FUNDAMENTAL AND SEDIMENTOLOGICAL CONTROLS ON LUMINESCENCE BEHAVIOUR IN QUARTZ AND FELDSPAR

Georgina Elizabeth King

A Thesis Submitted for the Degree of PhD
at the
University of St Andrews

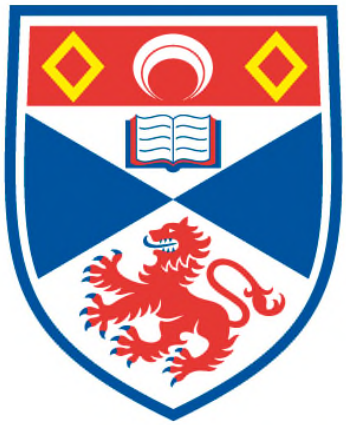

2012

Fundamental and sedimentological controls on luminescence behaviour in quartz and feldspar

Georgina Elizabeth King

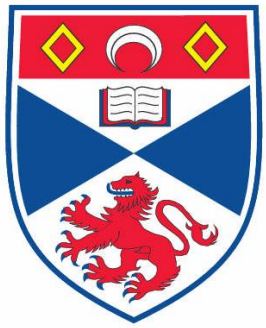

A thesis submitted to the University of St Andrews for the degree of Doctor of Philosophy

Department of Earth Sciences

School of Geography & Geosciences

January 2012

Declaration

I, Georgina King, hereby certify that this thesis, which is approximately 70,000 words in length, has been written by me, that it is the record of work carried out by me and that it has not been submitted in any previous application for a higher degree.

I was admitted as a research student in October, 2007 and as a candidate for the degree of PhD in October, 2007; the higher study for which this is a record was carried out in the University of St Andrews between 2007 and 2011.

Date 13/01/12

Signature of candidate

I hereby certify that the candidate has fulfilled the conditions of the Resolution and Regulations appropriate for the degree of PhD in the University of St Andrews and that the candidate is qualified to submit this thesis in application for that degree.

Date 13/01/12

Signature of supervisor

In submitting this thesis to the University of St Andrews I understand that I am giving permission for it to be made available for use in accordance with the regulations of the University Library for the time being in force, subject to any copyright vested in the work not being affected thereby. I also understand that the title and the abstract will be published, and that a copy of the work may be made and supplied to any bona fide library or research worker, that my thesis will be electronically accessible for personal or research use unless exempt by award of an embargo as requested below, and that the library has the right to migrate my thesis into new electronic forms as required to ensure continued access to the thesis. I have obtained any third-party copyright permissions that may be required in order to allow such access and migration, or have requested the appropriate embargo below.

The following is an agreed request by candidate and supervisor regarding the electronic publication of this thesis:

Access to all of printed copy but embargo of all of electronic publication of thesis for a period of one year on the following ground:

publication would preclude future publication;

Date 13/01/12

Signature of candidate

Signature of supervisor

Abstract

The optically stimulated luminescence (OSL) characteristics of a suite of quartz and feldspar samples from a range of modern glaciofluvial sediments have been explored to determine the use of OSL as a depositional pathway tracer. Paraglacial and subglacial source material and various glaciofluvial deposits have been analysed from the glacial catchments of Bergsetbreen, Fåbergstølsbreen, and Nigardsbreen as well as the Fåbergstølsgrandane sandur, Jostedalen, Norway.

The OSL distribution signatures have been characterised through exploration of sample skewness, kurtosis and overdispersion, and dose distributions of the different depositional settings and source materials are distinct for both quartz and feldspar. Residual ages are greatest for feldspar, indicating significant potential age overestimation where feldspar is used to date glaciofluvial deposits. Sample dose distributions and overdispersion characteristics are driven by source sediment properties, whereas residual ages are controlled by transport and depositional processes. Those transport and depositional processes which result in significant light exposure, also influence dose distributions, and processes that sort sediments least effectively have the highest residual doses.

Sample OSL characteristics, transport distance and grain size distributions have been investigated using factor analysis, as a means of predicting sediment source, facies, depositional process and deposit type. Although the depositional processes of the quartz samples can be clearly differentiated based upon OSL characteristics, factor analyses of feldspar and grain size characteristics are inconclusive.

The application of quartz OSL to the Norwegian samples was limited by its very poor luminescence sensitivity. Quartz is the preferred mineral for OSL, however, despite the plethora of successful quartz OSL applications, the precise origin of the UV/blue luminescence emission, measured during OSL, remains unclear. The origins of this emission and controls on its intensity were explored using a variety of spectroscopic techniques including photoluminescence, cathodoluminescence, radioluminescence (RL), ionoluminescence (IL) and x-ray excited optical luminescence (XEOL).

Exciting sample luminescence at a range of energies enables exploration of the different donor centres responsible for the luminescence emission. Cathodoluminescence and RL emission spectra are similar, comprising broad emissions at 1.5, 2.0 and 2.7 eV (detection in the UV part of the spectrum was not possible for these experiments). Ionoluminescence emission spectra were dominated by the ~ 3.3 eV emission, which is a component of the signal conventionally monitored during OSL. This emission depleted as a function of dose, to the benefit of the red emission (1.8-2.0 eV) for all samples throughout IL, and similar observations were made for the 3.4 eV emission observed from the XEOL emission spectra. The XEOL spectra are dominated by an emission at ~ 3.8 eV, not widely reported for quartz, which has tentatively been attributed to peroxy linkages. Differences between the IL and XEOL emission spectra are interpreted as evidence for the presence of multiple excited states.

Acknowledgements

First, I would like to thank my supervisors, Ruth Robinson and Adrian Finch, for always being both excited and enthusiastic about this project. They have been extremely patient and supportive and I have learned a huge amount from them both. Thanks also to David Sanderson, my SAGES affiliated supervisor, for forcing me to think things through, access to laboratory facilities at SUERC and the occasional lunch. Financial support from NERC under studentship F008589/1, from the QRA in the form of a New Workers Research Grant, from the Mineral Physics Group of the Mineralogical Society of Great Britain and Ireland in the form of a grant to attend LED 2008, and from the School of Geography and Geosciences postgraduate fund is gratefully acknowledged. SAGES are thanked for affiliation status.

Numerous people have helped me both directly and indirectly with this research over the past four years and from St Andrews I would like to thank Donald Herd, Angus Calder and Ross Somerville for assistance with many laboratory activities including SEM imaging, ICP-MS and HF etching. Helen Olaez is thanked for helping me negotiate the minefield of university bureaucracy and Colin Cameron for solving many of my IT problems and most of all for providing a computer that could cope in the final two weeks!

At SUERC I would like to thank Lorna Carmichael and Saffron for assistance navigating the laboratories, cups of tea and an excuse for a biscuit. At the University of Sussex I would like to acknowledge the help of David E. Hole in the collection of IL spectra, and Peter D. Townsend for subsequent discussions. At Diamond I would also like to acknowledge the input of Fred Mosselmans in collection of XEOL spectra.

Thanks to Henrik Friis and Richard Taylor for challenging and exciting debates about the fundamentals of luminescence, for help with IL and XEOL data collection respectively, and for numerous evenings in the pub. Thanks to Cheryl Wood for tolerating my grumpiness and training me to accept tardiness, and also thanks to the other postgrads of rooms 600 and 601 and Lyndsay Mitchell for plenty of coffee breaks and nights out. Thanks to Eleri Harris for keeping me sane and also together with Carlos Caballero, Liselotte, Andy Cullens and David Lowry for field assistance in Norway. Thank you to Nora Hanson and St Andrews Snowsports for making me adventure, especially Neil Graham and Alexis Jones.

Last but not least, thanks to my family for keeping it all in perspective, especially to my nephew Harry. Thank you to Peter Abbott for being fantastically supportive in the final few months, and more generally for just being brilliant.

Table of Contents

Table of Figures

List of Tables

Chapter 1. Introduction

1.1 Project Rationale

A key challenge faced by Earth scientists seeking to understand contemporary and ancient landscapes, is determining which transport and depositional processes have combined to create particular landform assemblages. Understanding the processes of landscape formation is essential in predicting landscape response under specific environmental conditions e.g. changing weather and climate. Glacial environments in particular, have been the focus of a huge volume of research over the past 100 years (c.f. Benn and Evans, 1998 and references therein), not least because Quaternary glaciation has provided the antecedent conditions for much of the contemporary Northern hemisphere landscape. Deciphering the scale, source material, duration and specific transport and depositional processes is key to understanding landscape response to past climatic changes, and also in predicting future responses. Provenance analysis techniques have the potential to address these questions, and a variety of methods have been developed within the Earth Sciences. These range from relatively simple techniques such as mineral assemblage examinations, from which source geology and thus provenance information can be determined (e.g. in the reconstruction of ice-sheet dynamics, Hibbert et al., 2010); to more complex methods such as detrital mineral isotope geochemistry (e.g. to reconstruct orogenic chronologies, Robinson et al., Submitted).

Optically stimulated luminescence (OSL) dating (Huntley et al., 1985) is a retrospective dosimetry method, most commonly applied to the dating of Quaternary landforms to aid palaeoenvironmental reconstruction (e.g. Jacobs et al., 2008; Stone and Thomas, 2008; Wallinga, 2002). Accurate chronologies are essential to understanding contemporary landscapes, as they delimit the duration and rate of landform development. More recently the potential of using OSL as a provenance tool has been recognised, through contrasting the properties of the OSL signals of different samples. Lü and Sun (2011) used the sensitivity (brightness) of the OSL and thermoluminescence (TL) signals of Quaternary loess and Tertiary aeolian deposits, to make inferences about changing provenance in Northern China. Tsukamoto et al. (2011) alternatively, used OSL signal properties to differentiate between source materials and therefore provenances, recording a relationship between OSL signal properties and source rock geological age. In addition to provenance, the OSL of a sample may encode information about the transport and depositional history of sediments, which potentially makes it a useful addition to the suite of existing provenance tracing tools available to Earth Scientists.

This thesis explores the extent to which OSL may be used as a depositional pathway tracer at the catchment scale. The premise of this technique is that different sediment source regions have specific luminescence dose distribution signatures, created

by different light exposure and geological histories. Similarly, the processes through which these sediments are transported, and their resultant deposits will also have specific luminescence fingerprints. If the technique is successful, then these fingerprints may be used by luminescence practitioners to inform sample selection and identification, as well as provide a means of reconstructing the depositional processes and their relative dominance within a specific environment.

A suite of modern glacial catchments were selected as the sample sites, within the Jostedalen region of Breiheimen in Southern Norway. The rationale for using modern sediments was that the process signatures, rather than depositional chronologies of the sediments could be investigated. In addition to providing an understanding of depositional pathway sediment characteristics, working on modern sediments provides a test of applying OSL within glacial catchments, the suitability and success of which has been long debated (see Fuchs and Owen, 2008; Lian and Roberts, 2006 for reviews).

Quartz within glacial catchments has been observed by various practitioners to have low luminescence sensitivity (e.g. Lukas et al., 2007; Rhodes and Pownall, 1994, see Chapters 4 and 6 for a discussion) and to be highly susceptible to recuperation and thermal transfer (Bailey et al., 1997; Rhodes, 2000). This may relate to the relatively limited transport distances experienced in comparison to other sedimentary environments, however an alternative and plausible explanation is that the geological history of quartz has dictated its luminescence emission spectroscopy (e.g. Botis et al., 2005; Rink, 1994). The emission and excitation spectroscopy of a suite of quartz samples comprising Norwegian and Scottish glaciofluvial material and calibration samples has thus also been analysed to explore the causes of differing luminescence sensitivities between quartz grains of different provenances.

1.1.1. **Objectives**

- Characterisation of the OSL properties (and by inference, bleaching characteristics) of the different source regions, transport pathways and sub-environments operating in the study catchments.
- Characterisation of the OSL properties of quartz and feldspar samples from each of the different catchments.
- Statistical determination of material from the different source deposits, transport and depositional pathways.

- Excited emission spectroscopy of Norwegian and Scottish glacial quartz samples relative to calibration material, to explore variability in luminescence sensitivity between samples of different provenances.

1.1.2. **Thesis Structure**

This thesis is structured in a hybrid form of traditional chapters and chapters based on published or submitted papers, in order that the full experimental details and rationale behind investigations can be communicated.

Chapter 1: Introduction

Chapter 2: Literature Review

An introduction into both optically stimulated and excited luminescence phenomena in minerals and the application of OSL in glacial environments

Chapter 3: Study Area & Sample Description

Details of Jostedalen and the Water of Tulla (Scotland) study areas, including an overview of the depositional context and processes that operate in the various catchments. Individual sample descriptions are listed in Appendix C.

Chapter 4: Quartz OSL

The OSL analysis protocol development is described, as well as the luminescence properties of the quartz samples under investigation. The implications of low aliquot numbers are considered statistically. Age model selection is discussed and sample residual ages quantified.

Chapter 5: Feldspar OSL

This chapter is similar to Chapter 4, but for the feldspar extract analysed. The grain size analysis methodology is also explained.

Chapter 6: OSL Results & Discussion

Residual luminescence properties and grain size data for both the quartz and feldspar extracts are contrasted for the different depositional sub-environments and catchments. Factor analysis is used to investigate common sample responses to the different variables. This analysis and discussion will form the basis of a paper on the applicability of using quartz and feldspar as depositional pathway tracers.

Chapter 7: Quartz Emission Spectroscopy

Photoluminescence, cathodoluminescence and radioluminescence investigations of quartz are investigated and emission spectra contrasted.

Chapter 8: Ionoluminescence of Quartz

This chapter is based on a paper published in Radiation Measurements and explores the emission spectra of a suite of quartz samples excited with proton implantation (King, G.E., Finch, A.A., Robinson, R.A.J., Hole, D.E., 2011. The problem of dating quartz 1: Spectroscopic ionoluminescence of dose dependence. Radiation Measurements 46, 1-9.). I collected the data with some lab assistance from D.E. Hole (the lab-technician of the beamline) and Adrian Finch, analysed the data myself and wrote the manuscript myself. Adrian Finch and Ruth Robinson provided normal supervisory input, in the form of discussions and proof reading, as they would to a chapter thesis. The manuscript was circulated to all authors prior to submission, but no comments were made.

Chapter 9: X-ray Excited Optical Luminescence of Quartz

This chapter is based on a paper accepted by Radiation Measurements and explores the emission spectra of the same suite of quartz samples investigated in chapters 7 and 8, excited with synchrotron x-irradiation (King, G.E., Finch, A.A., Robinson, R.A.J., Taylor, R.P., Mosselmans, J.F.W., 2011. The problem of dating quartz 2: Synchrotron generated x-ray excited optical luminescence (XEOL) from quartz. Radiation Measurements 46, 1082-1089). I collected the data together with Adrian Finch, Fred Mosselmans (the lab-technician for beamline I18) and Richard Taylor (another PhD student from St Andrews). I analysed the data and wrote the manuscript which Adrian Finch provided normal supervisory input to (discussions and proof reading). The manuscript was circulated to all authors prior to submission, only Fred made minor comments regarding the photon flux of the beam (I had made a mistake in my original draft).

Chapter 10: Spectroscopy synthesis

The emission spectra measured using the different excitation techniques, and their associated dose dependencies are compared and contrasted. Causes for the observed variations are proposed. This discussion will form the basis of a third paper on the fundamentals of quartz luminescence, and the benefits of exciting spectra with different energies and techniques.

Chapter 11: Synthesis & Conclusions

Chapter 2. Literature Review

2.1. Luminescence in Minerals

Luminescence is light emitted from a mineral following an input of energy. It is produced as an electron in an excited state migrates to a ground or lower energy state, resulting in photon production. Quartz is an insulator, and luminescence is produced either from recombination of excited electrons with hole traps intrinsic to the crystal structure (e.g. oxygen vacancies), or alternatively with extrinsic defects associated with substitutions (e.g. Al^{3+} may substitute for Si^{4+} charge compensated by a cation such as Li^{+}). It should be noted that various classifications of intrinsic and extrinsic defects have been used throughout the literature, for example some authors have classified oxygen vacancies as extrinsic defects, but they are regarded as intrinsic throughout this thesis (see Nasdala et al., 2004 for a discussion).

The processes controlling luminescence behaviour in quartz are conceptualised using a band-gap diagram (Figure 2.1). The band gap (E_g) of quartz is ~ 9 eV (O'Reilly and Robertson, 1983). Where excitation energy (E) is > E_g, quasi free electrons are excited into the conduction band, charge compensated by holes (regions of positive charge) in the valence band. Direct inter-band excitation of electrons from the valence to conduction bands, and the production of intrinsic luminescence is only possible where excitation energies are sufficient i.e. > E_g. However, defects create energy bands within the forbidden gap and enable production of extrinsic luminescence, even where $E < E_g$. This is because different elements interact as activators and sensitzers (Marfunin, 1979), thus the excitation and emission properties of a mineral provide insights into the structure and defects that are present. Energy interactions between defects result in stokes or anti-stokes shifts in emission, relative to absorption energy (Marfunin, 1979), in association with the Franck-Condon principle. This can be considered visually using a configurational co-ordinate diagram (Figure 2.2). Quartz OSL results in anti-stokes luminescence as excitation E is 2.6 eV and the monitored emission energy is > 3.4 eV, which relates to the stimulation of trapped charge, rather than excitation.

The energy levels of the different defects are dictated by their location within the energy gap which is dependent upon their crystal field, ligand strength and valence state. Traps are located closest to the conduction band, and recombination and activator centres closest to the valence band. The energy of emitted light is dependent upon the energy difference between the excited and ground states (Nasdala et al., 2004), furthermore crystal field effects influence the bandwidth of the emission. Defects such as Mn^{2+} which have significant interaction with the crystal lattice have broad emission bands in contrast to for example REE^{2+} (Marfunin, 1979).

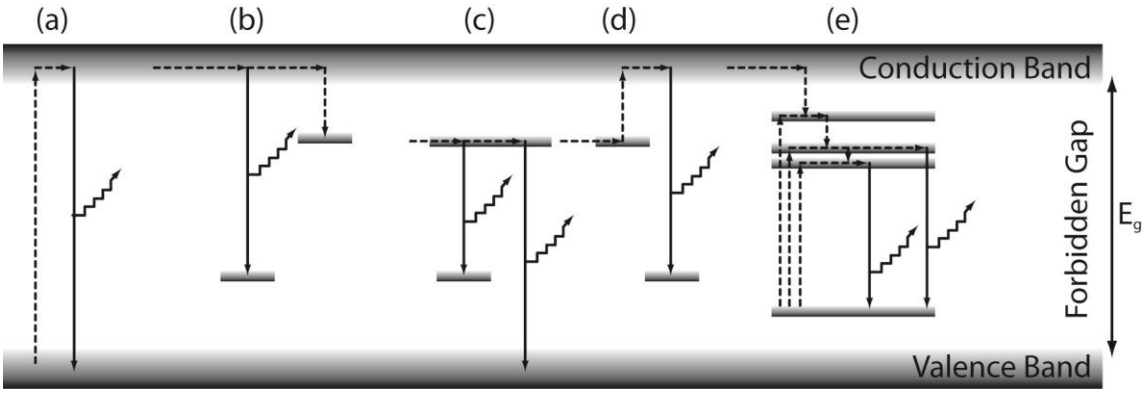

Figure 2.1: A band gap model reproduced after Nasdala et al., (2004) with permission from the European Mineralogical Union. The figure shows the key energy transitions that occur in an insulator: excitation, non-radiative energy transfer and luminescence production. a) Direct inter-band excitation of luminescence from the valence to the conduction band, direct recombination results in an emission at the same wavelength as excitation. b) The excited electron may recombine with an activator or become trapped, both features are defects within the crystal lattice. c) Trapped electrons may recombine directly with an activator or a hole in the valence band through tunnelling. d) Stimulated release of electrons from a trap via OSL or TSL. e) Extrinsic luminescence, electrons of defect ions recombine with the ground state.

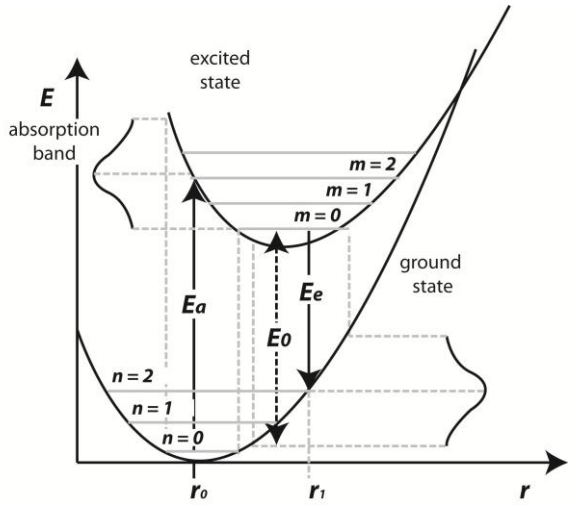

Figure 2.2: Configurational coordinate diagram explaining luminescence transitions following the Frank-Condon principle, reproduced after Nasdala et al. (2004) with permission from the European Mineralogical Union. Excitation from ground state *n=0* results in absorption of energy E_a. Relaxation from excited state *m=0* results in an emission of energy E_e. The difference between the minimum excited and ground state levels E_0 accounts for the stokes shift in the luminescence emission relative to the energy absorbed. $E_a > E_0 > E_e$.

2.2. Optically Stimulated Luminescence Dating

Luminescence dating exploits the ionizing radiation induced migration of electrons within certain crystalline insulating materials (Figure 2.1, part d). Ionizing radiation is derived from alpha (α) and beta (β) particles, and gamma (γ) rays from the decay of uranium (^{238}U, ^{235}U), thorium (^{232}Th), potassium (^{40}K) and rubidium (^{87}Rb) within minerals in the surrounding sedimentary environment (external) and the crystals being measured for luminescence (internal) (see Appendix A.4). Although the internal dose rate is greatest within K-feldspars, quartz crystals may also contain trace amounts of U, Th (Sutton and Zimmerman, 1978b) and Rb which are estimated to contribute up to 5% of annual dose (Mejdahl, 1987; Vandenberghe et al., 2004). Cosmic rays may also contribute to the radiation dose, dependent upon deposit depth, altitude and latitude (Prescott and Hutton, 1994).

Electrons stimulated by radiation migrate within the crystal between the valence and conduction bands, and become trapped in defects, which are also referred to as traps (Aitken, 1985). Thus, certain crystalline materials such as quartz may be treated as radiation dosimeters (e.g. Jain et al., 2003) or used to calculate sample age (e.g. Boe et al., 2007). If it is assumed that the radiation dose rate has remained constant throughout the period of deposition, then the number of electrons that have become 'trapped' is proportional to the period of time that has elapsed. This accumulated signal may be reset through exposure of the sample to energy in the form of either heat or light (or pressure, triboluminescence). The rate of electron escape is dependent upon the stimulation energy and the trap depth, and following thermal or optical stimulation, electrons are able to escape from their traps, referred to as sample bleaching. Luminescence dating methods comprise either optically stimulated luminescence (OSL) or thermally stimulated luminescence (TSL).

Electrons evicted from traps migrate to recombination centres where regions of positive charge, termed holes, created by the electrons initial migration, are available to receive them. Recombination centres may be radiative (L-centres) or non-radiative; where electron recombination occurs at the former energy is dissipated either as heat or as a photon of light, hence the name of the technique, luminescence; recombination at the latter results in phonon production. The specific nature of the various L-centres is discussed in Chapter 7.

Thus assuming that the number of electrons trapped is proportional to the total environmental dose, and that the amount of light produced upon recombination is proportional to the trapped charge, the amount of light released, following correction for

sample brightness (quantum efficiency, QE), must also be proportional to the sample age. The age of a sample may therefore be determined from:

Eq. 2.1: Age (ka) = P (Gy) / D_r (Gy ka^{-1})

where P is the palaeodose (Gy), which is the total radiation dose received during the period of deposition, and D_r is the environmental dose rate (Gy ka^{-1}). Within laboratory procedures P is estimated and termed the equivalent dose (D_e) to the natural dose accumulated during deposition (Murray and Roberts, 1997). Optically stimulated luminescence has benefited most from improvements in measurement precision and accuracy over recent decades (Duller, 2004), and thus discussion is appropriately restricted.

2.3. The Structure of Quartz

In order to understand the luminescence of quartz and feldspar, their structure must be considered: both minerals are insulators (e.g. Poolton et al., 2006). Quartz (SiO_2) has a simple structure (Figure 2.3) in comparison to feldspar (see Figure 2.4). It has two polymorphs but all quartz at room temperature and pressure comprises *α*-quartz; it crystallizes normally as *β*-quartz in a range of chemical, thermal and radioactive settings, which determine the number and type of chemical substitutions (see Götze, 2009; Götze et al., 2001 for reviews). Commonly Al^{3+} substitutes for Si^{4+}, which is charge compensated by interstitial alkali ions including Na^+, Li^+ and H^+; however Ti^{4+} and Ge^{4+} may also substitute for Si^{4+} under certain conditions (Götze et al., 2004). It is these chemical substitutions as well as structural variations such as oxygen vacancies, which create the defects exploited by luminescence dating (Figure 2.3). Defect type determines the stability and energy of the trapping and L-centres. Despite extensive research using a variety of analytical techniques (see Chapter 7) there remains little certainty as to which L-centres are responsible for the generation of which emissions (Bøtter-Jensen et al., 2003).

The thermal and optical stability of the discrete electron traps in quartz depends upon their location within the band-gap (Figure 2.1). All traps may be stimulated thermally (TSL), however only some traps are sensitive to optical stimulation, which has proven the major benefit of OSL (Murray and Roberts, 1998). Within many depositional environments quartz is bleached optically, thus within OSL only the rapidly bleached optical traps are analysed, resulting in reduced potential age overestimations.

The 110 ˚C and 325 ˚C TSL traps require most consideration when measuring OSL. The 110 ˚C trap is optically insensitive and is thermally unstable which results in loss of accumulated charge over geological time. The 325 ˚C trap can be both thermally and optically stimulated (Rhodes, 1988; Smith et al., 1986; Spooner, 1994b; Wintle and

Murray, 1997) and is thermally stable with a lifetime of 10^8 years at 20 ˚C (Murray and Wintle, 1999).

Owing to copyright restrictions, the electronic version of this thesis does not contain this image.

Figure 2.3: The molecular structure of quartz, after Gotze et al. (2001).

2.4. The Structure of Feldspar

Feldspars are aluminosilicates and are the most abundant constituent of igneous rocks (Deer et al., 2001). They vary widely in composition, but can be classified as members of two solid solution series: the alkali and plagioclase feldspars. The end-members of this ternary system are: Albite (Ab - $NaAlSi_3O_8$), K-feldspar (Orthoclase, Or - $KAlSi_3O_8$) and Anorthite (An - $CaAl_2Si_2O_8$) (Deer et al., 2001). Feldspar phases which occur on the continuum between $NaAlSi_3O_8$ and $CaAl_2Si_2O_8$ are the plagioclases, and those between $NaAlSi_3O_8$ and $KAlSi_3O_8$ are alkali feldspars. Some Na-rich feldspars contain broadly similar concentrations of K and Ca, and are termed ‘ternary feldspars’. That system includes feldspars such as Anorthoclase (Figure 2.5).

Feldspars are MT_4O_8 aluminosilicates, with structure composed of a charge compensating cation (M-site; K^+, Na^+, Ca^+), AlO_4 and SiO_4 tetrahedra (T-sites) (Figure 2.4, Krbetschek et al., 1997). Substitutions are determined by specific ionic characteristics and structural properties, and the physical and chemical conditions of mineral crystallisation (Krbetschek et al., 1997); for example the structure in plagioclase feldspars is such that only smaller cations are able to exchange with Na^+ at the M site.

Feldspars may be structurally classified as ordered or disordered, and the degree of order is dependent upon crystallisation temperature and thermal history. The degree of order relates to the distribution of Al^{3+} ions, substituted for Si^{4+}, and in high temperature feldspars such as sanidine this distribution is disordered (Deer et al., 2001; Visocekas and Zink, 1999). Visocekas et al. (1998) have attributed anomalous fading (discussed in Chapter 5) to the degree of ordering, and disordered feldspars are thought to be worst affected (Spooner, 1994a). Structural classifications are thus also important within the context of luminescence dating.

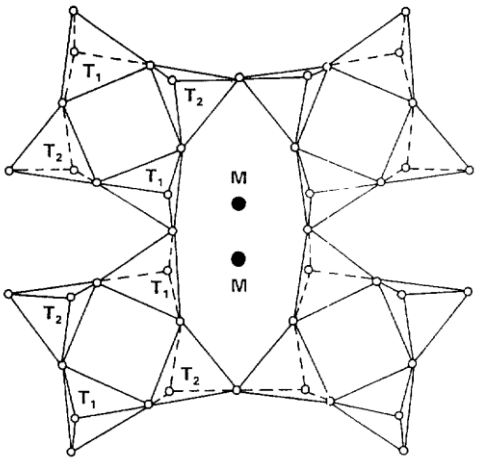

Figure 2.4: Schematic structure of feldspar reprinted from Krbetschek et al. (1997), Copyright 1997 with permission from Elsevier. The structure comprises four tetrahedral (T-) sites (AlO4 or SiO4), of which two are orientated upwards, and two downwards. Cations (M-sites) are located in the spaces between the tetrahedra.

Owing to copyright restrictions, the electronic version of this thesis does not contain this image.

Figure 2.5: A ternary diagram showing the classification of feldspars between the end members of Anorthite (An), Albite (Ab) and Orthoclase (Or). Curve A-B is the limit of the solid solution compositions, reproduced from Deer et al. (1992).

2.4.1. **OSL of Quartz and Feldspar**

Feldspars offer various advantages over quartz for OSL including greater intrinsic luminescence (Duller, 1997) which facilitates dating of younger samples (Baril, 2002). Consequently a suite of feldspar samples were analysed (Chapter 5) which provide a complimentary dataset to the quartz discussed in Chapter 4. Additional benefits of feldspar OSL are that electron traps become saturated at much higher radiation doses (extending the dating range of luminescence e.g. Martins et al., 2010) and that K-feldspars have an internal radiation dose rate which reduces the influence of external doses and associated uncertainty (Duller, 1997). However, due to their structural and chemical properties, feldspars are more complex radiation dosimeters, and it is anomalous fading (Wintle, 1973) which had until recently, generally obstructed their development relative to quartz. Anomalous fading comprises a loss of trapped charge over time, resulting in age underestimations. This phenomena has been recorded in most feldspars (e.g. Huntley and Lian, 2006), and is discussed more extensively in Chapter 5.

2.5. OSL in Glacial Environments

The complexity of glacial depositional settings and the associated challenges of taking appropriate samples have been highlighted by a number of authors (e.g. Fuchs and Owen, 2008; Richards, 2000). Consequently, previous applications, sampling strategies and analytical decisions (grain size, mineral selection) are reviewed to inform the analysis strategy of this research.

The use of OSL in glacial environments has been relatively restricted, despite its potential (Fuchs and Owen, 2008). The earliest applications of luminescence dating were to glacial sediments by scientists working in the Soviet Union during the 1960's (see Fuchs and Owen, 2008; Lian and Roberts, 2006 for reviews), however it was not until the 1980's that use became widespread. Early applications included analysis of residual TSL signals and OSL signals from suspended sediments in glacial meltwater channels (Gemmell, 1988, 1994, 1997, 1999) and from glaciofluvially deposited sediments (Forman and Ennis, 1991; 1992; Rhodes and Pownall, 1994). These authors were developing the work of Berger (1990) who recognised the challenge that partial bleaching of quartz and feldspar posed to dating within certain depositional environments. It is a fundamental requirement of the OSL method that the sample analysed has had its charge fully reset (bleached) through exposure to light, prior to deposition. If this requirement is only partially fulfilled (or the sediment is not bleached at all), then the age obtained will include a component from an earlier depositional phase. It is probable that this condition may not be

satisfied within glacial environments, where sediments are deposited in turbid meltwater streams, directly by the ice, or in an ice proximal location.

Due to the challenges posed by partial bleaching, many of the applications of OSL to glacial deposits have been restricted to glaciofluvial or glaciolacustrine materials, where the probability of light exposure prior to deposition is much greater (Fuchs and Owen, 2008; Thrasher et al., 2009a). However, successful OSL and ^{10}Be cosmogenic nuclide dating of Late Quaternary supraglacially-derived debris and glaciofluvial deposits in the Rongbuk valley (north of Everest) by Owen et al. (2009) may in part be a result of the extra bleaching potential of debris covered glaciers at high altitudes. Various methods have been developed to alleviate the challenges of partial bleaching, which can be broadly categorised into sample selection, partial bleaching identification and residual quantification, discussed below. Through analysing a range of modern glacial sediments, this thesis will enable the residuals of specific sediments to be quantified. In addition to problems associated with partial bleaching, Rhodes and Bailey (1997) observed that quartz in glacial systems exhibits very dim luminescence sensitivity and is highly susceptible to thermal transfer and recuperation. These phenomena have also been reported by other practitioners (e.g. Fuchs and Lang, 2001; Klasen et al., 2007; Lukas et al., 2007; Richards, 2000; Spencer and Owen, 2004; Thrasher et al., 2009a), and are discussed in Chapters 3 and 7.

2.5.1. **Sample Selection**

Sediments are bleached following erosion, during transport and deposition, consequently the specific transport and depositional processes operating and the scale and duration of those processes directly affect sediment luminescence properties. There is a large volume of research on the physics of sediment transport (e.g. physics of transport and deposition: Bridge and Bennett, 1992; grain sizes and sorting: Rice and Church, 2010; Robinson and Slingerland, 1998), however detailed investigations of these properties relative to sediment bleaching are beyond the scope of this research project. Instead the overarching transport and depositional processes, rather than the physics of individual grain transportation, are identified and related to specific bleaching characteristics.

Within glacial catchments, sediment may be deposited directly by the glacial ice, as is the case for subglacial landforms and tills, and supraglacial debris cones and fans. Depositional features in ice contact and proglacial settings include moraines and a diverse range of glaciofluvial and aeolian deposits. Furthermore, glaciofluvial processes rework subglacial material, as well as material derived from the supraglacial and proglacial

environments. Paraglacial material (Church and Ryder, 1972) on the valley sides may relate to earlier, more extensive glacial limits, and these can be reworked within the glacial foreland through a combination of hillslope and fluvial processes. Where a sandur is present in the proglacial zone, aeolian processes will both contribute material from beyond the immediate glacial environment and rework the sandur deposits. Fuchs and Owen (2008) describe the sediments which occur in the proglacial zone as *associated sediments*, together with glaciofluvial, glaciolacustrine, glaciomarine and glacioaeolian deposits, which may or may not be ice-deposited, but characterise the proglacial environment. The catchments analysed within this project are dominated by glaciofluvial processes, and thus the discussion is appropriately restricted.

Thrasher et al. (2009b) advocate a lithofacies approach whereby sub-environments are differentiated through analysis of their interaction with adjacent units and their process of deposition. They suggest that sandur bar features, especially bar-tops, are most likely to have been well bleached during deposition due to sub-aerial exposure during diurnal waning flow. Identification of genetic features most appropriate for OSL has also been attempted for fluvial environments. Murray et al. (1995) and Preusser (1999) determined that overbank deposits are more appropriate than channel deposits for dating purposes because of their increased probability for bleaching. Robinson et al. (2005) found that in Quaternary braided alluvial streams of NW Argentina, fluvial bar tops were well bleached. Because of the complex interactions of the different processes within glacial environments, it is important to consider each sedimentary sub-environment and deposit carefully. Finally, Lukas et al. (2007) suggest that processes rather than source areas are most important in determining the resultant D_e. Through investigating source and deposit material in each of the catchments of the study area, this assertion will be evaluated.

2.5.2. **Glaciofluvial Depositional Pathways**

With the exception of glacioaeolian processes (Thrasher et al., 2009b), the glaciofluvial system is regarded as the least likely to result in partial bleaching of sediments prior to deposition. Consequently glaciofluvial deposits and transport pathways have received the most attention from OSL practitioners working in glacial settings (see Fuchs and Owen, 2008; Thrasher et al., 2009a for a review), and are focussed on within this research. In its most simple form, a glaciofluvial system comprises a meltwater channel transporting material from the subglacial environment to the proglacial zone. Thus the resultant luminescence residual is the product of the initial residual of the source material and the degree of sunlight exposure that occurs throughout transport. Forman and Ennis (1992) confirmed that the residual luminescence of a sample reduces with increasing transport distance from the glacial snout. This correlation between transport

distance and bleaching has also been recognised within fluvial systems (e.g. Stokes et al., 2001). However, the bleaching rate is dependent upon the turbidity of the water, the suspended sediment load, the mineral grain size and type, the intensity of sunlight, ambient weather conditions and the time of day at which transportation takes place (Gemmell, 1997).

2.5.3. **Bleaching Characteristics of Quartz and Feldspar**

Glaciofluvial meltwater channels are turbulent throughout the ablation season, and often have high suspended sediment loads. This influences the bleaching rate of minerals as the incident sunlight is attenuated to longer, less energetic wavelengths. Water filters UV wavelengths, and turbidity increases spectral filtering, promoting a shift in peak transmission to 500-600 nm (Jerlov, 1976). Forman and Ennis (1992) investigated the bleaching properties of the TSL signal from polymineral fine grains (4-11 µm) at wavelengths > 400 nm, and observed slower bleaching at longer wavelengths. Ditlefsen (1992) developed this research using IRSL to examine the bleaching rates of K-feldspars in turbid water suspensions. Through varying the fine grain suspensions from 0.01 to 0.50 g l^{-1}, he demonstrated that bleaching rates reduced with increased suspended load, and that bleaching was most rapid in a stationary water-column. Furthermore, he demonstrated that the IRSL signal reduced to 5 % of its initial intensity over 20 h, whereas TSL was depleted to only 50 %, which shows the utility of IRSL over TSL in terms of bleaching potential.

The properties of the optical traps in quartz and feldspar differ, and thus it follows that their susceptibility to partial bleaching in glaciofluvial and fluvial environments will also vary. However, despite much research, little consensus has been reached on which of the minerals is least susceptible to partial bleaching. Despite having more rapidly recombining traps as identified via time-resolved (TR) OSL (Tsukamoto et al., 2006), feldspars have been shown to bleach more gradually than quartz upon exposure to sunlight (Godfrey-Smith et al., 1988) (Figure 2.6). However, Sanderson et al. (2007) have demonstrated experimentally that within turbid meltwater environments, where the incident light is severely attenuated, feldspars may actually bleach more rapidly than quartz (Sanderson et al., 2003) associated with the more severe attenuation of shorter wavelengths which bleach quartz most effectively. Klasen et al. (2007) investigated the bleaching rate of the IRSL and post-IR blue stimulated luminescence (BSL) signal of polymineral fine grains, determining that initially the IRSL signal was more rapidly reset, however after 10 h of bleaching, both signals were reset to the same extent. This experiment was supported by their earlier research where they observed that although quartz initially bleaches more rapidly than feldspar, that both minerals bleach to the same extent after 60 minutes

(Klasen et al., 2006). These observations have been contested by the experimental results of Hansen et al., (1999) who reported a two-fold increase in residual luminescence from feldspars in comparison to quartz for Holocene glaciofluvial sediments from Greenland. Numerous other practitioners have also observed an increased susceptibility of feldspar to partial bleaching (e.g. Owen et al., 2002; Spencer and Owen, 2004; Srivastava et al., 2001). When the optical parameters of quartz and feldspar are considered relative to the projected shift in wavelength with increasing turbidity (Figure 2.7), it is predicted that quartz will bleach more rapidly than feldspars at wavelengths > 500 nm (Spooner, 1994a, b; Wallinga, 2002). As empirical results vary, paired quartz and feldspar sample analyses have been contrasted where possible.

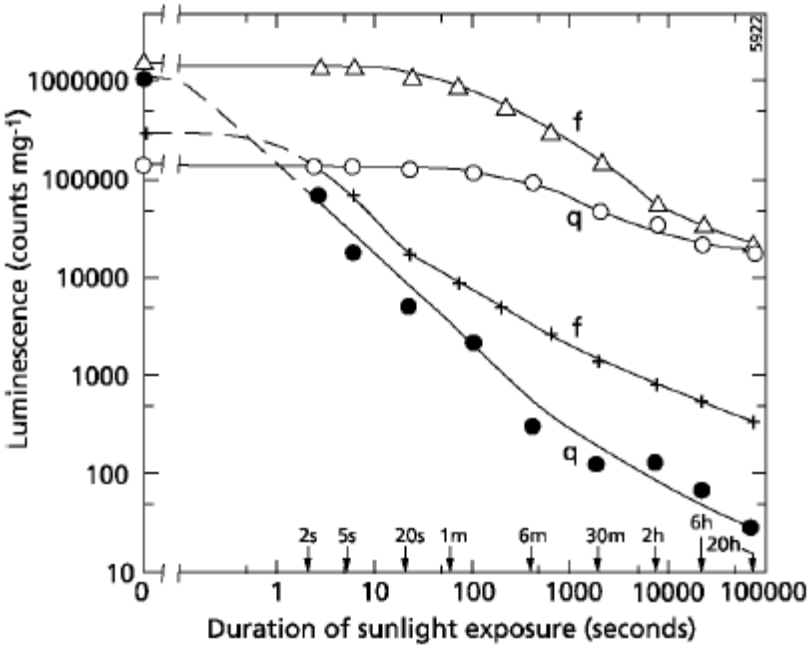

Figure 2.6: Sunlight bleaching of the natural TSL and OSL of quartz (q) and feldspar (f) (based on Godfrey-Smith et al., 1988; reprinted from Wallinga, 2002, Copyright 1988, 2002; with permission from Elsevier). It is apparent that the OSL signal is reset more rapidly than the TSL signal (filled circles and crosses), and that the quartz OSL is reset more rapidly than the feldspar OSL.

2.5.4. **Grain Size Selection**

Various practitioners have investigated which grain size is most appropriate for fluvial and glaciofluvial deposits, with the majority concluding that fine-grained deposits (< 125 µm) are more likely to exhibit partial bleaching (Alexanderson, 2007; Murray et al., 1995; Olley et al., 1998; Wallinga, 2002). In contrast, Rhodes and Bailey (1997) advocated use of the fine grain fraction for dating of Greenlandic and Himalayan glacial deposits. Although no causal mechanism for the increased partial bleaching of fine grained material has yet been found, flocculation of smaller particles may be responsible.

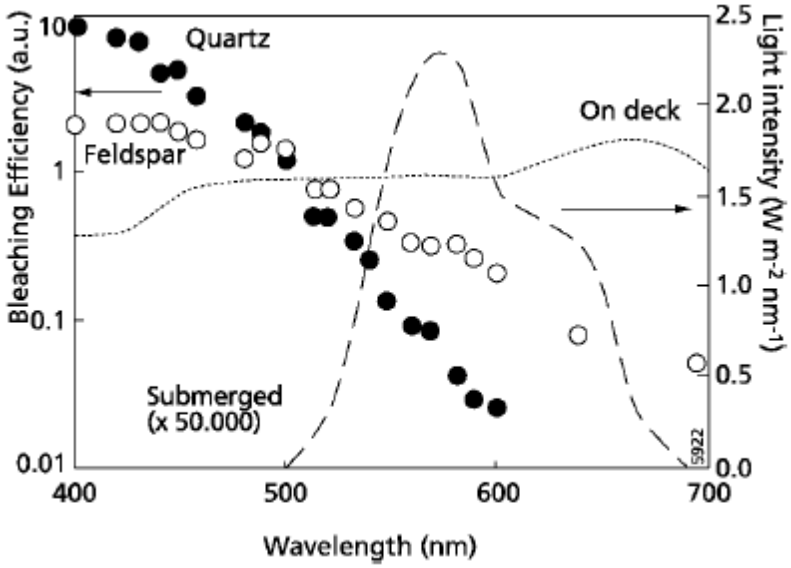

Figure 2.7: The light intensity at the surface (dotted line) and at 4 m depth (dashed line) of a turbid river (Berger and Luternauer, 1987). The light intensity at 4 m depth has been scaled up (5 x 10^4) to facilitate comparison. The bleaching efficiency of quartz (filled data points) and feldspar (unfilled data points) are shown (Spooner, 1994a, b). Figure reprinted from Wallinga (2002), Copyright 2002, with permission from Elsevier.

Owing to copyright restrictions, the electronic version of this thesis does not contain this image.

Figure 2.8: D_e variation with grain size for modern river deposits and the spring flood deposit ("Umingmakelv*") for four Greenlandic rivers. The inset shows the averaged behaviour of the different grains sizes analysed, relative to a control deposit. Figure reproduced from Alexanderson, (2007).

Alexanderson (2007) investigated the residual OSL signal within sediments from modern Greenlandic rivers and observed a strong negative correlation between residual dose and grain size (Figure 2.8) which resulted in the modern sediments having residual

ages between 50-500 years. This indicated that although such material is suitable for the dating of Pleistocene deposits, the uncertainty due to partial bleaching would be too great for Holocene sediments. In contrast Thrasher et al. (2009b) investigated the influence of grain size on D_e of four different sub-environments of a Pleistocene sandur system from the Isle of Man and observed no influence on D_e. Richards et al. (2000) and Preusser et al. (2001) have also reported no grain size dependence for quartz and feldspar respectively in glacial deposits, and thus grain size effects are not explored throughout this thesis.

2.6. Summary

A wide range of research has applied OSL within glacial environments, identifying a range of challenges and highlighting the importance of appropriate sample selection to circumvent the limitations of partial bleaching. A sampling strategy based upon this literature is detailed in Chapter 3, and the depositional environments of the different catchments investigated are described. Both quartz and feldspar extracts of samples have been analysed enabling empirical investigation of the bleaching properties of the different minerals within specific depositional contexts. Only the coarse (180-212 µm) grain size fraction has been dated in accordance with the grain size investigations discussed, avoiding the potential additional limitation of partial bleaching within the fine (< 125 µm) grain size fraction.

Chapter 3. Study Area & Sample Description

3.1. Study Area: Regional Overview

Jostedalen (61˚34' N, 7˚17' E), Breheimen, Southern Norway is the location of the Jostedalsbreen ice-cap which is the largest body of ice in mainland Europe. The various outlet glaciers which drain Jostedalsbreen provide contrasting depositional environments ideal for the examination of OSL as a depositional pathway tracer. This region was completely deglaciated throughout the mid Holocene climatic optimum (Nesje and Kvamme, 1991), however since ~ 5 ka to the present day, glaciers within Jostedalen have been extremely active (Shakesby et al., 2004). This is referred to as Neoglacial activity, and consequently Jostedalsbreen has been the subject of much previous research. Three glacial catchments were the focus of this research project: Bergsetdalen (61˚38' N, 7˚05' E), Fåbergstølsdalen (61˚42' N, 7˚17' E) and Nigardsdalen (61˚40' N, 7˚12' E, also known as Mjolverdalen), and the foreland of the Bergsetbreen, Fåbergstølsbreen and Nigardsbreen glaciers respectively. Additional sediments were also taken from the sandur in Fåbergstølsgrandane (61˚44' N, 7˚20' E), from Stordalen (61˚45' N, 7˚16' E), Jostedalen and Leirdalen (61˚28' N, 7˚15' E), and from deltaic sediments at Gaupne (61˚26' N, 7˚14' E).

3.1.1. **Geology & Climate**

Jostedalen is within the Western Gneiss region of Norway (Bryhni and Sturt, 1985), and is underlain by bedrock of Precambrian granitic to granodioritic gneiss (Holtedahl, 1960; Holtedahl and Dons, 1960), which is dissected by veins of quartz up to 30 cm thick and comprises quartz, feldspar and mafic minerals (Owen et al., 2007). The protoliths were metamorphosed during the Caledonian orogeny, when the Jostedal region was subjected to northwest extension (Andersen, 1998). The Jostedalsbre plateau is an elevated Precambrian peneplain, uplifted during the Tertiary, which has since been shaped by Pleistocene erosion and deposition (Strøm, 1948).

The upper catchments of Nigardsbreen and Bergsetdalen are underlain by quartz monzanite, whilst Fåbergstølsdalen and the majority of Jostedalen are underlain by quartz diorite (Figure 3.2). Consequently alkali feldspars, which are more suitable than plagioclase feldspars for luminescence dating, are more common within Nigardsbreen and Bergsetdalen than in the other catchments analysed, as typically quartz diorite is < 10% alkali feldspar. Furthermore, monzanite is associated with high Th concentrations, which indicates that the radiation exposure history of quartz derived from these source regions will be greater than those derived from quartz diorite bedrock (see Chapter 7 for a discussion on the influence of radiation history on luminescence emission properties).

A meteorological station at Bjørkhaug-i-Jostedalen (324 m.a.s.l.) near to Fåbergstølsbreen, indicates that mean average annual precipitation is currently 1380 mm, and mean monthly temperatures are - 4.9 ˚C and 13.4 ˚C in January and July respectively, with a mean annual temperature of 3.7 ˚C (Aune, 1993; Førland, 1993). A second weather station at the Fjaerland Glacier Museum in Luster (33 km from Jostedal) records similar average temperatures (Figure 3.1) but higher precipitation (annual average is 1769 mm) related to its location further west.

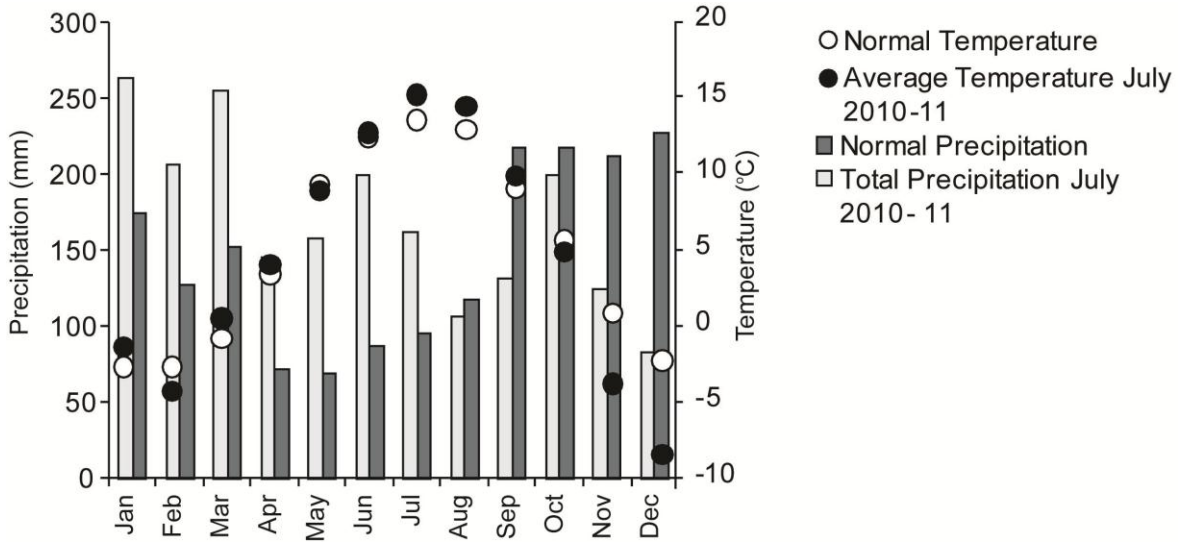

Figure 3.1: Climate data from the Luster, Sogn og Fjordane meteorological station (Norwegian Meteorological Institute). The station has been operating since 2005. No definition of how 'normal' precipitation and temperature values are calculated is provided on the website[1].

3.1.2. **Geomorphology**

The geomorphology of Jostedalen is characterised by glacial erosion and the reworking of glacial sediments, resulting in paraglacial sedimentation. Paraglacial processes are defined as 'nonglacial processes that are directly conditioned by glaciation' (Church and Ryder, 1972) and debris flows are a common paraglacial process within this region (e.g. Curry, 1999; Curry and Ballantyne, 1999). The various glaciers fed by the Jostedalsbreen ice-cap have a multitude of retreat moraines, attributed to the little ice-age (LIA) which has been the most substantial readvance of the Neoglacial period (Dahl et al., 2002). The presence of such recent glacial landforms has resulted in Jostedalen being studied intensely in an effort to produce accurate palaeoenvironmental reconstructions. The past research has been driven by the possibility that the glacial behaviour, and resulting geomorphology and sedimentology can be applied to better understand past glacial deposits and palaeoglacial environments, such as the Scottish highlands. Thus Jostedalen is thought to provide an excellent modern analogue for the behaviour of the ice

[1] http://www.yr.no/place/Norway/Sogn_og_Fjordane/Luster/Jostedal/statistics.html

sheets and glaciers that covered parts of the Northern hemisphere throughout the Quaternary period.

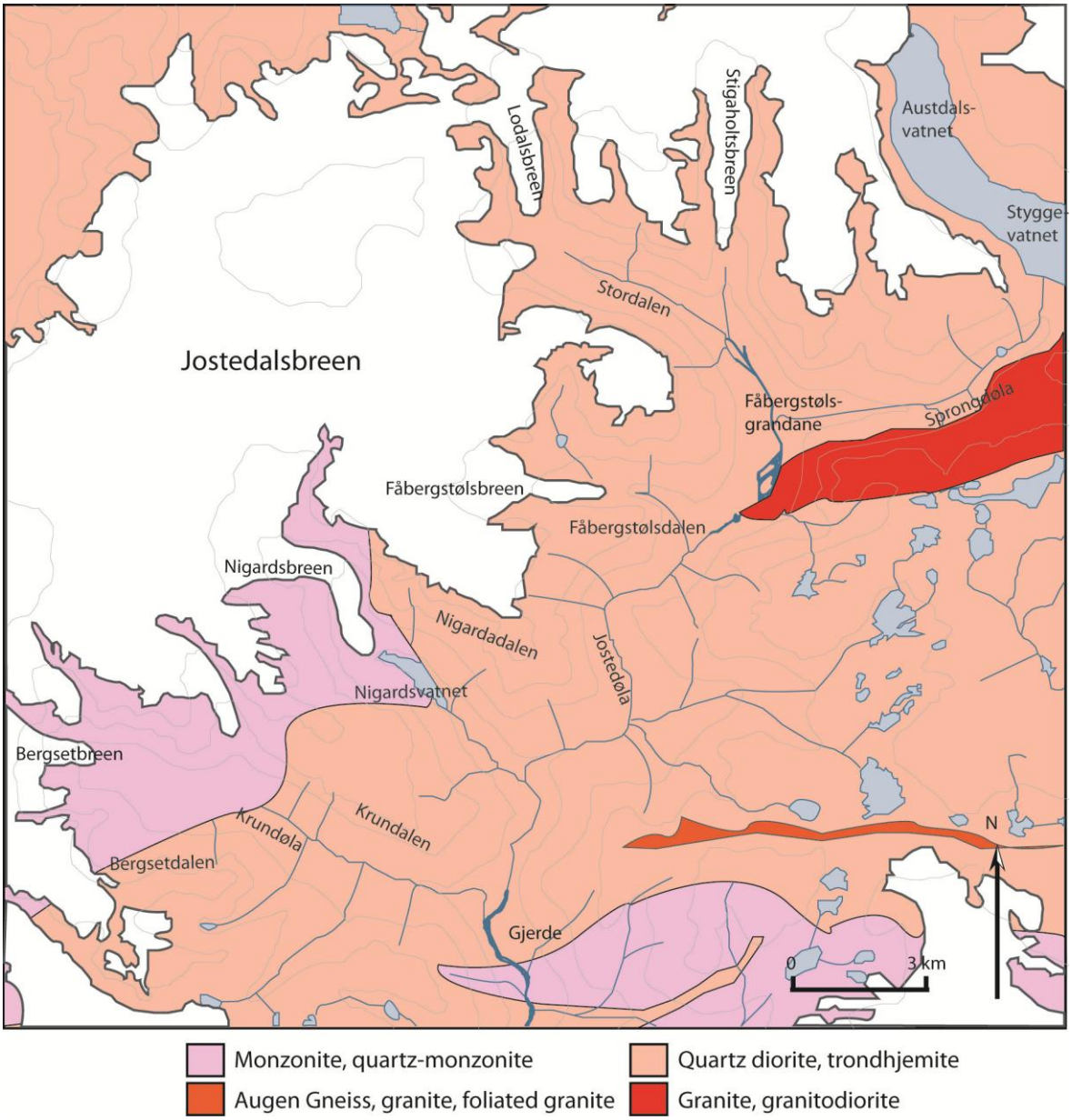

Figure 3.2: Geological map of Jostedalen, adapted from www.ngu.no (Norwegian Geological Institute) (61˚36 N, 7˚04 E)

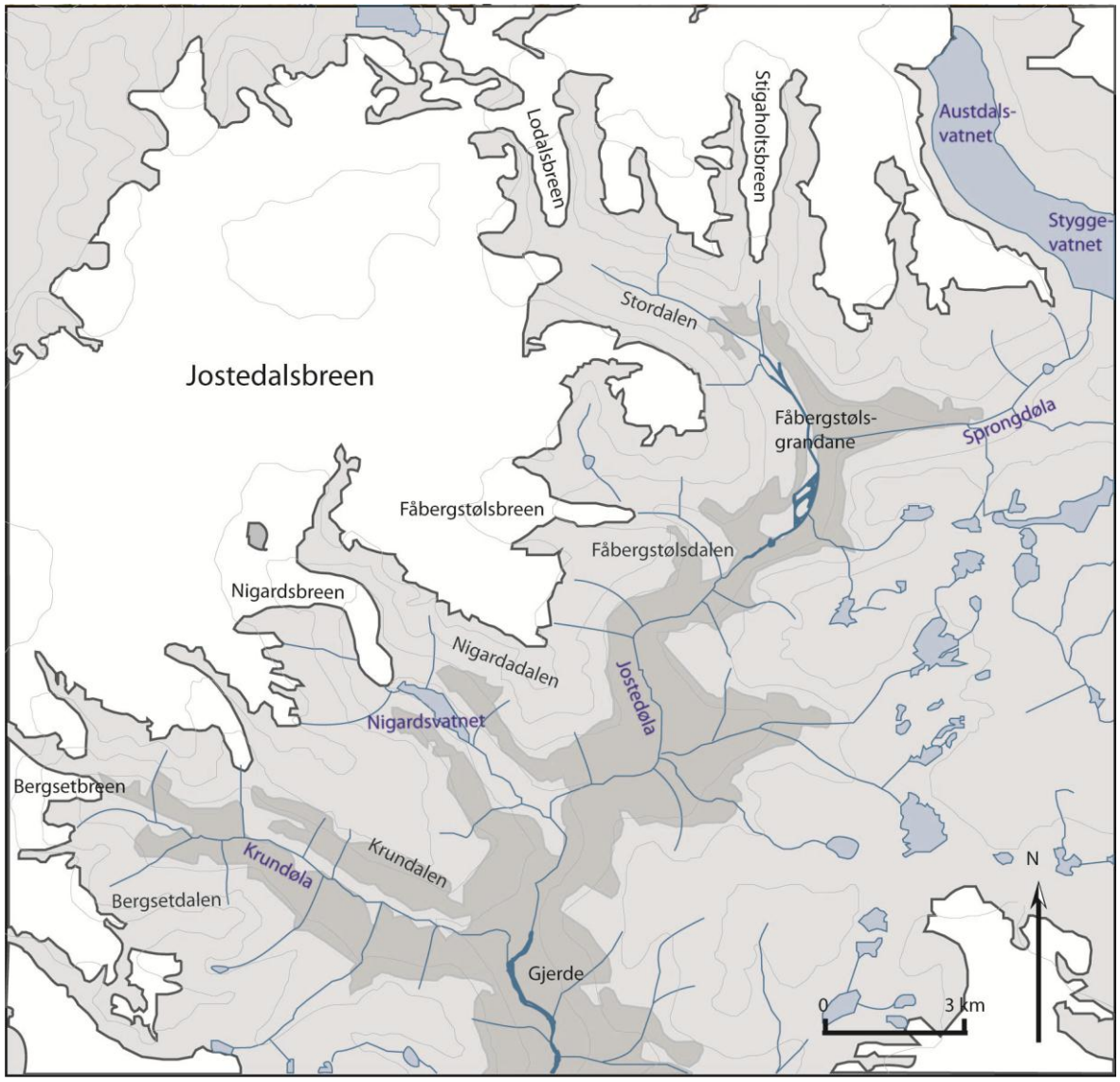

Figure 3.3: Upper Jostedalen (61˚36 N, 7˚04 E) with key features marked. Gaupne is 30 km south from this map.

3.1.3. **Geochronology**

The Jostedalsbre Plateau is believed to have been completely ice free 7.5-5.5 ka cal BP (Matthews et al., 2000; Nesje and Kvamme, 1991; Nesje et al., 2001; 2000). Consequently the various valleys containing outlet glaciers are thought to have been fully deglaciated by ~ 9 ka BP (Nesje et al., 1991). Much of the previous research in Jostedalen has focused upon constraining the timing of the recent Neoglacial activity using a variety of geochronological methods including lichenometry (e.g. Matthews, 2005; Shakesby et al., 2004; Winkler et al., 2003), Schmidt hammer (e.g. Matthews and Owen, 2010; Owen et al., 2007), and radiocarbon dating (e.g. Dahl et al., 2002). Despite challenges associated with these techniques (e.g. Matthews, 1980; Matthews and Owen, 2008), the onset of Neoglacial advance has been constrained to ~ 5 ka BP (Shakesby et

al., 2004), with substantial advances occurring in Jostedalen between 3.7 – 3.1 ka BP (Ballantyne, 1995; Ballantyne and Benn, 1994). Three main periods of glacial readvance have been identified for Norwegian glaciers throughout the Holocene: the Jondal events at 11,100 and 10,550 – 10,450 BP (Bakke et al., 2005) which correspond to the preboreal oscillation, the Erdalen events at 10,100-10,050 cal BP and 9,700 cal BP (Dahl et al., 2002), and the LIA readvance which culminated around 1750 AD (Nesje et al., 2001).

Radiocarbon dating has been heavily utilised in constraining Norwegian Neoglaciation. Organic deposits within moraine boundaries (e.g. Dahl et al., 2002) and lacustrine or mire deposits (e.g. Lie et al., 2004; Matthews, 2005; Matthews et al., 2000; Nesje et al., 2001) provide minimum ages for the event being dated. Podzol horizons have also been used, although these have been found to underestimate age due to contamination with young carbon (Matthews, 1980). The application of radiocarbon dating to material < 100 years old is limited by the occurrence of a number of plateaus within the radiocarbon production curve and reservoir effects, which result in large associated errors and reduced precision. Consequently luminescence dating can provide more precise date determinations throughout recent time periods (Duller, 2000).

The accurate chronological constraint of Quaternary glacial environments is fundamental to understanding future and past climatic and environmental change. However, dating former ice-limits is complicated by the paucity of material available for radiocarbon dating, furthermore radiocarbon dating is restricted to only the late Quaternary (~ 45 ka), due to the half-life of ^{14}C. Quartz OSL dating is commonly applicable over 1-200 ka, and in exceptional instances > 400 ka (Pawley et al., 2008), and thus enables constraint of the full Devensian climate oscillation. Feldspar saturates at a higher dose than quartz, and thus extends the dating range further (e.g. Kars et al., 2008; Porat and Botha, 2008). Also, as OSL is a direct dating method, the glacigenic landforms themselves can be dated, removing the errors associated with lag times between formation and deposition, which may affect indirect techniques such as radiocarbon dating (Lian and Roberts, 2006).

3.1.4. **Sedimentology**

The sedimentology of the study catchments is complicated because the valleys are comprised of an array of till, glaciofluvial and paraglacial deposits. As paraglacial sediments are, by definition, glacial in origin, they retain a substantial number of their original characteristics, such as clast size and shape, and their degree of sorting (Curry and Ballantyne, 1999). Detailed analyses of the paraglacial sediments at Bergsetbreen led Ballantyne and Benn (1994) to conclude that such sediments could be differentiated only

through using fabric analysis, although Curry and Ballantyne (1999) also observed some structural and facies distinctions in their investigation of Fåbergstølsbreen and Lodalsbreen. Clasts within till deposits align parallel with the direction of ice movements, whereas within paraglacial slope deposits these clasts become aligned perpendicular to flow direction. Ballantyne and Benn (1994) also observed a reduced fraction of fine sands in paraglacially modified sediments, indicative of the action of water which may have provided the initial impetus for slope failure.

Paraglacial modification of sediments is associated with increased precipitation (Matthews et al., 1997) and snowmelt (Ballantyne and Benn, 1994). These conditions have become more widespread throughout the Holocene and thus the situation is observed where Neoglacially deposited sediments may overlay older sediments which have also been paraglacially reworked, resulting in a complex cycle of sediment modification (Curry, 1999). However, as increased mass movements following landscape response to deglaciation are widespread, it is essential both to recognise these sediments and to quantify their suitability for OSL dating, to evaluate whether the method can be used on these sediments elsewhere.

3.2. Sampling Strategy & Facies Assemblages

The sampling strategy and facies assemblages are introduced first, and then an introduction to the specific sample sites is provided. Sample modernity was the key objective of the sampling strategy at all of the sites with the exception of Gaupne, and was achieved through sampling sediments proximal to the surface. In addition to sediment stratigraphic location, the sediment facies was key in sample selection, in order that depositional context, process and probable light exposure history, could be determined (Fuchs and Owen, 2008; Thrasher et al., 2009a). Samples were taken to characterise the main source materials, transport pathways and depositional environments of the study catchments, and are differentiated into subglacial, paraglacial, delta, sandur and glaciofluvial braided channel and point bars. Samples were either collected in opaque plastic tubes using conventional OSL methods, whereby the tubes were hammered into a cleaned face of the sediment, or alternatively using the opaque plastic bag method. The latter method comprises covering the sample site with an opaque, plastic bag, clearing a face of at least 2 cm from the sediment to remove any bleached surface material prior to sampling. Light penetration has been shown not to affect D_e after 0.5 cm in sandy limestone (Armitage and King, Submitted; King, 2007), and the additional 1.5 cm of material removed here will account for any additional light penetration associated with relatively loose sediment compaction (Ollerhead, 2001). The sample was then placed

directly into a transparent plastic bag within a second opaque bag, ensuring no light exposure occurred. Sample modernity is ensured by depositional context and stratigraphic location. Samples were prepared for luminescence analysis in the laboratories at the University of St Andrews and full details of the individual samples analysed are given in Appendix C.

3.2.1. **Subglacial Facies Assemblage**

Subglacial till deposits were sampled at the snouts of Fåbergstølsbreen and Nigardsbreen where it was safe to do so (FABSUB1-2, Appendix C.2.1). Using the facies approach of Eyles et al. (1983) these sediments are classified as massive, structureless diamicton (Dmm). The deposits are undergoing reworking by meltwater, identified from gullying of the sediment (Figure 3.4), however as only limited exposures are visible it is not possible to better characterise these assemblages. Clast sizes range from silt to boulders, although larger clasts were avoided when sampling.

Figure 3.4: Photograph of subglacial material sampled from Nigardsbreen.

Subglacial sediments comprise material that has been eroded from bedrock during the most recent glacial period, as well as reworked glacial deposits that relate to earlier glacial stades. Material eroded from bedrock and not exposed to sunlight is expected to have a saturated luminescence age, relating to its geological radiation dose which is beyond the dating range of OSL. Subglacial sediments are eroded, entrained and deposited underneath glacial ice, which provides a barrier to incident sunlight, attenuating the shortest wavelengths which result in most effective quartz bleaching (see Swift et al., 2010 for a review). Consequently the probability of sunlight exposure for such sediments is low, however Swift et al. (2010) observed the OSL of subglacial sediments sampled

from the Haut d'Arolla glacier to be partially bleached and tentatively attributed this to triboluminescence. Where the subglacial sediment comprises material reworked from earlier glaciations, a range of luminescence residual doses are anticipated which relate to the varied sunlight exposure histories of the different deposits.

3.2.2. **Paraglacial Facies Assemblage**

Paraglacial material was sampled from Fåbergstølsdalen (Figure 3.5, FAB41-42/85/86, Appendix C.2) and Bergsetdalen (BERG1-2, Appendix C.1.1), and comprises partially reworked subglacial material. The degree of reworking, and type of transport and depositional processes determine the facies of paraglacial sediments, and Dmm, Sr and Sh:Fl material have been sampled. Debris flows and slumping (Dmm) caused by snowmelt and precipitation are the dominant processes reworking these deposits within the catchments analysed here. Although material is also reworked via sheetwash (Sr, Sh:Fl) and avalanching (Dmm), which have much greater probability of bleaching in contrast to the aforementioned slope failure mechanisms.

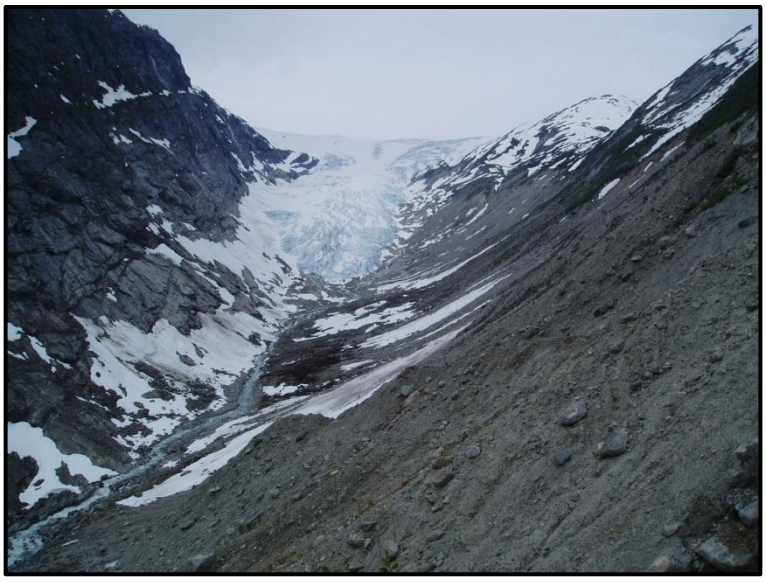

Figure 3.5: Photograph of paraglacial material sampled from Fåbergstølsdalen.

3.2.3. **Gilbert Style Delta Facies Assemblage**

Gilbert style deltas are formed where a river discharges into a standing body of water, and river channel and delta plain deposits are superimposed on the delta front (Bridge and Demicco, 2008). They have a distinctive suite of facies which can be grouped according to their bottomset, foreset and topset bedding geometries. Bottomsets comprise an assemblage of fine sand and silt, horizontal and ripple bedding (Flr, Flh) and grade laterally and upwards into ripple bedded foresets (Sr). Topsets overlay the foresets and are pebbly sand exhibiting well developed large-scale cross-bedding (Gp-Sp) (Jopling and

Walker, 1968). Bottomsets and topsets were sampled at Gaupne (GAUP1-2/40-41, Appendix C.7).

Although intuitively the topsets are most likely to have been fully bleached through fluvial reworking, the greater competency of flow required to transport the coarse material which these deposits are composed of, suggests that deposition may have been rapid and that sufficient sunlight exposure may not have occurred. The deposits in the bottom sets are deposited in deeper water, but if sediment transport is rapid as described, then topset and bottomset sediments will have similar histories of exposure to sunlight.

3.2.4. **Glaciofluvial Point and Braided Channel Bar Facies Assemblages**

Rivers evolve by developing alternate bar forms, as the river bed equilibrates with discharge and sediment supply. Bar length is related to width, and the ratio between length and width ranges from 3 – 12 (Bridge, 2003). Channel erosion and widening results in a drop in water level and bars become emergent (channel bars), comprising three morphological units: bar tail, crossover and bar head (Figure 3.6). These three units are referred to as unit bars, and develop with changes in discharge and sediment supply. Channel bars are compound features comprising multiple unit bars, and can be broadly categorised into point bars which form banks on the inside of river bends, and braid bars which are formed mid-channel (Figure 3.6). Bar forms migrate downstream, however the progression rate of braid and point bar forms is often considerably slower than their composite unit bars (see Bridge, 2003 for a review). Bar head lobes and bar tails interact within compound bar features, as sediment is transported along the bar length, with the former being topographically higher. Crossover channels form as erosion and sediment deposition cause changes in the gradient of bed and water surfaces.

The grain size and sorting of bar forms grades vertically; material is coarsest at the bar base comprising cobbles and gravels (Gm-Gt), fining upwards to sands (Sh-Sr). The competency of the river, sediment grain size and sediment availability determine the exact grain size distribution of bar features. Bar migration comprises erosion of bar heads and deposition on bar tails, which form foresets similar to delta deposits. Relict crossover channels fill with sand, silt and clay (Fl).

As channel bars are emergent for part of the discharge cycle, material is only reworked over the bar tops episodically. The discharge of glaciofluvial rivers has distinct seasonal and diurnal patterns. Throughout winter, discharge is negligible in contrast to summer discharge which initially comprises snowmelt prior to direct ice ablation. Discharge increases throughout the ablation season following expansion and increased connectivity of subglacial drainage pathways, and is also modulated by precipitation

events. Throughout the ablation season, diurnal variations in discharge are caused as ice melts in response to insolation, although this effect will be moderated in Norway relative to the Alps due to reduced diurnal insolation variation.

As for the sandur deposits, the sand-dominated facies deposited during periods of waning flow following a period of elevated discharge are most likely to be well bleached, and therefore the bar tops (Sh, Sr) and backs (Sh, Sr) were focussed upon during sampling. Samples were collected at the start of the ablation season; therefore bar top material relates to maximum discharge of the previous ablation season and should be well bleached. Braid bar deposits were collected from Bergsetdalen (BERG4/16/19/21/24-25, Appendix C.1) and Fåbergstølsdalen (FAB81, Appendix C.2), whilst point bar deposits were sampled from Bergsetdalen (BERG7/10, Appendix C.1), Fåbergstølsdalen (FAB81/90-92/94-95/98-100, Appendix C.2), Stordalen (LOD4-6, Appendix C.3) and Leirdalen (LEI13-14/18, Appendix C.4).

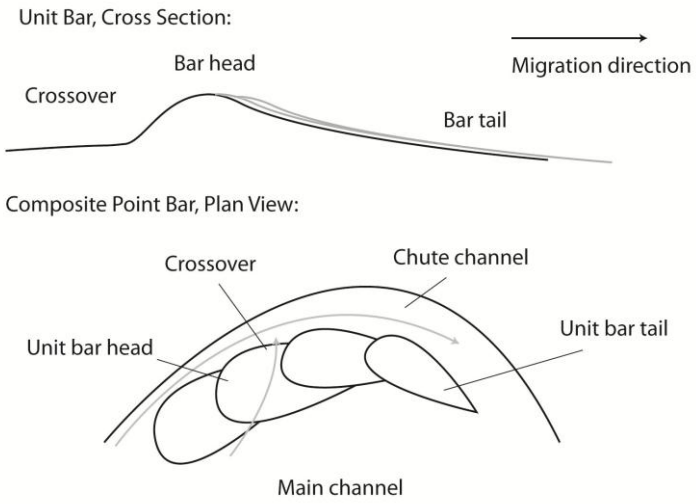

Figure 3.6: Schematic of composite unit bars forming a single point bar.

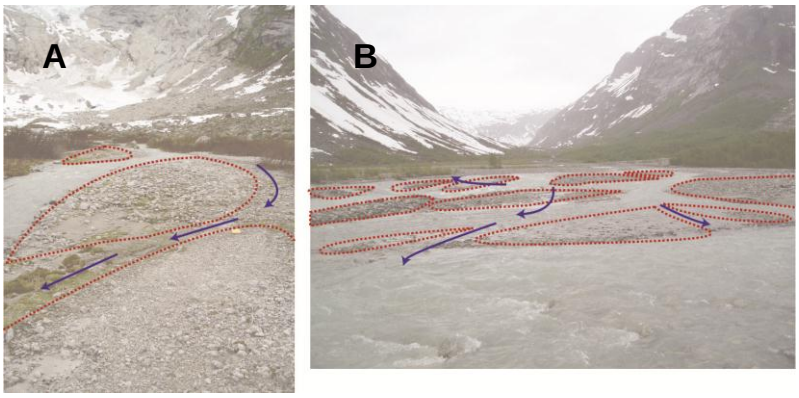

Figure 3.7: Composite braided bar units for (A) Bergsetdalen and (B) Fåbergstølsgrandane. The direction of water flow is shown by the arrows.

3.2.5. **Sandar Facies Assemblage**

Sandar comprise a complex facies assemblage both laterally and horizontally reflecting the varied discharge patterns and associated sediment fluxes of glacial environments. Thrasher et al. (2009b) developed a conceptual model which explores the

different depositional pathways and environments of a proglacial sandur, and associated facies (Boyce and Eyles, 2000; Brookfield and Martini, 1999; Miall, 1985) (Figure 3.8). The depositional processes that operate on a sandur are similar to braided river channels, although fine grained sediment accumulations on bar tops are rare or absent (Reineck and Singh, 1973).

Sand-dominated distal facies are most likely to have been effectively bleached (Thrasher et al., 2009b), therefore bar tops (Sh, Sr, Fl) and the bar tails (Sh, Sr) were focussed upon during sampling. The proglacial delta at Nigardsdalen (NIG3-4, NIG6-9, Appendix C.5) forms a similar depositional environment to the Fåbergstølsgrandane sandur (GRAN54-59, GRAN62, GRAN69, GRAN71, Appendix C.6), and these samples are also classified within the sandar facies assemblage. Total transport distance also influences the bleaching potential of some of these sub-environments (e.g. Forman and Ennis, 1992; Stokes et al., 2001), and this was accounted for through sampling similar deposits at increasing transport distances.

3.3. Grain Size Analyses

Grain size analyses can be used to make inferences about the dominant processes of deposition, however direct causality is often complicated by variables such as sediment source, availability and grain size. Consequently, it is necessary to consider other factors such as depositional context when making process determinations.

3.3.1. **Grain Size Analysis Method**

Grain size analyses were carried out at the University of St Andrews using a Coulter LS230 laser granulometer, which calculates particle size through diffraction of a 750 nm laser and can be used for the analysis of particles from 400 nm to 2 mm (Blott et al., 2004). Bulk material was not available for all samples either due to low sediment availability for dating, or where all bulk material had been prepared for ICP-MS analysis. Where material was available, it was visually inspected to confirm that no organics were present and then sieved to ensure that only grains < 2 mm were present. Material was carefully stirred to avoid settling effects and a subsample extracted. Water was added to the subsample which was mixed into a paste before being decanted through a 2 mm sieve into the laser granulometer for analysis. Material sufficient to result in 8-9% obscuration of the laser (0.5-1 g) was analysed, and duplicate analyses were made of all samples.

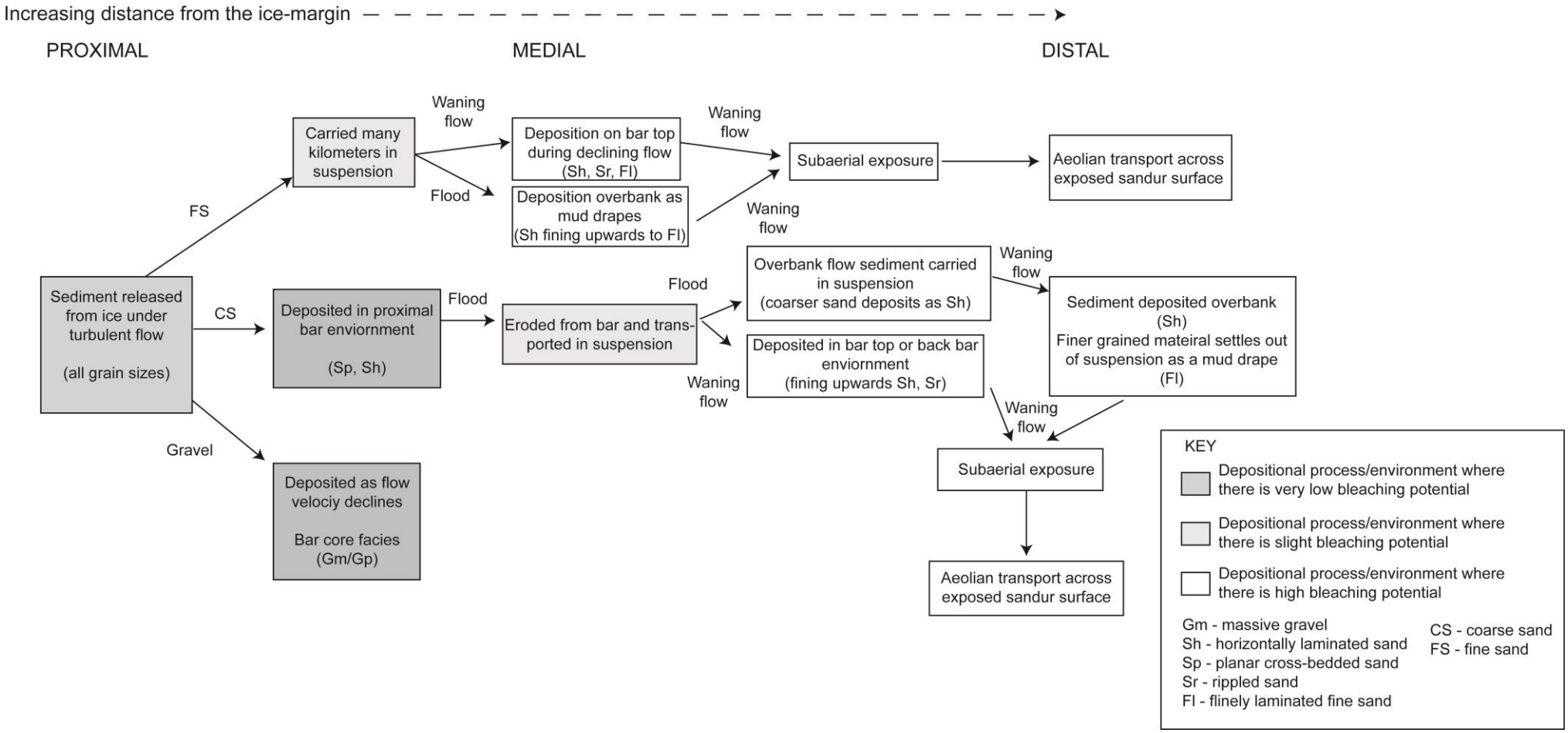

Figure 3.8: A conceptual model of the depositional processes and environments of a proglacial sandur reprinted from Thrasher et al. (2009b) with permission, © 2009 John Wiley & Sons, Ltd. The bleaching potential of the different depositional processes are highlighted.

Where significant deviation between initial and secondary analysis was observed, the sample was analysed a third time and particle size data averaged. Statistics were calculated using GRADISTAT (Blott and Pye, 2001).

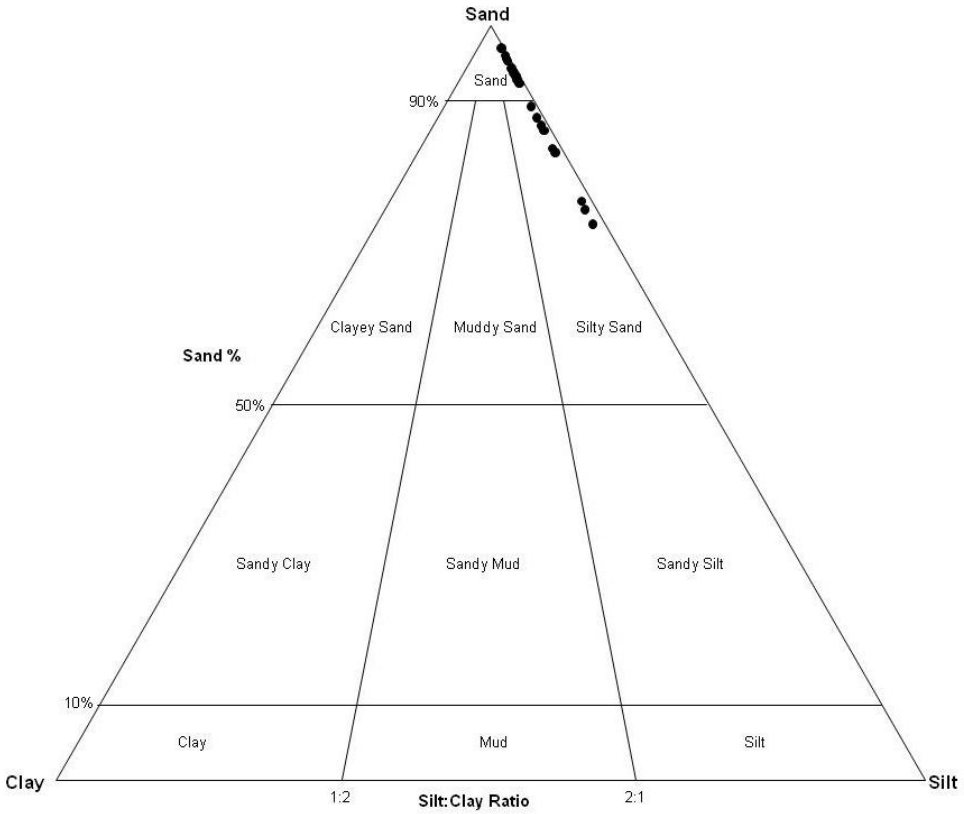

Figure 3.9: Sample particle size classification after Folk and Ward (1957) calculated in GRADISTAT (Blott and Pye, 2001).

All samples were classified as silty sand to sand following the classification scheme of Folk (1954) (Figure 3.9, Table 3.1). GRADISTAT returns a range of statistics, however the moment method of Folk and Ward (1957) was selected as Blott and Pye (2001) observe that it provides the most robust basis for the comparison of compositionally variable sediments. As the samples presented here are derived from a range of depositional environments, variability in composition is anticipated. However it should be noted that the target grain size for luminescence dating is 180-212 µm, therefore there will be bias towards sediments of the “fine sand” classification.

Table 3.1: Size scale adopted in the GRADISTAT program and used to plot the particle size data, adapted from Udden (1914) and Wentworth (1922). All analysed luminescence samples comprised the 180-212 µm grain size which this scheme classifies as “fine sand”.

Grain Size phi	mm	Descriptive term	
-6	64		
		Very coarse	
-5	32		
		Coarse	
-4	16		
		Medium	Gravel
-3	8		
		Fine	
-2	4		
		Very fine	
-1	2		
		Very coarse	
0	1		
	microns	Coarse	
1	500		
		Medium	Sand
2	250		
		Fine	
3	125		
		Very fine	
4	63		
		Very coarse	
5	31		
		Coarse	
6	16		
		Medium	Silt
7	8		
		Fine	
8	4		
		Very fine	
9	2		
		Clay	

Table 3.2: Moment particle size analysis results after Folk and Ward (1957) calculated in GRADISTAT (Blott and Pye (2001)

	Deposit	Material > 2mm?	Mean (φ)		Mode (φ)			Sorting		Skewness		Kurtosis	
FABSUB1	Subglacial	Yes	0.40	CS	-0.40			1.25	Poor	0.44	Very Fine Skewed	1.22	L
FABSUB2	Subglacial	Yes	0.47	CS	-0.26			1.23	Poor	0.40	Very Fine Skewed	1.17	L
FAB41	Paraglacial		0.72	CS	0.14			1.10	Poor	0.25	Fine Skewed	1.00	M
FAB42	Paraglacial	Yes	2.71	FS	3.10	-0.40	-0.13	1.95	Poor	-0.06	Symmetrical	1.07	M
FAB86	Paraglacial		3.02	VFS	2.84			1.30	Poor	0.10	Fine Skewed	1.07	M
FAB79	Point Bar Deposit		3.12	VFS	2.84			1.32	Poor	0.16	Fine Skewed	1.20	L
FAB84	Point Bar Deposit		1.56	MS	1.49			1.32	Poor	0.05	Symmetrical	1.10	M
FAB90	Point Bar Deposit		2.46	FS	2.03			1.12	Poor	0.18	Fine Skewed	1.09	M
FAB91	Point Bar Deposit		1.59	MS	1.49			0.92	Moderate	0.05	Symmetrical	1.15	L
FAB98	Point Bar Deposit	Yes	1.44	MS	1.22			1.31	Poor	0.10	Fine Skewed	1.10	M
FAB99	Point Bar Deposit		2.39	FS	2.57	-0.40		1.42	Poor	-0.04	Symmetrical	1.20	L
FAB100	Point Bar Deposit		2.65	FS	2.30			1.29	Poor	0.16	Fine Skewed	1.12	L
LEI18	Point Bar Deposit		0.58	CS	0.55			0.69	Moderate	0.05	Symmetrical	1.03	M
GRAN69	Point Bar Deposit		2.00	FS	1.49			1.15	Poor	0.39	Very Fine Skewed	1.29	L
FAB81	Braided Bar Deposit		1.95	MS	2.57	1.76	2.03	1.70	Poor	0.04	Symmetrical	0.94	M
NIG6	Sandar Braided Bar Deposit	Yes	0.60	CS	0.01			1.13	Poor	0.29	Fine Skewed	1.09	M
NIG7	Sandar Braided Bar Deposit		1.39	MS	1.89	-0.93		1.39	Poor	-0.11	Coarse Skewed	1.01	M
NIG8	Sandar Braided Bar Deposit	Yes	1.39	MS	-0.53	2.84		1.63	Poor	0.08	Symmetrical	0.73	P
NIG9	Sandar Braided Bar Deposit	Yes	2.71	FS	2.56			1.39	Poor	0.02	Symmetrical	1.45	L

CS – coarse sand, FS – fine sand, VFS – very fine sand, MS – medium sand, M – mesokurtic, L – leptokurtic, P - platykurtic

3.4. Bergsetdalen & Krundalen

Bergsetbreen (61˚38'51N 7˚06'16E) is a hanging glacier which discharges into the east-northeast orientated Krundalen valley, the upper section of which is referred to as Bergsetdalen (Figure 3.10). Meltwater from the glacier travels along the Krundøla for ~ 9 km until its confluence with the Jostedøla River at the village of Gjerde. It is the most southern valley sampled and has the lowest altitude. Krundalen is heavily vegetated relative to Fåbergstølsdalen, related to earlier glacial retreat and its lower altitude, consequently sediment transport processes within the catchment are dominated by the meltwater stream and some limited reworking of paraglacial material within the Little Ice Age (LIA) moraine limit.

Owing to copyright restrictions, the electronic version of this thesis does not contain this image.

Figure 3.10: Geomorphological map of Bergsetdalen/Krundalen (61˚37' N, 7˚04' E) modified from Ballantyne (1995). The largest debris cone is pre-LIA in age. The ice-limit has been modified to approximately reflect that observed in 2009, note also the reconstituted glacier.

Krundalen was fully deglaciated by ~ 9 ka BP, as were the other valleys in the Jostedal region (Nesje et al., 1991). Despite the first Neoglacial advances occurring from 3.7 ka BP in Jostedalen, there is no evidence of pre-LIA Neoglacial activity in Bergsetdalen (Ballantyne, 1995). Fourteen retreat moraines have been identified, and dated using lichenometry, of which the outermost pertains to the LIA (Bickerton and

Matthews, 1993). The moraines associated with the Jondal and Erdalen events lie beyond the LIA moraine limit (Dahl et al., 2002; Lukas, 2007).

Ballantyne (1995) identified five debris cones within Krundalen, the accumulation of which had ceased within 1-200 years of deglaciation, by 1965 AD. Paraglacial remobilisation of glacial sediments by debris flows was the key agent of development for two of the cones, whilst the largest debris cone was formed predominantly by sediment transported via snow avalanching. The absence of exposures prevented Ballantyne (1995) from investigating the sedimentological characteristics of the cone deposits, however Curry and Ballantyne (1999) observe that *in-situ* glacial deposits and paraglacially reworked material are sedimentologically similar, differing only in clast orientation and through their structural characteristics (see section 3.1.4). This has implications for the bleaching characteristics of paraglacial deposits, as if the sedimentology remains similar, it is unlikely that material other than that at the surface will have been exposed to sunlight. Consequently one would anticipate a mixture of low and high residual doses from paraglacial deposits.

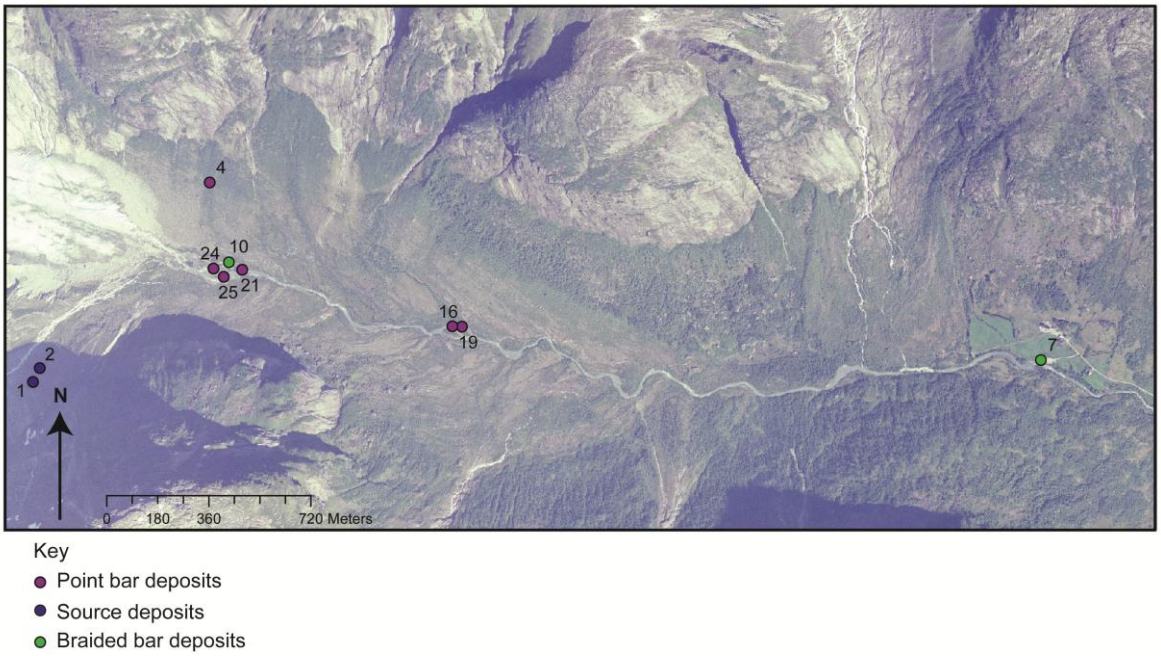

Figure 3.11: Aerial photograph of Bergsetdalen showing sample locations. Modified and reprinted with permission from Norway in Images (www.norgeibilder.no), Jotunheimen 2004, © Norwegian Mapping Authority.

Samples were taken along a transect from the reconstituted glacier snout, along the meltwater stream (the Krundøla, Figure 3.11). The Krundøla is an anastomosing river in the upper catchment due to the low valley gradient with a suite of active braided bars, but becomes a single channel ~ 250 m distal of Bergsetbreen. Dependent upon sample location key sediment sources were either subglacial material or paraglacial deposits, both of which were sampled, and specific details of the different samples analysed are

given in Appendix C.1. These samples formed the basis of David Lowry's (DBL) undergraduate thesis, and were sampled, prepared and measured under my supervision and re-analysed by me for inclusion in this thesis.

3.5. Fåbergstølsdalen

Fåbergstølsbreen (61˚42'49N 7˚19'14E) is a valley glacier which discharges into Fåbergstølsdalen, which trends east and then southeast towards Stordalen and the Jostedøla (Figure 3.3). The greater basal altitude of the valley and relatively narrow dimensions have meant that glacial retreat occurred slightly later here than in Krundalen. Vegetation is less well established and consequently valley side material is readily reworked by weather events contributing to the sediment flux of the valley. A single meltwater stream dominates the catchment and limited channel braiding occurs in the upper catchment, related to the increased gradient in the ice-proximal zone. The meltwater stream converges with the Jostedøla down valley (Figure 3.12).

Fåbergstølsdalen is characterised by the reworking of large volumes of glacial sediment derived from the valley sides through a variety of slope failure mechanisms (Figure 3.13). Ballantyne and Benn (1994) noted the occurrence of debris flows during warm weather, ascribing spring snowmelt as the key driver of paraglacial modification in contrast to high precipitation events, which have been suggested as the dominant driver for other areas of Norway (e.g. Matthews et al., 1997; Sletten and Blikra, 2007). They suggest that although some slope material fails as debris falls and slides, any sediment accumulates at the gully floor before remobilisation as a debris flow triggered by spring melt runoff. Furthermore, they suggest debris flows transport the majority of material within Fåbergstølsdalen, with avalanching and side valley streams contributing a limited volume. This paraglacial debris flow generated material is anticipated to have a high residual luminescence dose, as the rapid transit time and turbulent properties of debris flows afford limited opportunity for light exposure. Similarly translational debris slides will only provide sunlight exposure for the sediment at the surface, and the interior part of the main slide body may see no light exposure at all (e.g. Hungr et al., 2001).

The existing stratigraphy of material within the valley side source regions further complicates the sedimentology of Fåbergstølsdalen. The LIA till overlays early Holocene paraglacial material (Ballantyne and Benn, 1994), deposited during deglaciation of Fåbergstølsdalen around 9 ka BP (Nesje et al., 1991) (Figure 3.13). Consequently the optical exposure history of the sediments is extremely complicated, having a range of potential residual luminescence doses.

Within Fåbergstølsdalen, the LIA ice-advance has also been the most substantial of the Neoglacial activity. Seventeen retreat moraines have been identified by Ballantyne and Benn (1994), the outermost of which relates to the LIA and has been dated using a Schmidt hammer (Owen et al., 2007) and lichenometry (Bickerton and Matthews, 1993) to ~1750 AD. A moraine relating to the earlier Erdalen glacial advances, lies beyond the outermost LIA moraine (Dahl et al., 2002). Since the LIA maximum, the ice has retreated more than 2 km (Owen et al., 2007), 1.5 km of which has occurred since 1930 (Ballantyne and Benn, 1994). Fåbergstølsbreen is still fluctuating in extent, with glacial advance recorded between 1992 and 2000, retreat during 2000 until 2003, when the ice limit became stationary, prior to advancing between 2004 and 2005 (Institut für Geographie, Universität-Würzburg, 2008) (Institut für Geographie, Universität). Nesje (1989) determined a climatic response time of ~ 24 years for this glacier.

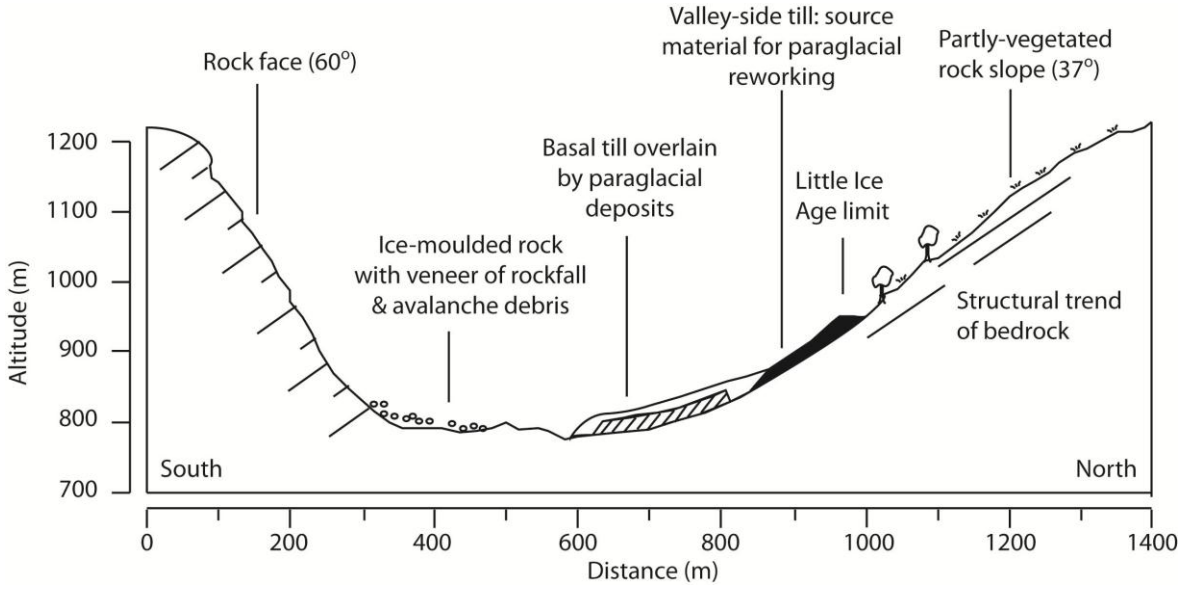

Figure 3.12: Cross-section of Fåbergstølsdalen modified from Ballantyne and Benn (1994) © Regents of the University of Colorado.

A similar and complimentary suite of samples to those collected for Bergsetdalen/Krundalen were collected within Fåbergstølsdalen using the opaque plastic bag method (Figure 3.14). The steep gradient of the North valley side rendered the collection of *in-situ* paraglacial material impossible, rather a range of material from source regions at the valley sides, which may have already undergone more significant paraglacial modification, was collected as well as a number of ice-proximal source material samples. Subglacial till deposits, snow avalanche, sheet wash, meltwater channel point and braided bar deposits were sampled. The influence of transport distance on residual luminescence was again investigated by sampling along an upstream to downstream transect of the meltwater channel, and full descriptions of individual samples are given in Appendix C.

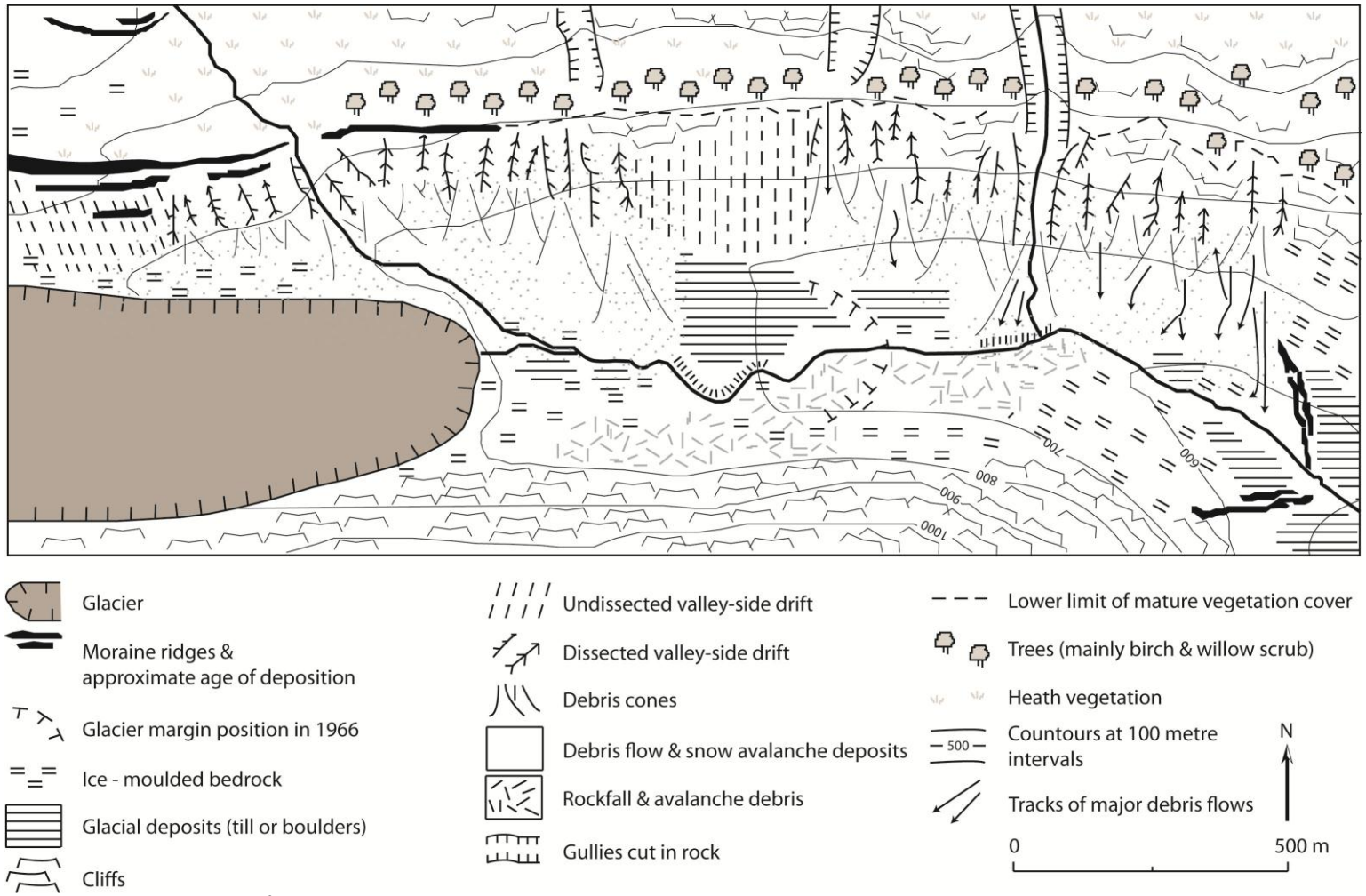

Figure 3.13: Geomorphological map of Fåbergstølsbreen (61˚42' N, 7˚16' E), reproduced from Ballantyne and Benn (1994), © Regents of the University of Colorado

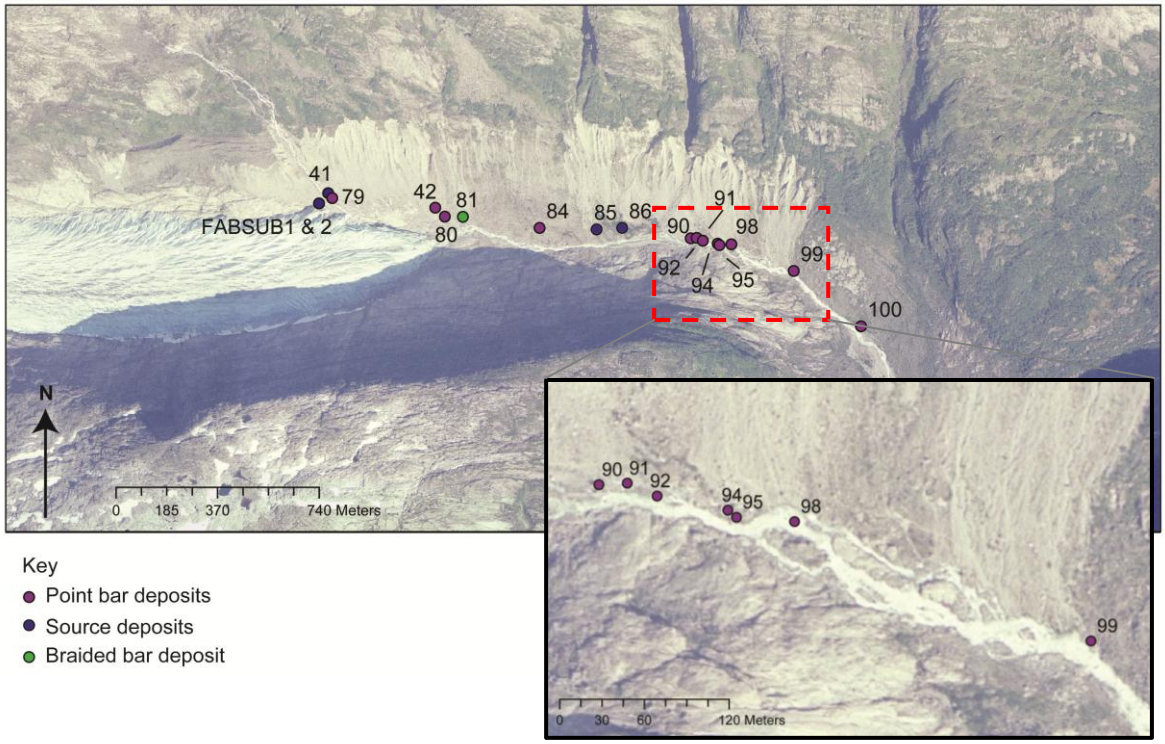

Figure 3.14: Aerial photographs of Fåbergstølsdalen showing sample locations. Modified and reprinted with permission from Norway in Images (www.norgeibilder.no), Jotunheimen 2004, © Norwegian Mapping Authority.

3.6. Nigardsdalen

Nigardsbreen (61°41′12N, 7°11′45E) discharges into a proglacial lake called Nigardalsvatnet, which formed in the 1930s and caused a dramatic increase in the rate of glacier retreat due to calving (Østrem et al., 1976). Several years of positive mass balance between 1962 – 1975 caused an increase in glacier thickness of > 6 m, however no advance in snout location had been observed by 1976 (Østrem et al., 1976). This supports the predicted response time for Nigardsbreen of 34.8 years (Oerlemans, 2007). The LIA maximum advance for Nigardsbreen occurred at 1748 AD (e.g. Matthews et al., 1986).

The Nigardsbreen catchment is dominated by near vertical jointing. The bedrock geology changes from quartz monzanite in the upper catchment, to quartz diorite and trondhjemite in the lower catchment. This geological shift is accompanied by a broadening in the catchment down valley reflecting the reduced resistance of quartz diorite and trondhjemite relative to quartz monzanite. Very little paraglacial material is present throughout the catchment and large volumes of bedrock are exposed. The glacier is drained by a single meltwater stream on the southern side of the valley, which switched from the north valley side in 2006 (Andy Cullens, Pers. Comm., 2008). Sediments are deposited into a

proglacial delta which is actively modified as the lake level varies throughout the meltwater season, in response to seasonal temperature changes and weather events.

Samples were taken from two longitudinal braid bars on the proglacial delta (Figure 3.15) and were collected in opaque plastic tubes. The proglacial delta sediments obtained from Nigardsbreen comprise braided bar deposits and therefore have a similar depositional process to the sandar deposits at Fåbergstølsgrandane.

3.7. Fåbergstølsgrandane

Fåbergstølsgrandane (61°43'39N, 7°21'50E) is the largest sandur in mainland Norway (Miljøvernavdelinga, 1994). It is supplied with sediment and meltwater from Lodalsbreen and Jostedalsbreen from the upper reaches of Stordalen, and also Stigaholtsbreen and Austedalsbreen. Lodalsbreen is partly debris covered which exerts an influence on the bleaching history of the sediments derived from it. Stordalen has very low vegetation density, reflecting its high altitude and recent deglaciation, but has reduced paraglacial sediment and hillslope connectivity between the valley sides and the meltwater channel, in contrast to Fåbergstølsdalen. The contribution of material from Austedalsbreen has been heavily influenced by the construction of an HEP dam and the formation of Austedalsvatnet and Styggevatnet in 1989 (McEwen and Matthews, 1998). However, sediments from Upper Jostedalen are still derived via the Sprongdøla which flows from beneath the dam to Fåbergstølsgrandane. The sandur is approximately 10 km^2 and is the origin of the Jostedøla.

Samples were collected in a transect across Fåbergstølsgrandane from the different sediment bars using the opaque bag method. Time constraints precluded the sampling of multiple transects, which may have provided insight into the contrast between different catchment source regions and contrasting transport velocities. Transport is more rapid on the western side of the sandur, due to the influence of meltwater from Lodalsbreen and Stigaholtsbreen, whereas water from Austdalsbreen is extracted for HEP generation via the Stygnevatnet dam (Figure 3.16). Glaciofluvial source material samples were also collected from the upper regions of Stordalen, to characterise the input of material from Lodalsbreen.

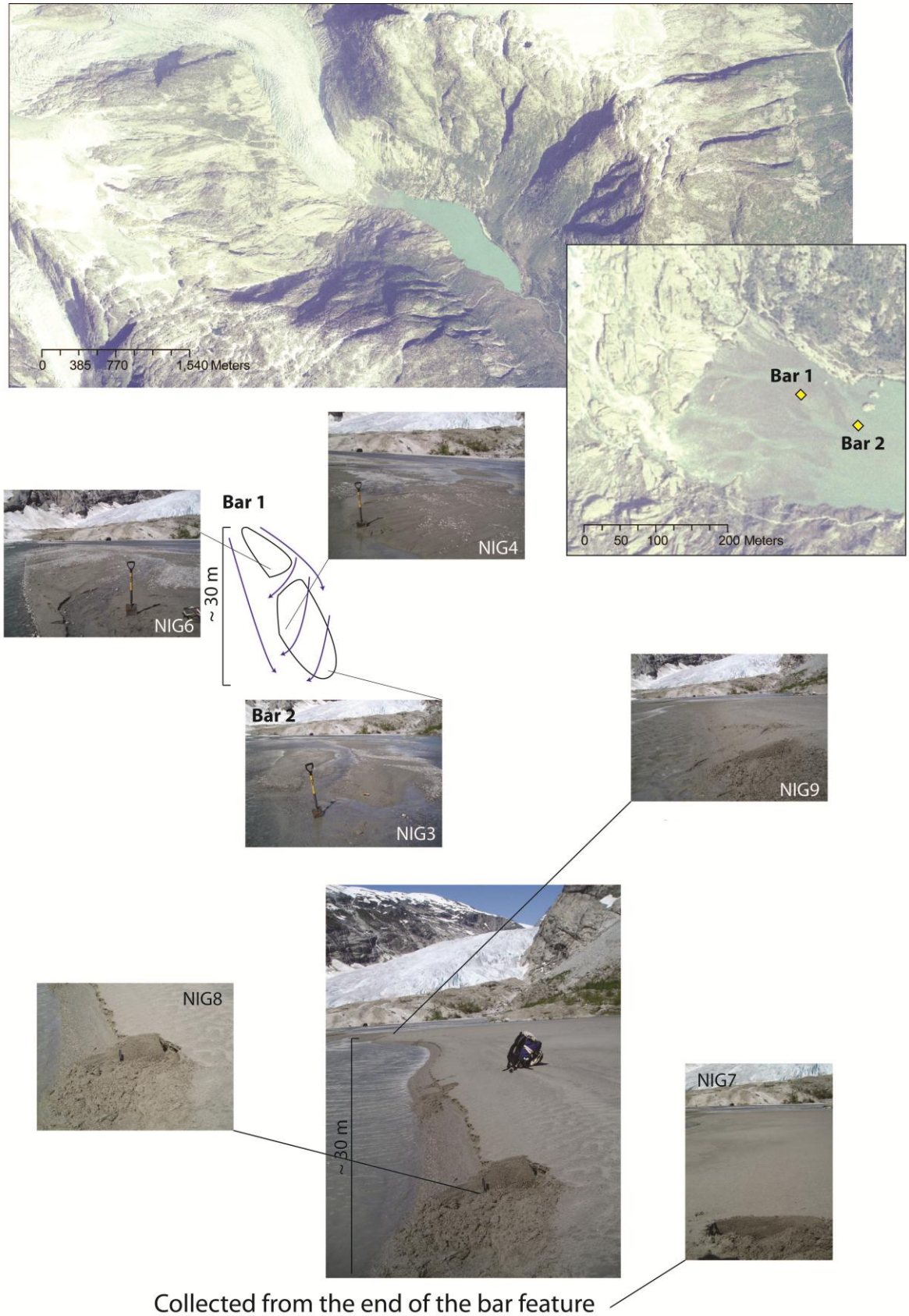

Figure 3.15: Photographs and schematic of the Nigardsdalen feldspar sample locations (61˚39' N, 7˚11' E). Aerial photographs modified and reprinted with permission from Norway in Images (www.norgeibilder.no), Jotunheimen 2004, © Norwegian Mapping Authority. Approximate bar head locations are indicated on the aerial photograph – variations in lake level, coupled with poor GPS signal due to high valley sides, have precluded indication of precise locations.

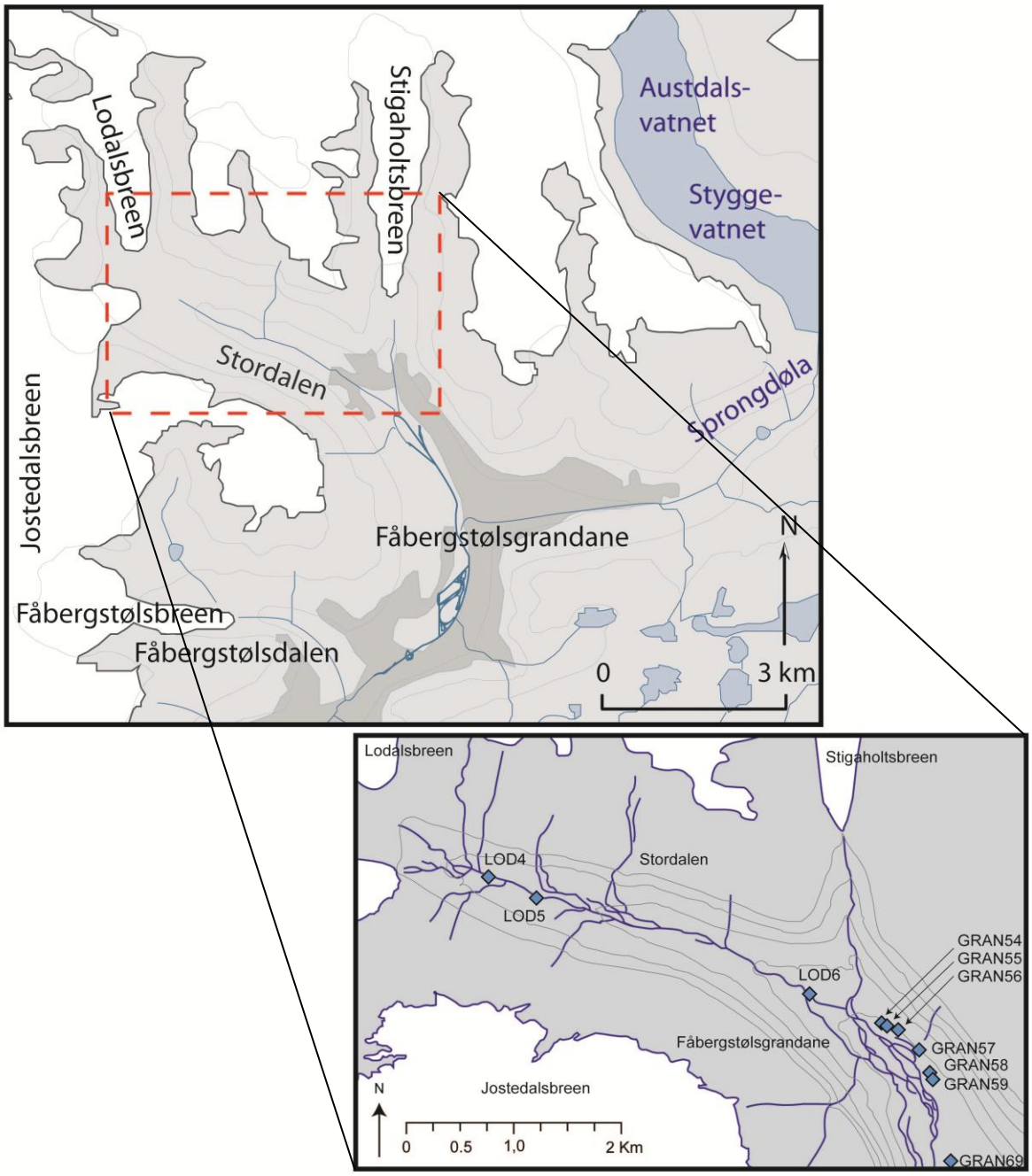

Figure 3.16: Map showing the sample locations of the Stordalen and Fåbergstølsgrandane point bar samples (61˚45' N, 7˚17' E), and the Fåbergstølsgrandane sandur samples.

3.8. Gaupne

Gaupne is 30 km south of the other sites investigated (Figure 3.17), at the far end of the Jostedal valley, where the Jostedøla discharges into the Gaupnefjorden and Lustrafjorden. There are extensive proglacial delta deposits at Gaupne, which have been associated with the Høgemoen stadial between 9.5 ± 0.2 and 9.1 ± 0.2 ka BP by Vorren (1973). These sediments are exposed through quarrying, and material was analysed at

Reidarmoen (82 m a.s.l.). The upper limit of this feature reflects sea level at the time of deposition.

Samples were taken from bottomsets comprising sandy horizons, interbedded with gravel deposits, and fluvial topset deposits (GAUP1-2, GAUP40-41, see Appendix C.7 for full sample details). Sampling locations were selected both in terms of accessibility, as a large amount of material within the quarries was loose and therefore hazardous, and also to bracket the period of deposit accumulation.

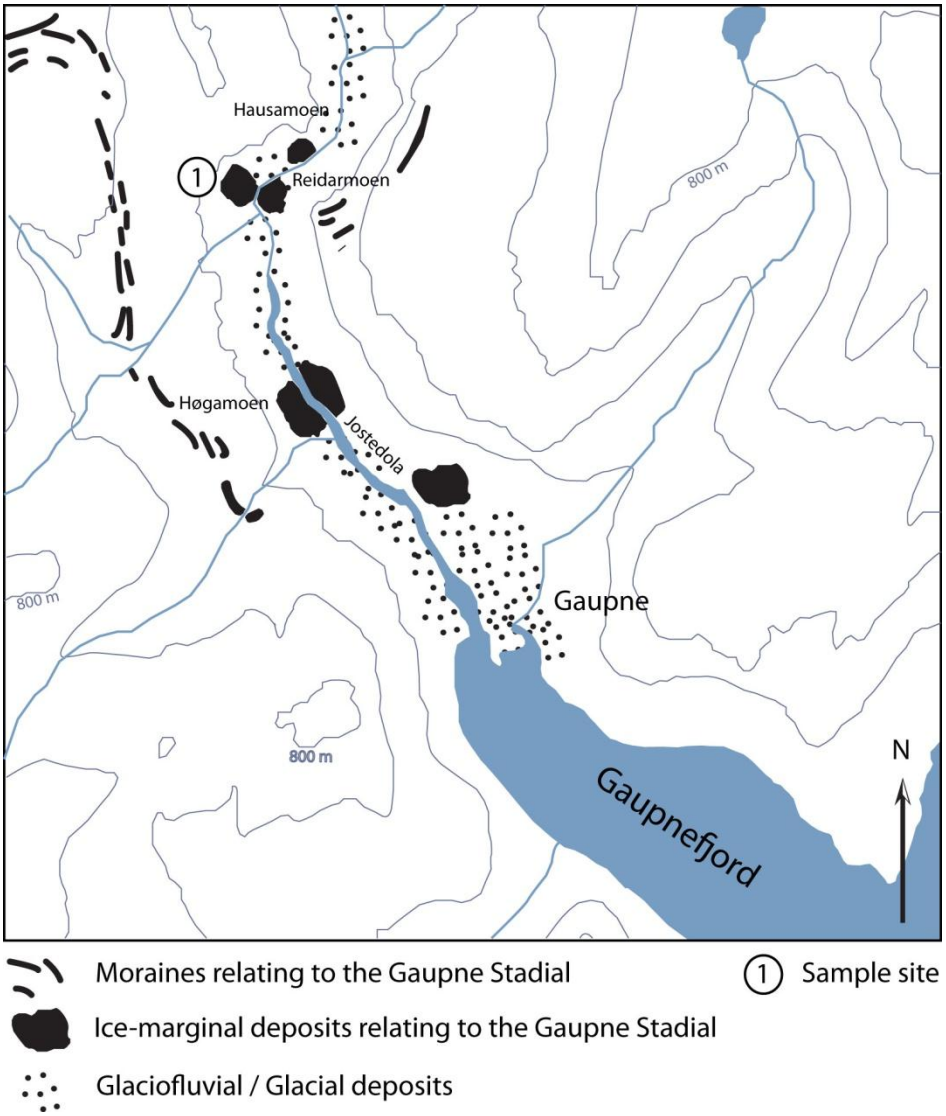

Figure 3.17: Map of the Gaupne deposits and landforms associated with the Høgemoen stadial (9.5±0.2 - 9.1±0.2 ka BP). Modified after Vorren (1973) (61˚22' N, 7˚13' E).

3.9. Water of Tulla, Scotland

In addition to the Norwegian samples, three samples from Scotland were also analysed to provide a comparative sample suite in terms of geological setting and

depositional environment (WTUL1-3, Appendix D). Samples are derived from granitic bedrock and were taken from a glaciofluvial deposit comprising inter-bedded sands and gravels adjacent to the Water of Tulla (56˚34' N, 4˚41'E). Loch Tulla, East Argyll, is surrounded by a series of terraces which have been related to a series of ice-dammed lakes that occupied the Tulla basin during the final stages of the Loch Lomond readvance (Ballantyne, 1979). More recently, cosmogenic nuclide dating has indicated a Loch Lomond Stadial age of 12.9-11.5 ka for moraines in the Western Grampians (see Ballantyne, 2010 for a review), which is in agreement with ages calculated for Greenland Stadial 1 (e.g. Lowe et al., 1999).

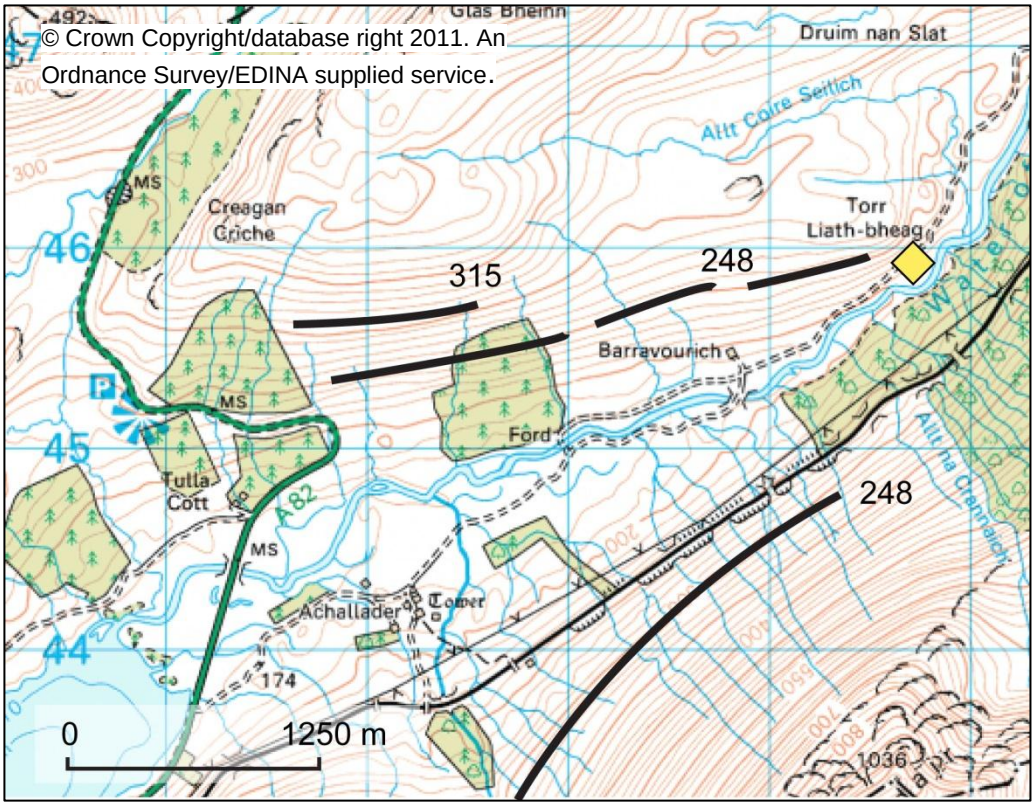

Figure 3.18: Water of Tulla location map, highlighting the sample location (56˚34' N, 4˚41'E) and abandoned lake shorelines and altitudes (thick black lines), identified by Ballantyne (1979).

3.10. Summary

A suite of samples from a number of glacial catchments in Jostedalen, southern Norway have been sampled for OSL analysis. The sedimentology, geomorphology, geology and climate of the study area, and the specific depositional characteristics of each study site, have been described. Three additional Scottish samples collected from the Water of Tulla, are thought to represent deposition during the final stages of deglaciation of this region, and thus have a similar depositional context to many of the Norwegian samples collected. These samples provide complimentary material to the

Norwegian samples and were used for emission spectroscopy experiments carried out prior to Norwegian sample suite collection (see Chapters 7 to 10). Grain size analyses were used to characterise samples taken from different depositional environments, and the rationale and analysis protocol are described.

Chapter 4. Quartz OSL

4.1. Luminescence Sample Preparation

Samples were prepared under subdued red light conditions, produced by wrapping fluorescent tubes with 2 layers of Lee 106 red paper (Jensen and Barbetti, 1979; Smith, 1988; Spooner and Prescott, 1986; Sutton and Zimmerman, 1978a), using conventional methods in the laboratories at the University of St Andrews. Samples were initially desiccated at 50 ˚C, and water content (%) calculated ([wet mass-dry mass]/wet mass x 100). Samples were sieved into four grain size fractions: <180, 180-212, 212-250 and >250 µm using a sieve shaker and either nylon sieve mesh and plastic collars or metal sieves. The 180-212 µm fraction was selected for preparation as it is known to be unaffected by grain size dependent dose rate effects during laboratory Sr^{90} β irradiation (Armitage and Bailey, 2005). Thrasher et al. (2009b) recently observed that for glaciofluvial sandur deposits, grain size had little influence on observed D_e, although this is in contrast with the observations of practitioners working on proglacial sediments (e.g. Klasen et al., 2007) and fluvial sediments (e.g. Olley et al., 1998).

Approximately 10 g of the 180-212 µm fraction, dependent on sediment availability, was given a 30 minute 30 % HCl wash to remove $CaCO_3$. The sample was agitated periodically at 5 minute intervals during the treatment. HCl was then decanted and replaced with 30 % H_2O_2 to remove organic material from the sample. The duration of H_2O_2 treatment varied between samples, dependent upon the amount of organic material present. Treatment was performed at room temperature and samples were agitated periodically. Once conspicuous effervescence had ceased the H_2O_2 was decanted and the sample rinsed three times with deionised water and twice with acetone. Samples were then dried at 50 ˚C before ~ 2 g of the sample was separated in a burette using 2.70 g cm^{-3} LST fastfloat, which is a heavy liquid comprising low toxicity sodium heteropolytungstate dissolved in water. Heavy minerals were retained and the < 2.70 g cm^{-3} fraction rinsed three times with deionised water to ensure all LST was removed. Some samples were then subjected to a second density separation using 2.58 g cm^{-3} LST to isolate the K-feldspar fraction (see Chapter 5, Figure 5.1), and both the > 2.58 g cm^{-3} (Quartz) and the < 2.58 g cm^{-3} (K-feldspar) fractions were then rinsed three times with deionised water. The dried > 2.58 g cm^{-3} samples were etched with 40 % HF for 40 minutes, and were agitated at 5 minute intervals. After 40 minutes the acid was decanted into a waste bottle, and the sample rinsed thoroughly three times with deionised water. Finally the etched quartz was treated with 30 % HCl for 30 minutes to remove any carbonates produced during etching, before being rinsed thoroughly in deionised water and then acetone. The pure quartz fraction was then ready for analysis.

4.2. Luminescence Analysis Protocol

All analyses, except where otherwise stated, were carried out using a TL-DA-15 (Bøtter-Jensen et al., 2003) or TL-DA-20 Risø reader at the University of St Andrews; these readers are referred to as Risø 1 and Risø 2 throughout the text, respectively. Stainless steel discs (10 mm diameter, 1 mm thick) were cleaned with acetone prior to spraying with silicone grease through a mask. The number of quartz grains was regulated through use of either a medium (5 mm Ø, ~ 125 grain) or large (8 mm Ø, ~ 400 grain) mask, as grains only adhered to the silicone grease coated region (grain size 180-212 µm). Quartz was mounted onto the discs and any loose grains removed by holding the discs with tweezers and vigorously tapping them against the bench to ensure deposition of a single quartz layer, prior to loading into the carousel.

Both Risø Readers are equipped with an EMI 9235QA photomultiplier and a 7.5 mm Hoya U-340 filter was used for the quartz measurements in each machine. Luminescence emissions between 275-370 nm (4.51-3.35 eV) only were detected (Hoya-Optics, 2011). Stimulation was carried out with blue diodes for BSL (470±20 nm, 2.64 eV) and infrared (IR) diodes for IRSL (870 nm (1.43 eV) in the TL-DA-15 and 875 nm (1.42 eV) in the TL-DA-20), operated at 90% power during conventional analyses (Table 4.1). Irradiation was achieved using a $^{90}Sr/^{90}Y$ beta source, which is calibrated using the calibration quartz prepared at Risø (CalQz Batches 8, 34 and 40, see Appendix A.5 for details).

Table 4.1: Risø Reader Diode Power at the sample position (100% power) (Risø, 2002, 2006)

Risø Reader Model	Blue diodes	IR diodes
TL-DA-15	40 mW·cm^{-2}	135 mW·cm^{-2}
TL-DA-20	50 mW·cm^{-2}	145 mW·cm^{-2}

4.3. Quartz D_e determination

4.3.1. The SAR Protocol

The single aliquot regenerative dose (SAR) protocol is distinct from previous OSL and TSL protocols in that it corrects for sensitivity changes that affect the sample throughout analysis (Blair et al., 2005; Murray and Mejdahl, 1999; Murray and Roberts, 1998; Murray and Wintle, 2000, 2003; Wallinga et al., 2000b). It comprises measurement of the equivalent dose (D_e) through stimulation of the natural luminescence (L_n), followed by measurement of the luminescence response (L_x) to multiple regenerative doses of different amounts, interspaced by measurement of the luminescence response (T_x) to test doses (T_D) of equal amount. The L_x of the regenerative doses are used to obtain a range of values which bracket L_n, and allow the D_e to be calculated through interpolation with

minimal associated errors (Banerjee et al., 2000). The luminescent response to the test dose is used to compensate for sensitivity changes of the quartz throughout analysis (L_x/T_x).

Quartz grains undergo sensitivity changes throughout analysis, manifested as a varying luminescence response to dose of equal amount. Increasing sensitivity is associated with sample heating (Zimmerman, 1971) and charge thermal transfer (Murray and Wintle, 2000). Reducing sensitivity is less commonly observed (although see Armitage et al., 2000), however repeated radiation dosing throughout analysis can promote the development of non-radiative centres which reduce the total OSL measured (e.g. Aitken, 1998; Bailey, 2004). Natural irradiation causes the same effect and the radiation exposure history of quartz may actually determine its overall sensitivity (e.g. Rink, 1994, see Chapters 7 - 10 for further discussion).

The SAR protocol is dependent upon three key assumptions: first that T_x provides an accurate estimation of sensitivity change throughout the analysis procedure, secondly that samples respond to both laboratory and geological dose rates in the same manner and thirdly that the charge population monitored within the sample remains constant (Murray and Wintle, 2003; Wintle and Murray, 1999). Multiple authors have addressed the first and second of these issues through analysis of a variety of independently dated samples (e.g. Stokes et al., 2000), although it should be noted that no test of sensitivity change between L_n and the first T_x measurement is made within the SAR protocol (Wallinga et al., 2000a). The final limitation may be addressed through performance of a dose-recovery test, whereby a sample is bleached and irradiated with a known dose, and the ability of the SAR protocol to return the laboratory D_e is assessed . The dose-recovery test is important because of the varying luminescence behaviour of different quartz and feldspar samples, which may be associated with trace element geochemistry, geological history or past radiation exposure (e.g. Duller, 2004; Murray and Wintle, 2003).

4.3.2. **Sample Preheating**

An essential part of the SAR protocol is preheating samples prior to stimulation, and stimulation at an elevated temperature. Preheating evicts charge from traps with lower thermal stabilities, such as the 110 ˚C TSL trap, which are populated during laboratory irradiation. Some of the evicted charge migrates to the 325 ˚C OSL trap where it contributes to the total observed luminescence upon stimulation (Zimmerman, 1971). Charge which accumulates in thermally unstable centres decays to the 325 ˚C OSL trap over geological time within the natural environment, and thus failure to include this electron population in the regenerative doses of the SAR protocol can result in sample

age overestimation. Preheating therefore ensures that the sampled electron population is equal throughout the SAR analysis protocol.

Optical stimulation of quartz is undertaken at 125 ˚C to ensure that the 110 ˚C TSL trap does not contribute to the observed signal. However, heating during stimulation causes thermal quenching (Figure 4 in Spooner, 1994b), whereby the probability of radiative (OSL), rather than non-radiative (phonon) recombination is reduced (Aitken, 1998).

4.3.3. **Thermal Transfer**

Preheating causes thermal transfer (TT) which comprises either 'basic transfer' of electrons from thermally stable optically-insensitive traps to optically-sensitive traps such as the 110 ˚C TSL trap, or 'double-transfer' which is a second order kinetic process and involves photo-transfer of electrons from the OSL trap to stable 'refuge' traps and back into the OSL trap after preheating (Aitken, 1998). Any TT electrons recombine upon stimulation, resulting in a cumulatively increasing charge throughout analysis which can be detected using a preheat (PH) plateau test. The D_e of multiple aliquots of the same sample are compared for the different PH treatments in order to determine a stable PH temperature (Murray and Wintle, 2000). If the D_e ratio from the lowest and highest PH temperature is less than 1.2, thermal transfer PH dependence is negligible, whereas a value > 1.2 indicates rising PH dependence (Ward et al., 2003). It is particularly important to avoid TT in young or dim samples as D_e values are low, and the transferred signal can be proportionally large (Ward et al., 2003). Samples of glacial origin often have low luminescence sensitivity and are particularly susceptible to TT (Rhodes and Pownall, 1994) which is pertinent to this research.

The preheat prior to T_x (PH2), also referred to as the 'cut heat', has a lower temperature (Murray and Wintle, 2000, 2003) and often a shorter duration than that used prior to measuring L_x, in order to minimise sensitivity changes between the L_n/L_x and T_x measurements, whilst always ensuring that the same proportion of signal is analysed.

4.3.4. **Recuperation**

Recuperation is manifested as non-zero sample response following zero-dose (Aitken and Smith, 1988; Murray and Wintle, 2000; Stokes et al., 2000) and is attributed either to optically insensitive traps which are only partially bleached during preheating, or alternatively to the thermal transfer of charge during PH2, which is then bleached during a more stringent PH1 (Murray and Wintle, 2000). Deconvolution of the OSL emission to isolate the fast component (C_F) (see section 4.7.1.2) in affected samples, has been shown

to successfully remove recuperation, indicating that recuperated charge may not be stimulated from the main OSL trap (Jain et al., 2003; Murray and Wintle, 2003). Murray and Wintle (2003) have proposed inclusion of a high temperature hot bleach (HB) at 280 ˚C in the SAR protocol. This HB fully empties the 110 ˚C TSL trap at the end of each SAR cycle and provides an experimental solution to recuperation. An alternative approach of recuperation measurement and correction has been proposed by Jain et al. (2002) whereby recuperation as a function of increasing PH temperature is explored (see Section 4.4.3). Recuperation is used as an indicator both of the thermal sensitivity of a quartz sample, and of its suitability for luminescence dating (Murray and Wintle, 2000, 2003).

4.4. Sample Analysis Protocol

An initial SAR protocol (Murray and Wintle, 2000) was selected to examine the sample luminescence characteristics (Table 4.2). Measurements were plotted using Analyst v.3.22b which was used for all analyses throughout this research (Duller, 2005). Twelve aliquots were analysed (two from six samples), revealing that the Norwegian quartz behaved poorly when analysed with SAR: no aliquots produced a dose response curve from which D_e could be calculated (Figure 4.1). Sample OSL sensitivities varied by a factor of two, and samples were significantly affected by recuperation (see Section 4.4.3). These initial results indicate that for these samples the SAR protocol requires significant modification, which was informed from the results of the dose recovery and PH plateau experiments.

Table 4.2: Initial SAR protocol

Natural/Regenerative Dose	N, 1, 2, 3, 4, 0, 1, 1 Gy
TSL	190 ˚C, 10 s, 5 ˚C/s
OSL	125 ˚C, 40 s, 5 ˚C/s, 90% power (Lx)
Test Dose	1 Gy*
TSL	180 ˚C, 10 s, 5 ˚C/s
OSL	125 ˚C, 40 s, 5 ˚C/s, 90% (Tx)

*The dose rates of Risø 1 and Risø 2 vary by ~ 20%, as Risø 2 has a more radioactive source. Analyses were carried out over a three year period, during which time the dose rate of both readers reduced by 0.10 Gy s^{-1}. Most sequences were run on both readers, therefore the dose in Gy listed in the protocols throughout this thesis are averages of both reader dose rates. This is more tangible than listing the dose as a unit of time. All data are corrected relative to the true dose rate, calculated specifically for each reader and measurement date.

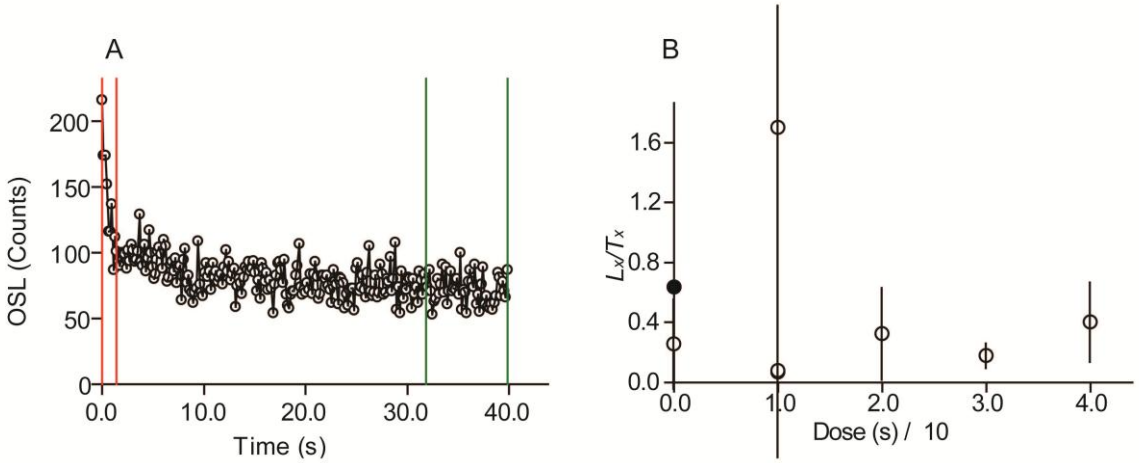

Figure 4.1: (A) OSL decay curve and (B) dose response data for a single aliquot of FAB79. The filled data point on the dose response plot is L_n/T_n. The signal integration interval is highlighted in red, and the background integration interval highlighted in green.

4.4.1. **Aliquot Acceptance Criteria**

Due to the poor luminescence sensitivity of the quartz analysed, and its susceptibility to thermal transfer, it has been necessary for the criteria to be more relaxed than those adopted by some luminescence practitioners (e.g. Jacobs et al., 2008; Rodnight et al., 2006; Thrasher et al., 2009b), however they are as stringent as many (e.g. Feathers, 2003; Klasen et al., 2007). As all uncertainties are appropriately accounted for this does not limit the utility of this data set, other than that the precision is necessarily reduced.

Aliquot acceptance criteria used in this study are 1) recycling ratios within 20% of unity; 2) signal intensities are ≥ 3 σ above background; 3) recuperation within 20% of the normalised natural signal; and 4) IR depletion ratio within 20% of unity (Duller, 2003). An additional fading test was performed to investigate the stability of the quartz luminescence for some samples (Fragoulis and Stoebe, 1990; Fragoulis and Readhead, 1991; Wintle, 1973). Fading experiments (e.g. Wallinga et al., 2000b) are discussed in more detail relative to feldspar in Chapter 5, and comprise the comparison of a prompt and delayed sensitivity corrected OSL measurement. The quartz samples were dosed with either 4.97 ± 0.34 or 24.87 ± 1.71 Gy prior to a pause of 7,200 s. Fading is identified by a reduction in the luminescence intensity of the delayed, relative to the prompt, stimulation. No samples exhibited fading, suggesting that the samples were pure quartz or that no fading feldspar grains were present. The delayed luminescence sensitivity was brighter for some of the samples, indicative of sensitivity changes throughout analysis.

4.4.2. **Preheat Plateau and Dose Recovery Experiments**

An initial dose recovery (N = 10 Gy) experiment was carried out on two aliquots from six different samples from Fåbergstølsdalen and Fåbergstølsgrandane (Table 4.3). Of the 12 aliquots analysed, 11 were accepted and had mean D_e of 8.57 ± 1.84 Gy (1 σ uncertainty) which despite its low level of precision, is within uncertainties of the administered dose. It should be noted that in these initial screening experiments, all aliquots that produced a dose response curve which allowed D_e interpolation were accepted, with no additional selection criteria employed (i.e. recycling ratio, recuperation and other acceptance criteria were not considered). Signals were integrated over the first 1.6 s (channels 1-10) and background from the final 8 s (final 50 channels).

Table 4.3: Dose recovery protocol

OSL	0 ˚C, 100 s, 90% power
Pause	7500 s
OSL	0 ˚C, 100 s, 90% power
Natural/Regenerative Dose	N=10, 10, 20, 30, 40, 0, 10, 10 Gy
TSL	190 ˚C, 10 s, 5 ˚C/s
OSL	125 ˚C, 40 s, 5 ˚C/s, 90% power (Lx)
Test Dose	1 Gy
TSL	180 ˚C, 10 s, 5 ˚C/s
OSL	125 ˚C, 40 s, 5 ˚C/s, 90% (Tx)

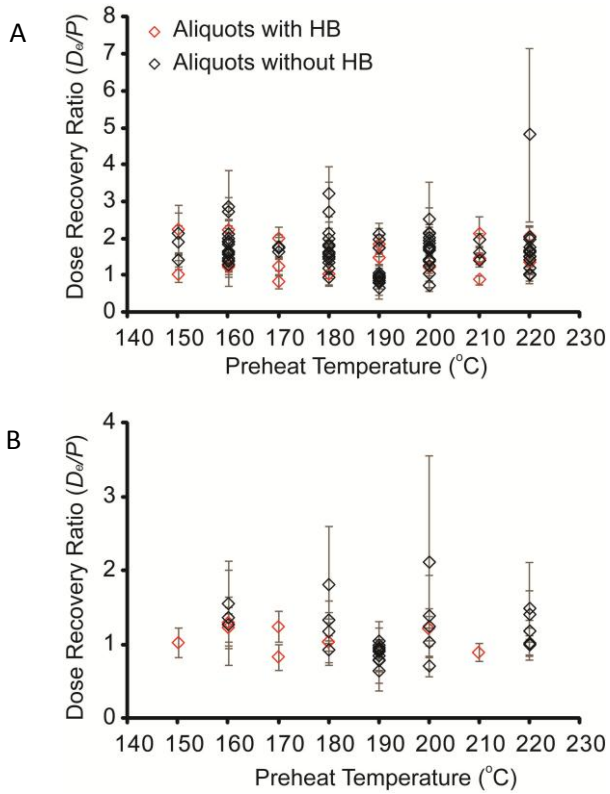

Figure 4.2: Dose recovery preheat plateau results. (A) All aliquots have a D_e within error of the given dose. (B) Aliquots that are within 10% of the given dose where uncertainties are included. HB refers to a hot bleach treatment of 280 ˚C at the end of each cycle (see section 4.4.2 for details).

As the initial dose recovery experiment demonstrated that the D_e was recoverable (Figure 4.2), the influence of PH temperature on dose recovery was explored, with a series of dose recovery pre-heat plateau experiments (Murray and Wintle, 2000). Pre-heat temperatures ranging from 150 – 220 °C were explored, with PH2 temperatures either equal to PH1, or 10 °C cooler. The duration of both pre-heat treatments was 10 s.

The intra- and inter-sample response to different PH temperatures varied. 132 aliquots of seven different samples were analysed and 102 aliquots fulfilled the analytical acceptance criteria (see Section 4.4.1), of which only 10% recovered a D_e within ± 10% of the administered dose (uncertainty not considered). No clear pattern of thermal influence on dose recovery could be derived and accepted aliquots had PH temperatures ranging from 150 to 220 ˚C, although half had PH of 190 ˚C. If a threshold of D_e recovery ± 20% is used, acceptance only increases to 18 %. If uncertainties are included, this percentage increases to 35% at a ± 10% threshold, and 46% at a ± 20% threshold, indicative of the low precision D_e values obtained. The consideration of dose recovery in isolation of uncertainties was prompted because of the large uncertainties associated with this sample suite.

In addition to testing PH temperature, the influence of a 280 ˚C HB (Murray and Wintle, 2003) for 10 s was investigated for 24 aliquots (see Section 4.3.4). 22 of these aliquots were accepted, however only 38% (8) returned the administered dose within uncertainties. A PH1 of 180˚C for 10 s was selected, followed by a PH2 of 180˚C for 10 s.

4.4.3. **Recuperation**

The zero-dose regeneration step of the SAR protocol is designed to detect recuperation (see section 4.3.4). Recuperation is particularly identified when signal intensities are low and a small proportion of charge transfer produces a large contribution to the total signal (Ward et al., 2003).

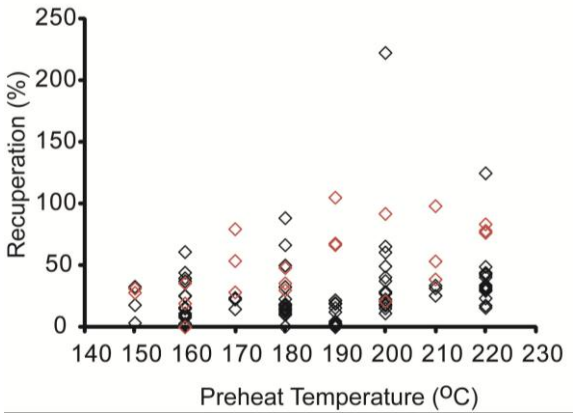

Figure 4.3: Recuperation of all aliquots used in the dose recovery and preheat plateau experiments, as a function of preheat temperature.

Figure 4.3 illustrates that there is a positive relationship between PH temperature and recuperation amount, indicating that recuperated charge may originate from traps deeper than the 325 ˚C trap. Thermal treatment can also produce recuperation and samples treated with a HB were most affected, consequently the HB was omitted from the final SAR protocol.

4.4.4. **Thermal Transfer derived Recuperation**

Recuperation may be caused by TT, therefore detailed investigations into the proportion of transferred charge were carried out following the experimental design of Jain et al. (2002). Recuperation due to thermal transfer was measured by assessing the 'natural' luminescence response of a bleached sample following a series of different preheat temperatures (Table 4.4). A small T_x is administered after each 'natural' to normalise the different aliquots, and T_x is kept low to minimise the amount of charge available for transfer during preheat. The amount of recuperation is then calculated:

Eq. 4.1: $TT_i' = (\Sigma N_i')/T_{160}$

Eq. 4.2: $N_i' = N_i/\alpha$

Eq. 4.3: $\alpha = T_i/T_{160}$

where TT_i' is thermal transfer over 130 – 300 ˚C, N_i' is the corrected thermal transfer signal, and T_i the measured response to a 1 Gy (10 s) test dose at i = 160 – 180 ˚C. The samples are so sensitive to thermal treatment, as demonstrated in the PH plateau experiments above, that in order to avoid thermal transfer from traps with thermal stabilities > 325 ˚C (see section 4.4.2), the lowest possible thermal treatments should be used. Minimum preheat temperatures adopted by OSL practitioners are typically in excess of 180 ˚C, however through calculating trap kinetics after Aitken (1998), it is apparent that charge in the unstable 110˚C TSL trap is reduced by 93% following a 10 s 130 ˚C preheat. Therefore PH temperatures as low as 130 ˚C were explored for a single sample, GAUP41.

Table 4.4: Thermal transfer OSL analysis protocol after Jain et al. (2002).

OSL	0 ˚C, 100 s, 90% power
Pause	1000 s
OSL	0 ˚C, 100 s, 90% power
TSL	130 ˚C – 300 ˚C (20 ˚C increments), 10 s, 5 ˚C/s (T_{160}, N_i)
OSL	125 ˚C, 40 s, heating rate – 5 ˚C/s, 90% power
Test Dose	1 Gy
TSL	160 to 180 ˚C, 10 s, heating rate – 5 ˚C/s
OSL	125 ˚C, 40 s, heating rate – 5 ˚C/s, 90% power (T_i)

The majority of samples exhibit clear TT dependence with increasing PH temperature; samples from Fåbergstølsgrandane are the worst affected (Figure 4.4). Uncertainties are calculated from the standard deviation (1σ) of the different signal

intensities. No increase in thermal dependence up to a PH temperature of 180 ˚C was detected. Therefore 180 ˚C was selected as the PH temperature, in accordance with the OSL convention of using the most stringent (highest) PH temperature possible. The TT_i' values can be interpolated onto dose response curves to give the apparent dose due to thermal transfer, i.e. TT_i (Gy), however due to the extremely low precision of the majority of samples, this provided no panacea and was not pursued.

These experiments support selection of 180 ˚C as the sample PH temperature, and indicate that a large number of samples will be rejected on grounds of recuperation. The influence of aliquot rejection due to recuperation was investigated through assessing changes in D_e with changing recuperation acceptance criteria (Figure 4.5A-C). Over 50% of the accepted quartz SAR aliquots were rejected with a recuperation threshold of > 10% of the D_e and increasing this threshold to 20% reduced rejection to 19%. As recuperation is calculated as a proportion of D_e, those samples with the lowest D_e values are the worst affected. All samples investigated exhibit reducing mean D_e and mean uncertainty with more relaxed acceptance criteria for recuperation (Table 4.5, Figure 4.5 A-C). Although it is acknowledged that mean D_e may not be a valid estimate of the palaeodose (see section 4.10), it provides a rapid mode of analysis for sample comparison. This is in agreement with the literature (e.g. Murray and Wintle, 2003) as recuperation is cited as a cause of palaeodose underestimation. However, these results indicate that where recuperation criteria are applied, age overestimation may result within partially bleached distributions containing aliquots with very young grains, as the best bleached samples are rejected. This challenge has been exacerbated by the very low sensitivity of this sample suite, attributed to the presence of a weak C_F (see section 4.7) and poor signal to noise ratios.

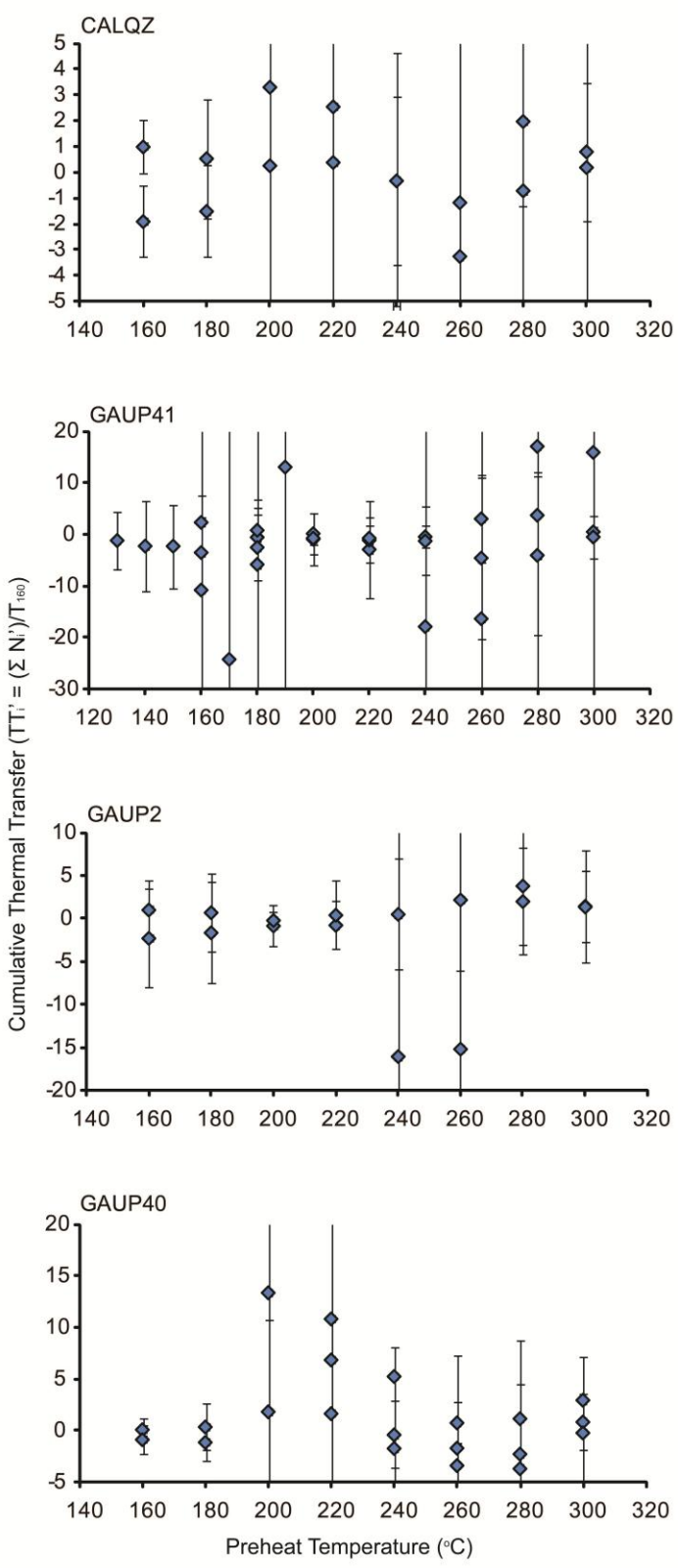

Figure 4.4: Thermal transfer results following the protocol of Jain et al. (2002). Note the varied response of the different samples to changing preheat temperatures.

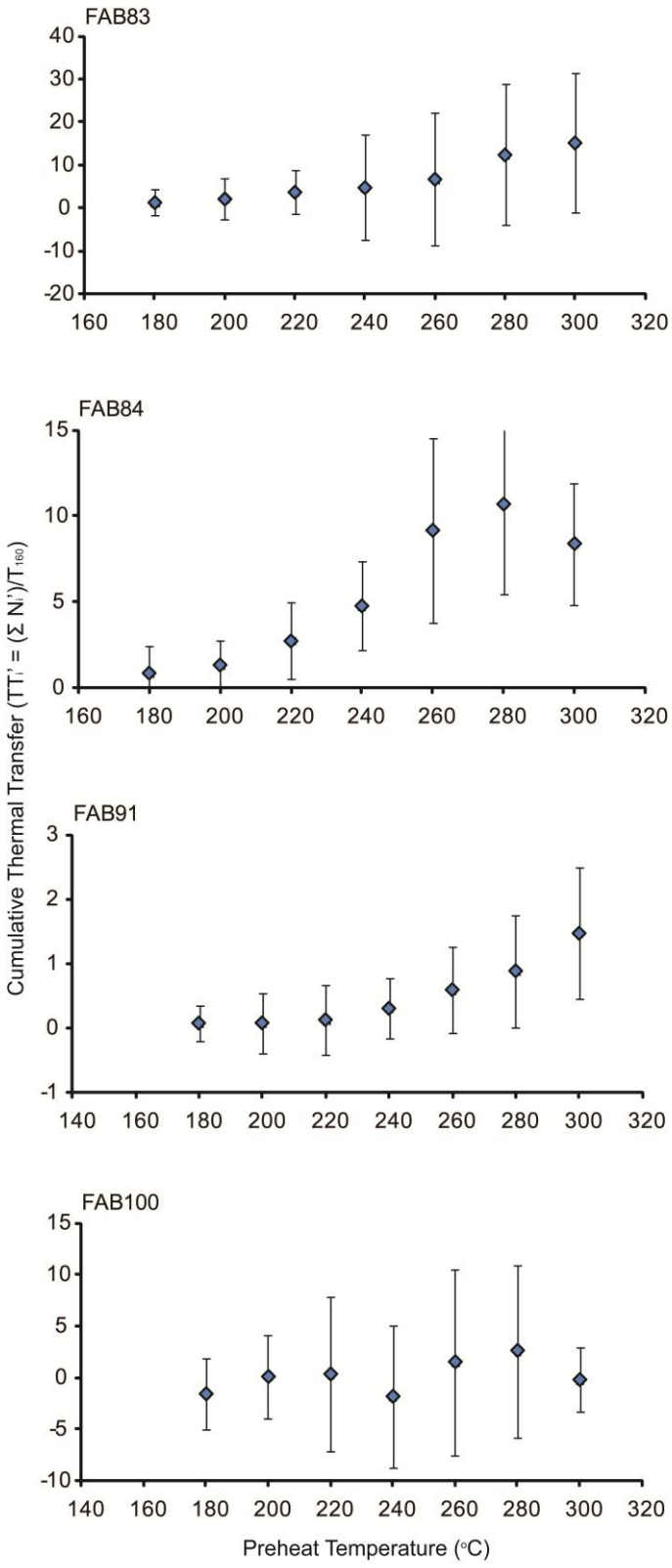

Figure 4.3 cont.: Thermal transfer results following the protocol of Jain et al. (2002). Note the varied response of the different samples to changing preheat temperatures.

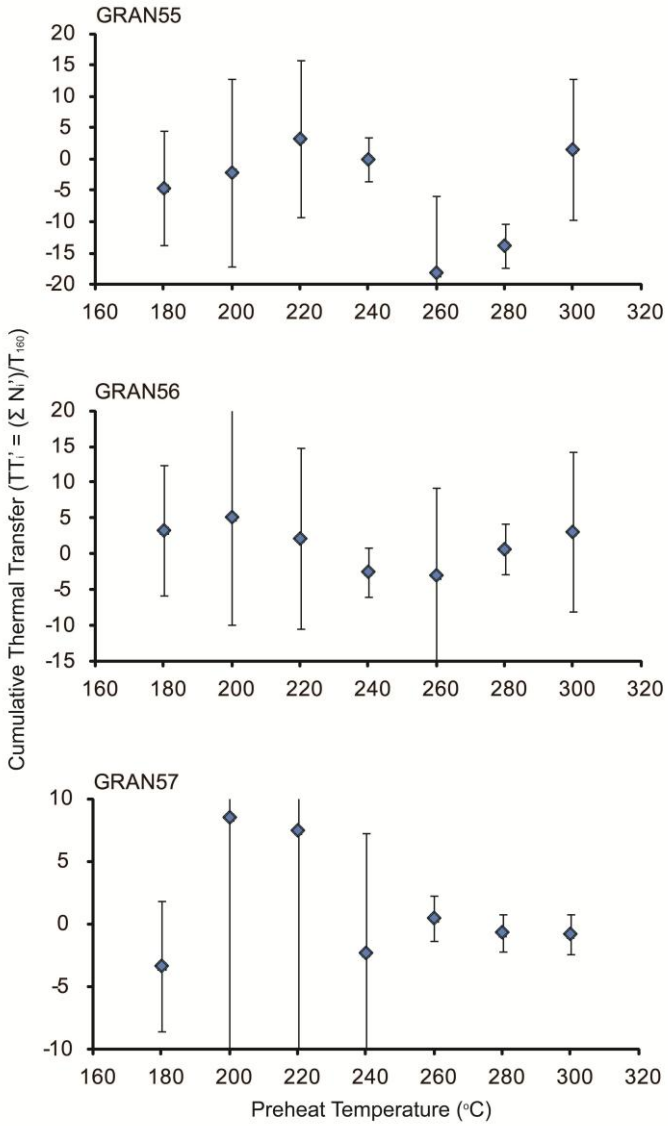

Figure 4.3 cont.: Thermal transfer results following the protocol of Jain et al. (2002). Note the varied response of the different samples to changing preheat temperatures.

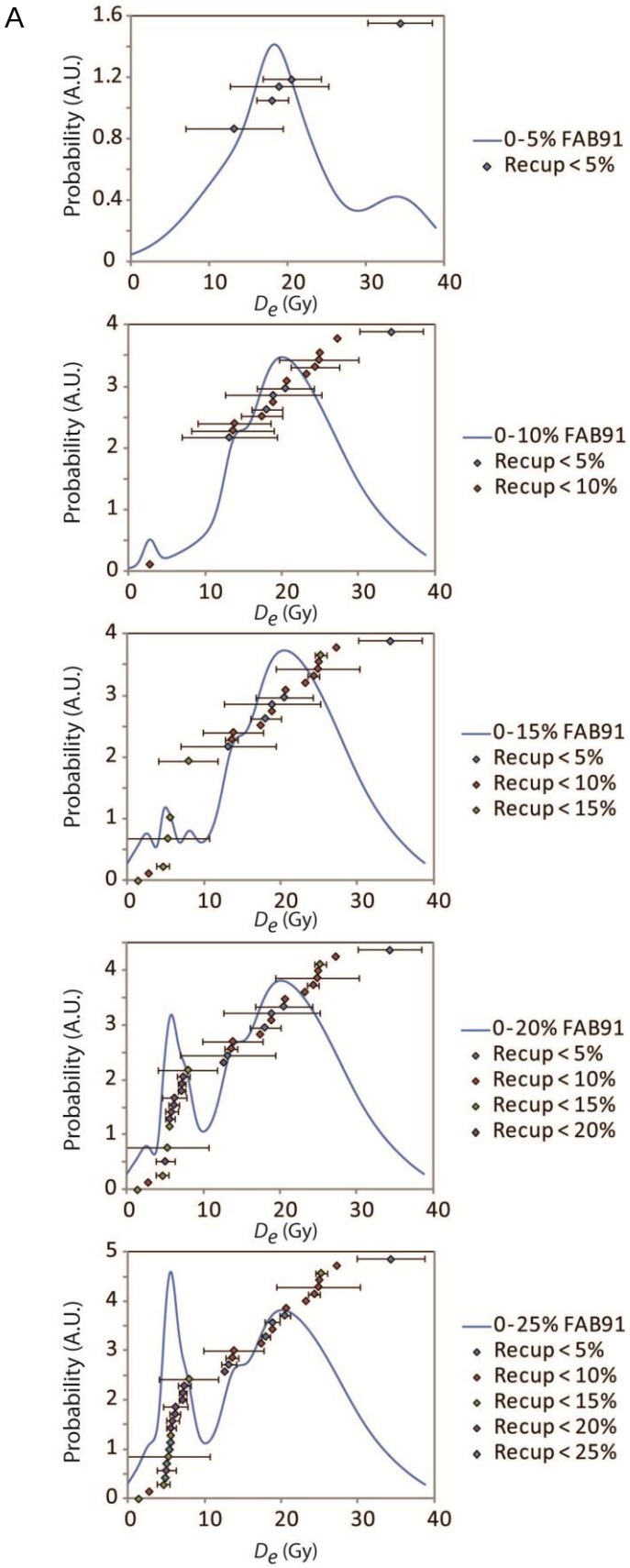

Figure 4.5: A series of probability density functions derived from the inclusion of aliquots with different degrees of recuperation. (A) FAB91 and (B) FAB86 were two of the samples most affected by recuperation, whereas (C) FAB94 was least affected.

B

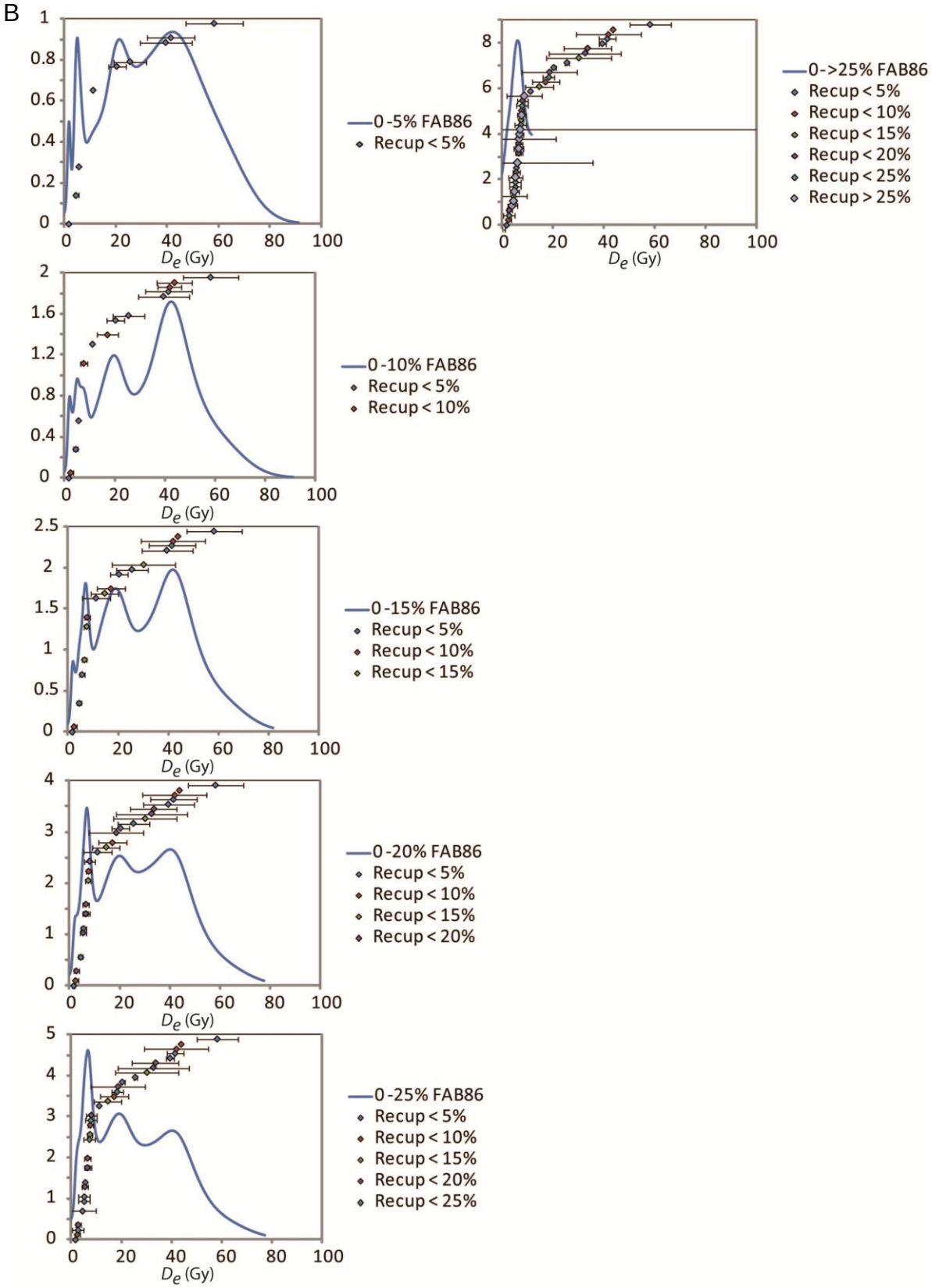

Figure 4.4 cont: A series of PDFs derived from the inclusion of aliquots with different degrees of recuperation. FAB86 was one of the samples most affected by recuperation.

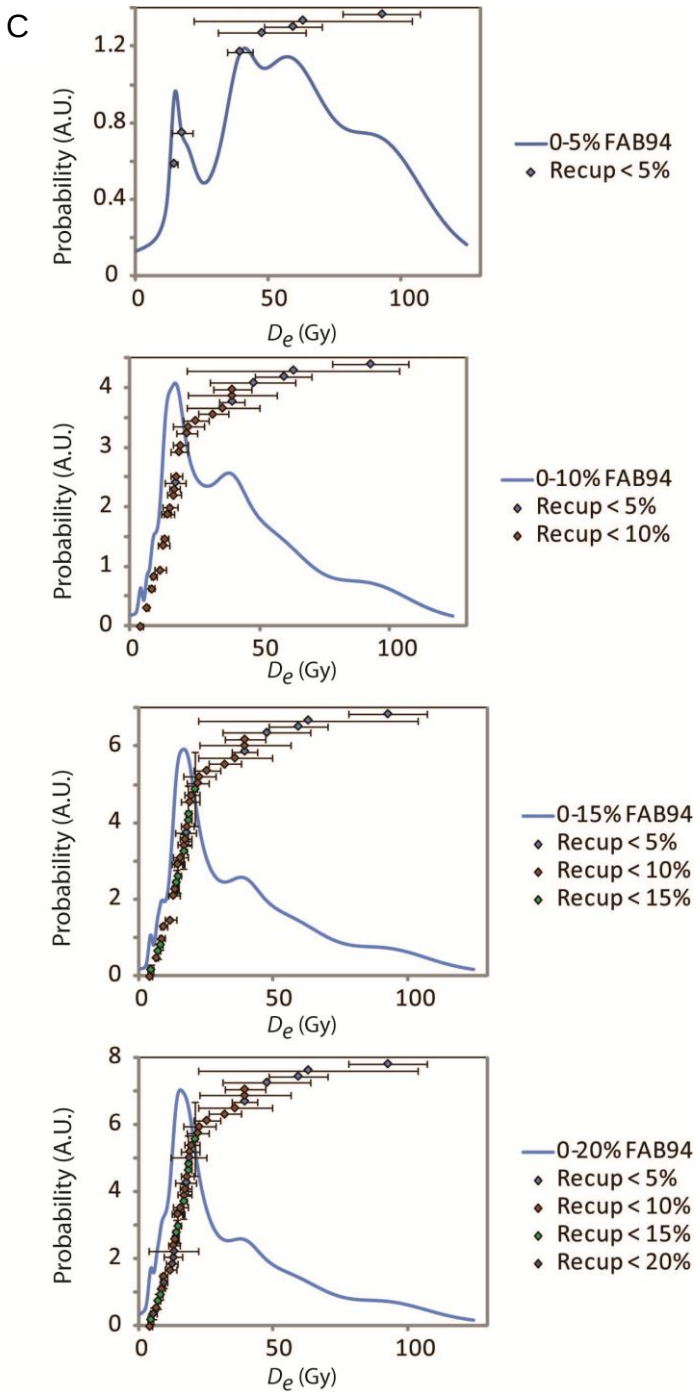

Figure 4.4 cont.: A series of probability density functions derived from the inclusion of aliquots with different degrees of recuperation. FAB94 was least affected by recuperation.

Table 4.5: Changing mean D_e for three samples with different recuperation criteria

	FAB91		FAB86		FAB94	
Recuperation	n	D_e (Gy)	n	D_e (Gy)	n	D_e (Gy)
0 – 5%	5	20.97 ± 4.49	9	23.15 ± 5.38	7	47.63 ± 13.28
0 – 10%	16	19.76 ± 3.71	14	22.97 ± 4.76	28	26.31 ± 6.42
0 – 15%	22	16.64 ± 3.13	18	21.12 ± 4.80	37	23.19 ± 5.53
0 – 20%	31	13.84 ± 2.58	26	19.03 ± 4.91	43	21.59 ± 5.32
0 – 25%	32	13.57 ± 2.52	32	16.91 ± 4.62		
0 – > 25%	35	12.85 ± 2.43	44	13.86 ± 7.57		

4.4.5. **Selected SAR protocol**

Based on the results outlined in the preceding sections the final SAR protocol that was selected and used for the analysis of all of the Norwegian quartz samples is listed in Table 4.6.

Table 4.6: Quartz SAR protocol

Natural/Regenerative Dose	5, 10, 20, 30, 0, 5, 5 Gy
TSL	180˚C, 10 s, 5˚C/s
IRSL	20˚C, 40 s, 5˚C/s (final cycle only
OSL	125˚C, 40 s, 5˚C/s, 90% power (Lx)
Test Dose	5 Gy
TSL	180˚C, 10 s, 5˚C/s
OSL	125˚C, 40 s, 5˚C/s, 90% (Tx)

4.4.6. **Single Grain Analyses and Aliquot Size Selection**

Recent developments have facilitated the rapid analysis of single grains of quartz and feldspar (Bøtter-Jensen et al., 2000; Duller et al., 2000; Duller and Murray, 2000), and such analyses are especially recommended where partial bleaching of a sample suite is suspected (Duller, 2008). A sub-set of material was sent to Aberystwyth University where it was analysed using a single-grain laser luminescence attachment. 400 grains of FAB80 were analysed with the protocol listed in Table 4.7.

Table 4.7: Quartz single-grain SAR protocol

Natural/Regenerative Dose	50, 100, 200, 400, 500, 1000, 2000, 0, 50, 50 s
TSL	180˚C, 10 s, 5˚C/s
IRSL	40 ˚C, 40 s, 5˚C/s, 90% power – IR Test cycle only)
Green Laser OSL	125˚C, 1 s, 5˚C/s, 90% power (Lx)
Test Dose	100 s
TSL	180˚C, 10 s, 5˚C/s
Green Laser OSL	125˚C, 1 s, 5˚C/s, 90% (Tx)

Single grain analyses are characterised by variations in grain signal intensity over several orders of magnitude (Duller et al., 2000; Murray and Roberts, 1997). Duller and Murray (2000) observe that 95% of the observed signal from an aliquot may be derived from just 5% of the grains (cf. McFee and Tite, 1994; Murray and Roberts, 1997). The signal intensity of a single grain is the product of its sensitivity and palaeodose, thus within large aliquots D_e values are skewed towards those of the brightest grains (Duller et al., 2000; Thomsen et al., 2003), which may cause D_e overestimation. Grain populations where this is likely to be problematic can be identified through plotting the total light sum relative to the proportion of grains that contribute to it (Duller et al., 2000) (Figure 4.6). Some quartz have extremely poor luminescence sensitivity, and glacial sediments in particular have been shown to yield a very small proportion of luminescent grains (e.g. Duller, 2006).

Only 1 of 400 grains measured produced both a dose response curve from which D_e could be interpolated (Figure 4.7), and satisfied the acceptance criteria applied to the single aliquot analyses (see Section 4.4.1). Systematic uncertainties are higher in single grain analyses, and were estimated at 3% (Duller et al., 2000; Thomsen et al., 2005; Truscott et al., 2000).

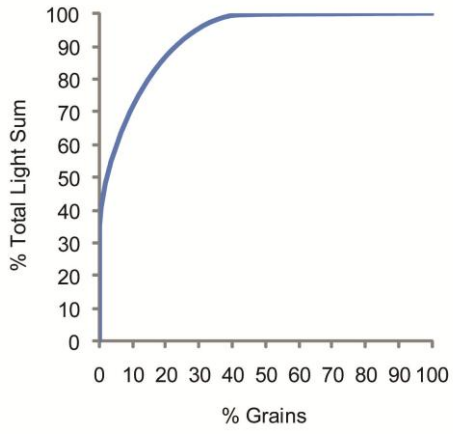

Figure 4.6 (left): Total light sum of the 400 grains of FAB80 analysed.

Figure 4.7 (below): Single grain natural luminescence (A) and dose response curve (B) for a single grain of FAB80.

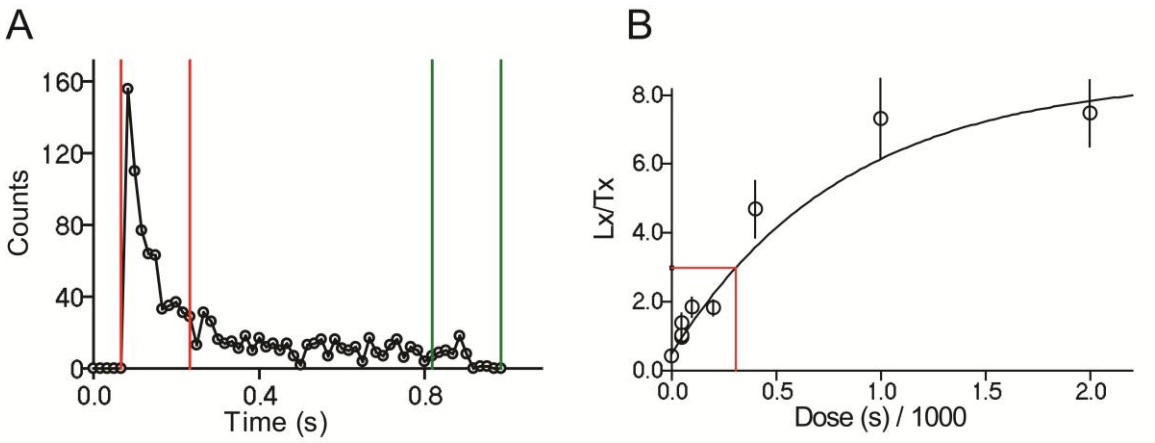

Where the light sum of all grains is calculated, irrespective of their ability to produce independent dose response curves, it is apparent that one grain contributes > 40% of the total observed luminescence, and this is not the grain from which a D_e could be interpolated. 95% of the signal is derived from 30% of the grains. The low single grain acceptance rate (0.25%) means that this sample suite is not suitable for single grain analysis because of the time required to produce a data set large enough to be statistically robust. That a single grain contributes > 40% of the total signal is concerning, as it suggests that within single aliquot analyses, D_e values will be skewed disproportionately towards these values (Duller et al., 2000; Rhodes, 2007; Thomsen et al., 2003). However, that 30% of grains contribute to 95% of the total signal indicates that such averaging will be mediated.

Thrasher et al. (2009b) advocate the use of small aliquots (SA) of ~ 20 grains for the dating of glacigenic sediments, as if 5% of those grains are luminescent, then it is

equivalent to single grain dating. As the luminescence sensitivity of these samples is so poor, large aliquots of ~ 400 grains have been analysed in order to improve aliquot acceptance rates, the number of replicates and thus increase the rigour of the D_e obtained.

4.5. Background Calculation

4.5.1. The Early Background (EBG) Method

Recently some members of the OSL community has determined that use of an early background rather than a late background measurement is most appropriate, because the contribution of the slow (C_S) component is minimized relative to the C_F for young samples, which is the preferred signal for luminescence analysis, and the component that the SAR protocol is designed to measure (Murray and Wintle, 2000). Cunningham and Wallinga (2010) have proposed a quantitative method for determining appropriate signal and background integration intervals. Initially they fit the CW-OSL decay curve to three components, the C_F, medium (C_M) and C_S components, with fixed decay rates (α) of 2.2 s^{-1}, 0.44 s^{-1} and 0.02 s^{-1} using the formula:

Eq. 4.4: $$n_{oi}\alpha_i \exp(-\alpha_i t)$$

where α_i is the decay rate of the component, n_{oi} is the initial start population of electrons for each component, fixed at 100 for the first two components, and 1000 for the final component, and *t* is the stimulation time (s).

Once the components have been fitted, the contribution of each to total signal as a function of time is calculated. The derived values are used to determine the integration time, which minimises the contribution of the C_S and C_M to the signal and background, respectively. Cunningham and Wallinga (2010) advocate a balance between maximising C_F contribution whilst 1) not exceeding 5% for RSE of the net, background corrected signal, 2) calculating the background immediately after the signal, and 3) using a background integration period not exceeding 2.5 times the signal integration period.

Three aliquots of FAB42 were analysed as it has the brightest natural luminescence sensitivity of the Norwegian quartz sample suite. In contrast to Cunningham and Wallinga (2010), the nonlinear least squares (*nls)* function (Bates and Watts, 1988) was used in R 2.11.1 to fit each component (Figure 4.8). All R code is provided in Appendix B. Dose response curves calculated with the EBG method were plotted in Analyst v.3.22b (Duller, 2005). Results indicate that FAB42 has a C_F for only 0.64 or 0.80 s (4 or 5 channels), therefore iterations to determine the RSE for net background corrected signals within this

period were calculated (Table 4.8), in order that the criteria of Cunningham and Wallinga (2010) outlined above could be applied. Figure 4.8 also indicates that for aliquot 2 the fast component never contributes the maximum proportion of total signal, in contrast to the other two aliquots. This may be indicative of partial bleaching, whereby the fast component is preferentially depleted relative to the medium or slow components, or alternatively that even the Norwegian quartz with highest OSL sensitivity, is not always fast component dominated.

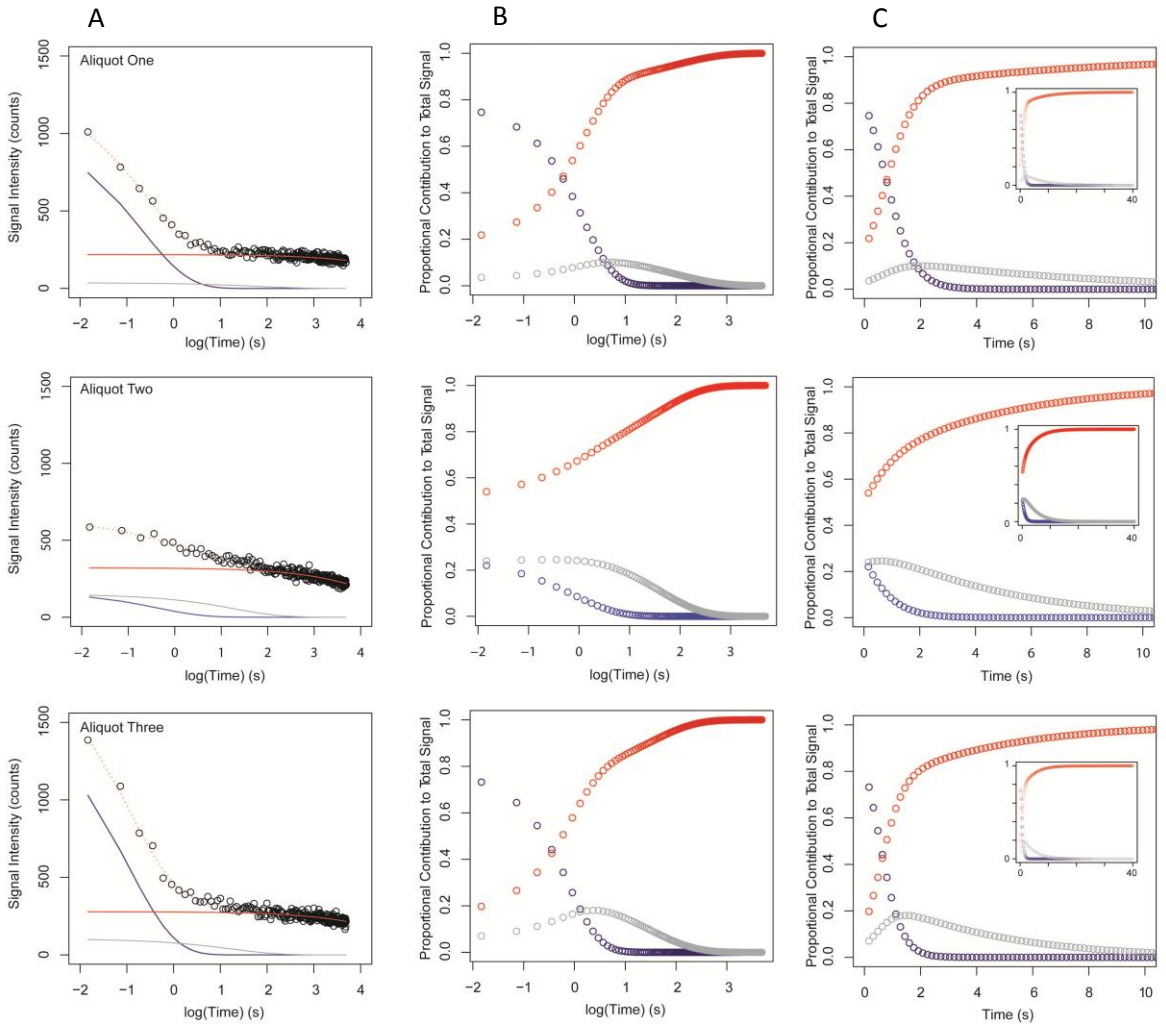

Figure 4.8: EBG model results for three aliquots of FAB42 which are presented in Table 4.8. Blue data points represent the C_F, grey the C_M and red the C_S. Graphs in column (A) present the model fit, (B) the proportion of the signal from each component as a function of log (time), and (C) as a function of time over the first 10 s of stimulation. The inset in column C shows contributions for the full 40 s stimulation period. Note that for aliquot 2, the fast component never contributes the greatest signal proportion.

With the exception of a signal integration period of 0.16 s, all integrations fulfil the RSE <5% criterion, but the dose response curve fitting improves with longer integration periods (Figure 4.9), reflecting improved signal to noise ratios. The minimum ratio at which a dose response curve can be plotted is 0.8 s for all aliquots (background as listed in

Table 4.8). When these integration intervals were applied to other samples which had lower luminescence signal intensities, such as FAB84, the shape of the dose response curves was still severely affected which may be indicative of 1) sensitisation of the C_S throughout analysis, 2) an unstable C_M, or 3) poor signal to noise ratios.

Table 4.8: RSE values for three aliquots of FAB42 using different integration periods. Background integrations are always 2.5 times greater than signal integration after Cunningham and Wallinga (2010).

Signal Int. (s)	Background Int. (s)	RSE Aliquot 1	RSE Aliquot 2	RSE Aliquot 3
0.16	0.32 - 0.64	8.12	44.43	6.30
0.32	0.48 - 0.80	3.06	4.72	2.49
0.48	0.64 - 1.76	2.32	3.21	1.98
0.64	0.80 - 2.24	2.00	2.54	1.73
0.80	0.96 - 2.88	1.83	2.21	1.60
0.96	1.12 - 3.36	1.70	1.98	1.51
1.12	1.28 - 4.00	1.62	1.82	1.44
1.28	1.44 - 4.48	1.55	1.70	1.39
1.44	1.60 - 5.12	1.50	1.60	1.33
1.60	1.76 - 5.60	1.45	1.52	1.29

The EBG method is not suitable for this sample suite, because of the low signal to noise ratios. Extending the signal integration period would address this, however as it would involve integration over the C_M and C_S, the benefits of the EBG method would be negated. Consequently it was decided to continue using a late light subtraction, as has been used conventionally in luminescence dating over the past twenty years. Signals were integrated over the initial 1.6 s and backgrounds over the final 8 s. Investigation of the different quartz components using the EBG indicated that these samples may not be C_F dominated, and this was explored further using the Fast ratio of Durcan and Duller (2011).

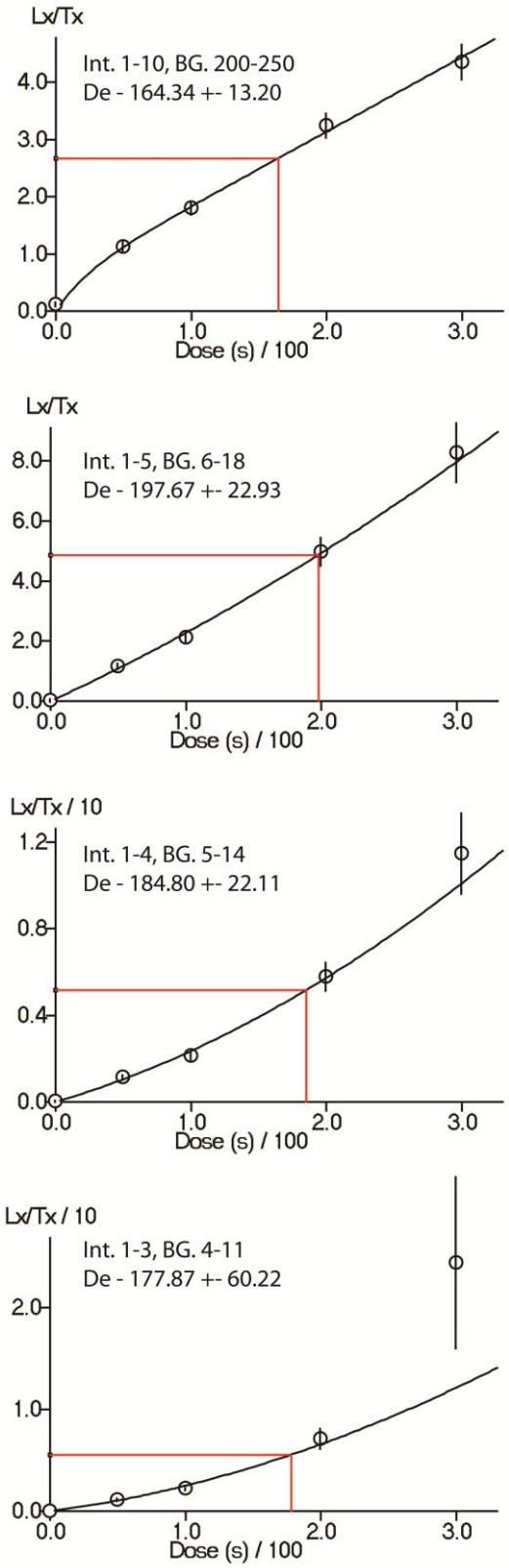

Figure 4.9: Four graphs showing the influence on interpolation of the D_e of changing the signal and background integration intervals for an aliquot of FAB42, the integration intervals are indicated on each of the graphs, and the top values (Int. 1-10, BG 200-250 were those adopted. See text for details.

4.5.2. **The Fast Ratio**

An alternative method through which the C_F can be isolated is through using the Fast ratio proposed by Durcan and Duller (2011). This technique is more rapid than LM-OSL analyses and enables samples to be rapidly screened through isolating components using the energy (*E*, mJ•cm^{-2}) required to stimulate them:

Eq. 4.5: $$E = \frac{-ln\left(\frac{x}{100}\right)}{\sigma_p}\lambda_{470}$$

where $\boldsymbol{x}$ is the percentage of the initial signal, λ_{470} is the energy input from 470 nm blue diodes (4.23 x 10^{-19}, mJ photon^{-1}) and σ_p is the photoionisation cross section of the component of interest e.g. C_F has σ_p 2.41 x 10^{-17} cm^{-2} (values calculated for Risø 1, see Section 4.7.2). The times required to bleach the different components are listed in Table 4.9, and this information can be used to calculate the Fast ratio (Durcan and Duller, 2011), which is a measure of the proportion of signal derived from C_F at the outset of stimulation (L_1) (Table 4.9).

Table 4.9: Energy and time required to bleach each of the different components. Photoionisation cross sections are calculated for Risø 1, see Section 4.7.2.

		σ_p (cm^2)	C_F 2.41 x 10^{-17}	C_M 4.30 x 10^{-18}	C_{S1} 6.97 x 10^{-19}	C_{S2} 6.87 x 10^{-20}	C_{S3} 2.46 x 10^{-20}	C_{S4} 1.56 x 10^{-21}
% reduction of the initial signal	50%	mJ·cm^{-2}	12	68	420	4,267	11,905	187,393
		s	0.4	2	15	154	429	6,746
	25%	mJ·cm^{-2}	24	136	841	8,533	23,811	374,786
		s	0.9	5	29	299	833	13,111
	10%	mJ·cm^{-2}	40	227	1,396	14,173	39,549	622,506
		s	1.5	8	50	510	1,424	22,410
	5%	mJ·cm^{-2}	53	295	1,816	18,440	5,1454	809,899
		s	1.9	11	65	664	1,852	29,156
	2.5%	mJ·cm^{-2}	65	363	2,236	22,706	63,360	997,292
		s	2	13	81	817	2,281	35,902
	1%	mJ·cm^{-2}	81	453	2,792	28,346	79,098	1,245,012
		s	3	16	101	1,020	2,848	44,820
	0.1%	mJ·cm^{-2}	121	680	4,188	42,519	118,647	1,867,518
		s	4	24	151	1,531	4,271	67,230

When the Fast ratio is less than 20, less than 90% of the initially stimulated signal is derived from the C_F (Durcan and Duller, 2011) and greater contributions from the C_S and C_M are anticipated. The Fast ratio method therefore provides a rapid, quantitative method of screening samples for their suitability for OSL analysis. Calculation of the Fast ratio is achieved from:

Eq. 4.6: $$Fast\ ratio = \frac{L_1 - L_3}{L_2 - L_3}$$

L_2 is set to coincide to the peak relative contribution of the C_M, when the C_F has been depleted to 1% (Table 4.9) and L_3 is averaged over the energy range where the C_M is depleted to 1 and 0.1%. The equivalent time (s) of L_2 and L_3 are calculated from:

Eq. 4.7: $$t_{(L2)} = \frac{-\ln\left(\frac{1}{100}\right)\lambda_{470}}{\sigma_F P}$$

Eq. 4.8: $$t_{(L3\ Start)} = \frac{-\ln\left(\frac{1}{100}\right)\lambda_{470}}{\sigma_M P}$$

Eq. 4.9: $$t_{(L3\ End)} = \frac{-\ln\left(\frac{0.1}{100}\right)\lambda_{470}}{\sigma_M P}$$

where $t_{(L2)}$, $t_{(L3\ Start)}$ and $t_{(L3\ End)}$ are the time (s) at which L_2, $L_{3\ start}$ and $L_{3\ end}$ occur respectively, all other variables have been defined in the text previously. Under the experimental conditions used here, L_1 is 0 s (channels 1-2), L_2 is 3 s (channels 18-19), $L_{3\ start}$ is 16 s (100 channels), and $L_{3\ end}$ is 24 s (150 channels). All continuous wave (CW) quartz SAR stimulations were 40 s in duration, over 250 channels, resulting in channel width of 0.16 s or 5.8 mJ·cm^{-2}. This is in line with the maximum channel width of ~ 5 mJ·cm^{-2} suggested by Durcan and Duller (2011). L_1 is the photon counts between 0.0 and 5.8 mJ·cm^{-2} (channels 1 - 2), L_2 is between 104.4 and 110.2 mJ·cm^{-2} (channels 18 - 19) and L_3 is the average of 580 to 870 mJ·cm^{-2} (channels 100 – 150) (Figure 4.10).

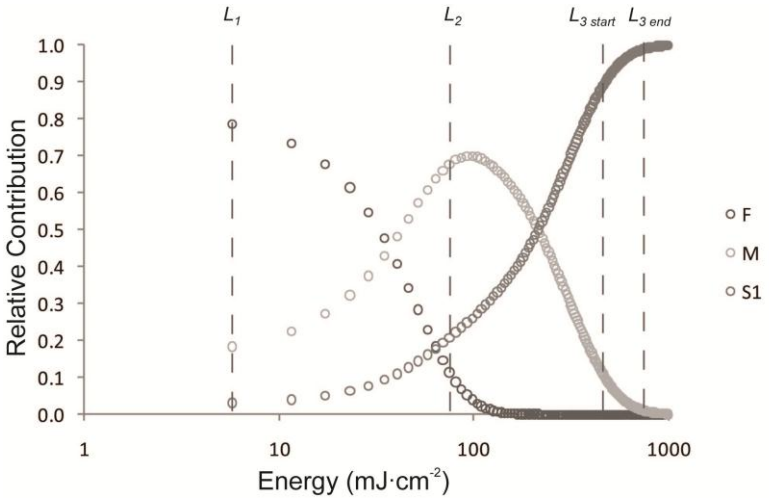

Figure 4.10: The relative contribution of the different components of FAB42 to total luminescence emission as a function of cumulative stimulation energy. The various components (L_1, L_2 and L_3) necessary for calculation of the F ratio have been indicated.

The five Norwegian samples that were examined for Fast ratio analysis (FAB81, GRAN54/55/56/57) failed to pass the acceptance criterion of > 20, although values ranged from 1.14 ± 0.54 to 14.24 ± 1.24 for FAB81. The Fast ratio was calculated for both L_n and the first T_x (4.72 ± 0.13 Gy) in order to account for any depletion of the fast component due to partial bleaching. The T_x Fast ratios were greater than those for L_n where L_n Fast ratios were small, but smaller where L_n ratios were large (Table 4.10). This indicates that the majority of samples are affected by partial bleaching, rather than by the presence of an unstable C_M (e.g. Steffen et al., 2009), but more importantly it indicates that ***some*** samples may not be partially bleached and could return a true depositional age following OSL analysis. The bleaching properties of the Norwegian samples were explored through a series of bleaching experiments described in Section 4.6, whilst further exploration of the different components was achieved using LM-OSL (see Section 4.7).

Table 4.10: Fast ratio results for L_n and T_x measurements of 24 aliquots of FAB81. The % difference between the L_n and T_x fast ratios is given to demonstrate changes in the proportion of the C_F between the natural and regenerated doses. Positive % differences indicate partial bleaching of the natural signal, which affects the majority of aliquots. However, a small number of aliquots are unaffected, suggesting that no partial bleaching has occurred and that a D_e representative of the burial age can be recovered.

Fast Ratio (Ln)	Fast Ratio (*T*x)	% Difference
1.14 ± 0.54	1.31 ± 0.62	15.05
1.60 ± 0.67	1.95 ± 0.73	21.73
1.18 ± 0.53	4.75 ± 1.03	302.70
1.36 ± 0.58	2.40 ± 0.81	76.65
5.46 ± 0.71	2.54 ± 0.68	-53.54
1.75 ± 0.54	2.95 ± 0.70	68.26
1.17 ± 0.43	1.63 ± 0.57	39.98
12.06 ± 1.20	4.09 ± 0.71	-66.10
2.98 ± 0.60	3.34 ± 0.90	11.91
1.32 ± 0.60	1.91 ± 0.76	44.48
5.83 ± 0.78	3.78 ± 0.75	-35.10
2.43 ± 0.59	2.38 ± 0.63	-2.01
3.52 ± 0.65	3.08 ± 0.75	-12.50
2.27 ± 0.76	2.20 ± 0.73	-3.25
1.41 ± 0.60	2.08 ± 0.63	48.26
8.42 ± 0.86	4.24 ± 0.71	-49.72
1.45 ± 0.64	1.80 ± 0.69	24.33
1.32 ± 0.58	2.68 ± 0.82	102.85
2.01 ± 0.51	2.69 ± 0.66	33.72
5.25 ± 0.74	3.91 ± 0.85	-25.47
1.35 ± 0.62	2.98 ± 0.98	121.34
14.24 ± 1.24	6.39 ± 0.84	-55.11
2.06 ± 0.59	3.21 ± 0.79	55.76
2.33 ± 0.64	1.99 ± 0.67	-14.41

4.6. Bleaching Experiment Methodology

Two types of bleaching experiment were used to test whether samples were bleachable within the natural environment, and that the luminescence signal bleaches during analysis with the SAR protocol. The former was carried out at Scottish Universities Environmental Research Centre (SUERC) (see section 4.6.1) whilst the latter was carried out at the University of St Andrews (see section 4.6.3).

4.6.1. **Natural Bleaching Experiment**

Two bleaching experiments were carried out using a light box at SUERC, the emission spectrum of which approximates daylight and is shown in Figure 4.11. The first bleaching experiment monitored depletion of the natural signal as a function of time, and the second depletion of a regenerated signal. Three Norwegian quartz samples were

selected for analysis, which are representative of the main valleys studied (FAB98, GRAN57 and NIG7). 24 hand dispensed medium aliquots of each were mounted on stainless steel discs using Silikospray. Three aliquots of each sample were retained as a standard of zero exposure, the remaining aliquots were grouped into sets of 3 and were bleached for 0.25, 0.5, 1, 2, 4, 8 and 16 hours respectively. The luminescence of 2 aliquots from each set were then analysed using a TL-DA-15 Risø reader (reader 2 at SUERC), which has the same filters as the Risø readers in St Andrews (see section 4.2) using the protocol listed in Table 4.11, and the third aliquot was retained as a standard.

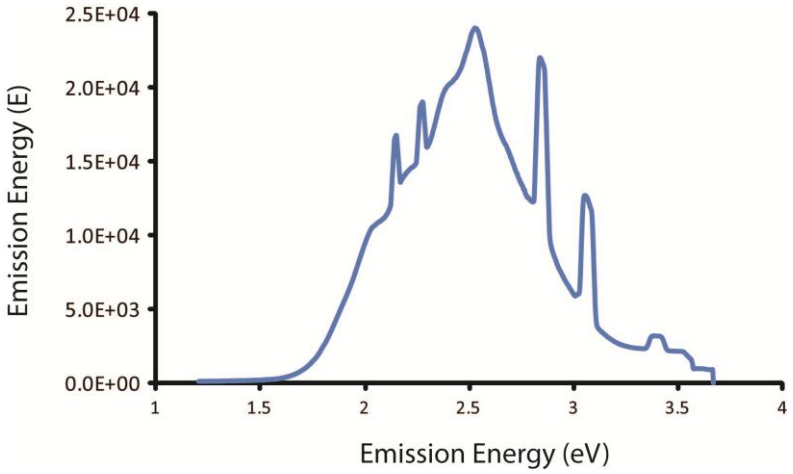

Figure 4.11: Emission spectrum of the SUERC lightbox, measured using an Ocean Optics USB2000 Fibre Optic Spectrometer. The emission energy of the lightbox is ~5.48 $mW \cdot cm^{-2}$ (Marc Smillie, 2010, pers. commun.) whereas that for natural daylight is ~136.8 ± 0.5 $mW \cdot cm^{-2}$ (Kopp and Lean, 2011)

Table 4.11: Bleaching Experiment Analysis Protocol

TSL	180 ˚C, 10 s, 5 ˚C/s
OSL	60 s, 60% power, 125 ˚C
TSL	500 ˚C
Test Dose	4.7 Gy*
TSL	180 ˚C, 10 s, 5 ˚C/s
OSL	60 s, 60% power, 125 ˚C
TSL	500 ˚C
Regenerative Dose	200 s (~20 Gy)

*The dose rate listed here is specific to the reader used at SUERC and the measurement date

It is apparent that of all the samples, only FAB98 exhibited significant depletion in the natural signal with increasing exposure time (Figure 4.12). After 15 minutes of exposure, 60% of the natural signal remained, however no further depletion in residual luminescence was observed. It should be noted that this experiment was carried out on multiple aliquots of each sample, which because of the partially bleached nature of the samples (see section 4.9), will have very different initial luminescence signals. GRAN57 and NIG7 may also exhibit less relative bleaching, because the sample is already bleached to its maximum residual level.

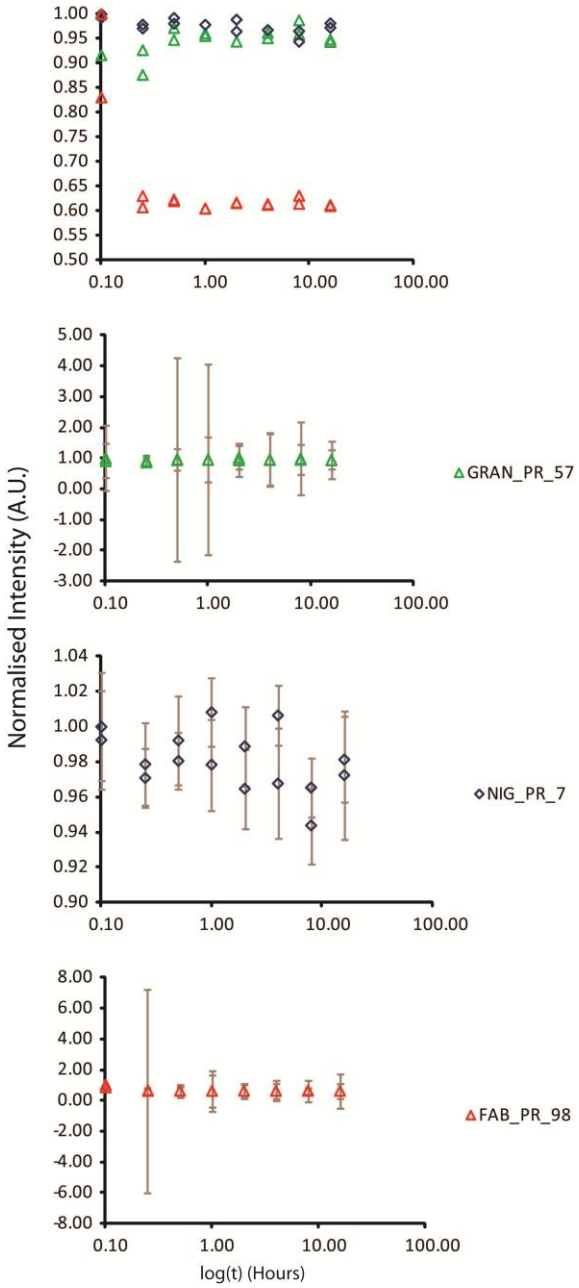

Figure 4.12: OSL results of the natural bleaching experiment for GRAN57, NIG7 and FAB98. All data are test dose corrected and then normalised to the most intense emission. No error bars are shown in the upper, comparative plot to enable the relative behaviour of the emissions to be observed. FAB98 exhibits the most rapid bleaching.

4.6.2. **Regenerative bleaching experiment**

Following analysis of the residual luminescence from the natural bleaching experiment, the same aliquots were given a beta dose of 18.80 ± 0.07 Gy for the regenerative dosing experiment. A well characterised quartz standard obtained from BDH Lab Supplies Ltd. (BDH) which has a dose of 36.98 ± 2.27 (D. Sanderson, Pers. Comm.) was also analysed.

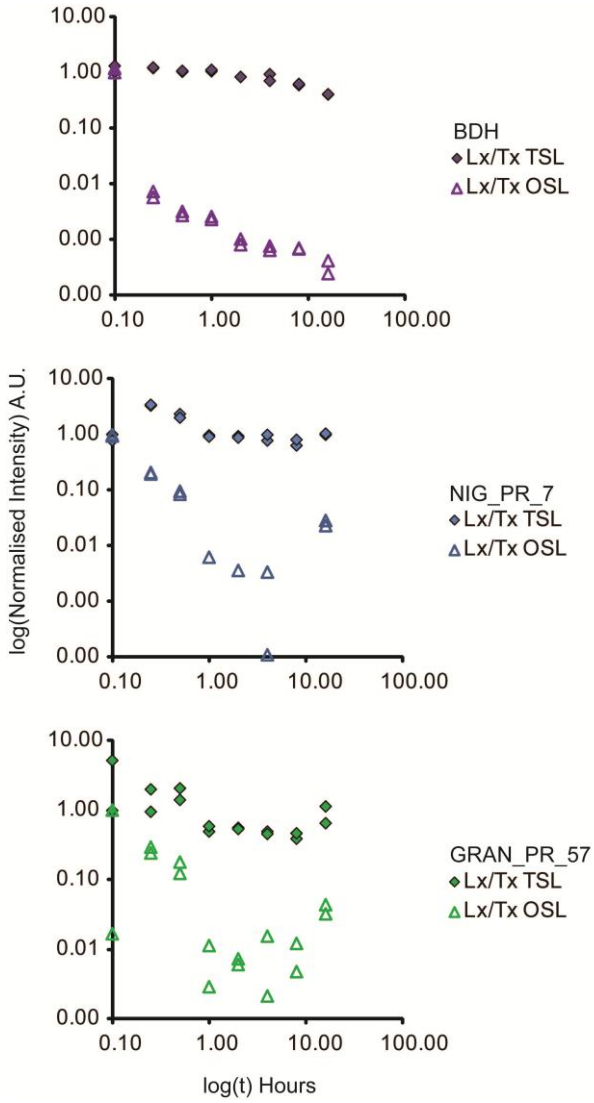

Figure 4.13: TSL and OSL results of the regenerative bleaching experiment. All data are test dose corrected and then normalised to the most intense emission. Uncertainties are not shown to facilitate plotting in log-log space.

The residual luminescence of BDH reduced to < 1% of the initial luminescence intensity after 0.25 hours exposure (Figure 4.13). The TSL signal reduced less rapidly, with ~ 40% of the signal remaining after 16 hours of bleaching. NIG7 and GRAN57 bleached to ≤ 10% after 1 hour of exposure, which indicates that the samples are bleachable and therefore suitable for luminescence dating. However, as samples were dosed with 18.80 ± 0.07 Gy, a residual of 10% is approximately 2 Gy, which equates to a residual age of ~ 500 years where an average D_r across the entire sample suite is used to calculate age (see section 4.12). This presents a serious limitation to the minimum ages that can be calculated, especially as the samples collected are known to have ages < 100 years. However, as age distributions are of greater interest within this thesis, rather than absolute ages, this limitation can be accommodated. The scatter between aliquots is indicative of the poor luminescence sensitivity of the Norwegian samples. The probability of prolonged (~ 1 hr) exposure periods within the glacial environment, and the influence of reduced solar intensity due to cloud cover, seasonality or attenuation through fluvial transport are discussed in Chapters 2 and 3**.**

As signals depleted to > 10% within 1 hour, a second regenerative bleaching experiment was carried out which explored the rate of initial signal depletion through bleaching samples for 450, 225, 112, 56, 28 and 14 seconds. After 225 s, < 10% of the initial signal remained within BDH, whereas < 40% of the signal remained in FAB98 (Figure 4.14).

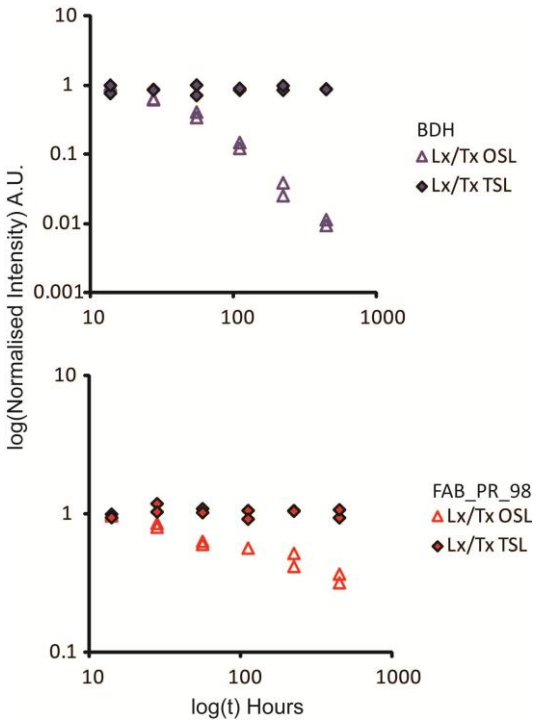

Figure 4.14: OSL and TSL rapid regenerative bleaching experiment results. Errors are not shown to facilitate plotting in log-log space.

4.6.3. **Laboratory Bleaching Experiment**

Part of the PH plateau and dose recovery tests discussed in section 4.4.1 involves bleaching aliquots with the blue diodes (90% power) in the Risø reader. Bleaching duration within these experiments comprises 200 s at room temperature, consisting of two 100 s bleaches, interspaced by a 7200 s pause which enables charge evicted to unstable centres, to decay to the main luminescence centres (Table 4.3). Comparison of the two OSL intensities measured in these steps enables some quantification of the suitability of the samples for OSL dating to be made, as successful bleaching with blue diodes is integral to analysis with a conventional SAR protocol.

Where the luminescence signal of the first and second stimulations were integrated and contrasted over the first 4 s (10 channels) it was evident that 95% of the signal had been bleached in the first exposure, however, where the signal was integrated over 80 s (199 channels) the proportion of total signal depletion dropped to just 59%. This was anticipated due to the slower rate of bleaching of the C_M and C_S components and demonstrates the importance of integrating signals over the first few seconds.

4.7. Linearly Modulated OSL (LM-OSL)

Linearly modulated OSL (Bulur, 1996) comprises stimulation with linearly increasing power. It enables differentiation of the quartz OSL components (C_F, C_M and C_S) by their photoionisation cross-sections (σ_p, cm^{-2}) (Bailey et al., 1997), which are determined through calculating detrapping probability (b, s^{-1}) relative to maximum stimulation light intensity (I_o, W·s) (Choi et al., 2006):

Eq. 4.10: $b = \sigma_p I_0$

The absolute number of components varies between different quartz samples (Bailey et al., 1997; Jain et al., 2003; Singarayer and Bailey, 2003), and the number of components may be limited by the power or duration of bleaching (e.g. Kiyak et al., 2007). Choi et al. (2006) observed > 80% of quartz had five components, a conclusion supported by Singarayer and Bailey (2003), whilst Jain et al. (2003) have identified seven components. LM-OSL has provided further evidence that OSL traps exhibit first-order kinetic behaviour, determined through observation of linearly increasing b with increasing stimulation light power up to 50 $mW \cdot cm^{-2}$ (Jain et al., 2008).

LM-OSL is substantially more time consuming than conventional analyses due to the integration periods necessary to ensure isolation of the individual components, but provides a valuable comparison to the other component investigations reported here. Integration periods range from 1,000 to 4,000 s (Jain et al., 2008), which are ~100 times longer than conventional analyses. Sensitivity corrections remain important (Kiyak et al., 2007, 2008) and Choi et al., (2006) have identified that background increases with increasing stimulation power. However unlike CW-OSL deconvolution, LM-OSL does not suffer from elevated background levels derived from the mathematical transformation (Jain and Lindvold, 2007).

Component identification is dependent upon analytical protocol PH and stimulation duration (Kiyak et al., 2007; Polymeris et al., 2009), and even where protocols are similar, σ_p may still vary significantly, which makes drawing universal conclusions about the optical traps within quartz challenging. For instance, Kiyak et al. (2007) obtained σ_p values that agree with Jain et al. (2003) for the C_S, but not for the ultrafast component (C_{UF}), C_F or C_M.

4.7.1. **Components**

4.7.1.1. The Ultrafast Component

The C_{UF}, first recognised by Jain et al. (2001) and Choi et al. (2003) is a thermally unstable component with very shallow trap depth of 0.9-1.4 eV (Jain et al., 2008). Due to its short lifetime, it is generally absent from natural D_e measurements, and thus may result in age underestimation where an inadequate PH temperature is used. Jain et al. (2008) recommend PH temperatures > 200 ˚C, in agreement with Choi et al.'s (2003) finding that a 160 ˚C PH temperature was inadequate and resulted in an isothermal TSL emission during stimulation of regenerated doses. As the trap depth of the C_{UF} is so shallow, blue-light stimulation requires no phonon assistance to bleach it (Jain et al., 2008).

4.7.1.2. The Fast Component

The C_F is thermally stable and is most suitable for dating applications due to its rapid bleaching rate. In contrast to other components, the C_F is less prone to sensitivity change (Kiyak et al., 2007) and recuperation (Jain et al., 2003), which render it ideal for precise D_e determinations. However, sensitivity changes and recuperation of the C_F have been reported (e.g. Jain et al., 2003) and are attributed to depletion of other components, thus sample thermal stability must still be characterised (Jain et al., 2003; Kiyak et al., 2007).

4.7.1.3. The Medium Component

The C_M has been reported to be both thermally stable (Bailey et al., 2003) and unstable (Li and Li, 2006; Steffen et al., 2009), and is present within all quartz. When exposed to the full UV spectrum, as occurs with unobstructed daylight, the C_F and C_M recombine at the same rate, whereas at longer wavelengths the C_M bleaches less readily (Bailey, 2003; Singarayer and Bailey, 2003, 2004) (see section 1.4.3). Consequently, in some environments it is possible to examine the relative signals of the C_F and C_M to determine sample partial bleaching, and also to extract true (or at least a minimum age estimation) D_e (Bailey, 2003).

4.7.1.4. The Slow Component

Between three and four different C_S have been reported for quartz, depending upon the duration of LM-OSL stimulation, as the least light sensitive of these components is often only partially analysed throughout the selected protocol (e.g. Kiyak et al., 2007).

Deconvolution of the different components from LM-OSL and CW-OSL is based on the assumption of first order kinetics, however Bailey (2000) observed that some C_S exhibit non-first order kinetics and that their decay-rate is dependent upon initial charge concentration. This renders the C_S inappropriate for dose determinations and its incorporation within the measured OSL signal is therefore avoided where possible (see section 4.5.1).

4.7.2. **The LM-OSL Method**

Medium sized aliquots were used for all of the LM-OSL analyses (see section 4.2) and were measured using Risø 1, which has a maximum stimulation power intensity of 40 mW·cm^{-2} at the sample position (Table 4.1). Stimulation was ramped linearly from 0-90% power for all analyses, thus maximum stimulation power was 36 mW·cm^{-2}.

Table 4.12: LM-OSL protocol after Choi et al. (2006)

CalQz Standard & Procedural Blank	OSL	0 ˚C, 100 s, 90% Power
	Pause	1000 s
	OSL	0 ˚C, 100 s, 90% Power
	Dose	9.52 Gy*
	TSL	200 ˚C (5 ˚C/s), 10 s
	LM-OSL	Blue diodes, 4000 s, 90% Power, 125 ˚C (5 ˚C/s)
	Dose	9.52 Gy*
	TSL	TSL – 160 ˚C (5 ˚C/s), 10 s
	LM-OSL	LM-OSL – Blue diodes, 4000 s, 90% Power, 125 ˚C (5 ˚C/s)
Samples	TSL	200 ˚C (5 ˚C/s), 10 s
	LM-OSL	Blue diodes, 4000 s, 90% Power, 125 ˚C (5 ˚C/s)
	Dose	62.84 Gy*
	TSL	160 ˚C (5 ˚C/s), 10 s
	LM-OSL	Blue diodes, 4000 s, 90% Power, 125 ˚C (5 ˚C/s)
Procedural Blank Only	LM-OSL	LM-OSL – Blue diodes, 4000 s, 90% Power, 125 ˚C (5 ˚C/s)

* Dose rate relates to Risø 1 during June 2009. Only Risø 1 was used for the LM-OSL analyses

All LM-OSL analyses used a protocol similar to that listed in Table 4.12 after Choi et al. (2006). Each analysis set consisted of an aliquot of CalQz as a standard, the samples under analysis, and a procedural blank comprising a stainless steel disc covered with Silikospray. The CalQz was bleached twice for 100 s with blue diodes, interspaced by a 1000 s pause before preheating at 200 ˚C for 10 s prior to analysis.

All data were BG corrected using the LM-OSL measurement obtained from the procedural blank. As some samples analysed had very poor luminescence sensitivity, this correction resulted in negative values which were replaced with zero for the purpose of modelling. Curve deconvolution was carried out using Sigmaplot 10.0 after Choi et al. (2006) and the equation of Bulur et al. (2002):

Eq. 4.11: $L(t) = n_0\, b\, (t/T) \exp(-bt^2/2T)$

where L(t) is the luminescence emission intensity as a function of time (t), n_0 is the number of electrons trapped, T is the total stimulation time (s) and b (s^{-1}) is the detrapping probability. The detrapping probability is related to the photoionisation cross section (cm^2):

Eq. 4.12: $b = \sigma_p I_0$

where I_0 is the maximum stimulation light intensity (W·s). I_0 is a function of the maximum intensity of the diodes (*P*) and the energy (E) of photons derived from 470 nm blue LEDs:

Eq. 4.13: $E = h \nu$

where *h* is Planck's constant (6.63×10^{-34} W·s^2) and ν is frequency (s^{-1}). The frequency for light of this wavelength (λ_{470}) is determined from:

Eq. 4.14: $\nu = c / \lambda_{470}$

$\nu = 3 \times 10^8$ (m·s^{-1}) / 470×10^{-9}(m)

$\nu = 6.38 \times 10^{14}$ (s^{-1})

where *c* is the speed of light. Therefore, *E* has a value of 4.23×10^{-19} W·s^{-1}. Maximum *P* in these experiments is 36 mW·cm^2, thus the number of photons per unit time per unit of area is:

Eq. 4.15: $I_0 = P / E$

$I_0 = 0.036$ (W·cm^{-2}) / 4.23×10^{-19} (W·s^{-1})

$I_0 = 8.51 \times 10^{16}$ (photons s^{-1}·cm^{-2})

The photoionisation cross sections of the sample analysed are summarised in Figure 4.16.

The deconvolution model works through iterating different parameters of b and n to calculate the best fit with the measured emission, whilst satisfying the condition that $n_N > 0$ and $b_N > 0$. Initial values of n_N (10^5), step size (10^2) and tolerance (10^{-500}) were based on Choi et al. (2006). Initial *b* values were amended from Jain et al. (2003) to reflect the maximum diode power of Risø 1, 36 mW·cm^{-2} in contrast to 47 mW·cm^{-2}, see Table 4.13.

Table 4.13: Detrapping parameter (b) value calculation after Jain et al. (2003)

Component	b (s^{-1}) after Jain et al. (2003) 47 mW·cm-2	b (s^{-1}) 36 mW·cm-2
Ultrafast (C_{UF})	32	24.67
Fast (C_F)	2.5	1.97
Medium (C_M)	0.62	0.48
Slow 1 (C_{S1})	0.15	0.11
Slow 2 (C_{S2})	0.023	0.02
Slow 3 (C_{S3})	0.0022	0.0018
Slow 4 (C_{S4})	0.0003	0.0002

Although the *b* values for the various components varied significantly as additional components were included in the model, the model fit did not improve, with r^2 increasing from 0.816 to 0.827 where four and five components were included, respectively. A maximum r^2 value of 0.828 was achieved where seven components were fitted (Table 4.14). Choi et al. (2006) identify false components from very high *b* values or very low *n* values, however false components for FAB42 are manifested as extremely small *b* values, which Choi et al. (2006) attribute to inappropriate initial parameters. As the r^2 values did not increase significantly from 0.827 for the five component fit (Figure 4.15), with the addition of further components, this fit is selected as the most appropriate (Table 4.14).

The model sensitivity to initial starting parameters was investigated through using *b* values published in Choi et al. (2006), and the results are listed in Table 4.15. The model behaves better with these starting parameters, producing fewer false components, and demonstrates the sensitivity of the modelling to the initial starting parameters (Choi et al., 2006). However, as the r^2 values remain similar irrespective of which start parameters are used, those calculated for the specific power of the diodes in Risø 1 are regarded as more appropriate.

Table 4.14: Fitting results for the natural LM-OSL of FAB42 using initial *b* value starting parameters calculated for Risø 1 (see Table 4.13)

Relative σ_p	Initial b Values		N = 3	b_N/b_1	N = 4	b_N/b_1	N = 5	b_N/b_1	N = 6	b_N/b_1	N = 7	b_N/b_1
σ_{UF}											5.98×10^{2}	
	24.67										8.74	
σ_F / σ_F		n_1	151×10^{6}		1.90×10^{3}		7.99×10^{3}		5.99×10^{2}		2.841×10^{3}	
= 1.0	1.97	b_1	0.141	1	0.087	1	0.413	1	8.713	1	0.841	1
σ_M / σ_F		n_2	4.11×10^{5}		6.01×10^{6}		2.40×10^{4}		2.85×10^{3}		6.68×10^{3}	
= 0.2	0.48	b_2	1×10^{-3}	0.004	4×10^{-8}*	5×10^{-6}	2.4×10^{-3}	0.059	0.838	0.096	0.198	0.235
σ_{S1} / σ_F		n_3	3.39×10^{3}		1.23×10^{7}		4.28×10^{5}		6.68×10^{3}		1.63×10^{7}	
= 0.06	0.11	b_3	3×10^{-3}	0.024	7×10^{-6}	8×10^{-5}	2×10^{-3}	0.006	0.197	0.023	2×10^{-7}*	2×10^{-6}
σ_{S2} / σ_F		n_4			4.27×10^{5}		1.30×10^{7}		2.01×10^{4}		2.00×10^{4}	
= 0.01	0.02	b_4			3×10^{-3}	0.03	5×10^{-6}	1×10^{-5}	0.024	3×10^{-3}	0.024	0.0284
σ_{S3} / σ_F		n_5					4.23×10^{6}		3.88×10^{5}		3.84×10^{5}	
= 0.001	0.0018	b_5					2×10^{-6}	5×10^{-6}	0.003	3×10^{-4}	3×10^{-3}	3×10^{-3}
σ_{S4} / σ_F		n_6							5.02×10^{5}		2.91×10^{5}	
= 0.0001	0.0002	b_6							2×10^{-4}	3×10^{-5}	0.0004	4×10^{-3}
R^2			0.820		0.816		0.827		0.827		0.828	

*False parameters, identified from their extremely low *b* values (<10^{-6}, after Choi et al. 2006)

The fitting results listed in Table 4.14 indicate that for the selected, five component fit, the S3 component is dominant ($n = 1.30 \times 10^7$). The initial LM-OSL investigation was carried out on the natural luminescence intensity of the sample, which may explain the dominance of the C_{S3}, and supports the EBG and Fast ratio investigations which indicate that L_n is not always C_F dominated. This was investigated through analysis of the LM-OSL of a 62.84 Gy regenerative dose (Figure 4.16, Table 4.16); a large dose was selected to improve the signal to noise ratio.

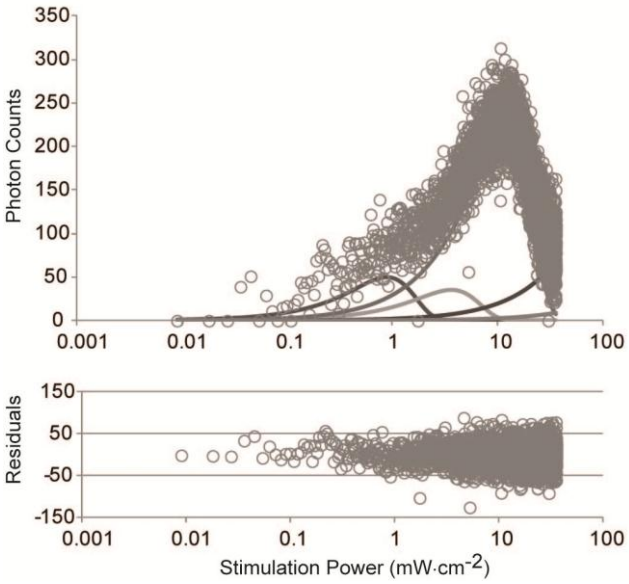

Figure 4.15: Natural LM-OSL emission of FAB42 (upper plot) and curve fitting residuals (lower plot), fitted with five components.

Table 4.15: Fitting results for the natural LM-OSL of FAB42 using initial b values after Choi et al. (2006) (see Table 4.13)

Relative σ_p	Initial b values		N = 3	b_N / b_1	N = 4	b_N / b_1	N = 5	b_N / b_1	N = 6	b_N / b_1
σ_F / σ_F		n_1	1.90×10^4		8.00×10^3		7.40×10^3		7.40×10^3	
= 1.0	1.65	b_1	0.087	1	0.412	1	0.457	1	0.457	1
σ_M / σ_F		n_2	4.73×10^7		2.40×10^4		2.77×10^7		1.98×10^4	
= 0.2	0.40	b_2	2×10^{-6}*	2×10^{-5}	0.024	0.059	1×10^{-5}	3×10^{-6}	0.031	0.068
σ_{S1} / σ_F		n_3	4.28×10^5		2.23×10^7		1.97×10^4		1.66×10^6	
= 0.06	0.09	b_3	3×10^{-3}	1508	$4\ 10^{-5}$	1×10^{-4}	0.031	2.58×10^4	2×10^{-5}	0.001
σ_{S2} / σ_F		n_4			4.28×10^5		2.37×10^5		1.26×10^{-5}	
= 0.01	0.01	b_4			2×10^{-3}	708	1×10^{-3}	0.017	0.000	0.000
σ_{S3} / σ_F		n_5					3.69×10^5		3.73×10^5	
= 0.001	0.0015	b_5					3×10^{-3}	2335	3×10^{-3}	0.090
σ_{S4} / σ_F		n_6							2.70×10^5	
= 0.0001	0.0002	b_6							5×10^{-4}	0.014
R^2			0.816		0.827		0.827		0.827	

*False parameters, identified from their extremely low *b* values (<~10^{-6}, after Choi et al. 2006)

Table 4.16: Fitting results for FAB42 using calculated b values (see Table 4.13) following regenerative dosing of 62.84 Gy

Relative σ_p	Initial b Values		N = 3	b_N / b_1	N = 4	b_N / b_1	N = 5	b_N / b_1	N = 6	b_N / b_1	N = 7	b_N / b_1
σ_{UF}											5.96×10^3	
	24.67										8.737	
σ_F / σ_F		n_1	3.26×10^4		2.01×10^4		1.66×10^4		8.82×10^3		1.38×10^4	
= 1.0	1.97	b_1	0.459	1	0.947	1	1.17	1	2.05	1	0.841	1.000
σ_M / σ_F		n_2	1.50×10^5		3.69×10^7		2.73×10^4		2.05×10^4		1.66×10^4	
= 0.2	0.48	b_2	0.001	0.012	2×10^{-6}	2×10^{-6}	0.132	0.113	0.365	0.178	0.198	0.269
σ_{S1} / σ_F		n_3	3.64×10^5		2.91×10^4		1.92×10^5		1.83×10^4		1.57×10^4	
= 0.06	0.11	b_3	0.0001	0.002	0.086	0.09	0.004	0.004	0.059	0.029	2×10^{-7}*	0.051
σ_{S2} / σ_F		n_4			3.09×10^5		3.38×10^5		7.48×10^4		1.03×10^5	
= 0.01	0.02	b_4			0.003	0.003	7×10^{-4}	6×10^{-4}	0.001	0.003	0.024	0.007
σ_{S3} / σ_F		n_5					3.48×10^{-2}		2.53×10^5		2.19×10^5	
= 0.001	0.0018	b_5					0.000	0.000	0.003	0.001	0.003	0.003
σ_{S4} / σ_F		n_6							5.41×10^5		4.55×10^5	
= 0.0001	0.0002	b_6							0.0001	6×10^{-5}	4×10^{-4}	0.0003
R^2			0.671		0.714		0.724		0.732		0.732	

*False parameters, identified from their extremely low *b* values (<10^{-6}, after Choi et al. 2006)

A six component fit was selected as this had the maximum r^2 of 0.732, and no improvement in r^2 was recorded with additional components. In contrast to the natural signal the C_F and C_M dominate the initial signal of the regenerated dose (Table 4.16). This is indicative of partial bleaching of the natural signal, as where quartz is only partly exposed to sunlight prior to deposition, the C_F and C_M components are most rapidly bleached (Bailey, 2003; Bailey et al., 2003; Singarayer and Bailey, 2003, 2004).

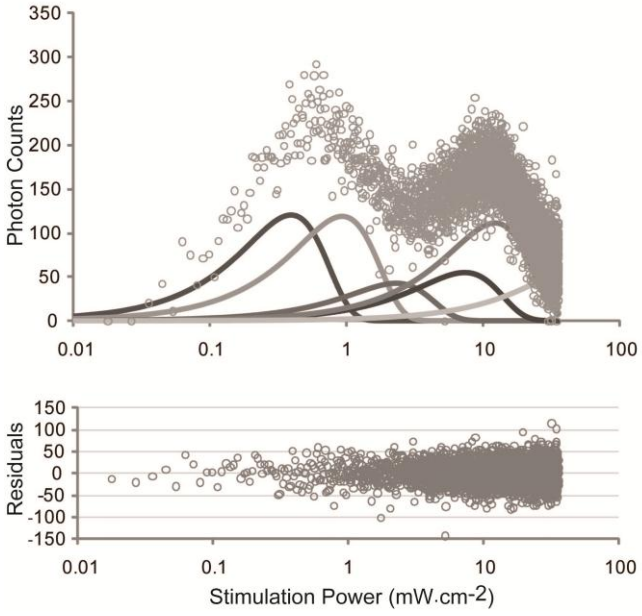

Figure 4.16: LM-OSL emission of FAB42 following a 62.84 Gy regenerative dose (upper chart) and curve fitting residuals (lower chart), fitted with 6 components.

The σ_p calculated for FAB42 are similar to those previously reported e.g. Choi et al. (2006); Singarayer and Bailey (2003); Durcan and Duller (2011), and a comparison to Jain et al. (2003) is made in Table 4.17.

Table 4.17: Calculated photo-ionisation cross sections compared to those published by Jain et al. (2003)

	σ_p Jain et al. (2003a)	σ_p Calculated
F	$2.32 \pm 0.16 \times 10^{-16}$	2.41×10^{-17}
M	$5.59 \pm 0.44 \times 10^{-18}$	4.30×10^{-18}
S1	$1.33 \pm 0.26 \times 10^{-18}$	6.97×10^{-19}
S2	$2.08 \pm 0.46 \times 10^{-19}$	6.87×10^{-20}
S3	$2.06 \pm 0.16 \times 10^{-20}$	2.46×10^{-20}
S4	$0.17 \pm 0.17 \times 10^{-21}$	1.56×10^{-21}

LM-OSL emissions can also be used to evaluate PH temperature suitability. The regenerative LM-OSL curves for PH temperatures ranging from 160 ˚C to 200 ˚C are shown in Figure 4.17. The C_{UF} is removed by an increase in PH temperature from 160 ˚C to 170 ˚C, supporting the selection of a 180 ˚C preheat temperature for this sample suite (See section 4.4.1).

Recently, the use of LM-OSL particularly with regard to the time required for measurement and analysis has been questioned (e.g. Wallinga et al., 2008). Non-linearity in stimulation power due to increasing diode temperature during stimulation (Choi et al., 2006), and limited response of diodes within Risø TL-DA-15 machines to power settings < 0.14% have been identified (Wallinga et al., 2008). Failure to correct for such system-responses will influence lifetime calculations, and may explain the discrepancies in calculated σ_p (e.g. Jain et al., 2003; Kiyak et al., 2007).

Despite these limitations, the few LM-OSL analyses presented here provide an explanation for the poor behaviour of some of the Norwegian quartz throughout SAR analysis. The SAR protocol is designed for C_F dominated quartz (Murray and Wintle, 2000), and thus where quartz are not C_F dominated, this protocol operates less well (Thrasher et al., 2009b). Lukas et al. (2007) examined their Scottish glacigenic sediment with LM-OSL and concluded that the C_F was weak within the majority of their quartz samples, which was believed to contribute to their poor luminescence sensitivity. Such characteristics are apparent within the Norwegian samples suite examined here.

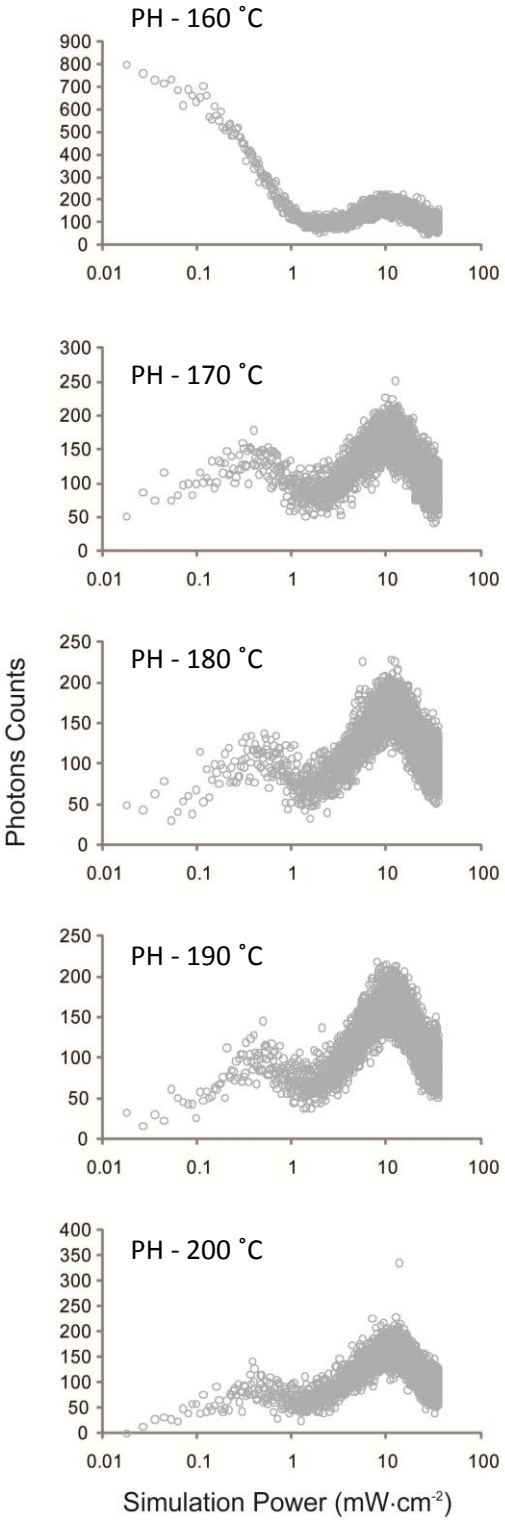

Figure 4.17: LM-OSL curves for repeated 62.84 Gy regenerative doses on the same aliquot of FAB42 treated with different PH temperatures prior to stimulation. PH temperatures varied from 160 ˚C (top chart) to 200 ˚C (bottom chart) in 10 ˚C increments for a period 10 s.

4.8. De(t) Plots

Partial bleaching of the OSL signal can also be determined through examining whether the D_e changes when integrated over different portions of the decay curve. This can be observed graphically using D_e(t) plots which show variation in the D_e of a sample as a function of stimulation time (Bailey, 2003; Bailey et al., 2003). If a sample has been partially bleached then D_e is anticipated to increase with stimulation time, as the unbleached C_M is stimulated. Alternatively, if a sample has been fully bleached the D_e(t) plot exhibits a plateau. This technique builds upon the earlier TSL plateau method proposed by Hütt and Jungner (1992), and has been successfully applied to glacial sediments by a number of authors. Thomas et al. (2006) determined that their glacigenic sediments from Arctic Russia were fully bleached from a non-rising D_e(t) plot, and Pawley et al. (2008) confirmed their glaciofluvial sediments from Norfolk were not partially bleached, but observed a falling D_e(t) profile which they attributed to an unstable C_F.

Integration intervals for the D_e(t) plots were calculated after Bailey (2003), and comprised 1.6 s integrations from channels 1-10, 10-20 etc. Signal from 32-40 s (channels 200-250) was used to calculate the background. Rising D_e with integration time was observed for all samples investigated (Figure 4.18), which further confirms that the samples under investigation are partially bleached.

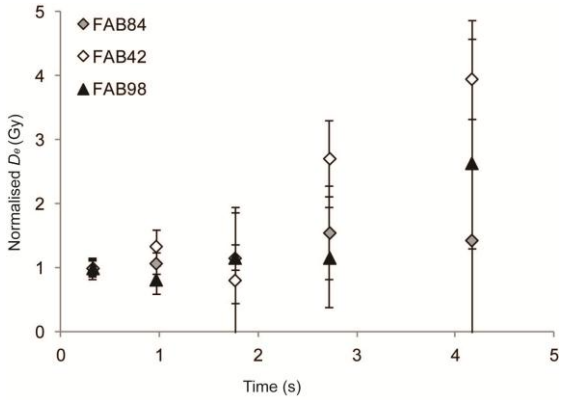

Figure 4.18: D_e(t) plots after Bailey (2003; Bailey et al., 2003) for three samples (FAB84/42/98). Data points are the average of 5 aliquots and are integrated over 0-0.32, 0.48-0.96, 1.12-1.76, 1.92-2.72 and 2.88-4.16 s. Doses have been normalised relative to the first D_e to facilitate plotting on a single graph.

4.9. Summary of Quartz OSL Investigations

Sections 4.3 to 4.9 have outlined the various different techniques used to evaluate the luminescence properties of the Norwegian quartz investigated throughout this thesis, and a protocol is suggested for future analyses of samples which exhibit similar properties of poor luminescence sensitivity and high recuperation levels (Figure 4.19). The

regenerative doses in the dose recovery experiments can be adjusted depending upon the luminescence sensitivity of the samples under investigation. Similarly, preheat temperatures are at the discretion of the analyst, however the protocols detailed in section 4.4 could be adopted. Acceptance values for each of the tests are as discussed throughout this chapter, e.g. recuperation < 20%.

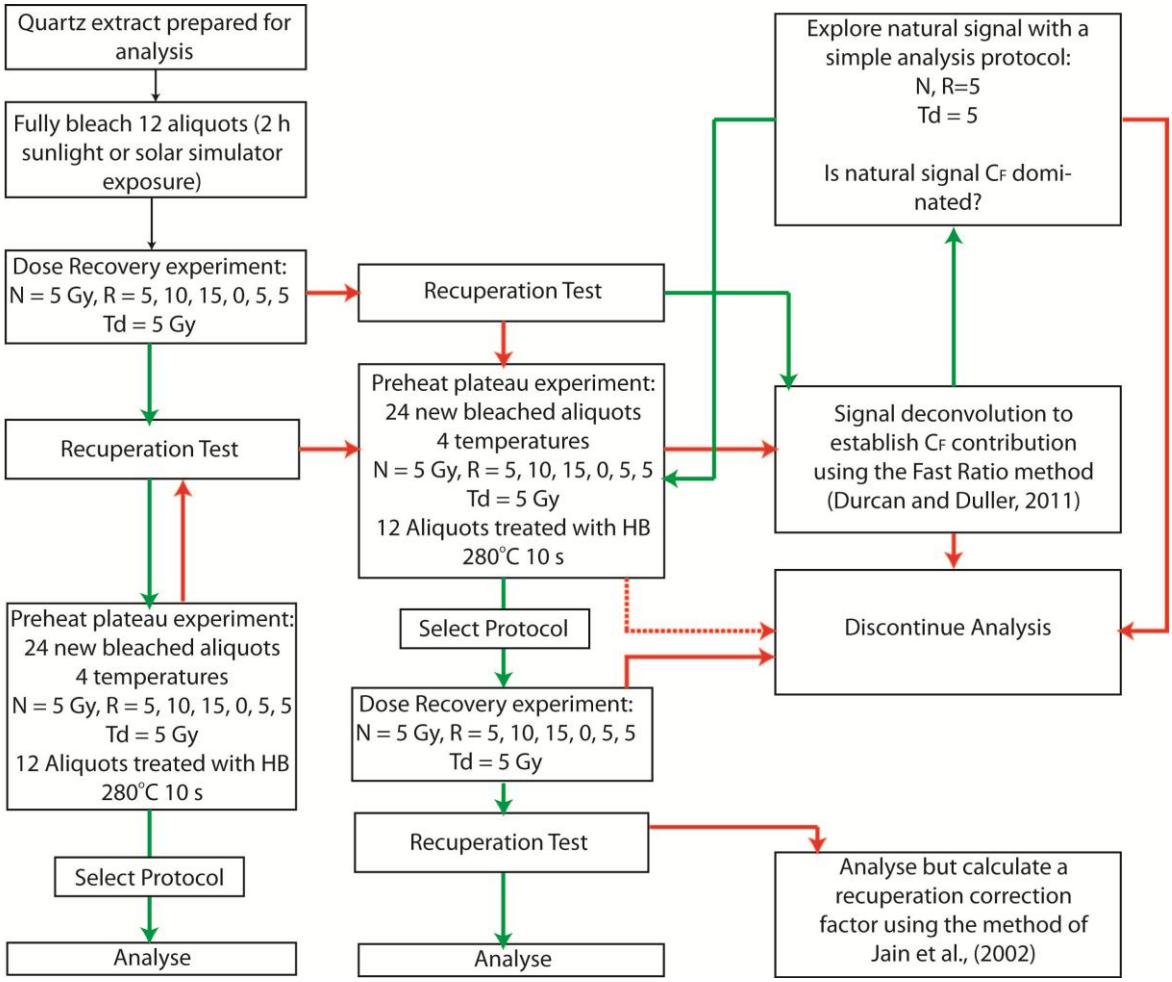

Figure 4.19: Sample analysis flowchart for effective screening of quartz samples with limited suitability for OSL dating. Green arrows denote that the acceptance criteria have been passed, e.g. that recuperation is < 20% as discussed in the text, and red arrows those that have not been accepted. The dotted arrow is used to illustrate the route where the box has already been used.

4.10. Age Models

It has been demonstrated that the samples analysed within this thesis display heterogeneous bleaching (e.g. see Section 4.5.2) and have produced a range of D_e values that may not be normally distributed (e.g. Figure 4.20). As such, an appropriate age model must be chosen in order to determine the true burial dose (Galbraith et al., 1999). The scatter in D_e values of a sample is termed the overdispersion (σ_d) and is the relative standard deviation of D_e values once systematic and statistical uncertainties have been

accounted for (Galbraith et al., 1999). Overdispersion may be caused by heterogeneous bleaching (Murray et al., 1995), post depositional mixing, beta dose heterogeneity (Murray and Roberts, 1997; Nathan et al., 2003; Olley et al., 1997), or poor accounting for variable sample behaviour due to inappropriate analysis protocols. As many of these samples are heterogeneously bleached, it is predicted that this will exert the greatest influence on σ_d. Overdispersion is calculated using the central age model (CAM) which weights the mean values relative to an underlying (assumed) normal distribution (Galbraith et al., 1999). The CAM, common age model (COM), finite mixture model (FMM, Galbraith and Green, 1990), minimum age model (MAM, Galbraith and Laslett, 1993) and lowest 5% model (L5%, Olley et al., 1998) have been applied to this sample suite.

All modelling was carried out using R; the code for the CAM, COM, MAM-4 and FMM were provided by Rex Galbraith, and the code for the MAM-3 model by Geoff Duller. An Excel spreadsheet was constructed to calculate the L5% model.

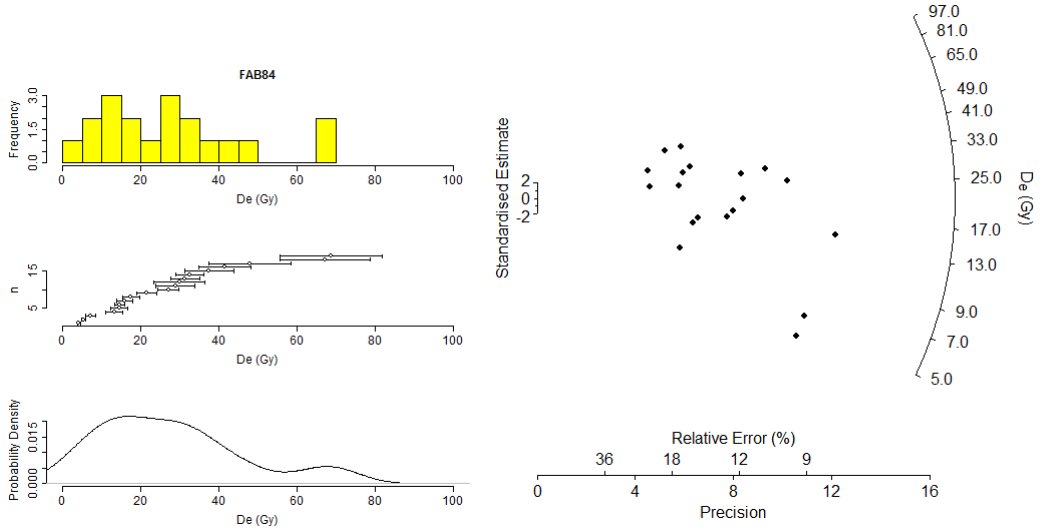

Figure 4.20: Histogram, scatter graph, probability density function and radial plot showing the D_e distribution of FAB84 which is a glaciofluvial point bar deposit.

4.10.1.1. The Central and Common Age Models

The COM and CAM are related models for different σ_d values (COM σ_d = 0, and for CAM σ_d > 0) (Galbraith et al., 1999). Overdispersion was calculated using the CAM for all samples, however where σ_d = 0, the model reduces to COM, indicating a common D_e for the sample population.

4.10.1.2. The Finite Mixture Model (FMM)

The FMM was initially designed for fission track dating and was first applied to OSL dating by Roberts et al. (2000). Using stochastic modelling of multi-grain aliquots, Arnold and Roberts (2009) found that the FMM was unable to recover the true D_e and

recommend that it should be used with single grain analyses only. Despite being designed for mixtures of individual mineral grains, rather than single aliquot applications, a number of studies have utilised it with single aliquot data sets (e.g. Guralnik et al., 2011; Rodnight et al., 2006).

The FMM fits a number of closely spaced component populations to an D_e distribution, enabling identification of the different components present; the deposits' true burial age is typically identified as the lowest mean D_e value (Rodnight et al., 2006). This is contingent on the assumption that full bleaching prior to deposition occurred for at least some of the grains within the sample, and thus age models should not be applied in isolation of sample depositional and sedimentological context. The model returns the Bayesian Information Criterion (BIC) calculated from the maximum log likelihood, which reduces as the model fit improves (Galbraith et al., 2005; Jacobs et al., 2008).

In contrast to the MAM (discussed below), the FMM enables objective selection of the lowest age component, as the number of aliquots that form the component can be identified (Rodnight et al., 2006). Rodnight et al. (2006) rejected components which contained < 10% of the sample population. The FMM requires an σ_d start parameter to be selected, which is indicative of the σ_d of a well bleached sample, and provides the basis for the individual components identified within the sample D_e distribution. A value of 10% was used after Rodnight et al. (2006), based on Duller and Augustinus (2006) and Jacobs (2006) observations of σ_d values of 10% and 12% for well bleached aeolian sand, respectively. More recently Arnold and Roberts (2009) have reviewed σ_d values from a range of studies for aliquots of different sizes, and the mean σ_d value for samples believed to be well bleached is 13 ± 7%, which is consistent with the value of 10% used here.

4.10.1.3. The Minimum Age Model (MAM)

The MAM has either three or four parameters (MAM-3 and MAM-4, respectively) and is specifically designed for heterogeneously bleached deposits. Prior to modelling, an σ_d value of 15% is added to each of the D_e values, which accounts for the relative scatter in a well bleached OSL sample (see above, Galbraith et al., 2005). The model operates through approximating the D_e distribution with a truncated log-normal distribution, and the truncation point provides the estimate of sample age (Galbraith et al., 1999).

4.10.1.4. The Lowest 5% Model (L5%)

The L5% model was developed by Olley et al. (1998) to determine the true depositional age of heterogeneously bleached fluvial sediments. They ranked D_e values derived from 78 small (60-100 grain) aliquots and calculated the mean D_e from the

youngest 5% (n = 4). The percentage of values from which D_e should be calculated is expected to vary between depositional environments and requires calibration. The maximum number of accepted aliquots for a single Norway sample is 56, 5% of which is 3 aliquots; for the majority of samples the L5% method derived D_e is based on only a single aliquot. Increasing the percentage will increase inclusion of heterogeneously bleached sediments, and since it is not possible to reduce the aliquot number, a value of 5% has also been adopted.

4.10.1.5. Model selection

Model selection was initially done using the criteria of Bailey and Arnold (2006) who, using modelled single grain data, have developed a flow chart (Figure 4.21) through which appropriate age models can be selected using statistical criteria including σ_d, weighted skewness (c_w) and kurtosis (k_w) (see Thrasher et al., 2009b for a discussion). Weighted skewness is calculated as:

Eq. 4.16: $$c_w = \sum_i \left\{ w_i \left(\frac{De_i - \overline{De}}{sDe} \right)^3 \right\} \frac{1}{\sum_i w_i}$$

Eq. 4.17: $$w_i = \frac{1}{\left(\frac{\sigma De_i}{De_i} \right)}$$

where sD_e is the standard deviation of the D_e population for a sample. Kurtosis (*k), is* defined as:

Eq. 4.18: $$k_w = \left\{ \frac{n(n+1)}{(n-1)(n-2)(n-3)} \sum \left(\frac{De_i - \overline{De}}{sDe} \right)^4 \right\} - \frac{3(n-1)^2}{(n-2)(n-3)}$$

where n is the total number of D_e values in the sample set.

These values were calculated for all samples where > 5 aliquots had been accepted and were tested for statistical significance against the standard error of skewness and kurtosis (σ_{cw} and σ_{kw}, respectively). Dose distributions where c_w or k_w values were > $2\sigma_{cw}$ or > $2\sigma_{kw}$ are statistically significant (Bailey and Arnold, 2006; Tabachnick and Fidell, 1966), and are indicative of heterogeneous bleaching:

Eq. 4.19: $$\sigma_{cw} = \sqrt{\left(\frac{6}{n} \right)}$$

Eq. 4.20: $$\sigma_{kw} = \sqrt{\frac{24}{n}}$$

Bailey and Arnold (2006) proposed critical values of k_{wcrit} = 2.18 and c_{wcrit} = 7.25 which were used initially and then contrasted with revised values of $k_{wcrit} = 0.6/(2\sigma_{kw})$ and $c_{wcrit} = 1/(2\sigma_{cw})$ (Arnold, 2006) after Thrasher et al. (2009b). The calculated values of c_w and k_w

are normalised to their respective significance values (i.e. $c/2\sigma_{cw}$ and $k/2\sigma_{kw}$) prior to use with the flowchart for model selection.

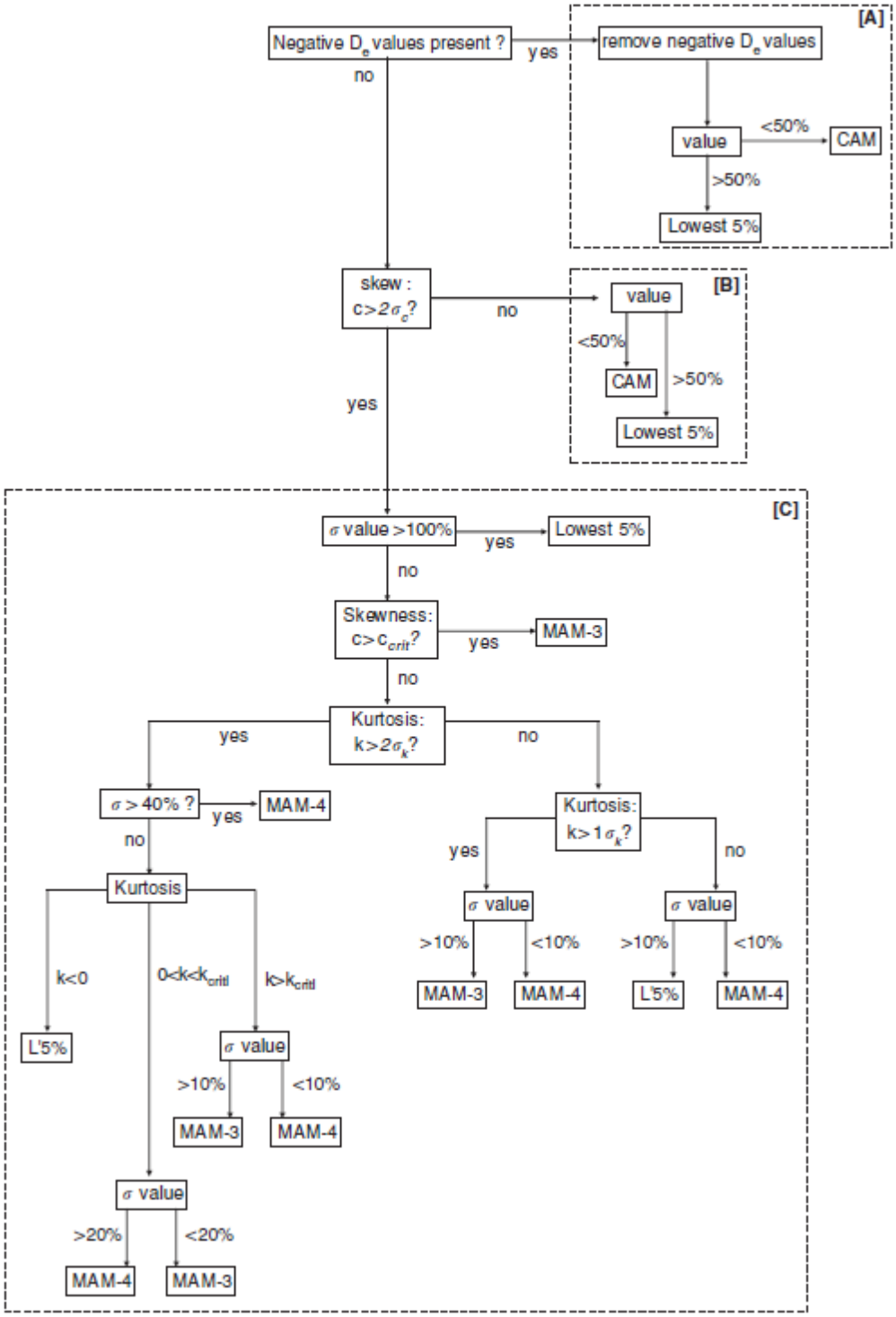

Figure 4.21: Statistical model selection criteria reprinted from Bailey & Arnold (2006), with permission from Elsevier. Section A deals with young samples, section B with well bleached samples and section C with heterogeneously bleached samples.

In addition to analysing the data with Bailey and Arnold's (2006) model selection flowchart, all samples were also assessed using Arnold's (2006) flowchart specifically for single aliquot data (Figure 4.22). In contrast to the former flowchart which provides an

objective means of selecting between the MAM-3 and MAM-4 (which have three and four components respectively), CAM and L5% models, the latter flowchart only allows differentiation between the MAM and CAM, as these provided the best age estimates for the empirical D_e data sets derived from fluvial samples analysed in the original research (Arnold, 2006; Arnold et al., 2007). Model selection results are tabulated in Table 4.18.

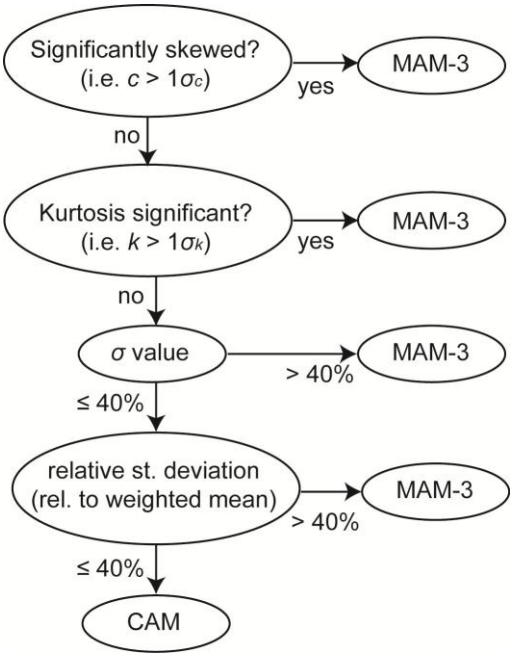

Figure 4.22: Single aliquot model selection flowchart after Arnold (2006).

The selected models varied significantly where the selection criteria of Bailey and Arnold (2006) were used in contrast to either the revised critical values or the SA flowchart, although the latter two selection protocols identified the same models for all samples with the exception of GAUP2. The selection criteria of Bailey and Arnold (2006) identified the L5% model as most appropriate for five of the samples (Olley et al., 1998), however because of the low number of replicates and the arbitrary manner through which the appropriate percentage of aliquots that form the true dose population is selected, this model is regarded as inappropriate for this sample suite. Therefore the selection criteria of Bailey and Arnold (2006) with revised critical values (Arnold, 2006) after Thrasher et al. (2009b) has been selected as the most appropriate method of model selection. However, for FAB95 and FAB41 the MAM-3 model returns extremely large uncertainty (see sample D_e distributions in Figure 4.23), and therefore these samples were analysed using the models returned by Bailey and Arnold's (2006) selection criteria.

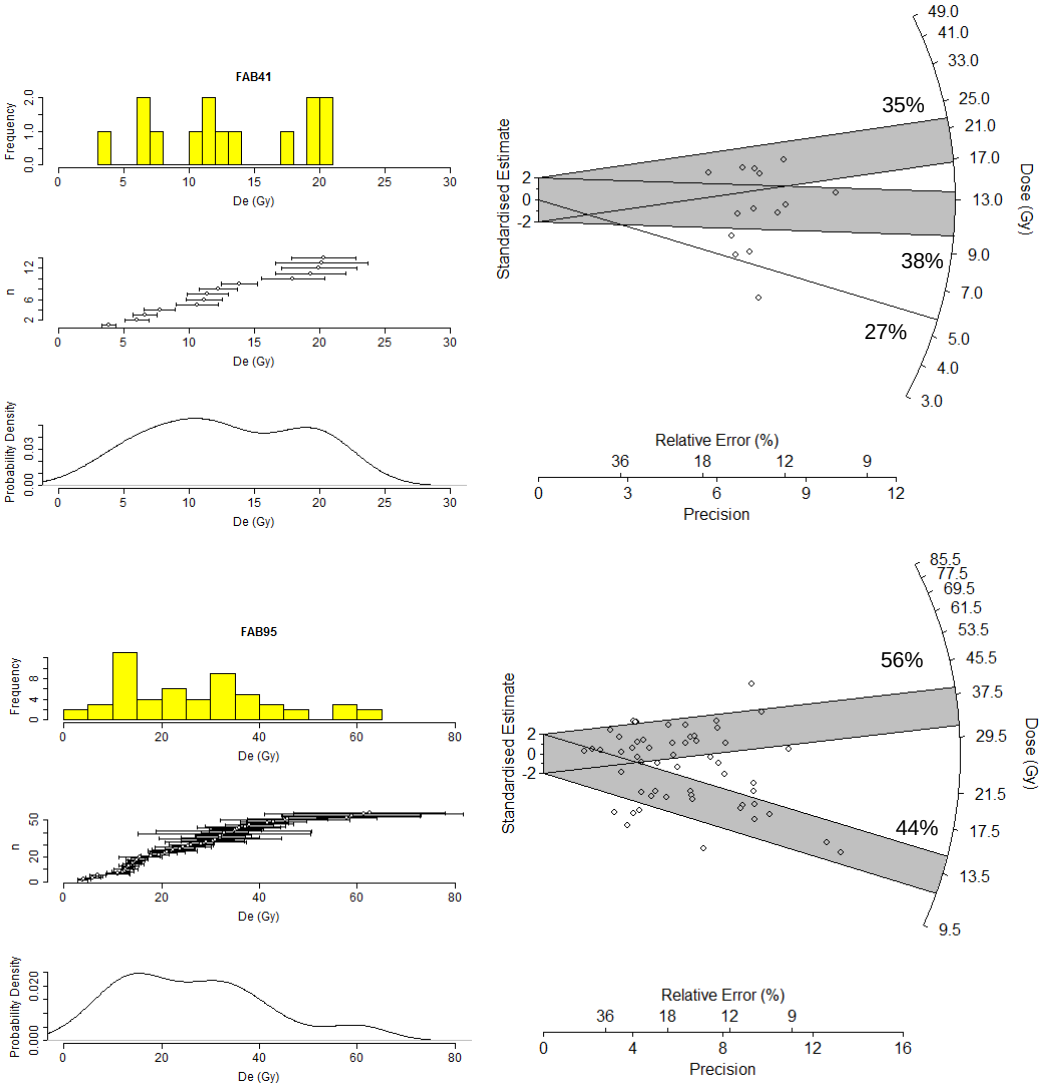

Figure 4.23: Histograms, scatter graphs, probability density functions and radial plots for FAB41 and FAB95, which the MAM-3 model returned extremely high uncertainties for (see Table 4.18). The different components identified with the FMM are identified on each radial plot.

The FMM does not feature in either flowchart (Figure 4.22 or Figure 4.21, see Section 4.10.1.2 for a discussion on the suitability of the FMM for single aliquot data sets) however all samples were analysed with it to explore the nature of components within the different dose populations (Table 4.19).

Table 4.18: Quartz sample model selection results after Arnold (2006) and Bailey and Arnold (2006), see section 4.10.1.5 for details.

Sample	Type	n	Average D_e (1 σ Error)	D_e CAM/COM	σ_d	$2\sigma c_w$	norm c_w	c crit ($1/2\sigma c_w$)	$2\sigma k_w$	norm k_w	k_w crit ($0.6/2\sigma k_w$)	Bailey & Arnold 2006	Arnold 2006 (after Thrasher et al., 2009)	SA Arnold 2006
FABSUB1	Subglacial	20	15.24 ± 10.41	12.10 ± 2.34	0.78 ± 0.10	1.44	2.65	0.69	1.44	-0.06	0.42	L5% 1.50 ± 0.46	MAM-3 3.34 ± 0.87	MAM-3 3.34 ± 0.87
FABSUB2		25	13.99 ± 12.65	11.00 ± 1.73	0.68 ± 0.07	1.42	9.95	0.70	1.42	-1.84	0.42	MAM-3 5.00 ± 1.26	MAM-3 5.00 ± 1.26	MAM-3 5.00 ± 1.26
FAB41*	Paraglacial	14	12.94 ± 5.76	11.57 ± 1.55	0.48 ± 0.03	1.28	1.08	0.78	1.28	-2.94	0.47	MAM-4 3.94 ± 1.51	MAM-3 4.79 ± 8.94	MAM-3 4.79 ± 8.94
FAB42		27	1.62 ± 6.18	2.90 ± 0.50	0.89 ± 0.10	0.96	22.70	1.04	0.96	-2.78	0.63	MAM-3 0.99 ± 1.43	MAM-3 0.99 ± 1.43	MAM-3 0.99 ± 1.43
FAB85		23	6.96 ± 6.12	5.05 ± 0.92	0.84 ± 0.10	1.03	8.01	0.97	1.03	5.20	0.58	MAM-3 1.44 ± 0.25	MAM-3 1.44 ± 0.25	MAM-3 1.44 ± 0.25
FAB86		27	18.50 ± 14.96	12.42 ± 2.29	0.91 ± 0.12	1.49	3.26	0.67	1.49	1.50	0.40	MAM-3 5.68 ± 13.16	MAM-3 5.68 ± 13.16	MAM-3 5.68 ± 13.16
FAB79	Glaciofluvial Point Bar	28	28.95 ± 19.45	25.30 ± 2.38	0.47 ± 0.02	1.67	9.32	0.60	1.67	-1.94	0.36	MAM-3 14.63 ± 1.81	MAM-3 14.63 ± 1.81	MAM-3 14.63 ± 1.81
FAB80		19	13.23 ± 6.99	11.59 ± 1.34	0.49 ± 0.03	1.21	2.12	0.82	1.21	-2.00	0.49	L5% 4.54 ± 0.49	MAM-3 6.09 ± 0.83	MAM-3 6.09 ± 0.83
FAB84		19	27.72 ± 18.71	21.40 ± 3.76	0.75 ± 0.08	1.98	2.22	0.50	1.98	-0.07	0.30	L5% 4.12 ± 0.39	MAM-3 5.22 ± 1.03	MAM-3 5.22 ± 1.03
FAB90		19	22.13 ± 10.49	19.70 ± 2.44	0.47 ± 0.03	1.49	1.11	0.67	1.49	-2.27	0.40	MAM-3 10.69 ± 2.06	MAM-3 10.69 ± 2.06	MAM-3 10.69 ± 2.06
FAB91		31	13.45 ± 8.55	10.91 ± 1.36	0.66 ± 0.05	1.05	2.72	0.95	1.05	-0.47	0.57	L5% 1.92 ± 1.00	MAM-3 4.45± 0.84	MAM-3 4.45± 0.84
FAB92		7	3.57 ± 1.40	11.72 ± 0.66	0.00	-	-	-	-	-	-	-	-	-
FAB94		43	20.85 ± 17.08	15.84 ± 1.64	0.64 ± 0.04	1.26	9.38	0.79	1.26	7.66	0.48	MAM-3 6.40 ± 0.80	MAM-3 6.40 ± 0.80	MAM-3 6.40 ± 0.80
FAB95*		56	26.79 ± 15.26	22.09 ± 1.88	0.61 ± 0.03	1.04	3.21	0.96	1.04	-0.26	0.57	L5% 4.67 ± 1.27	MAM-3 9.22 ± 26.50	MAM-3 9.22 ± 26.50
FAB98		41	26.11 ± 15.46	21.35 ± 2.30	0.66 ± 0.04	1.23	2.87	0.81	1.23	-1.16	0.49	MAM-3 7.47 ± 0.97	MAM-3 7.47 ± 0.97	MAM-3 7.47 ± 0.97
FAB99		18	11.67 ± 6.60	10.95 ± 1.42	0.48 ± 0.03	1.21	1.85	0.83	1.21	-1.05	0.50	L5% 3.43 ± 2.50	MAM-3 5.78 ± 1.28	MAM-3 5.78 ± 1.28
FAB100		25	11.95 ± 9.62	8.99 ± 1.43	0.75 ± 0.08	1.24	3.65	0.81	1.24	-0.15	0.48	L5% 1.78 ± 2.20	MAM-3 3.14 ± 0.54	MAM-3 3.14 ± 0.54

*The MAM-3 model returns extremely large uncertainty, therefore these samples have been analysed with the models selected using Bailey and Arnold's (2006) selection criteria.

Table 4.18 continued.

Sample	Type	n	Average D_e (1 σ Error)	D_e CAM/COM	σ_d	$2\sigma c_w$	norm c_w	c crit ($1/2\sigma c_w$)	$2\sigma k_w$	norm k_w	k_w crit ($0.6/2\sigma k_w$)	Bailey & Arnold 2006	Arnold 2006 (after Thrasher et al., 2009)	SA Arnold 2006
FAB81	Glaciofluvial Braided Channel Bar Deposit	22	9.93 ± 5.27	9.25 ± 1.00	0.46 ± 0.03	0.98	2.62	1.02	0.98	-1.40	0.61	L5% 3.48 ± 1.03	MAM-3 5.15 ± 0.87	MAM-3 5.15 ± 0.87
GRAN54	Sandur Braided Channel Bar	13	17.90 ± 3.81	17.90 ± 1.28	0.00	-	-	-	-	-	-	-	-	-
GRAN55		30	11.25 ± 4.83	10.89 ± 0.87	0.30 ± 0.01	0.80	3.17	1.25	0.80	0.56	0.75	L5% 4.27 ± 3.36	MAM-3 10.86 ± 3.20	MAM-3 10.86 ± 3.20
GRAN56		5	3.53 ± 3.39	4.31 ± 1.94	0.19 ± 0.11	1.65	0.79	0.61	1.65	-4.86	0.36	L5% 0.68 ± 5.37	MAM-3 4.33 ± 0.002	MAM-3 4.33 ± 0.002
GRAN57		6	1.76 ± 1.02	2.03 ± 0.59	0.00	-	-	-	-	-	-	-	-	-
GRAN58		12	11.01 ± 4.53	11.72 ± 1.42	0.26 ± 0.02	1.23	1.98	0.81	1.23	-3.28	0.49	MAM-3 11.92 ± 3.86	MAM-3 11.92 ± 3.86	MAM-3 11.92 ± 3.86
GRAN59		24	17.71 ± 5.52	16.94 ± 1.00	0.16 ± 0.00	0.96	1.99	1.04	0.96	-3.25	0.63	MAM-3 14.24 ± 2.06	MAM-3 14.24 ± 2.06	MAM-3 14.24 ± 2.06
GRAN62		5	6.13 ± 1.49	6.25 ± 1.45	0.00	-	-	-	-	-	-	-	-	-
GAUP2	Delta	8	37.43 ± 10.41	36.59 ± 4.17	0.20 ± 0.01	2.28	0.00	0.44	2.28	-2.15	0.26	CAM 36.59 ± 0.11	CAM 36.59 ± 0.11	CAM 36.59 ± 0.11
GAUP41		13	21.56 ± 5.54	20.01 ± 1.71	0.00	-	-	-	-	-	-	-	-	-

Table 4.19: Quartz FMM results, see section 4.10.1.5 for details, CAM and MAM-3 model results are shown for comparative purposes.

Sample	Type	n	Average D_e (1 σ Error)	σ_d	FMM D_e (Gy) C1	FMM D_e (Gy) C2	FMM D_e (Gy) C3	FMM D_e (Gy) C4	CAM D_e (Gy)	MAM-3 D_e (Gy)
FABSUB1	Subglacial	20	15.24 ± 10.41	0.78 ± 0.10	4.20 ± 0.45 31%	20.31 ± 1.54 69%	-	-	12.10 ± 2.34	3.34 ± 0.87
FABSUB2		25	13.99 ± 12.65	0.68 ± 0.07	10.02 ± 0.70 90%	47.41 ± 5.93 10%	-	-	11.00 ± 1.73	5.00 ± 1.26
FAB41	Paraglacial	14	12.94 ± 5.76	0.48 ± 0.03	7.17 ± 1.34 38%	23.73 ± 1.84 35%	3.77 ± 0.71 27%	-	11.57 ± 1.55	4.79 ± 8.94
FAB42		27	1.62 ± 6.18	0.89 ± 0.10	2.54 ± 0.09 49%	1.27 ± 0.10 25%	6.38 ± 0.06 15%	18.21 ± 1.29 11%	2.90 ± 0.50	0.99 ± 1.43
FAB85		23	6.96 ± 6.12	0.84 ± 0.10	7.98 ± 0.50 41%	3.22 ± 0.26 26%	1.44 ± 0.24 21%	19.34 ± 2.04 13%	5.05 ± 0.92	1.44 ± 0.25
FAB86		27	18.50 ± 14.96	0.91 ± 0.12	31.82 ± 2.27 50%	5.88 ± 0.39 50%	-	-	12.42 ± 2.29	5.68 ± 13.16
FAB79	Glaciofluvial Point Bar	28	28.95 ± 19.45	0.47 ± 0.02	30.88 ± 1.52 73%	15.05 ± 0.08 27%	-	-	25.30 ± 2.38	14.63 ± 1.81
FAB80		19	13.23 ± 6.99	0.49 ± 0.03	9.04 ± 0.73 32%	21.57 ± 1.30 31%	5.80 ± 0.51 19%	11.98 ± 1.22 18%	11.59 ± 1.34	6.09 ± 0.83
FAB84		19	27.72 ± 18.71	0.75 ± 0.08	31.85 ± 2.49 41%	15.89 ± 1.19 30%	5.14 ± 0.45 16%	63.91 ± 10.77 13%	21.40 ± 3.76	5.22 ± 1.03
FAB90		19	22.13 ± 10.49	0.47 ± 0.03	30.22 ± 3.11 46%	10.43 ± 1.41 31%	19.64 ± 3.43 23%	-	19.70 ± 2.44	10.69 ± 2.06
FAB91		31	13.45 ± 8.55	0.66 ± 0.05	19.28 ± 0.92 54%	5.74 ± 0.26 46%	-	-	10.91 ± 1.36	4.45± 0.84
FAB94		43	20.85 ± 17.08	0.64 ± 0.04	15.66 ± 0.69 60%	46.95 ± 4.30 18%	6.73 ± 0.42 22%	-	15.84 ± 1.64	6.40 ± 0.80
FAB95		56	26.79 ± 15.26	0.61 ± 0.03	13.37 ± 0.57 44%	34.80 ± 1.48 56%	-	-	22.09 ± 1.88	9.22 ± 26.50
FAB98		41	26.11 ± 15.46	0.66 ± 0.04	11.48 ± 0.63 42%	34.24 ± 1.61 58%	-	-	21.35 ± 2.30	7.47 ± 0.97
FAB99		18	11.67 ± 6.60	0.48 ± 0.03	6.54 ± 0.65 45%	16.40 ± 0.99 55%	-	-	10.95 ± 1.42	5.78 ± 1.28
FAB100		25	11.95 ± 9.62	0.75 ± 0.08	7.17 ± 1.34 38%	23.73 ± 1.84 35%	3.77 ± 0.71 27%	-	8.99 ± 1.43	3.14 ± 0.54
FAB81	Glaciofluvial Braided Channel	22	9.93 ± 5.27	0.46 ± 0.03	9.55 ± 0.59 46%	4.74 ± 0.58 27%	16.85 ± 1.27 27%	-	9.25 ± 1.00	5.15 ± 0.87
GRAN55	Sandur Braided Channel Bar	30	11.25 ± 4.83	0.30 ± 0.01	8.34 ± 1.01 55%	14.95 ± 1.97 45%	-	-	10.89 ± 0.87	10.86 ± 3.20
GRAN58		12	11.01 ± 4.53	0.26 ± 0.02	10.35 ± 1.18 85%	20.15 ± 6.56 15%	-	-	11.72 ± 1.42	11.92 ± 3.86
GRAN59		24	17.71 ± 5.52	0.16 ± 0.00	15.08 ± 1.54 67%	21.42 ± 3.23 33%			16.94 ± 1.00	14.24 ± 2.06

4.11. Investigations into Sample Number

Rodnight (2008) recently proposed that a minimum of 50 aliquots are required for a D_e distribution to be reproducible through examination of a heterogeneously bleached fluvial sample. She identified that non-normally distributed datasets which contain < 20 aliquots, have a > 50% chance of appearing to be normally distributed. However she also identified that the MAM and FMM return a stable D_e once > 30 aliquots are analysed. Due to the low acceptance rates of the quartz analysed here, 24 samples have less than 20 aliquots, 9 samples have between 21 and 30 aliquots, and 3 have n > 30 (Table 4.18). Consequently the influence of n on both D_e determination and sample distribution must be explored.

Rodnight (2008) determined the threshold value of n = 50 through bootstrapping 20 populations (B_{20}) of n = 5, 10, 15, 20, 30, 40, 50 and 60 aliquots, and testing for normality using the Kolmogorov-Smirnov test. Bootstrapping operates through sampling from the original data set, with replacement, until population size is equal to the original dataset (see Efron and Tibshirani, 1993). This experiment has been repeated on CalQz Batch 8 (CalQzB8) which is normally distributed (p = 0.73, α = 0.05, Figure 4.24, and four Norwegian samples which have apparently non-normal distributions (Figure 4.23 and Figure 4.25). Sample details are listed in Table 4.20. Subpopulations of n (increments of 5) of each of the samples were bootstrapped 20 times. The Shapiro-Wilk test (Shapiro and Wilk, 1965) has been reported to provide a better assessment of normality (Stephens, 1974) than the Kolmogorov-Smirnov test and is used in R 12.2.0 (Royston, 1982a, b, 1995) to test the bootstrapping output reported here (R code is provided in Appendix B).

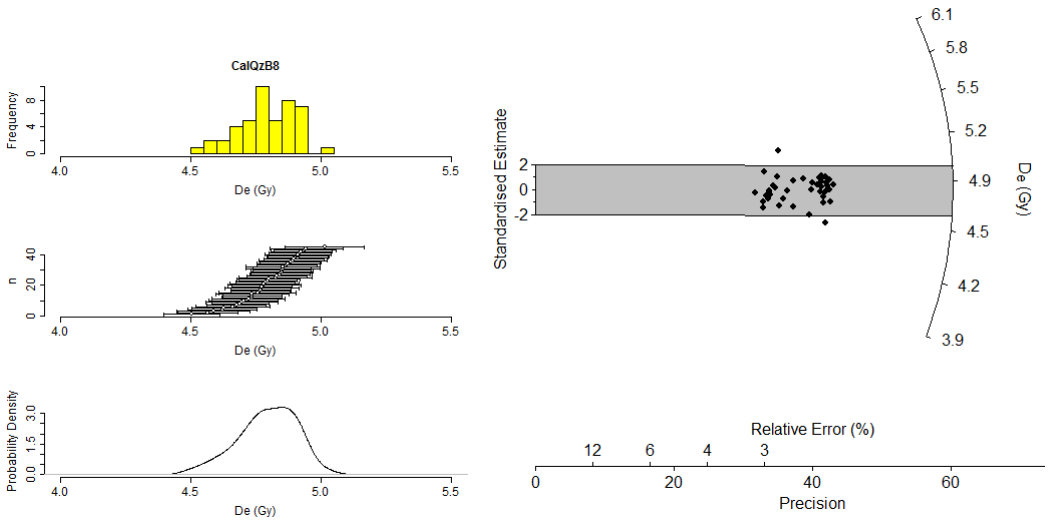

Figure 4.24: Histogram, scatter graph, probability density function and radial plot of CalQz Batch 8, analysed in the bootstrapping experiments. This sample has zero overdispersion and is normally distributed (p = 0.73, α = 0.05).

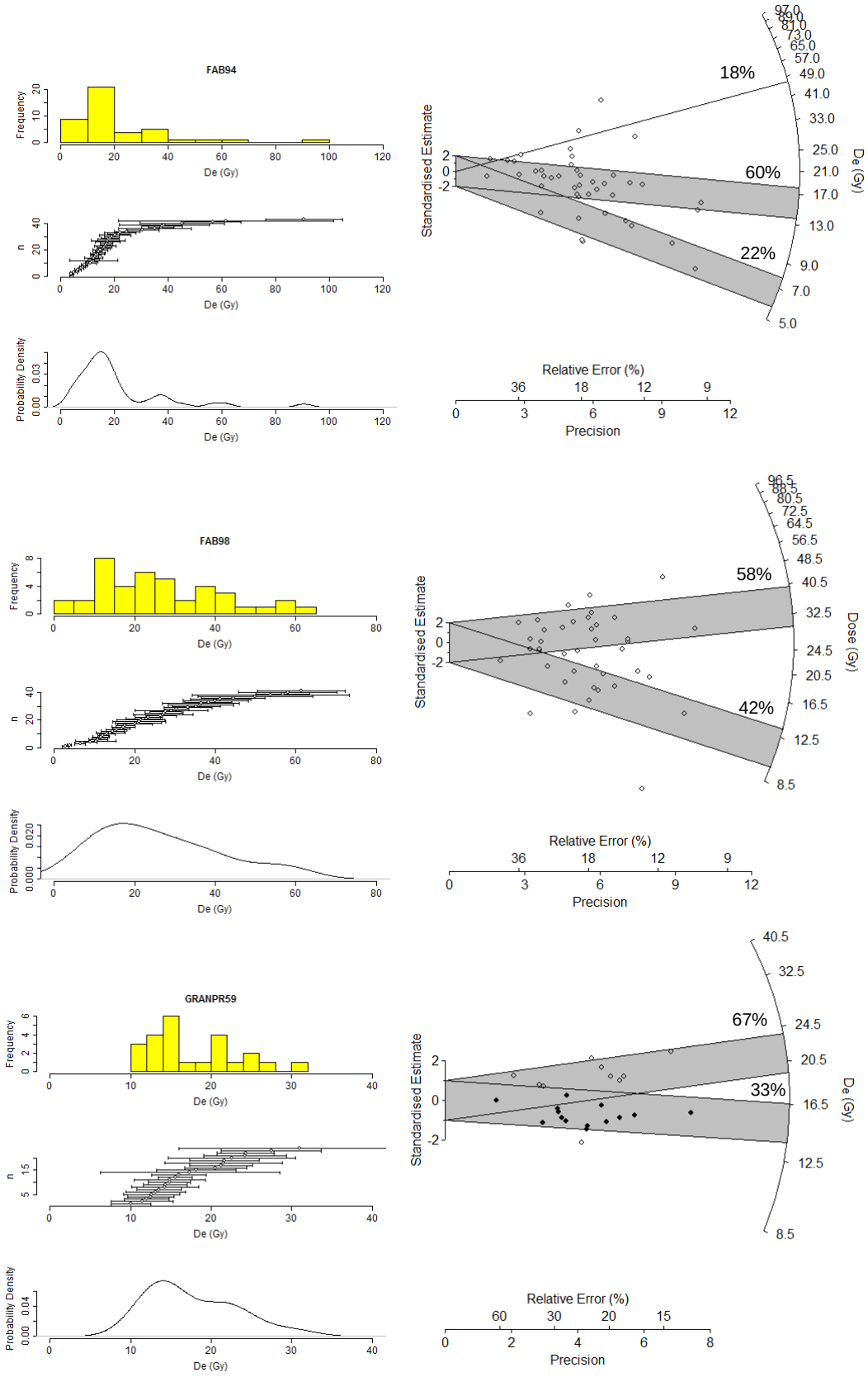

Figure 4.25: Histograms, scatter graphs, probability density functions and radial plots of FAB94, FAB98 and GRAN59 which have been used in the bootstrapping experiments. Distributions of FAB95 have been shown previously on page 95.

Table 4.20: Properties of samples analysed with bootstrapping

Sample	n	σd	FMM Components	Bootstrapped Populations
FAB94	43	0.64 ± 0.04	3	8
FAB95	56	0.61 ± 0.03	2	10
FAB98	41	0.66 ± 0.04	2	8
GRAN59	24	0.16 ± 0.00	2	4
CalQzB8	44	0.00	1	8

Where *n* = 10, 55 to 85% of the Norwegian bootstrap samples returned normal distributions (Table 4.21), supporting Rodnight's observations (2008). For *n* > 20, all distributions calculated for FAB94 were non-normal, anticipated due to its highly non-normal distribution. However FAB98 which has greater σ_d than FAB94, and returns two components with FMM, returned 45% normal distributions when *n* = 30. CalQzB8 was investigated to provide a control as it has known dose, zero σ_d and is normally distributed. Where *n* = 40, 25% of bootstrapped populations were not normally distributed. This indicates the sensitivity of the Shapiro-Wilk test. Increasing to 50 bootstraps was explored for CalQzB8; for *n* = 40 only 14% of bootstrapped populations had non-normal distributions, indicating an improvement in model power with increasing bootstrap cycles as would be anticipated.

Table 4.21: Shapiro-Wilks test results for the bootstrapped populations. 20 bootstrapped populations were analysed for each population size (*n*).

n	% Normally distributed populations				
	FAB94	FAB95	FAB98	GRAN54	CalQzB8
5	80	85	90	90	90
10	55	85	80	70	100
15	40	75	80	55	95
20	0	70	70	35	85
25	0	65	40	-	80
30	0	40	45	-	95
35	0	30	30	-	95
40	0	25	20	-	75
45	-	15	-	-	70
50	-	15	-	-	-

These results suggest that small *n* may falsely indicate normal distributions, but that these normality tests are too sensitive for OSL D_e distributions as CalQzB8 is normally distributed, yet returns some non-normal results. Consequently, the influence of varying sample *n* on the mean D_e was investigated for a range of samples with different σ_d values, as this may provide a better indication of the likely influence of *n* on D_e. Again using the bootstrap function in R.12.2.0; 10,000 sub-sample populations of *n* = 5, 10, 15, 20, 25, 30, 35 and 40 were calculated with replacement, and their mean average D_e values calculated. Where sample *n* is < 40, the sample function in R creates populations of > *n*

through sampling with replacement. The data are summarised in Figure 4.26, and it is apparent that for samples with σ_d > 40% (e.g. FAB79, σ_d 47 %), mean D_e varies significantly with n, but stabilises where n > 30, in support of Rodnight's observations (2008). Samples with low σ_d that are well characterised (e.g. GRAN59, σ_d 17 %, sample n = 24) exhibit lower variation than samples with high σ_d values, or those that are characterised with few aliquots (e.g. GRAN56, σ_d 19%, n = 5; Figure 4.26).

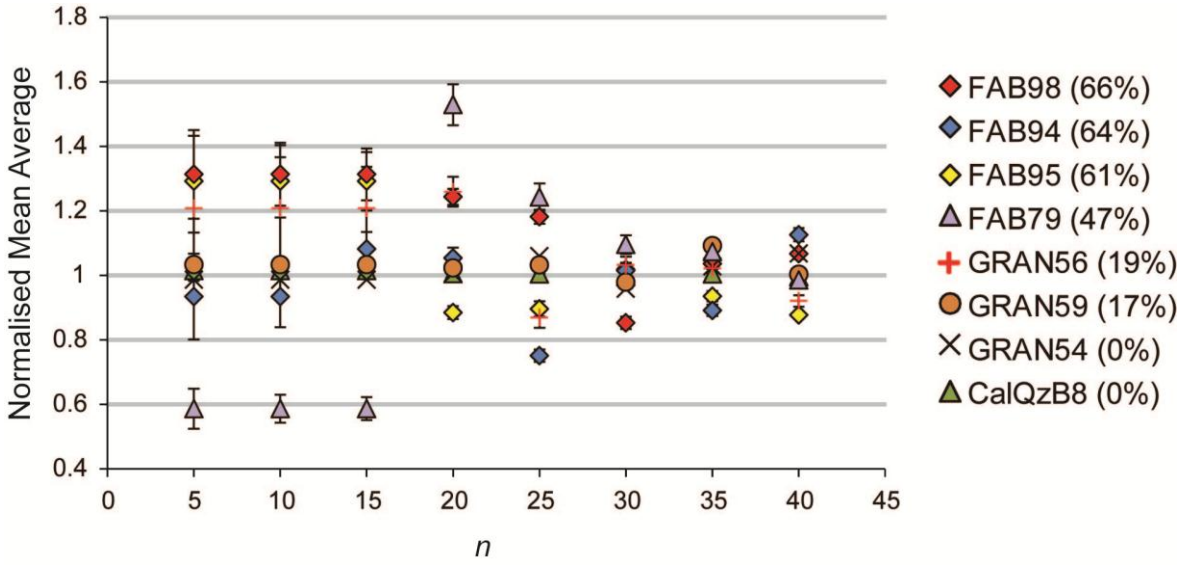

Figure 4.26: Variation in sample mean D_e as a function of n, calculated from 10,000 bootstrap populations (see Appendix B for R code). Data are normalised to the original sample mean D_e and σ_d values are listed in the key.

The influence of sample n on σ_d was also assessed through sub-sampling populations using the replicate function in R of n = 5, 10, 15, 20, 25, 30, 35, 40, 45 and 50, for samples with different σ_d properties (Figure 4.27). The results of CalQzB8 and GRAN54 which have zero σ_d are not shown as no deviation was observed as a function of n. With the exception of GRAN59, the other samples analysed exhibited little variation in σ_d where n > 10. The variance in GRAN59 is unexplained, however within the context of this research the broad characteristics of the different deposits are investigated, thus fluctuation between ~ 10 and ~ 20% σ_d is of little consequence. However it is acknowledged that this may influence age model selection where the criteria of, for example, Bailey and Arnold (2006) are used, and the same is also true of sample skewness and kurtosis, which will also be affected by sample size.

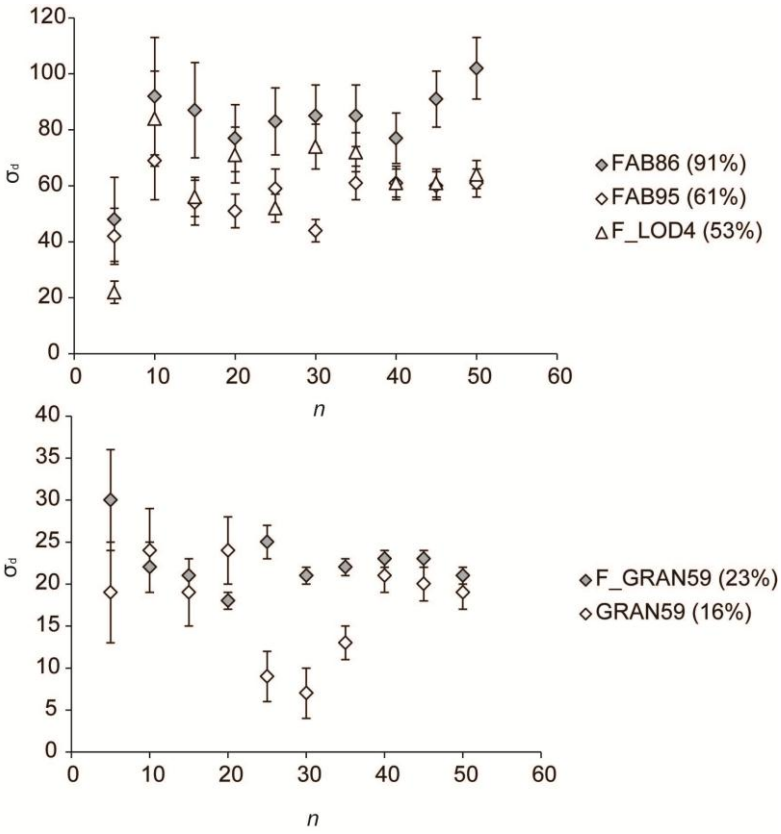

Figure 4.27: Variation in sample σ_d as a function of *n*. Sub-samples were derived using the Resample function in R, which enabled populations beyond measured *n* to be calculated, i.e. GRAN59 has sample *n* of 24 aliquots. Feldspar extracts of GRAN59 (F_) and LOD4 have also been included to explore whether quartz and feldspar behave in the same way. Analysis code is provided in Appendix B.

4.11.1. Investigations of Bootstrap Population Distribution Statistics

The nature of the majority of the samples analysed in this thesis is such that non-normal distributions are anticipated, so rather than assessing whether low *n* values result in false assumptions of normality, consideration should instead be given to whether *n* appropriately represents the parent populations, regardless of distribution. This has been explored through bootstrapping the different samples, and calculating the skewness (B_c), kurtosis (B_k) and mean (B_x) of the bootstrapped populations. Where *n* provides a sufficient estimation of the underlying population, according to the central limits theorem these statistics should have a normal distribution irrespective of sample distribution. CalQzB8 (*n* = 44) is known to have uniform dose and 5,000 bootstrap populations with replacement, of equal size to the original sample, were calculated. The B_c, B_k and B_X were calculated and distributions tested for normality using the Shapiro-Wilk test. Only B_X had normal distribution ($p = 0.10$, $\alpha = 0.05$), indicating that even for a well characterised, normally distributed sample, greater *n* is required for full sample characterisation.

As CalQzB8 has known age and distribution, a synthetic population of 100 aliquots was created from the measured sample, using the "sample" function with replacement in R 2.12.0 (Becker et al., 1988; Ripley, 1987; R Development Core Team, 2010; R code is listed in Appendix B) and the experiment repeated. Even with increased *n,* B_k and B_c still

did not exhibit normal distributions (p = 0.05). Only following creation of a sample of n = 3,000 were normal B_k and B_c populations derived. This reinforces the earlier observation that using this kind of test for sample size is too stringent to be practically applicable within luminescence dating, due to the time and expense of analysing such vast numbers of aliquots. An alternative assessment of distribution normality could be made through evaluation of c and k, however time has precluded further investigations into this at present.

4.11.2. Investigation of Bootstrap Population Distribution Statistic Bias

Rather than seeking a normal distribution in all three of the exploratory statistics, a normal distribution for B_X could instead be used to evaluate whether n is sufficient, however where samples are multimodal, larger n values will be required (Figure 4.26). Alternatively, through exploring the ***bias*** in the B statistics relative to the distribution properties of the original sample, a qualitative inference regarding the need for additional aliquots can be made on a sample by sample basis.

All quartz and feldspar samples were bootstrapped 10,000 times (n equal to the original sample, sampled with replacement, Figure 4.28) and confidence intervals (1σ) were derived for B_X, B_c and B_k. These B statistics are contrasted with the x, c, and k, values of the original samples suite (Table 4.22 and Table 4.23) to calculate bias (b) using:

Eq. 4.21 $$\left|B_k - k\right| = \mathrm{b}B_k$$

where bB_k is the bias of the bootstrapped value of kurtosis, relative to the value measured for the original sample. The Norwegian feldspar data described in Chapter 5 are also discussed here to facilitate comparison.

CalQzB8 has been investigated to provide a control, and its derived bias values were explored as potential threshold values; B_X bias (bB_X) is -0.0001 ± 0.0170 (< 1%), bB_c is -0.10 ± 0.62 (29%) and bB_k is -0.03 ± 0.48 (62%). Uncertainties are large, which reflects the sensitivity of these statistics to population distribution. All samples produced bB_X < 1% indicating that, for all samples, sample means are insensitive to variations in sample population where n is kept the same. This is because the mean is an unbiased statistic and therefore cannot provide a robust method for evaluating sample size. CalQzB8 has bB_K of 62% which is greater than the bB_K of 24 of the 29 Norwegian quartz samples analysed (Table 4.22). The sensitivity of k to sample size was evaluated through sub-sampling four populations from CalQzB8, with replacement (n = 10, 20, 30 and 40), and it reduces with increasing n. The % bias of bB_k ranged from 0.5 – 234 % for the different samples, indicating considerable sensitivity of k to sample population. Interestingly the

quartz samples with minimum and maximum bias had similar sample *n*, but different σ_d: GRAN55 (*n*=31, σ_d: 30 ± 1%) had maximum bias in contrast to FAB91 (*n*=30, σ_d: 66 ± 5%) illustrating that there is no simple relationship between sample distribution characteristics and bias.

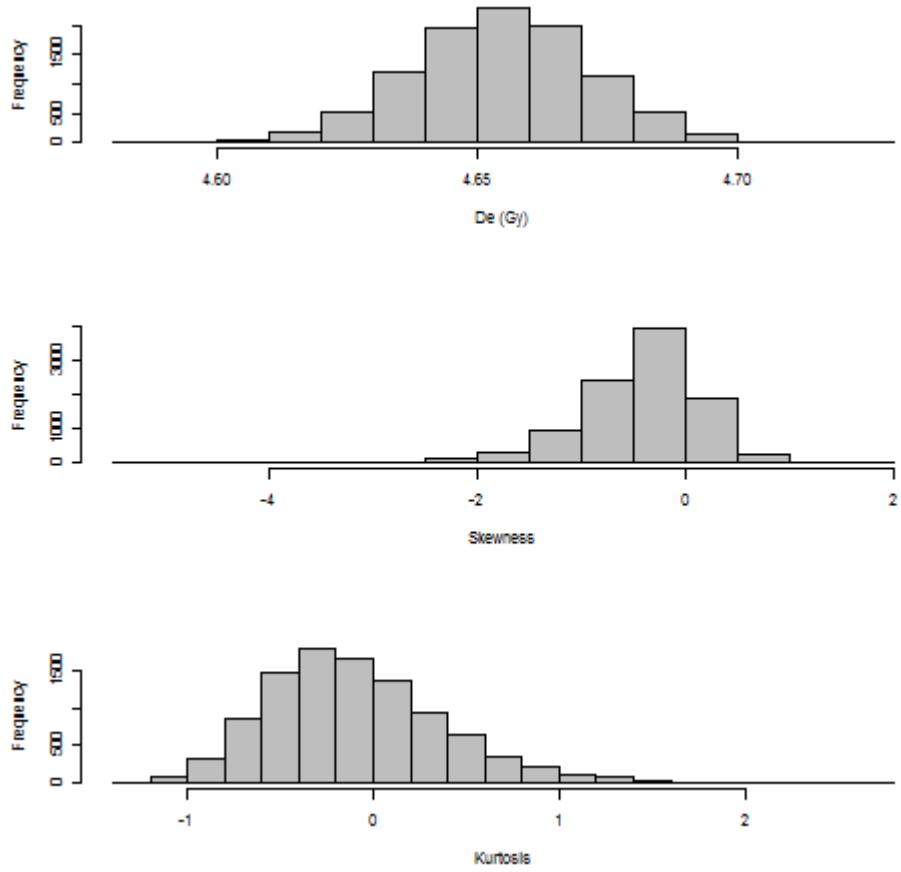

Figure 4.28: Histograms of CalQzB8 bootstrapped results following 10,000 iterations.

The significance of measured *k* relative to a normal distribution was evaluated for the quartz samples using Eq. 4.20; nine quartz samples have significant *k*, and are listed in Table 4.22. However, little association was observed between significant *k* and bB_k, further illustrating the sensitivity of *k* to sample population. In contrast, six of the 26 feldspar samples analysed had significant *k*, and these samples exhibited the least bias (Table 4.23).

Where the CalQzB8 threshold of bB_C 29% is used, only two quartz samples are accepted, FAB95 (n=56) and FAB98 (n=41). This result is consistent with Rodnight's assertion that a minimum aliquot number of 50 is required in order to fully characterise a sample distribution, however evaluation of the feldspar data indicated that only four samples fulfilled this acceptance criterion, although 15 samples have $n > 30$ (see Chapter 5 for sample details). The % bias of the bB_c estimates range from 18 – 1,637%, indicating that *c* is extremely sensitive to variations in population. Bootstrapping CalQzB8 100,000 times failed to reduce its bB_c significantly (b$B_{c\text{-}10,000}$ 29%, b$B_{c\text{-}100,000}$ 28%), furthermore,

sub-sampling populations of n = 10, 20, 30 and 40 exhibited significant variation in derived c. The significance of measured c can be evaluated using Eq. 4.19, and eight quartz samples have significant c (Table 4.22). However, as for k, little correlation between significant c and bB_c is observed. Of the four feldspar samples which have significant k, three have low bias, but none pass the 29% acceptance criterion (Table 4.23).

Where sample c or k are correlated relative to bB_c or bB_k for both the quartz and feldspar samples as a function of n, it is apparent that a series of thresholds exist (Figure 4.29). For low n values, bB_c and bB_k are generally low, irrespective of c or k, however when n approaches ~ 20, bias increases. This is an artefact of investigating samples with low n values, as the finite number of potential population iterations is reduced. Those samples with the greatest n values exhibit the lowest bias, which supports Rodnight (2008). However, those samples with the greatest c and k values also exhibit the greatest bias, indicating that for some samples with multi-modal distributions, an assumption that 50 aliquots is sufficient may not be valid. In the quartz samples analysed this threshold is < -0.1 and > 1 for c, whereas for feldspar it is > 3. Samples exhibiting c beyond these boundaries require additional analyses relative to those within the threshold range, relating to the increased likelihood that the underlying sample distribution comprises multiple modes. Similarly, the largest values of k are subject to the greatest bias, and a threshold of > 0 has been assigned, above which further analyses may be required. Bias reduces for quartz extracts with > 30 aliquots and for feldspar extracts with > 50 aliquots, indicating that suitable n should be considered on an individual sample basis.

4.11.3. Aliquot Number Analysis Protocol

The investigations into the influence of aliquot number on sample distribution indicate that using a threshold value of 50 aliquots for confidence in sample distribution is over-simplistic, and that bootstrapping and evaluation of the bootstrapped population's statistical bias relative to c and k provides an alternative and effective screening mechanism. Visual analysis of sample D_e distributions provides insights into the number of aliquots required, which are lost where only σ_d and other distribution statistics are considered. For example, σ_d is diagnostic of the worst bleached samples, and also those nearing complete bleaching, as significant outliers may relate to the best bleached grains or those that have not been fully reset, thus σ_d should be regarded as a hysteretic parameter. Further research into the relationship of sample distributions relative to true distribution may enable the use of bootstrapping to generate complete and statistically robust distributions, from which improved D_e determinations can be made. Rather than adopting a threshold value of 50 aliquots throughout this thesis, sample n, c, k, and bB_c and bB_k relative to CalQzB8 are instead considered. Samples are tested with the following

Table 4.22: Mean, *c* and *k* statistics for the original quartz datasets and averages from the bootstrap populations. Biases are calculated from the difference between original and calculated values derived from 10,000 bootstraps, standard errors are quoted at 1σ. *P* indicates bootstrap criteria passed.

Sample	*n*	Mean	Bias (bB_x)	SE	% Bias	*c*	*c* Sig?	bB_c	% Bias	SE	*k*	*k* Sig?	bB_k	% Bias	SE	*n*	*c*	< bB_c *CalQzB8*	k	< bB_k *CalQzB8*
FABSUB1	20	15.24	0.0086	2.28	0.06	0.63		0.44	69.45	1.56	-0.45		-0.09	20.26	0.69					P
FABSUB2	25	13.99	0.0286	2.46	0.20	1.80		2.91	162.00	8.00	2.73		-0.35	12.70	2.46				*P*	*P*
FAB41	14	12.94	-0.0281	1.50	0.22	0.00		0.04	1245.70	1.51	-1.58		0.19	12.07	0.42					*P*
FAB42	27	4.62	-0.0026	1.17	0.06	2.77		11.72	422.56	47.65	8.01		-2.64	32.90	4.04				*P*	*P*
FAB85	23	6.96	0.0019	1.24	0.03	1.48		1.68	113.96	4.38	2.00	*Y*	-0.89	44.39	1.80				*P*	*P*
FAB86	27	18.50	-0.0090	2.81	0.05	0.69		0.29	42.06	1.16	-0.70	*Y*	-0.07	10.64	0.74					*P*
FAB79	28	28.95	-0.0178	3.62	0.06	3.28		16.39	499.75	28.65	12.47		-6.25	50.10	5.76				*P*	*P*
FAB80	19	13.23	-0.0100	1.56	0.08	0.63		0.50	79.26	2.48	-1.20		0.27	22.31	0.91					*P*
FAB84	19	27.72	-0.0046	4.12	0.02	0.80		0.72	90.39	2.33	-0.27		-0.02	7.18	0.90					*P*
FAB90	19	22.13	0.0040	2.37	0.02	0.11		0.07	59.47	1.00	-1.40		0.10	7.31	0.37					*P*
FAB91	31	13.45	-0.0002	1.51	0.00	0.39		0.14	35.81	0.75	-1.13	*Y*	0.01	0.54	0.41	*P*				*P*
FAB92	7	3.57	0.0011	0.49	0.03	-0.23	*Y*	-3.73	1636.73	61.54	-1.85		0.28	15.33	0.55		*P*			*P*
FAB94	43	20.85	-0.0051	2.53	0.02	2.10		1.65	78.25	4.40	4.94		-1.16	23.53	2.97	*P*			*P*	*P*
FAB95	56	26.79	0.0131	2.02	0.05	0.63		0.12	18.35	0.62	-0.34	*Y*	0.01	2.99	0.40	*P*		*P*		*P*
FAB98	41	26.11	0.0365	2.40	0.14	0.63		0.16	26.08	0.78	-0.55	*Y*	0.05	8.39	0.50	*P*		*P*		*P*
FAB99	18	11.67	-0.0231	1.50	0.20	0.62		0.52	82.88	2.11	-0.93		0.04	4.75	0.73					*P*
FAB100	25	11.95	0.0124	1.90	0.10	0.87		0.50	57.59	2.09	-0.68	*Y*	0.23	33.49	1.03					*P*
BERG24	8	2.95	0.0018	0.28	0.06	-0.11	*Y*	-0.52	449.99	24.81	-1.60		0.13	8.01	0.54		*P*			*P*
FAB81	22	9.93	-0.0119	1.09	0.12	0.73		0.48	65.68	1.73	-0.57		0.06	10.14	0.80					*P*
GRANPR54	13	17.90	0.0026	1.00	0.01	-0.11	*Y*	-0.11	100.95	1.48	-1.61		0.17	10.87	0.41		*P*			*P*
GRANPR55	30	11.31	-0.0147	0.97	0.13	0.78		0.41	52.13	1.38	-0.07	*Y*	-0.17	233.76	0.87					
GRANPR56	5	3.53	0.0061	1.35	0.17	0.70	*Y*	-	-	-	-1.43		-0.21	14.59	0.50					*P*
GRANPR57	6	1.76	0.0017	0.38	0.10	-1.00		-	-	-	-0.59		-0.65	110.33	0.74		*P*			
GRANPR58	12	11.01	-0.0031	1.25	0.03	1.34		6.47	481.98	28.19	1.27	*Y*	-1.01	79.18	1.42				*P*	
GRANPR59	24	17.71	0.0002	1.10	0.00	0.66		0.36	55.34	1.40	-0.60		-0.06	9.60	0.72					*P*
GRANPR62	5	6.13	0.0082	0.59	0.13	0.18	*Y*	-	-	-	-1.90		0.12	6.50	0.39					*P*
GAUP2	8	37.43	-0.0012	3.42	0.00	-0.82	*Y*	-4.99	610.96	33.04	-0.64		-0.45	70.86	0.76		*P*			
GAUP41	13	21.56	-0.0003	1.47	0.00	-0.03	*Y*	-0.09	314.00	1.99	-1.60		0.18	11.15	0.48					*P*
CALQZB8	44	4.65	-0.0001	0.02	0.00	-0.34	*Y*	-0.10	28.57	0.62	-0.06	*Y*	-0.03	62.34	0.48	*P*	*P*	*P*		*P*

*Where $n < 7$ no bias could be calculated for skewness.

Table 4.23: Mean, *c* and *k* statistics for the original non-fading corrected feldspar datasets and averages from the bootstrap populations. Biases are calculated from the difference between original and calculated values derived from 10,000 bootstraps, standard errors are quoted at 1σ. *P* indicates bootstrap criteria passed.

Sample	*n*	Mean	Bias (bB_x)	SE	% Bias	*c*	*c* Sig?	bB_c	% Bias	SE	*k*	*k* Sig?	bB_k	% Bias	SE	*n*	*c*	< bB_c *CalQzB8*	k	< bB_k *CalQzB8*
BERG2	21	178.33	0.156	20.01	0.09	-0.04	*Y*	-0.03	88.06	0.93	-0.97		0.08	-8.46	0.42					*P*
FAB86	12	219.33	-0.013	13.39	0.01	0.40		0.53	133.12	2.19	-0.76		-0.18	24.25	0.63					*P*
LOD4	46	27.11	0.020	2.68	0.07	2.60		2.76	106.38	6.36	8.40		-2.36	-28.15	4.23	*P*			*P*	*P*
LOD5	24	52.37	-0.057	5.18	0.11	0.67		0.37	55.54	1.31	-0.14		-0.19	133.09	0.77					
LOD6	48	24.15	-0.042	2.71	0.05	1.58		0.64	40.27	2.12	2.02		-0.02	-0.75	1.65	*P*			*P*	*P*
FAB94	12	195.53	-0.115	11.84	0.06	0.71		1.04	147.25	4.16	-0.46		-0.41	89.95	0.84					
FAB100	12	68.94	0.064	4.65	0.09	-0.09	*Y*	-0.07	79.31	1.78	-0.98		0.05	-4.71	0.64					*P*
JOS51	47	3.81	0.001	0.22	0.00	4.00		10.37	259.31	18.20	19.89		-9.38	-47.15	8.88	*P*	*P*		*P*	*P*
FAB81	12	96.06	-0.121	5.72	0.13	0.07		0.05	67.23	2.02	-1.48		0.15	-10.17	0.46					*P*
LEI13	48	10.86	-0.001	2.04	0.06	4.89		28.20	577.20	50.46	26.88		-12.68	-47.18	11.45	*P*	*P*		*P*	*P*
LEI14	45	8.89	0.018	1.46	0.67	2.71		3.20	118.00	11.16	8.08		-1.81	-22.41	4.25	*P*			*P*	*P*
LEI18	47	5.37	-0.003	0.81	0.09	5.82		130.64	2243.20	199.37	35.25		-18.48	-52.42	15.38	*P*	*P*		*P*	*P*
GRAN54	48	147.97	-0.026	4.80	0.02	-0.11	*Y*	-0.06	55.17	0.85	-0.60		-0.02	3.79	0.49	*P*				*P*
GRAN55	48	102.09	-0.019	4.83	0.02	-0.39	*Y*	-0.22	56.75	1.25	-0.77		0.09	-12.19	0.63	*P*				*P*
GRAN56	55	16.62	-0.001	0.56	0.03	0.92		0.26	28.23	0.91	1.53		-0.16	-10.71	0.96	*P*		*P*	*P*	*P*
GRAN57	54	13.79	0.001	0.67	0.01	0.97		0.25	25.78	0.89	1.06		-0.23	-21.78	0.86	*P*		*P*	*P*	*P*
GRAN58	24	124.44	-0.120	5.65	0.10	-0.04	*Y*	-0.08	181.52	1.09	0.13		-0.08	-61.10	0.92				*P*	*P*
GRAN59	60	167.25	-0.054	5.14	0.06	0.47		0.09	18.23	0.51	-0.30	*Y*	-0.03	8.45	0.38	*P*		*P*		*P*
GRAN69	60	15.82	-0.009	1.58	0.05	2.44		1.49	61.14	3.85	7.24		-1.22	-16.79	3.53	*P*			*P*	*P*
NIG3	47	7.87	-0.010	0.71	0.00	5.11		40.70	796.74	69.61	28.72		-14.10	-49.10	12.21	*P*	*P*		*P*	*P*
NIG4	33	188.16	0.209	16.18	0.11	0.63		0.23	37.14	0.96	-0.23	*Y*	-0.07	28.48	0.67	*P*				*P*
NIG6	23	5.44	-0.008	0.46	0.15	3.14		18.19	579.23	29.80	10.87	*Y*	-5.96	-54.80	5.36		*P*		*P*	*P*
NIG7	48	5.18	-0.005	0.32	0.05	3.16		6.13	193.84	14.65	11.21		-1.66	-14.82	6.16	*P*	*P*		*P*	*P*
NIG8	48	6.70	-0.002	0.23	0.01	0.66		0.14	21.94	0.69	-0.47	*Y*	-0.08	16.29	0.55	*P*		*P*		*P*
NIG9	48	17.52	0.043	3.07	0.70	3.74		9.50	253.73	24.60	16.32		-5.33	-32.66	7.06	*P*	*P*		*P*	*P*
GAUP1	24	173.28	-0.016	8.73	0.01	-0.47	*Y*	-1.05	223.00	5.22	-0.79		0.05	-6.26	0.85					*P*

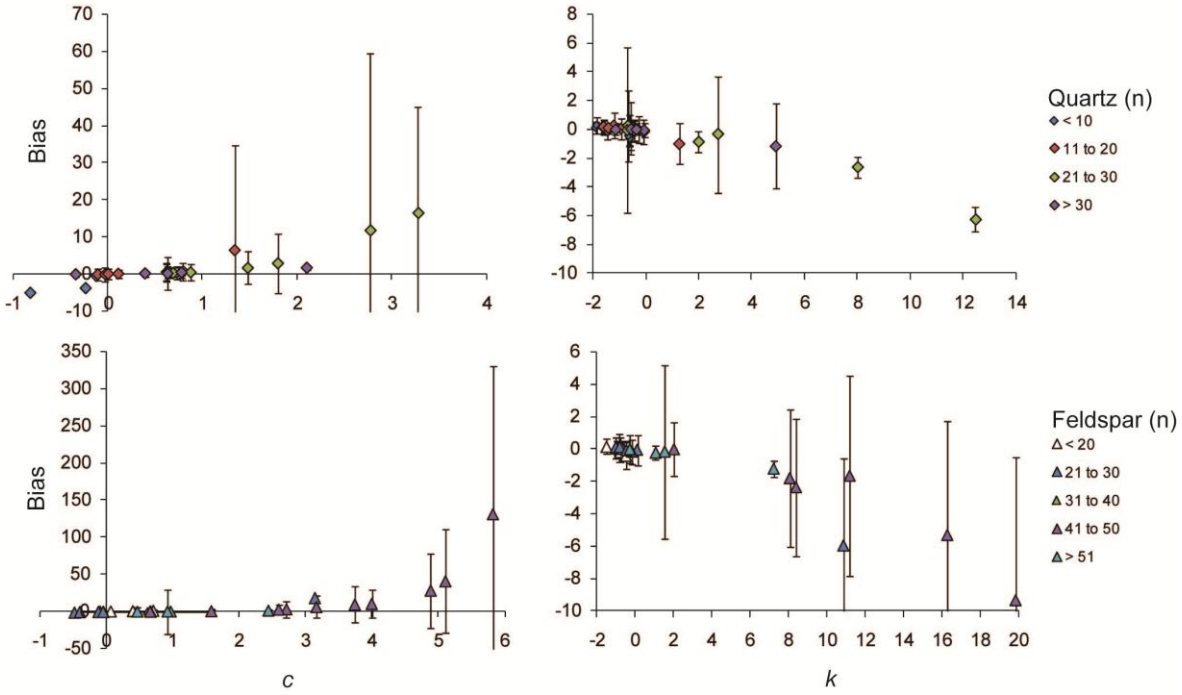

Figure 4.29: Graphs showing bias, relative to sample *c* and *k* for the quartz and feldspar samples. Sample *n* is highlighted. Error bars are the standard error of the bias, calculated from the bootstrapped populations.

criteria: $n > 30$, *c* and *k* within acceptance limits detailed in Section 4.11.2 and bB_c and bB_k > CalQzB8, results are listed in Table 4.23 and Table 4.22. Overdispersion values areinsensitive once $n > 10$ (Figure 4.27) and so at least the σ_d of samples with low *n* may be considered reliable where the other bootstrap acceptance criteria are not fulfilled. The normality test used here was overly sensitive to sample D_e distribution, observed in the failure of CalQzB8 to routinely return a normal distribution. These experiments into sample number require development through exploration of the influence of changing *n* and D_e distribution on the various age model calculated D_e values (e.g. Rodnight, 2008), which has not been possible throughout the duration of this research.

4.12. Environmental Dose Rate & Age Determination

The environmental dose rate (D_r) must be determined in order to derive sample residual age (Eq. 2.1). It is produced by ionizing radiation from the decay of radioisotopes both external and internal to the quartz and feldspar grains, and cosmic radiation (see Appendix A.3 for full D_r calculation detail). Careful calculation of dosimetry is essential in dating applications as microdosimetric variations can result in significant sample σ_d if they

are not properly incorporated (e.g. Nathan et al., 2003). The samples in this research are mostly significantly overdispersed, therefore microdosimetry will have a reduced influence on observed scatter. Furthermore, as the samples in this research are partially bleached and should have near zero age, the D_r that they have been exposed to relates to their previous depositional context, and not to the deposit sampled, meaning that the samples' dosimetric history can only be estimated.

It was not possible to calculate D_r for some samples due to limited material availability. Where this is the case, the U, Th, K and Rb values of samples from the same catchment have been averaged and the associated standard error calculated; these values are used to provide an approximate age. Those samples where average D_r has been used are clearly indicated in Table 4.24. Following calculation of D_r, sample ages were calculated using Eq. 2.1 (Table 4.24).

4.13. Summary

An OSL analysis protocol suitable for the Norwegian quartz samples has been developed, and an experiment protocol for screening quartz with challenging OSL properties proposed. Three different age model selection protocols have been considered, and the criteria of Bailey and Arnold (2006) with revised critical values (Arnold, 2006) after Thrasher et al. (2009b) has been selected as most appropriate for this sample suite. All samples have been age modelled and residual ages are calculated using the D_r calculation given in Appendix A. The challenging nature of the quartz samples analysed in this thesis has resulted in low aliquot acceptance, the implications of which have been considered in detail through a range of statistical bootstrapping experiments.

Table 4.24: Quartz dosimetry and age calculations, samples listed in italics have been calculated using average catchment U, Th, K and Rb concentrations.

Sample	Type	N	D_e (Gy)	Model	Water Content* (%)	Sample Depth** (m)	K (%)	Th (ppm)	U (ppm)	Rb (ppm)	Wet Dose Rate (Gy ka^{-1})	Age (ka)	Max Age (ka)	c	K
FABSUB1	Subglacial	20	3.34 ± 0.87	MAM-3	10.00	1.00	2.85	7.68	1.69	100	3.49 ± 0.21	0.96 ± 0.26	5.78 ± 0.58	0.57	0.03
FABSUB2		25	5.00 ± 1.26	MAM-3	10.00	1.00	3.00	10.13	2.33	100	3.90 ± 0.22	1.28 ± 0.33	12.09 ± 1.70	2.01	4.14
FAB41	Paraglacial	14	3.94 ± 1.51	MAM-4	14.96	0.02	*3.25 ± 0.26*	*8.39 ± 0.93*	*3.28 ± 0.70*	*100*	*3.66 ± 0.26*	*1.07 ± 0.42*	*6.49± 0.71*	*0.00*	*-1.43*
FAB42		27	0.99 ± 1.43	MAM-3	27.75	0.02	3.59	14.44	2.71	100	4.04 ± 0.23	0.25 ± 0.35	4.51 ± 0.43	3.10	10.98
FAB85		23	1.44 ± 0.25	MAM-3	10.57	0.02	2.91	10.83	3.85	100	4.18 ± 0.23	1.21 ± 0.09	4.63 ± 0.60	1.69	3.42
FAB86		27	5.68 ± 13.16	MAM-3	21.20	0.02	3.00	7.65	3.03	100	3.52 ± 0.20	1.67 ± 0.15	9.05 ± 0.87	0.69	-0.51
FAB79	Glaciofluvial Point Bar	28	14.63 ± 1.81	MAM-3	16.69	0.02	2.77	8.02	3.89	100	3.69 ± 0.20	3.99 ± 0.55	8.42 ± 0.67	4.00	19.04
FAB80		19	6.09 ± 0.83	MAM-3	22.29	0.02	*3.25 ± 0.26*	*8.39 ± 0.93*	*3.28 ± 0.70*	*100*	*3.75 ± 0.27*	*1.62 ± 0.25*	*5.75 ± 0.56*	*0.74*	*-0.91*
FAB84		19	5.22 ± 1.03	MAM-3	12.93	0.02	3.22	8.47	3.47	100	4.12 ± 0.24	1.27 ± 0.26	15.50 ± 2.80	0.95	0.47
FAB90		19	10.69 ± 2.06	MAM-3	14.19	0.02	3.04 ± 0.01	8.65 ± 0.12	4.15 ± 0.09	100	4.07 ± 0.23	2.63 ± 0.53	4.83 ± 0.90	0.13	-1.21
FAB91		31	4.45± 0.84	MAM-3	8.28	0.02	3.53 ± 0.02	7.03 ± 0.13	2.64 ± 0.03	100	4.33 ± 0.26	1.03 ± 0.21	1.33 ± 0.11	0.28	-1.31
FAB92		7	11.72 ± 0.66	COM	11.24	0.02	*3.25 ± 0.26*	*8.39 ± 0.93*	*3.28 ± 0.70*	*100*	*4.13 ± 0.29*	*0.93 ± 0.69*	*1.24 ± 0.50**	*-0.37*	*-1.66*
FAB94		43	6.40 ± 0.80	MAM-3	20.35	0.02	3.14	7.87	4.06	100	3.86 ± 0.22	1.66 ± 0.23	12.17 ± 1.36	2.61	8.68
FAB95		56	4.67 ± 1.27	L5%	15.77	0.02	*3.25 ± 0.26*	*8.39 ± 0.93*	*3.28 ± 0.70*	*100*	*3.99 ± 0.28*	*1.17 ± 0.33*	*8.72 ± 0.77*	*0.94*	*0.94*
FAB98		41	7.47 ± 0.97	MAM-3	11.66	0.02	3.16 ± 0.1	8.63 ± 0.13	3.41 ± 0.07	100	4.12 ± 0.24	1.81 ± 0.26	8.30 ± 0.66	0.95	0.21
FAB99		18	5.78 ± 1.28	MAM-3	8.95	0.02	3.37 ± 0.05	7.50 ± 0.01	3.68 ± 0.07	100	4.41 ± 0.26	1.31 ± 0.30	3.72 ± 0.33	0.74	-0.50
FAB100		25	3.14 ± 0.54	MAM-3	19.61	0.02	3.22 ± 0.05	8.62 ± 0.02	3.22 ± 0.01	100	3.81 ± 0.54	0.82 ± 0.15	6.20 ± 0.63	1.12	0.44

Table 4.24 continued.

Sample	Type	N	D_e (Gy)	Model	Water Content* (%)	Sample Depth** (m)	K (%)	Th (ppm)	U (ppm)	Rb (ppm)	Wet Dose Rate (Gy ka^{-1})	Age (ka)	Max Age (ka)	c	K
BERG24	Braided Channel Bar	8	3.12 ± 0.62	COM	21.44	0.02	4.22	17.12	3.25	100	4.73 ± 0.27	0.66 ± 0.14	1.26 ± 0.23*	-0.21	-0.99
FAB81		22	5.15 ± 0.87	MAM-3	16.86		3.19	8.63	2.61	100	3.79 ± 0.22	1.36 ± 0.25	4.45 ± 0.44	0.84	-0.10
GRAN54	Sandur Braided Channel Bar	13	17.90 ± 1.28	COM	21.62	0.02	*2.89*	*13.53 ± 1.87*	*2.91 ± 0.73*	*121.8 ± 4.5*	*3.72 ± 0.24*	*4.82 ± 0.34*	*6.07 ± 1.38**	*-0.38*	*-0.66*
GRAN55		30	10.86 ± 3.20	MAM-3	22.74	0.02	*2.89*	*13.53 ± 1.87*	*2.91 ± 0.73*	*121.8 ± 4.5*	*3.68 ± 0.23*	*2.95 ± 0.89*	*4.07 ± 0.61*	*0.72*	*-0.26*
GRAN56		5	4.31 ± 0.45	MAM-3	15.85	0.02	*2.89*	*13.53 ± 1.87*	*2.91 ± 0.73*	*121.8 ± 4.5*	*3.92 ± 0.25*	*1.10 ± 0.14*	*2.32 ± 1.44**	*1.46*	*1.77*
GRAN57		6	2.03 ± 0.59	COM	23.70	0.02	*2.89*	*13.53 ± 1.87*	*2.91 ± 0.73*	*121.8 ± 4.5*	*3.65 ± 0.23*	*0.56 ± 0.10*	*0.75 ± 0.74**	*-1.79*	*3.86*
GRAN58		12	11.92 ± 3.86	MAM-3	16.91	0.02	*2.89*	*13.53 ± 1.87*	*2.91 ± 0.73*	*121.8 ± 4.5*	*3.88 ± 0.25*	*3.07 ± 1.02*	*5.19 ± 1.73*	*1.69*	*3.21*
GRAN59		24	14.24 ± 2.06	MAM-3	10.51	0.02	*2.89*	*13.53 ± 1.87*	*2.91 ± 0.73*	*121.8 ± 4.5*	*4.13 ± 0.27*	*4.56 ± 0.32*	*5.19 ± 0.86*	*1.01*	*0.10*
GRAN62		5	6.25 ± 1.45	COM	17.10	0.02	*2.89*	*13.53 ± 1.87*	*2.91 ± 0.73*	*121.8 ± 4.5*	*3.87 ± 0.25*	*6.11 ± 0.37*	*2.10 ± 1.87**	*1.42*	*2.05*
GAUP2	Delta	8	36.59 ± 0.11	CAM	0.72	9.00	2.89	10.65	3.15	100	4.00 ± 0.23	9.15 ± 0.60	11.65 ± 2.59*	-1.24	1.58
GAUP41		13	20.01 ± 1.71	COM	5.15	0.50	3.91	10.47	5.81	100	5.72 ± 0.33	3.50 ± 0.27	5.30 ± 9.70*	-0.17	-1.28

*Maximum age calculated from maximum D_e

Chapter 5. Feldspar OSL

5.1. Sample Preparation

Initial sample preparation is the same as for quartz, and K-feldspar was isolated from the 180 – 212 µm grain size fraction through density separation in LST (see Section 4.1 for methodology and for details regarding laboratory lighting). Orthoclase dominates the < 2.58 g cm^{-3} density fraction, and was primarily analysed (Figure 5.1). Feldspar extracts were not treated with HF (Duller, 1992). The structural and chemical properties of feldspar influence their luminescence behaviour, consequently it is important to limit the range of feldspar analysed within a single aliquot. Ideally a single feldspar phase would be isolated, however as feldspar exist in a solid solution series, hand picking of grains from the density separate would be required to achieve this. Magnetic separation may improve the isolation of individual feldspar, however such facilities are not commonly available in luminescence laboratories and were not readily available under subdued light conditions at the University of St Andrews. Optical microscopy of the < 2.58 g cm^{-3} separate indicates that it comprises mainly orthoclase, although some quartz and biotite were present. In addition to pure orthoclase, some grains contain intergrowths or perthitic albite ($NaAlSi_3O_8$), which were observed with back-scattered electron (BSE) imaging using a JEOL JCXA733 electron microprobe at the University of St Andrews (Figure 5.2).

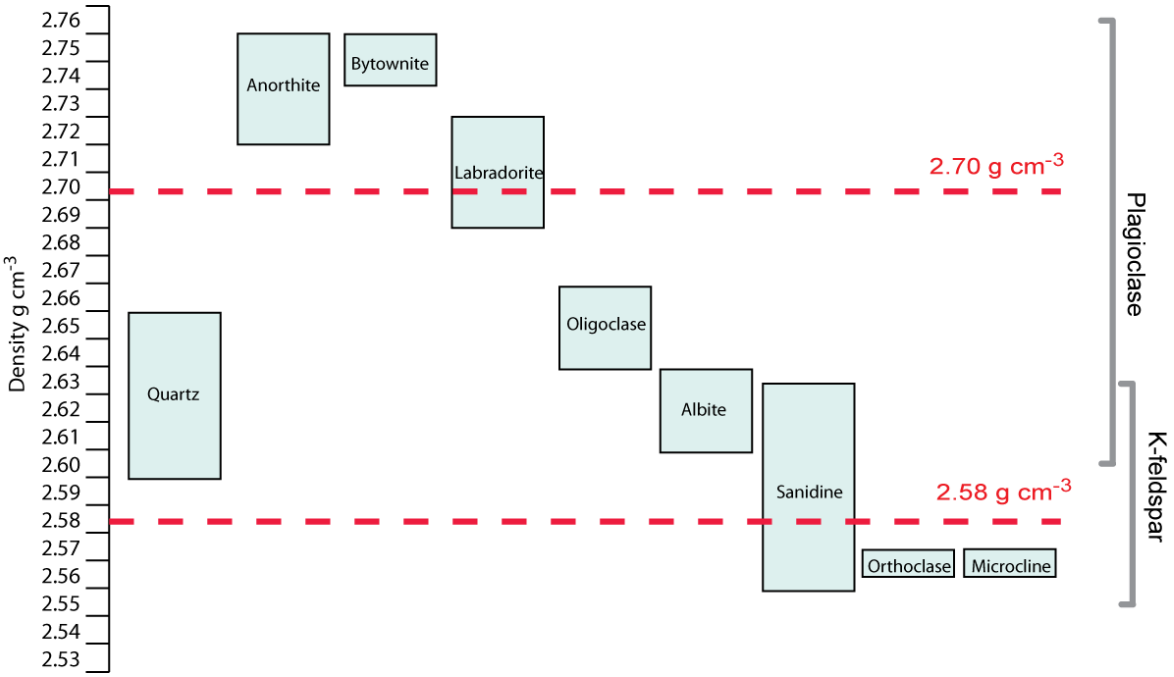

Figure 5.1: Densities of the different feldspar minerals obtained from www.mindat.org. The specific gravities of LST used in the density separations are indicated.

Providing feldspar inclusions are absent, quartz do not respond to low temperature (< 70 ˚C) IR stimulation (Singarayer and Bailey, 2003, 2004), and so will not influence measurements made with the selected luminescence analysis protocol (see section

5.4.3). The presence of albite may however exert an influence on the monitored luminescence signal and is discussed in section 5.2.

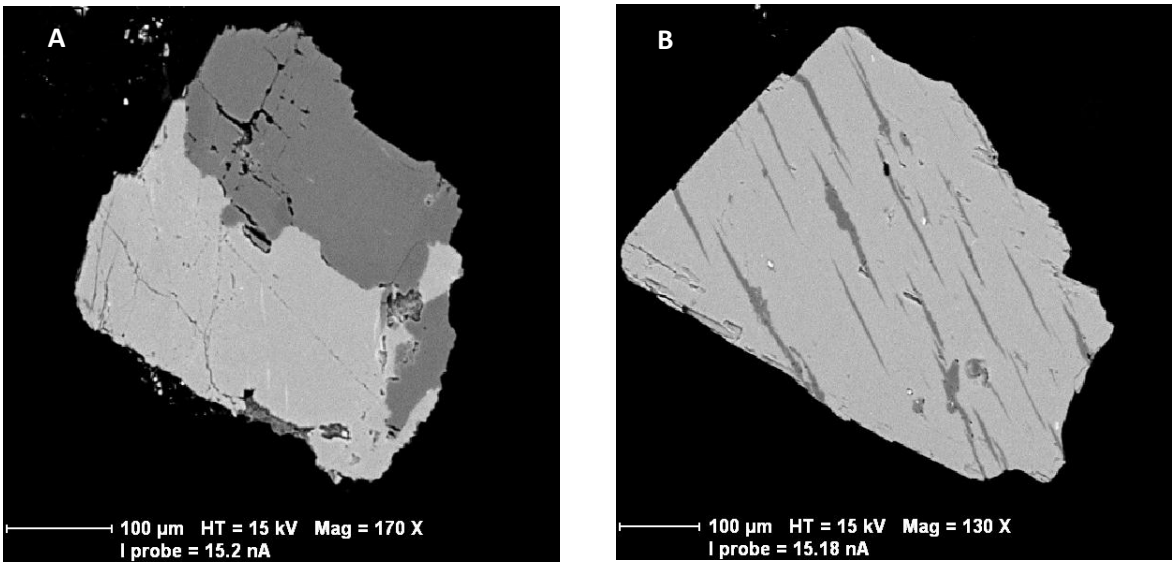

Figure 5.2: BSE images of feldspar grains. A) Orthoclase and albite (darker section) intergrowth, B) orthoclase with perthitic albite.

5.1.1. **Biotite Emission Experiment**

Biotite grains are present in all of the feldspar extracts as despite its greater density (average 3.09 gcm^{-3}, http://webmineral.com/data/Biotite.shtml), biotite may float during heavy liquid separation. This is because of its sheet silicate structure and high surface area to volume ratio. An experiment on hand picked grains of biotite indicated weak IRSL and bright TSL (Figure 5.3), in contrast to the findings of Li and Yin (2006), who observed no IRSL, but a TSL and weak BSL response. The pIR-$IRSL_{250}$ L_n luminescence emission (see Section 5.4.3 for protocol details) is most intense, and the regenerated TSL has a broad 110˚C emission.

Biotite has the chemical composition $K(Mg,Fe)_3(AlSi_3O_{10})(OH,F)_2$ and contains, on average, 6 % Fe. Consequently it behaves as a conductor rather than semi-conductor and is regarded as a non-fluorescent material (http://webmineral.com/data/Biotite.shtml). The observed luminescence may alternatively relate to biotite inclusions in feldspar grains, not differentiated during picking. Although the pIR-$IRSL_{250}$ signal has the highest intensity the $IRSL_{50}$ measured luminescence is negligible in proportion to the total luminescence intensity of the small aliquots analysed (typical counts > 7,000 – 50,000), therefore its influence on monitored luminescence is considered minimal.

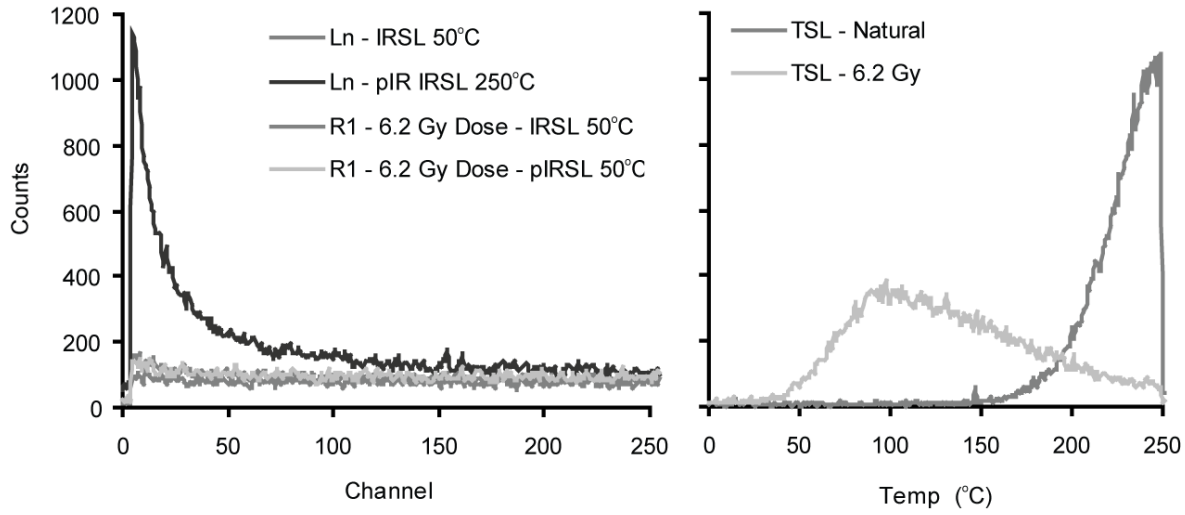

Figure 5.3: TL and $IRSL_{50}$ emissions of hand-picked biotite from GRAN57

5.2. Excitation and Emission Properties of Feldspar

Hütt et al. (1988) initially proposed a single trap for the source of IRSL in feldspars. Subsequent work by a range of authors (e.g. Poolton et al., 1994; Sanderson and Clark, 1994) has indicated more complex trap structure (Duller, 1997; Duller and Wintle, 1991), however recently the single trap modelled has returned to favour (e.g. Baril and Huntley, 2003; Jain and Ankjærgaard, 2011) although remains debated. Whereas cation substitutions in quartz are uncommon because of the charge compensation required to substitute Si^{4+} (see Chapters 7-10), Fe^{3+} readily substitute Al^{3+} within feldspars, consequently the excitation and emission properties of feldspar are diverse. Feldspars are usually stimulated in the blue or infrared, which releases charge in different proportions from traps of differing stabilities, meaning that inferences about total trapped charge, essential in OSL, also vary (e.g. Fattahi and Stokes, 2004; Sanderson and Clark, 1994).

Krbetschek and Rieser (1995) explored the emission spectra of alkali-feldspars and plagioclases in response to IR (880 nm, 1.41 eV) stimulation. They observed that the IRSL of albite emits brightly at 330 nm (3.76 eV) and 560 nm (2.21 eV), with intensities two orders of magnitude greater than orthoclase, which has a broad blue emission at ~ 400 nm (3.10 eV) and a brighter yellow emission at 560 nm (2.21 eV). This yellow emission is associated with the presence of Mn^{2+} (560nm, 2.21 eV) (Clark and Bailiff, 1998) and the blue emission with paramagnetic oxygen defects (O^-) identified through cathodoluminescence (CL) explorations of alkali feldspars (Finch and Klein, 1999). Because of their specific gravities (Figure 5.1) it is apparent that sanidine and microcline may also be present within the separate analysed, although these were not identified in the BSE imaging. Furthermore microcline is anticipated due to the bedrock geology of granitic gneiss of the study area (see Chapter 3). Sanidine ($(K,Na)(Si,Al)_4O_8$) exhibits very

poor IRSL sensitivity and so will not influence the observed luminescence if present (Krbetschek and Rieser, 1995), whereas microcline exhibits a blue (410 nm, 3.02 eV) and yellow (560 nm, 2.21 eV) emission, the latter of which has been identified as thermally unstable and not suitable for OSL analysis (Rieser et al., 1997).

As feldspars emit at a longer wavelength than the UV emission of interest for quartz, the filter arrangement of Risø 2 was changed to comprise a 2 mm Schott BG 39 (transmittance 310-700 nm, 4.0-1.77 eV) and a 4 mm Corning 7-59 filter (transmittance 320-430 nm, 3.87-2.88 eV), and the blue diodes were disabled. Stimulation was carried out using the IR diodes (870 nm, 1.43 eV) and emissions were detected between 320-430 nm (3.87-2.88 eV). This limits detection to the blue emission only, avoiding the unstable yellow emission of microcline (Rieser et al., 1997). The blue TSL emission has also been observed to fade less than the UV TSL emission (Balescu and Lamothe, 1992), further indicating the suitability of the selected emission.

5.3. Luminescence Analysis Protocol

Despite the apparent advantages of the SAR protocol, some authors have found applying it to feldspars problematic, with poor recovery of known D_e attributed to causes other than anomalous fading. Equivalent dose underestimations have been observed and are attributed to changing electron trapping probabilities associated with sample preheating, which the SAR protocol is unable to account for (Wallinga et al., 2000a; Wintle and Murray, 2006). Wallinga et al. (2001) contrasted single-aliquot regeneration added dose (SARA) (Mejdahl and Bøtter-Jensen, 1994), and SAR derived D_e values to explore this and determined that SARA derived ages exhibited the least underestimation. However within the SARA protocol, D_e values are determined through linear extrapolation, rather than interpolation, and have lower precision than SAR derived values (Wallinga et al., 2001).

Multiple authors have sought to develop the SAR protocol's applicability to feldspars, and research has particularly focussed on sample thermal treatment, e.g. Wallinga et al. (2000a) explored the SARA and multiple aliquot additive dose (MAAD) protocols (Sanzelle et al., 1996) which generally do not include thermal treatments prior to adding dose. They concluded that the loss of precision associated with these protocols was prohibitive and instead employed minimal preheat temperatures and mathematical correction factors. Blair et al. (2005) investigated the influence of preheating on sample sensitivity change throughout SAR analysis, and attributed poor dose recovery to charge build up. They overcame this through administration of a TSL measurement at the end of

each regenerative cycle, similar to the HB proposed by Murray and Wintle (2003) for quartz SAR, and through having PH1 equal to PH2.

Samples were analysed using a modified SAR protocol (Table 5.1), as proposed by Wallinga et al. (2007) whereby the PH1 and PH2 temperatures were identical in order to improve sensitivity corrections (after Blair et al., 2005; Huot and Lamothe, 2003), and a high-temperature IR bleach was incorporated at the end of each SAR cycle (Blair et al., 2005; Buylaert et al., 2007; Murray and Wintle, 2003). In addition to the conventional IR measurements at 50 ˚C ($IRSL_{50}$), a post-IR IRSL stimulation at 250 ˚C (pIR-$IRSL_{250}$) was also included (Buylaert et al., 2009; Thomsen et al., 2008) as this signal is regarded as less susceptible to anomalous fading.

Table 5.1: Feldspar pIR-$IRSL_{250}$ protocol

Natural/Regenerative Dose	Dependent on cycle
TSL	250 ˚C, 60 s, 5 ˚C/s
IRSL	50˚C, 100s, 5˚C/s, 90% power
IRSL	250˚C, 100s, 5˚C/s, 90% power
Test Dose	6.2 Gy
IRSL	250 ˚C, 60 s, 5 ˚C/s
IRSL	50˚C, 100s, 5˚C/s**,** 90% power
IRSL	250˚C, 100s, 5˚C/s, 90% power
IRSL	290˚C, 100s, 5˚C/s, 90% power

Due to the high signal intensity of feldspar, small aliquots were mounted using a mask of 2 mm Ø and the average aliquot size was 30 grains (grain size 180-210 µm). Some samples were analysed using stainless steel cups, rather than discs, which meant that they were hand mounted. However, counting individual grains has confirmed that the average aliquot number is the same as the disk mounted samples (30 grains). Aliquot acceptance is 98 %, much greater than the 38 % acceptance rate of quartz (see Section 6.1.2). Due to the luminescence sensitivity of feldspar, no aliquots failed due to poor signal to noise ratios, high recuperation or poor recycling (Figure 5.4). However the D_e obtained from the pIR-$IRSL_{250}$ signal is much greater than that obtained for the initial $IRSL_{50}$ signal, e.g. the $IRSL_{50}$ D_e for GRAN54 is 148 ± 5 Gy in contrast to 497 ± 33 Gy for the pIR-$IRSL_{250}$ D_e. Thiel (2011) reports age overestimations in pIR-IRSL age determinations for young samples, which she attributes to either an unbleached residual, or to thermal transfer. Li and Li (In Press) have also reported that the pIR-IRSL signal at multiple elevated temperature (MET) stimulations has a high residual dose, and also that higher temperature stimulations bleach more gradually (Figure 5.5). An alternative explanation for this discrepancy may relate to different rates of signal fading. Fading rates are lower for the pIR-$IRSL_{250}$ signal (e.g. Buylaert et al., 2009; Li and Li, 2011, see Appendix A.9), however fading alone is unable to account for a > 300 % D_e discrepancy. Therefore, a number of bleaching experiments have been carried out to evaluate both

feldspar suitability and the suitability of the pIR-IRSL$_{250}$ protocol for the sample suite, as well as a range of dose recovery and pre-heat plateau experiments.

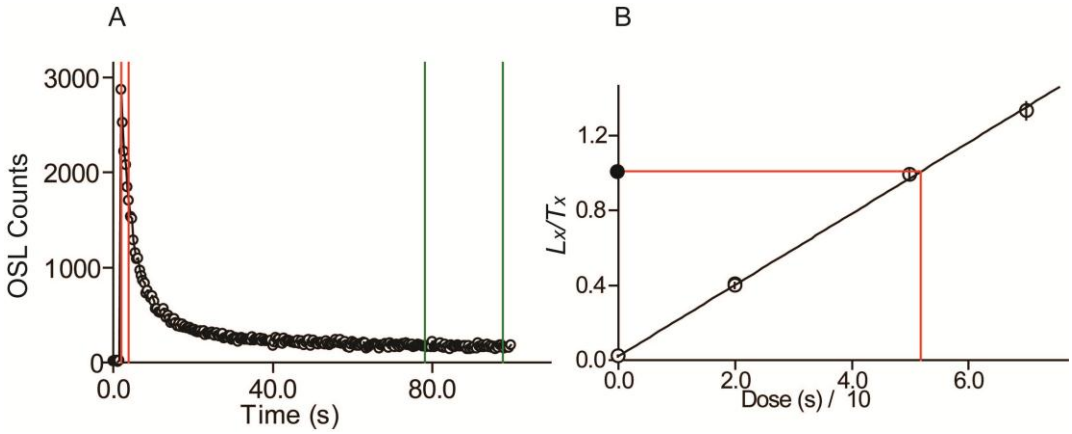

Figure 5.4: (A) IRSL$_{50}$ decay curve and (B) dose response data for a single aliquot of F_GRAN56. The filled data point on the dose response plot is L_n/T_n. The signal integration interval is highlighted in red, and the background integration interval highlighted in green.

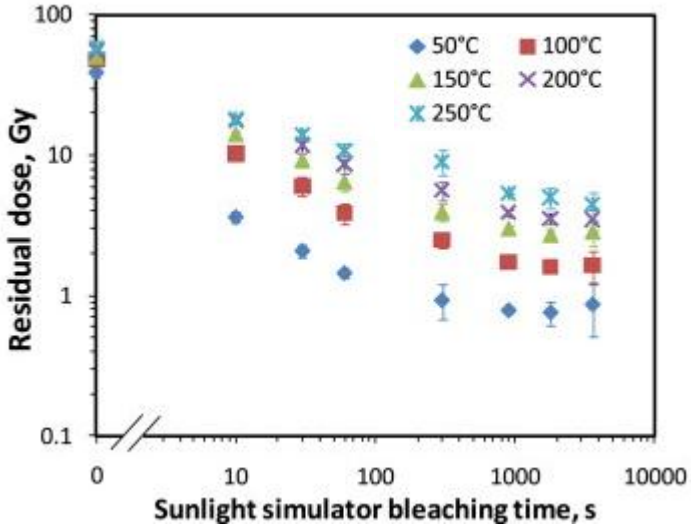

Figure 5.5: Residual doses of a single sample (WG3) as a function of bleaching time reprinted from Li and Li (In Press), Copyright 2011, with permission from Elsevier. The temperatures listed are the OSL stimulation temperatures within their multiple elevated temperature (MET) pIR-IRSL protocol.

5.4. Sample Characterisation

5.4.1. **Bleaching Experiments**

Six aliquots of GRAN56 were exposed to ambient light conditions on a bright, overcast July day in St Andrews, for 300 minutes. The latitude of St Andrews (56˚ N) is similar to the study area (61˚ N), and therefore provides a reasonable proxy for light intensity, albeit that sunlight in Scotland has slightly higher UV intensity. The D_e values of the samples were measured following light exposure using the protocol outlined in Table

5.2. A D_e value of 2.34 ± 0.12 Gy was obtained for the $IRSL_{50}$ measurement and 10.84 ± 0.37 Gy for the pIR-$IRSL_{250}$, indicating that either the pIR-$IRSL_{250}$ is slower to bleach, and/or that it bleaches to a higher residual level in accordance with Li and Li (In Press).

These residual values are lower than the D_e for GRAN56 (320.80 ± 14.60 Gy), which has a number of implications, the most important of which is that these samples are suitable for $IRSL_{50}$ analysis. This is because we can be confident that the residual observed in the GRAN56 samples relates to the depositional process experienced, rather than the optical bleaching limit of the feldspar. A further implication is that these samples have either experienced a lower light intensity during transport, or a more limited exposure time, than during the bleaching experiment presented here, or both. This was investigated through a more detailed bleaching experiment using a solar simulator light box at SUERC.

5.4.1.1. Natural dose bleaching experiment

The first solar simulator light box bleaching experiment monitored the depletion of the natural signal as a function of exposure time, and the second experiment measured the depletion of a regenerated signal. Four feldspar samples were analysed: FAB98, GRAN56, GRAN57 and NIG7. Twenty-four hand dispensed medium aliquots of each sample were mounted on stainless steel discs using Silikospray, and 3 aliquots retained as a standard of 0 minutes exposure. The remaining aliquots were grouped into threes, and were bleached for 0.25, 0.5, 1, 2, 4, 8 and 16 hours, respectively. The luminescence of two aliquots from each set were then analysed using a TL-DA-15 Risø reader equipped with a 3 mm Hoya U-340 filter[2] and EMI 9235QA photomultiplier, and the third aliquot was retained as a standard. The analysis protocol is listed in Table 5.2. A final beta dose of 5 Gy provides the regenerative dose for the next experiment (see section 5.4.1.2).

Table 5.2: Natural bleaching experiment protocol

TSL	250 ˚C, 60 s, 5 ˚C/s
IRSL	50 ˚C, 100 s, 5 ˚C/s, 60 % power
pIR-IRSL	250 ˚C, 100 s, 5 ˚C/s, 60 % power
Test Dose	5 Gy
TSL	250 ˚C, 60 s, 5 ˚C/s
IRSL	50 ˚C, 100 s, 5 ˚C/s, 60 % power
pIR-IRSL	250 ˚C, 100 s, 5 ˚C/s, 60 % power
Regenerative Dose	5 Gy

The luminescence emission of all the samples reduces as bleaching time increases (Figure 5.6); FAB98 and GRAN56 bleach most rapidly and to the greatest extent, with residuals of ~ 20 % and 15 % after 16 hours for the pIR-$IRSL_{250}$ and $IRSL_{50}$ signals respectively. NIG7 and GRAN57 alternatively have residuals of ~ 50 % after 16 hours for $IRSL_{50}$, and ≥ 40 % for pIR-IRSL. These bleaching characteristics are influenced by the

[2] As the Risø reader at SUERC was equipped with Hoya U-340 filters, it was only possible to monitor the UV, rather than the blue feldspar emission during these experiments.

different residual ages of these samples, due to their partially bleached nature. NIG7 and GRAN57 may have smaller residual doses than FAB98 and GRAN56 at the outset of the bleaching experiment, which will reduce their relative signal depletion. This was investigated through assessing bleaching behaviour relative to a known 5 Gy dose.

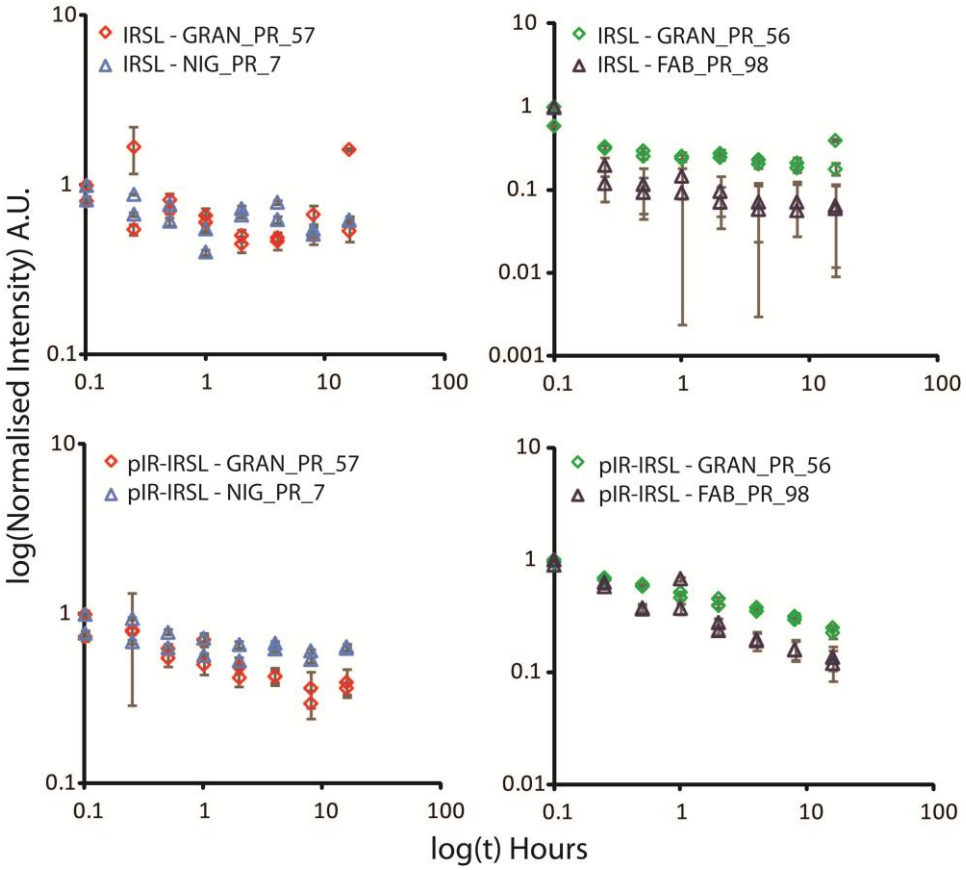

Figure 5.6: Natural bleaching experiment results. Samples are test dose corrected, and then normalised to an unbleached aliquot. Error bars depict the RSE after Li (2007).

5.4.1.2. Results: Regenerative Bleaching Experiments

The results from the regenerative bleaching experiment differ markedly from the natural bleaching experiment (Figure 5.7). In addition to two Norwegian feldspar samples (GRAN57 and NIG7), a well characterised K-feldspar sample, International Atomic Energy Agency (IAEA) F1 was analysed (see Sanderson and Clark, 1994). All samples bleach rapidly for the $IRSL_{50}$ analyses, and signals reduced to < 10 % within 1 hour of exposure. Scatter in the data beyond this point is related to low signal to noise ratios. In contrast to the $IRSL_{50}$ data, the pIR-$IRSL_{250}$ signal is more variable between aliquots, and generally bleaches less rapidly. After 1 hr of bleaching > 30 % of the initial signal remains in all samples, although such a generalisation is made cautiously given the scatter in the data series.

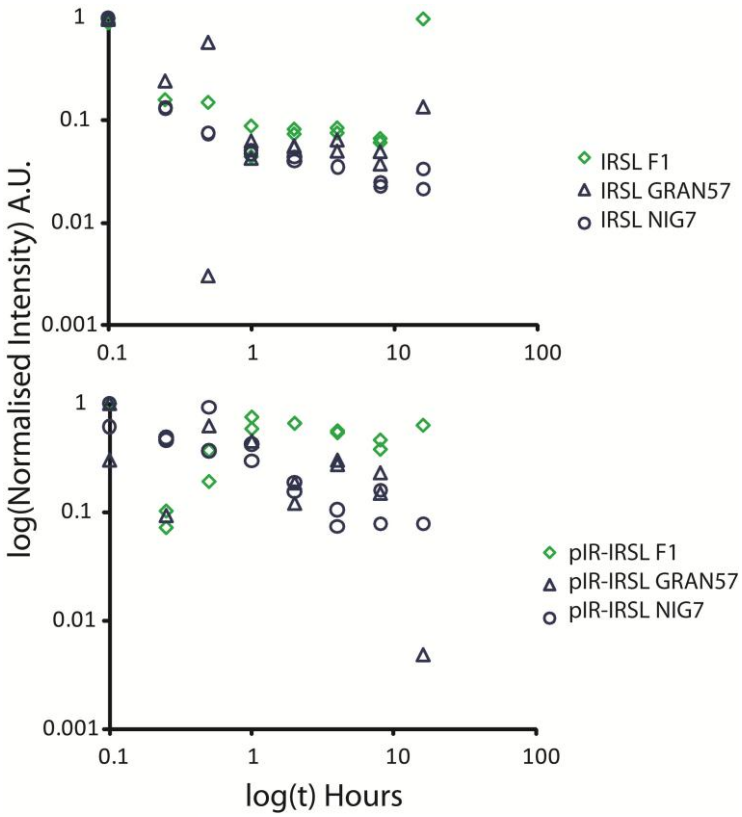

Figure 5.7: $IRSL_{50}$ and pIR-$IRSL_{250}$ of the regenerative bleaching experiment. All data are test dose corrected and then normalised to the highest emission. Errors are not shown to facilitate plotting in log log space.

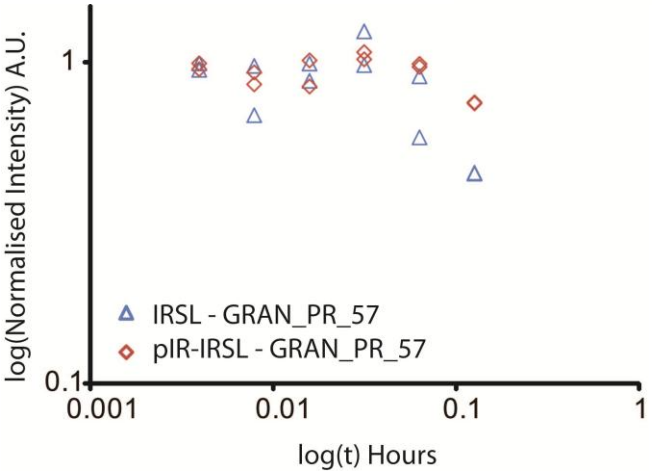

Figure 5.8: $IRSL_{50}$ and pIR-$IRSL_{250}$ of the rapid regenerative bleaching experiment. All data are test dose corrected and then normalised to the highest emission. Errors are not shown to facilitate plotting in log log space.

Despite the differences between the pIR-$IRSL_{250}$ and $IRSL_{50}$ data, both signals are bleachable and thus are appropriate for OSL analysis (Figure 5.7), although as the $IRSL_{50}$ signal depletes more rapidly it will be less susceptible to partial bleaching and is therefore preferred. A final experiment determined which of the two signals bleaches fastest during initial exposure (Figure 5.8). Initial signal depletion was explored through bleaching for 14, 28, 56, 112, 225 and 450 s. After 450 s bleaching, 45 % and 75% of the initial signal remained for $IRSL_{50}$ and pIR-$IRSL_{250}$ analyses respectively. The sample suite analysed here has short bleaching periods prior to deposition, therefore the $IRSL_{50}$ signal is most appropriate and has been used here.

It should also be noted that in accordance with other studies (e.g. Klasen et al., 2006; Spooner, 1994b; Wallinga, 2002), the Norwegian quartz signal bleaches more rapidly than the feldspar signals (see 1.4.3 for a discussion and 4.7 for quartz results),

indicating that quartz is the preferred mineral for OSL dating in glacial environments, although its application is often limited by its poor luminescence sensitivity (see Chapter 2 for a discussion).

5.4.2. **Dose Recovery and Preheat Plateau Experiments**

A dose recovery experiment was carried out on 12 aliquots of GRAN56. The aliquots were bleached within the Risø reader at room temperature using IR diodes for 100 s, followed by a 7500 s pause and a further 100 s IR bleach. Six aliquots were analysed using pIR-IRSL, and six with conventional IRSL. The dose of 6.21 ± 0.28 Gy was recovered to an average of 6.44 ± 0.19 Gy with $IRSL_{50}$ and 6.63 ± 0.14 Gy with pIR-$IRSL_{250}$ (Figure 5.9). Both sample sets overestimate the administered dose which may be indicative of thermal transfer, recuperation, or residual charge present at the outset of analysis. Recuperation was < 5 % for both the $IRSL_{50}$ and pIR-$IRSL_{250}$ analyses. The pIR-$IRSL_{250}$ dose recovery exhibited the greatest overestimation; however this is not sufficient to account for the 300 % D_e overestimation described in Section 5.3, which is instead related to the slower bleaching rate of the pIR-$IRSL_{250}$ signal.

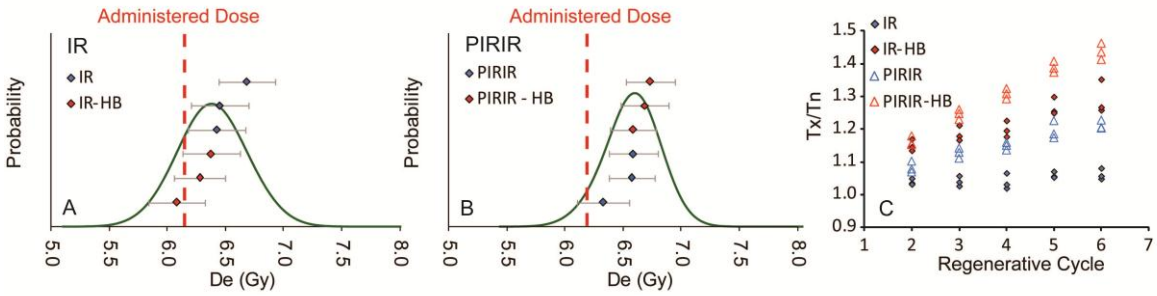

Figure 5.9: Probability density functions of recovered D_e values for the (A) $IRSL_{50}$ and (B) pIR-$IRSL_{250}$ stimulated signals of twelve aliquots of GRAN56. (C) Test dose (T_x) intensity variation (T_x/T_n) as a function of regenerative cycle, where T_n is the first test dose.

Examination of T_x for each regenerative cycle demonstrates that sensitivity changes are greatest where the pIR-$IRSL_{250}$ protocol is combined with a HB. Note that sensitivity changes are smaller when the $IRSL_{50}$ protocol does not include a HB, but are affected by the preceding dosing treatment (Figure 5.9C), which is indicative of thermal transfer. For this reason, the HB step has been retained and the pIR-$IRSL_{250}$ protocol rejected in favour of conventional $IRSL_{50}$.

A preheat plateau dose recovery experiment was carried out (Table 5.3). All samples recovered the administered dose within 10 % (Figure 5.10). Those samples treated with a HB tended to overestimate dose (1.95 ± 0.01 %), whilst those without it exhibit slight underestimation (-0.18 ± 0.01 %).

Table 5.3: Dose recovery experiment protocol

IRSL	0 ˚C , 100 s, 90 % power
Pause	7500 s
IRSL	0 ˚C , 100 s, 90 % power
Natural/Regenerative Doses	N = 6.2, 2.5, 6.2, 8.6, 0, 2.5 Gy
TSL	100/150/200/250 ˚C, 60 s, 5 ˚C/s
IRSL	50 ˚C, 100 s, 5 ˚C/s, 90 % power
Test Dose	6.2 Gy
TSL	100/150/200/250 ˚C, 60 s, 5 ˚C/s
IRSL	50 ˚C, 100 s, 5 ˚C/s, 90 % power
IRSL	290 ˚C, 40 s, 5 ˚C/s, 90 % power

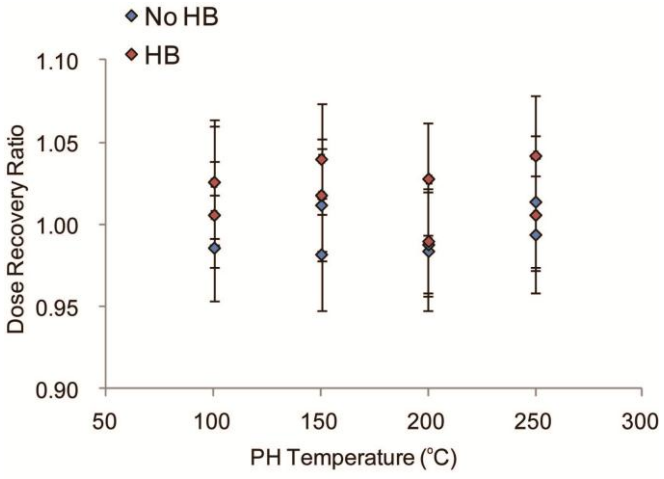

Figure 5.10: $IRSL_{50}$ dose recovery, preheat plateau experiment results. Red data points have been treated with a HB, whereas blue data points have had this stage of the protocol omitted. The protocol is listed in Table 5.3.

5.4.3. **Selected SAR Protocol and associated acceptance criteria**

As the feldspar samples recover dose within 10 %, have recycling ratios within 10 % and are unaffected by recuperation, no further sample characterisation was carried out prior to protocol selection. The selected protocol is listed in

Table 5.4. Aliquot acceptance criteria are 1) recycling ratios within 10 % of unity; 2) signal intensities ≥ 3 σ above background; and 3) recuperation within 10 % of the normalised natural signal. All samples were also tested for anomalous fading discussed in section 5.7.

Table 5.4: Feldspar SAR protocol

Natural/Regenerative Doses	6.2, 12.4, 18.6, 0, 6.2 Gy*
TSL	250 ˚C, 60 s, 5 ˚C/s
IRSL	50 ˚C, 100 s, 5 ˚C/s, 90 % power
Test Dose	6.2 Gy
TSL	250 ˚C, 60 s, 5 ˚C/s
IRSL	50 ˚C, 100 s, 5 ˚C/s, 90 % power
IRSL	290 ˚C, 100 s, 5 ˚C/s, 90 % power

*Regenerative doses varied dependent upon sample D_e but initial analyses were carried out with these doses

5.5. Sample reproducibility

The highly overdispersed nature of the D_e distributions of the different Norwegian samples necessitates that sample reproducibility is investigated. This was achieved through splitting GRAN69 into two sub-samples: a (n=24) and b (n=36), which were prepared and analysed separately. GRAN69a has σ_d 64 ± 4% and residual dose of 17.35 ± 1.94 Gy, and GRAN69b has σ_d 58 ± 3% and residual dose of 14.80 ± 1.28 Gy. The σ_d and residual dose values overlap within uncertainties between the two samples, indicating that this sample's luminescence behaviour is reproducible. Both sub-samples comprise three components when analysed with FMM, and two of the components overlap within errors between samples. As GRAN69a and GRAN69b are indistinguishable, they are considered as a single sample (GRAN69) in the results and discussion (Figure 5.11, Table 5.5).

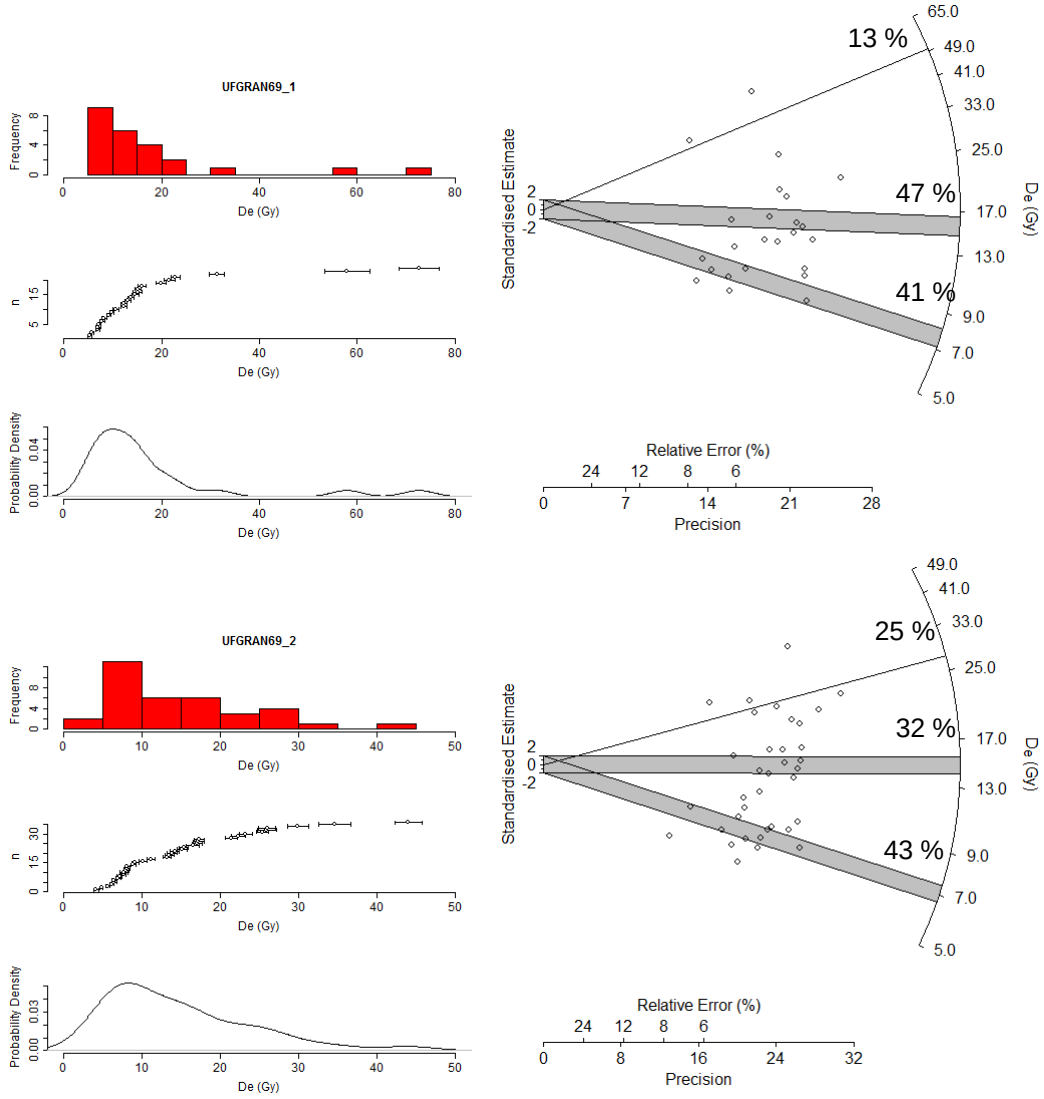

Figure 5.11: Histograms, probability density functions, scatter graphs and radial plots of GRAN69a & GRAN69b. The relative proportions of the different components indicated by the FMM are indicated on the radial plots. Radial plots were plotted using Radial Plot (Reed and Olley, 2003), all other plots are produced using the gplots package in R (Warnes et al., 2010).

Table 5.5: FMM Component summary for the different GRAN69 fractions

	C1		C2 (Gy)		C3 (Gy)	
	D_e (Gy)	%	D_e (Gy)	%	D_e (Gy)	%
GRAN69a	49.94 ± 3.39	13	15.63 ± 0.57	41	7.67 ± 0.31	41
GRAN69b	27.27 ± 1.00	25	14.66 ± 0.60	32	7.05 ± 0.43	43
GRAN69	34.98 ± 1.57	15	15.92 ± 0.42	42	7.31 ± 0.18	43

5.6. Standardised Growth Curve

Standardised growth curves (SGC) for quartz and polymineral fine grains have recently been investigated by a number of authors (e.g. Burbidge et al., 2006; Roberts and Duller, 2004; Telfer et al., 2008). A suite of standardised growth curves were calculated for individual samples which interpolate onto the linear part of the growth curve, in order to facilitate more rapid analysis. Average dose response values (L_x/T_x) for different regenerative doses were fitted with a linear function to form SGCs from which D_e values could be interpolated. The accuracy of the SGCs was evaluated through testing the SGC D_e values against those obtained from SAR and fitted in Analyst. Samples were not corrected for T_x dose (T_D), as all doses were equal with the exception of 12 aliquots of JOS51, which had T_D of 2.5 Gy, rather than 5 Gy. The SGC for JOS51 was calculated from $L_x/T_x \bullet T_D$ after Roberts and Duller (2004).

In order to avoid circularity when testing the SGCs, available aliquots are separated into two populations and three SGC are constructed; one for each population (SGC_{P1} and SGC_{P2}) and one for the whole population (SGC_{WP}, Figure 5.13). The SGC_{P1} was used to calculate SGC D_e values for population two, and vice versa (Table 5.6 and Table 5.7); the SGC_{WP} was used to calculate D_e values for all samples. Aliquots with D_e values that interpolate onto the non-linear part of the growth curve are not included in SGC calculation or testing as a linear fit results in D_e overestimation. SGCs affected by this are indicated in Table 5.8. A different function could be used to fit a SGC that extends into the non-linear part of the dose-response curve, however this has not been investigated here.

Curve fit error was calculated using LINEST in Excel 2007, and incorporated together with 1.5 % analytical error in D_e error estimations. Standardised growth curve aliquot D_e (s) values are calculated from:

Eq. 5.1: $$D_e = \frac{\left(\frac{L_x}{T_x}\right) - b}{a}$$

where a is the slope, and b the intercept of the curve fit. Calculating uncertainties in this manner does not account for counting statistics, and the % uncertainty is the same for all aliquots, manifest in the radial plots of those samples with SGC derived D_e values (Figure 5.12).

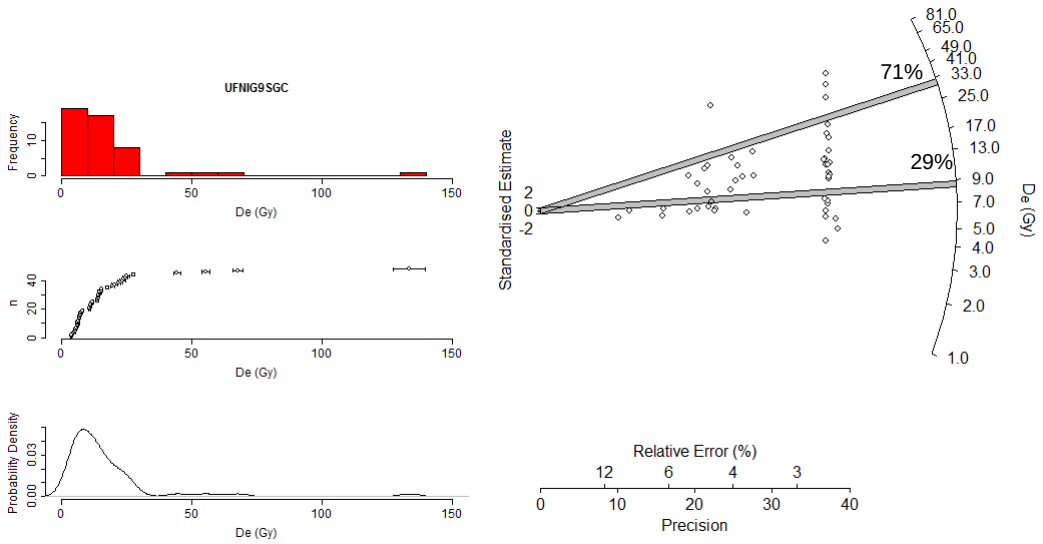

Figure 5.12: Histogram, scatter graph, probability density function and radial plot for F_NIG9. D_e values calculated using a SGC are clearly apparent in the radial plot, due to their similar uncertainties, however they are not apparent in the any of the other distributions (e.g. the histogram) confirming that the D_e distributions are not affected by this artefact. Two FMM components have been identified for F_NIG9 and are indicated on the radial plot.

With the exception of NIG9 (Table 5.8), all of the SGC_{WP} interpolated aliquots return average SAR:SGC D_e values within 10 %. Where the SGC_{P1} and SGC_{P2} are explored, LEI14, NIG9 and NIG7 do not produce SAR:SGC ratios within 10 %. This is attributed to differences in the regenerative doses used in the sample analysis protocols from which the two SGCs are calculated, and highlights sensitivity of the dose response curve to different regenerative dose treatments. These effects are averaged by the SGC_{WP}, however as the SAR:SGC_{P2} ratios are closest to unity (see Table 5.8) this has been used for SGC D_e interpolation.

Luminescence analyses for SGC interpolation comprised L_x/T_x followed by a single regenerative dose cycle (after Burbidge et al., 2006), where the regenerative dose was equal to T_D. A T_D of 6.2 Gy was used throughout all analyses, which is equal to the T_D used in the feldspar SAR protocol for all samples with the exception of JOS51 discussed above. The SAR L_x/T_x are plotted onto the SGC, providing an independent test of SGC validity (Figure 5.13).

As the Norwegian sample suite comprises partially bleached material, some D_e doses are derived which interpolate onto the non-linear part of the dose response curve. In these instances those aliquots were excluded as interpolation on the linear SGC would be inappropriate. This does result in a slight bias towards younger ages in the additional SGC measurements, however only one sample, LOD4 was affected (two aliquots had D_e values > 500 s). The SGC can therefore be reliably applied to this sample suite to increase aliquot number and reduce measurement time.

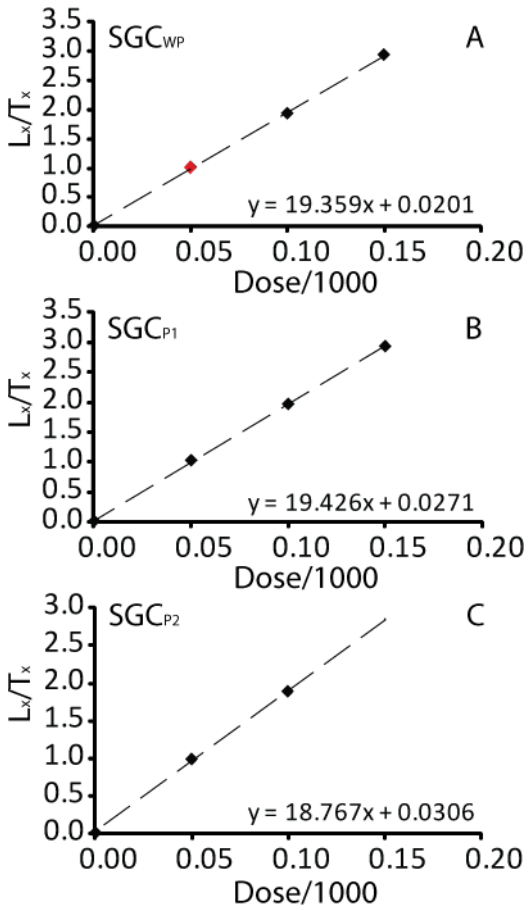

Figure 5.13: SGC for GRAN57, (A) the regenerative L_x/T_x (red data point) is plotted onto SGC_{WP}, confirming SGC validity. (B) SGC_{P1} and (C) note the slight difference in slope for SGC_{P2}, attributed to the absence of the final regenerative dose in that protocol.

Table 5.6: SAR:SGC_{P1} for GRAN57, SAR values are from population 2, used to develop SGC_{P2}

Aliquot	SAR D_e s)	SGC_{P1} D_e (s)	% Difference
1	56.2	53.08	0.94
3	85.7	80.88	0.94
5	58.4	54.84	0.94
7	72.4	68.41	0.94
9	142.6	130.18	0.91
11	85.9	80.52	0.94
13	82.9	78.78	0.95
15	195.5	177.34	0.91
17	58.8	55.91	0.95
19	60.1	57.50	0.96
21	84	79.80	0.95
23	53.8	50.49	0.94
		Average	0.94
	Standard Deviation		0.015
		SE	0.004
		RSE	0.463

Table 5.7: SAR:SGC_{P2} for GRAN57, SAR values are from population 1, used to develop SGC_{P1}

Aliquot	SAR D_e (s)	SGC_{P2} D_e (s)	% Difference
1	87	84.73	0.97
3	67.8	66.59	0.98
5	80.1	77.51	0.97
7	90.1	87.21	0.97
9	91.6	89.26	0.97
11	106.3	105.10	0.99
13	77.0	75.04	0.97
15	80.8	77.63	0.96
17	69.3	68.51	0.99
19	69.3	67.86	0.98
21	82.4	79.73	0.97
23	88.5	86.59	0.98
		Average	0.98
	Standard Deviation		0.009
		SE	0.002
		RSE	0.256

Table 5.8: SGC curve fits, fit ratios and standard errors for the three different SGC developed

	SGC_{WP}				SGC_{P1}				SGC_{P2}			
	n	Curve fit (y = ax + b)	SAR D_e/SGC_{WP} D_e	SE	n	Curve fit (y = ax + b)	SAR D_e/SGC_{P1} D_e	SE	n	Curve fit (y = ax + b)	SAR D_e/SGC_{P2} D_e	SE
GRAN56	25	a: 19.39 ± 0.19 b: 0.03 ± 0.18	0.93	0.004	13	a: 18.43 ± 0.33 b: 0.05 ± 0.03	0.99	0.003	12	a: 19.01 ± 0.30 b: 0.04 ± 0.03	0.95	0.03
GRAN57	24	a: 19.36 ± 0.22 b: 0.02 ± 0.02	0.95	0.003	12	a: 19.43 ± 0.21 b: 0.03 ± 0.02	0.94	0.004	12	a: 18.77 ± 0.46 b: 0.03 ± 0.03	0.98	0.002
JOS51	23	a: 18.72 ± 0.43 b: 0.01 ± 0.04	1.01	0.005	12	a: 19.07 ± 0.66 b: 0.01 ± 0.01	0.96	0.010	11	a: 18.70 ± 0.28 b: 0.01 ± 0.02	0.98	0.007
LEI13	24	a: 18.86 ± 0.33 b: 0.02 ± 0.03	0.99	0.024	12	a: 17.78 ± 0.40 b: 0.04 ± 0.04	0.94	0.006	12	a: 18.10 ± 0.47 b: 0.05 ± 0.05	0.95	0.013
LEI14	21	a: 19.28 ± 0.21 b: 0.06 ± 0.02	0.95	0.013	9*	a: 18.66 ± 0.14 b: 0.14 ± 0.03	0.86	0.012	12	a: 19.56 ± 0.30 b: 0.01 ± 0.01	0.92	0.013
LEI18	24	a: 18.76 ± 0.24 b: 0.01 ± 0.02	0.98	0.008	12	a: 18.97 ± 0.38 b: -0.01 ± 0.04	1.02	0.006	12	a: 18.85 ± 0.43 b: 0.02 ± 0.02	0.95	0.014
NIG3	23	a: 22.97 ± 1.08 b: -0.15 ± 0.09	0.96	0.017	12	a: 23.76 ± 1.20 b: -0.23 ± 0.13	0.95	0.012	11*	a: 19.17 ± 0.63 b: 0.02 ± 0.03	0.96	0.033
NIG7	24	a: 19.24 ± 0.37 b: 0.02 ± 0.02	1.08	0.056	12	a: 18.35 ± 0.37 b: 0.05 ± 0.03	1.49	0.114	12	a: 19.11 ± 0.44 b: 0.02 ± 0.02	0.98	0.004
NIG8	24	a: 18.03 ± 0.48 b: 0.09 ± 0.04	0.97	0.003	12	a: 18.29 ± 0.44 b: 0.06 ± 0.04	0.99	0.003	12	a: 18.76 ± 1.44 b: 0.06 ± 0.07	0.96	0.002
NIG9	24	a: 17.27 ± 0.39 b: 0.11 ± 0.05	0.84	0.049	12	a: 18.24 ± 0.32 b: 0.05 ± 0.03	0.73	0.085	12	a: 17.18 ± 0.44 b: 0.10 ± 0.06	0.98	0.022
LOD4	22	a: 17.85 ± 0.41 b: 0.09 ± 0.06	0.97	0.006	10*	a: 19.04 ± 0.30 b: 0.01 ± 0.03	0.92	0.007	12	a: 17.70 ± 0.33 b: 0.08 ± 0.05	1.01	0.007
LOD6	24	a: 17.98 ± 0.29 b: 0.06 ± 0.04	0.98	0.005	12	a: 18.42 ± 0.26 b: 0.04 ± 0.02	0.96	0.008	12	a: 17.89 ± 0.33 b: 0.06 ± 0.04	0.98	0.007

*SGC where aliquots are not included due to interpolation on the non-linear part of the dose response curve.

5.7. Anomalous Fading

Anomalous fading in feldspars was first recognized by Wintle (1973), and refers to the loss of accumulated charge from electron traps which ***should*** be stable over geological time, subject to Arrhenius' equation of chemical kinetics:

Eq. 5.2: $p_T = p_o \exp(-\varepsilon/kT)$

Where p_T is the probability of thermal ionization at a certain temperature, p_o is a constant, $-\varepsilon$ is trap depth (eV), k is Boltzman's constant (8.617343×10^{-5} eV K^{-1}) and T is temperature (K) (Zink et al., 1995). Aitken (1985) showed that the loss of luminescence signal over time t^* will be $\approx \log(t^*/t_c)$, where t_c is the luminescence signal at an arbitrary time, thus escape becomes more difficult as the population of trapped electrons is reduced (Aitken, 1998).

Most of the experimental protocols used to measure anomalous fading show that it affects the majority of K-feldspars (Huntley and Lamothe, 2001) and all disordered feldspars (Visocekas and Zink, 1999). Within the density separate analysed here, sanidine is the only disordered feldspar that may be present (see Figure 5.1), however due to its poor IRSL sensitivity it will have negligible influence on the IRSL detected (see section 5.2). If uncorrected, anomalous fading results in sample age underestimation, and both TSL and IRSL emissions are affected (Balescu and Lamothe, 1994). Various models have been proposed to account for this loss of charge including the localized transition model (Templer, 1985, 1986), decay of luminescence centres (Wintle, 1977), changing competition between radiative and non-radiative centres (Chen and Hag-Yahya, 1997), mid-term fading (Grun, 1989; Hornyak et al., 1993; Xie and Aitken, 1991) and migration of defects (for a review see Aitken, 1998).

However, the most widely accepted model is that of quantum mechanical tunnelling initially proposed by Visockeas (1979; 1985; Visocekas et al., 1976), which states that in addition to escape via the conduction band, a trapped electron has a small probability of escape via wave mechanical tunnelling. Tunnelling requires no energy from lattice vibrations, and is an athermal process. Visocekas et al. (1976) made their proposal following observation of a post-irradiation red luminescence afterglow at low temperatures. Where thermal dependence of anomalous fading has been observed (e.g. Chen and Hag-Yahya, 1997; Visocekas, 2002), fading is most probably the result of an inappropriate thermal treatment protocol, which fails to evict charge from traps unstable over geological time that then 'fade'. Apparent anomalous fading may also be observed where sensitivity changes caused by thermal treatments or irradiation are not corrected for (Aitken, 1998).

5.7.1. **SAR and Anomalous Fading Detection**

The SAR protocol has been adapted by Wallinga et al (2000b) for use with coarse grained feldspar through inclusion of an additional regenerative dose after storage, which assesses sample susceptibility to anomalous fading. Thus the analysis protocol comprises a regenerative dose (R_1) prior to sample storage, then (L_1/T_1)/(L_2/T_2) to determine fading and then (L_2/T_2)/ (L_3/T_3) to determine whether the recycling ratio is acceptable. If a sample is unaffected by fading, the ratio (L_1/T_1)/(L_2/T_2) should be unity. The SAR protocol has numerous advantages over previous fading analysis methods as it is a single rather than multiple-aliquot technique, and sample sensitivity changes are better accounted for. Furthermore, as the results are normalized relative to T_x, it is unaffected by loss of grains which would be problematic were absolute light values being contrasted (Wallinga et al., 2000b).

Anomalous fading was calculated for a minimum of 6 aliquots of each sample (see Appendix A.9 for individual sample numbers), using a protocol similar to that proposed by Wallinga et al. (2007) albeit with a range of different time delays. The protocol used (Table 5.9) was designed by Huot (2006) and enables calculation of fading using either the *g* method (Huntley and Lamothe, 2001) or the dose rate correction (DRC) method (Lamothe et al., 2003; Wallinga et al., 2007) which are applicable to D_e values interpolated onto the linear and exponential parts of the dose response curve respectively. All samples were preheated prior to storage after Auclair et al (2003). The fading test protocol was carried out on samples immediately following their initial analysis with the SAR protocol.

Table 5.9: Fading Test Protocol

Dose	Between 25 and 100 % of D_e (Auclair et al., 2003)
TSL	250 ˚C, 60 s, 5 ˚C/s
Pause	Pause (0 s, 250 s, 750 s, 1500 s, 3000 s, > 86400 s)
IRSL	50 ˚C, 100s, 90% power, 5 ˚C/s
IRSL	250 ˚C, 100s, 90% power, 5 ˚C/s
Test Dose	25 % of initial dose (Auclair et al., 2003)
TSL	250 ˚C, 60 s, 5 ˚C/s heating rate
IRSL	50 ˚C, 100s, 90% power, 5 ˚C/s
IRSL	250 ˚C, 100s, 90% power, 5 ˚C/s
IRSL	290 ˚C, 100s, diodes 90% power, 5 ˚C/s

5.7.2. **Calculation of *g***

The *g* method (Huntley and Lamothe, 2001) was used to estimate the fading rate of the samples analysed and *g* was calculated using the following equation from Huntley & Lamothe (2001):

Eq. 5.3: $I = I_c \left[I - \frac{g}{100} \, log_{10} \left(\frac{t^*}{t_c} \right) \right]$

where I is the luminescence intensity at time t^*, I_c is the luminescence intensity at an arbitrary time t_c, t^* is the time after irradiation, including half of the irradiation period throughout which fading will also occur (Aitken, 1985; Auclair et al., 2003; Visocekas, 1985), and g is the fading rate in %/decade, a decade being a factor of 10 in time since irradiation (Huntley and Lamothe, 2001). This equation can be rearranged in terms of g:

Eq. 5.4: $$\frac{I}{I_c} = -\frac{g}{100}\, log_{10}\left(\frac{t}{t_c}\right)$$

Eq. 5.5: $$\frac{I}{I_c} - 1 = -\frac{g}{100}\, log_{10}\left(\frac{t}{t_c}\right)$$

Eq. 5.6: $$\frac{\left(\frac{I}{I_c}\right)-1}{log_{10}\left(\frac{t}{t_c}\right)} = \frac{-g}{100}$$

Eq. 5.7: $$\frac{\left(\frac{I}{I_c}\right)-1}{log_{10}\left(\frac{t}{t_c}\right)} * 100 * -1 = g$$

Values of g_{2days} (%/decade) were calculated from the measured fading (Table 5.9) through linear regression of I[log(t/t$_c$)] against log(t/t$_c$) (Huot, 2006) (Figure 5.14). Fading rates varied between the different catchments, and ranged from 1 ± 2 to 7 ± 8 %/decade (Table 5.10). The precision of these estimates is very low, relating to large uncertainties in the linear regression caused by scatter between the different aliquots, which ranged from 6 to 21 aliquots (modal average is 6).

The cause of scatter between aliquots is uncertain, but may relate to sensitivity changes occurring throughout the measurement cycles, or insufficient correction by T_x. Where the ratio T_n/T_x is explored, significant variation is observed for some samples throughout analysis, however despite this almost all aliquots passed the recycling ratio acceptance threshold of 10 %, indicating that T_x corrections are adequate. Huot (2006) advocates bleaching samples with a solar simulator to ensure no residual charge remains (Blair et al., 2006). Although samples are bleached throughout SAR analysis prior to measurement of fading, some residual charge may remain, causing scatter amongst the fading measurements as it is depleted throughout analysis. This is especially true where the final SAR measurements are likely to have been additional large regenerative doses, which were added to sequences at the end of analysis as required.

Table 5.10: Average measured g_{2days} (%/decade) values for the different catchments analysed

Valley	g_{2days} (%/decade)	*n*
BERG	6.98 ± 7.61	11
FAB	2.36 ± 1.09	24
GAUP	1.32 ± 2.42	6
GRAN	4.11 ± 2.55	97
JOS	2.08 ± 5.06	17
LEI	2.84 ± 4.38	51
LOD	4.11 ± 3.84	54
NIG	3.25 ± 1.72	80

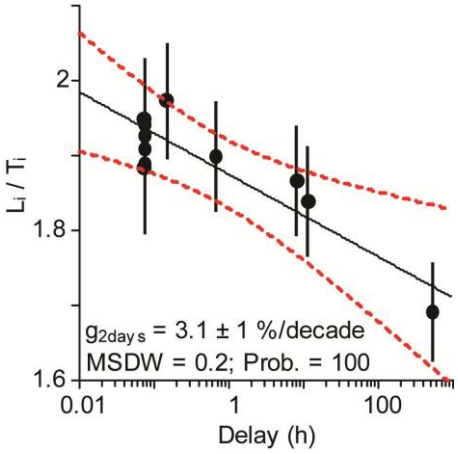

Figure 5.14: Calculation of g_{2days} after Huot (2006) through linear regression of measured D_e values for an aliquot of NIG9.

5.7.3. **Anomalous Fading Correction**

The fading correction applied to D_e values interpolated from the linear part of the dose response curve can be achieved using the *g* method of Huntley & Lamothe (2001), where the fading corrected D_e (D_{eF}) is calculated as:

Eq. 5.8: $$D_{eF} = D_e * \left(\frac{1-g_{2days}}{100*log_{10}\left(\frac{t}{t_c}\right)} \right)$$

If the D_e is interpolated from the exponential part of the dose response curve, the dose rate correction (DRC) method of Lamothe *et al*. (2003) should instead be used, which derives D_{eF} from interpolation of D_e on a fading corrected dose response curve.

The uncertainty of fading corrected ages must incorporate the uncertainty of *g* through error propagation, which because of the low precision of derived *g* presented here, results in uncertainties > 500 % in some instances. Additional experiments to determine the causes of *g* uncertainty including solar bleaching of samples prior to analysis, measurement of aliquots which have not been subject to SAR, and investigation of intra-sample variability are necessary, however time has precluded their further investigation here. Therefore the feldspar ages presented have not been fading corrected.

However, within the context of this thesis which explores the residual doses, rather than absolute ages of the different samples, this is not regarded as prohibitive.

5.8. Age Modelling

Details of the different age models are given in Chapter 4 and age model selections are listed in Table 5.11. Fading uncorrected D_e values were modelled with the CAM to calculate σ_d in order to select the appropriate age model (Arnold, 2006; Arnold et al., 2007; Bailey and Arnold, 2006; Thrasher et al., 2009b) (see Section 4.10.1.5). In contrast to the quartz model selection criteria, a greater variety of models are selected using the different flowcharts. The SA criteria of Arnold (2006; 2007) select the CAM for FAB81, FAB100 and GRAN55 and MAM-3 for the remainder of the sample suite. The criteria of Bailey and Arnold (2006) also return the CAM for FAB81 and GRAN55, as well as for FAB86 and FAB94, with the remaining samples being allocated either the MAM-3 or L5% models. Where the revised critical values are used (Arnold, 2006) after Thrasher et al. (2009b) the CAM is also indicated for FAB86, FAB94, FAB81 and GRAN55, with the remainder selecting the MAM-3 or L5% models.

The residual doses for the feldspar samples are significantly greater than for the quartz samples analysed (see Chapter 4), which precludes model selection through comparison with independent (quartz) age control. The MAM-3 model produces very large uncertainties for some samples e.g. NIG4, and the L5% model may be more appropriate in these instances. This is the selected model using the criteria of Bailey & Arnold (2006) for two of the five affected samples. However, the arbitrary nature of this model in contrast to the MAM-3 model, especially where samples sizes are relatively small, means that it is less favoured. Consequently the model selection criteria of Bailey & Arnold (2006) with critical values from Arnold (2006) after Thrasher et al. (2009b) have been adopted, which are the same criteria used for the quartz analyses. Where uncertainties larger than sample age occur with the MAM-3 model, the L5% model has instead been used, and affected samples are clearly identified.

All samples were also explored with FMM in order that the different components of the distributions could be identified. The majority of samples consisted of two different components, except NIG7 and GRAN57 which comprise a single component.

5.9. Environmental Dose Rate & Age Calculations

In contrast to the quartz samples, as the feldspar samples were not etched, a component of the D_r is derived from alpha decay of U and Th (Table 5.13). K-feldspars

also have a significant internal dose due to the inclusion of K in the crystal structure. Environmental dose rate calculations are detailed in Appendix A.4, and fading uncorrected ages are listed in Table 5.13. Due to limited material it was not possible to calculate D_r for all samples. Where material was unavailable, the average catchment U, Th, K and Rb values have instead been used to calculate D_r and to provide an approximate age calculation; affected samples are clearly identified within Table 5.13.

5.10. Summary

The 2.58 g cm^{-3} K-feldspar extract is analysed using the conventional $IRSL_{50}$ protocol as the pIR-$IRSL_{250}$ exhibits greater residual dose, attributed to slower bleaching of this luminescence signal. This interpretation is supported by bleaching experiments (Section 5.4.1), preheat plateau and dose recovery investigations (Section 5.4.2). Standardised growth curves are developed for samples which interpolate onto the linear part of the dose response curve, and these rapid analyses enable measurement of a greater number of replicates within the available analysis time. Investigations into the anomalous fading of the feldspar signals demonstrate that the pIR-IRSL signal fades more gradually, however uncertainties in calculated *g* values are large, possibly related to inadequate bleaching throughout the analysis protocol prior to the fading experiments. As this thesis explores the residual ages of different sedimentary deposits, rather than absolute ages, the feldspar data are not fading corrected. The high luminescence sensitivity of the feldspar extracts means that few aliquots fail the acceptance criteria, and these data are contrasted with the quartz OSL data in the following chapter.

Table 5.11: Fading uncorrected feldspar samples model selection results after Arnold (2006) and Bailey and Arnold (2006).

Sample		n	Average D_e (Gy) (1 σ Error)	D_e CAM	σ_d	$2\sigma c_w$	Norm c_w	c crit ($1/2\sigma c_w$)	$2\sigma k_w$	Norm k_w	k_w crit ($0.6/2\sigma k_w$)	Bailey & Arnold 2006	Arnold 2006 (after Thrasher et al., 2009)	SA Arnold 2006
BERG2*	Paraglacial	21	178.33 ± 15.52	142.27 ± 25.05	0.800 ± 0.09	1.07	2.23	0.94	2.14	0.24	0.28	L5% 17.01 ± 1.39	MAM-3 132.71 ± 115.69	MAM-3 132.71 ± 115.69
FAB86		12	219.33 ± 10.30	214.38 ± 12.71	0.200 ± 0.004	1.41	0.85	0.71	2.83	0.22	0.21	CAM 214.38 ± 12.71	CAM 214.38 ± 12.71	MAM-3 34.06 ± 23.83
LOD4	Glaciofluvial Point Bar	46	27.11 ± 1.00	23.23 ± 1.80	0.525 ± 0.040	1.00	10.54	1.00	2.00	4.74	0.30	MAM-3 11.87 ± 1.02	MAM-3 11.87 ± 1.02	MAM-3 11.87 ± 1.02
LOD5		24	52.37 ± 2.24	46.02 ± 4.92	0.523 ± 0.029	0.88	2.60	1.14	1.76	0.09	0.34	MAM-3 6.99 ± 1.15	MAM-3 6.99 ± 1.15	MAM-3 6.99 ± 1.15
LOD6		48	24.15 ± 0.80	18.51 ± 1.97	0.735 ± 0.065	1.00	4.09	1.00	2.00	1.64	0.30	MAM-3 5.78 ± 0.66	MAM-3 5.78 ± 0.66	MAM-3 5.78 ± 0.66
FAB94		12	195.53 ± 9.50	191.45 ± 11.07	0.194 ± 0.004	1.41	1.11	0.71	2.83	0.49	0.21	CAM 191.45 ± 11.07	CAM 191.45 ± 11.07	MAM-3 191.39 ± 43.47
FAB100		12	68.94 ± 2.97	66.93 ± 4.86	0.248 ± 0.006	1.41	0.52	0.71	2.83	-0.05	0.21	CAM 66.93 ± 0.07	L5% 37.60 ± 1.56	CAM 66.93 ± 0.07
JOS51		47	3.82 ± 0.21	3.65 ± 0.14	0.268 ± 0.015	0.71	19.46	1.40	1.43	17.89	0.42	MAM-3 2.78 ± 0.16	MAM-3 2.78 ± 0.16	MAM-3 2.78 ± 0.16
FAB81	Glaciofluvial Braided Bar	12	96.06 ± 4.13	93.88 ± 5.80	0.210 ± 0.004	1.41	0.49	0.71	2.83	-0.35	0.21	CAM 93.88 ± 5.80	CAM 93.88 ± 5.80	CAM 93.88 ± 5.80
LEI13		48	13.50 ± 0.81	7.94 ± 0.77	0.670 ± 0.056	0.71	69.19	1.41	1.41	25.72	0.42	MAM-3 3.63 ± 0.43	MAM-3 3.63 ± 0.43	MAM-3 3.63 ± 0.43
LEI14		45	10.05 ± 0.75	6.30 ± 0.70	0.742 ± 0.068	0.73	25.26	1.37	1.46	9.29	0.41	MAM-3 2.52 ± 0.27	MAM-3 2.52 ± 0.27	MAM-3 2.52 ± 0.27
LEI18		47	6.38 ± 0.39	4.56 ± 0.30	0.460 ± 0.032	0.71	69.88	1.41	1.41	31.95	0.42	MAM-3 2.76 ± 0.21	MAM-3 2.76 ± 0.21	MAM-3 2.76 ± 0.21
GRAN54	Sandur Braided Bar	48	147.97 ± 5.17	145.77 ± 4.39	0.201 ± 0.010	1.00	0.54	1.00	2.00	-0.09	0.30	L5% 96.73 ± 3.62	L5% 96.73 ± 3.62	MAM-3 131.08 ± 9.37
GRAN55		48	102.09 ± 3.25	99.10 ± 5.15	0.253 ± 0.005	1.00	0.47	1.00	2.00	-0.28	0.30	CAM 99.10 ± 0.05	CAM 99.10 ± 0.05	CAM 99.10 ± 0.05
GRAN56		55	320.80 ± 14.60	16.13 ± 0.53	0.244 ± 0.012	0.66	2.89	1.51	1.32	0.31	0.45	L5% 8.89 ± 0.30	MAM-3 12.68 ± 0.69	MAM-3 12.68 ± 0.69
GRAN57		54	10.37 ± 0.37	12.98 ± 0.62	0.348 ± 0.020	0.67	3.41	1.50	1.33	0.10	0.45	L5% 6.88 ± 0.31	MAM-3 8.56 ± 0.57	MAM-3 8.56 ± 0.57

Table 5.11 continued.

Sample		n	Average D_e (Gy) (1 σ Error)	D_e CAM (Gy)	σ_d	$2\sigma c_w$	Norm c_w	c crit ($1/2\sigma c_w$)	$2\sigma k_w$	Norm k_w	k_w crit ($0.6/2\sigma k_w$)	Bailey & Arnold 2006	Arnold 2006 (after Thrasher et al., 2009)	SA Arnold 2006
GRAN58	Sandur Braided Bar	24	124.44 ± 4.30	120.99 ± 5.92	0.237 ± 0.004	1.00	1.03	1.00	2.00	0.45	0.30	L5% 67.68 ± 2.73	MAM-3 120.90 ± 36.08	MAM-3 120.90 ± 36.08
GRAN59		60	173.28 ± 7.80	162.38 ± 5.00	0.234 ± 0.011	0.63	2.76	1.58	1.26	-0.20	0.47	MAM-3 128.80 ± 6.78	MAM-3 128.80 ± 6.78	MAM-3 128.80 ± 6.78
GRAN69#1		24	17.35 ± 0.97	13.47 ± 1.78	0.644 ± 0.048	1.00	11.59	1.00	2.00	5.05	0.30	MAM-3 6.08 ± 0.76	MAM-3 6.08 ± 0.76	MAM-3 6.08 ± 0.76
GRAN69#2		36	14.80 ± 0.64	12.42 ± 1.22	0.588 ± 0.031	0.82	6.27	1.22	1.63	2.17	0.37	MAM-3 5.55 ± 0.55	MAM-3 5.55 ± 0.55	MAM-3 5.55 ± 0.55
GRAN69		60	15.82 ± 0.78	12.82 ± 1.02	0.612 ± 0.044	0.63	2.70	1.58	1.26	-1.62	0.47	MAM-3 5.73 ± 0.44	MAM-3 5.73 ± 0.44	MAM-3 5.73 ± 0.44
NIG3		47	7.55 ± 0.46	7.27 ± 0.36	0.335 ± 0.021	0.71	38.55	1.40	1.43	25.69	0.42	MAM-3 6.27 ± 0.92	MAM-3 6.27 ± 0.92	MAM-3 6.27 ± 0.92
NIG4		33	188.16 ± 9.95	164.56 ± 15.55	0.540 ± 0.027	0.85	3.62	1.17	1.71	0.81	0.35	L5% 48.25 ± 2.95	MAM-3 288.81 ± 171.77	MAM-3 288.81 ± 171.77
NIG6*		26	61.76 ± 3.69	50.09 ± 6.36	0.607 ± 0.043	1.02	11.08	0.98	2.04	5.88	0.29	MAM-3 7.45 ± 178.18	MAM-3 7.45 ± 178.18	MAM-3 7.45 ± 178.18
NIG7		48	5.44 ± 0.25	4.89 ± 0.22	0.306 ± 0.018	0.71	15.21	1.41	1.41	10.81	0.42	MAM-3 3.56 ± 0.21	MAM-3 3.56 ± 0.21	MAM-3 3.56 ± 0.21
NIG8		48	7.27 ± 0.33	6.52 ± 0.21	0.224 ± 0.011	0.71	2.25	1.41	1.41	-0.06	0.42	MAM-3 5.23 ± 0.30	MAM-3 5.23 ± 0.30	MAM-3 5.23 ± 0.30
NIG9*		48	17.36 ± 0.79	12.35 ± 1.34	0.751 ± 0.067	0.71	46.16	1.41	1.41	16.86	0.42	MAM-3 6.23 ± 17.56	MAM-3 6.23 ± 17.56	MAM-3 6.23 ± 17.56
GAUP1	Delta	24	406.53 ± 25.87	393.03 ± 20.56	0.248 ± 0.005	1.00	1.50	1.00	2.00	0.41	0.30	MAM-3 391.80 ± 124.32	MAM-3 391.80 ± 124.32	MAM-3 391.80 ± 124.32

*The MAM-3 returns very large uncertainties for these samples, therefore they have been modelled with the L5% model.

Table 5.12: Fading uncorrected feldspar FMM results.

Sample		n	Average D_e (Gy) (1 σ Error)	σ_d	FMM D_e (Gy) C1	FMM D_e (Gy) C2	FMM D_e (Gy) C3	FMM D_e (Gy) C4	CAM D_e (Gy)	MAM-3 D_e (Gy)
BERG2	Paraglacial	21	178.33 ± 15.52	0.80 ± 0.09	197.10 ± 6.19 81 %	30.76 ± 2.05 19 %	-	-	142.27 ± 25.05	132.71 ± 115.69
FAB86		12	219.33 ± 10.30	0.200 ± 0.004	242.23 ± 11.85 64 %	172.06 ± 12.36 36 %	-	-	214.38 ± 12.71	34.06 ± 23.83
LOD4	Glaciofluvial Point Bar	46	27.11 ± 1.00	0.525 ± 0.040	14.14 ± 0.41 37 %	25.54 ± 0.64 46 %	53.14 ± 2.09 17 %	-	23.23 ± 1.80	11.87 ± 1.02
LOD5		24	52.37 ± 2.24	0.523 ± 0.029	48.68 ± 2.36 34 %	80.42 ± 3.17 33 %	24.37 ± 1.15 32 %	-	46.02 ± 4.92	6.99 ± 1.15
LOD6		48	24.15 ± 0.80	0.735 ± 0.065	23.34 ± 0.56 48 %	10.86 ± 0.49 22 %	5.97 ± 0.34 15 %	62.30 ± 2.60 15 %	18.51 ± 1.97	5.78 ± 0.66
FAB94		12	195.53 ± 9.50	0.194 ± 0.004	224.38 ± 11.42 53 %	160.35 ± 9.80 47 %	-	-	191.45 ± 11.07	191.39 ± 43.47
FAB100		12	68.94 ± 2.97	0.248 ± 0.006	73.12 ± 2.66 83 %	43.51 ± 4.13 17 %	-	-	66.93 ± 4.86	66.95 ± 21.97
JOS51		47	3.81 ± 0.15	0.268 ± 0.015	3.45 ± 0.06 90 %	6.61 ± 0.39 10 %	-	-	3.65 ± 0.14	2.78 ± 0.16
FAB81	Glaciofluvial Braided Bar	12	96.06 ± 4.13	0.210 ± 0.004	109.56 ± 4.99 60 %	74.58 ± 4.15 40 %	-	-	93.88 ± 5.80	93.88 ± 5.80
LEI13		48	13.50 ± 0.81	0.670 ± 0.056	5.93 ± 0.11 75 %	20.02 ± 0.63 25 %	-	-	7.94 ± 0.77	3.63 ± 0.43
LEI14		45	10.05 ± 0.75	0.742 ± 0.068	4.91 ± 0.26 55 %	26.21 ± 1.15 16 %	2.68 ± 0.24 16 %	9.62 ± 1.01 13 %	6.30 ± 0.70	2.52 ± 0.27
GRAN54	Sandur Braided Bar	48	147.97 ± 5.17	0.201 ± 0.010	149.21 ± 3.98 73 %	196.52 ± 12.77 16 %	99.64 ± 6.18 11 %	-	145.77 ± 4.39	131.08 ± 9.37
GRAN55		48	102.09 ± 3.25	0.253 ± 0.005	112.42 ± 2.85 75 %	67.00 ± 3.10 25 %	-	-	99.10 ± 5.15	99.22 ± 33.07
GRAN56		55	320.80 ± 14.60	0.244 ± 0.012	14.17 ± 0.62 64 %	20.29 ± 1.37 36 %	-	-	16.13 ± 0.53	12.68 ± 0.69
GRAN57		54	10.37 ± 0.37	0.348 ± 0.020	9.36 ± 0.22 44 %	16.82 ± 0.33 56 %	-	-	12.98 ± 0.62	8.56 ± 0.57
GRAN58		24	124.44 ± 4.30	0.237 ± 0.004	134.08 ± 3.32 79 %	80.54 ± 3.96 21 %	-	-	120.99 ± 5.92	120.90 ± 36.08

Table 5.12 cont.: Fading uncorrected feldspar FMM results.

Sample		n	Average D_e (Gy) (1 σ Error)	σ_d	FMM D_e (Gy) C1	FMM D_e (Gy) C2	FMM D_e (Gy) C3	FMM D_e (Gy) C4	CAM D_e (Gy)	MAM-3 D_e (Gy)
GRAN59	Sandur Braided Bar	60	173.28 ± 7.80	0.234 ± 0.011	178.00 ± 5.98 51 %	126.97 ± 3.97 37 %	237.08 ± 15.24 12 %	-	162.38 ± 5.00	128.80 ± 6.78
GRAN69#1		24	17.35 ± 0.97	0.64 ± 0.05	15.63 ± 0.57 47 %	7.67 ± 0.31 41 %	49.94 ± 3.39 12.5 %	-	13.47 ± 1.78	6.08 ± 0.76
GRAN69#2		36	14.80 ± 0.64	0.59 ± 0.03	7.05 ± 0.23 43 %	14.66 ± 0.57 32 %	27.27 ± 1.00 25 %	-	12.42 ± 1.22	5.55 ± 0.55
GRAN69		60	15.82 ± 0.78	0.61 ± 0.04	7.31 ± 0.02 43 %	15.92 ± 0.03 42 %	34.98 ± 0.04 15 %	-	12.82 ± 1.02	5.73 ± 0.44
NIG4		33	188.16 ± 9.95	0.540 ± 0.027	215.41 ± 4.99 73 %	80.91 ± 3.08 27 %	-	-	164.56 ± 15.55	288.81 ± 171.77
NIG6		26	61.76 ± 3.69	0.607 ± 0.043	76.19 ± 3.10 51 %	30.77 ± 1.32 49 %	-	-	50.09 ± 6.36	7.45 ± 178.18
NIG8		48	7.27 ± 0.33	0.224 ± 0.011	5.39 ± 0.26 46 %	8.45 ± 0.33 35 %	6.41 ± 0.95 19 %	-	6.52 ± 0.21	5.23 ± 0.30
NIG9		48	17.36 ± 0.79	0.751 ± 0.067	8.62 ± 0.16 71 %	30.99 ± 0.88 29 %	-	-	12.35 ± 1.34	6.23 ± 17.56
GAUP1	Delta	24	406.53 ± 25.87	0.25 ± 0.00	444.05 ± 16.05 72 %	288.78 ± 18.89 28 %	-	-	393.03 ± 20.56	391.80 ± 124.32

Table 5.13: Dosimetry and age calculations, fading uncorrected Feldspar. Samples in italics have had D_r calculated from the average catchment D_r. Sample depth is 0.02 m for all samples with the exception of GAUP1 which has depth 10 m.

Sample	Type	n	D_e (Gy)	Model	Water Content* (%)	K (%)	Th (ppm)	U (ppm)	Rb (ppm)	Dry Alpha Dose Rate (Gy ka^{-1})	Wet Dose Rate (Gy ka^{-1})	Age (ka)	Max Age (ka)	c	k
BERG2	Paraglacial	*21*	*132.71 ± 115.69*	*MAM-3*	*20.00*	*4.11 ± 0.36*	*19.53 ± 3.59*	*3.50 ± 0.77*	*100*	*0.46 ± 0.56*	*5.94 ± 0.58*	*22.34 ± 19.61*	*56.52 ± 5.68*	*-0.04*	*-0.63*
FAB86		12	214.38 ± 12.71	CAM	21.20	3.00	7.65	3.03	100	0.26 ± *0.34*	4.14 ± 0.33	51.78 ± 5.42	58.50 ± 4.46	0.52	0.20
LOD4	Glaciofluvial Point Bar	*46*	*11.87 ± 1.02*	*MAM-3*	*15.40*	*2.89*	*13.53 ± 1.87*	*2.91 ± 0.73*	*121.8 ± 4.5*	*0.34 ± 0.35*	*4.64 ± 0.36*	*2.56 ± 0.31*	*24.17 ± 1.68*	*2.72*	*9.81*
LOD5		*24*	*6.99 ± 1.15*	*MAM-3*	*20.70*	*2.89*	*13.53 ± 1.87*	*2.91 ± 0.73*	*121.8 ± 4.5*	*0.34 ± 0.35*	*4.43 ± 0.34*	*1.58 ± 0.29*	*18.15 ± 1.26*	*0.76*	*0.41*
LOD6		*48*	*5.78 ± 0.66*	*MAM-3*	*19.30*	*2.89*	*13.53 ± 1.87*	*2.91 ± 0.73*	*121.8 ± 4.5*	*0.34 ± 0.35*	*4.48 ± 0.35*	*1.29 ± 0.18*	*19.40 ± 1.18*	*1.71*	*2.72*
FAB94		12	191.45 ± 11.07	CAM	20.35	3.14	7.87	4.06	100	0.31 ± *0.35*	4.52 ± 0.35	42.33 ± 4.29	49.61 ± 3.83	0.93	0.77
FAB100		*12*	*37.60 ± 1.56*	*L5%*	*19.61*	*3.22 ± 0.05*	*8.62 ± 0.02*	*3.22 ± 0.01*	*100*	*0.28 ± 0.35*	*4.48 ± 0.35*	*8.40 ± 0.79*	*16.34 ± 1.13*	*-0.12*	*-0.21*
JOS51		47	2.78 ± 0.16	MAM-3	25.30	3.55	14.86	3.66	100	0.40 ± *0.36*	5.00 ± 0.36	0.56 ± 0.05	2.48 ± 0.19	4.17	22.6
GRAN69a		24	6.08 ± 0.76	MAM-3	14.04	2.89	14.85	3.42	118.60	0.38 ± *0.36*	4.91 ± 0.38	1.24 ± 0.19	6.48 ± 0.47	2.57	6.65
GRAN69b		36	5.55 ± 0.55	MAM-3	14.04	2.89	14.85	3.42	118.60	0.38 ± *0.36*	4.91 ± 0.38	1.13 ± 0.15	5.55 ± 0.37	1.28	1.59
GRAN69		60	5.73 ± 0.44	MAM-3	14.04	2.89	14.85	3.42	118.60	0.38 ± *0.36*	4.91 ± 0.38	1.17 ± 0.13	7.12 ± 0.45	2.56	8.29
FAB81	Glaciofluvial Braided Bar	12	93.88 ± 5.80	CAM	16.86	3.19	8.63	2.61	100	0.25 ± *0.34*	4.42 ± 0.36	21.25 ± 2.25	24.80 ± 1.85	0.09	-1.15
LEI13		*48*	*3.63 ± 0.43*	*MAM-3*	*14.78*	*3.05 ± 0.33*	*12.21 ± 0.79*	*2.52 ± 0.67*	*124.30 ± 12.59*	*0.30 ± 0.35*	*4.26 ± 0.33*	*0.85 ± 0.12*	*23.18 ± 1.98*	*5.19*	*31.4*
LEI14		45	2.52 ± 0.27	MAM-3	18.54	2.82	12.77	2.99	115.40	0.33 ± *0.35*	4.28 ± 0.33	0.59 ± 0.08	12.65 ± 1.47	2.89	9.61
LEI18		47	2.76 ± 0.21	MAM-3	21.74	3.28	11.65	2.04	133.20	0.27 ± *0.35*	4.36 ± 0.34	0.63 ± 0.07	9.76 ± 0.74	6.16	40.5
GRAN54	Sandur Braided Bar	*48*	*96.73 ± 3.62*	*L5%*	*21.62*	*2.89*	*13.53 ± 1.87*	*2.91 ± 0.73*	*121.8 ± 4.5*	*0.34 ± 0.45*	*4.40 ± 0.42*	*22.00 ± 2.36*	*56.44 ± 4.10*	*0.46*	*1.47*
GRAN55		*48*	*99.10 ± 5.15*	*CAM*	*22.74*	*2.89*	*13.53 ± 1.87*	*2.91 ± 0.73*	*121.8 ± 4.5*	*0.34 ± 0.45*	*4.36 ± 0.42*	*22.74 ± 2.57*	*25.80 ± 1.77*	*-0.43*	*-0.43*
GRAN56		*55*	*12.68 ± 0.69*	*MAM-3*	*15.85*	*2.89*	*13.53 ± 1.87*	*2.91 ± 0.73*	*121.8 ± 4.5*	*0.34 ± 0.45*	*4.62 ± 0.45*	*2.74 ± 0.32*	*6.34 ± 0.44*	*1.00*	*2.16*

Table 5.13 cont.: Dosimetry and age calculations, fading uncorrected Feldspar.

Sample	Type	n	D_e (Gy)	Model	Water Content* (%)	K (%)	Th (ppm)	U (ppm)	Rb (ppm)	Dry Alpha Dose Rate (Gy ka^{-1})	Wet Dose Rate (Gy ka^{-1})	Age (ka)	Max Age (ka)	c	k
GRAN57		*54*	*8.56 ± 0.57*	*MAM-3*	*23.70*	*2.89*	*13.53 ± 1.87*	*2.91 ± 0.73*	*121.8 ± 4.5*	*0.34 ± 0.45*	*4.32 ± 0.41*	*1.98 ± 0.24*	*6.68 ± 0.46*	*1.00*	*1.38*
GRAN58		*24*	*120.90 ± 36.07*	*MAM-3*	*16.91*	*2.89*	*13.53 ± 1.87*	*2.91 ± 0.73*	*121.8 ± 4.5*	*0.34 ± 0.45*	*4.58 ± 0.44*	*26.41 ± 8.32*	*29.29 ± 2.01*	*-0.02*	*0.84*
GRAN59		*60*	*128.80 ± 6.78*	*MAM-3*	*10.51*	*2.89*	*13.53 ± 1.87*	*2.91 ± 0.73*	*121.8 ± 4.5*	*0.34 ± 0.45*	*4.85 ± 0.48*	*26.55 ± 3.07*	*54.96 ± 4.68*	*0.52*	*-0.04*
NIG3	Sandur Braided Bar	*47*	*6.27 ± 0.92*	*MAM-3*	*24.24*	*3.17 ± 0.24*	*12.93 ± 2.17*	*2.21 ± 0.58*	*131.80 ± 6.91*	0.30 ± 0.35	4.33 ± 0.34	1.45 ± 0.24	8.92 ± 0.68	*5.49*	*34.03*
NIG4		33	48.25 ± 2.91	MAM-3	22.48	3.38	10.96	1.60	135.60	0.24 ± 0.34	4.29 ± 0.34	67.32 ± 40.44	50.21 ± 3.22	0.69	0.14
NIG6		23	14.29 ± 0.70	L5%	22.44	3.46	12.43	1.76	141.30	0.27 ± 0.35	4.49 ± 0.35	3.18 ± 0.31	16.97 ± 1.22	2.61	8.5
NIG7		48	3.56 ± 0.21	MAM-3	15.44	3.06	12.37	2.31	125.60	0.29 ± 0.35	4.56 ± 0.36	0.78 ± 0.08	3.40 ± 0.25	3.38	13.2
NIG8		48	5.23 ± 0.30	MAM-3	20.74	3.09	12.15	2.34	131.60	0.29 ± 0.35	4.37 ± 0.34	1.20 ± 0.12	2.51 ± 0.18	0.71	-0.27
NIG9		48	3.84 ± 0.25	L5%	19.28	2.88	16.65	3.07	124.90	0.39 ± 0.36	4.72 ± 0.36	0.81 ± 0.08	28.26 ± 2.04	3.94	18.7
GAUP1	Delta	24	391.80 ± 124.32	MAM-3	2.40	2.80	9.82	4.58	100	0.43 ± 0.37	6.61 ± 0.49	59.25 ± 19.39	67.15 ± 4.69	0.40	0.44

Chapter 6. OSL Results & Discussion

6.1. Sample Characteristics

6.1.1. **Quartz Sensitivity**

Many of the quartz samples analysed for this research project were rejected and low sample acceptance is attributed to the poor sensitivity of the sample suite. Where acceptance is correlated with average T_x signal intensity, 67% of Fåbergstølsgrandane sample acceptance is accounted for (Figure 6.1), however the same correlation is not observed for Fåbergstølsdalen (r^2 = 0.06). It was not possible to explore this relationship within the other catchments as insufficient data are available due to analysis of fewer samples and low aliquot acceptance.

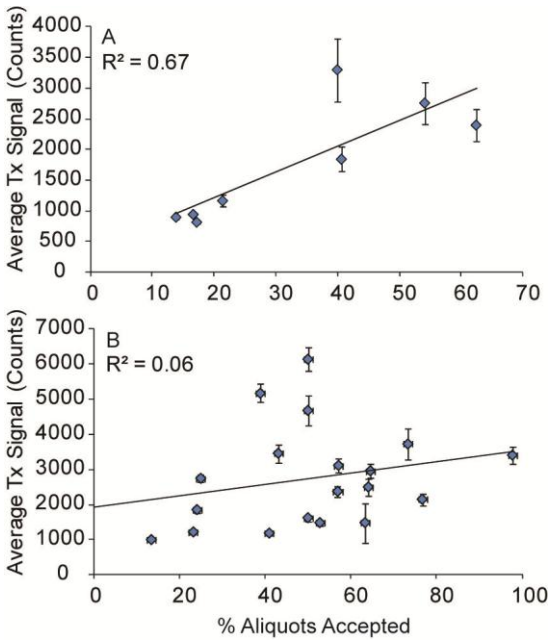

Figure 6.1: Correlations between the percentage of aliquots accepted and average T_x intensity for (A) Fåbergstølsgrandane and (B) Fåbergstølsdalen.

The quartz luminescence sensitivity varies between the different catchments (Figure 6.2), and sediment sampled from Fåbergstølsdalen is most sensitive. Sensitivity does not vary systematically as a function of deposit type (Figure 6.3), which may be related to differences in sample number. However, subglacial material is least sensitive, consistent with the association of improved sensitivity with sample reworking (e.g. Preusser et al., 2006). Across the entire sample set, little association between sediment reworking and sensitivity is observed, which relates either to the restricted spatial scale over which quartz samples are considered (maximum transport distance ~ 4 km), or to geological controls on the luminescence properties of quartz.

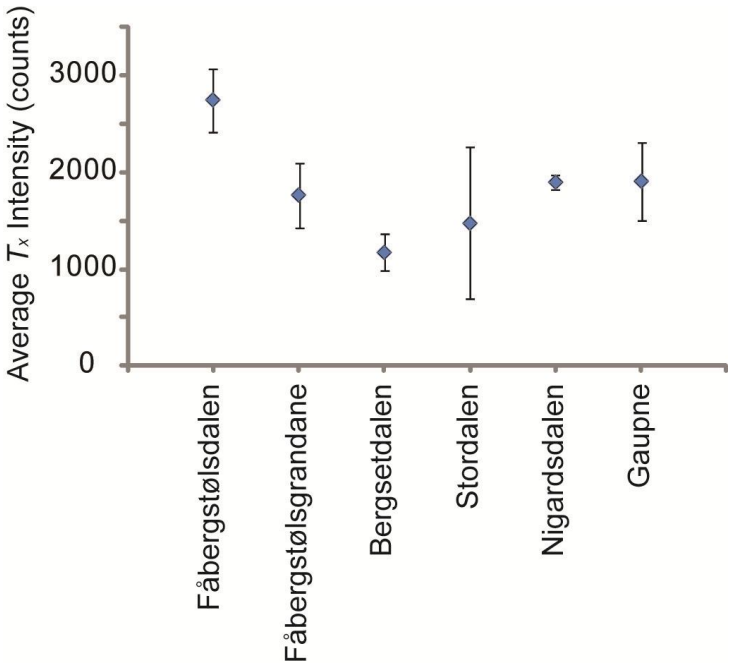

Figure 6.2: Average T_x intensity (counts) and standard errors for all accepted aliquots for the different catchments, note that the data for Nigardsdalen are derived from only 4 aliquots of a single sample.

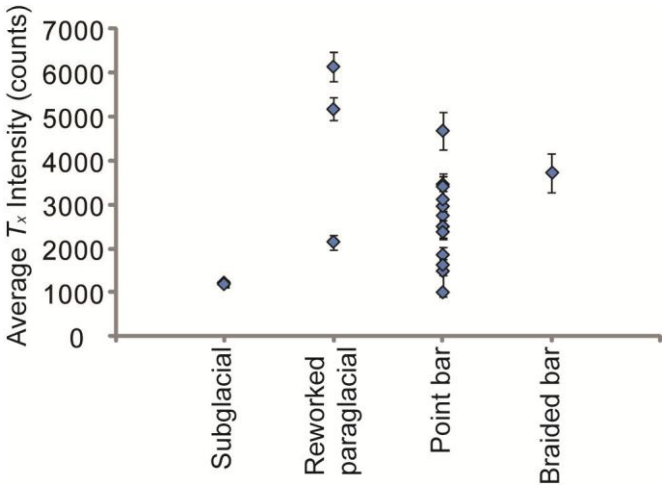

Figure 6.3: Average T_X intensity with standard errors for the different deposit types sampled from Fåbergstølsdalen.

Fåbergstølsdalen has the most sensitive quartz and has different bedrock geology to the other catchments analysed, comprising quartz diorite. Bergsetdalen, Fåbergstølsgrandane and Nigardsdalen are underlain by quartz monzonite which has higher Th content to quartz diorite, and which is reflected in the average ICP-MS data for each catchment (Table 6.1). Although the ICP-MS data relate to the sedimentary, rather than geological irradiation history of the different quartz samples, it is apparent that Bergsetdalen, has very poor quartz luminescence sensitivity (Figure 6.2) and the greatest dose rates, whereas Fåbergstølsdalen has the most sensitive quartz, and one of the

lowest dose rates. Irradiation history is known to influence the luminescence efficiency of quartz (e.g. Rink, 1994) and is discussed more extensively in Chapters 7-10.

Table 6.1: Mean average ICPMS data for each of the catchments analysed with standard errors. The WTUL samples are included for comparative purposes.

	K (%)	Th (ppm)	U (ppm)	Rb* (ppm)	Dry Dose Rate*
BERG	4.11 ± 0.11	19.53 ± 1.13	3.50 ± 0.23	100	6.13 ± 0.36
FAB	3.25 ± 0.05	8.39 ± 0.19	3.28 ± 0.15	100	4.49 ± 0.27
GAUP	3.30 ± 0.27	10.02 ± 0.35	4.11 ± 0.68	100	4.85 ± 0.29
GRAN	2.89 ± 0.00	13.53 ± 1.33	2.91 ± 0.51	121.80 ± 3.20	4.41 ± 0.26
JOS	3.39 ± 0.13	13.02 ± 1.07	3.23 ± 0.35	100	4.93 ± 0.29
LEI	3.05 ± 0.19	12.21 ± 0.46	2.52 ± 0.39	124.30 ± 7.27	4.39 ± 0.26
NIG	3.17 ± 0.24	12.93 ± 2.17	2.21 ± 0.58	131.80 ± 6.91	4.48 ± 0.27
WTUL	1.84 ± 0.04	5.69 ± 0.35	2.11 ± 0.18	100	2.67 ± 0.16

*Dry dose rate calculated assuming zero water content and no cosmic dose contribution. Where no measured Rb values are available for the catchments, a value of 100 ppm has been used.

6.1.2. **Sample Acceptance**

The causes of sample rejection varied both by deposit type (Table 6.2) and catchment (Table 6.3). Fewer than 40% of the total quartz aliquots analysed fulfilled the acceptance criteria (see Chapter 4). In contrast, almost all of the feldspar samples analysed were accepted (98%) associated with the much greater luminescence sensitivity of feldspar relative to quartz (Duller, 1997; see Chapter 2). The reasons for the rejection of 12 feldspar aliquots are given in Appendix A. Sample recuperation was the greatest cause of quartz aliquot rejection (19%), closely followed by poor recycling (18%), and both are associated with low sample sensitivity. Almost 5% of aliquots were rejected because the signal was < 3 σ from the background value (see Appendix A for acceptance rates of all samples analysed).

Total acceptance varies when considered relative to the different deposit types (see categorisations in Chapter 3 and individual sample characteristics in Appendix C). Subglacial samples and glaciofluvial bars attached to braided river channels have the lowest acceptance rates of 25 and 20% respectively (Table 6.2), whereas material collected from glaciofluvial (bank-attached) point bars has the highest acceptance rate (48%). Rather than reflecting depositional context, this relationship reflects differences between catchments, attributed to localised geological variations. This is supported where the acceptance rates for Fåbergstølsdalen are considered for each of the deposit types: minimum acceptance is 31% for subglacial samples, and the maximum value of 73% is for glaciofluvial braided channel bar deposits. In contrast, for Bergsetdalen maximum acceptance is 13% for channel point bar deposits, 8% for braided channel bar deposits and no aliquots are accepted for any of the quartz paraglacial deposits from this catchment.

The low aliquot numbers for some of the quartz samples, which is a consequence of the poor sample acceptance rates, is too low for robust conclusions regarding D_e distribution or residual age to be drawn. Where possible quartz data are supported by feldspar data, however where this is not possible, and $n < 10$, the quartz samples are rejected. For unsupported quartz samples which have $n < 30$, the data are considered within the limitations of the available number of aliquots. A full list of quartz samples analysed and those that are not considered in the discussion for this reason, is provided in Appendix A.1.

Table 6.2: Summary table by deposit type where N is total number of aliquots analysed, *n* are those aliquots accepted and Acc. % the percentage accepted. The remainder of the table relates to the causes of sample rejection following the criteria outlined in Chapter 4. RR = recycling ratio, Oversat = aliquots which have D_e beyond the saturation level of the dose response curve, Sig < 3 σ BG = signal less than 3 σ above the background, IRSL = IR depletion test, Plot = unable to interpolate D_e, Calc = unable to calculate D_e, Recup = recuperation.

Summary	N	n	Acc.%	RR	Oversat	Sig < 3 σ BG	IRSL	Inad. Regen	Plot	Calc	Recup
Subglacial Samples	201	51		44	5	33	24	3	8	4	29
%			25	21.9	2.5	16.4	11.9	1.5	4.0	2.0	14.4
Paraglacial Samples	298	113		48	19	36	9	21	8	5	40
%			38	16.1	6.4	12.1	3.0	7.0	2.7	1.7	13.4
Glaciofluvial Point Bars	648	312		89	52	11	33	30	9	0	113
%			48	13.7	8.0	1.7	5.1	4.6	1.4	0.0	17.4
Gilbert-style Delta	62	22		12	9	1	3	0	1	3	11
%			35	19.4	14.5	1.6	4.8	0.0	1.6	4.8	17.7
Glaciofluvial Braided Channel Bar	162	32		41	1	30	8	9	5	3	33
%			20	25.3	0.6	18.5	4.9	5.6	3.1	1.9	20.4
Sandur Braided Channel Bar	245	98		37	7	23	3	2	5	2	68
%			40	28.0	5.3	17.4	2.3	1.5	3.8	1.5	51.5
Total All Aliquots	1586	606		270	92	133	78	63	36	17	293
%	100		38	17.0	5.8	8.4	4.9	4.0	2.3	1.1	18.5

Table 6.3: Summary table by catchment

	Acceptance Rate (%)						
Sample	Subglacial	Paraglacial	Fluvial	Gilbert-	Fluvial	Sandur	Average
FAB	31	41	53	-	73	-	50
BERG	-	0	13	-	8	-	11
NIG	11	-	-	-	-	-	11
LOD	-	-	6	-	-	-	6
GAUP	-	-	-	36	-	-	36
GRAN	-	-	-	-	-	40	40

6.2. D_e Distributions and Residual Ages

The D_e distributions and residual ages of the different deposits are discussed first by deposit type and then by catchment so that interrelationships between the two can be explored. Residual ages indicate that all of the modern sediments which have a known age of < 100 years (see Chapter 2) are higher than anticipated, and have an average age > 1 ka.

6.3. Source Material

Only source material from Fåbergstølsdalen, comprising subglacial and paraglacial samples, had sufficient quartz acceptance for discussion (see Table 6.2, Table 6.3). The bootstrap experiments described in Chapter 4 indicate that samples with n < 30 may not have well characterised distributions. FAB86, FAB42 and FABSUB2 have $n \geq 25$ and bB_k < CalQzB8 and so have moderately well characterised distributions, suitable for discussion.

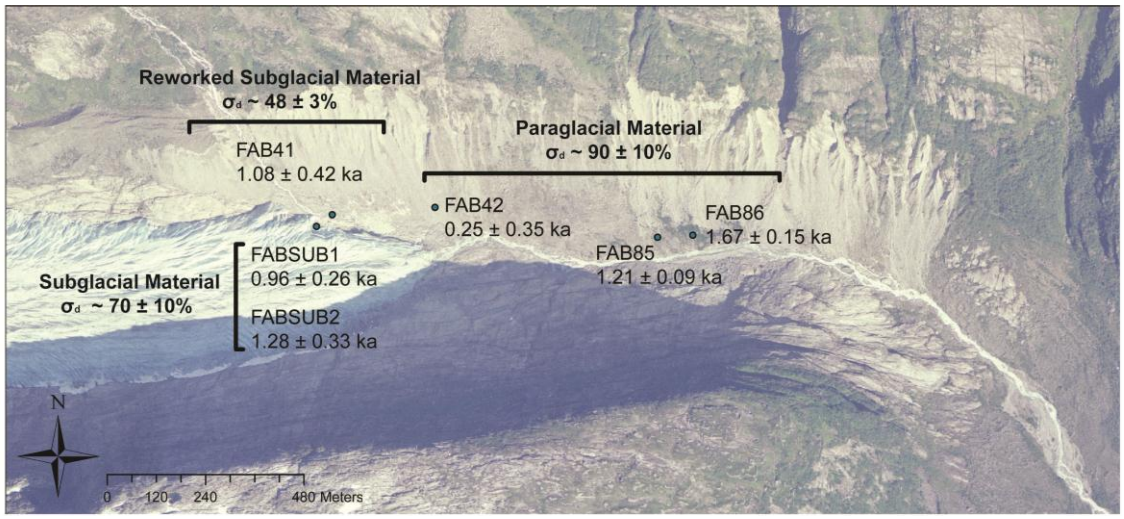

Figure 6.4: Aerial photograph of Fåbergstølsdalen with source sample locations and quartz residual ages indicated. Modified and reprinted with permission from Norway in Images (www.norgeibilder.no), Jotunheimen 2004, © Norwegian Mapping Authority.

The subglacial material (Dmm) has σ_d of ~ 70 ± 10%, indicative of partial bleaching, the residual ages of these samples is low and they have highly skewed D_e distributions (Figure 6.5). Grain size analyses (GSA, Figure 6.7) indicate that as anticipated, the subglacial till (Dmm) deposits are poorly sorted and skewed towards coarser material. Residual ages are younger than anticipated for *in-situ* deposits (< 1.5 ka), which should have a minimum age of ~ 5 ka associated with the onset of Neoglaciation (e.g. Shakesby et al., 2004, see Chapter 3), and may be because the sample site was at the glacier front. Material was gathered here due to logistical constraints and therefore some sunlight

exposure due to sediment reworking by meltwater may have occurred prior to sample collection. Alternatively, low residual ages may be caused by signal bleaching by intense pressure at the glacier bed (triboluminescence, Swift et al., 2010).

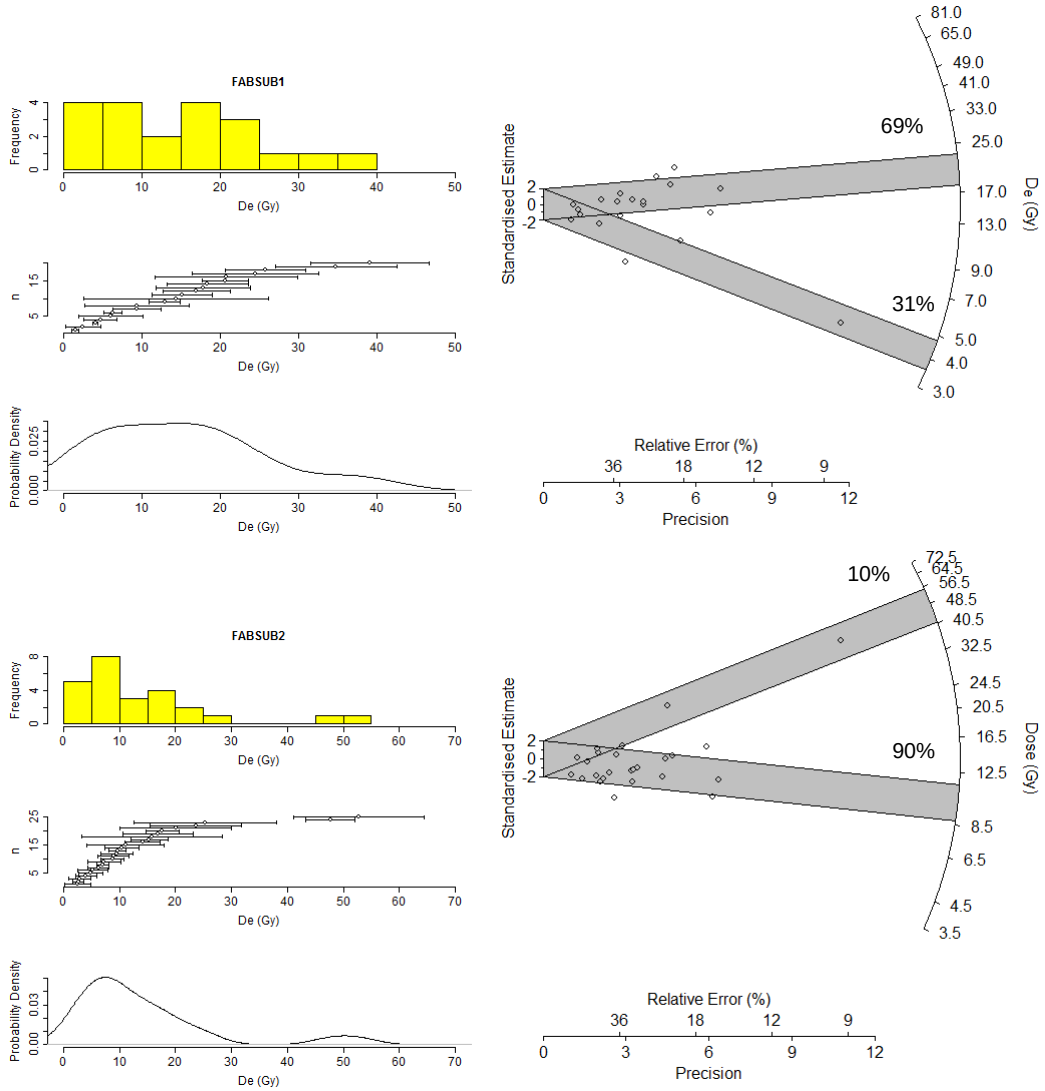

Figure 6.5: Histograms, probability density functions, scatter graphs and radial plots of the quartz subglacial source samples. The relative proportions of FMM components are indicated on radial plots.

The paraglacial material quartz samples (Dmm, Sr, Sh:Fl) have σ_d of 90 ± 10% which is consistent for material reworked by different processes, e.g. FAB42 comprises avalanche debris whereas FAB85 and FAB86 are sheetwash deposits (see Appendix C for individual sample descriptions, Figure 6.6). These different transport processes are reflected in the contrasting residual ages of these deposits, suggesting that although the source material dictates sample σ_d and D_e distribution shape, that residual age is governed by specific transport and depositional processes, even over limited transport distances. The GSA characteristics of these samples are also similar, but distinct to those of the subglacial material. They comprise mean phi of fine to very fine sand, are poorly sorted and have identical kurtosis (1.07, mesokurtic, see Table 3.2).

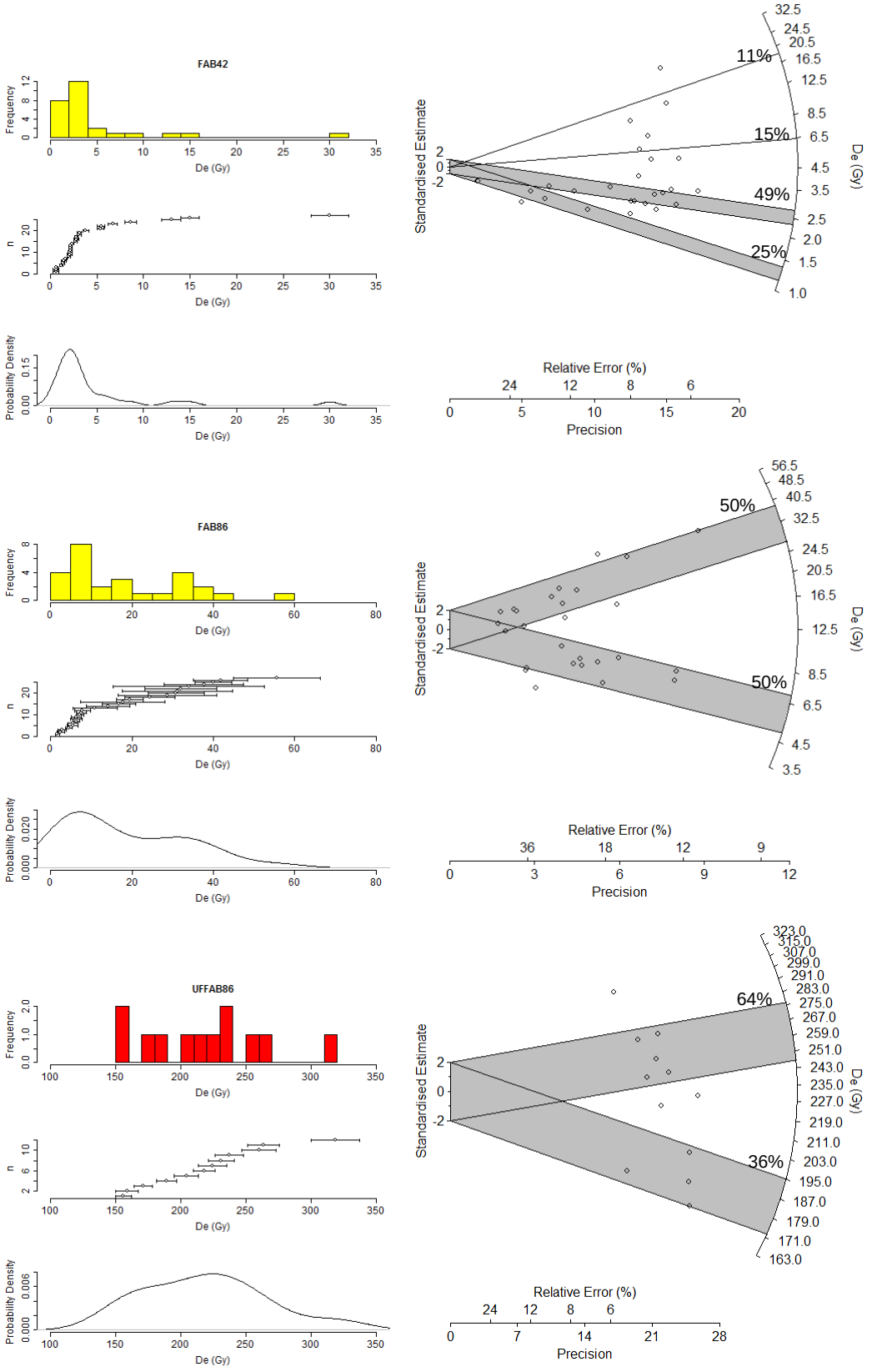

Figure 6.6: Histograms, probability density functions, scatter graphs and radial plots of the quartz extract of FAB42 and the quartz (light grey) and feldspar (dark grey) extracts of FAB86 paraglacial source samples. The relative proportions of FMM components are indicated on radial plots.

Two paraglacial feldspar samples were also analysed. F_BERG2, which is sampled from Bergsetdalen, has σ_d consistent with the quartz data (80 ± 9%), however the feldspar extract of FAB86 (F_FAB86) has σ_d of 20 ± 0.4%, significantly less than the partner quartz extract (91 ± 12%). The residual age of F_FAB86 is also much greater (51.78 ± 5.42 ka) than for the partner quartz extract (1.67 ± 0.15 ka). Although different residual ages are anticipated between quartz and feldspar due to the variance in bleaching rates (see Chapter 2), σ_d values may be expected to be similar as the feldspar and quartz grains are exposed to the same processes and are derived from the same source material. Furthermore, as $n > 10$, the measured σ_d values are thought to be representative of the samples (see Chapter 4). Maximum residuals are > 50 ka for both feldspar samples indicating that paraglacial materials are not fully bleached between periods of glaciation.

In contrast to the subglacial and paraglacial deposits described, FAB41 (n=12, Figure 4.23) has lower σ_d (48 ± 3%). Investigations into the dependence of σ_d on n described in Chapter 4 demonstrated that where $n > 10$, σ_d exhibits little variation, thus this value is regarded as real, although additional replicates would make it more robust. The GSA data for FAB41 are similar to those for the subglacial material, although it has been significantly reworked, comprising Sh coarse sand. Its location indicates that it is sourced from both paraglacial and subglacial deposits, however the similarities in the GSA data (Figure 6.7) indicate that subglacial sources are dominant and thus FAB41 is interpreted as a reworked subglacial deposit. If the subglacial samples are considered diagnostic of the source material, then the reduced σ_d of this sample must be related to depositional processes, which contrasts with the observations for the paraglacial material, and suggests that a threshold level may exist after which sediment modification during transport is sufficient to affect σ_d as well as residual age. This may occur where bleaching heterogeneity is sufficient to exert an influence over the existing D_e distribution. An alternative proposal is that under uniform bleaching conditions, when some grains in an existing heterogeneous population become fully bleached, σ_d will reduce. The bleaching experiments described in Chapter 4 indicate that the minimum residual dose in a fully bleached quartz sample is ~ 2 Gy, however the minimum residual for FAB41 is ~ 4 Gy, indicating that none of the aliquots of FAB41 are fully bleached. Therefore the latter proposal cannot be accepted whilst assuming sample modernity, instead the former proposal that depositional processes also influence sample σ_d provides an explanation for the observed modification.

The maximum residual age of the different samples has been calculated from the single greatest D_e of the aliquots measured. Where these maximum ages, rather than the modelled ages, of the different samples are considered (Table 4.18), FAB86 has a maximum residual of 9.05 ± 0.87 ka and FABSUB2 of 12.09 ± 1.70 ka. The Jostedalsbre

plateau is thought to have been completely ice free by 7.5-5.5 ka cal BP (e.g. Nesje and Kvamme, 1991; see section 1.6.1.2.) and Neoglacial activity started around 5 ka BP (Shakesby et al., 2004), indicating that subglacial and paraglacial material retains a residual dose which is older than the youngest period of ice advance and retreat in the valley (assuming similar dosimetric rates through time). These observations are also supported by the two feldspar samples analysed, which had maximum residuals > 50 ka. Subglacial material was also sampled from Nigardsbreen, however only 4 aliquots were accepted of the 48 analysed. The maximum residual age of those aliquots, modelled with the CAM, is 4.99 ± 0.44 ka, and is consistent with the onset of Neoglacial activity within Jostedalen, however replicates are insufficient for these results to be any more than indicative.

6.3.1. **Source Material Grain Size Analysis Results**

Grain size distributions for the source material are plotted relative to their phi values and associated classification using the size scale adopted in GRADISTAT, modified from Udden (1914) and Wentworth (1922) (Table 3.1). All of the source material is poorly sorted. The subglacial material is leptokurtic and skewed towards finer material (Figure 6.7), in contrast to the paraglacial material which has a mesokurtic and fine skewed distribution. Mean phi is least for the subglacial samples, indicative of their larger grain sizes, and greatest for FAB42 (avalanche deposit). FAB42 is the only source sample to have a multimodal grain size distribution. The -0.40 phi mode (very coarse sand) is also recorded for FABSUB1, and may be indicative of subglacial Dmm deposits, from which paraglacial deposits originate (see Chapter 2). However the extreme variability of subglacial sediments make generalisations about their specific sedimentology inappropriate (see Benn and Evans, 1998 for a review).

There is some correlation between the degree of GSA skewness (Table 3.2), indicative of sediment sorting, and the oldest OSL components of the source materials identified with FMM (Table 4.19). FABSUB1, FABSUB2 and FAB41 have greatest GSA skewness, and their largest population FMM components have the greatest residual ages for the source materials: FABSUB1: 20.31 ± 1.54 Gy (69%), FABSUB2: 10.02 ± 0.70 (90%), FAB41: 7.17 ± 1.34 Gy (38%). This reflects the limited opportunities for bleaching with depositional processes which lead to poorly sorted sediments. However this relationship is complex as FAB86 has very fine skewness and is poorly sorted, but contains a component with residual dose of 31.82 ± 2.27 Gy (50%).

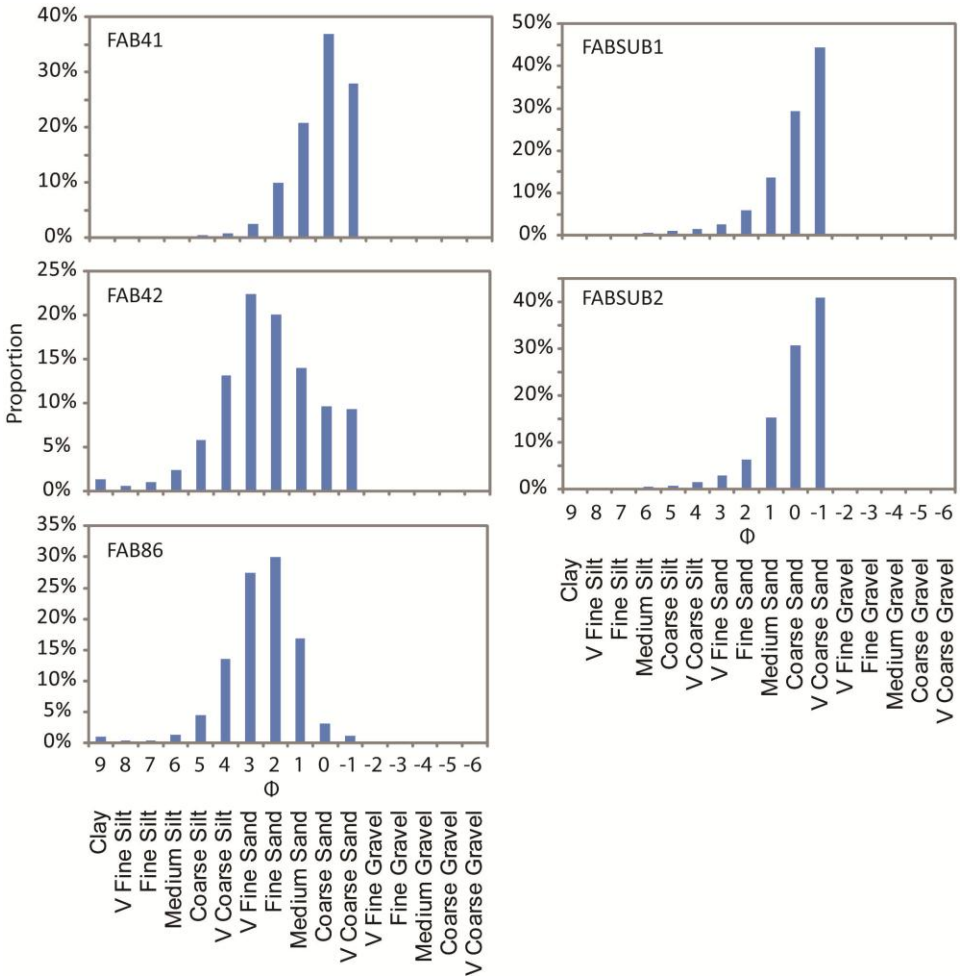

Figure 6.7: Grain size analysis results for source material, data have been grouped using the size scale detailed in Chapter 4.

6.3.2. **Source Material Summary**

Source material is partially bleached and exhibits a range of residual doses. Subglacial, paraglacial and reworked subglacial samples can be differentiated through σ_d values and using GSA statistics. Subglacial material from this area has σ_d of ~ 70 ± 10%, paraglacial material has σ_d of 90 ± 10% and reworked subglacial material of 48 ± 3% although the σ_d properties of the reworked subglacial deposits are characterised by a single sample. These values may vary between catchments, however poor sample acceptance has precluded investigation of this, although F_BERG2 which is a paraglacial deposit from Bergsetdalen has σ_d consistent with the Fåbergstølsdalen samples. A sample with 80 % σ_d may be classified as either paraglacial or subglacial using these criteria alone, which is a consequence of the common origin of these sediments from till deposits (see Chapter 3), thus consideration of the depositional setting of a sample may also be required to inform categorisation.

Paraglacial D_e distributions appear to be more skewed than subglacial material, whereas GSA skewness is reduced for paraglacial samples, relative to subglacial

material. Clear associations between sediment sorting, degree of σ_d, and residual luminescence signal for the different source sediments have been identified. The feldspar residual ages are significantly greater than the quartz samples, and this theme is recurrent throughout the entire dataset.

6.4. Glaciofluvial Point Bar Deposits

Low sample acceptance again restricts the quartz sample discussion to Fåbergstølsdalen, where 11 point bar samples were taken at locations increasingly distal from the glacial snout (Figure 6.8). Of the Fåbergstølsdalen samples seven are almost within the bootstrap acceptance criteria of $n \geq 30$, and all samples have bB_k < CalQzB8 (62%). Two of the quartz samples are supported by feldspar analyses, and a further five feldspar samples from Stordalen, Fåbergstølsgrandane and the Jostedøla river are discussed.

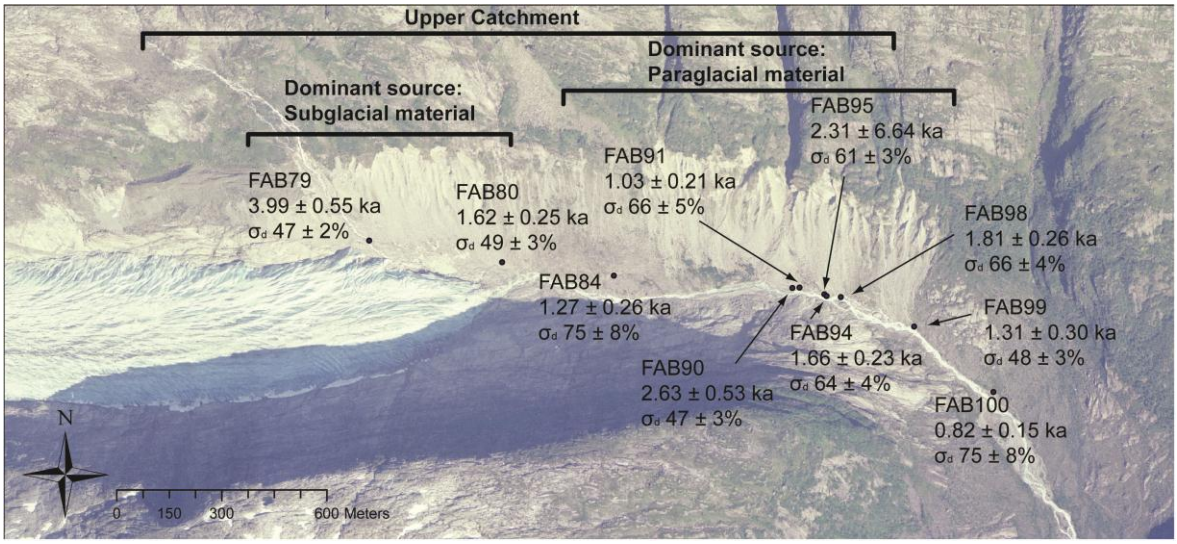

Figure 6.8: Point bar deposit sample locations from Fåbergstølsdalen (61˚42' N, 7˚18' E) with quartz residual ages (ka) indicated. Modified and reprinted with permission from Norway in Images (www.norgeibilder.no), Jotunheimen 2004, © Norwegian Mapping Authority.

6.4.1. Fåbergstølsbreen Point Bar Deposits

The point bar deposits (Sr, Sh, Sh:Fl) comprise paraglacial and subglacial material, confirmed by their GSA characteristics, which are similar to the paraglacial samples analysed. Samples have fine-symmetrical skewness, poor-moderate sorting and mostly comprise medium-fine sand (Table 3.2). The dominant source materials vary, with samples from the upper catchment (< 1 km distal from the ice margin) incorporating subglacial and paraglacial material transported over very short distances in addition to the reworked glaciofluvial, paraglacial and subglacial sediments transported by the main

meltwater stream (Figure 6.8). This is partly reflected in the different residual ages of the sediments; those samples with dominant subglacial or paraglacial inputs exhibit higher residual ages, e.g. FAB79 has a residual age of 3.99 ± 0.55 ka and is predominantly sourced from subglacial material. In contrast FAB100 has no direct subglacial or paraglacial input and has the youngest residual age of 0.82 ± 0.15 ka, although further aliquots are required for its distribution (n = 25) to be fully characterised.

Depositional processes have been demonstrated to dictate residual age for the source materials (consistent with Lukas et al. 2007), and thus the variations observed in Fåbergstølsdalen reflect a complex interplay between different source materials transported in the meltwater channel for different durations. The sedimentology and sample location of the point bar deposits confirm that glaciofluvial deposition is the final depositional process. However, within this extremely active catchment material is transported directly into the meltwater stream via a range of processes including sheetwash and debris flow mechanisms from the hillslope. Thus material may only be transported over very short distances, resulting in elevated residual ages. This can be considered with a simplified conceptual model (Figure 6.9) whereby the different inputs of three deposits (A, B and C) are calculated. Assuming that the rate of sediment bleaching and σ_d modification in the meltwater channel is constant, the luminescence properties of deposits A, B and C depend upon the relative flux of the subglacial (*S*), paraglacial (*P*) and other source sediments (*O*, e.g. supraglacial material) into the meltwater channel, their transport distance, and ultimately their relative contribution to the resultant deposit.

Other authors have observed residual age to rapidly reduce as a function of transport distance within fluvial and glaciofluvial systems (e.g. Forman and Ennis, 1992; Stokes et al., 2001), however this relationship is complicated within Fåbergstølsdalen e.g. FAB90 has residual age of 2.63 ± 0.53 ka despite its location relatively far from the ice margin compared to other samples.

The σ_d values of the point bar deposits vary throughout the catchment, which indicates a transition from predominantly subglacial source deposits in the upper catchment, to paraglacial sediment sources in the lower catchment. This is supported as the σ_d values of FAB79 and FAB80 are similar to FAB41, which is also reworked subglacial material (Figure 6.10). FAB41 was reworked via a sheetwash process rather than by a meltwater stream, which is reflected in its lower residual age, as sheetwash offers greater opportunity for sediment bleaching during surface transport. The σ_d values of the point bar deposits vary relative to the source materials, which demonstrates that depositional process is also influencing sample D_e distribution through heterogeneous bleaching. However the specific process signatures operating within this catchment are difficult to identify because of the complexity caused by the multiple source deposit inputs.

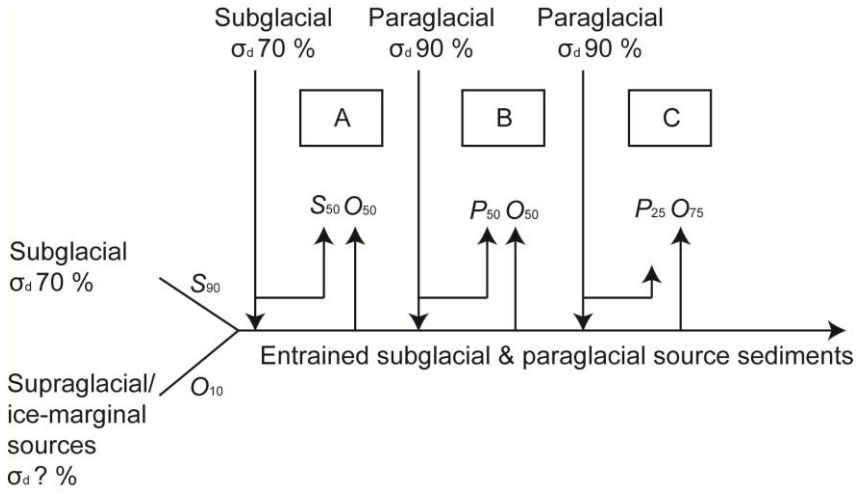

Figure 6.9: Conceptual model showing how the variations in source sediment input influence the luminescence characteristics of the point bar deposits of Fåbergstølsbreen. Subglacial *(S)*, paraglacial (*P*) and other source deposits (*O*) are entrained in the meltwater channel over different distances and contribute to deposits A, B and C in different proportions, indicated in subscript.

In addition to quartz, feldspar data are available for FAB100 and FAB94 (Figure 6.11), however both feldspar samples have lower σ_d values than their quartz counterparts (σ_d ~ 20%), and residual ages are an order of magnitude larger. The feldspar fraction of FAB86 (paraglacial deposit) also has a lower σ_d than the quartz fraction, and although the feldspar samples have < 30 aliquots, σ_d has been demonstrated to be insensitive to *n* where *n* > 10 (Chapter 4). The high residual ages of these feldspar deposits relate to the input of partially bleached paraglacial material, entrained in the meltwater stream over short transport distances in Fåbergstølsdalen. In catchments where paraglacial inputs are relatively reduced, feldspar residuals are much lower, for example in Stordalen (see Section 6.4.2). The residual age of F_FAB94 (42.33 ± 4.29 ka) is much greater than that of F_FAB100 (8.40 ± 0.79 ka), which further supports this interpretation as F_FAB94 is located in the upper catchment where entrainment of fresh inputs of paraglacial material are possible (Figure 6.8). Furthermore the residual age and σ_d characteristics of the feldspar samples are consistent with F_FAB86 (51.78 ± 5.42 ka, σ_d 20 ± 1%), which is a paraglacial deposit, i.e. residual ages are high relative to the quartz samples, and σ_d values are generally lower. Thus although the feldspar characteristics differ from the quartz characteristics, σ_d is still dictated by source material and residual age by depositional process and transport distance.

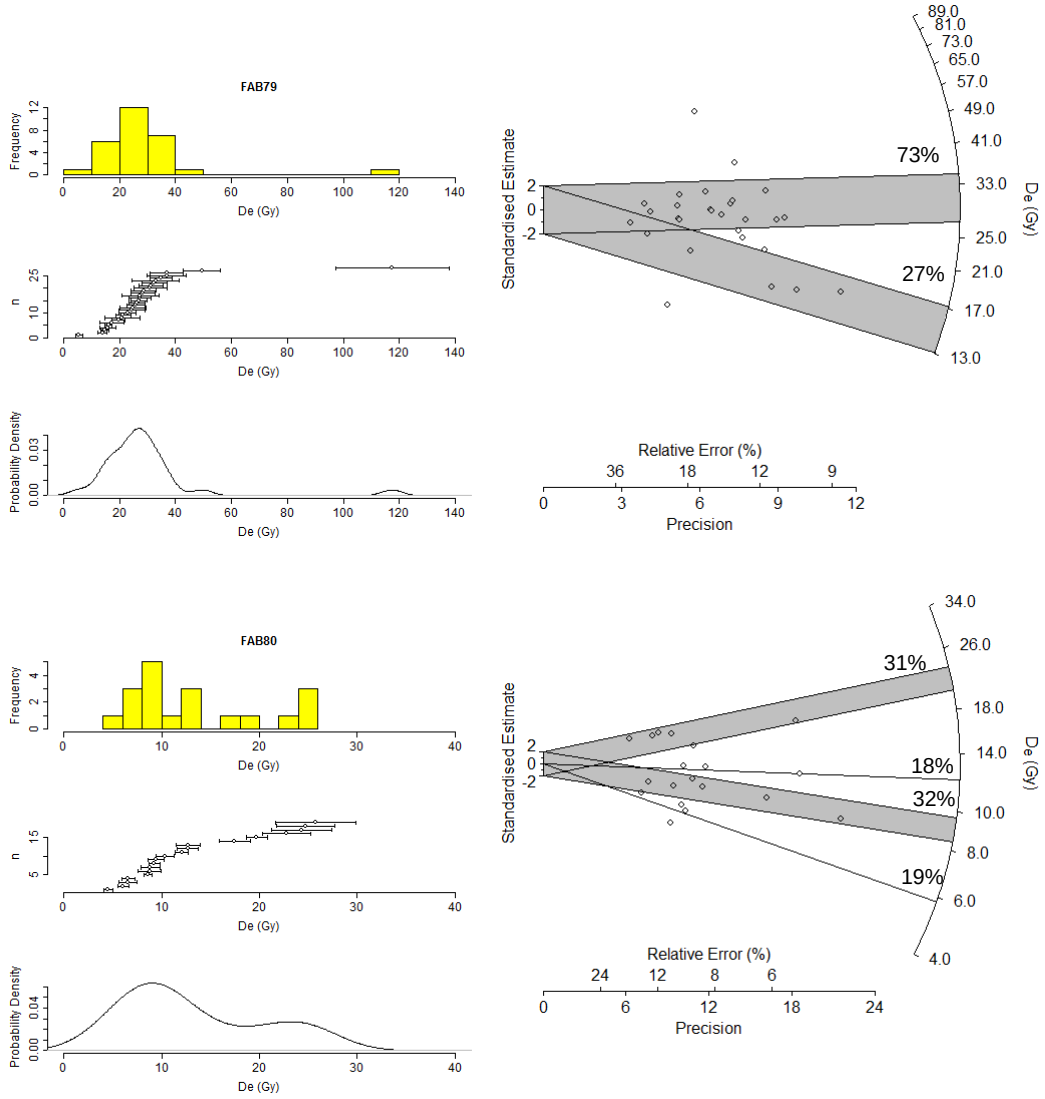

Figure 6.10: Histograms, probability density functions, scatter graphs and radial plots of quartz glaciofluvial point bar deposits, derived from subglacial source material. The relative proportions of FMM components are indicated as appropriate.

The D_e distributions of the different deposits exhibit heterogeneous bleaching, and FMM analysis indicates that the point bar samples comprise between two and four components (Table 4.19 and Table 5.12). Five quartz samples were dominated by a ~ 32 Gy component (average age 8.01 ± 0.78 ka), and overlap within errors (Figure 6.12). A component with this residual was also observed within FAB86 (paraglacial deposit, 50%) and it is coincident with deglaciation of these catchments prior to the onset of Neoglacial activity (Nesje and Kvamme, 1991), suggesting a common origin. Ballantyne and Benn (1994) observed that the LIA till in this catchment overlies early Holocene paraglacial material (Figure 3.12). Deglaciation (~ 9 ka ago) will have resulted in exposure and bleaching of formerly subglacial material, and subsequent paraglacial modification. However for these paraglacial deposits to have retained an age of 8 ka, they must have been covered prior to the LIA re-advance, possibly through slope failure of material further up the valley sides, i.e. paraglacial reworking, or alternatively from glaciofluvially reworked sediments. The OSL data presented here suggest that these early Holocene paraglacial

sediment sources have only recently been accessed, consistent with Ballantyne and Benn's (1994) geomorphological observation.

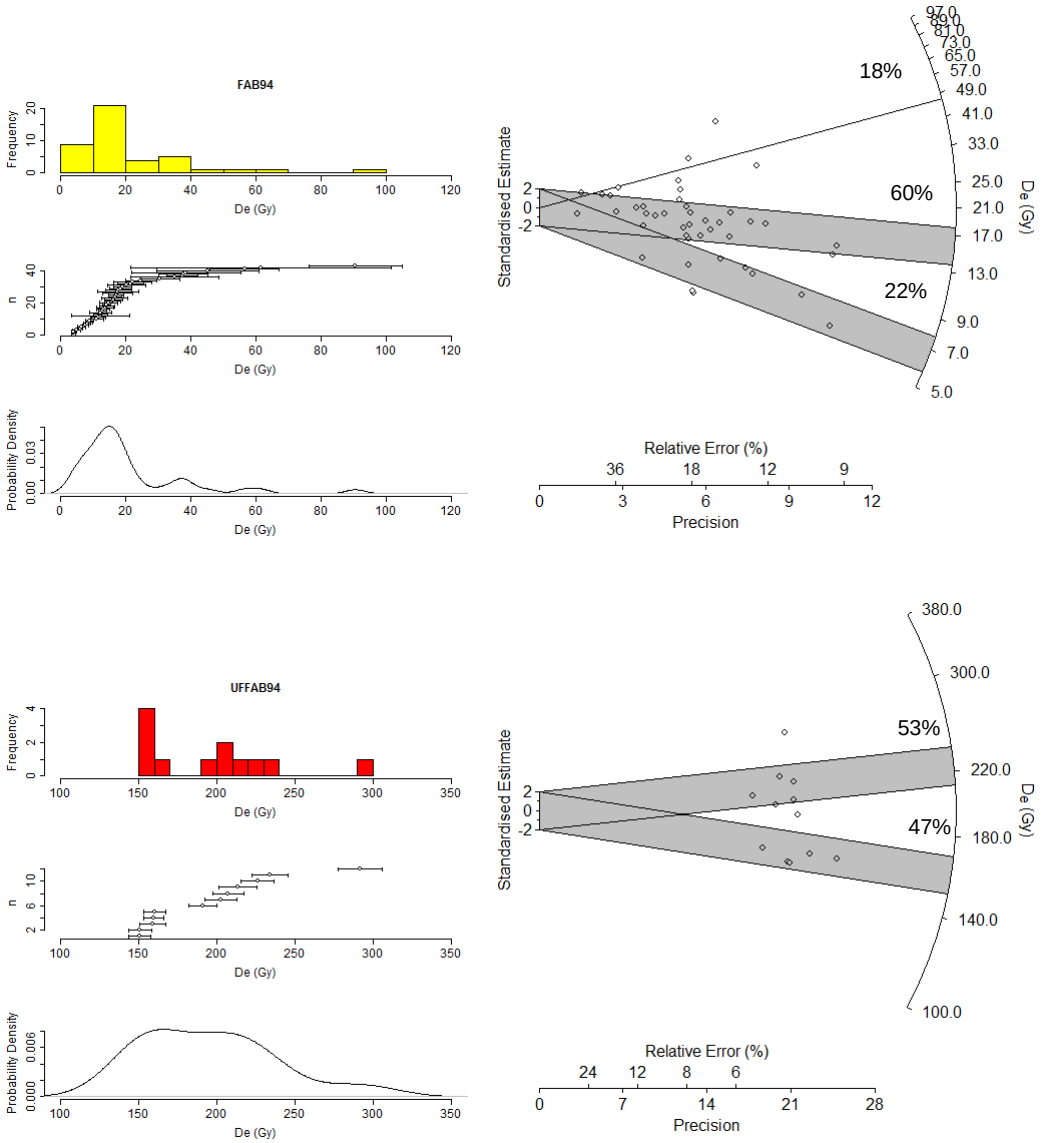

Figure 6.11: Histograms, probability density functions, scatter graphs and radial plots of quartz (light grey) and feldspar (dark grey) extracts of FAB94, a glaciofluvial point bar deposit derived from paraglacial source material. The relative proportions of FMM components are indicated as appropriate.

The consistency of the age of these components suggest that the paraglacial material was well bleached prior to deposition, which conflicts with the observed σ_d and large residuals identified in the modern analogue deposits. Uniform bleaching of the original subglacial deposit with triboluminescence may account for this, however a second challenge is that during erosion, transport and entrainment in the meltwater channel, this material also remained fully unbleached, which is also difficult to reconcile with the modern analogue observations reported here. Irrespective of these caveats, it is unlikely

that a uniform residual would be present in all of the samples given their significant heterogeneity, and thus it is attributed to the early Holocene paraglacial deposit.

A second common component of ~ 6 Gy was also present in four of the samples, and relates to an average age of 1.47 ± 0.15 ka. This component is also observed in FAB86 (1.67 ± 0.15 ka, 50%) and may also relate to a period of glacial re-advance. Nesje et al. (2004) identified a cool period at 1700-1600 cal years BP from the sediment records of a non-glacial lake in Jotunheimen, which they attributed to either changes in solar forcing or internal oscillations in the climate system.

Sample	Age (ka)	% Aliquots
FAB79	8.42 ± 0.67	73
FAB84	7.73 ± 0.78	41
FAB90	7.43 ± 0.90	46
FAB95	8.72 ± 0.77	56
FAB98	8.30 ± 0.66	58

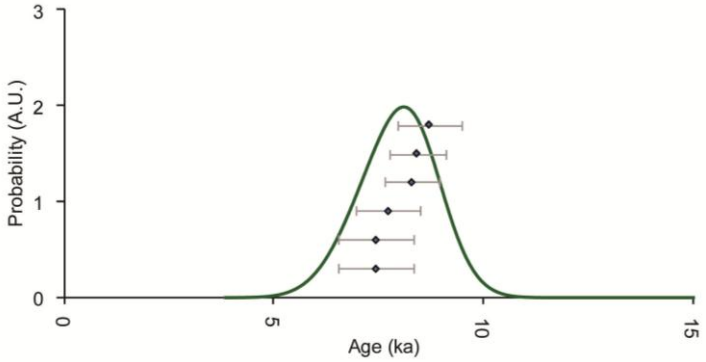

Figure 6.12: Table and probability density function of the ~ 32 Gy component identified to be present within six of the glaciofluvial point bar deposits analysed.

6.4.2. **Stordalen & Jostedalen Point Bar Deposits**

Three samples (F_LOD4-6) were collected from a transect along the single meltwater channel from Stordalen, which drains onto Fåbergstølsgrandane, where a single sample was collected (F_GRAN69, Figure 3.16). Although some paraglacial material is present in Stordalen, there is less channel-hillslope coupling in this valley compared to Fåbergstølsdalen, consequently the main sediment source is subglacial sediment derived from the debris covered glacier, Lodalsbreen. Overdispersion values for the Stordalen and Fåbergstølsgrandane samples range from 52 ± 3 to 74 ± 7% (Table 5.11), which is consistent with the σ_d properties identified for the quartz subglacial source material samples (FABSUB1 and 2), although these values are greater than the σ_d of 48 ± 3% for FAB41 (reworked subglacial material). However, whereas FAB41 has been transported via sheetwash, the Stordalen deposits are transported via the meltwater channel. This illustrates the effect that depositional process has on σ_d where significant sunlight exposure may occur. Residual ages reduce as a function of increasing transport distance, which supports the observation for the paraglacial deposits that sediment sources initially dictate σ_d and depositional process dictates residual age. This also reinforces the common sediment source origin of these samples, and that the opportunity

for sediment bleaching increases with transport distance, in agreement with previous observations (e.g. Forman and Ennis, 1992).

F_GRAN69 (Figure 6.14) was collected adjacent to the main meltwater stream on Fåbergstølsgrandane which is partly sourced from Stordalen. The residual age of F_GRAN69 is younger, but consistent with the Stordalen samples (1.17 ± 0.13 ka), and its σ_d is similar (61 ± 4%), supporting the hypothesis that source deposits dictate σ_d and that depositional processes and transport distance dictate residual age.

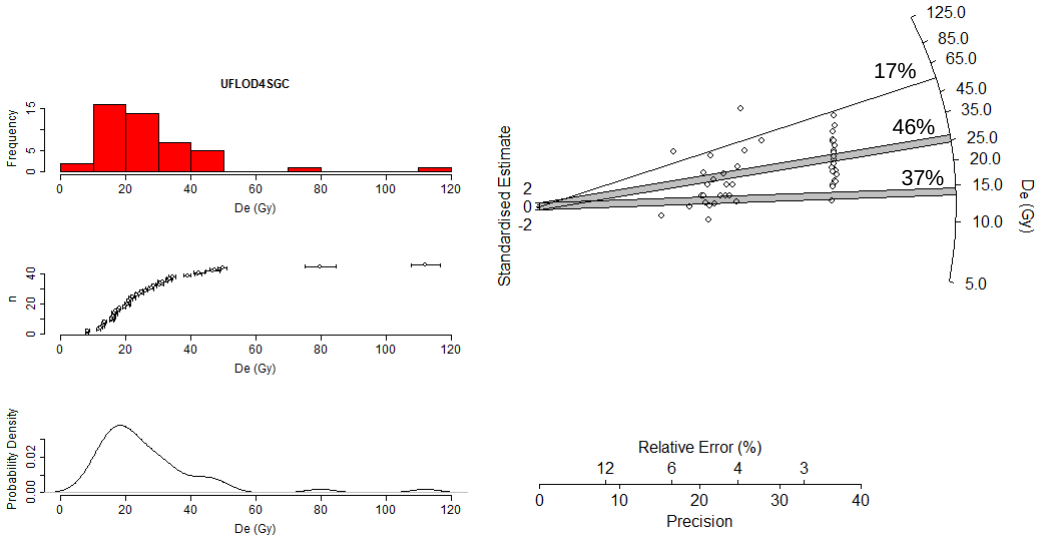

Figure 6.13: Histograms, probability density functions, scatter graphs and radial plot of F_LOD4, a glaciofluvial point bar deposit. The relative proportions of FMM components are indicated on the radial plot.

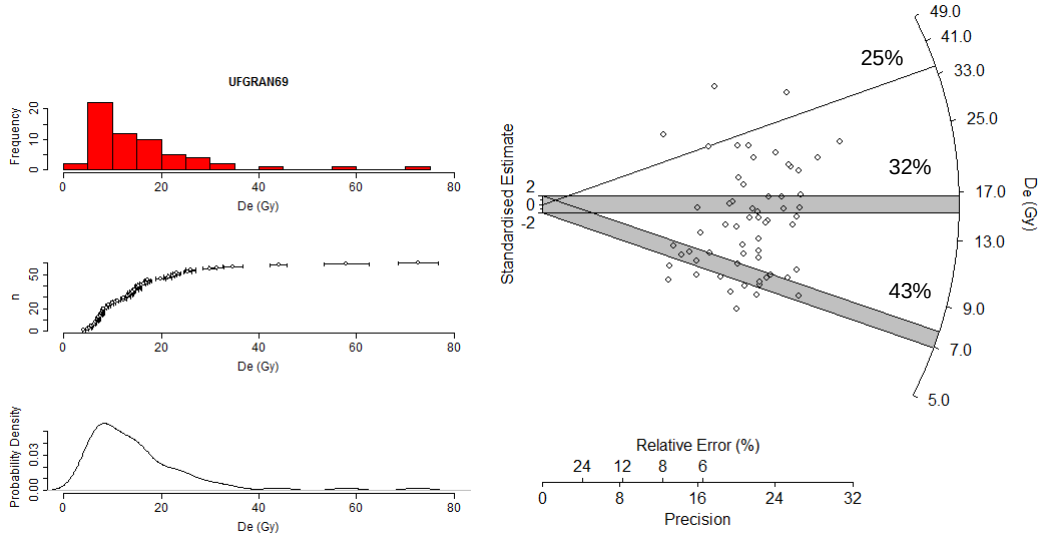

Figure 6.14: Histogram, probability density function, scatter graph and radial plot of GRAN69. The relative proportions of the FMM components are indicated.

A final point bar deposit (F_JOS51) was sampled from the Jostedøla river, ~ 20 km distal of Fåbergstølsgrandane, where the Jostedøla originates. This sample provides a

contrasting ice-distal depositional context to the other point bars sampled. The Jostedøla river is a larger scale system than any of the glacial catchment meltwater systems explored, however it provides the best available contrast due its geographical proximity. F_JOS51 has the smallest residual age (0.56 ± 0.05 ka) and sample σ_d (27 ± 2%) confirming the influence of source material and specific depositional context on sample luminescence characteristics, irrespective of depositional process (Figure 6.15).

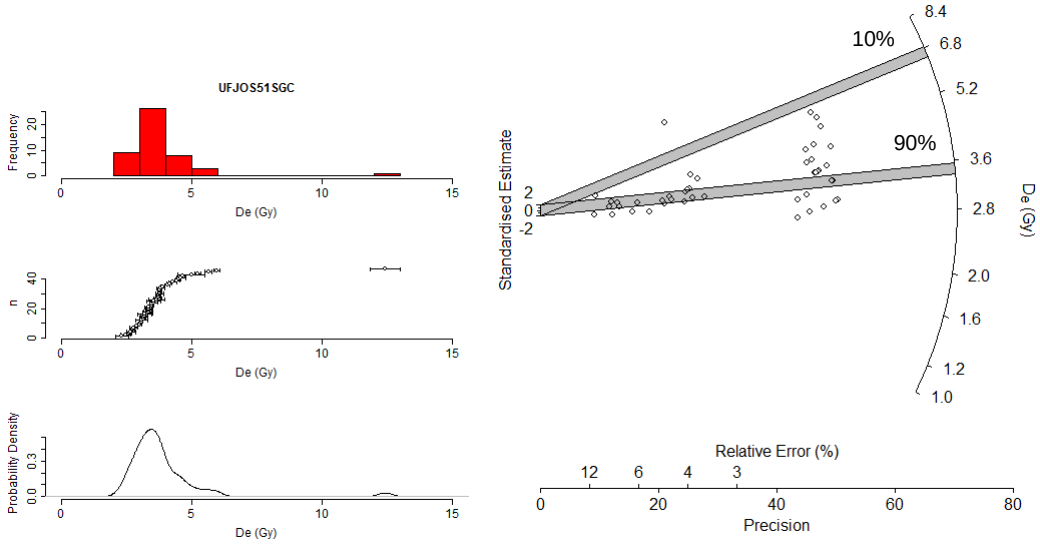

Figure 6.15: Histograms, probability density functions, scatter graphs and radial plots of F_JOS51, a glaciofluvial point bar deposit. The relative proportions of FMM components are indicated on the radial plot.

6.4.3. **Glaciofluvial Point Bar Grain Size Analyses**

The grain size analysis results indicate variability between the mean grain size and sorting for the point bar samples (Figure 6.16), and this is reflected in their varied luminescence σ_d and residual age characteristics. All of the samples are poorly sorted medium or fine sand, with the exception of FAB91 which is moderately sorted and has low skewness. F_GRAN69 has very fine (negative) skewness, which is a GSA characteristic of the source material analysed (see Section 6.3.1). Kurtosis ranges from leptokurtic to mesokurtic.

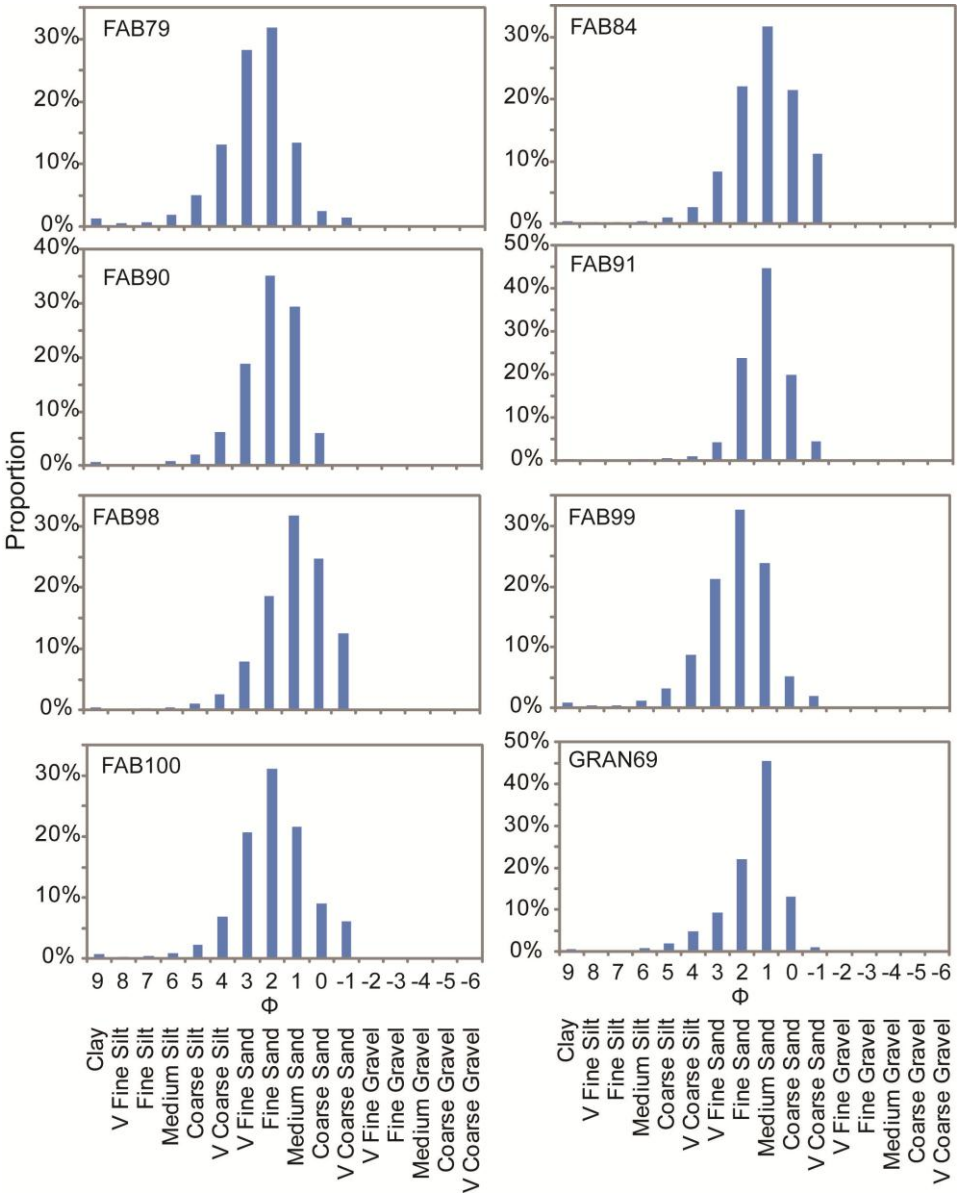

Figure 6.16: Grain size analysis results for glaciofluvial point bar deposits, data have been grouped using the size scale detailed in Chapter 4.

FAB79 has the greatest residual age and is the most ice proximal sample, comprising very fine sand with a leptokurtic and fine skewed distribution. The source material for this sample is likely to be dominated by fines washed from subglacial deposits and transported via sheetwash; it is poorly sorted with high residual age and σ_d similar to FAB41 (reworked subglacial deposit). FAB84 exhibits the same degree of poor sorting (1.32), however it is mesokurtic and has symmetrical skewness which are properties more similar to the paraglacial source materials, in agreement with its σ_d value of 75 ± 8% and location further along the catchment where paraglacial inputs are dominant (Figure 6.8).

6.4.4. **Point bar Deposit Summary**

The point bar quartz sample σ_d in Fåbergstølsdalen is dictated by both source material and depositional processes, and a transition from predominantly subglacial to paraglacial sediment incorporation is apparent throughout the catchment. Residual age is predominately influenced by depositional processes, which is also observed within the Stordalen feldspar samples. Supporting feldspar samples have lower σ_d values than the Fåbergstølsdalen quartz fractions, which is tentatively attributed to differential bleaching between minerals. However, feldspar σ_d is consistent with source deposit characteristics identified from F_FAB86 (paraglacial material) and residual ages also reflect depositional processes and transport distances, consistent with the quartz samples. F_JOS51 has the lowest σ_d and residual age of the samples investigated, confirming that the σ_d and residual age characteristics explored in the remaining sample suite are the product of the glacial source materials, and do not solely relate to modification associated with transport and depositional processes.

A common residual age of 8.01 ± 0.78 ka within six of the point bar deposits and FAB86, a paraglacial deposit, has been identified. This is attributed to erosion of early Holocene paraglacial deposits, with the assumption that these sediments were fully bleached prior to deposition and have experienced no bleaching throughout transport and deposition as point bar deposits. It is not possible to assign specific σ_d or residual age properties to the point bar deposits, as for the source sediments, due to their clear dependencies on sediment source deposit D_e distribution and residual age characteristics.

6.5. Braided Channel Bar Deposits

Insufficient aliquots were accepted from the seven Bergsetdalen samples to enable discussion of their luminescence properties, consequently three samples from Leirdalen (F_LEI13/14/18, Figure 6.17), a site on the Jostedøla and a single braided channel bar deposit from Fåbergstølsdalen (FAB81, Figure 6.18) are considered. The Leirdalen samples comprise distal material, similar to F_JOS51 (point bar deposit), but are sampled from further downstream in the Jostedøla.

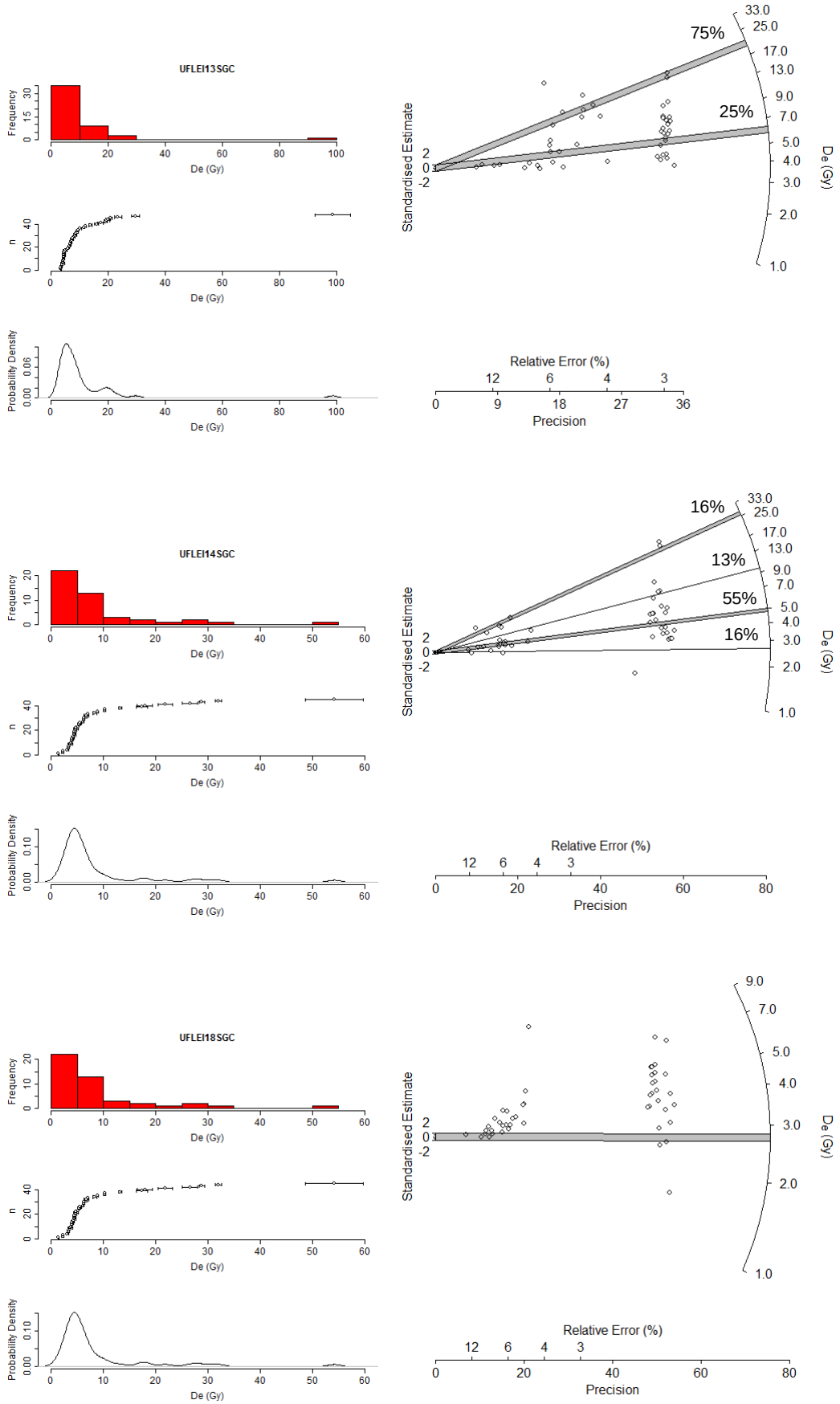

Figure 6.17: Histograms, probability density functions, scatter graphs and radial plots of F_LEI13, 14 and 18. The relative proportions of FMM components are indicated as appropriate.

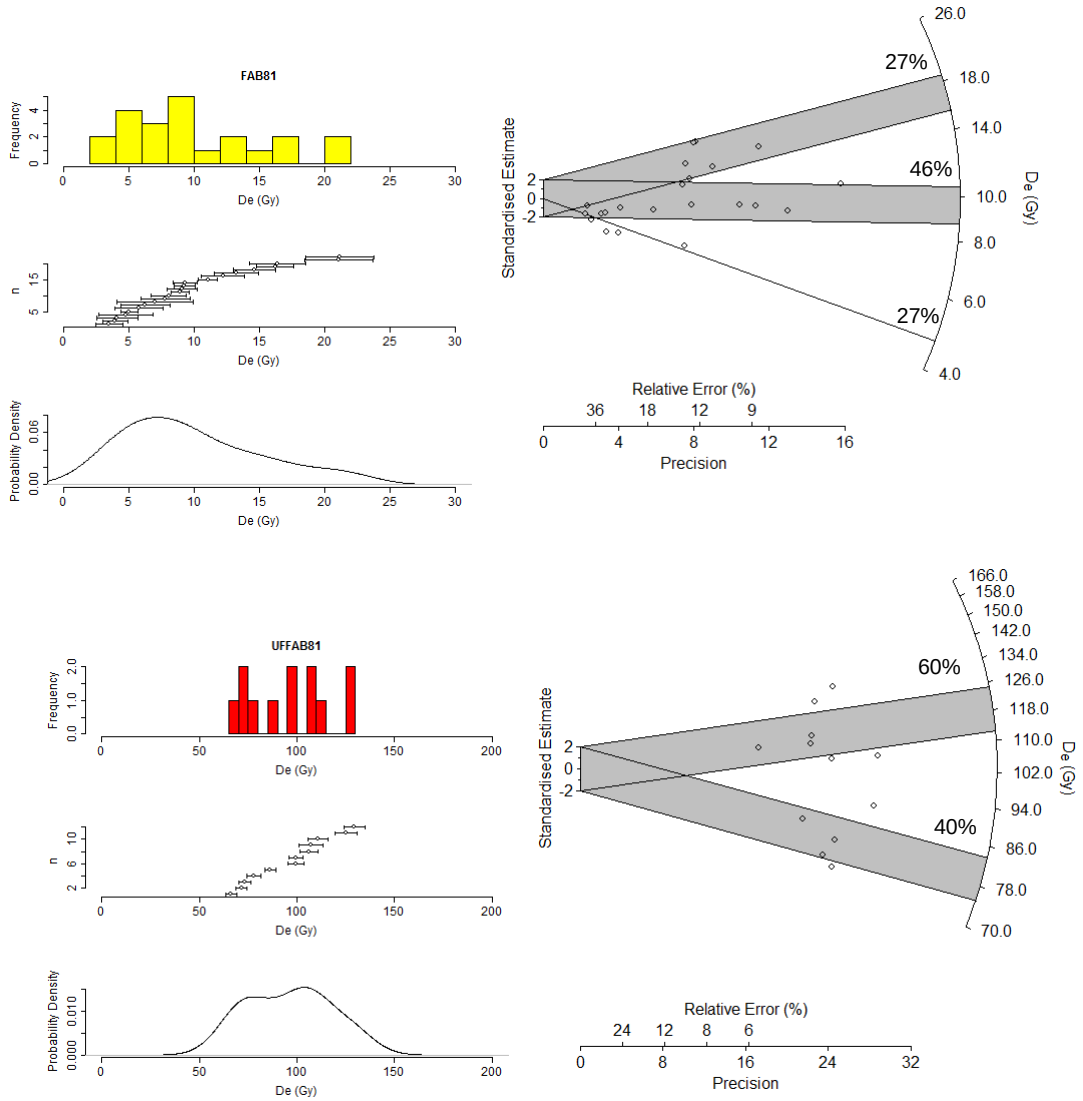

Figure 6.18: Histograms, probability density functions, scatter graphs and radial plots of quartz (light grey) and feldspar (dark grey) extracts of FAB81, a glaciofluvial braided bar deposit. The relative proportions of FMM components are indicated on the radial plots.

Three braided channel bar deposits were sampled from the Jostedøla river at the confluence of Leirdalen and Jostedalen (F_LEI13/14/18). The Tunsbergdalsbreen glacier which discharges into Leirdalen, via Tunsbergdalsvatnet is ~ 20 km distal from the sample site. F_LEI18 was sampled from a bar tail, and F_LEI13 and 14 from mid-bar. Sample D_e distributions are extremely skewed (> 2.89) and σ_d is > 50%. All of the F_LEI samples have $n \geq 45$ and bB_k < CalQzB8. Residual ages are < 1 ka for all samples, but are lowest for F_LEI14 and F_LEI18 which are sampled from the bar-mid and bar tail respectively. F_LEI18 has the lowest σ_d value, which is associated with improved sorting of bar tail deposits, and is supported by the GSA results of symmetrical skewness and moderate sorting. The degree of σ_d for the Leirdalen samples is larger than may be anticipated, given their ice distal location, however these values are interpreted to indicate the influence of source material derived from Leirdalen. This is because, even accounting for the different flow regimes that operate at braided, rather than point bars, similar σ_d values

to F_JOS51 are anticipated because of their relatively distal location. This illustrates the influence of source sediment on σ_d. The low residual ages of these samples are attributed to a combination of depositional processes and transport distance.

The residual age of FAB81 is 1.36 ± 0.25 ka, and σ_d is 46 ± 3 %, which is comparable to the σ_d values of point bar deposits sourced dominantly from subglacial material. Its location adjacent to the main meltwater channel in Fåbergstølsdalen suggests that the proportional contribution from paraglacial and subglacial sources should be equal, and thus these σ_d properties may relate more to transport processes rather than source sediments. The supporting feldspar sample for FAB81 has greater residual age (16.87 ± 1.38 ka) and reduced σ_d (21 ± 0.4%) as observed for the other Fåbergstølsdalen feldspar samples.

6.5.1. **Glaciofluvial Braided Channel Grain-size Analyses**

Grain size analysis is available for FAB81 and F_LEI18. FAB81 is dominantly medium sand with three modal peaks of 2.57, 1.76 and 2.03 phi, indicative of its poor sorting. It has no skewness, is mesokurtic, and grain sizes range from clay to very coarse sand, indicative of varied energies of deposition. The multimodal grain size characteristics are reflected in the bleaching properties of FAB81, as indicated from FMM. F_LEI18 is moderately sorted, which reflects improved sediment sorting at braided bar tails, and may also be influenced by the more ice distal nature of these samples.

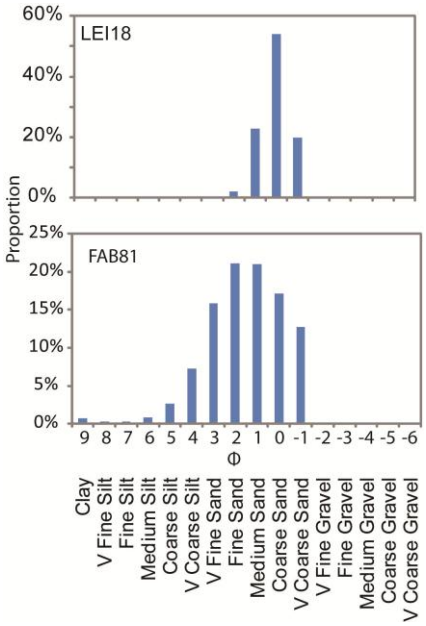

Figure 6.19: Grain size analysis results for FAB81, a glaciofluvial braided bar deposit, data are grouped using the size scale detailed in Chapter 4.

6.5.2. **Glaciofluvial Braided Channel Summary**

Of the five quartz and feldspar samples analysed from braided bar deposits, only FAB81 has a residual age > 1 ka, which might be expected given the influence of paraglacial material within Fåbergstølsdalen. The residual ages of the Jostedøla samples are lower, which is attributed to greater opportunity for sediment bleaching with increasing transport distance. The relatively high σ_d values of the Leirdalen samples relative to F_JOS51 (point bar deposit) is related to different sediment source regions between the samples sites. Whereas F_JOS51 primarily reworks material from upper Jostedalen, the LEI samples rework material from Leirdalen, and Tunsbergdalsbreen.

6.6. Sandur Braided Channel Bar Deposits

A transect of braided bar deposits were analysed from Fåbergstølsgrandane sandur (GRAN54-59, Figure 3.16) and the proglacial delta at Nigardsdalen (F_NIG3/4/6/7/8/9, Figure 3.15). These samples enable exploration of how luminescence characteristics are modified as a function of transport distance and position on a braided channel bar, in two contrasting depositional environments.

6.6.1. **Fåbergstølsgrandane Sandur**

Quartz and feldspar extracts of six complimentary braided bar samples (GRAN54-59) were analysed, however acceptance for the quartz samples was low and all samples with the exception of GRAN55 fail the bootstrap acceptance criteria outlined in Chapter 4 (Table 4.22). Consequently the feldspar data which all fulfil at least two of the bootstrap criteria and have $n > 48$ for all samples (with the exception of F_GRAN58) are considered. The braided channel bars in Fåbergstølsgrandane comprise multiple elevations and lengths, reducing in scale from elevations of ~ 1 m with distance further southeast across the catchment. The samples were taken from similar scale features, which have elevations of ~ 30 cm and lengths of approximately 50 m.

Overdispersion values are low (< 35%) for all samples (Table 5.11) and are in broad agreement with the quartz analyses (Table 4.18). Only minor modification of σ_d with increasing sediment reworking and bleaching across the bars is observed, although bar tail deposits have the greatest σ_d values. This relationship was also indicated from the quartz data (Figure 6.20), but is not observed for the pIR-$IRSL_{250}$ measurements, where σ_d exhibits a slight reduction between the bar head and tail. Only F_GRAN54/55 and 56 were analysed with the pIR-$IRSL_{250}$ protocol as the large residuals and reduced rate of bleaching associated with this emission limited applicability to young samples, and these

experiments were not continued (see Chapter 5). Residual age reduces with increasing reworking across the composite bar forms. F_GRAN54/58/59 are sampled from bar heads and have the greatest residual ages, F_GRAN55 is sampled from mid bar, and F_GRAN56/57 are sampled from the bar tails and have the lowest residuals. Where the percentage reduction in age is considered between a bar head (GRAN54) and tail (GRAN56) deposit, a reduction of age by ~ 80% is observed for all luminescence measurements (quartz BSL, feldspar $IRSL_{50}$ and pIR-$IRSL_{250}$, Figure 6.20).

Feldspar have greater residuals than their partner quartz samples for all deposits analysed in this research, and bleaching experiments demonstrate that the pIR-$IRSL_{250}$ luminescence signal bleaches less readily than the $IRSL_{50}$ signal, and that quartz bleaches most rapidly (see Sections 4.6 and 5.4.1). All three signals bleach at the same rate during transport across the braided bar (Figure 6.20), indicating first that bar-mid and bar-tail deposits are not deposited by the same process as bar-head deposits, and secondly that this depositional process provides greater opportunities for sample bleaching than bar-head deposition. Bar-head deposits essentially comprise channel material, which is known to sort less rapidly than material transported across channel bars (Rice and Church, 2010), and these properties are encoded in the luminescence response. In contrast, signal bleaching during transport across braided channel bars is homogeneous, as heterogeneous bleaching would result in a slower rate of $IRSL_{50}$ and pIR-$IRSL_{250}$ signal depletion as these signals are more sensitive to partial bleaching effects, consequently σ_d exhibits little modification throughout transport, as the D_e distribution remains approximately constant under homogeneous bleaching conditions.

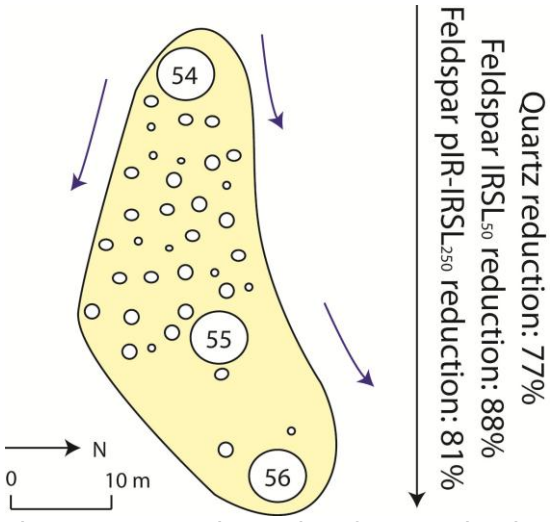

GRAN54	*n*	Residual Age (ka)	σ_d
Quartz	13	4.81 ± 0.34	0%
$IRSL_{50}$	48	22.00 ± 2.36	20 ± 1%
pIR-$IRSL_{250}$	12	83.19 ± 6.68	18 ± %

GRAN55	*n*	Residual Age ka)	σ_d
Quartz	30	2.95 ± 0.89	30 ± 1%
$IRSL_{50}$	48	22.74 ± 2.57	25 ± 1%
pIR-$IRSL_{250}$	12	77.61 ± 5.52	16 ± 1%

GRAN56	*n*	Residual Age (ka)	σ_d
Quartz	5	1.10 ± 0.14	19 ± 1%
$IRSL_{50}$	55	2.74 ± 0.32	24 ± 1%
pIR-$IRSL_{250}$	12	15.35 ± 0.19	12 ± 1%

Figure 6.20: Schematic of a sandur braided bar sampled from Fåbergstølsgrandane. Residual ages and σ_d values for the quartz and feldspar extracts measured for each sample are listed, pIR-$IRSL_{250}$ ages are also available for these samples and are included. Note the similarity in % age reduction between samples GRAN54 and GRAN56 for all measurements.

The Fåbergstølsgrandane bar head deposits have high residual ages and low σ_d. Examination of the other glaciofluvial sediments has indicated that source sediments determine sample σ_d and that residual ages are determined by depositional process. None of the source sediments discussed have σ_d as low as the bar-head deposits, which also have the greatest residual ages of any of the sediments explored. Potential sediment sources are subglacial material from Stigaholtsbreen and Lodalsbreen, and paraglacial material within those catchments; although these values conflict with the high σ_d and low D_e values of the Stordalen (LOD4/5/6) point bar deposits. Galbraith et al. (1999) suggests that samples with σ_d < 20% are not partially bleached. The D_e distributions of the bar head deposits reported here are significantly skewed (F_GRAN54, c = 0.46), despite having low σ_d, however they may be classified as a form of Type A sediment, which are uniformly, partially bleached (Duller, 2008), or may not have been bleached at all. These observations are considered relative to the proglacial delta deposits at Nigardsdalen.

In contrast to the glaciofluvial material collected from the other catchments, the Fåbergstølsgrandane sandur is relatively distant from the ice margins of Lodalsbreen and Stigaholtsbreen. Consequently it is surprising that residual ages are so significant, in contrast to the other valleys. One possible explanation is that the key sediment fluxes onto the sandur are driven by storm events, which are known to cause significant reworking of paraglacial material within other parts of Norway (e.g. Matthews et al., 1997; Sletten and Blikra, 2007). These events also result in routing more meltwater subglacially and thus a greater flux of subglacial material. Such high energy pulses of material onto the sandur offer limited opportunity for bleaching due to their associated high suspended sediment load and turbulence (e.g. Jerlov, 1976), and explain why it is the lower energy transport across the braided bars that results in more significant sunlight exposure in Fåbergstølsgrandane.

6.6.2. **Nigardsdalen**

Two composite bar features were sampled from Nigardsdalen at positions ~ 200 m (Bar 1) and ~ 300 m (Bar 2) downstream from the glacial snout. Both bars are ~ 30 m in length, and have elevations of ~ 30 cm, which makes them similar in scale to the bars sampled from Fåbergstølsgrandane (Figure 3.15, Table 6.4). A number of contrasts are immediately apparent relative to the Fåbergstølsgrandane samples; first the residual ages from feldspar in Nigardsdalen are much lower, with the exception of NIG4 (Table 5.13); secondly σ_d values are much greater (Table 5.11), and thirdly σ_d reduces with transport across both bar features.

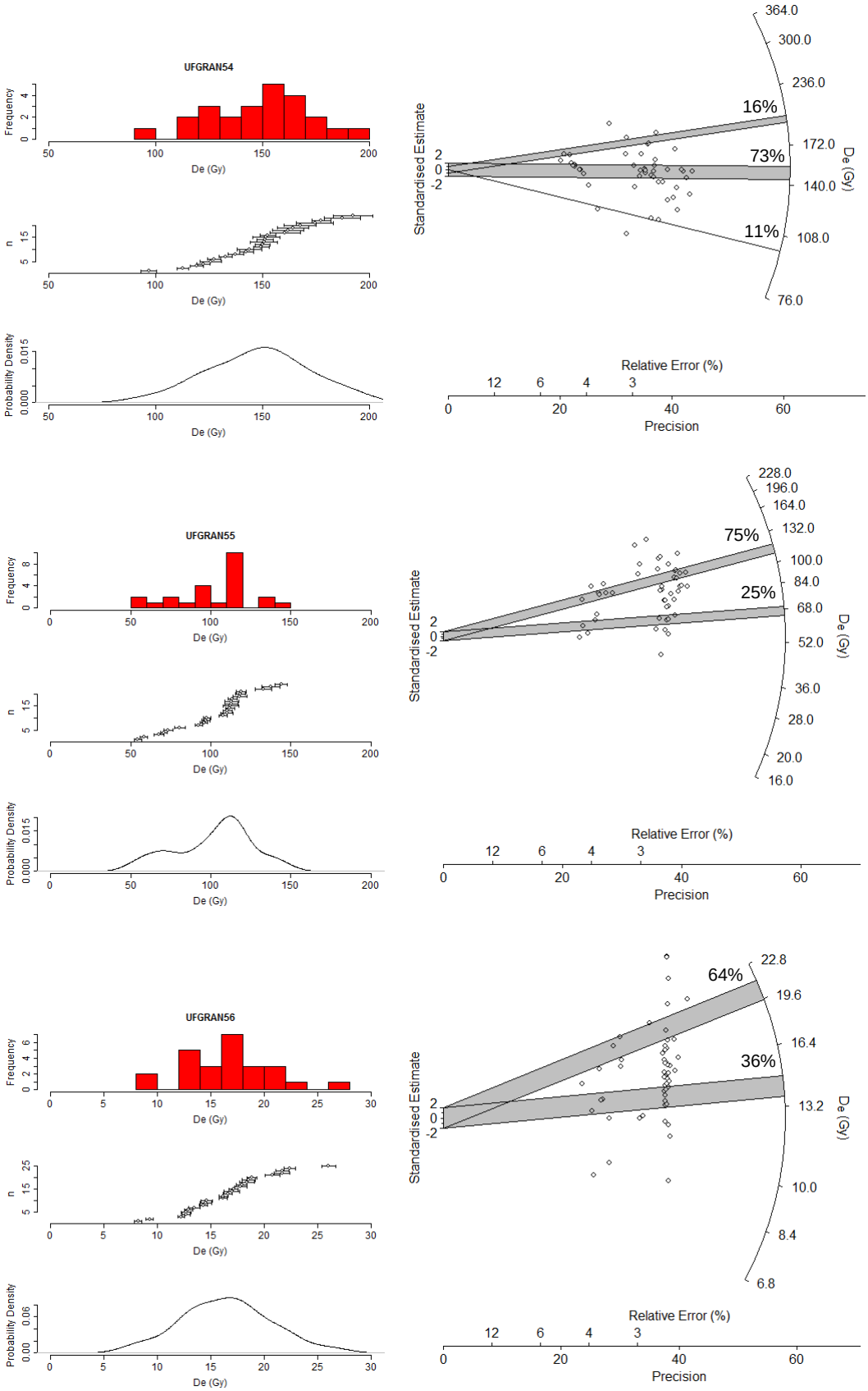

Figure 6.21: Histograms, probability density functions, scatter graphs and radial plots of F_GRAN54/55/56. The relative proportions of components identified from FMM are indicated.

Table 6.4: Residual ages and σ_d values for the Nigardsdalen feldspar samples. See Figure 3.15 for sample locations.

	Sample	n	Age (ka)	σ_d
Bar 1	NIG6	23	3.18 ± 0.31	61 ± 4%
	NIG4	33	67.32 ± 40.44	54 ± 3%
	NIG3	47	1.45 ± 0.24	34 ± 2%
Bar 2	NIG9	48	0.81 ± 0.08	75 ± 7%
	NIG8	48	1.20 ± 0.12	22 ± 1%
	NIG7	48	0.78 ± 0.08	31 ± 2%

The bar head deposits in Nigardsdalen have much smaller residual ages, and also greater σ_d than the equivalent deposits in Fåbergstølsgrandane (Table 5.11, Table 5.13, Figure 6.22), which can be explained either by a different sediment source or by contrasting the transport and depositional processes. The proglacial delta deposits at Nigardsdalen are predominately sourced from subglacial material, and the σ_d characteristics of the bar head deposits support this as they are similar to the 70 ± 10% σ_d value assigned to the quartz subglacial material in Fåbergstølsdalen. The processes of deposition are similar between the two catchments, in that they both have low gradient and comprise anastomosing meltwater channels, however, whereas in Fåbergstølsgrandane the different braided bar features have elevations of ~ 1 m in the upper catchment, maximum elevations are ~ 30 cm throughout Nigardsdalen. Elevation values are approximate and fluctuate throughout the ablation season in response to changing meltwater channel discharge, however Nigardsdalen comprises a shallower system, where sediments have much greater opportunity for reworking across channel bars, because of their relatively low relief. This equates to better bleaching opportunities prior to deposition at the bar-heads, and thus the Nigardsdalen bar-head deposits are categorised as Type B deposits (Duller, 2008), which have experienced heterogeneous bleaching.

The residual ages of the Nigardsdalen samples, calculated with the L5% and MAM3 models are lower for Bar 2 than Bar 1, which is attributed to greater bleaching opportunities with increasing transport distance. No uniform reduction in residual age across Bar 2 is observed as a consequence of the almost fully bleached nature of these deposits. Transport and depositional processes influence both σ_d and residual age for these samples, as σ_d reduces as samples become more completely bleached, where bleaching is homogeneous.

F_NIG4 has a much greater residual age than the other Nigardsdalen samples, which is related to its specific sample location, adjacent to a crossover chute channel on Bar 1. F_NIG6 and F_NIG4 are multimodal, and an ~ 80 Gy component is present in both samples, however no component associated with the 215.41 ± 4.99 Gy (73%) F_NIG4 component is modelled for F_NIG3. This indicates that material from elsewhere is being reworked across the bar and deposited at F_NIG4, which is most probably related to

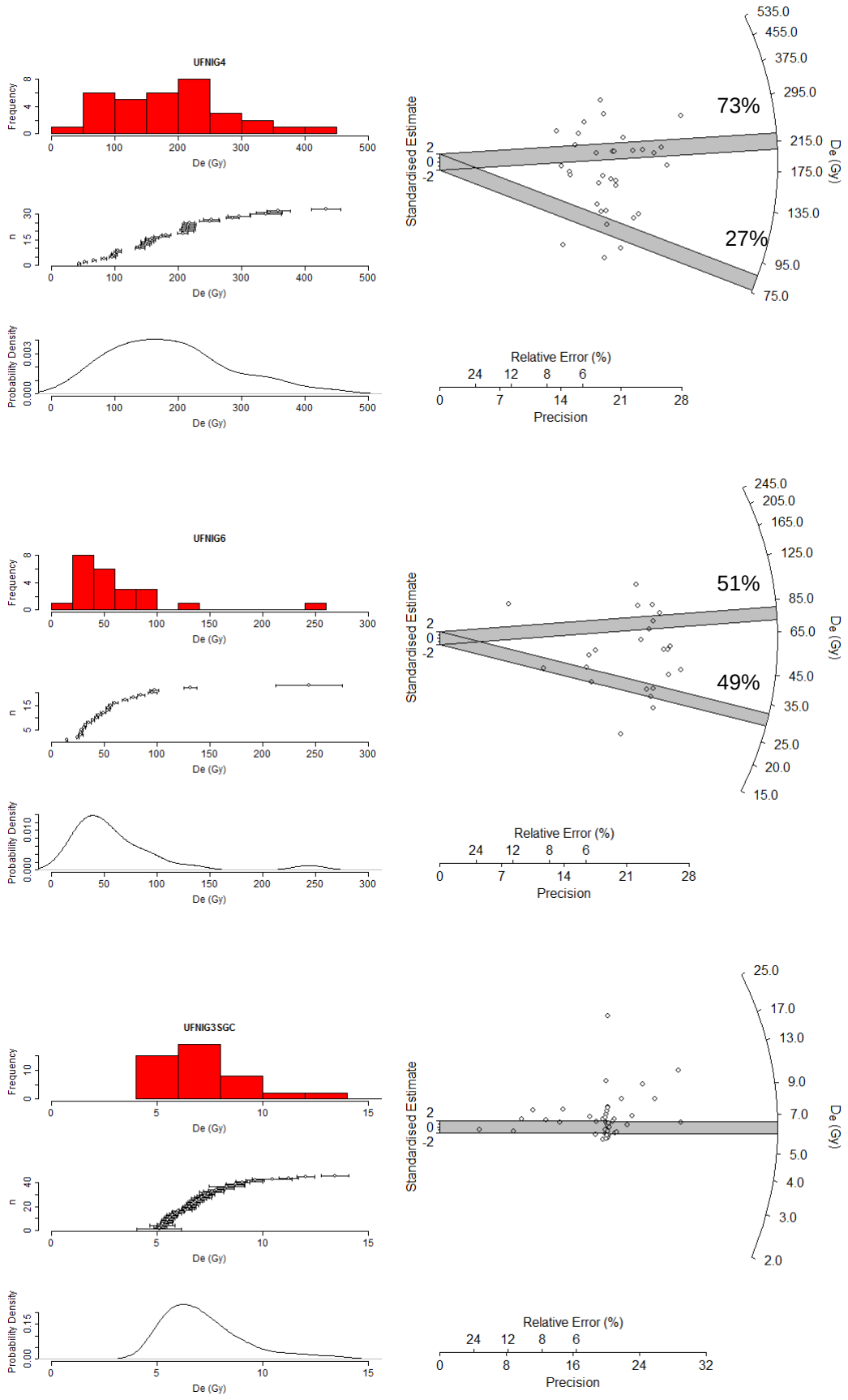

Figure 6.22: Histograms, probability density functions, scatter graphs and radial plots of F_NIG3/4/6. Where FMM indicated the presence of multiple components, the relative proportions of these components are indicated.

sediments transported via crossover flow during higher discharges. During periods of elevated discharge, which may occur following a storm event, sediments are reworked across the proglacial delta more rapidly resulting in reduced bleaching opportunities. Such material could be deposited directly at F_NIG4 resulting in a greater residual age than if the material were reworked across the bar feature from F_NIG6, as occurs during periods of reduced discharge. Material transported along this route at lower discharges has better opportunity for sample bleaching as the shallow channel has reduced competency, increasing transport duration, and thus sunlight exposure.

Overdispersion and residual age reduce with reworking across the bar features, and FMM indicates that all samples except the bar tail deposits comprise at least two components (Table 5.12). This supports a transition from Type B to Type A sediments with sediment reworking across the bar features as material becomes more uniformly bleached.

6.6.3. **Nigardsdalen Braided Channel Bar Deposit Grain Size Characteristics**

F_NIG6 and F_NIG9 are both sampled from bar heads, however the GSA characteristics are significantly different (Figure 6.23) which reveals the variability present in the specific sub-environments of the different depositional classifications. F_NIG9 has modal phi of 2.71 in contrast to 0.60 for F_NIG6. The interrelationships between F_NIG7/8/9 have been discussed, and a contrast in GSA characteristics supports the luminescence results observed. Modal phi fluctuates from 2.56 to 2.84 and 1.89 with transport downstream, and kurtosis shifts from leptokurtic, to mesokurtic in the same direction.

6.6.4. **Sandur Braided Channel Bar Deposit Summary**

The contrasts between Nigardsdalen and Fåbergstølsgrandane have highlighted the controls of transport and depositional processes on sample σ_d characteristics, as well as residual age. In Fåbergstølsgrandane, bar head deposits have high residuals and low σ_d which reflect the limited bleaching opportunities for sediments transported onto the sandur during storm events. In contrast the Nigardsdalen bar head deposits have low residual ages and high σ_d, as a consequence of multiple, heterogeneous bleaching opportunities. The source sediments are similar in both catchments, although transport distances are ~ 20 times greater in Fåbergstølsgrandane.

The process of bar head erosion and transport across the braided bar features is the same in both catchments. Homogeneous bleaching of the Type A deposits of Fåbergstølsgrandane results in little variation in σ_d as a function of transport.

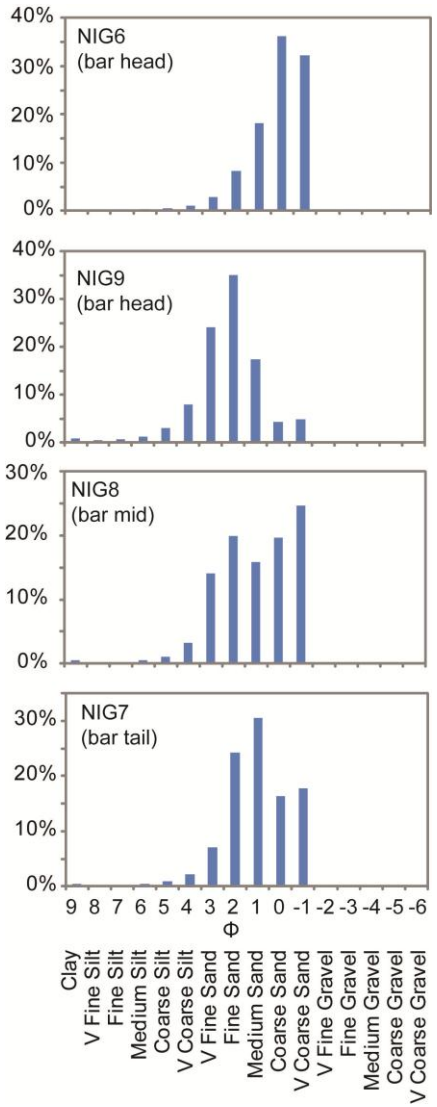

Figure 6.23: Grain size analysis results for NIG6/7/8/9, data are grouped using the size scale detailed in Chapter 4.

Homogeneous bleaching is confirmed by the uniform behaviour of both the quartz and feldspar ($IRSL_{50}$ and $pIR\text{-}IRSL_{250}$) extracts, as under heterogeneous bleaching conditions contrasting behaviour associated with the different minerals' bleaching properties would be anticipated. In contrast, the Type B bar head deposits in Nigardsdalen exhibit a marked reduction in σ_d as sediments are bleached. If this bleaching is homogeneous and all grains bleach at the same rate, it may be anticipated that σ_d of the bar head deposits would be preserved, however this is not observed. Homogeneous bleaching could cause a reduction in σ_d where sediments are becoming fully bleached, however the bleaching experiments described in Chapter 5 identified a maximum residual of < 1 Gy for fully bleached feldspar samples, which equates to an age of ~ 200 years. The Nigardsdalen samples with the lowest residuals have ages > 500 years and thus this explanation for reducing overdispersion cannot be accepted. Furthermore, as the proglacial lake at Nigardsbreen developed in the 1930's (Østrem et al., 1976), fully

bleached samples cannot have an age > 1 ka, and so sample modernity is certain and thus residual ages are a consequence of partial bleaching. Heterogeneous bleaching must therefore be occurring within Nigardsdalen, as the samples become more fully bleached. The relative bleaching behaviour of the braided bar sediments can be considered with the conceptual model in Figure 6.24.

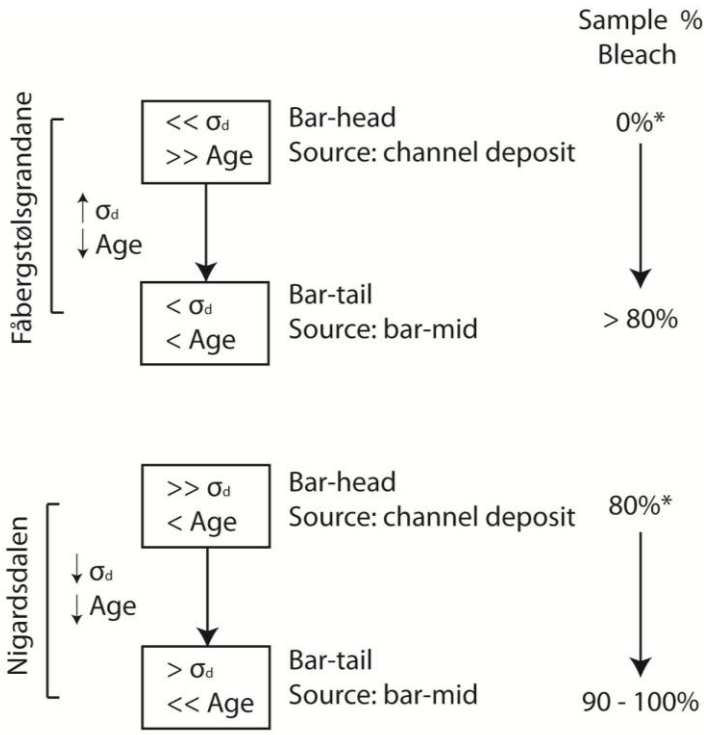

Figure 6.24: Conceptual model of sediment bleaching for the Fåbergstølsgrandane and Nigardsdalen samples. The properties of the source channel deposits are key in determining the bar-head characteristics. Although the same transport and depositional processes rework samples across the bar features at both sites, the resultant bar-tail luminescence properties are different, illustrating the influence of source sediments on both luminescence residual ages and distributions. The sample bleaching percentages highlighted with * are estimated.

The Fåbergstølsgrandane sandur braided channel bar deposits have greater residual modelled ages than the glaciofluvial braided channel bar and point bar deposits, exhibiting the greatest residuals at the bar heads which are caused by initial deposition of poorly sorted sediments by highly competent flow. Bar tail deposits have the smallest residuals, which is in agreement with the findings of previous research (e.g. Thrasher et al., 2009b), however the observation that only the bar tail deposits exhibit the best bleached sediments has not been previously reported. This has implications for improving sampling protocols in environments that are challenging to date using luminescence methods. The contrasting variations in σ_d as a function of transport across the bar features between the Nigardsdalen and Fåbergstølsgrandane catchments is unexplained, but illustrates the complex interrelations of σ_d and residual age in complimentary depositional environments.

6.7. Gilbert-style Delta Deposits

A delta bottomset was sampled at Gaupne, and two samples were analysed: F_GAUP1 and GAUP2. GAUP40 and GAUP41 were sampled from the top of the exposure, which is approximately 10 m thick, from an extensive cross bedded exposure of coarse, to medium grained sand deposits which are attributed to infilled river channels (Figure 6.25 and Figure 6.26). Acceptance rates were low, related to poor recycling, high recuperation and sample oversaturation. Only one aliquot of GAUP40 was accepted and this sample is not discussed further.

6.7.1. **Gilbert-style Delta Deposit Summary**

GAUP2 (*n*=8) has an σ_d value of 20 ± 1% which may be underestimated following the bootstrap experiments described in Chapter 4, however due to the paucity of material available for these sites, this sample is considered. GAUP41 (*n*=13) has zero σ_d. GAUP2 has an age of 9.15 ± 0.60 ka and GAUP41 of 3.50 ± 0.27 ka, modelled using the COM and CAM, respectively. These ages are stratigraphically consistent and the GAUP2 age fits within the Høgemoen stadial, dated to 9.5 ± 0.2 - 9.1 ± 0.2 ka BP. Vorren (1973) suggested, without chronology, that the Gaupne delta developed during the Høgemoen stadial. The overlying GAUP41 sediments are contemporaneous with substantial glacial advances that occurred in Jostedalen between 3.7 – 3.1 ka BP (Ballantyne, 1995; Ballantyne and Benn, 1994). This age has significance for constraining fjord and sea levels during the Late Holocene, and the duration of sedimentation in the Gaupne delta.

F_GAUP1 (*n*=24*)* has σ_d of 25 ± 1% and age, modelled using MAM-3, of 59.25 ± 19.39 ka. This age is inconsistent with that obtained for GAUP2 in the quartz analyses, which was 9.15 ± 0.60 ka, indicating that feldspar are inappropriate for dating delta bottom sets, associated with their slower bleaching rate (e.g. Hansen et al., 1999). Despite this, σ_d values were similar for GAUP2 (20 ± 1%) and GAUP1, which is consistent with less rapid bleaching of feldspar, in contrast to quartz.

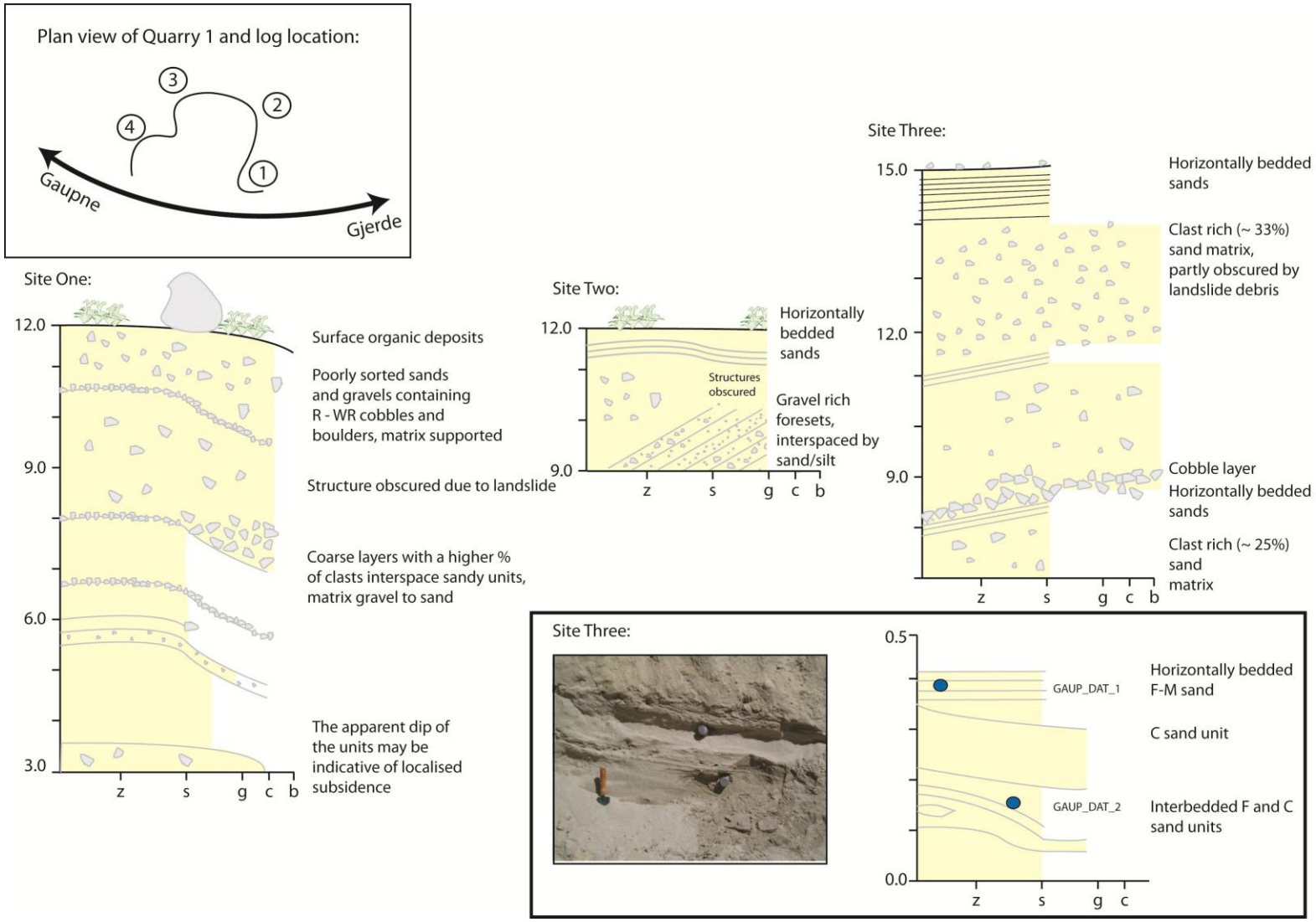

Figure 6.25: Logs of the sediments exposed at Gaupne (61˚ 26' N, 7˚14' E), with sampling locations at Site Three identified

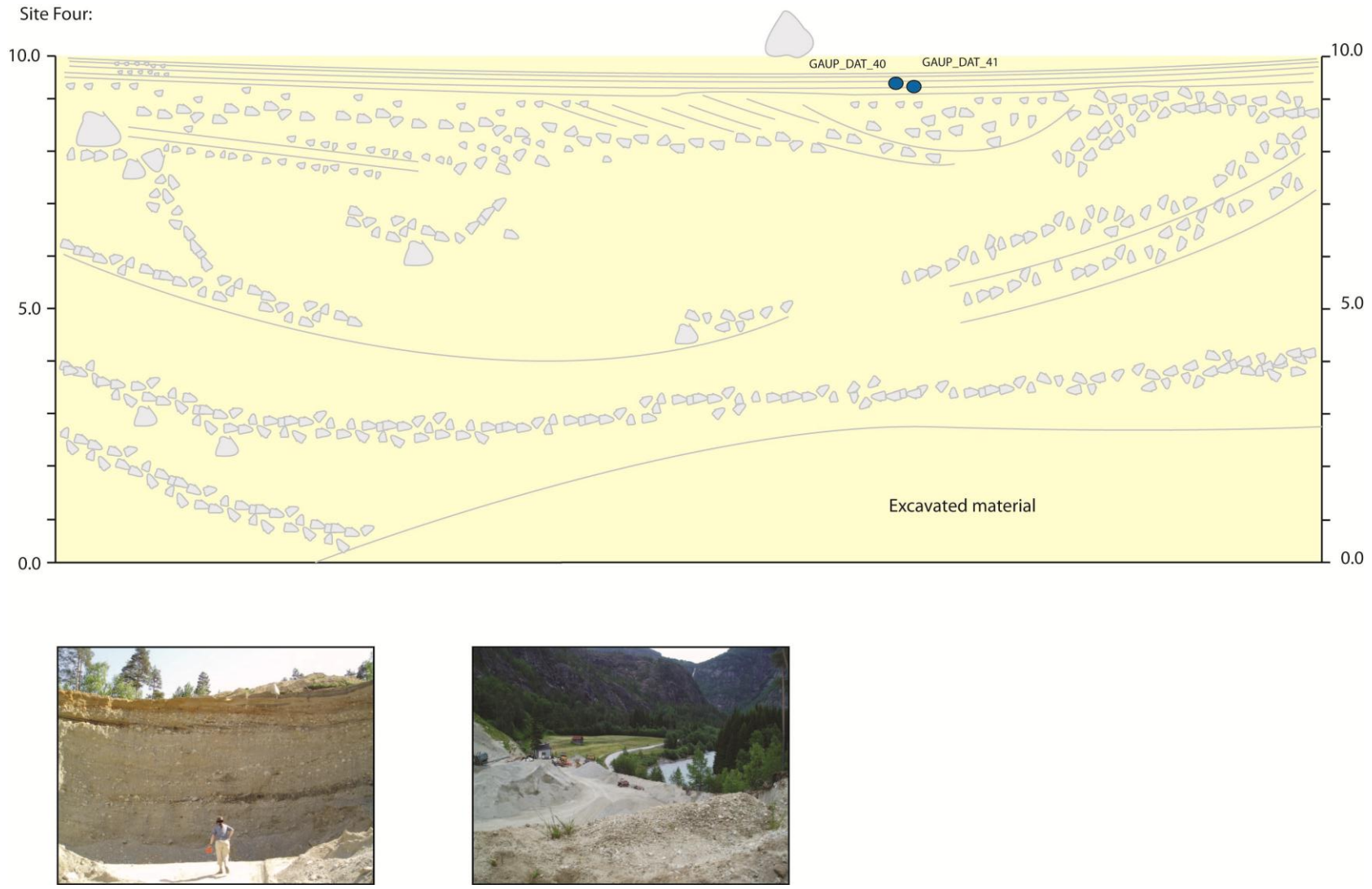

Figure 6.26: Sedimentary log of the largest exposure at Gaupne (61˚ 26' N, 7˚14' E), Site Four, with sampling locations highlighted.

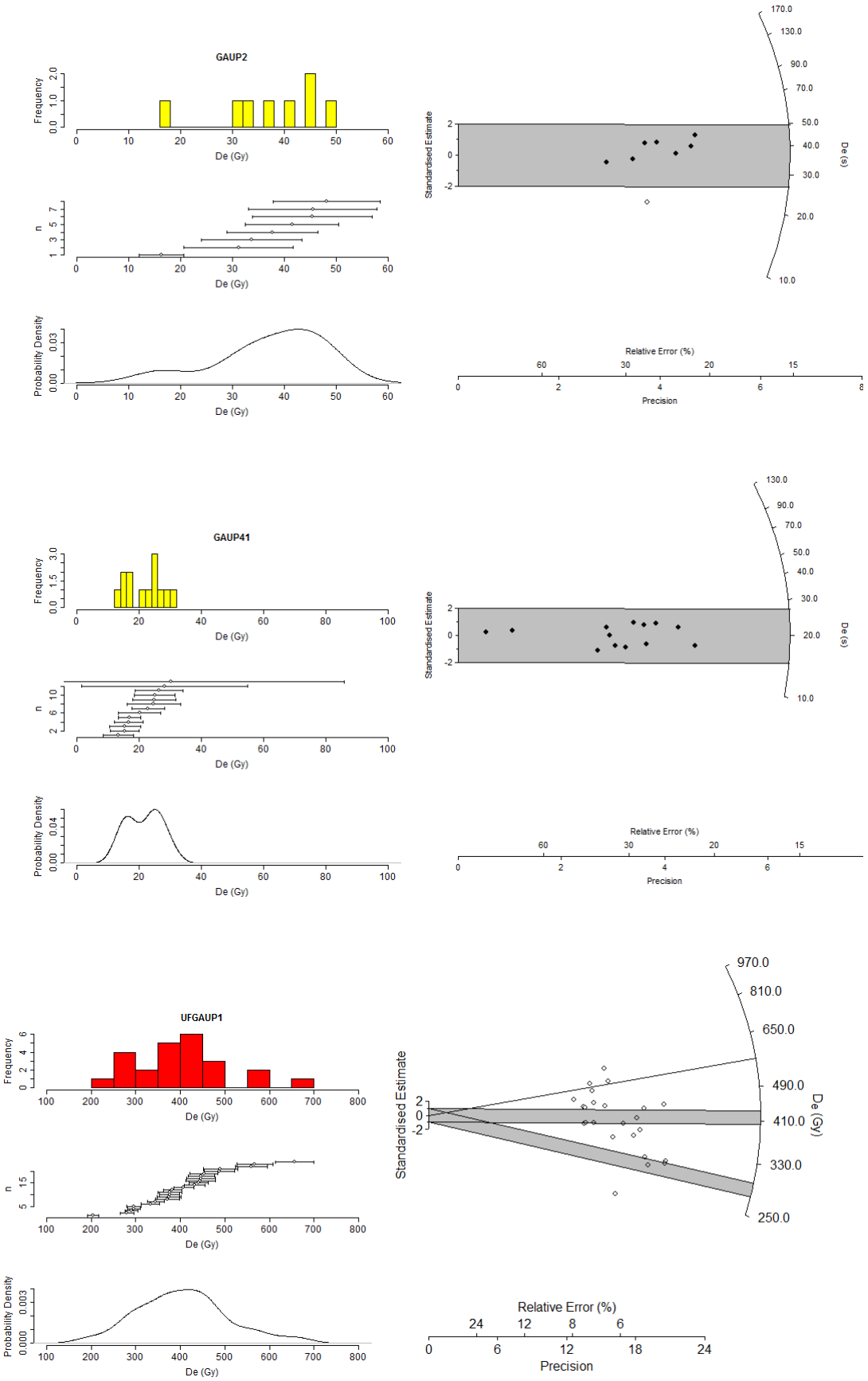

Figure 6.27: Histograms, probability density functions, scatter graphs and radial plots of GAUP2, GAUP41 and F_GAUP1.

6.8. Summary

Analysis of the different source and deposit luminescence properties of the various samples have indicated that source deposits initially control sample σ_d characteristics, and transport and depositional processes control residual age. However, following a threshold of sediment modification via transport (i.e. sunlight exposure and bleaching), transport and depositional processes also exert an influence on sample σ_d. The proximity of the sediment deposit to the sediment source is therefore important in determining the key driver of observed σ_d. The modification of σ_d by the same depositional process contrasts, dependent upon the source materials, as illustrated by the different behaviour of the Nigardsdalen and Fåbergstølsgrandane bar deposits. Factor analysis of the different luminescence and GSA variables may provide insights into these complex interrelationships, as well as a means of predicting sediment sources, and is considered next.

6.9. Factor Analysis

Factor analysis is a multivariate method of data reduction which enables exploration of the inter-relationship between variables and samples (Davis, 1986). It has been used to explore sediment source linkages from mineral magnetic data (Walden et al., 1992) and in a range of geochemical applications (e.g. Abesser et al., 2006). R-mode analysis is similar to principle components analysis and comprises the transformation of data from a sample (*n*) by variable (*m*) matrix, into an *m x m* matrix, which enables calculation of the similarity of variables in terms of the sample response to them (Walden and Smith, 1995). Variables are reduced into a set of uncorrelated, orthogonal factors. Each factor is associated with a degree of *m* variance and these are quantified through its loadings, and factor loadings can be plotted in two-dimensional space. Q-mode analysis alternatively seeks to identify samples which respond to the different variables in a similar manner, and is also similar to some principle coordinates analysis (Walden and Smith, 1995). An *n x n* matrix is constructed and factors calculated; those samples which plot closely to one another relative to the calculated factors can be interpreted to respond to all of the variables in a similar manner.

Factor analysis involves standardisation of data values (Davis, 1986), therefore where R- and Q-mode analyses are calculated simultaneously, common factors can be calculated (Davis, 1986; Gower, 1966; Zhou et al., 1983) and the loadings of both variables and samples contrasted. Factor analysis assumes the data are multivariate, normally distributed, and that $m > n$. Interpretation of the factors and loadings is qualitative

and has no significance testing, therefore slight deviations from these assumptions are not thought to be critical (Walden and Smith, 1995). Simultaneous R- and Q-mode analyses were calculated using Minitab v.16 and no factor rotation was used, avoiding the main criticism of this technique (Temple, 1978).

The luminescence properties of the different samples relative to their depositional context are explored to determine whether they are diagnostic of 1) deposit type, 2) source deposit, 3) transport process and 4) facies. Sample categorisations are based on field observations and analysis of the luminescence and dose distributions described in the first half of this chapter and summarised in Appendix A.1. If they are diagnostic this will provide a tool through which these variables can be predicted for sediments where they are unknown. For example, the contribution of hillslope material to a fluvial deposit could be calculated, potentially enabling reconstruction of sediment flux from different source deposits in palaeoenvironmental reconstructions. Factors with eigenvalues (E) < 1 are rejected (Nunnally, 1978). Sample depositional properties are considered initially, followed by luminescence properties (see Table 6.5) and then a combination of the two sets of properties are examined. Samples are categorised by deposit type and facies in all biplots, and where clustering of sediment source and transport process characteristics are identified, these are indicated.

Table 6.5: Variables explored with Factor Analysis

Luminescence Variables	Transport and depositional Variables**
Modelled Age (ka)	Transport Distance (m)
Maximum Age (ka)*	GSA Sorting
σ_d	GSA *k*
k	GSA *c*
c	GSA mean
Average T_x Intensity	% V Coarse Sand
% Acceptance***	% Coarse Sand
	% Medium Sand
	% Fine Sand
	% V Fine Sand
	% Coarse Silt
	% Medium Silt
	% Fine Silt
	% V Fine Silt
	% Clay

*Calculated from the maximum D_e value.
**Distance data are available for all samples, only 13 samples have both GSA and quartz luminescence data, and 9 samples have both GSA and feldspar luminescence data
***Not considered in the feldspar analysis as acceptance rates were all > 90%

Interrelationships exist between the different luminescence and depositional properties listed in Table 6.5, which indicates that analyses may be limited by auto-correlation. For example average T_x Intensity is correlated with % acceptance for some of the quartz data (Figure 6.1), as many samples were rejected due to low signal to noise ratios. A second example is that the degree of GSA Sorting is related to the GSA *k* and GSA *c* values, with large *k* or *c* being indicative of low sorting. A final example is that as sample σ_d is calculated from the D_e distribution, this will also be related to luminescence *k*

and *c*. However, exclusion of the auto-correlating parameters will limit the inferences that can be made from the factor analysis, as the objective here is to identify which parameters are most indicative of transport and depositional processes and facies. However, through iterative exploration of various factor analyses, those parameters which are redundant due to significant correlation with other parameters are rejected. Factor loading scores for the different variables are listed in Appendix A.11.

6.9.1. **Depositional Variables Factor Analysis**

Grain size analysis data were collected for 19 samples (see Section 3.3). All variables were initially included in the factor analysis and four factors with loadings > 1 identified, explaining 92% of total variance. However the cluster of % V Fine Sand to % Clay loadings on the first factor (E = 9.82) is indicative of redundancy, and these values were summed into a new category ("% V fine sand:clay"), and reanalysed. Three factors with loadings > 1 were identified, which explain 83% of total variance. Where the R-mode data are analysed, the % V fine sand:clay exhibits no loading on the factors identified and therefore was removed from the dataset. The number of calculated factors and % variance explained remain unchanged.

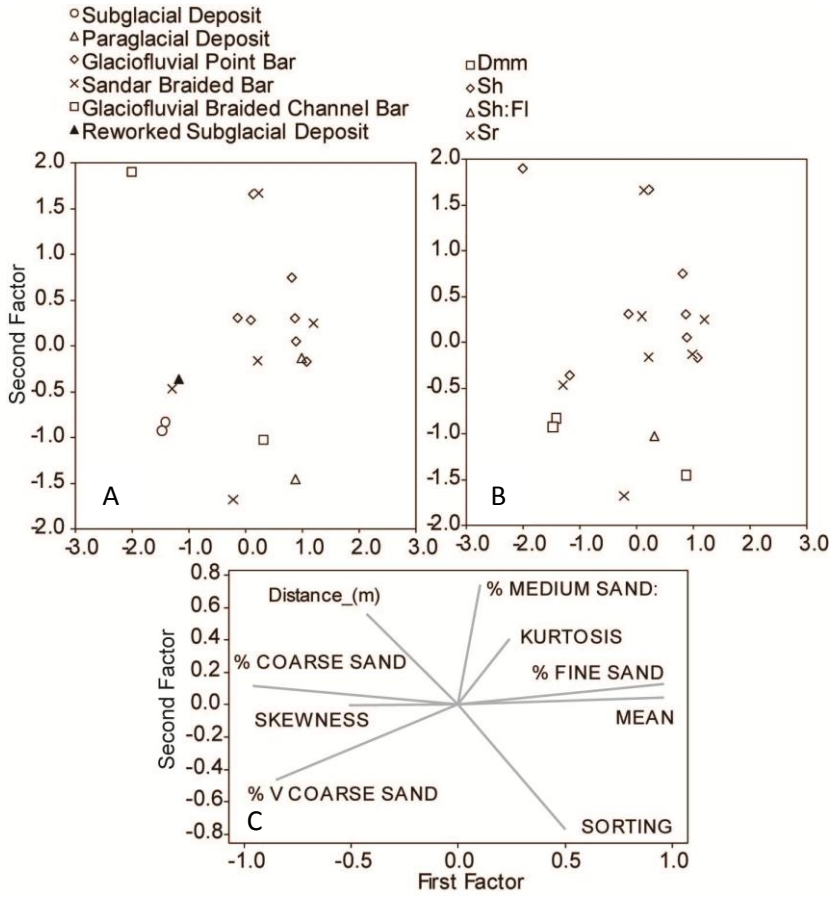

Figure 6.28: Q-mode biplots of samples plotted against the first and second factors calculated from the depositional environment variables (see Table 1). Samples are classified by deposit type (A) and facies (B). R-mode loading plot of variable loading against the first and second factors (C).

From the Q-mode plots and the R-mode loading plot (Figure 6.28), it is apparent that only the subglacial samples are distinct. There is significant overlap between the point bar and sandur bar deposits, although the sandur samples group towards the paraglacial and subglacial source material, indicative of their coarse-medium sand composition. The different facies overlap. The subglacial Dmm samples have strong negative loadings on the first and second factors, however FAB42 (also Dmm) exhibits strong loading on the first factor (Figure 6.28), indicative of its elevated amount of fine sand relative to FABSUB1 and 2. Similarly, no differentiation between sediments of different sources or transport processes is apparent.

It is clear that the GSA data presented here are insufficient to clearly distinguish between the different deposits, depositional processes, sediment sources and/or facies sampled. This may relate to the sampling strategy employed throughout this research, as well as sample luminescence characteristics which have dictated sample acceptance, and has resulted in underrepresentation of source material relative to the other deposit types.

6.9.2. **Luminescence Variables Factor Analysis**

6.9.2.1. Quartz Luminescence Factor Analysis

The luminescence properties of the samples were also investigated with factor analysis. Only samples with $n > 10$ were included, and all quartz luminescence variables were explored in the first analysis. Three factors had loadings > 1 and explain 75 % of the observed variance. The sandur deposits are clearly differentiated by their correlation with factor two, which has substantial positive loadings from age (0.87), and negative loadings from σ_d (-0.72). However the remainder of the deposits are clustered, relating to the relatively strong correlation of all other variables with the first factor (Figure 6.29). The interdependence of the different luminescence variables contributes to this clustering e.g. average T_x and % acceptance are closely related, as sample acceptance is governed by sensitivity for this sample set. Maximum age and average T_x are also closely associated, which is surprising as no intrinsic relationship between these variables should exist, unless it is an artefact caused by rejecting young samples due to their dim L_n emissions; this interpretation is supported by the correlation of both of these variables with % acceptance.

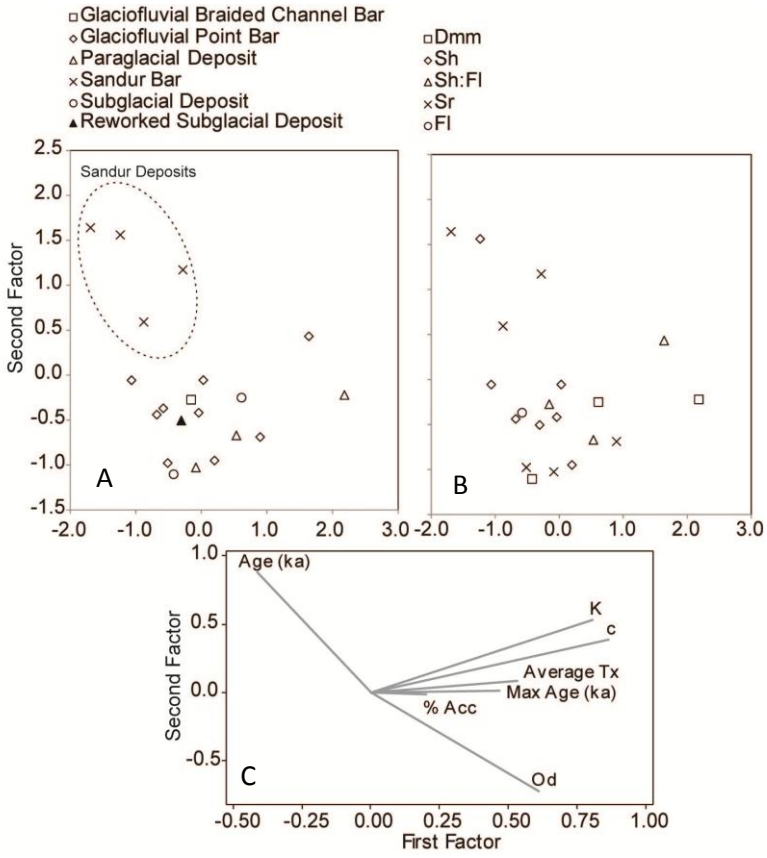

Figure 6.29: Q-mode plots of samples plotted against the first and second factors calculated from the luminescence variables (see Table 6.5). Samples are classified by deposit type (A) and facies (B). R-mode loading plot of variable loading against the first and second factors (C). See Appendix A.11 for associated table.

Where sample transport distance relative to the glacier snout is also included in the analysis, the different deposits are more easily distinguished, and better distinction between depositional processes is also achieved. Distance from the ice margin is known for these samples, and can be reconstructed for palaeoenvironments based on facies assemblages and geomorphological evidence. Three factors with loadings > 1 are identified, and explain 73% of observed variance. Clear differentiation is possible between the sandur and glaciofluvial point bar deposits, driven largely by the negative loading of transport distance (-0.72) and positive loading of σ_d (0.74) on factor one. This indicates that samples with high σ_d have experienced short transport distances, consistent with the proposal that over short transport distances, dose distributions are governed by sediment source, but that over longer distances, transport process exerts the maximum influence. This relationship is more complicated than a simple reduction in σ_d and residual age with distance, as revealed by the negative loadings of distance and age on factor two: the Fåbergstølsgrandane samples have experienced the greatest transport distances of the quartz samples, but have the greatest residual ages and lowest σ_d values. Thus transport processes are key in dictating the sediment residual age.

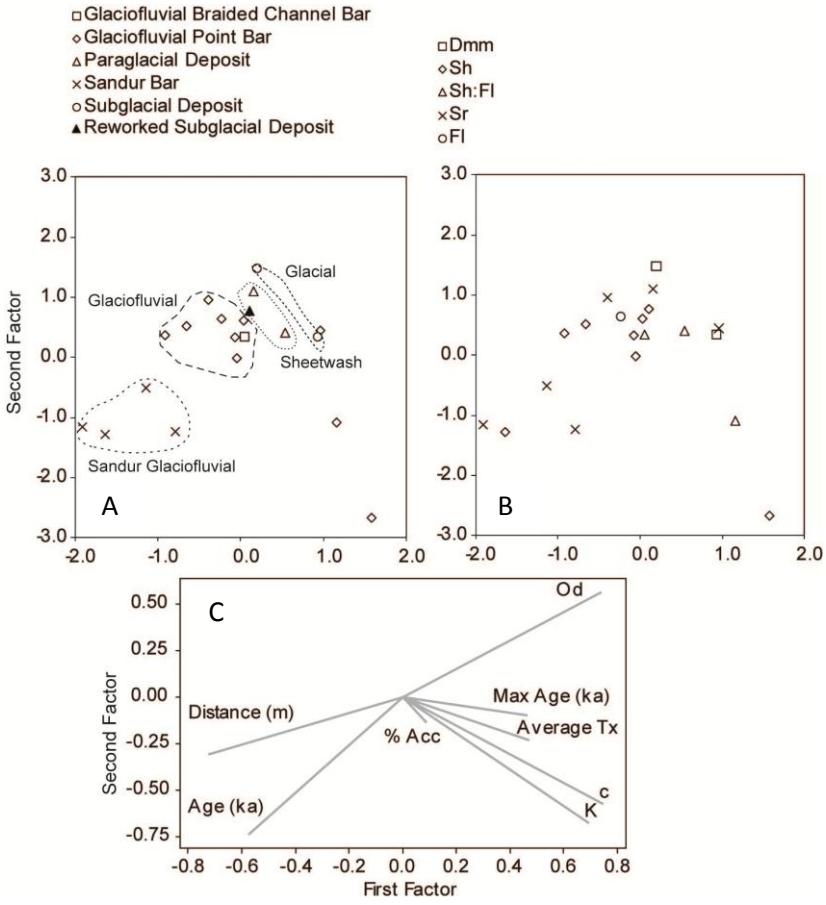

Figure 6.30: Q-mode biplots of samples plotted against the first and second factors calculated from the quartz luminescence variables and transport distance (see Table 6.5). Samples are classified by deposit type (A) and facies (B). R-mode loading plot of variable loading against the first and second factors (C). See Appendix A.11 for associated table.

The source deposits are more strongly associated with factor one, along with *k*, *c*, and σ_d, which is anticipated given their more skewed distributions and high σ_d values. Clear differentiation of the various facies or sediment sources is not possible, although it should be recognised that these samples are not a comprehensive suite from a glacial catchment, but are biased towards material perceived to be suitable for OSL.

Finally, an inverse relationship between age and σ_d is apparent from the R-mode loading plot, which suggests that those samples with lowest residual ages have greatest σ_d. This is an artefact due to age modelling of the majority of samples using the MAM-3 model, and could be overcome through consideration of sample age range (i.e. the different between maximum and minimum residual doses), although this has not been investigated here.

6.9.2.2. Feldspar luminescence factor analysis

All of the feldspar luminescence variables were explored in the first analysis, however significant auto-correlation was observed between D_e, maximum age, and age; consequently D_e was excluded and the analysis repeated (Figure 6.31). Two factors had E > 1 and explain 75% of the observed variance. No clear differentiation of deposit or facies

type is possible, although the paraglacial material is distinguished by its positive loading on the second factor due to its high σ_d values.

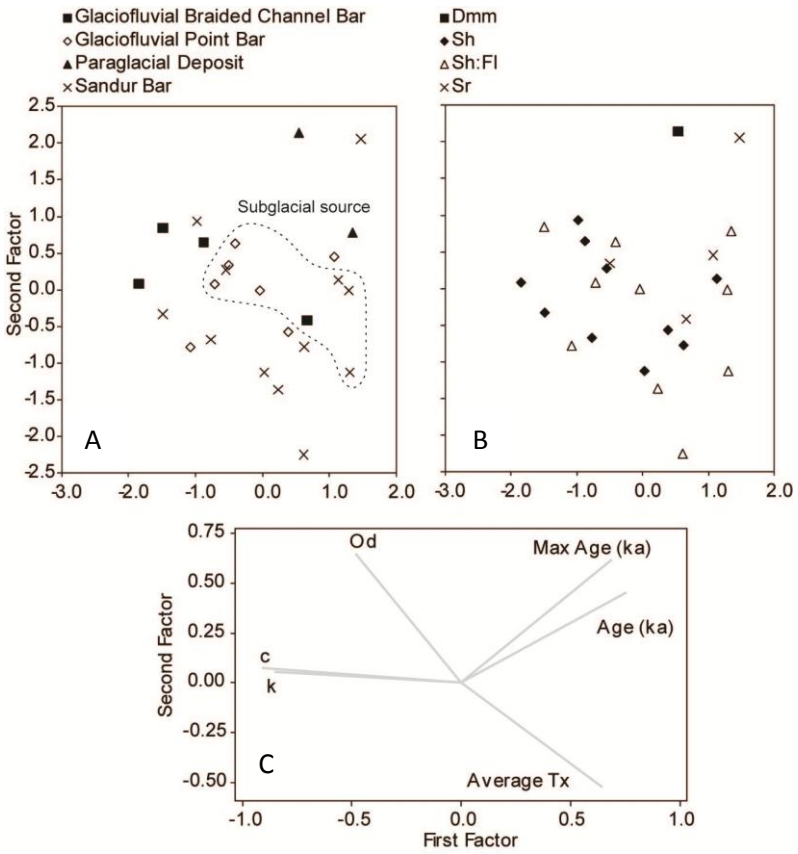

Figure 6.31: Q-mode plots of samples plotted against the first and second factors calculated from all feldspar luminescence variables excluding D_e (Gy) (see Table 6.5). Samples are classified by deposit type (A) and facies (B). R-mode loading plot of variable loading against the first and second factors (C). See

Samples sourced from subglacial material cluster together, however sediments sourced from paraglacial and glaciofluvial deposits (e.g. the Nigardsdalen samples except NIG6 which has subglacial source) cannot be distinguished. The sandur deposits generally plot more negatively on the second factor, however F_NIG4 (Sr) correlates positively with both factors, due to its high residual age.

Transport distance from the ice front was incorporated into the analysis (Figure 6.32), to explore whether this could better differentiate the deposits, and two factors with E > 1, explaining 69% of the variance were obtained. Deposit and facies differentiation is not improved, and it is no longer possible to isolate sediments sourced from subglacial material (Figure 6.32). This contrasts with the quartz data where residual age increases as a function of transport distance driven by the Fåbergstølsgrandane samples, facilitating deposit and source sediment differentiation (Figure 6.30). However, for the feldspar samples, glaciofluvial braided bar deposits are better differentiated as they are more positively correlated with the first factor, with the exception of F_FAB81, related to its greater residual age, in contrast to the other braided bars deposits.

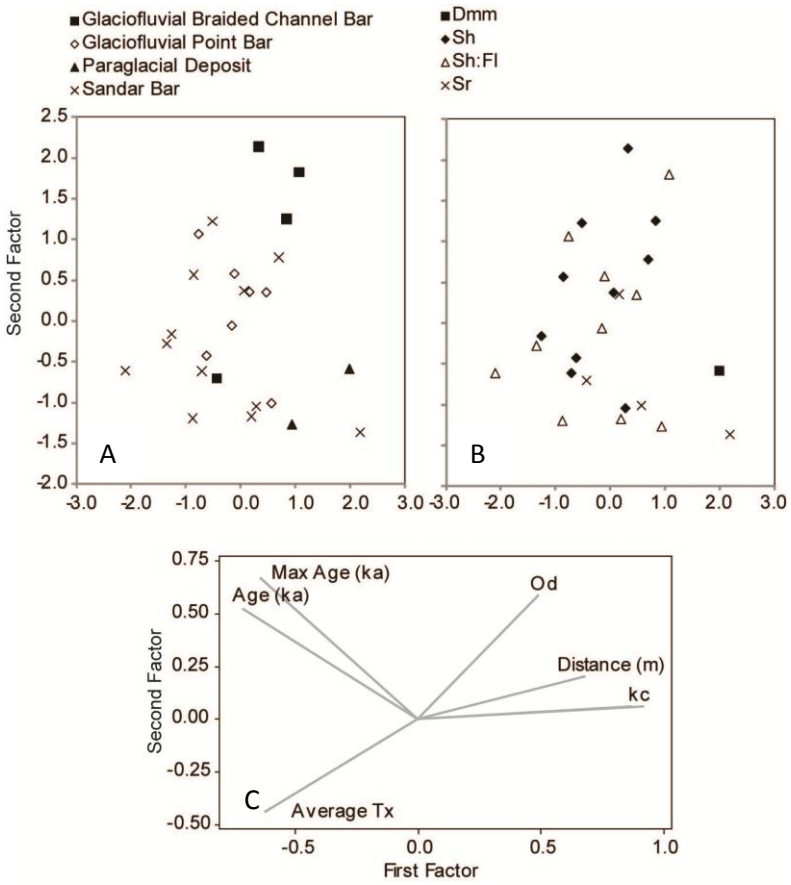

Figure 6.32: Q-mode plots of samples plotted against the first and second factors calculated from all feldspar luminescence variables excluding De (Gy) (see Table 6.5), and including distance from the ice margin. Samples are classified by deposit type (A) and facies (B). R-mode loading plot of variable loading against the first and second factors (C). See Appendix A.11 for associated table.

Factor one has strong negative loadings from variables: age (-0.71), maximum age (-0.64) and average T_x (-0.62); and positive loadings from *c* (0.92), *k* (0.87) and σ_d (0.49). Variable loadings on the second factor are less clearly defined, although *c* and *k* load least upon it, with the remainder of the variables loading positively (~ 0.5). The exception is average T_x which loads negatively (-0.44). All of the deposits are clustered, possibly related to the interdependence of the different luminescence variables e.g. *k* and *c* are mathematically related statistical parameters. Maximum age and age are closely correlated, which is surprising as most samples were analysed with the MAM-3 model, and due to the high σ_d values of the sample set no correlation is anticipated.

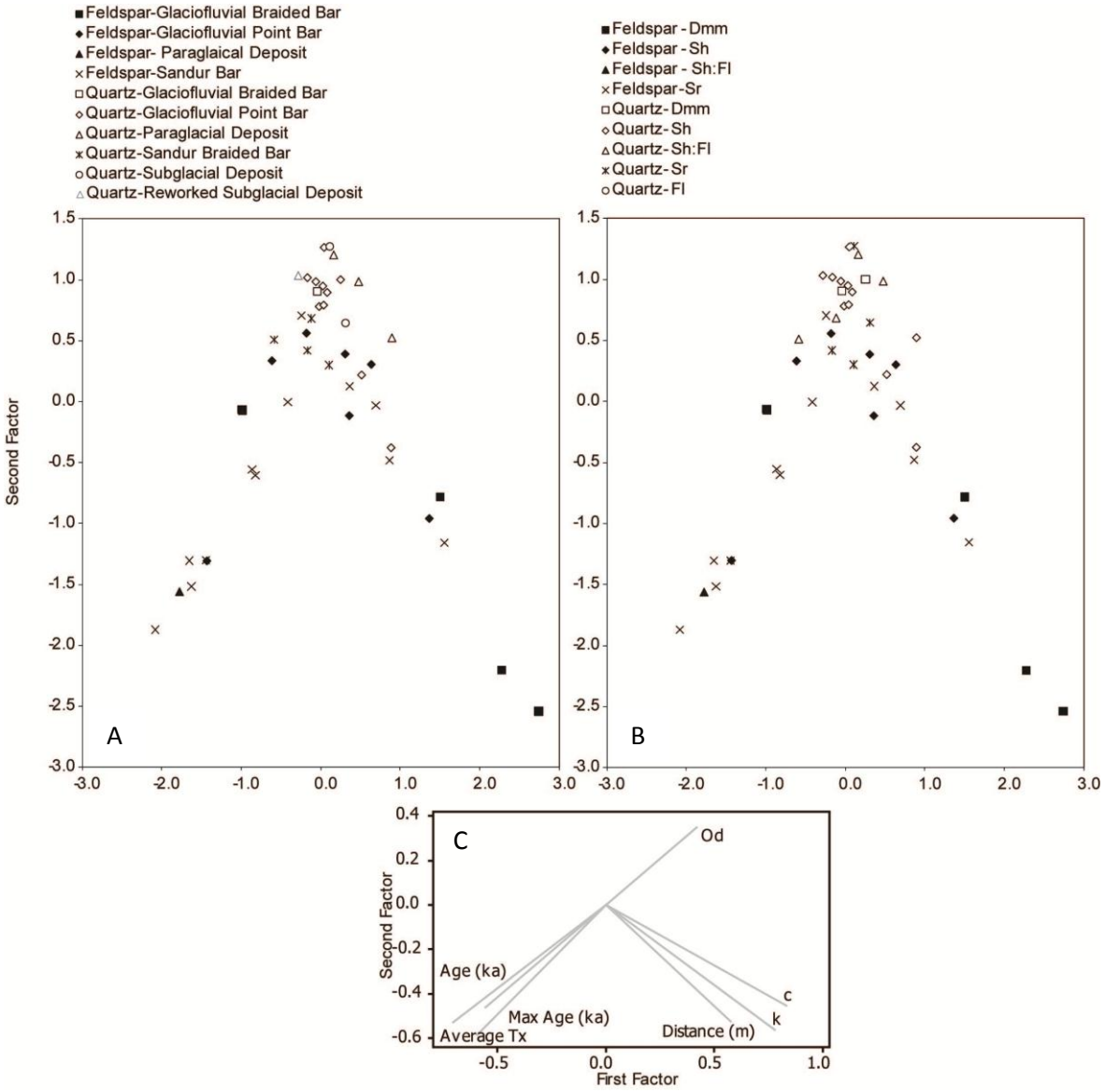

Figure 6.33: Q-mode plots of samples plotted against the first and second factors calculated from all feldspar and quartz luminescence variables excluding De (Gy) (see Table 1), and including distance from the ice margin. Samples are classified by deposit type (A) and facies (B). R-mode loading plot of variable loading against the first and second factors (C). See Appendix A.11 for associated table.

6.9.2.3. Quartz and feldspar luminescence factor analysis

Factor analysis of the quartz and feldspar luminescence variables was unsuccessful, revealing significant autocorrelation between average T_x, age (ka) and maximum age (ka) as well as between distance, *k*, *c*. Overdispersion was inversely correlated with average T_x, age (ka) and maximum age (ka). The covariance observed here is reinforced by the different behaviour of the quartz and feldspar sample suites, and precludes extraction of common causal factors.

Three factors of E > 1 are identified, which explain 82% of the variance, however from the Q-mode plots it is apparent that the quartz and feldspar data are clustered relating to variance intrinsic to the two sample populations. As the feldspar samples analysed were collected from the most distal locations and have the greatest ages, they are at the extremes of the different variables investigated, reflected in their associations at the extremes of the first two factors. In contrast, the quartz samples are clustered, because of their relatively moderate values. Repeating this analysis on only those samples which had both quartz and feldspar fractions analysed provided no further insights, except to confirm that the quartz and feldspar luminescence properties were distinct.

6.9.3. **Depositional and Luminescence Variables Factor Analysis**

Factor analysis is extremely sensitive to missing values, due to its foundation on matrix algebra. Grain size analysis data are not available for the full sample suite, and therefore it has been only partially possible to explore whether a combination of GSA and luminescence variables provides the best distinction of the different glacial deposits.

6.9.3.1. Quartz Luminescence and GSA Factor Analysis

Thirteen quartz samples were analysed (the remaining GSA data relate to feldspar samples), however within factor analysis $m > n$ cannot be violated. Where all of the variables used in the final GSA and luminescence models are incorporated, m is 15, therefore variables with identical loadings on factors were excluded i.e. maximum age and average T_x have identical loading on factor one, therefore average T_x was excluded. % fine sand, % acceptance and k were also excluded, reducing m to 12.

Four factors are identified which have E > 1 and account for 86% of the observed variance. The GSA variables load most heavily on the first factor and the luminescence variables on the second factor, indicating little association between the datasets, however average T_x, c and GSA sorting have very similar loadings on the second factor. Clear differentiation of the subglacial deposits is achieved, which is driven by the loading of % coarse sand and GSA skewness on the first factor. As no GSA data are available for the sandur deposits, isolation of all the different depositional environments is precluded, however these investigations indicate that more rigorous GSA and OSL property comparisons may provide valuable insights into deposit differentiation. Sediment sources and transport processes also cannot be distinguished, but again this may relate to the limited dataset analysed.

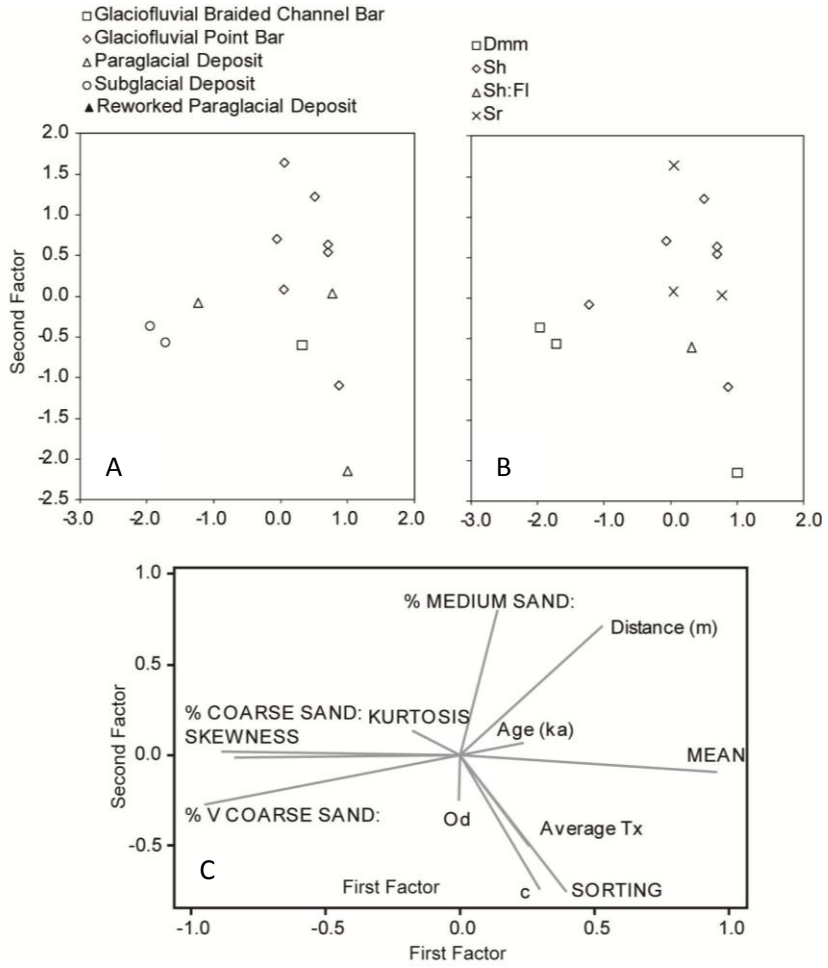

Figure 6.34: Q-mode biplots of samples plotted against the first and second factors calculated from a combination of quartz luminescence and depositional variables (see Table 6.5 and text for discussion of variable selection). Samples are classified by deposit type (A) and facies (B). R-mode loading plot of variable loading against the first and second factors (C). See Appendix A.11 for associated table.

6.9.3.2. Feldspar Luminescence and GSA Factor Analysis

Eight of the feldspar samples had GSA information which limited the number of variables that could be explored with factor analysis in order that $m < n$ is not violated. Distance, average T_x, c, σ_d, age, GSA mean, GSA sorting and GSA skewness were initially investigated, however because of the limited sample number conclusive differentiation of deposit, facies, sediment source or process was not possible (Figure 6.35).

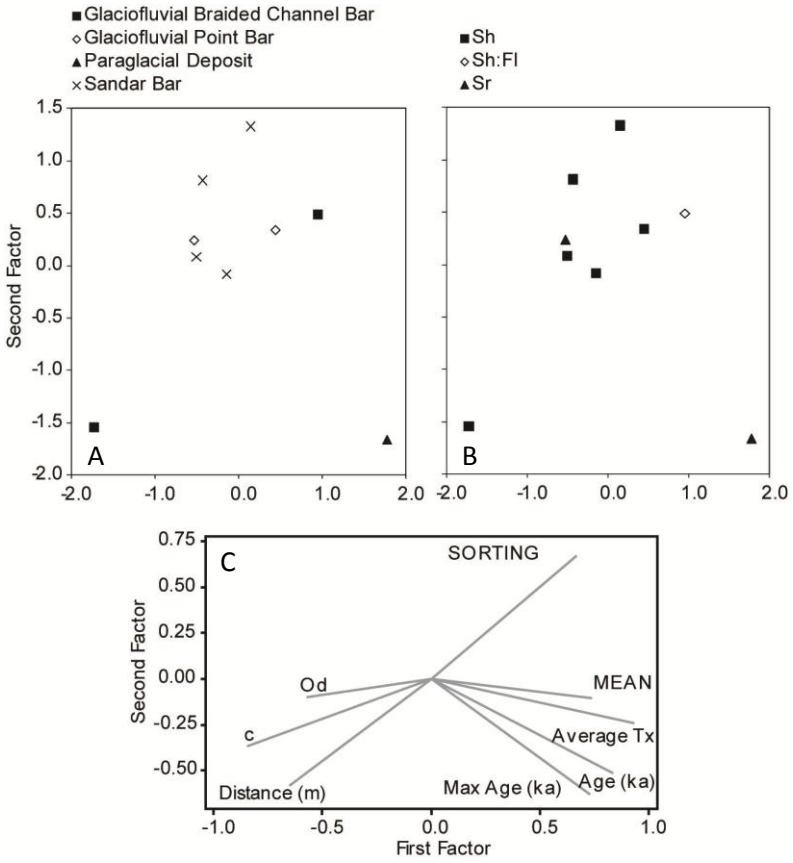

Figure 6.35: Q-mode biplots of samples plotted against the first and second factors calculated from a combination of feldspar luminescence and depositional variables (see Table 6.5 and text for discussion of variable selection). Samples are classified by deposit type (A) and facies (B). R-mode loading plot of variable loading against the first and second factors (C). See Appendix A.11 for associated table.

6.9.3.3. Quartz and Feldspar Luminescence and GSA Factor Analysis

Start parameters for the investigation of the 22 samples which have complete luminescence and depositional (i.e. including GSA) datasets were selected from the results of the previous GSA and luminescence investigations for quartz and feldspar, and are comprised of age, maximum age, average T_x, c, σ_d, % V coarse sand, % coarse sand, % medium sand, distance, GSA skewness, GSA kurtosis, GSA Mean and GSA Sorting. Although % acceptance was important in the initial quartz investigations, this parameter is not important for the feldspar samples and it was excluded. Residual age and average T_x values are significantly influenced by whether samples are quartz or feldspar, however these variables were not the key drivers of the identified factors, and so they were kept in the analyses. Five factors with E > 1 were identified, which explain 88% of the variance; the first two factors explain 54% of the variance. % V coarse sand loads most heavily on factor 1 (0.71) and GSA mean least heavily (-0.86), followed by age (-0.59) and average T_x (-0.56). The close association between age and average T_x is related to the quartz data as discussed previously. Overdispersion loads most significantly on the second factor (0.70), which age (-0.50), average T_x (-0.59) and % V coarse sand (-0.49) load least heavily on. This suggests an inverse relationship between σ_d and the other variables which is driven by the properties of the paraglacial material for both quartz and feldspar,

as well as the quartz glaciofluvial braided bar deposits, which have high σ_d but low age, related to MAM-3 age modelling. However there is significant scatter in the different depositional environments and facies prohibiting conclusive deposit, sediment source or transport process determination.

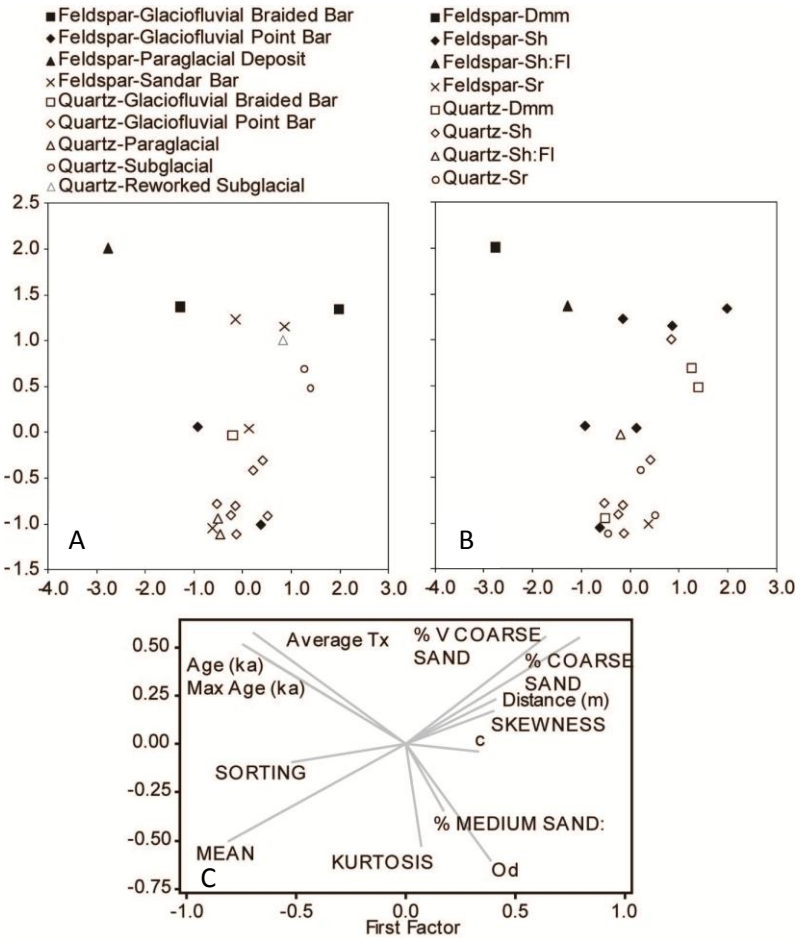

Figure 6.36: Q-mode biplots of samples plotted against the first and second factors calculated from a combination of feldspar and quartz luminescence and depositional variables (see Table 6.5 and text for discussion of variable selection). Samples are classified by deposit type (A) and facies (B). R-mode loading plot of variable loading against the first and second factors (C). See Appendix A.11 for associated table.

6.10. Summary of Factor Analysis Results

The sandur, source and glaciofluvial point bar deposits can be partly distinguished in the different factor analyses. The quartz luminescence data can be well differentiated by depositional process (Figure 6.30), which supports the observations that sediment source dictates sample dose distribution over short transport distances, but that transport and depositional processes dictate sample dose distribution over greater transport distances. This analysis has also illustrated the influence of transport and depositional processes on residual dose. A weak positive relationship between residual dose and transport distance is observed for the quartz samples, primarily due to the Fåbergstølsgrandane bar head deposits which have large transport distance from the ice margin, but high residual dose related to the deposition of channel material.

The same differentiation by depositional process is not observed for the feldspar data, which may be a consequence of the different sediments analysed. Alternatively this may relate to the different luminescence properties of feldspar in comparison to quartz, which are apparent in the contrasting σ_d and residual dose values of the Fåbergstølsdalen samples analysed, although as the feldspar samples only have n = 12 for these samples, greater replicates are required to fully evaluate these differences.

Where distance is not included in the analyses, no conclusive differentiation of the various deposits, transport processes, source sediments or facies is possible for these samples. This may be related to the similarities in the depositional environments under investigation, and also the complexity of these partially bleached sediments. The majority of the sample suite comprises glaciofluvial deposits which are poorly sorted sands. Investigation of depositional environments which vary more significantly, such as a contrast between equal sample numbers of subglacial, paraglacial, glaciofluvial and glacioaeolian sediments, may enable clearer trends to be identified. The sediments explored within this research are almost all partially bleached, and the feldspar samples analysed are worst affected, resulting in larger residual ages. Furthermore as the feldspar extracts analysed are from the samples with the greatest transport distances, this has skewed the dataset considerably, because the feldspar sample properties are at the extremes of the variables considered. Consequently comparative quartz and feldspar factor analysis was unsuccessful, limiting the size of the dataset investigated here, but may be informative in an environment where well bleached deposits have been analysed, and the quartz and feldspar ages are comparable.

Although factor analysis of the quartz luminescence properties is successful, the other analyses are inconclusive; however, the potential of factor analysis applied to luminescence data has been demonstrated. Its application can be further explored through investigation of existing datasets comprising sediments from contrasting depositional environments (e.g. fluvial and aeolian) with distinct facies, source sediments and transport and depositional processes. If sediments with similar properties (e.g. source sediment, σ_d, luminescence sensitivity, grain size characteristics etc.) are observed to cluster, then factor analysis of OSL characteristics may provide a powerful tool for provenance analysis. Furthermore, these investigations will develop our understanding of how transport and depositional processes modify luminescence behaviour.

6.11. Conclusions

- The luminescence distribution of the different glacial samples is dictated primarily by source material, and secondly by transport and depositional processes.

- The residual ages of the different glacial samples are dictated primarily by transport and depositional processes.
- Increased transport distances promote a reduction in the influence of sediment source material and an increase in the influence of transport and depositional processes, in determining the residual age and σ_d characteristics of deposits.
- Subglacial and paraglacial samples have maximum residual ages beyond the period of most recent glaciation, indicating that these deposits are unsuitable for luminescence dating.
- *In-situ* subglacial material and paraglacial material can be differentiated by GSA and have σ_d values > 70%.
- It is not possible to assign a specific σ_d value to point bar deposits because of the complex interrelationships between sediment sources, transport distances and depositional processes which dictate their dose distributions.
- Source material, as well as the calibre of glaciofluvial streams, dictates both the σ_d and residual ages of bar head deposits.
- The residual ages and σ_d properties of mid-bar and bar tail deposits are dictated by the immediate source material at the bar head.
- Feldspar are more susceptible to partial bleaching than quartz within high calibre depositional systems, but are rapidly and effectively bleached during sediment reworking across bar deposits.
- Bar-tail deposits represent the best bleached samples within the glaciofluvial system, indicating that these deposits may be suitable for luminescence dating.
- Samples with the least sediment sorting have greatest residual age.
- Factor analysis potentially provides a means of differentiating deposit types and depositional process based upon combined OSL and GSA analyses, although the sample suite investigated here was limited through poor acceptance rates of quartz from some of the catchments investigated.
- Quartz and feldspar residuals cannot be compared effectively in factor analysis due to their different bleaching responses during deposition in glacial environments.

6.12. Further Avenues of Research

The catchments selected for this investigation are complex depositional environments. Investigation of a more constrained system of limited sediment sources,

transport and depositional processes would provide a robust proof of concept for the use of OSL as a provenance and depositional pathway tracer. This would improve understanding of the specific provenance and transport controls on sample luminescence properties, and would enable more successful application of the technique in complex depositional environments, such as the glacial environment analysed here.

The poor luminescence sensitivity of the quartz sample suite investigated here has limited this research. Repeating this investigation in a catchment where quartz has improved luminescence sensitivity would improve quantification of absolute residuals for the different source materials and deposits. Evaluation of signal evolution at a larger scale (e.g. 10^2 or 10^3 km), with a reduced sampling resolution, may also provide a more efficient means of investigating depositional process signatures. This would also enable changing quartz sensitivity as a function of sediment reworking to be explored more fully, which may also contribute valuable provenance information.

The comparisons drawn between the quartz and feldspar data explored here are valuable as they illustrate the increased bleaching of quartz, in comparison to feldspar within some depositional environments and over short transport distances. The results also illustrate the importance of bar top transport and deposition, and how the bleaching rate on bars can be very rapid. This is similar to the difference between the rates of transport and downstream fining and sorting trends in channels (low) versus bars (high). Quantifying how sediment transport rates and luminescence characteristics are linked would further enhance our understanding of how transport and depositional processes modify luminescence behaviour. Time limitations have precluded analysis of quartz and feldspar pairs for all of the samples, and given the poor luminescence sensitivity of the quartz under investigation sufficient replicates may not be achievable. However, it is recommended that comparisons are investigated in future research, as identifying depositional environments where feldspar are well bleached will provide the best opportunity for successful OSL dating where quartz luminescence sensitivity is poor. More effective screening of quartz luminescence properties at the outset of any future OSL investigation using the protocol proposed in Chapter 4 is also recommended, to improve analytical efficiency.

Chapter 7. Quartz Emission Spectroscopy

7.1. Introduction

The first part of this thesis has demonstrated how OSL dating can be used to answer geomorphological questions; however, the challenges of dating quartz with poor luminescence QE have become apparent. The controls over quartz OSL QE remain unclear but have been linked to geological provenance (Götze et al., 2004; Rink et al., 1993; Westaway, 2009), irradiation (Rink, 1994), transport and thermal histories (Pietsch et al., 2008; Preusser et al., 2006). However, quartz with the same irradiation, source and depositional histories often exhibit highly variable emission intensities (Duller et al., 2000; McFee and Tite, 1998). The light emitted by quartz most commonly comprises bands in the UV-blue and red/IR (Krbetschek et al., 1997). Risø readers, the most widely used OSL instrumentation, stimulate the quartz with diodes at 470±20 nm (2.6 eV) and measure the response through Hoya U340 filters (Bøtter-Jensen et al., 2000). The transparency of these filters lies between 3.4 and 4.6 eV and only a part of the UV-blue emission band is monitored. The remainder of the emission (below 3.4 eV and above 4.6 eV) is unmeasured in conventional OSL but may contain significant dosimetry or geological provenance information. Therefore, the objective of the second part of this thesis is to explore the specific characteristics of the different luminescence centres in quartz to determine why some quartz have low luminescence QE and are therefore challenging OSL dosimeters. This has been achieved through emission spectroscopy using a variety of different excitation methods. Photoluminescence, cathodoluminscence and radioluminescence are described in this chapter; ionoluminescence investigations are described in Chapter 8 which is based on a paper, published in Radiation Measurements (King et al., 2011a), and x-ray excited optical luminescence (XEOL) investigations are discussed in Chapter 9, which is based on a paper presently in review for Radiation Measurements (King et al., 2011b). The different explorations are synthesised in Chapter 10.

7.2. Excitation Methods

Examination of luminescence emission spectra provides insights into the charge recombination centres (e.g. Krbetschek et al., 1997; Rink et al., 1993), in contrast excitation spectra enable exploration of the different electron donor-centres. Few authors have contrasted the excited and stimulated luminescence emission spectra of quartz (notable exceptions are Krbetschek et al., 1997; Martini et al., 1995; Rink et al., 1993; Schilles et al., 2001; Townsend et al., 1993), and few have contrasted emission spectra derived from different excitation methods. Five complimentary techniques were used to

explore the luminescence emission of quartz: photoluminescence (PL), cathodoluminescence (CL), radioluminescence (RL), ionoluminescence (IL) and x-ray excited optical luminescence (XEOL). The excitation energies of the different techniques vary markedly, as does charge carrier flux (e.g. protons in the case of ionoluminescence), and the degree of sample penetration (Table 7.1 and Figure 7.1). Brooks et al. (2002) demonstrated that CL, IL and RL are complimentary and that using a multi-excitation approach is valuable in exploring the emission centres of feldspar. Friis et al. (2011) more recently have used a similar approach and contrasted PL, CL, RL and IL of leucophanite and meliphanite to explore luminescence absorption and emission properties. Contrasting the different excitation techniques and energies will provide valuable insights into the nature of the different luminescence centres and defects of quartz and also controls on quartz luminescence QE.

Table 7.1: Excitation energies for the different techniques used within this research.

				X-irradiation	
Technique	PL*	CL	IL	RL	XEOL
Excitation Energy (eV)	2.4 - 4.1	15×10^3	0.95×10^6	20×10^3	7×10^3
Carriers s^{-1}		1×10^{15}	6.2×10^{11}		3×10^{12}
Carriers s^{-1} μm^{-2}		4×10^{15}	2.4×10^{10}		1.1×10^{16}
Estimated Dose Rate (Gy s^{-1})**		1.8×10^8	1×10^5	0.03	2.5×10^8
Sample penetration depth**	Surface to bulk	< 2 µm	10 µm	Bulk	200 µm

*The penetration depth of PL is dependent upon the wavelength used, the wavelengths used are not ionising, and therefore no dose rate has been calculated.
**Dose rate and sample penetration are sample dependent, all calculations are relative to quartz

Marfunin (1979) differentiates between three types of irradiation based excitation methods: 1) electromagnetic irradiation which encompasses PL and x-irradiation (RL and XEOL); PL excites without ionising samples whereas x-irradiation causes ionisation. 2) corpuscular irradiation which excites with charged particles and includes CL and IL, which result in the formation of defects, ionization, and centre formation; and 3) excitation by electrons trapped during irradiation, which Marfunin (1979) limits to release by heat (TSL) but is extended to optical release (OSL, Huntley et al., 1985).

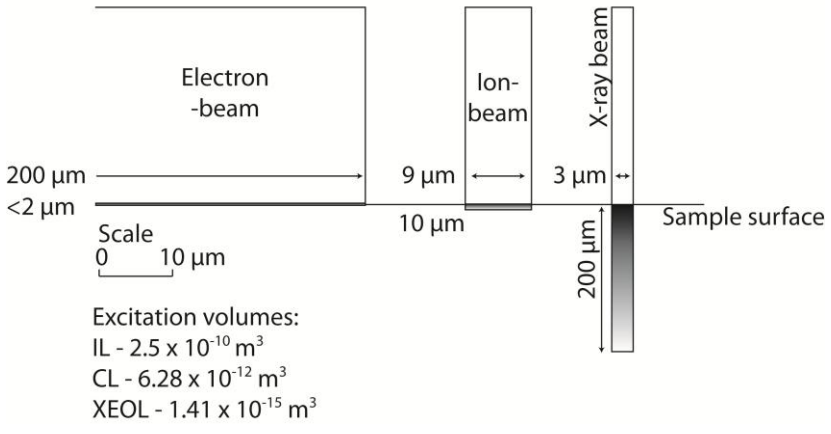

Figure 7.1: Beam diameters, penetration depths and excitation volumes for IL, CL and XEOL of quartz, density 2.65 kg m^{-3}

7.2.1. **Photoluminescence**

Photoluminescence comprises excitation through irradiation with photons typically within the UV or visible light range (Nasdala et al., 2004). As quartz has E_g of ~ 9 eV, type 'a' excitations as listed in Figure 2.1 are not possible as $E < E_g$ and rather type 'e' transitions are observed. Photoluminescence therefore offers an extremely versatile method through which the different defects of a mineral can be probed, especially where the excitation wavelength can be tuned (e.g. Friis, 2009). Photoluminescence has been used to characterise the 4.4 eV emission of quartz e.g. Gee and Kastner (1979) first reported observation of the 4.4 eV intrinsic emission of unirradiated, and irradiated (α)SiO_2 using *E* of 7.6 eV under vacuum at 15 K

7.2.2. **Cathodoluminescence**

Cathodoluminescence comprises electron irradiation of a sample and is sufficiently energetic to promote direct inter-band excitation and luminescence emission. It is widely used to characterise geological samples (see Pagel et al., 2000), particularly quartz (see Götze et al., 2001 for a review). Quartz CL spectra have been used to make inferences about crystal composition (e.g. Rusk et al., 2006), and irradiation history (e.g. Botis et al., 2006) although overlap in emission spectra has made provenance analyses challenging (e.g. Boggs et al., 2002).

The great disadvantage of CL is that it has very shallow sample penetration, which causes rapid sample degradation due to its high excitation density. The caveat is that the emission intensity is bright, making this a suitable technique for exploration of dimly luminescent materials, such as quartz. The interaction of CL with quartz has been modelled using CASINO v 2.42 (Drouin et al., 2007). At an incident energy of 15 kV and an electron beam diameter of 2 mm (see section 7.5) quartz is excited to a maximum depth of ~ 2 µm, although maximum excitation is at ~ 1.3 µm penetration (Figure 7.2).

The current for the CL analyses fluctuated significantly throughout analysis (see discussion in section 7.5), but was kept to approximately 2.0 x 10^{-4} A. Beam voltage (*E*) was 15 kV and dose rate (Gy) can also be calculated using Eq. 7.1, where *t* is time (s), *e* is the electron charge constant 1.6 x 10^{-19} C, and *m* is the mass of the irradiated area (see Table 1).

Eq. 7.1: $$Dose\ rate\ (Gy\ s^{-1}) = \frac{\left[t\left(I\left(\frac{1}{e}\right)\right)E\right]e}{m}$$

The excited mass is low for CL because of its shallow penetration (see Table 7.1), thus for a beam of 200 µm diameter and penetration 2 µm, the excited mass is 1.67 x 10^{-8}

kg and excitation energy is 1.9 x 10^{19} eV s^{-1}, with a charge carrier flux of 4 x 10^{15} μm^{-2} s^{-1} and an approximate dose rate of ~ 1.8 x 10^{8} Gy s^{-1}. As maximum energy delivery occurs at 1.3 µm, the true dose rate will be greater at depths < 1.3 µm and reduced at greater depths, averaging dose rate across the entire excitation volume overcomes these penetration dependencies.

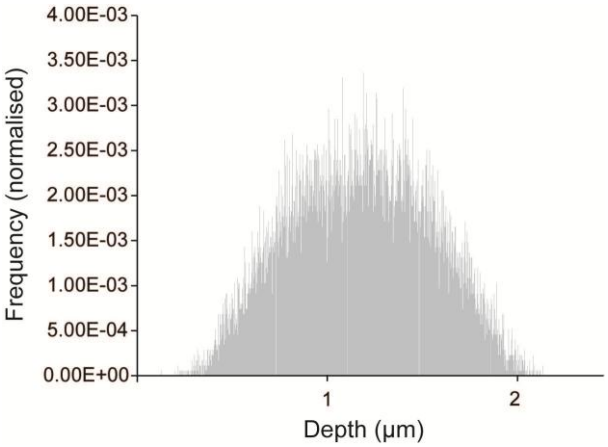

Figure 7.2: CASINO model results for sample excitation with an electron beam of 15 keV and 2 mm Ø. The frequency histogram indicates that most energy is deposited at ~ 1.3 µm depth.

7.2.3. **Ionoluminescence**

Ionoluminescence comprises the implantation of a sample with ions of specific mass and charge e.g. protons (see Chapter 8), accelerated to energies of MV. The current for the IL analyses was recorded at the outset and end of each measurement, and the mean average used for normalisation, the voltage (E) was kept at 9.5 x 10^{5} V for all experiments. Dose rate was calculated from Eq. 7.1 and the excited mass was 6.63 x 10^{-7} kg. The ion flux for a current of 1 x 10^{-7} A, was 6.9 x 10^{11} ions s^{-1}, and each ion had energy of 1.52 x 10^{-13} J. This corresponds to a typical dose rate 6.6 x 10^{17} eV s^{-1}, or 1.3 x 10^{5} Gy s^{-1}. Where this is calculated relative to the beam area the delivery rate of charge carriers is 2.5 x 10^{10} μm^{-2} s^{-1}. The high excitation energy of this method makes direct inter-band excitation possible and IL enables observation of emission bands absent from PL (Marfunin, 1979).

7.2.4. **X-irradiation**

Two types of x-irradiation have been contrasted throughout this research: polychromatic x-irradiation (referred to as RL throughout this thesis) which delivers a range of excitation energies, and monochromatic synchrotron x-irradiation (referred to as XEOL). The XEOL experiments comprised excitation with monochromatic synchrotron light of ~ 7 keV = 1.14 x 10^{-15} J $photon^{-1}$. The photon flux at Diamond is ~ 3 x 10^{12} photons s^{-1} (Mosselmans et al., 2009) although filtering and mirrors reduce this by ~ 75 % at the

sample position which equates to a flux of ~ 7.5 x 10^{11} photons s^{-1}, not dissimilar to that delivered in IL. However, whereas the ion beam has an area of 250 μm^2, the x-ray beam has an area of 0.0007 μm^2, which results in an excitation energy of 6.25 x 10^{15} eV s^{-1}, or dose rate of 2.48 x 10^8 Gy s^{-1}. Furthermore as charge carriers are delivered over a more restricted area, delivery is 1.06 x 10^{16} μm^{-2}, which is significantly greater than for the IL or CL under the experimental conditions presented here.

7.3. Samples

7.3.1. **Calibration Quartz**

Calibration quartz (CalQz) has predictable OSL behaviour and was used to provide a standard for both the OSL analyses and spectroscopic investigations described in this thesis (see Appendix A for details). Batch 8 was used for the PL, CL, RL and IL investigations, and Batch 34 for the XEOL investigations, as Batch 8 had been exhausted.

A series of CL images of CalQzB8, were taken using the CL imaging system at the University of St Andrews, which is a Technocyn 8200 mk V cold-cathode luminoscope on a Nikon Optiphot microscope. Beam conditions were maintained at ~600 µA and ~15 kV, which correspond to power density ~ 40 kW m^{-2}. Images were collected with a DVC high sensitivity CCD camera using EPIX software. Typical exposure times were 8 s. It is apparent that few of the grains exhibit bright CL, and that two distinct populations of grains are present: bright material that luminesces in the blue, and less bright material that luminesces in the yellow. Image contrast and brightness has been amended in Adobe Photoshop CS.

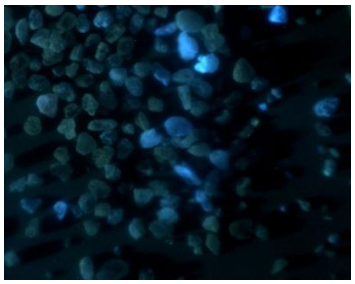

Figure 7.3: CL image of CalQzB8. No scale is provided on the image but quartz grains are ~ 200 µm in diameter.

7.3.2. **Water of Tulla Quartz (WTUL1 & WTUL2)**

The OSL properties of the Water of Tulla samples are described in Appendix D. They are derived from granitic bedrock and geomorphological evidence indicates that they were deposited in a glaciofluvial outwash deposit during final deglaciation of Scotland, confirmed by OSL dating. These samples are similar in geological and depositional history

to the Norwegian samples, and were investigated in their stead for the IL and XEOL experiments. This was because the IL experiments were carried out prior to Norwegian sample collection. To facilitate inter-comparison between the emission spectra derived from the two different excitation methods, the same sample suite was explored for XEOL as for IL. The WTUL samples were also analysed with CL and RL.

CL imaging of the WTUL samples demonstrates that two populations are apparent, those that are brightly luminescent in the blue, and a larger population of dimly luminescent yellow grains. These grains were observed to be IR responsive throughout OSL analyses, however optical examination confirmed that no discrete feldspar were present. It may therefore be that these grains contain feldspar inclusions, which may account for the yellow grain population (see Chapter 5 for a discussion of the emission spectra of feldspar). Interestingly the population of brightly luminescent grains for WTUL2 (Figure 7.4) is similar in size to that of CalQzB8 (Figure 7.3) despite WTUL2 having less favourable OSL characteristics (see Appendix D). The CL imaging reported here was qualitative, and therefore it is not possible to make any absolute determinations regarding the relative proportions of brightly CL luminescent and non-luminescent grains.

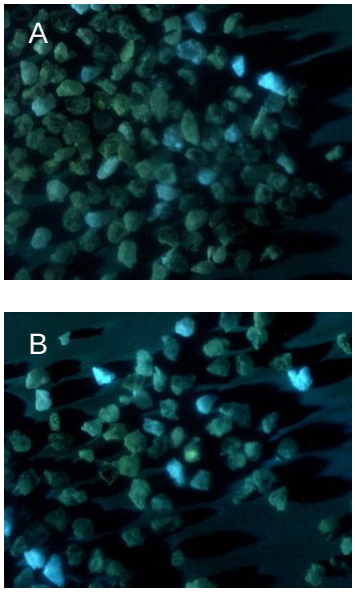

Figure 7.4: CL image of WTUL1 (A) and WTUL2 (B). No scale is provided on the image but quartz grains are ~ 200 µm in diameter.

7.3.3. **Norwegian Quartz**

The OSL properties of the Norwegian quartz sample suite have been extensively characterised in Chapter 4, therefore only a brief description of the individual samples analysed for emission spectroscopy is provided. Details regarding specific sample location are provided in Appendix C. FAB42/79/92 were analysed with CL and FAB84 with RL only. FAB42 has the greatest OSL sensitivity of the Norwegian samples analysed for emission spectroscopy, and FAB92 the lowest OSL sensitivity. Only FAB79 was

investigated with CL imaging, which showed that the grains are sub-angular to angular, suggestive of limited fluvial transport and therefore sediment reworking (Figure 7.5). Only one grain is brightly luminescent which is indicative of the poor luminescence sensitivity associated with the Norwegian sample suite.

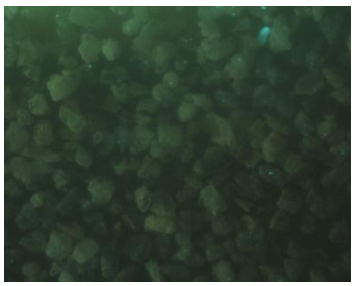

Figure 7.5: CL image of FAB79. No scale is provided on the image but quartz grains are ~ 200 µm.

7.3.4. **Hydrothermal Quartz Macrocrystal**

A natural hydrothermal quartz macrocrystal was also analysed in addition to the polygrain 180 – 212 µm Ø samples. The macrocrystal had *c*-axis length of ~ 35 mm, and was cut parallel (QzPara) and perpendicular (QzPerp) to *c*, in order that the effects of crystal anisotropy on the emission spectroscopy of quartz could be explored.

7.4. Photoluminescence

Samples were screened using two different photoluminescence systems at the University of St Andrews. CalQzB8 only, was explored with the first system: a modified Spex Fluorolog 2 fluorescence spectrometer, which has a peltier-cooled Hamamatsu 928R PMT and for which the excitation source is a Xe lamp (emission 240-600 nm), filtered with a monochromator (see Friis, 2009 for system details). All samples were analysed with the second system which is a UV laser (375 nm, 3.31 eV) Edinburgh Instruments time-resolved imaging system. As $E < E_g$, only transitions of type 'e' (Figure 2.1) could be observed, and thus PL examinations of the quartz provided a screening mechanism for defects of specific absorption characteristics.

No luminescence emissions were observed for either system. As the Xenon lamp PL involved excitation from 300 – 600 nm (2.1 – 4.1 eV), no defects with absorption in this range were identified for CalQzB8. Similarly for those samples analysed with the Edinburgh Instruments system, no defects with absorption of 375 nm (3.3 eV) were identified. Pure quartz (i.e. SiO_2) is transparent within the < 5 eV UV range (e.g. Gurkovskii et al., 1974), however the PL results are surprising as an absorption band at 3.8 eV has been associated with peroxy linkages (≡Si-O-O-Si≡) (Nishikawa et al., 1989) in oxygen rich quartz, although Itoh et al. (1988) did not record this absorption band for

Sawyer premium grade synthetic quartz which is known to be oxygen deficient (Stevens-Kalceff and Phillips, 1995). Thus, tentatively, it might be inferred that the samples analysed here may be oxygen deficient, although this is not supported by the XEOL analyses (Chapter 9).

At the time of these experiments facilities were unavailable for low temperature PL analyses in the Department of Earth Sciences at the University of St Andrews, which would have increased resultant luminescence emissions through reduced phonon interaction with the luminescence centres, similarly more energetic PL excitation light sources were unavailable, as were facilities for PL either under vacuum or with UV detection, and consequently these experiments were not continued.

7.5. Cathodoluminescence

Spectroscopic CL and RL experiments were carried out on the CL/RL/TL system developed by Peter Townsend at the University of Sussex, which was moved to the University of St Andrews in June 2008. Full details of the system and later modifications are given in Luff and Townsend (1993) and Wang (2007). The instrument has f2/2 optics and due to an intermittent fault in the UV sensitive PMT, spectra were detected with a single PMT sensitive between 400 - 800 nm (1.6 - 3.1 eV). Excitation for CL is delivered by an electron beam, and for RL from a Philips MSN-101 X-ray tube. The instrument is equipped with a heating and cooling stage, which enables spectra to be collected in the range 40-700 K, however the temperature stages were not fully functioning throughout the experiment period and all data reported here were collected at room temperature. Samples are mounted on a horizontal stage at 45˚ to the spectrometers.

Cathodoluminescence causes rapid sample degradation due to the high excitation density caused by its relatively low sample penetration depth (Figure 7.1), consequently the duration of sample exposure is important to interpreting emission spectra. This presented a number of problems with the experimental setup as full beam stabilisation was not possible within 10 minutes, therefore samples analysed inevitably had some modification. The beam focus was extremely variable and required manual monitoring and adjustment throughout analysis, achieved through positioning a magnet adjacent to the beam, on the system outer casing. All analyses were carried out at 0.2 mA and 15 kV. Two filters, one at 400 nm and a second at 450 nm are positioned in front of the PMT to ensure that doublets from lower wavelength emission are not detected (Luff and Townsend, 1993). No system correction has been applied to either the CL or RL spectra, however all spectra have been background corrected and converted to energy space

through calculation of eV from wavelength, and by calculation of I(E)dE from I(λ)dλ by multiplication by energy^2 (Hamilton et al., 1978).

7.5.1. **Background Calculation**

As the objective of the spectroscopic analyses is to relate observed emissions to the properties of OSL samples, samples were initially mounted on stainless steel discs, coated with silicone grease as is conventional in OSL analyses (see Chapter 4). However, CL analyses indicated that the silicone grease has a broad blue (2.6 eV) luminescence emission (Figure 7.6). Spurious OSL from silicone grease has previously been reported (Vandenberghe et al., 2008), although the physical process responsible has not been suggested. Consequently two other substrates were investigated: UHU glue diluted with acetone on stainless steel discs, and 12 mm carbon tabs manufactured by Agar which are conventionally used to mount samples for SEM analyses. The glue exhibits a 2.5 eV blue emission, and the carbon tabs a 2.45 eV emission (Figure 7.6). All CL spectra also exhibit a red emission at ~ 2.2 eV which is attributed to filament glow and may have substantial influence where the sample CL emission is dim.

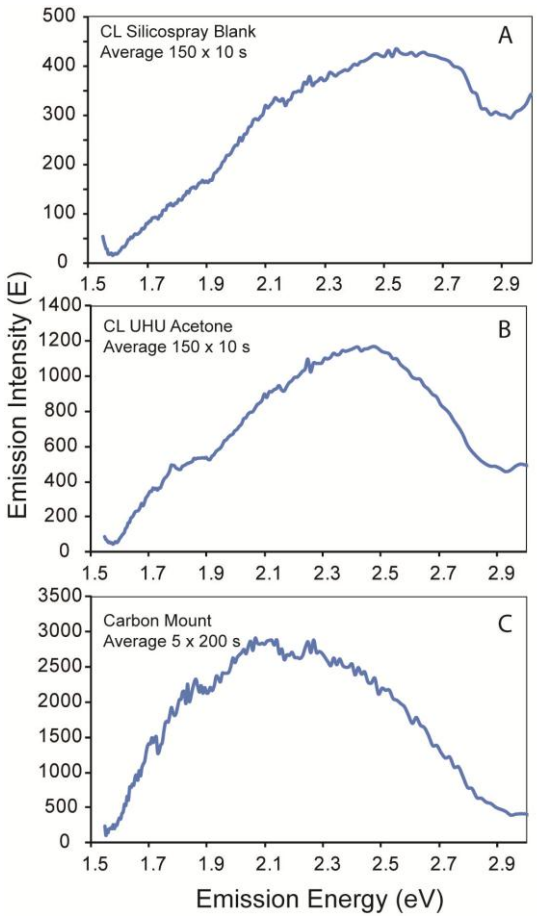

Figure 7.6 (left): CL emission spectra of (A) a silikospray coated stainless steel disc, (B) a stainless steel disc coated with UHU, diluted with acetone, and (C) a carbon tab. The filter stack used in the sample analyses was not used during collection of these spectra.

Figure 7.7 (below): CL emission spectrum of a blank stainless steel disc. The 400 and 450 nm filter stack has been used, explaining the curtailment of the emission at ~ 2.7 eV.

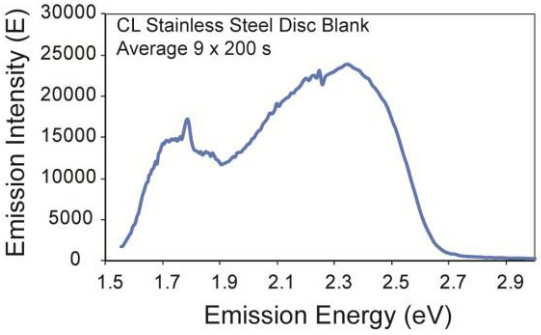

Analysis of a completely blank stainless steel disk which had been cleaned with acetone had a red emission at 1.8 eV. Steel is a conductor and so does not luminesce, therefore the emissions observed in Figure 7.7 may also relate to filament glow, an oxidation layer on the disk itself or on the brass sample holder, or to residue within the sample chamber. As the carbon tabs exhibited the lowest background when corrected for integration time, these were selected as the substrate for all further CL analyses.

The stability of the signal from the carbon tabs as a function of exposure time was explored in a further experiment. Three tabs were analysed and all exhibited depletion in total emission with increasing exposure to the electron beam. This is problematic as the emission spectrum of quartz is known to be sensitive to irradiation, and modifies rapidly throughout CL analysis (e.g. Luff and Townsend, 1990; Perny et al., 1992). The UV emission is observed to reduce to the benefit of the red emission (see Chapters 8 and 9), consequently similar behaviour in a tab could result in false positive results. The ratio of the blue (501 nm, 2.5 eV) to red (651 nm, 1.90 eV) emission, as a function of irradiation time were explored, to characterise better the shift in luminescence observed here. It should be noted that the 2.5 eV emission peak identified is most probably the shoulder of a broad emission, centred at higher energy, but has been truncated by the filter stack. It is apparent that both the blue and red emissions reduce as a function of irradiation (Figure 7.8), and that the blue emission depletes more rapidly than the red emission. Importantly, no relative increase in the red emission is observed, providing a means of determining whether the luminescence spectra recorded are influenced by the substrate.

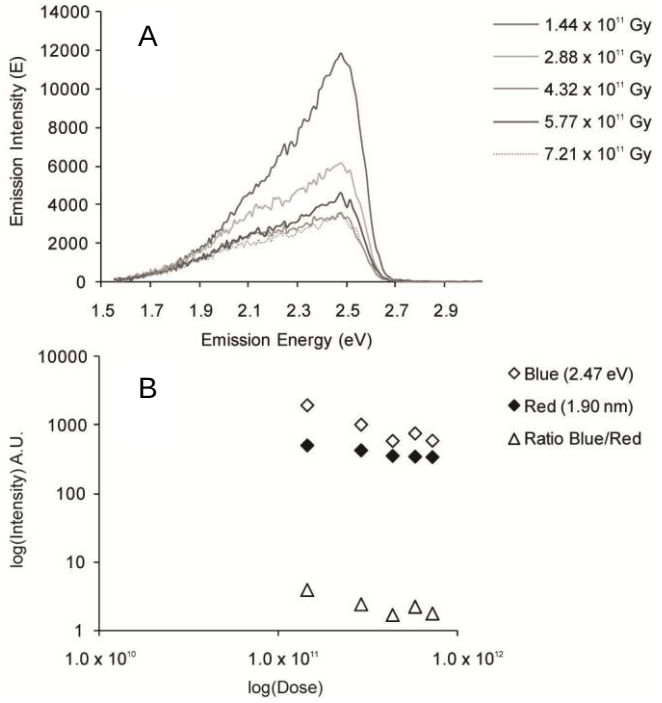

Figure 7.8: Dose dependence experiment results for a carbon mount. (A) The total emission reduces as a function of irradiation time, and (B) the blue emission depletes more rapidly than the red emission.

The carbon tab background signal has been determined from the most intense emission recorded i.e. the initial emission which was integrated over 800 s of irradiation

(Figure 7.8). It is acknowledged that this signal was most probably more intense during initial irradiation (i.e. t < 100 s), but also that increased integration periods will have improved the signal to noise ratio. Therefore where this emission is contrasted with quartz emissions collected over shorter durations, a correction factor is applied, e.g. the emission spectra of FAB42 are collected over 230 x 10 s intervals, which are binned into 300 s groupings, therefore a correction factor of 300/800 = 0.375 has been used to reduce the intensity of the carbon background signal appropriately.

7.5.2. **Cathodoluminescence of Calibration Quartz**

The CL emission spectrum of CalQzB8 is dominated by a broad emission at 2.5 eV, which is truncated by the filter stack (Figure 7.9). The emission intensity is significantly greater than that of the carbon tab. Current fluctuations throughout analysis precluded examination of emission modification as a function of irradiation time as although depletion in the blue emission to the benefit of the red was observed throughout analysis, recovery of the blue emission was apparent following 7 x 10^{11} Gy. Rather than indicating a recovery of the blue emission centres, this is interpreted to reflect migration of the beam onto a previously unexposed sample section. An emission at 2.16 eV developed after 2.8 x 10^{11} Gy, which was not observed in the other samples analysed (Figure 7.10). This is a similar energy to the filament glow recorded during the background measurements, however, as the filament glow is constant throughout analysis, this origin is discounted.

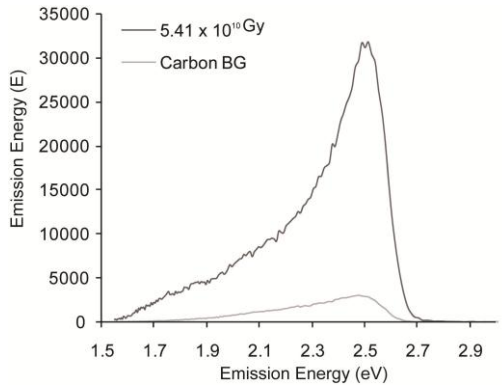

Figure 7.9: CL emission spectrum of CalQzB8 integrated over the initial 300 s (5.4 x 10^{10} Gy) of excitation.

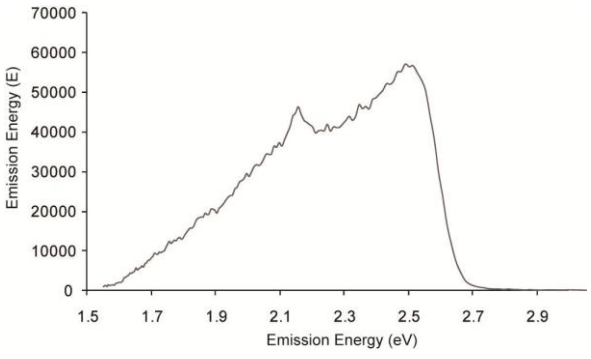

Figure 7.10: CL emission spectrum of CalQzB8, integrated over 300 s from 3000 – 3300 s excitation (5.95 x 10^{11} Gy to 5.77 x 10^{11} Gy). Note the emergence of the 2.16 eV emission.

7.5.3. **Cathodoluminescence of Norwegian Quartz**

7.5.3.1. FAB42

The emission spectrum is dominated by a 2.54 eV emission (Figure 7.11), which is more intense than, but the same energy as the carbon tab. This emission reduces as a function of irradiation time. The red emission is fully encompassed by the tab background, and no conclusions can be drawn regarding modification as a function of irradiation.

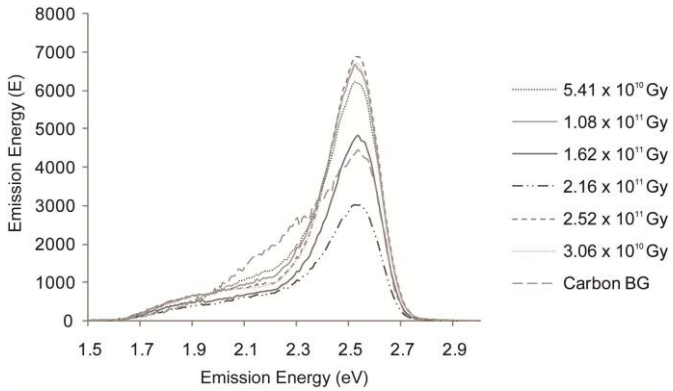

Figure 7.11: CL emission spectra of FAB42 mounted on a carbon tab. The carbon tab background is plotted alongside the emission spectra to highlight similarities and differences between the emission profiles.

7.5.3.2. FAB79

In contrast to FAB42, FAB79 exhibits clear dose dependence, whereby the initially dominant 2.48 eV emission depletes to the benefit of the red emission (1.9-2.0 eV, Figure 7.12). Although the blue emission cannot be distinguished from that of the carbon tab, the increase in red emission intensity is not a background effect, and is therefore attributed to FAB79.

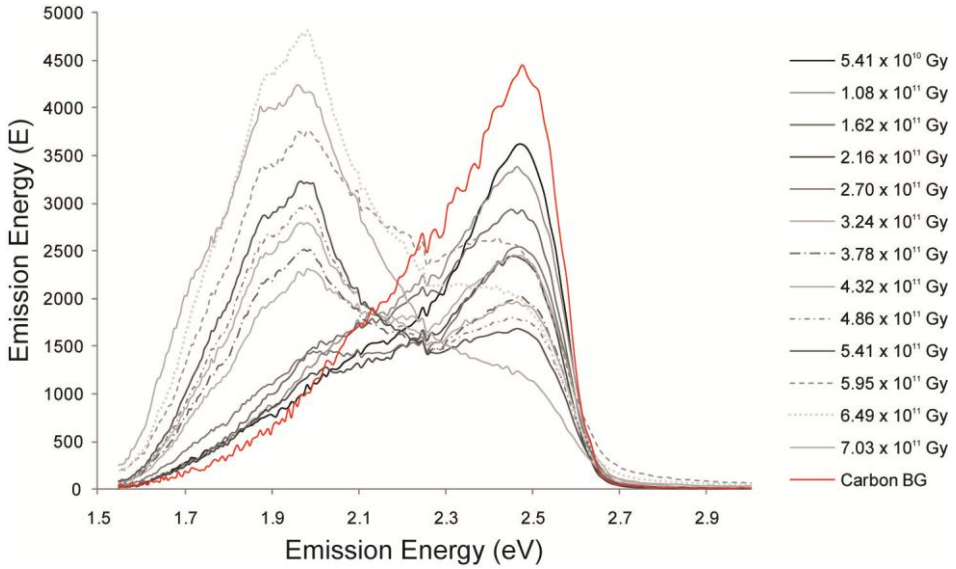

Figure 7.12: CL emission spectra following increased exposure of FAB79 to CL irradiation.

Deconvolution of the emission spectra was carried out using the Multipeak Fit 2.0 package in Igor pro V.6.2 (WaveMetrics, 2011). This program performs non-linear least squares fitting of the spectra using the Levenberg-Marquardt algorithm to iterate component fits which minimize χ^2. All components are assumed to be Gaussian in energy space and the autofit option is used. Deconvolution indicates a shift in the luminescence emission from the blue, to the benefit of the red, however curve fitting is adversely affected by truncation of the major, 2.7 eV blue emission (Figure 7.13). In the initial spectra, the red emission comprises a combination of a 1.8 and ~ 2.2 eV emission, whereas in the final spectrum a suite of red emissions are identified, ranging from 1.7 – 2.1 eV.

7.5.3.3. FAB92

The CL emission spectrum of FAB92 is similar to that of FAB42, no red emission development was observed, despite analysis for > 1,800 s which was the duration of irradiation prior to red emission development for FAB79. The intensity of the FAB92 spectrum does not exceed that of the carbon tab, however the emission spectra differ, as the emission centred at ~ 2.7 eV for FAB92 is narrower.

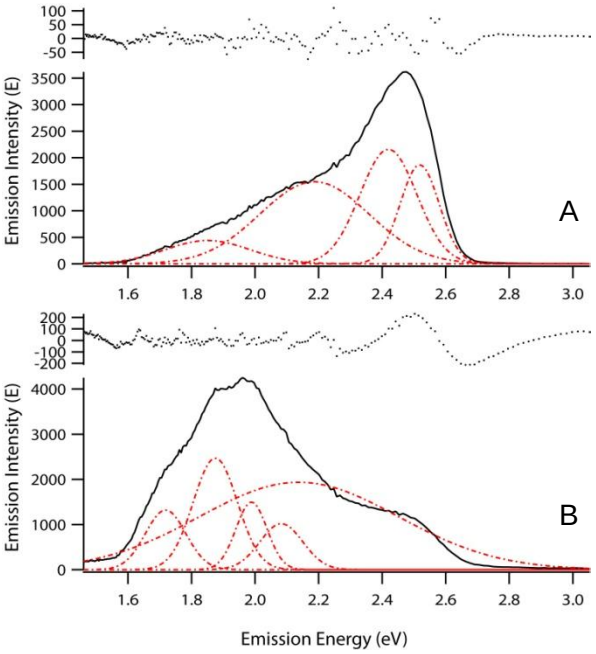

Figure 7.13: CL emission spectra and deconvolution of the (A) initial (5.41 x 10^{10} Gy) and (B) final (7.03 x 10^{11} Gy) CL emission spectra for FAB79

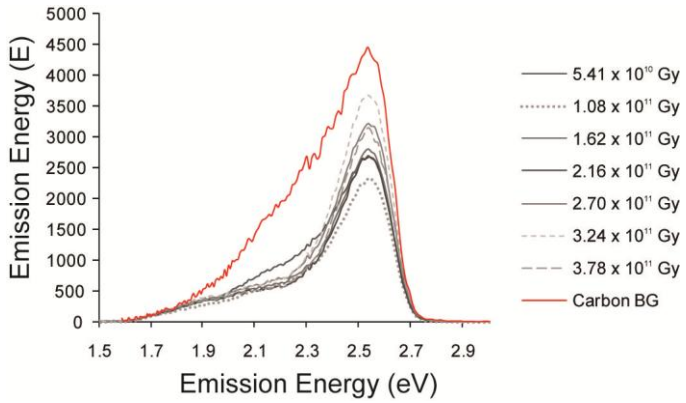

Figure 7.14: CL emission spectra for FAB92.

7.5.4. **Cathodoluminescence of a hydrothermal Quartz Macrocrystal**

The hydrothermal quartz macrocrystal was mounted directly onto the sample stage, rather than onto a carbon tab, and 30 x 10 s emission spectra were collected. The emission intensity of this sample was much greater than for the remainder of the sample suite, however due to the variable stability of the electron beam, this cannot be regarded as a true indication of improved luminescence quantum efficiency (QE). The emission spectra have been averaged into three spectra which are plotted in Figure 7.15, to enable clearer comparison. This sample is also dominated by a blue emission, despite not being mounted on a carbon stub, confirming that at least part of the observed emissions for the other samples originates from the quartz itself.

A shift in emission from the blue to the red with increased sample exposure is apparent, as for FAB79, which is more clearly considered where the ratios of the blue/red emissions are contrasted. This shift occurs following 3.6 x 10^{10} Gy for this sample, in contrast to following 2.7 x 10^{11} Gy of exposure for FAB79.

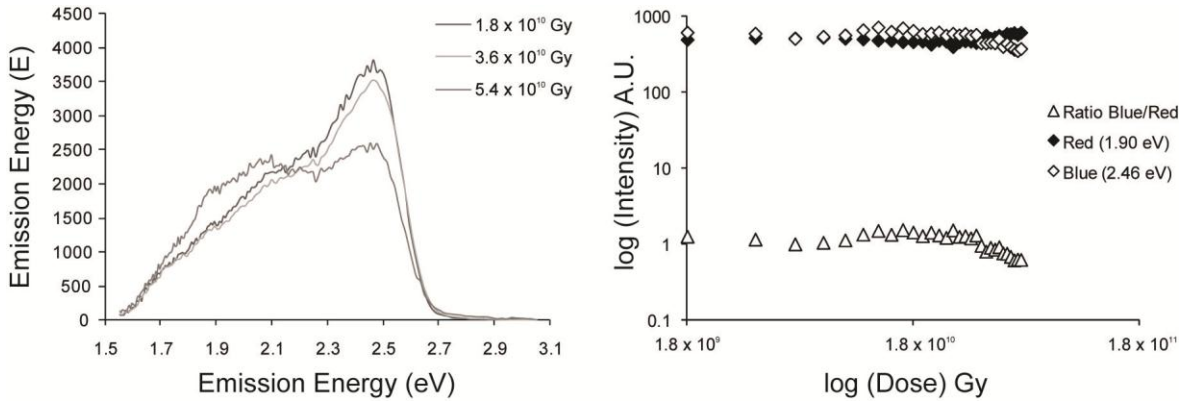

Figure 7.15: CL emission spectra and dose dependence of the blue (498 nm) and red (605 nm) emissions of the hydrothermal quartz macrocrystal.

Deconvolution of the QzMacro emission spectra indicates that the red emission is dominated by an emission at 1.9 eV, which shifts to 1.86 eV at the end of excitation

(Figure 7.16). The two other emission peaks identified are at ~ 2.2 and 2.5 eV and also do not shift significantly throughout excitation, although the 2.2 eV emission which also contributes to the red emission, increases in intensity.

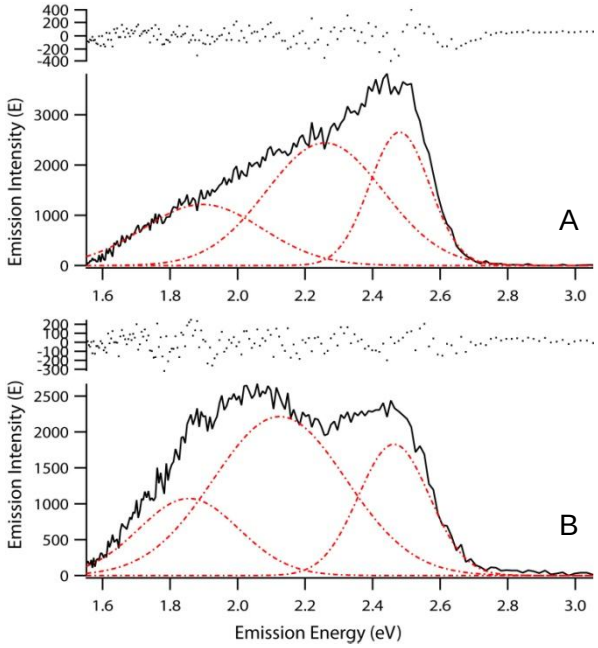

Figure 7.16: Deconvolution of the (A) initial (1.8 x 10^{10} Gy) and (B) final (5.4 x 10^{10} Gy) CL emission spectra for QzMacro.

7.5.5. **Discussion of CL emission spectra**

All samples were initially dominated by a broad blue emission which was truncated at ~ 2.7 eV (450 nm) by the filter stack. This emission is likely to comprise a composite of the 2.7 eV (450 nm), 2.5 eV (500 nm) and 2.1 eV (580 nm) emissions which have been widely reported for quartz (e.g. Götze et al., 2001; Stevens-Kalceff and Phillips, 1995). The 2.7 eV emission is attributed to the self-trapped exciton (STE) (Stevens-Kalceff and Phillips, 1995; see Chapters 9 and 10 for a discussion) and the 2.5 eV emission to ion impurities of Al^{3+} charge compensated by Li^{+} (Perny et al., 1992). The 2.1 eV emission has been related to either oxygen vacancies (E' centres) (Götze et al., 1999; Rink et al., 1993) or to the STE (Itoh et al., 1988; Stevens-Kalceff and Phillips, 1995), see Götze et al. (2001) for a review. Other red emissions in quartz have been related to non-bridging oxygen hole centres (NBOHCs) e.g., 1.88 eV, Stevens-Kalceff and Phillips (1995) or to the substitution of Si^{4+} with tetrahedral Fe^{3+} e.g. 1.75 eV, Pott and McNicol (1971). The emission spectra could be deconvolved to assess the relative contributions of these different emission centres, however the truncation of the main emission peak seriously affects curve fitting.

CalQzB8 exhibits a distinct 2.16 eV emission not identified in the emission spectra of the other samples, which develops following 2.7 x 10^{11} Gy of irradiation (Figure 7.10). Excitation at 15 kV and 0.2 A, which were the parameters used in the CL spectroscopy

experiments, delivers an excitation density of ~ 13 kW m^{-2} at the sample surface, causing rapid sample modification throughout analysis. The 2.16 eV emission is likely to reflect increased modification of the crystal lattice as additional defects are created in the form of oxygen vacancies (*E'* centres). This is consistent with Götze et al.'s (1999) observation that yellow, 580 nm emissions (2.14 eV) are most commonly observed in hydrothermal vein quartz of acidic volcanoes which are noted for their high concentration of oxygen vacancies.

The emission spectra of FAB42 and FAB92 are very similar, which is interesting given their extremely different OSL QE. FAB42 has an average OSL signal response 6 times greater than FAB92. FAB79 in contrast exhibits significant irradiation dose dependence, whereby the blue emission at 2.5 eV depletes to the benefit of a red emission, which comprises a range of components with energies of 1.7-2.0 eV. The broad red emission present in the carbon tab spectra exhibits no increase in luminescence intensity as a function of dose, and therefore this emission is attributed to an irradiation induced shift in the luminescence emission centres of quartz. This phenomenon is also observed for the hydrothermal quartz macrocrystal (Figure 7.15 & Figure 7.16), and has been observed in CL by a range of authors (e.g. Stevens-Kalceff and Phillips, 1995) who have attributed it to the development of non-bridging oxygen hole (NBOHC) centres, which are formed through the irradiation induced modification of precursor centres such as Silinol groups (≡Si-O-H) which form a NBOHC (≡Si-O$^{\bullet}$) after the O-H bond has been broken by the incident beam; or through the development of oxygen vacancies (Luff and Townsend, 1990). Natural crystals may also exhibit regions where the red emission is dominant, termed halos (e.g. Botis et al., 2005; Owen, 1988), which are attributed to alpha irradiation damage from the decay of adjacent radionuclide bearing grains (Komuro et al., 2002). The irradiation sensitivity observed here is also recorded in quartz IL (see Chapter 8) and XEOL (see Chapter 9), and is discussed more extensively in the synthesis in Chapter 10.

The relationship of blue emission depletion to the red can be fitted with a power-law relationship, which forms a straight line in log-log space (Figure 7.17), using the calculation $A e^{-mD}$ where A is the pre-exponential factor, dependent on initial signal intensity, *m* is the gradient of the relationship and *D* is the duration of irradiation (s). These data are listed for QzMacro and FAB79 in Table 7.2. Little association is observed between the A and *m* values of the different samples, which may relate to fluctuations in beam *I* throughout analysis, although consideration of the ratio between emissions should average out beam effects; dose dependent relationships are considered in more detail in Chapter 10.

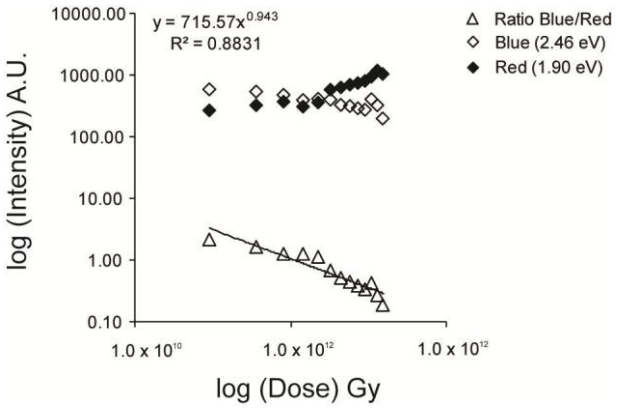

Figure 7.17: Dose dependence of the blue (498 nm) and red (605 nm) CL emissions of FAB79. The ratio of the blue/red emissions has been fitted with a power relationship in log-log space, the equation of which is shown on the plot.

The CL data presented here are limited by the background signal of the carbon tabs used as the substrate for the quartz samples, although analyses of the quartz macrocrystal which was not mounted onto a carbon tab exhibited the same blue emission, confirming that it originates from quartz. Beam instability has limited the comparisons that can be made both between spectra of different samples and the carbon tab background spectra, due to fluctuations in intensity. Beam migration during analysis also influences emission spectra, as observed for CalQzB8 (see Section 7.5.2) and so limits exploration of dose dependent effects. A final limitation is the intermittent fault of the UV detector, which precluded analyses between 200 – 400 nm where much of the quartz emission occurs, and the necessary truncation of the emission spectra by the 400 and 450 nm filters.

Table 7.2: Slope and pre-exponential factors (A) calculated for FAB79 and QzMacro for emissions at 2.47 eV, 1.97 eV and the ratio 2.47/1.97 eV. 2.47 eV is not the true peak of the blue emission (2.7 eV) due to curtailment of the spectra by filters, discussed in the text.

Sample	$A^{2.47}$	$m^{2.47}$	r^2
FAB79	3.63 ± 0.40	-0.33 ± 0.12	0.72
QzMacro	3.00 ± 0.14	-0.14 ± 0.07	0.36
	$A^{1.97}$	$m^{1.97}$	
FAB79	0.78 ± 0.54	0.61 ± 0.16	0.84
QzMacro	2.62 ± 0.10	0.03 ± 0.04	0.07
	$A^{2.47/1.97}$	$m^{2.47/1.97}$	
FAB79	2.85 ± 0.68	-0.94 ± 0.20	0.88
QzMacro	0.37 ± 0.23	-0.17 ± 0.11	0.26

7.6. Radioluminescence

The equipment used for the RL experiments is detailed in section 7.5. Samples were irradiated at either 20 or 40 kV and spectra integrated between 100 and 300 s. CalQzB8,

FAB84, WTUL1 and a different quartz macrocrystal sample, from the same crystal but cut perpendicular to the *c*-axis (QzPerp) were analysed. With the exception of QzPerp all samples were mounted on carbon tabs which had the lowest background emission for RL of the substrates analysed (Figure 7.18). QzPerp was mounted directly onto the brass sample holder. All samples are background corrected and where emission integrations are shorter than the 300 s background integration, they have been adjusted as detailed for the CL emission spectra (see section 7.5.1). A 400 nm filter was used for all emissions with the exception of QzPerp where the 450 nm filter was also used.

Emission intensity varied significantly between samples, and CalQzB8, which was the only sample irradiated at 40 kV, exhibited extremely dim RL intensity (Figure 7.19), as did FAB84 which was irradiated at 20 kV. In the case of CalQzB8 this may be related to the relatively short signal integration period (100 s, 6 Gy). Deconvolution of the CalQzB8 emission spectra indicated 3 emission peaks at 1.5, 2.0 and 2.8 eV (826, 620 and 442 nm). The 1.5 eV emission may be a doublet of the 2.8 eV emission, as the 450 nm filter was not used in spectra collection.

In contrast WTUL1 and QzPara have bright emission spectra (Figure 7.20), and WTUL1 also exhibits emissions at 1.5, 2.0 and 2.7 eV (826, 620 and 459 nm). As the RL emission of QzPara was collected with both the 400 and 450 nm filters, the emission spectrum indicates a peak at 2.5 eV which is interpreted as the shoulder of the 2.7 eV emission observed for this sample in IL and XEOL analyses (see Chapters 8 and 9), and for the CalQzB8 and WTUL1 RL spectra. The 2.0 eV emission is not discernable from the emission spectrum and deconvolution identified only a single emission peak at 2.4 eV, demonstrating that where filters have significantly truncated the emission spectrum, curve fitting is seriously affected.

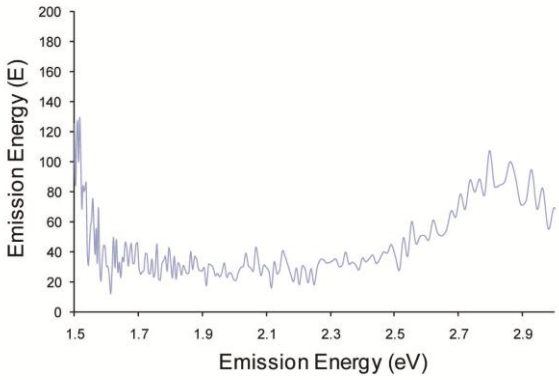

Figure 7.18: Carbon tab RL background emission spectrum, integrated over 300 s (9 Gy). Note that maximum emission energy is 140 and that the background increases towards the spectrometer detection limit.

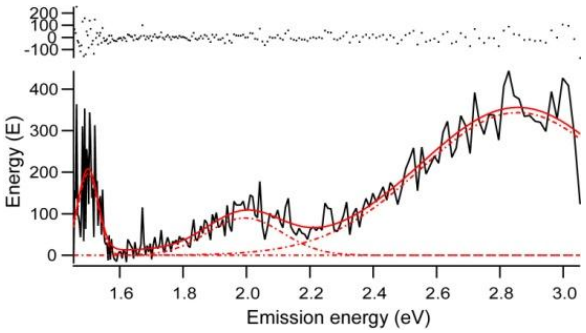

Figure 7.19: Background corrected RL emission spectra for CalQzB8, integrated over 100 s (3 Gy). Note that no filters were used during collection of this spectrum.

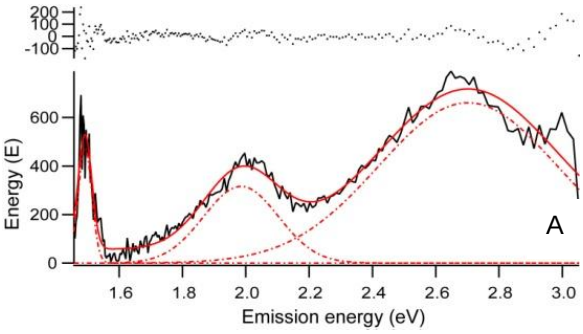

Figure 7.20: (A) WTUL1 RL emission spectrum and (B) QzPara RL emission spectrum. Note that in contrast to the other spectra collected, the 450 nm (2.76 eV) filter was also used for QzPara.

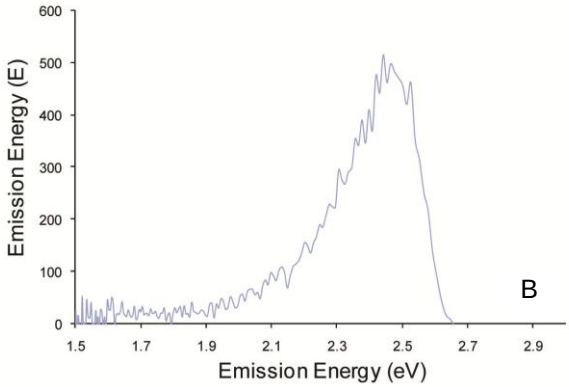

7.6.1. **Discussion of RL Emission Spectra**

Various authors have investigated the RL of quartz e.g. Schilles et al. (2001) identified three RL emission bands at 360, 470 and 630 nm (3.4, 2.6 and 2.0 eV) which are in agreement with Krbetschek's earlier research (1997). The 3.4 eV emission is unfortunately beyond the detection range of the spectrometer used here, however the 2.6 and 2.0 eV emissions are observed for WTUL1 and CalQzB8. The 1.5 eV emission observed in the CalQzB8 and WTUL1 RL spectra may be a doublet, recorded due to analysis without the 400 and 450 nm filters, although an emission of this energy is recorded in the IL analyses (see Chapter 8). The origins of these emissions have been discussed in section 7.5.5, and are not repeated here. The 2.0 eV emission is absent in QzMacro, which is not regarded as a filtering effect, but may relate to a lower population of NBOHC as discussed in section 7.5.5.

7.7. Discussion of PL/CL and RL Emission Spectra

The emission spectra derived from the CL and RL experiments detailed here are limited due to low signal intensities, variable background emissions and challenging system set-up. The CL spectra have dramatically varying intensity due to beam instability which cannot be used to derive any conclusive inferences regarding the varying QE of quartz from different provenances. Similarly the RL experiments are incomplete, are not easily contrasted due to varying integration periods and cannot be used to make inferences about the different defects that characterise the quartz emission.

However, despite these challenges, these experiments have facilitated the following insights: 1) that the 2.7 and 2.0 eV RL emissions are present in both hydrothermal quartz, and quartz derived from granitic bedrock; and 2) that CL results in depletion of the blue emissions to the benefit of the red emission, although it is not possible to evaluate the rate at which this change occurs between samples due to changes in the electron beam intensity and focus throughout analysis (and thus changes in dose rate); 3) the RL and CL emission spectra are similar. Both sets of spectra are dominated by two emissions at ~ 2.0 eV and ~ 2.7 eV. Deconvolution of the emission spectra would better facilitate intercomparisons, however with the limited data that are available here, and the emission truncation caused by the necessity for the 400/450 nm filters, deconvolution of the CL spectra is inappropriate. These experiments are complemented by the IL and XEOL investigations detailed in Chapters 8 and 9 respectively and a full synthesis of the different emission spectroscopy experiments is provided in Chapter 10.

Relating the RL and CL spectra to the quartz OSL QE is interesting, as from these limited experiments little correlations in absolute intensity are observed. CalQzB8 emits a bright CL signal, however the emission of FAB79 is almost 2 orders of magnitude more intense. This may relate to beam instability, however the RL emission spectra are similar, CalQzB8 exhibits a less intense signal than WTUL1 or QzMacro. The correlation of emission spectra energy and intensity with OSL QE is considered further in Chapters 8, 9 and 10.

Future CL experiments require modification of the CL system to include a faraday cup, whereby the beam could be interrupted and thus sample degradation avoided. An alternative, but more technically demanding solution would be installation of a moveable stage whereby the sample could be moved into the path of the incident beam, following beam stabilisation. The latter suggestion is more challenging as the sample chamber must remain at vacuum in order for CL analyses to be possible. The UV spectrometer has recently been replaced within this system, and future CL, RL, TL and OSL experiments are planned.

Chapter 8. Ionoluminescence of Quartz

8.1. Introduction

Ionoluminescence (IL, also known as ion beam luminescence, IBL) is the study of light emitted from a sample when it is implanted with ions. By selecting specific ion species and implantation energy, ion-implantation can be applied at conditions equivalent to irradiation with ionising radiation. In the present study, quartz is implanted with protons at 0.95 MV to explore the luminescence as a function of dose. This mimics the processes that occur in natural samples during irradiation over geological timescales, and allows the influence of radiation history, one of the proposed controls of quartz OSL QE, to be understood more fully. The results are compared and contrasted with the luminescence spectra of natural quartz samples. Furthermore because IL involves high excitation energies, it is possible to examine the full UV-IR (6.2-1.1 eV) emission spectrum of quartz which provides a clearer indication of the complex quartz luminescence emission.

These experiments explore a number of hypotheses: 1. that quartz of different provenances exhibit different luminescence emission spectra; and 2. that radiation dosing promotes a change in the luminescence emission of quartz at both room temperature (RT) and liquid nitrogen (LNT) temperatures. Testing and accepting hypotheses 1 and 2 could help identify how trace elements influence luminescence centre behaviour, why quartz from certain geological histories have different emissions, and why dose history influences luminescence sensitivity. Hypothesis 3 is that the luminescence emission of quartz exhibits anisotropic effects. Unlike feldspar, quartz does not contain good cleavage, which results in a much greater range of probable orientations when multiple 180-250 µm grains are deposited onto discs during single aliquot analyses. Therefore relative to their structure, there is a greater chance of random orientations occurring, making measurements of single grains more prone to anisotropic effects.

8.2. Materials and Methods

8.2.1. **Samples**

Calibration quartz (CalQz), from the Risø National Laboratory, Denmark, is used globally to calibrate both individual Risø reader machines (see Appendix A.5). It has a very bright OSL signal, typically two orders of magnitude greater than the Scottish samples (WTUL1 and WTUL2; see Appendix D). Batch 8 CalQz is sedimentary quartz from Jutland, Denmark, which has been annealed at 500 °C and dosed with 4.81 Gy. It was prepared using conventional OSL methods at Risø and comprises 180-250 µm grains. Two Scottish samples (WTUL1 and WTUL2) are derived from Younger Dryas

glacial outwash deposits, collected from a sediment exposure adjacent to the Water of Tulla, Central Highlands (56° 34'N, -4° 41'W). WTUL quartz samples were extracted from bulk material, following conventional OSL sample preparation involving desiccation, sieving to isolate the 180-212 µm grain size fraction, H_2O_2 treatment, density separation using 2.70 g cm^{-3} LST fastfloat, which is a heavy liquid comprising low toxicity sodium heteropolytungstates dissolved in water, and two 40 minute, 40 % HF etches prior to a final HCl wash (see Section 4.1). The quartz grain samples were mounted using UHU glue diluted with acetone, onto 10 mm^2 stainless steel discs (conventionally used for OSL dating) which were then mounted on an aluminium sheet and inserted into the sample chamber. A natural hydrothermal quartz macrocrystal is also analysed to explore response as a function of crystal orientation. Two 10 mm x 5 mm x 5 mm sections were cut parallel (QzPara) and perpendicular (QzPerp) to the *c*-axis and were finely polished. The quartz macrocrystal samples were mounted directly onto an aluminium sheet using UHU glue diluted with acetone. All errors are quoted at the 95 % confidence interval (2 σ).

8.3. Ionoluminescence

Ionoluminescence was performed under vacuum using the 3 MV van de Graaff particle accelerator at the University of Sussex following the methodology of Brooks et al. (2002). The ion-beam was focussed to a spot of 0.25 cm^2 and the IL of quartz was explored using H^+ ion species at an acceleration potential of 0.95 MV, with repeated 190 s exposures. The ion current was ~50 nA. Protons were selected because their low mass causes the least sample modification. Their behaviour can be very precisely modelled using packages such as SRIM (The Stopping and Range of Ions in Matter: Ziegler et al., 2008), which provide excellent constraint of energy dynamics during the interaction. SRIM modelling indicates that within these experiments, energy is transferred as electronic excitation over depths of ~11 µm.

Analyses were conducted at both room (RT=300 K) and liquid nitrogen temperatures (LNT=77 K). The sample was aligned at an angle of 22.5° to the incident beam, to enable emission collection at an angle of 45° relative to the excitation energy, and thus ensure maximum signal recording. Light emissions were collected by a quartz fibre optic coupled to a *ƒ*/4 SpectroPro 300i monochromator. The detector used was a Roper Scientific image intensified CCD camera operated using the WinSpec software package. Experiments were conducted at RT with the exception of several spectra for QzPara and QzPerp collected at 77 K. The system operates between 1.1-6.2 eV using a coarse grating to perform two separate spectral analyses between 1.1-2.5 eV and 2.0-6.2 eV respectively. The two spectra were matched in the 2.0-2.5 eV region. Intensity data

were normalised linearly for variations in the ion beam current. The spectra are corrected for background and system response against a W lamp by assuming a modified grey body radiation profile (Finch et al., 2004) using software written in house. Corrected spectra have then been converted to energy space through calculation of eV from wavelength, and by calculation of I(E)dE from I(λ)dλ by multiplication by energy^2 (Hamilton et al., 1978).

8.4. Results

8.4.1. **Modelling of the Interaction by SRIM**

The interaction of protons and quartz were modelled using TRIM (Transport of Ions in Matter), part of the SRIM package, through exploration of the interaction of 10^5 ions with a 180 µm thick quartz sample, density 2.66 g cm^{-3} (Figure 8.1). TRIM calculates the amount of energy lost by the implantation ions to the target through ionization, phonon release and ion displacements at 0 K. Although the model does not account for temperature, which influences bond energies within the material, it is still useful for estimating the effects of implantation. TRIM estimates that > 99% of the implantation energy is lost as ionization. The remaining < 1% energy loss is due to phonon production, predominantly from atom recoil. Few vacancies are produced due to the low mass of protons relative to oxygen or silicon atoms. TRIM indicates that ionization is concentrated at shallower depths (<10.8 µm) than phonon production. Luminescence is produced from the ionized region, and thus IL predominantly provides insights into the unaltered bulk of the sample, rather than the modified sample portion, which develops at the end of the ion track.

8.4.2. **IL Emission Spectra and Dose Dependence**

The initial IL emission spectra of the samples are given in Figure 8.2. The alignment process and first integration time typically took 190 s and hence these spectra are the integral luminescence associated with the first ~4 x 10^7 Gy. The spectra comprise multiple emission bands, which can be deconvolved to comprise between 5 and 7 Gaussian components (Figure 8.3). The fit of the model was tested using the χ^2 parameter after Stevens-Kalceff (2009), whereby no further components were added once improvement in χ^2 had stabilised.

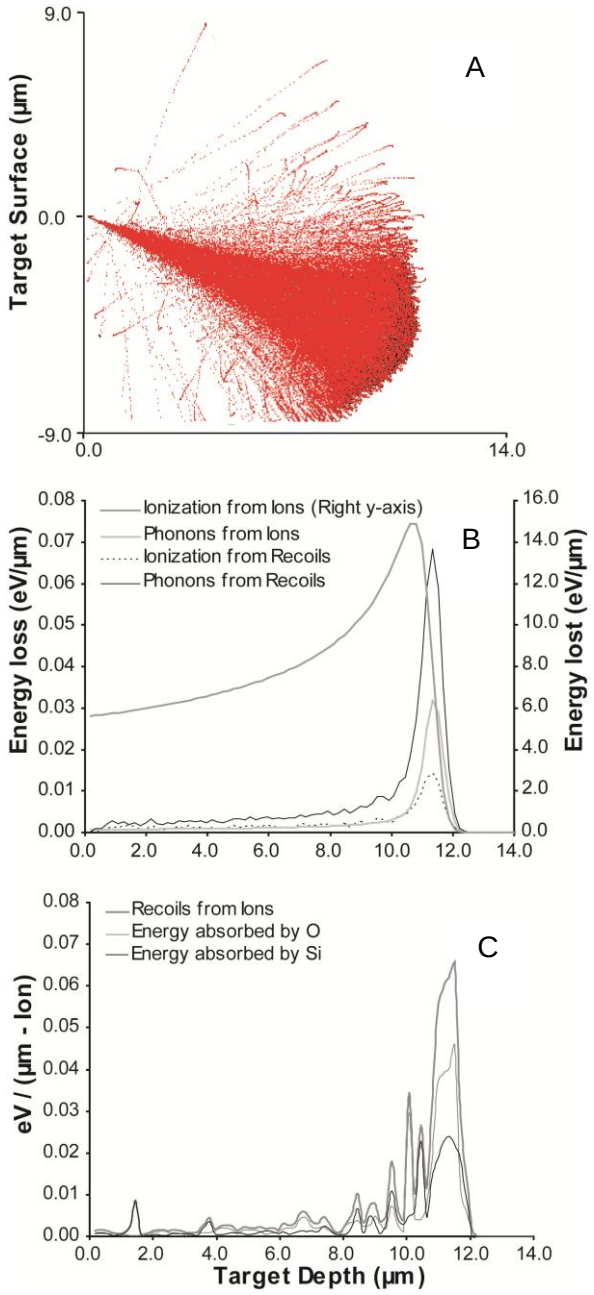

Figure 8.1: TRIM model of 10^5 protons at 0.95 MV implanting quartz 180 µm thick, density 2.66 g cm^{-3} (Ziegler et al., 2008). The upper graph (A) predicts the pathway of incident ions, indicating clustering over ~9 µm and that maximum sample penetration is ~11 µm. The middle graph (B) indicates ion derived ionization peaks at 10.8 µm which accounts for > 2 orders of magnitude more energy dissipation than recoil derived ionization or phonon production, which both peak at 11.3 µm. The lower graph (C) indicates that recoil production is low, and is clustered at ~11 µm depth.

Visual analysis of the emission spectra resulted in the identification of four different emissions at 1.8-1.9 eV (red), 2.6-2.7 eV (blue), 3.2-3.4 eV (UV-violet) and 3.6-3.7 eV (UV) (Figure 8.2). Deconvolution indicated that the 1.8-1.9 eV emission is a composite of at least two emissions at 1.7-1.9 (red) and 2.0 eV (orange), and also revealed an additional emission at 1.4-1.5 eV (IR). All spectra are dominated by the red and UV-violet emissions, the energies of which vary between the different quartz, with CalQzB8 exhibiting peak emissions at 1.9 and 3.4 eV, QzPerp at 1.8 and 3.3 eV, and both WTUL samples at 1.8 and 3.2 eV. All samples with the exception of CalQzB8 also exhibit a 3.7 eV emission, QzPerp exhibits a 2.6 eV emission and WTUL1 and WTUL2 a 2.7 eV emission. Due to difficulties with ion-beam stability, QzPara was irradiated during system

alignment and the first spectrum recorded corresponds to 1.6 x 10^8 Gy implantation, thus it is excluded from Figure 8.2.

The width of the filter conventionally used during OSL dating of quartz using a Risø reader is also shown in Figure 8.2. The UV-blue emission is not entirely covered by the OSL detection window (3.4-4.6 eV) and just the tail of this emission is measured in OSL. CalQzB8 has the most intense UV-violet relative to red emission of all of the samples analysed, whereas the UV-violet is much less pronounced in WTUL and QzPerp.

As proton implantation continues for all samples, the UV and UV-violet emission intensity reduces and the red emission increases in intensity. The UV-violet and red emissions also broaden (Figure 8.4). The blue emission disappears from QzPerp, WTUL1 and WTUL2. The median red emission energy shifts from ~1.8 eV to ~1.7 eV in WTUL and from ~1.9 to ~1.85 eV in CalQzB8. These results on natural materials are similar to data reported from high-grade synthetic quartz (Bettiol et al., 1997). Although those authors recorded no UV emission, they did observe a single broad red emission at 660 nm (1.88 eV), which increased in intensity with increasing dose.

In order to determine whether the changes in the spectra were transitory or permanent, one sample (QzPerp) was left at RT for 15 hours, and the spectrum repeated. No recovery of the sample is observed, and thus it is inferred that these radiation dose effects are stable over timescales of days. This experiment also confirms that the modification of the IL is not just due to local thermal effects.

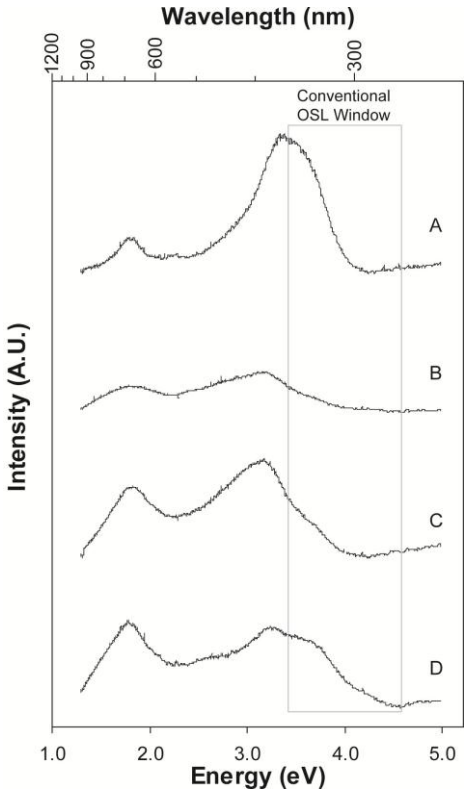

Figure 8.2: Initial IL spectra obtained from each of the samples at RT. Data are plotted in energy space and have not been scaled for intensity (see text for details). Spectrum A: CalQzB8, B: WTUL2, C: WTUL1, D: QzPerp. The initial spectra comprise two main emission peaks at 1.8-1.9 eV and 3.2-3.4 eV. The conventional OSL detection window (3.4-4.6 eV), where Hoya U-340 filters are used is indicated (Ballarini et al., 2005).

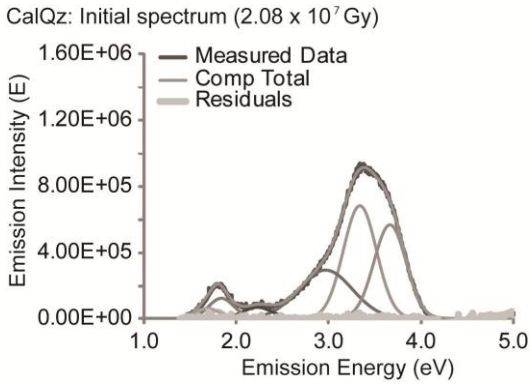

Component	mean (eV)	sigma (eV)	Intensity (E)	% Total Emission
1	3.66	0.17	5.67×10^5	32
2	3.34	0.18	6.82×10^5	38
3	2.97	0.29	2.92×10^5	16
4	2.23	0.16	7.21×10^4	4
5	1.84	0.14	1.22×10^5	7
6	1.69	0.13	6.20×10^4	3

Sum Squared Residuals: 6.57×10^{10}

Figure 8.3: Deconvolution of the initial CalQzB8 emission spectra in energy space using multiple Gaussian components which indicate that the UV-violet and red emissions which dominate all samples, are composites of at least two emission centres.

8.4.3. **Anisotropy of the Light Emitted**

Comparison of QzPara and QzPerp allows the anisotropy of luminescence to be determined. Analysis of the spectrum at 1.6×10^8 Gy shows that the relative amplitude of the red to the UV-violet emission is much greater for QzPara than for QzPerp (Figure 8.5). After implantation with 2.3×10^8 Gy, the UV-violet emission was significantly reduced relative to the red in both samples, although both emissions were still present. IL was also measured at 77 K on fresh areas of QzPara and QzPerp (Figure 8.6) and a single pronounced blue emission at 2.7 eV was recorded. This emission was apparent in QzPerp at RT, although was rapidly quenched by implantation. Counts for the intensity of the blue emission were an order of magnitude greater than for the UV-violet emission observed at RT. No spectra or intensity shift was observed for either QzPara or QzPerp when exposed as a function of dose at LNT, however there was some emission variability which may relate either to local sample warming or short (s) period fluctuations in the beam.

8.5. Discussion

8.5.1. **Room Temperature IL**

The origins of the luminescence emissions of quartz have been explored using contrasting spectroscopic techniques including CL, RL, PL and electron spin resonance (ESR; see Stevens-Kalceff and Phillips, 1995 for a review). The RT (300 K) IL spectra are similar to those observed from quartz and silica glass by other authors (e.g. rose quartz: Kibar et al., 2007; silica glass: Kononenko et al., 2007) and are similar to quartz RL (Fujita and Hashimoto, 2006) and CL spectra (Götze et al., 2001; Stevens-Kalceff, 2009; see also Chapter 7). Each excitation method differs energetically; for example, CL delivers energies of kV and excites only the surface region of the sample, whereas IL delivers MV

but excites the sample bulk (Brooks et al., 2002; Townsend et al., 1999; Townsend and Rowlands, 2000; see also Table 7.1). Despite these differences, useful insights into the emission properties of quartz can be obtained as the same centres are excited.

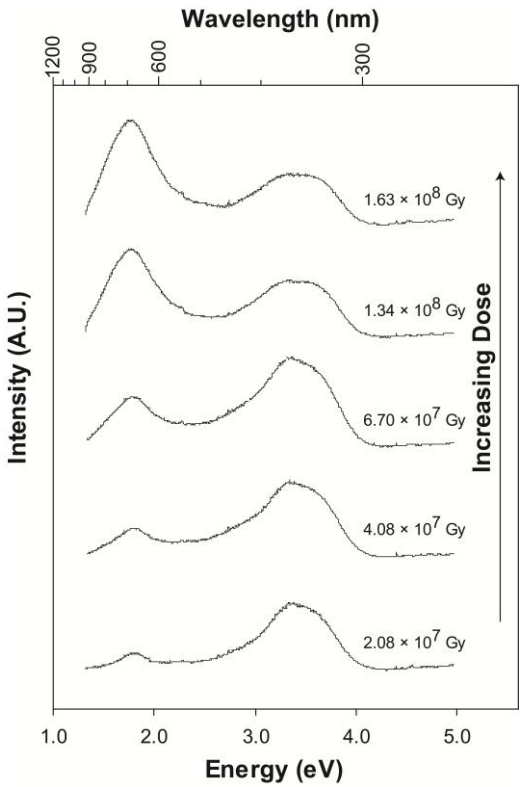

Figure 8.4: Modification of the CalQzB8 emission spectrum as a function of cumulative implantation dose (Gy). The initial spectrum is shown at the bottom of the figure.

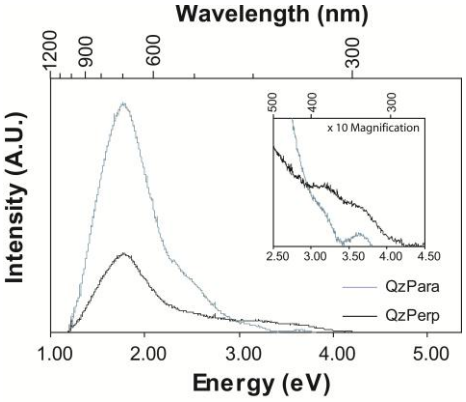

Figure 8.5: QzPara and QzPerp emission spectra at RT following 1.6 x 10^8 Gy radiation dosing. The 3.2-3.4 eV UV-violet emission is highly amorphized in QzPerp, and is indistinct in QzPara, these emissions are shown at x 10 magnification in the inset. QzPara and QzPerp exhibit small 3.6 eV and 3.7 eV UV emissions respectively.

8.5.2. **The UV-blue Emissions**

Although some debate in its origin remains (e.g. McKeever, 1991; Yang and McKeever, 1990), it is widely assumed that the 380 nm (3.3 eV) UV-blue emission is associated with the substitution of Si^{4+} with Al^{3+}, charge compensated by protons or interstitial alkali ions (Alonso et al., 1983; Itoh et al., 2002; Perny et al., 1992). This results in the formation of $[AlO_4/M^+]^\circ$ centres, where the Al^{3+} is charge compensated by either Li^+, Na^+ (Perny et al., 1992) or H^+ (Itoh et al., 2002; Luff and Townsend, 1990). It should be

noted that other entities such as Ge^{4+}, Ti^{4+} and H_3O_4 may also substitute for Si^{4+}, although such substitutions are less thermodynamically favoured and are dependent upon the crystallisation conditions (Götze et al., 2004). Similarly the abundance of the different charge-compensating alkali ions is also determined by the crystallisation conditions: e.g. Li^+ occurs in higher concentrations in pegmatitic quartz (Rink et al., 1993). The process of electron recombination at this centre is complex, and may reflect the development and decay of precursor centres (see Itoh et al., 2002; McKeever, 1991; Yang and McKeever, 1990 for a discussion). The role of the interstitial alkali ions as charge carriers for the $[AlO_4/M^+]^\circ$ centres has been confirmed through comparison of 'swept' and 'unswept' quartz luminescence emissions, where the swept quartz has been exposed to intense electron irradiation in a hydrogen atmosphere, causing removal of alkali ions (Alonso et al., 1983). Swept quartz exhibited no UV emission at 380 nm (3.3 eV), in contrast to an unswept portion of the same sample (Alonso et al., 1983). However, Martini et al. (1995) have more recently observed the TSL 380 nm emission to be unaffected by sample sweeping, inferring that although this emission relates to the $[AlO_4]^\circ$ centre, it cannot be charge compensated by H^+ or M^+ ions. Although the specific charge compensator remains debated, it has been inferred that this is the same centre accessed during OSL through comparative OSL, TSL, CL and ESR spectroscopies (Itoh et al., 2002; Martini et al., 2009; Martini et al., 2000; Martini et al., 1995). Thus it is inferred that the UV-violet IL in these samples comes from the same centre, as the emission energies are the same. This is consistent with the observation that CalQzB8 exhibits the most intense IL UV-violet emission, in addition to the most intense OSL UV-blue emission. Martini et al. (2009) suggest that the population of $[AlO_4/M^+]^\circ$ centres is linked to low photon luminescence of quartz, thus CalQzB8 must have an enhanced population of these centres relative to the other samples analysed.

The UV-violet emission modifies during implantation (Figure 8.4), where depletion of the emission is observed, with increasing radiation dose. This dependence of the UV-violet emission to irradiation has also been observed (Botis et al., 2006; Krbetschek and Trautmann, 2000; Rink, 1994), although no precise mechanisms have been determined (Alonso et al., 1983; Halperin and Sucov, 1993; Itoh et al., 2002; Yang and McKeever, 1990). Exploration of the properties of the extrinsic $[AlO_4/M^+]^\circ$ defect using CL and ESR, has revealed that the population is highly sensitive to irradiation (Luff and Townsend, 1990; Perny et al., 1992; Weil, 1984). This can also be identified by the depletion of the signal with increasing exposure, as observed within these IL experiments (Figure 8.4). This is attributed to the accelerated migration of the interstitial alkali ions (Halliburton et al. 1981), which are mobile along the c-axis of the quartz crystal at temperatures > 200 K (Durrani et al., 1977; McKeever 1984; Stevens-Kalceff and Phillips, 1995). Furthermore

radiation dosing has been identified as affecting the OSL and TSL emissions of quartz, (Durrani et al., 1977; Hochman and Ypma, 1988; Levy, 1979; Rink, 1994). All of these observations are consistent with IL accessing the same centres observed by OSL and other spectroscopies.

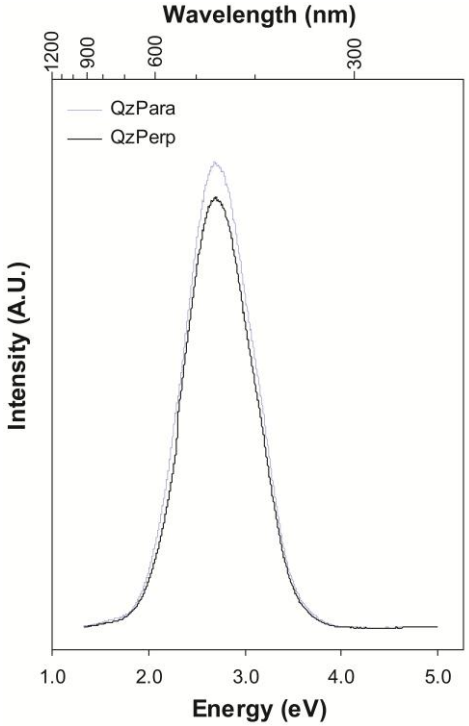

Figure 8.6: QzPara and QzPerp emission spectra at 77 K. The 1.8, 3.2 and 3.6-3.7 eV emissions at room temperature are replaced with an intense blue 2.7 eV emission. This emission is an order of magnitude brighter than the room temperature spectra.

UV-blue luminescence has also been attributed to other causes. Al^{3+} substituted for Si^{4+} can also be charge-compensated by a bridging electron hole, a centre given the annotation $[AlO_4]^\circ$ (Martini and Galli, 2007) and, in a clustered form, believed to contribute to the blue CL of feldspar (Finch and Klein, 1999). Such centres would be formed if the alkali ion were removed from $[AlO_4/M^+]^\circ$ centres and ion migration is expected to shift luminescence between these two centre types. Second, UV-blue luminescence has been linked to oxygen vacancies in a variety of different guises, called the *E'*-centres (see Weil, 1984 for a review). In many cases, the vacancy can couple with other defects such as protons. These may produce UV-blue luminescence, or they may compete with UV-blue centres to dissipate energy non-radiatively (Poolton et al., 2000). The formation of *E'*-centres has been linked to irradiation, as oxygen vacancies are created (Durrani et al., 1977; McKeever 1984).

Understanding the dose dependence of IL provides insights into which of the above scenarios is most likely in these quartz samples. The interplay between $[AlO_4/M^+]^\circ$ and $[AlO_4]^\circ$ hinges on alkali and proton mobility during IL. Ion diffusion in quartz is believed to lie predominantly parallel to the c-axis as the structure has channels in this direction. Implantation would reduce the activation energy (Brooks et al., 2001) associated with hopping between adjacent channels. However, it is unclear from first principles whether

such mobility would cause the motion of alkali metals away from $[AlO_4/M^+]^\circ$ centres to create $[AlO_4]^\circ$ centres or vice versa. The luminescence profile of the UV-violet region changes significantly during the implantation, in addition to the gross reduction of the overall UV-violet signal (Figure 8.3). The UV-violet peak is initially at 3.3 eV but broadens progressively. Deconvolution indicates that the UV-violet band comprises at least two components at 3.3 and ~3.6 eV and that implantation modifies the relative proportions of these two components. If it is accepted that the 3.3 eV emission results from $[AlO_4/M^+]^\circ$ (Alonso et al., 1983; Itoh et al., 2002; Perny et al., 1992), it is possible to suggest that the 3.6 eV centre is from $[AlO_4]^\circ$ and that ion migration during implantation is away from the centre. QzPara and QzPerp exhibit UV emissions at 3.6-3.7 eV before significant implantation. Only a small amount of literature has been published about the origins of this emission, however it has been attributed to the recombination of electrons at oxygen vacancies (Itoh et al., 2002; Rink et al., 1993). Heavy ion implantation generates oxygen vacancies, but the use of protons means that this is minimal (see Section 8.4.1) and the few vacancies that are formed are at the end of the ion track. As this region contributes very little to the luminescence signal, oxygen vacancy formation is not considered to be a credible explanation for the substantial changes seen here. Similarly the formation of AlOH centres and $[H_3O_4]^\circ$ centres (Nuttall and Weil, 1980; Yang and McKeever, 1990) as a consequence of proton implantation will be concentrated in this region, and thus are also unable to explain the observed depletion of the UV-violet to the benefit of the red.

8.5.3. **The Red Emission**

All samples exhibit a red emission at 1.8-1.9 eV. Deconvolution indicated that this emission is a composite of at least two emissions at 1.7-1.8 eV and 2.0 eV, which are attributed to Fe^{3+} impurities and non-bridging oxygen hole centres (NBOHC) respectively. The substitution of Si^{4+} with tetrahedral Fe^{3+}, has been associated with emissions at 1.75 eV (Kempe et al., 1999; Pott and McNicol, 1971) and 1.65 eV (Stevens-Kalceff, 2009). Red-IR (1.7 eV) luminescence in feldspar, another framework silicate, has also been linked to tetrahedral Fe^{3+} using ESR (Finch and Klein, 1999). Red emissions at 1.88 eV have been related to a NBOHC, the concentration of which is dependent on precursor peroxy linkage and hydroxyl group populations (Bettiol et al., 1997; Götze, 2009; Stevens-Kalceff and Phillips, 1995).

In contrast to the UV-violet emission, the red emission exhibits an increase in luminescence intensity with increasing radiation dose. Similar observations have been reported previously for both CL and IL, and were interpreted as either due to development of NBOHC as peroxy linkages are broken and the radiolysis of hydroxyl groups occurs

(Stevens-Kalceff and Phillips, 1995), or to the creation of oxygen vacancies throughout irradiation (Luff and Townsend, 1990; Stevens-Kalceff and Phillips, 1995).

Luff and Townsend (1990) observed dose dependent effects in quartz luminescence during electron irradiation (CL), whereby the 2.6 eV emission was quenched whilst the 1.9 eV emission increased in intensity throughout exposure. The sensitization in the orange-red emission was permanent. Bettiol et al. (1997) also observed similar emission modification throughout 3 MV proton–excited IL of a sample for ten minutes at 295 K, which they also attributed to formation of NBOHC.

8.5.4. **Interrelationships between the UV-blue and red emissions**

All of the samples have different ratios of the intensity of UV-violet to red light emission at the onset of the experiment. Variations in this ratio are indicative of the specific precursor defect populations in samples prior to irradiation, which are the product of their crystallisation history (Götze, 2009) and dose history. Despite differing initial ratios of red and UV-violet emissions, all of the samples exhibit reduction in the intensity of the UV-violet emission alongside enhancement of the red emission as a function of ion implantation. There are three ways in which to interpret the data. The interaction may:

1. reduce the population of those centres that give rise to UV-violet luminescence through one mechanism and create the red luminescent centres through another,
2. reduce the population of UV-violet centres and increase the population of red centres through a single mechanism, or
3. have no effect on the population of red centres, but by reducing the population of UV-violet centres, energy which would have previously been emitted from a UV-violet recombination site is able to cascade to the red luminescent recombination site.

The overall reduction in the UV-violet emission is inferred to result from reductions in the populations of $[AlO_4/M^+]^\circ$ and $[AlO_4]^\circ$ type centres caused by ion and electron migration. The $[AlO_4]^\circ$ centre would be charged (-1) if it were not for the coupling of the Al defect with a paramagnetic oxygen hole centre, effectively a coupled NBOHC. The data are consistent with a mechanism in which ion and electron migration causes a change in the centre types from:

Eq. 8.1: $[AlO_4/M^+]^\circ >> [AlO_4]^\circ + M^+_{(free)} >> [AlO_4]^- + NBOHC_{(free)}$

Luminescence: 3.3 eV 3.6 eV 1.9 eV

Such an interpretation implies that the increase in the red luminescence represents increasing the population of NBOHC and does not call upon oxygen vacancy formation, in accordance with TRIM model results. To understand this further, the luminescence dose dependence of the UV-violet/red ratio has been examined. The dose dependence exhibits an exponential relationship (Figure 8.7), the gradient of which is negative and ranges from -2.08 ± 1.19 for QzPara, to -1.14 ± 0.13 for WTUL2, which have the steepest and most shallow slopes respectively (Table 8.1). The power dependencies of all samples overlap within errors, and where QzPara is excluded, the average slope is -1.12 ± 0.11. Exclusion of QzPara is justified due to its greater implantation throughout experimentation (see Section 8.4.2). The slope consistency in these graphs indicate that, whatever the mechanism, it is the same process occurring in all the quartz samples studied. On average the dose dependence of quartz is determined to be governed by the relationship:

Eq. 8.2: $$\frac{I_{UV-violet}}{I_{red}} = Ae^{-1.12D}$$

where $I_{UV\text{-}violet}$ is the emission count at 3.26 eV, and I_{red} the emission count at 1.9 eV, which are the average central values for the UV-violet and red composite emissions identified visually for the different quartz samples. D is the dose (Gy) and A represents different initial ratios of the UV-violet and red luminescence. The pre exponential factor A is within error for all samples, ranging from 7.64 ± 0.93 for WTUL1 and 8.43 ± 1.22 for CalQzB8 where QzPara is excluded. The annealing treatment that CalQzB8 has received is known to increase OSL QE. One mechanism through which this could be achieved is the recovery of $[AlO_4/M^+]^\circ$ centres through thermally induced remobilisation of alkali ions. The brighter luminescence of CalQzB8 is thus reflected in its larger A value.

The slope of Figure 8.7 is not significantly different to 1. If the power dependence had been significantly greater or less than 1, it would have been possible to infer that the rate of formation of red luminescence was significantly different to that of the reduction of the UV-violet light. As it is, the rate of generation of quanta of red luminescence parallels within error the depletion in quanta of UV-violet. This is consistent with the model of NBOHC formation presented above. However it is also consistent with a model whereby reduction of the populations of UV-violet luminescent centres allows energy that would have been emitted at one of these centres to cascade further to the red luminescence centre. Such a model does not involve changes in the luminescence centre populations, rather that these are now accessible to the excited energy. If the latter model is accepted, then luminescence from Fe^{3+} centres (Kempe et al., 1999; Pott and McNicol, 1971; Stevens-Kalceff, 2009) may indeed be the cause of the red luminescence, perhaps also

associated with NBOHC formation. The contributions to red luminescence from these two types of centre may, in due course, be deconvolved by time-resolved luminescence spectroscopies.

Table 8.1: Dose Dependence and Pre-Exponential Terms for Implantation of Quartz.

Sample	Provenance	$\text{Log}_{10}\ A$	Power Dependence
CalQzB8	Risø Labs	8.4 ± 1.2	-1.11 ± 0.16
WTUL1	Glaciofluvial deposit	7.6 ± 0.9	-1.11 ± 0.11
WTUL2	Glaciofluvial deposit	8.2 ± 1.1	-1.14 ± 0.13
QzPara*	Hydrothermal	15.2 ± 9.9	-2.08 ± 1.19
QzPerp	Hydrothermal	7.8 ± 0.5	-1.11 ± 0.06

*The relatively large error for QzPara is due to its analysis with shorter acquisition periods (130 s), selected to minimise modification following its enhanced exposure during ion beam tuning.

8.5.5. **Dose Rate effects**

Dose rate effects are problematic in all luminescence investigations, since laboratory experiments are completed over timescales that are geologically 'instantaneous'. Whether dose rate, rather than integral dose, brings about the changes observed has been considered. Brooks et al. (2001) contrasted IL from H^+ implantation with that of H_2^+ ions for sapphire. The H_2^+ ions dissociate on entering the sample to form separate excitation tracks which overlap both spatially and temporally. Such comparisons double the dose rate whilst all other conditions, notably the incident power, are kept constant. Brooks et al. (2001) recorded no dose rate effects. This is also consistent with Fujita and Hashimoto (2006) who explored the dose rate dependence of the RL of quartz. During sample dosing at RT, they also observed a strong RL emission at 3.1 eV for a range of dose rates from 0.1 to 10 Gys^{-1}. The RL emission intensity did not vary with dose rate. The total cumulative dose varied throughout the IL analyses whereas the dose rate remained approximately constant, thus it is tentatively concluded that the observed luminescence emission changes are an effect of cumulative dose rather than dose rate.

8.5.6. **LNT IL Spectra**

The 2.7 eV emission observed for all samples at LNT (Figure 8.6) coincides with the 2.8 eV emission observed during low temperature CL of quartz (Itoh et al., 1989; Luff and Townsend, 1990) and IL of rose quartz (Kibar et al., 2007). It is an order of magnitude more intense than the RT spectrum, in agreement with Itoh et al. (1989), Luff and Townsend (1990) and Kibar et al. (2007). However, Bettiol et al. (1997) did not observe

this emission peak when performing IL at 80 K on synthetic quartz, although the 1.88 and 2.3 eV emissions were enhanced.

Numerous origins for the 2.7 eV emission have been proposed. It may originate from an intrinsic oxygen-vacancy defect, attributed to the self-trapped exciton (STE; e.g. Itoh et al., 1989; Itoh et al., 2002). It has been associated with *E'*-centre annihilation in glass (Sigel, 1973), although non-linearity in this relationship is indicative of some non-radiative *E'*-centre recombination in quartz (see McKeever 1984 for a review; Poolton et al., 2000). Alternatively it may be associated with the $[AlO_4/M^+]^\circ$ defect that produces the UV-violet emission at RT (Stevens-Kalceff and Phillips, 1995). This is regarded as the most plausible explanation as alkali ions are unable to diffuse through the crystal lattice at temperatures < 200 K, which renders the centre insensitive to radiation exposure at LNT. No dose dependence was observed in either sample, following exposure to 1.25 x 10^8 Gy and 6.08 x 10^7 Gy for QzPara and QzPerp respectively.

8.5.7. **Anisotropic Effects**

The emissions of both QzPara and QzPerp were similar at LNT, both being dominated by the intense 2.7 eV emission, although QzPara exhibits a slightly stronger luminescence signal. At RT following exposure to 1.6 x 10^8 Gy, the UV-violet signal has depleted dramatically in both samples (Figure 8.5), although the 3.2-3.3 eV and 3.6-3.7 eV emissions are still visible. QzPara exhibits the most intense red (1.9 eV) luminescence signal, whereas QzPerp exhibits the most intense UV-violet (3.2-3.3 and 3.6-3.7 eV) luminescence signal. These results indicate that grains aligned perpendicular to their *c*-axis will luminesce most brightly overall and in the red, however those aligned parallel to their *c*-axis will emit most brightly in the UV-violet.

8.6. Conclusions

The exposure of quartz to ion implantation results in an increasing red emission and decreasing UV-violet emission, the latter of which is conventionally used in OSL dating. This is consistent with irradiation-induced migration of charge compensating alkali ions from $[AlO_4/M^+]^\circ$ centres, which are considered responsible for the 3.3 eV UV-violet emission. The red emission may be enhanced through development of NBOHC as a direct consequence of irradiation, coupled with an increased availability of energy both at these centres and at Fe^{3+} centres. The dose dependence behaviour of all samples overlaps within error. Variability between samples may relate to differences in provenance, specifically crystallisation environment and geological irradiation history, or alternatively to anisotropic effects.

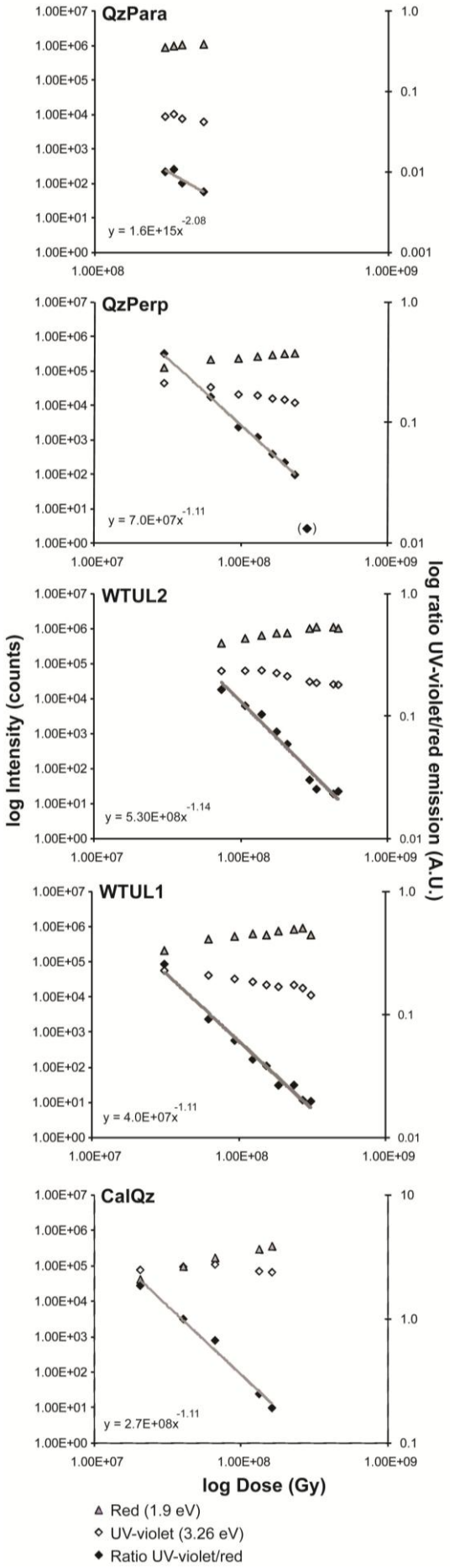

Figure 8.7: A log-log plot of luminescence intensity versus dose. The UV-violet/red (filled diamonds) ratios are plotted relative to the second (right) y-axis, and are fitted with a power-law trendline (in log-log space). The UV-blue emission (open diamonds) exhibits reducing intensity with increasing dose, in opposition to the red emission (filled triangles). The bracketed data point on the QzPerp plot has not been included in calculation of the trendline, but is shown here in the interest of transparency.

Spectroscopic profiling using excitation methods such as IL, CL or RL provide valuable insights regarding which samples are likely to be suitable for OSL dating. These experiments provide an explanation for the observation that recently eroded quartz has poor luminescence sensitivity. If quartz is derived from relatively radioactive bedrock, such as granite, the UV-blue luminescence emission will already have been quenched. Thus their poor luminescence sensitivity is explained by their immediate, geologically determined, radiation history. Conversely the observation that highly weathered quartz which have undergone many cycles of deposition and transport have good OSL properties, can be explained as exposure to high temperatures or mechanical processes during transport may enable remigration of the alkali ions to their charge compensating interstitial locations, resulting in $[AlO_4/M^+]^\circ$ centre formation and UV-blue emission recovery.

Spectroscopic analyses of quartz luminescence emission are valuable in informing sample selection and analytical protocols, and should be utilised within OSL dating (Krbetschek et al., 1997; Townsend et al., 1993). These would enable identification of quartz likely to respond well in OSL analyses and may facilitate protocol development for more challenging samples.

Chapter 9. XEOL of quartz

9.1. Introduction

X-ray excited optical luminescence (XEOL) is a spectroscopic luminescence technique which monitors the light emitted by matter when exposed to x-rays. The development of synchrotrons, which, in contrast to bench top x-ray generators, produce tuned, microfocused x-rays, enables specific energy ranges to be targeted on particular regions of a crystal. For instance, Jürgensen et al. (2009) examined the XEOL of a zoned quartz crystal across the Si K-edge (see also Rogalev and Goulon, 2002; Sham and Rosenberg, 2007 for reviews).

This chapter demonstrates how synchrotron XEOL enables exploration of both the emission spectrum of quartz and the nature of specific defects. The XEOL of quartz between 200 and 850 nm (6.2 to 1.5 eV) as a function of x-ray dose is also considered. These experiments explore a number of hypotheses: 1) quartz of different provenances exhibit different emission spectra; 2) x-irradiation changes the luminescence of quartz; and, 3) luminescence of quartz exhibits anisotropic effects. Testing and accepting hypotheses 1 and 2 supports the outcomes of the research presented in Chapter 8 on the radiation susceptibility of quartz and conclusions that geological dose history influences luminescence sensitivity. If hypothesis 3 is correct, this would provide an explanation for the high uncertainties associated with single grain OSL, reflecting the variety of orientations experienced by quartz grains, as well as a distribution in luminescence characteristics to which these errors are usually attributed.

9.2. Materials and Methods

9.2.1. **Samples**

The sample suite is described in Chapter 8, and comprises a range of quartz of different geological and/or depositional histories. Calibration quartz (Batch 34) (CalQz), from the Risø National Laboratory, Denmark, is used globally for the calibration of Risø reader machines. Batch 34 CalQz is sedimentary quartz from Jutland, Denmark, and has been annealed at 700 $^{\circ}$C and dosed with 4.81 ± 0.06 Gy. Two Scottish samples (WTUL1 and WTUL2; see Appendix D) are derived from Younger Dryas glacial outwash deposits, collected from a sediment exposure adjacent to the Water of Tulla, Central Highlands (56° 34'N, -4° 41'W). CalQzB34 has an OSL signal typically two orders of magnitude greater than WTUL1 and WTUL2. A natural hydrothermal quartz macrocrystal is also analysed to explore response as a function of crystal orientation. Two 10 mm x 5 mm x 5 mm sections were cut parallel (QzPara) and perpendicular (QzPerp) to the *c*-axis and were finely polished.

Sample grains were mounted on sellotape. Signals from the sellotape were small and the responses of quartz mounted on sellotape or pressed into Al-foil could not be distinguished, confirming that quartz XEOL dominates the data.

9.2.2. **X-ray Excited Optical Luminescence (XEOL)**

Experiments were carried out at the third generation Diamond synchrotron (www.diamond.ac.uk, beamtime reference NT1237), on the I18 Microfocus Spectroscopy beamline (Mosselmans et al., 2009). Monochromatic x-rays were delivered to the experimental hutch and experiments were performed using x-rays of two energies: 7148 and 6972 eV. These energies were initially selected to explore the K-edge of Fe, however as varying the excitation energy over this range exerted no discernable influence on light emission, it is not considered further. The experimental chamber of beamline I18 was covered with a white, thick-cloth hood. Emission spectra from procedural blanks were flat with counts < 140, two orders of magnitude smaller than the dimmest signal from the quartz, confirming that the spectra are truly representative of the XEOL of the samples. All spectra were collected at room temperature (RT = 300 K) and pressure.

Samples were aligned at 22.5˚ to the incident x-rays using optical microscopy, and at 22.5˚ to the detector to enable maximum signal collection. The x-ray beam was ~ 3 μm in diameter. Light emissions were collected by a quartz fibre optic coupled to an f/4 SpectroPro 300i monochromator. The detector used was a Roper Scientific image intensified CCD camera operated using the WinSpec software package. This spectrometer is the same used in Chapter 8, and has a resolution of < 2 nm. The system operates between 1.5-6.2 eV using a coarse grating to perform two separate spectral analyses between 1.5-2.5 eV and 2.0-6.2 eV, respectively. The two spectra were matched in the 2.0-2.5 eV region. The spectra are corrected for background and system response against a W lamp by assuming a modified grey body radiation profile (Finch et al., 2004) using software written in house. Corrected spectra were converted to energy space through calculation of eV from wavelength, and by calculation of I(E)dE from I(λ)dλ by multiplication by energy^2 (Hamilton et al., 1978).

Spectra were collected over different integration periods dependent upon signal intensity; shorter integration intervals (down to 10 s) were preferable as modification of the sample as a function of dose could be rapidly detected. Consequently, absolute emission intensities are only contrasted with like integrations throughout this chapter. The radiation dose rate was estimated as the product of the photon energy, photon flux and % of x-rays absorbed. The photon flux at Diamond is 3 x 10^{12} photons s^{-1} (Mosselmans et al., 2009). The combination of mirrors and slit closures used reduced this by 75 % to ~ 8 x 10^{11} at the sample site, and ~ 95 % of the incident irradiation is absorbed (Henke et al., 1993). The

mass of the sample illuminated can be calculated as the product of the volume and density giving an estimate of the dose rate as 248 MGy s^{-1}. Initial current measurements (I_0) prior to the analyses were unnecessary as, with the exception of four beam drop outs, average current was 249.3 ± 1.16 mA throughout the experimental period, indicating that variability was < 1 %.

Corrected spectra were deconvolved into their different components using the Multi-peak Fitting 2 package in Igor v6.21 (WaveMetrics). This program performs non-linear least squares fitting of the spectra using the Levenberg-Marquardt algorithm to iterate component fits which minimize χ^2. All components were assumed to be Gaussian in energy space and the autofit option was used, only the deconvolved emission energies are discussed, unless otherwise stated. All errors are cited to the 95% confidence interval (2σ). Two sets of measurements were collected for CalQzB34 and QzPara, denoted (a) and (b) throughout the text respectively.

9.3. Results

9.3.1. **XEOL Emission Spectra and Dose Dependence**

X-irradiation causes XEOL from all the quartz. All samples are initially dominated by UV emissions, although the number of emission peaks and their energies vary between samples (Figure 9.1). There is significant noise in the hard UV part of the emission spectrum (> 4 eV) for all samples except CalQzB34, which is caused by reduced sensitivity of the spectrometer at these energies.

Intensity is defined as the maximum peak amplitude of the deconvolved spectra, and CalQzB34, WTUL1 and QzPerp are dominated by a ~ 3.8 eV emission, which is less intense but also present in QzPara and WTUL2. All samples also exhibit UV emissions at 3.3-3.4 eV, and CalQzB34, QzPerp and WTUL1 have an additional emission at ~ 3.6-3.7 eV. The relative maximum peak intensity and breadth of these emissions varies between the different samples. All samples with the exception of QzPara exhibit emissions at ~ 4.1 eV. The 4.4 eV emission is the most intense emission for QzPara. QzPara and QzPerp exhibit a blue emission at ~ 2.7 eV, not recorded in the other samples.

Modification in emission energy is observed for all samples during irradiation (Figure 9.1). Total emission intensity reduces for all samples, although this is less apparent for WTUL1 which may relate to its more limited exposure of 3.15 x 10^{10} Gy in contrast the remainder of the sample suite. The ~ 3.8 eV emission becomes dominant in all samples, and a weak red emission at 1.9-2.0 eV develops for all samples with the exception of WTUL1, which is attributed to its reduced irradiation.

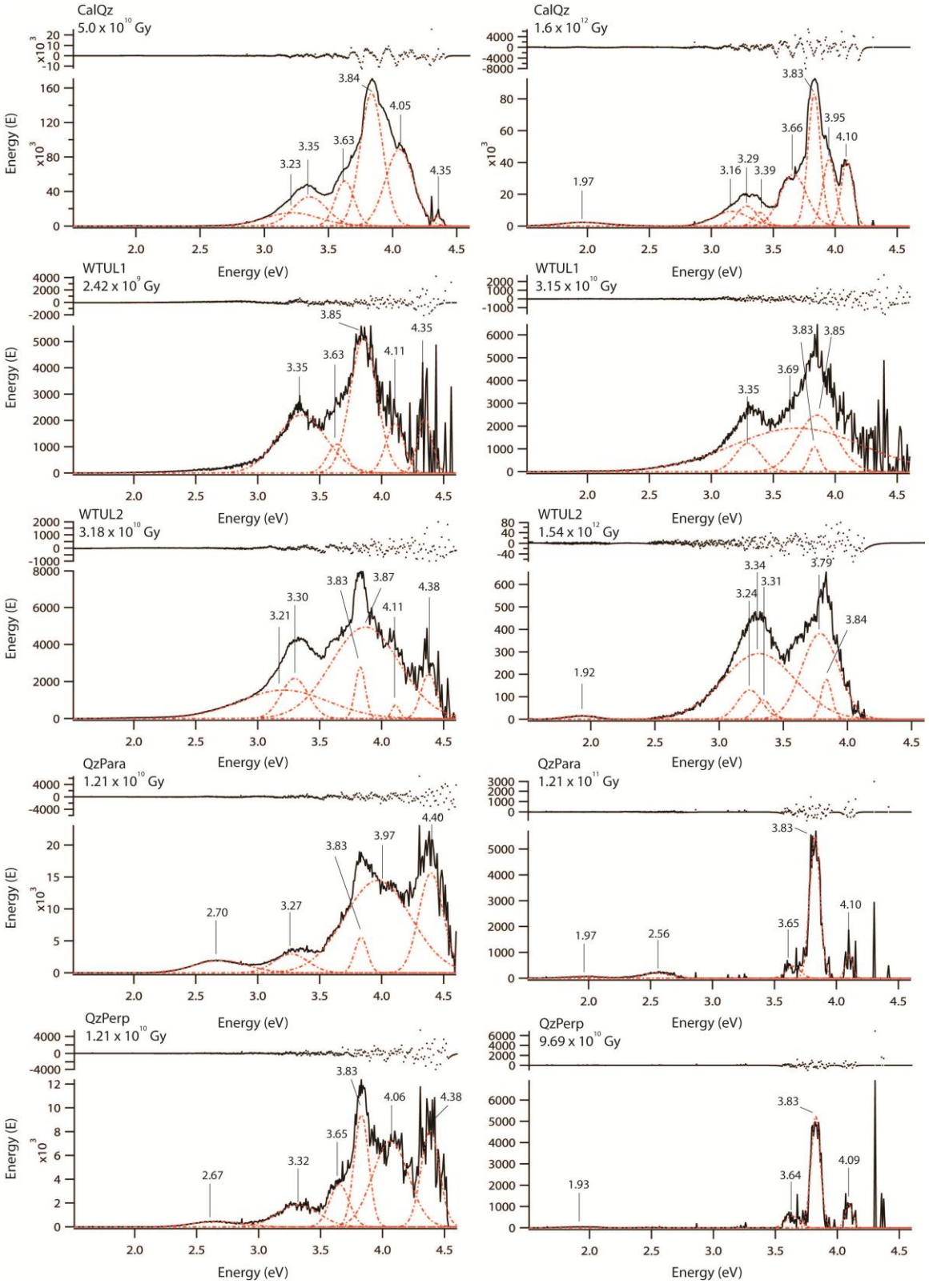

Figure 9.1: Initial and final emission spectra for the samples, note variation in the y-axis between plots to accommodate the range of signal intensities. Spectra are plotted in energy space and have been deconvolved into their composite emission. Residuals from curve fitting are shown. The amount of radiation exposure for each spectrum is indicated, variations in radiation exposure are caused by differing integration intervals, dependent upon signal intensity. The initial and final spectra for each of the samples contrasted here, have been collected over the same integration period: CalQzB34, 10 s; WTUL1, 10 s; WTUL2, 10 s; QzPara, 50 s; QzPerp, 50 s.

X-irradiation prompts the various UV emissions to shift in energy. The ~ 4.4 eV emission is lost from all samples. The 4.1 eV emission depletes from WTUL1 and WTUL2, but develops in QzPara. The ~ 3.9 eV emissions deplete from QzPara and WTUL2, although a 3.95 eV emission develops in CalQzB34, similarly the ~ 3.3 eV emissions are depleted from QzPara and QzPerp but remain in CalQzB34, WTUL1 and WTUL2. Finally the ~ 2.7 eV emission, identified in only QzPara and QzPerp is depleted, although an emission at ~ 2.6 eV develops in QzPara. The response to x-irradiation is broadly similar for CalQzB34, QzPara and QzPerp, although the signal intensity of QzPara is most significantly affected (Figure 9.1).

9.3.2. **Anisotropy of the Light Emitted**

The initial luminescence from QzPara is brighter than that from QzPerp at the same dose and dose rate (Figure 9.1). The emission bands and intensities present are similar between the two samples, but are distinct from the other samples analysed. QzPara is initially dominated by the ~ 4.4 eV emission in contrast to QzPerp where the ~ 3.8 eV emission dominates. Despite this, the final emission spectra following irradiation exposure, are almost identical for the two samples (Figure 9.1). Both QzPara and QzPerp are dominated by the 3.8 eV emission, however whereas the ~ 2.7 eV emission is fully depleted from QzPerp (Figure 9.2), a ~ 2.6 eV emission remains for QzPara. This cannot be attributed to a difference in irradiation levels, as QzPara has received the higher dose of the two samples.

9.4. Discussion

9.4.1. **XEOL Emission Spectra**

The emission spectra of the quartz samples at the onset of irradiation vary in both intensity and energy (Figure 9.1). Although only a few quartz are analysed in the present study, this variability is consistent with a dependence on provenance since CalQzB34 is coastal sand which has been annealed, QzPara and QzPerp are hydrothermal quartz, and the WTUL samples are derived from granitic bedrock. Although other authors have investigated the luminescence of quartz using a range of different spectroscopic methods and excitation energies, and cite provenance as a controlling factor on the luminescence profile, the causal factors of this relationship have not been fully explored (see Preusser et al., 2009; Stevens-Kalceff and Phillips, 1995 for a review).

9.4.2. **The 4.1 eV and 4.4 eV Emissions**

All samples exhibit emissions at ~ 4.4 eV. QzPerp, CalQzB34, WTUL1 and WTUL2 also have an emission at ~ 4.1 eV, and QzPara exhibits a less energetic emission at ~ 4.0 eV. The origin of these emissions is uncertain, although emissions in quartz at 4.28 and 4.77 eV have been associated with recombination at *E'* centres (Jones and Embree, 1976), and at 4.4 eV with *E'* centres in oxygen deficient amorphous silicon dioxide (Nishikawa et al., 1994). Although crystalline SiO_2 and amorphous silica are structurally distinct, their luminescence is often similar (Götze, 1996), and thus it is appropriate to contrast their emissions (Krbetschek et al., 1997). Schilles et al. (2001) also observed an emission at this energy during RL of quartz which they tentatively attributed to the *E'* centre, although this was at the limit of their spectrometer's detection range. *E'* centres have a variety of forms, but comprise oxygen vacancies (see Weil, 1984 for a review) which may be coupled with other defects. Pacchioni and Ieranò (1997) alternatively relate this emission to the neutral oxygen vacancy centre (V_o) in α-quartz (≡Si-Si≡, where ≡ denotes bonding to three oxygen atoms).

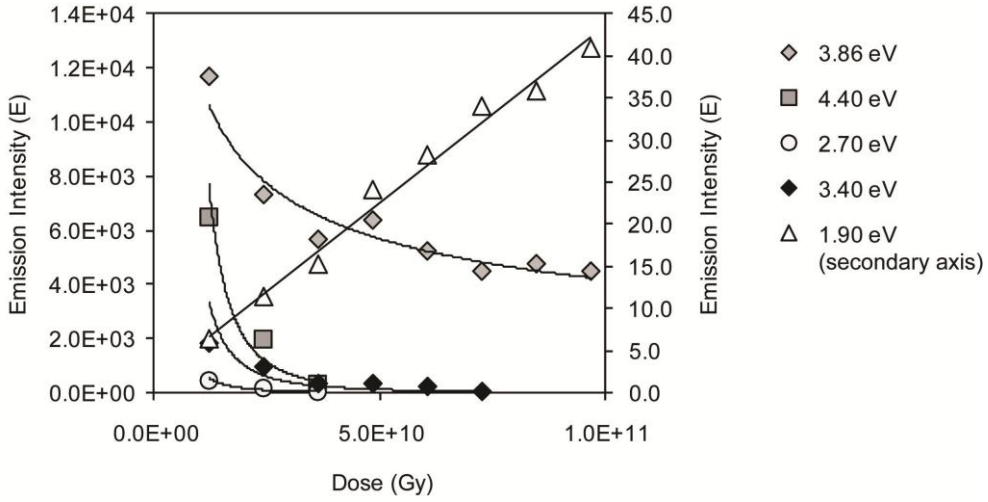

Figure 9.2: Plot showing the changes in intensity for the different emissions analysed for QzPerp, this sample was selected as it contains the full suite of emissions discussed throughout the text. Note that the axes are not in log-space. All emissions are fitted with a power-law function, with the exception of the red (1.9 eV) which is fitted with a linear function and is the only emission plotted against the secondary axis.

The 4.4 eV emission depletes rapidly as a function of dose for all samples and its decay can be fitted with a power function (Figure 9.2). The emission is fully absent from CalQzB34 (a) following 9.9 x 10^{10} Gy, from QzPara (a) following 7 x 10^{10} Gy, from QzPara (b) following 6 x 10^{10} Gy and from QzPerp following 4.9 x 10^{10} Gy. The emission does not fully deplete from CalQzB34 (b) following 1 x 10^{11} Gy, or from either WTUL sample.

As the 4.4 eV emission depletes so rapidly from CalQzB34 (a), QzPara and QzPerp, repeat analyses at a lower excitation energy are required in order to fully characterise its decay. Low temperature analyses may also improve the signal intensity of this emission, reducing phonon interactions with the defects under investigation. *E'* centres develop within quartz during irradiation (Griscom, 1980; Rink and Odom, 1991) it is therefore surprising that the 4.4 eV emission depletes throughout analysis, unless the specific type of *E'* centre responsible for this emission is being modified. Alternatively, where the 4.4 eV emission is due to the V_o centre, these centres may dissociate forming Si_3^- centres (Friebele et al., 1985; Griscom,1985; $Si^{\cdot}$:Si≡), charge compensated by H^+. The $[Si_3^-/H^+]^\circ$ centre has been associated with a red emission at 1.91 eV (Stevens-Kalceff and Phillips, 1995), consistent with the relationship between the UV and red emissions reported here. The charge compensating H^+ for this centre may be derived from interstitial protons, or the decay of $[AlO_4/H^+]^\circ$ centres, associated with the 3.3 eV or potentially the 2.7 eV emission discussed in sections 9.4.3 and 9.4.4, or alternatively from $[H_3O_4]^\circ$ centres (Nuttall and Weil, 1980; Yang and McKeever, 1990).

In contrast to the 4.4 eV emission, the 4.1 eV emission is present in CalQzB34, QzPerp and QzPara at the end of excitation, although it is not deconvolved for either WTUL sample. An absorption band at this energy has been previously reported for fused quartz (e.g. Levy and Varley, 1955) and a neutral oxygen vacancy centre of this energy has also been identified (Song et al., 2001).

9.4.3. **The UV Emissions (3.3-3.9 eV)**

The intensity and energy of the 3.3-3.4, 3.6-3.7 and 3.8-3.9 eV emissions vary between the different samples, and their energies and relative intensities change throughout analysis. The origin of the 3.3 eV emission in quartz has been explored by a number of authors, and was observed to dominate these samples during ionoluminescence (IL; see Chapter 8). Although some debate about its origin remains, the 3.3 eV emission is most commonly attributed to the substitution of Si^{4+} with Al^{3+}, charge compensated by either protons or interstitial alkali ions (Alonso et al., 1983; Itoh et al., 2002; Perny et al., 1992), forming $[AlO_4/M^+]^\circ$ centres. Poolton et al. (2000) and Schilles et al. (2001) have associated the OSL emission with $[TiO_4/Li^+]^\circ$ and $[TiO_4/H^+]^\circ$ donor centres, which recombine at the $[AlO_4]^\circ$ recombination centre to emit at 380 nm (Martini et al., 1995).

Quartz emissions at 3.6 eV have been attributed to the recombination of electrons at oxygen vacancies (Itoh et al., 2002; Rink et al., 1993). However, during IL these emissions were observed to develop following exposure to irradiation (Chapter 8), and

have tentatively been attributed to $[AlO_4]^{\circ}$ centres, charge compensated by $M^{+}_{(free)}$. These centres form following irradiation induced migration of charge compensating cations from $[AlO_4/M^{+}]^{\circ}$ centres, which occurs at temperatures > 200 K (Durrani et al., 1977; Halliburton et al., 1981; McKeever 1984; Stevens-Kalceff and Phillips, 1995). Although this emission develops in QzPara throughout analysis, no relative increase in intensity is apparent from the deconvolved spectra of the other samples, in contrast to the IL emission spectra (see Chapter 8). If this emission is instead associated with the oxygen vacancy centre, then recombining charge may compete with that of the 4.4 eV emission, which is favoured during x-irradiation (Figure 9.1).

The 3.8-3.9 eV emission is less frequently reported in the literature. Demars et al. (1996) recorded a 330 nm (3.76 eV) emission in quartz overgrowths using cathodoluminescence (CL), and linked it to high Al and Li concentrations determined through SIMS. Rink et al. (1993) also observed an emission at 330 nm (3.76 eV) in pegmatitic and volcanic quartz samples using spectroscopic thermoluminescence, which they linked to contamination of the quartz with feldspar. Emissions at this wavelength have been recorded in a variety of feldspar minerals (see Krbetschek et al., 1997 for a review), and have been associated with stressed silicate lattices (Garcia-Guinea et al., 2007a). Discrete feldspar are rejected as the origin of the 3.8-3.9 eV emission reported here for a number of reasons: 1) it is present in all samples; 2) the CalQzB34 has been tested for feldspar contamination both through SEM microscopy and IR (880 nm) OSL stimulation which resulted in no luminescence, which would be anticipated were feldspar present; and, 3) QzPerp and QzPara are derived from a quartz macrocrystal and are therefore unlikely to contain feldspar impurities.

The 3.8-3.9 eV emission may instead reflect luminescence of multiple excited states which are not usually observed at lower ionisation densities. Similar observations were made by Garcia-Guinea et al. (2007b) who found that the IL emission of albite was strongly dependent on the excitation ionisation density when they varied the ion implantation species from H^{+} to H_2^{+}. An absorption band at 3.8 eV, associated with peroxy linkages, has been observed in quartz (Nishikawa et al., 1989) and it is tentatively suggested here that the high excitation energies achieved in XEOL limit the stokes shift of an associated luminescence emission, however coupled absorption and emission spectroscopy are required to validate this suggestion.

9.4.4. **The 2.70 eV Emission**

The blue-violet emission at ~ 2.7 eV was only observed in the initial QzPara and QzPerp emission spectra, although a less energetic ~ 2.6 eV emission is recorded in the

final QzPara spectrum. The ~ 2.7 eV emission has been previously reported, using a range of excitation methods, and has been attributed to the self-trapped exciton (STE) (e.g. CL, Stevens-Kalceff and Phillips, 1995; x-rays, Trukhin and Paludis, 1979), or to intrinsic defects (e.g. photoluminescence (PL), Friebele et al., 1985; CL, Luff and Townsend, 1990).

Jürgensen et al. (2009) observed this emission in the XEOL of hydrothermal quartz crystals, and attributed it to a composite of three emissions centred at 2.5, 2.8 and 3.1 eV. The 2.5 eV emission is related to an extrinsic process (Itoh et al., 1988; Stevens-Kalceff and Phillips, 1995; Tanimura and Halliburton, 1986), the 2.8 eV emission to radiative recombination of the STE (Itoh et al., 1988; 1989), possibly associated with peroxy bonding sites (≡Si-O-O-Si≡) (Hayes et al., 1984; Jürgensen et al., 2009), and the 3.1 eV emission to radiative recombination at $[AlO_4/M^+]^\circ$ centres (Alonso et al., 1983; Jürgensen et al., 2009; see Chapter 8 for a review). Deconvolution of the initial QzPara and QzPerp emissions does not support this proposal in the present samples, as none of the component emission intensities are identified, however the 2.56 eV emission identified in the final QzPara spectrum may relate to the extrinsic process.

The 2.7 eV emission is absent in the final spectra following irradiation exposure (Figure 9.1). This contrasts with Götte et al. (In Press) who observed no irradiation sensitivity for a 448 nm (2.77 eV) emission from hydrothermal quartz explored with CL, which may be explained by the distinct excitation energies of XEOL and CL analyses (see Table 7.1). If the 2.7 eV emission is related to a centre involving hydrogen such as $[AlO_4/H^+]^\circ$ centres, then its dose dependency may be explained. The relatively light mass of hydrogen makes it susceptible to irradiation induced migration, thus it is likely that these centres will dissociate rapidly, reflected in the rapidly depleting 2.7 eV emission. Furthermore, liberated H^+ will react readily with available vacancies, possibly charge compensating the Si_3^- centres produced during V° centre dissociation, and contributing to the red emission at 1.9 eV.

9.4.5. **The Red Emission (1.9-2.0 eV)**

None of the quartz samples initially exhibit a red emission (Figure 9.1), however an emission at ~ 1.9 eV was observed to develop with radiation dosing for all samples with the exception of WTUL1. Similar observations have been reported by other authors for CL (e.g. Botis et al., 2006) and IL (e.g. Bettiol et al., 1997). This emission is attributed either to the NBOHC (Munekuni et al., 1990) or alternatively to development of Si_3^- centres following the irradiation induced decay of oxygen vacancies (Friebele et al., 1985; Stevens-Kalceff and Phillips, 1995). If these oxygen vacancies are the precursor centres

of the red emission during XEOL, then it may also explain why the 3.6 eV and 4.4 eV emissions are observed to deplete throughout irradiation (see Sections 9.4.3 and 9.4.2). Red emissions at 1.75 eV have been associated with the substitution of Si^{4+} with tetrahedral Fe^{3+} (Pott and McNicol, 1971), however no emissions at this energy are observed here.

The increase in the red emission intensity was satisfactorily modelled as linear for all samples, with the exception of CalQzB34, which increases asymptotically. There are several ways to fit saturation behaviour and here it is approximated with a saturating exponential (Figure 9.3). It may either be that CalQzB34 has a distinct dose dependence or that dose dependence of this centre is sigmoidal for all samples, but that all but CalQzB34 are close to saturation, at which point sigmoidal and linear dependences are difficult to distinguish. A potential explanation for the saturating behaviour of CalQzB34 is that an equilibrium situation is arising whereby irradiation induced creation and destruction of the centres responsible for the red emission is occurring at the same rate. However, other samples were exposed to the same amount of irradiation throughout the experiment and no such saturation phenomenon was observed. Berger (1990) comments on similar dose response behaviour observed for quartz during OSL and TSL. Stevens-Kalceff and Phillips (1995) observe development of a 1.9 eV emission, associated with non-hydroxyl NBOHC precursors, which exhibits similar dose dependence under electron beam irradiation.

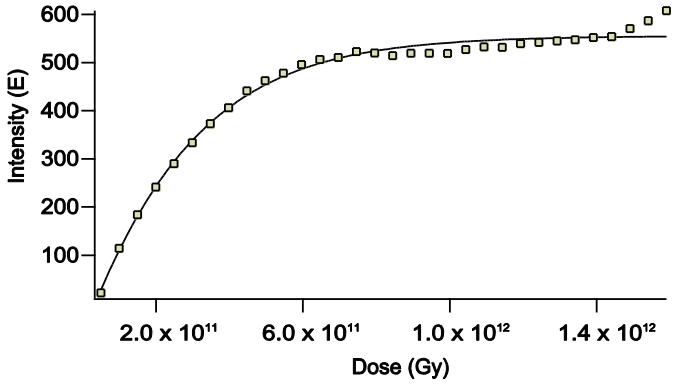

Figure 9.3: Plot showing the increase in the 1.97 eV emission as a function of irradiation dose for CalQzB34 (a).

9.4.6. **Interrelationships between the UV, Blue-violet and Red Emissions**

All of the UV/blue emissions reduce in intensity, to the benefit of the red emission, as a function of dose in all samples (Figure 9.4). This can be considered quantitatively through calculating the ratio of the visually identified composite 3.8, 3.4 and 2.7 eV emissions, to the composite red 1.9 eV emission. Composite emissions rather than the individual deconvolved signals were fitted in this manner to enable a general comparison

between the different quartz samples which exhibit slight variations in specific signal intensities and energies. Furthermore, OSL dating conventionally operates through measurement of a composite signal under continuous wave light stimulation. The depletion of the UV and blue emissions to the benefit of the red can be fitted with a power-law relationship: $A_{3.8/1.9}e^{-mD}$, where $A_{3.8/1.9}$ is the ratio of composite emissions 3.8/1.9 eV in the first analysis, and *m* is the slope as a function of dose *D* (Gy). The pre-exponential factor A varies significantly between the different samples, and is dependent upon the initial emission intensity (Table 9.1), which is also dependent upon signal integration period. The signals of CalQzB34 (a) and the WTUL samples are integrated over 10 s and CalQzB34 always has a greater A value, indicative of its greater luminescence QE, in contrast the WTUL samples have A factors < 5.

The power law function fits all samples well ($r^2 \geq 0.87$) with the exception of the WTUL samples ($r^2 \leq 0.28$), attributed to their poor signal to noise ratios. It was not possible to investigate the interrelationship of the 4.4 and 1.9 eV emissions, because of the rapid depletion of the 4.4 eV emission throughout irradiation (see section 9.4.2). The average slope values for the 3.8/1.9 and 3.4/1.9 eV emission ratios overlap within error; $m_{3.8/1.9}$ is -1.46 ± 0.41 and $m_{3.4/1.9}$ is -1.16 ± 0.47. The similarity in dose dependence between the two emissions indicates three possible scenarios: 1) there is a direct physical relationship between the luminescence centres; 2) the same processes are operating to affect the centres; and/or, 3) unrelated processes are operating at the same rate. The average slope for the 2.7/1.9 eV emission ratio is distinct from the 3.8/1.9 and 3.4/1.9 eV ratios, indicating that the 2.7 eV emission is derived from a physically different centre and consistent with the first proposal that the 3.8 and 3.4 eV emission have a direct physical association.

The nature of the interrelationship between the UV and red emissions is uncertain and more complicated than the behaviour exhibited during IL suggests (see Chapter 8). Götte et al. (In Press) recently discounted a coupling between these centres as CL of hydrothermal quartz produces more rapid depletion of the 395 nm (3.1 eV) emission relative to increase of the 648 nm (1.9 eV) emission. The linear increase of the red emission reported here from XEOL, relative to the power-law decay of the UV and blue emissions, supports a more complex interdependence of the two centres which varies with the form of excitation. Further work is required to elucidate fully the relationships between the interrelated centres responsible for the range of emissions observed.

9.4.7. **Dose Rate Effects**

All experiments seeking to simulate natural radiation damage accumulated over geological timescales use far greater dose rates than the natural environment. Sedimentary quartz is typically exposed to dose rates of ~ 1 mGy a^{-1}, whereas those in granite (and quartz grains adjacent to zircons) may experience dose rates of up to 60 Gy a^{-1}. In contrast the estimated dose rate for the synchrotron x-rays at 7148 eV is 7.9 x 10^{15} Gy a^{-1}. Dose rate effects are different by 14 orders of magnitude and may have a significant influence on the emission spectra and the dynamics of the modification. For example, dose rate effects could explain the differences in the emission spectra reported here to Jürgensen et al. (2009) who excited quartz XEOL under vacuum with softer x-rays of 1.8 keV.

The key observation that the UV and blue quartz emissions deplete with increasing irradiation exposure to the benefit of the red emission, are supported by a range of complimentary excitation methods, such as CL and IL which have different radiation dose rates. Cathodoluminescence excites only the surface of a sample, as penetration is ~ 1.3 µm at 15 kV (Drouin et al., 2007), which equates to a dose rate of ~ 1 x 10^{8} Gy s^{-1}. In contrast IL excitation with protons at 0.95 MV excites samples to ~ 11 µm depth, delivering a dose rate of ~ 1.3 x 10^{5} Gy s^{-1} (see Chapters 7 and 8) and yet the resultant spectroscopies are broadly similar, therefore tentatively the data are interpreted as independent of radiation dose rate.

9.4.8. **Anisotropy of Emitted Light**

QzPara has a more intense initial signal than QzPerp, an observation consistent with the IL experiment results (Chapter 8). Initial spectra vary as the 4.4 eV emission dominates QzPara in contrast to QzPerp which is dominated by the 3.8 eV emission (Figure 9.1). The rate at which the UV emission declines to the benefit of the red emission is greater for QzPara (Table 9.1). This is unexpected as the migration of charge compensating cations, associated with the 3.4 eV emission, is anticipated to be most rapid along the *c*-axis (see Section 9.4.8).

The final emission spectra of the samples are almost indistinguishable, both in emission profile and intensity (Figure 9.1) indicating that the same processes are operating, albeit at different rates (Figure 9.4). The key contrast is the presence of the 2.56 eV emission in the final spectrum of QzPara, which is absent from QzPerp. This emission may be related to the 2.7 eV emission, present in both hydrothermal samples at the outset of analysis, and is attributed to an extrinsic process. The precise origin of this emission has not been reported previously, however extrinsic emissions are attributed to

element impurities which may be present either as substitutions or interstitial ions. Therefore, the persistence of this emission in QzPara relative to QzPerp may reflect the reduced rate of ion migration in this orientation. An alternative explanation for the differences in the emission spectra reported here may be localised structural or compositional variations in the quartz macrocrystal, which cannot be discounted. However, assuming that the crystal is homogenous these results indicate that quartz grains aligned parallel to the *c*-axis luminesce most brightly, but that radiation dosing reduces the magnitude of the difference.

Table 9.1: Dose dependence (*m*) and Pre-Exponential (A) terms for x-irradiation of quartz. No data for the 3.40 eV emission are available for QzPara because of low emission intensity, the 2.70 eV emission is only observed for QzPara and QzPerp.

Sample	$A^{3.86/1.90}$	$m^{3.86/1.90}$	r^2
CalQz (a)	11.33 ± 1.45	-0.85 ± 0.12	0.87
CalQz (b)	29.24 ± 2.62	-2.47 ± 0.24	0.96
WTUL1	4.41 ± 2.73	-0.23 ± 0.27	0.20
WTUL2	4.36 ± 2.08	-0.23 ± 0.18	0.28
QzPerp	17.07 ± 0.94	-1.37 ± 0.09	0.99
QzPara (a)	28.59 ± 5.94	-2.47 ± 0.54	0.94
Qz Para (b)	31.67 ± 6.81	-2.76 ± 0.62	0.94
Average		*-1.48 ± 0.41*	

Sample	$A^{3.40/1.90}$	$m^{3.40/1.90}$	r^2
CalQz (a)	11.69 ± 1.43	-0.93 ± 0.12	0.89
CalQz (b)	25.13 ± 3.37	-2.13 ± 0.31	0.91
WTUL1	3.52 ± 2.59	-0.16 ± 0.25	0.12
WTUL2	4.15 ± 2.13	-0.22 ± 0.19	0.26
QzPerp	26.37 ± 3.35	-2.37 ± 0.32	0.99
QzPara (a)	-	-	-
QzPara (b)	-	-	-
Average		*-1.16 ± 0.47*	

Sample	$A^{2.70/1.90}$	$m^{2.70/1.90}$	r^2
QzPerp	35.33 ± 9.07	-3.31 ± 1.75	0.93
QzPara (a)	34.71 ± 5.09	-3.12 ± 0.47	0.97
QzPara (b)	41.01 ± 3.96	-3.71 ± 0.36	0.99
Average		*-3.38 ± 0.17*	

CalQzB34, WTUL1 and WTUL2 comprise multiple 180-212 µm grains. As the incident beam is ~ 3 μm^2 in diameter, it is inferred that single grains have been analysed. The orientation of these grains is unknown; however the crystal anisotropy results indicate that as the ~ 3.8 eV emission dominated the initial spectra of these samples, they are all aligned perpendicular to the *c*-axis.

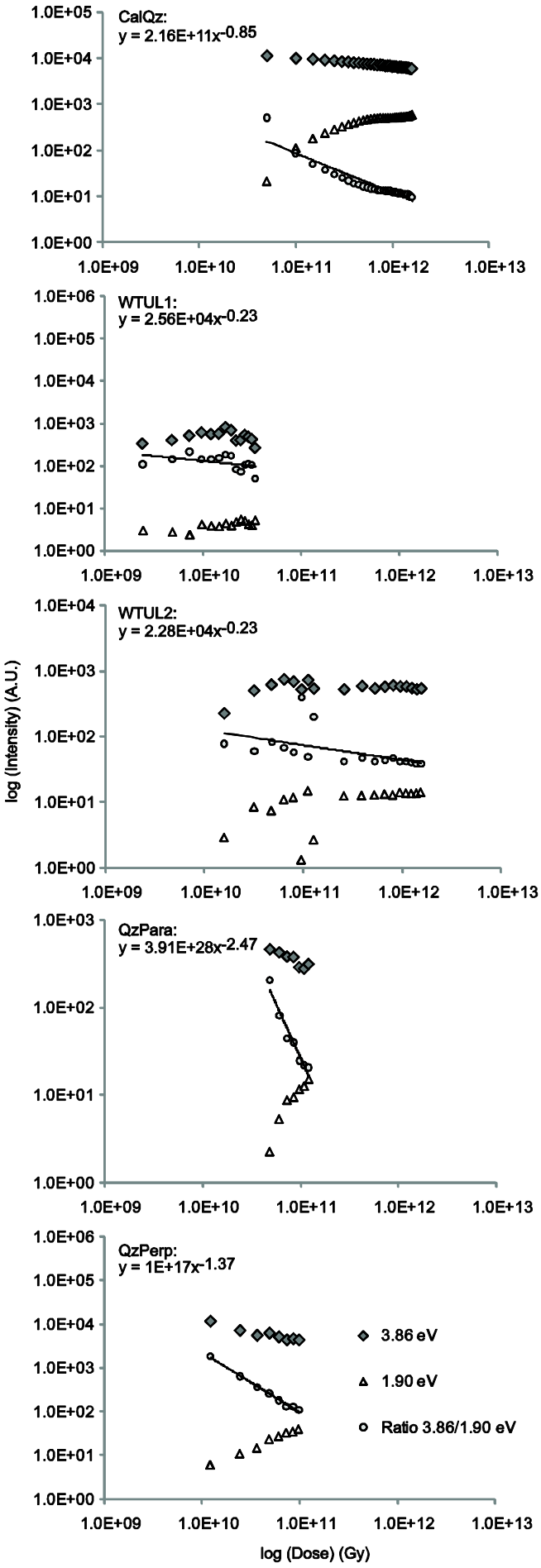

Figure 9.4: Log-log plots of luminescence emission intensity as a function of irradiation time (dose) for all samples. The 3.86 eV and 1.9 eV emissions are plotted, as is the ratio 3.86/1.9, which is fitted with a power-law relationship in log-log space. Note that as the initial three spectra of QzPara exhibited no 1.9 eV emission, data are only plotted following 4.85 x 10^{10} Gy. The red emission drops significantly in intensity for WTUL2 in two of the collected spectra, however as the 3.8 eV emission is unaffected, beam instability or localised heating are unlikely to be responsible for this fluctuation.

9.5. Conclusions

The analysis of quartz XEOL enables exploration of complex luminescence pathways not observed at lower excitation energies and provides insights into the processes occurring in naturally irradiated quartz. These experiments complement published work carried out using IL and CL and demonstrate that 1) quartz of different provenances exhibit different XEOL, attributed to their specific geological histories; 2) radiation dosing promotes a reduction in the UV XEOL to the benefit of the red in all samples; 3) a physical relationship between the 3.8 and 3.4 eV emission centres may exist, inferred from the similarity in the rate of emission depletion; 4) the 2.7 eV emission is independent of the 3.4 and 3.8 eV emissions and exhibits greater irradiation sensitivity than the other UV emissions; and, 5) the luminescence emissions of a natural hydrothermal quartz crystal cut parallel and perpendicular to the *c*-axis are different. QzPara initially exhibits a dominant 4.4 eV emission whereas QzPerp is dominated by the 3.8 eV emission. Grains orientated perpendicular to the *c*-axis will luminesce more brightly than those orientated parallel to the *c*-axis.

Chapter 10. Spectroscopy Synthesis

10.1. Introduction

The various spectroscopic techniques explored within this thesis have analysed the same suite of samples, and thus might be expected to have similar luminescence. Where emission spectra vary in response to the different types and energies of excitation, it provides insights into the physical nature of the defects present, which is one of the key objectives of mineral spectroscopy. Such insights allow inter-relationships between the emission centres to be identified and better understood, and allow luminescence models to be improved.

All of the excitation techniques explored, with the exception of PL, have revealed that the quartz emission is dominated by a range of UV-blue emissions, part of which is conventionally monitored during OSL. These emissions are generally attributed to structural extrinsic (substitution) and intrinsic (vacancy) defects within the crystal (Chapter 2). Throughout irradiation, the emission intensity and energy of the UV-blue emissions change, consistent with these centres being intrinsic in nature and increased mobility of these defect structures throughout the crystal.

Ionoluminescence and XEOL are complimentary methods. Although the dose rate of XEOL is much greater (see Chapter 7), both techniques excite luminescence primarily through sample ionization. Ionoluminescence and XEOL are also sufficiently energetic to break structural bonds within the crystal (particularly Si-O), which will influence the luminescence spectrum. Bonds which have been broken form two dangling bonds; bond breakages are usually transient and recover within short (e.g. ns) lifetimes, although some may be metastable and hence effectively permanent. This process could be explored through time-resolved spectroscopies, and future experiments are planned. The dose dependence of the IL and XEOL emissions may be a consequence of broken bonds failing to recover, and the resultant increase in ion/defect mobility. In the experiments presented here, the IL excitation delivers charge carrier densities 6 orders of magnitude less than XEOL. XEOL delivers 1.1×10^{16} photons μm^{-2} in contrast to IL which delivers 2.4×10^{10} ions μm^{-2}, thus although the charge carriers in IL are more energetic (1.52×10^{-13} J) than XEOL (1.14×10^{-15} J), the total excitation energy and the dose rates delivered in XEOL are greater. Hence in these experiments, there is a far greater probability that x-irradiation will interact with metastable, excited states, such as the transient, dangling bonds caused by bond breakage.

Ionoluminescence is a form of ‘corpuscular’ excitation, thus although protons have very low mass and SRIM modelling indicates that 99 % of energy delivery results in ionisation (Figure 8.1), some atomic displacements occur within the target sample. Elastic collisions occur between implanted ions and the nuclei of the solid, which can physically

knock atoms from sites creating frenkel defects (i.e. vacancies in one part of the structure and interstitial ions elsewhere). It is possible to predict that implantation of quartz with heavier elements, such as He or N, or at greater acceleration energies would result in different IL emission spectra to those observed, as vacancy development influences possible recombination pathways. This may also account for the minor variations between the IL spectra reported in Chapter 8, and those of Bettiol et al. (1997) who implanted quartz with protons at 3.0 MV. In contrast as x-rays have no mass, physical displacements are not possible during XEOL. Thus it may be anticipated that emissions relating to vacancy development or loss of short-range order may be present within IL emissions, but not within the XEOL spectra. However, as quartz is opaque in the UV at depths > 250 nm (e.g. Gurkovskii et al., 1974) and physical displacements created during IL are largely concentrated at the end of the ion-track (> 10 µm; SRIM modelling of the experimental conditions reported here, Chapter 8), such emissions may not be visible at the sample surface.

Contrasting and comparing the emission spectra of the IL and XEOL experiments provides insights into the origins of the different emission energies, and associated recombination centres. The results from the CL and RL analyses presented in Chapter 7 are also considered with the IL and XEOL data in a summary table, and implications for OSL discussed.

10.2. Similarities in emission spectra

Both the IL and XEOL emissions are initially dominated by a suite of UV emissions of varying intensities and energies. The 3.3 eV and 3.6 eV emissions are common to both excitation methods, however emissions > 3.6 eV are only observed for the XEOL spectra. Both the IL and XEOL exhibit similar irradiation dose dependence, whereby the UV-blue emissions deplete to the benefit of the red/IR, although the rate of this relationship varies between emissions, techniques and samples.

10.2.1. **The 3.3 eV Emission**

The 3.3 eV emission, which is believed to relate to the quartz OSL and 110 ˚C TSL emission (Martini et al., 2009), was dominant in the IL emission spectra (Figure 8.2) and was identified in all initial XEOL spectra by deconvolution (Figure 9.1). This emission is attributed to $[AlO_4/M^+]^\circ$ or $[AlO_4/H^+]^\circ$ centres, charge compensated by interstitial H^+ or cations (Alonso et al., 1983; Itoh et al., 2002; Luff and Townsend, 1990; Perny et al., 1992 see Chapter 8 for a review). An alternative proposition is that it arises from $[AlO_4]^\circ$ centres, charge compensated by a bridging electron hole, h^+ (Martini et al., 2009; Martini and Galli,

2007; Martini et al., 1995). Durrani et al. (1977) and McKeever (1984) have also suggested that this emission is associated with *E'* centres, and Schilles et al. (2001) and Poolton et al. (2000) have associated it with $[TiO_4/M^+]^\circ$ or $[TiO_4/H^+]$ donor centres, identified from ESR.

The IL and XEOL observations in Chapters 8 and 9 indicate that $[AlO_4/M^+]^\circ$, $[AlO_4/H^+]^\circ$ or $[AlO_4/h^+]^\circ$ centres are the most probable origin of this emission, although these analyses do not enable differentiation between Al^{3+} or Ti^{4+} substitutions. Ge^{4+} may also substitute for Si^{4+}, however as Al^{3+} substitutions are most common within quartz, our discussion is restricted to these centres (Götze, 2009). ESR analyses would enable differentiation of these centres when they are paramagnetic, rather than diamagnetic, and combinations of ESR and IL/XEOL will constitute future work.

The dominance of the 3.3 eV emission in IL spectra, relative to XEOL, indicates complexity in the recombination pathways under investigation. Since ionisation constitutes the primary means of energy deposition in both methods, it might be expected that XEOL and IL spectra will be identical. However, the XEOL experiment delivers 6 orders of magnitude greater number of charge carriers to the sample, which enhances the opportunity for excitation of metastable, multiple excited states. The resultant excitons may recombine via alternative pathways, potentially quenching the 3.3 eV emission intensity due to competition effects. In contrast to the IL spectra, the XEOL spectra are dominated by a 3.8 eV emission, and also have a range of emissions > 4.0 eV which may be accessed by these excitons (see Chapter 9 for a discussion). Therefore it is possible to hypothesise that these high energy recombination sites are from metastable doubly-excited recombination centres.

10.2.2. **Dose Dependence of the 3.3 eV Emission**

The depletion of the 3.3 eV emission to the benefit of the red emission is within uncertainties for both the IL ($Ae^{-1.115 \pm 0.007\ D}$, see Chapter 8) and XEOL ($Ae^{-1.16 \pm 0.47\ D}$, see Chapter 9) measurements. This suggests that irrespective of the influence of multiple excited states on the emission spectra, the depletion of quanta of UV luminescence at this energy is linked to the development of quanta of red luminescence. However, whereas all of the pre-exponential factors (*A*) overlap within error for the IL analyses of every sample (except QzPara, see Chapter 8), those analysed with XEOL do not. The uncertainties of the XEOL 3.4 eV dose dependence are much greater than for IL, and are associated with reduced total signal intensities, and the reduced dose dependence of the WTUL samples, discussed in Section 9.4.6.

The dose quenching of the 3.3-3.4 eV emissions is attributed to the migration of charge compensating ions away from $[AlO_4]^-$ centres, which has been widely reported

elsewhere (e.g. Perny et al., 1992; see Chapter 8 for a review). However the precise interrelationships between precursor centres, $[AlO_4]^\circ$ and their respective charge compensators is still debated. For example Itoh et al. (2002) have proposed a model whereby TSL is produced through the migration of defects (M^+) and recombination at $[AlO_4]^-$ centres, in contrast to the Randall and Wilkins model (1945) of electron recombination normally adopted within retrospective luminescence dosimetry e.g. Bailey (2001). Itoh et al. (2002) propose that OSL is produced through the migration of electrons and holes, whereas Martini et al. (2009) propose recombination of the TSL and OSL 3.3 eV emissions at $[AlO_4/h]^\circ$ traps. Thus further research is required to fully understand the specific energy transitions that generate quartz luminescence, and also how it is modified.

10.2.3. **The 3.6 eV Emission**

The 3.6 eV emission was recorded in both IL and XEOL. Itoh et al. (2002) and Rink et al. (1993) attribute this emission to intrinsic oxygen vacancy defects, which occur naturally within quartz samples. In the IL experiments, as the UV emission depletes, its peak intensity shifts from 3.3 eV to 3.6 eV throughout irradiation. Oxygen vacancy development is rejected as the cause of this emission shift, since, although IL will result in some elastic collisions and physical displacements, SRIM modelling indicates that only 1% of implantation energy is dissipated in this manner and is concentrated at depths greater than ~ 10 μm during ion implantation (Figure 8.1). However luminescence originating from centres at this depth is reabsorbed and may not contribute to the emission from the crystal surface (e.g. Gurkovskii et al., 1974). This shift in emission intensity to 3.6 eV is instead interpreted to reflect an increasing population of $[AlO_4]^\circ$ centres, charge compensated by $M^+_{(free)}$ produced through the irradiation induced dissociation of $[AlO_4/M^+]^\circ$ centres (see Chapter 8).

In the XEOL spectra, the 3.6 eV emission is more intense than the 3.3 eV emission for CalQzB34 and QzPerp, but is not present in all of the samples analysed, and does not exhibit uniform dose dependence (see Chapter 9). The contrast between the XEOL and IL spectra in this respect may relate to the development of multiple excited states during XEOL, and increased competition for recombining charge. This can also explain the relative quenching of the 3.3 eV emission in contrast to the other XEOL UV emissions recorded.

10.2.4. The 2.6-2.7 eV Emission

A blue emission at 2.6-2.7 eV was recorded for QzPerp, WTUL1 and WTUL2 during IL and for QzPara and QzPerp during XEOL. A bright 2.7 eV emission replaced all other emissions during LNT IL of QzPara and QzPerp (Figure 8.6). Itoh et al. (1989; 2002) have attributed this emission to the STE, although other authors have suggested that it originates from E' centres (Sigel, 1973), or from $[AlO_4/M^+]^\circ$ centres because of its insensitivity to irradiation at low temperatures (Stevens-Kalceff and Phillips, 1995).

10.2.5. Dose Dependence of the 2.6-2.7 eV Emission

The 2.6-2.7 eV RT emission exhibits significant dose dependence during IL and XEOL, although the IL spectra for QzPara and QzPerp collected at LNT exhibit no dose dependence. The XEOL and IL experiments indicate that the 2.7 eV emission exhibits greater dose dependence than the 3.4 eV emission during x-irradiation, and for the XEOL emissions it can be characterised by the relationship $A e^{-1.59 \pm 0.46\ D}$ where the absolute signal intensity of the 2.7 eV emission is calculated relative to dose (Table 10.1). The 2.7 eV emission emits a smaller proportion of total energy during RT IL, and it was not possible to fit the signal decay of this relationship with a power-law function ($r^2 \leq 0.19$). For the XEOL spectra, the slope of blue signal depletion is greater than that of the 3.4 eV XEOL emission, but overlaps within uncertainties; consequently it is not possible to conclude whether this emission originates from a different centre to the 3.4 eV emission. However, where the ratio 2.7/1.9 eV is considered (i.e. dividing out beam current fluctuation), $A e^{-3.39 \pm 0.17\ D}$ is derived (see Chapter 9), which is distinct from the 3.4/1.9 emission depletion gradient. This allows the conclusion to be drawn that the blue emission is derived from a centre other than the $[AlO_4/M^+]^\circ$ centre involved in 3.4 eV emission production.

These data may indicate that the blue emission originates from the $[AlO_4/H^+]^\circ$ centre, (i.e. a centre with a broadly similar dose dependence as the 3.4 eV emission) but with a different numerical decay rate. H^+ has the greatest mobility of the various charge compensators, which is consistent with the greater irradiation sensitivity of this centre. This is also consistent with the persistence of the 2.7 eV emission during LNT IL analysis, as at LNT H^+ mobility is considerably reduced. Although H^+ is mobile under electron beam irradiation at < 100 K (Griscom, 1985b), it exhibits enhanced mobility at 170-200 K (Stevens-Kalceff and Phillips, 1995). Griscom (1985b) has alternatively proposed that atomic hydrogen may act as a charge compensator for *E'* centres ($\equiv Si^\bullet$) at low temperatures (80 K):

Eq. 10.1 ($\equiv Si^\bullet + H^\circ \rightarrow \equiv Si.\text{-}H^+$)

which may also explain this emission. Although, as *E'* centres are able to develop throughout irradiation at low temperatures (Stevens-Kalceff and Phillips, 1995), an increase in this emission may be anticipated. However no increase in emission intensity as a function of dose was recorded for the LNT, IL experiments. The centre proposed by Griscom (1985b) has a lifetime of ~ 1 ms, thus time-resolved spectroscopies would enable more precise assignment of the true recombination defect.

10.2.6. **The Red Emission (1.7-2.0 eV)**

A red emission develops as UV depletes during the IL and XEOL analyses. Whereas the red emission is initially present in IL spectra, it is absent at the beginning of XEOL and develops throughout exposure. The IL red emission can be deconvolved into two overlapping bands at 1.7 eV and 2.0 eV, which are related to the Fe^{3+} defect and NBOHC respectively (see Chapter 8 for a review). Increasing dose results in a shift of the IL red emission towards lower energies, interpreted as an increase in NBOHCs and also an increase in the efficiency of the Fe^{3+} centre due to reduced competition from $[AlO_4/M^+]^\circ$ centres for recombining charge. Deconvolution of the XEOL spectra indicate a single emission at 1.92-1.97 eV. The red IL emission is bright relative to the IL UV emissions (Figure 8.2), in contrast to the XEOL spectra (Figure 9.1), which may again indicate differential cascading of charge between the two excitation methods.

10.2.7. **Dose Dependence of the Red Emission**

The development of a red emission as a function of dose during XEOL is attributed to an increasing NBOHC population. Radiolytic damage of quartz is possible at energies > 9 eV (Griscom, 1985b), and will contribute to an increasing population of NBOHC throughout analysis as permanent bond breakages develop. The luminescence characteristics of NBOHC are dependent upon their precursor centres (Figure 10.3): hydroxyl precursors luminesce at 1.95 eV whereas non-hydroxyl precursors luminesce at ~ 1.9 eV (see Stevens-Kalceff and Phillips, 1995 for a review). Stevens-Kalceff and Phillips (1995) observed depletion of a 1.98 eV emission in CL with increased electron beam exposure, whereas an emission at 1.9 eV increased in intensity with exposure, before stabilising. These results are consistent with the IL and XEOL, and thus hydroxyl groups are not regarded as the main precursors for NBOHC within these samples. The red XEOL emission of CalQzB34 increases asymptotically as a function of irradiation (Figure 9.3), consistent with the non-hydroxyl NBOHC precursor centre described by Stevens-Kalceff and Phillips (1995).

≡Si-O-H → ≡Si-O• + H°
Hydroxyl Centre → NBOHC and atomic hydrogen

≡Si-O-O-Si≡ → ≡Si-O• .O-Si≡
Peroxy Centre → 2 NBOHC

≡Si-O- -Si≡ → ≡Si-O.•Si≡
Strained Silicon Centre → NBOHC and *E'*

Figure 10.1: Precursors of NBOHC in quartz (Stevens-Kalceff and Phillips, 1995)

$[Si_3^-/H^+]^\circ$ centres have also been associated with a red emission at 1.91 eV (Stevens-Kalceff and Phillips, 1995). This centre, which comprises a three-coordinated silicon atom, with a trapped electron, has been recorded to develop throughout irradiation in silica, (Friebele et al., 1985; Griscom, 1985a), and develops from dissociation of the neutral oxygen vacancy (V_o) (Pacchioni and Ieranȯ, 1997).

Eq. 10.2: ≡Si-Si≡ + H^+ → ≡Si. :Si≡ / H^+

The V_o centre is thought to contribute to the 3.8 eV XEOL emission, and it is therefore plausible that Si_3^- centres may develop as a consequence of irradiation, and contribute to the red, XEOL emission.

10.3. The ≥ 3.8 eV Emissions

A suite of UV emissions are recorded only in XEOL, despite the energy of carriers for both the XEOL and IL being significantly > 9 eV, the band gap of quartz. The XEOL emissions recorded at energies ≥ 3.8 eV are attributed to the development of multiple excited states, associated with the increased flux of charge carriers within XEOL rather than IL. I infer that these centres form for excited structures, such as excitation of transient bond breakages. The origin of these different centres is considered only briefly, as further details are given in Chapter 9.

10.3.1. **The 3.8 eV Emission**

The origin of the 3.8 eV emission has not been widely reported but a 3.64-3.75 eV (330-340 nm) emission has been associated with high Al and Li content (Demars et al., 1996). However as 3.8 eV is also the average bond energy between Si and O in quartz (Gilman, 2008), this suggests that the defect responsible for this emission is intrinsic. An absorption band at 3.8 eV is associated with peroxy linkages by Nishikawa et al. (1989), and it is tentatively suggested here that the high excitation energies achieved in XEOL limit the stokes shift of an associated luminescence emission. Coupled absorption and emission spectroscopy are required to validate this suggestion. If peroxy linkages are the

cause of this emission, then it also follows that these may form precursor centres for peroxy radicals and *E*' centres (≡Si-O-O-Si≡ → ≡Si-O-O$^{\bullet}$ + ≡Si$^{\bullet}$) as proposed by Friebele et al. (1979), or NBOHC (Munekuni et al., 1990). Peroxy radicals are associated with the STE and blue luminescence (Itoh et al., 1989; Itoh et al., 2002). *E*' centres influence the luminescence of quartz in a variety of ways, and may contribute as radiative (e.g. Jones and Embree, 1976), or non-radiative acceptor centres (e.g. Poolton et al., 2000).

10.3.2. Dose Dependent Effects on the 3.8 eV Emission

The 3.8 eV emission reduces in intensity as a function of dose, which may be explained by the irradiation-induced breakdown of peroxy linkages, resulting in NBOHC development. This explains the observed increase in red luminescence intensity and may also account for the linearity observed in red emission development for most of the XEOL samples. The development of *E'* centres, which are also formed during peroxy radical dissociation, may also contribute to the reduced UV emission as the population of non-radiative recombination pathways increases (Corazza et al., 1996; Poolton et al., 2000; Schilles et al., 2001). The depletion of this centre to the benefit of the red emission in XEOL has been characterised by $Ae^{-1.46 \pm 0.41\ D}$ (see Chapter 9 for a discussion).

10.3.3. The 4.4 & 4.1 eV Emissions

The origins of the 4.4 and 4.1 eV emissions are discussed in Chapter 9, however briefly they have been attributed to neutral oxygen vacancies (V_o) (Pacchioni and Ieranò, 1997; Song et al., 2001). The 4.4 eV emission has also been attributed to *E'* centres (Jones and Embree, 1976) .

10.3.4. Dose Dependent Effects on the 4.4 eV Emissions

Of the emissions identified during the XEOL experiments, the 4.4 eV emission depleted most rapidly throughout x-irradiation (see Chapter 9 for a discussion). It is proposed that the V_o centre responsible for the 4.4 eV emission may dissociate to form Si_3^- defects as increasing interstitial hydrogen becomes available, associated with the migration of interstitial H^+ away from $[AlO_4]^\circ$ centres and the potential dissociation of hydroxyl groups (≡Si-O-H) and $[H_3O_4]^\circ$ centres. If $[AlO_4/H^+]^\circ$ centres are responsible for the blue emission, then this may also account for the irradiation sensitivity of this centre.

Eq. 10.3: $[AlO_4/H^+]^\circ \rightarrow [AlO_4]^- + H^+$

$\equiv Si\text{-}Si\equiv + H^+ \rightarrow \equiv Si.\ :Si\equiv / H^+$

The increased sensitivity of the 4.4 eV emission to radiation inferred from the XEOL experiments and the interconnected role of H^+ in V_o centre dissociation is further

supported by the increased mobility of H^+ in contrast to the other charge compensating cations responsible for the 3.4 eV emission. This may also explain the steep gradient of blue to red emission depletion recorded in the XEOL spectra, where blue emissions are related to a centre charge compensated by hydrogen (see Section 10.2.4).

10.4. Crystal Anisotropy

Anisotropic effects of crystal orientation were investigated throughout both the XEOL and IL experiments, and both indicated that quartz analysed perpendicular to the *c*-axis (QzPara) has higher luminescence QE. The emission spectra of both samples was similar, however QzPara was dominated by the 4.4 eV emission in the XEOL experiments, whereas QzPerp was dominated by the 3.8 eV emission. Where these emissions are related to oxygen vacancy and peroxy centres respectively, obvious crystal orientation effects relating to the *c* axis are unable to explain this contrast, rather it may relate to localised structural or compositional variations in the crystal. Dose dependence was similar between samples, and QzPara exhibited more rapid depletion of the UV emissions to the benefit of the red for both the IL and XEOL analyses. This was unanticipated as the migration of charge compensating cations is most rapid parallel to the *c*-axis, but indicates that quartz analysed perpendicular to *c* will luminescence most brightly.

These anisotropic effects have direct implications for luminescence dating, as within single aliquot analyses, grains are aligned in multiple orientations, averaging crystal anisotropy. Within single grain analyses however, crystal orientation will influence the monitored luminescence emission. Thus crystal anisotropy potentially contributes to the high σ_d values observed for well bleached, single grain D_e distributions (see Arnold and Roberts, 2009 for a review of measured values).

10.5. Complexities in the Dose Dependence Relationships

The interactions between the different centres responsible for the observed XEOL and IL emissions are complex. Acceptor centre populations fluctuate throughout excitation, and the resultant luminescence is a sensitive indicator of centre interdependence. Although broadly similar dose dependence effects are reported for the XEOL and IL emissions, a number of contrasts and complexities exist in these relationships. First, the XEOL spectra exhibit a pronounced reduction in emission intensity, as a function of dose, which was absent from IL. This may be explained by the greater flux of charge carriers in the XEOL experiments, which increase the opportunities for excitation of broken bonds. If a multiple excited state is created whereby two photons

excite the same bond in quick (e.g. ps-ns) succession, bond recovery is less likely to occur and the sample may adopt a metastable physical state in which short range order is lost and the sample may be considered to begin to amorphize. This suggestion can be tested through measuring spectra using excitation techniques with different rates of charge carrier delivery, which can be achieved through synchrotron beam attenuation, maintaining *E* whilst reducing charge carrier flux.

Both the IL and XEOL UV emission depletions are well approximated by a power-law function, however, whereas all of the pre-exponential factors (*A*) overlap within errors for the IL analyses, those analysed with XEOL do not (Figure 10.2). This cannot simply be explained by the varied durations of x-irradiation between samples, and no correlation is observed between A and either minimum (r^2 0.36) or maximum cumulative dose (r^2 0.42). Those samples with the largest A factors exhibit the greatest rate of 3.4 eV emission depletion to the benefit of the red, and those with the smallest *A* factors the converse, i.e. samples with the brightest 3.4 eV emissions deplete most rapidly.

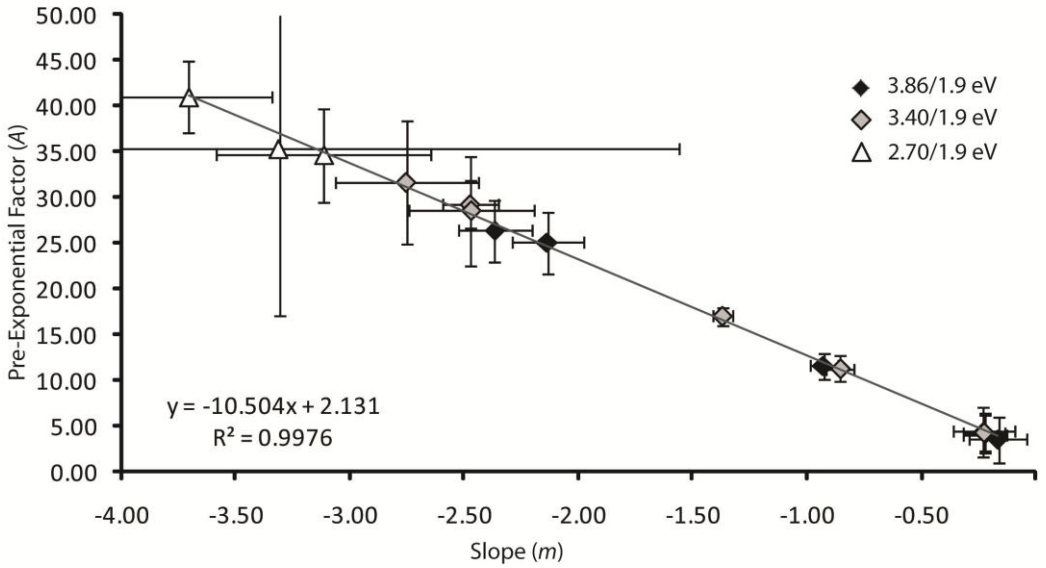

Figure 10.2: Plot showing the relationship between the pre-exponential factors (A) and the slopes (*m*) for the 3.86/1.9, 3.40/1.9 and 2.70/1.9 eV emissions for all samples analysed with XEOL.

Comparisons of *A* and *m* show an almost perfect (r^2 = 0.99) linear relationship (Figure 10.2This relationship is absent for the IL data (r^2 = 0.13) and the reasons for it are uncertain. A possible explanation, which may also account for the absence of a dominant 3.3 eV emission in the XEOL spectra, may be that during x-irradiation all recombination pathways are saturated, which promotes emissions at intrinsic defects such as peroxy linkages (3.8 eV) and oxygen vacancies (4.4 eV), rather than at the extrinsic defect sites associated with the 3.3 eV emission. If the present XEOL experiment delivers excitation energies sufficient to saturate all of the quartz recombination pathways, the gradient of the relationship between A and *m* indicates the rate at which emission modification is occurring, as a function of the excitation energy. Thus for XEOL a gradient of -10.5 is

observed. Therefore it is possible to predict that repeating the XEOL experiments with a different x-ray energy and different x-ray delivery rates should result in observation of a different gradient. Thus this relationship offers a means of exploring dose dependent effects for high excitation methods. This is because although $E > E_g$ during all synchrotron experiments, the probability of a bond recovering following excitation with photons of different energies will vary. Lower energy photons deliver less excitation to a bond during photoelectric transfer than photons of higher energies, thus disruption to the molecular structure is less, improving the opportunity for bond recovery and influencing the rate of dose dependence.

Table 10.1: Dose dependence (*m*) and Pre-Exponential (A) terms for x-irradiation and ionoluminescence of quartz. No data for the 3.40 eV emission are available for QzPara (b) because of low emission intensity, the 2.70 eV emission is only observed for QzPara and QzPerp

XEOL	Provenance	$A^{3.86}$	$m^{3.86}$	r^2
CalQz (a)	Aeolian	6.05 ± 0.09	-0.19 ± 0.15	0.87
CalQz (b)	Aeolian	17.39 ± 2.45	-1.23 ± 0.23	0.98
WTUL1	Glaciofluvial Deposit	2.47 ± 2.30	0.02 ± 0.23	0.20
WTUL2	Glaciofluvial Deposit	2.16 ± 0.95	0.05 ± 0.08	0.09
QzPerp	Hydrothermal	8.49 ± 1.11	-0.44 ± 0.09	0.92
QzPara (a)	Hydrothermal	9.12 ± 0.80	-0.60 ± 0.07	0.97
Qz Para (b)	Hydrothermal	10.46 ± 3.13	-0.73 ± 0.62	0.84
Average			*-0.44 ± 0.17*	

XEOL	Provenance	$A^{3.40}$	$m^{3.40}$	r^2
CalQz (a)	Aeolian	6.35 ± 0.13	-0.26 ± 0.01	0.87
CalQz (b)	Aeolian	13.27 ± 0.74	-0.89 ± 0.07	0.97
WTUL1	Glaciofluvial Deposit	1.58 ± 2.28	-0.09 ± 0.22	0.05
WTUL2	Glaciofluvial Deposit	1.95 ± 1.15	-0.06 ± 0.10	0.07
QzPerp	Hydrothermal	27.60 ± 17.24	-2.39 ± 1.63	0.68
QzPara (a)	Hydrothermal	21.93 ± 5.64	-1.91 ± 0.54	0.94
Qz Para (b)	Hydrothermal	-	-	-
Average			*-0.88 ± 0.43*	

XEOL	Provenance	$A^{2.70}$	$m^{2.70}$	r^2
QzPerp	Hydrothermal	27.99 ± 18.82	-2.50 ± 1.82	0.88
QzPara (a)	Hydrothermal	12.70 ± 0.78	-1.01 ± 2.03	0.99
QzPara (b)	Hydrothermal	14.98 ± 1.90	-1.24 ± 0.18	0.96
Average			*-1.59 ± 0.46*	

IL	Provenance	$A^{3.26}$	$m^{3.26}$	r^2
CalQz	Aeolian	5.71 ± 2.08	-0.10 ± 0.27	0.87
WTUL1	Glaciofluvial Deposit	9.29 ± 1.12	-0.60 ± 0.14	0.92
WTUL2	Glaciofluvial Deposit	6.25 ± 2.91	-0.20 ± 0.35	0.14
QzPerp*	Hydrothermal	10.98 ± 2.57	-0.83 ± 0.32	0.82
QzPara	Hydrothermal	4.64 ± 17.25	-0.09 ± 2.08	0.00
Average			*-0.44 ± 0.17*	

*QzPerp (IL) was not included in calculation of average *m* because r^2 was zero, where it is included *m* is -0.37 ± 0.15.

Power-law fits of individual emission reduction as a function of irradiation dose (Table **10**.**1**) indicate depletion rates of -0.44 ± 0.17 for the 3.8 eV emission, ~ -0.88 ± 0.43 for the 3.4 eV emission -1.59 ± 0.46 for the 2.7 eV emission for XEOL, and -0.44 ± 0.17

for the 3.26 eV IL emission. The average depletion rates of the 3.8 eV XEOL and 3.26 eV IL emissions are identical, which may indicate an interrelationship between donor centres. These power-law exponents are in broad agreement with the results of simple equation models which calculate the luminescence centre saturation with increasing excitation energy. Exponents of 0.5, 1.0 and 1.5 have been predicted, dependent upon defect concentration and excitation power (Phillips et al., 2003). The excitation power of the XEOL experiments is sufficient to saturate all centres, supported by the relationship observed in Figure 10.2, and thus it follows that the power dependency of centre saturation may also predict centre quenching as a function of dose. Although the IL power is less, it may be sufficient to saturate all accessible recombination pathways, i.e. those not accessed through the development of multiple excited states, which accounts for the similarities in dose dependence exponent values.

There are also similarities in the A factors derived for the IL and XEOL (see Table 8.1 and Table 9.1); WTUL1 and WTUL2 have the lowest A factors for both techniques, associated with their poor luminescence sensitivity (Appendix D), which further demonstrates that spectra excited within different energies are complimentary, and also suggests that a technique such as CL may provide an effective screening mechanism for the QE of quartz used for OSL. Although the CL experiments reported here do not exhibit such a correlation, associated with the limited detection range and electron beam instability (see Chapter 7).

10.6. Summary of Emission Spectroscopy Experiments

A huge breadth of research has investigated the luminescence of quartz (see Götze et al., 2001; Krbetschek et al., 1997; Stevens-Kalceff and Phillips, 1995 for reviews), and both complimentary and contradictory results, hypotheses and models are prevalent throughout the literature. Through detailed investigations into the origins of the various emission centres, a series of assignments have been made for the emissions recorded in the experiments reported here. These are listed in Table 10.2, although it is recognised that further investigations into the defect centres using different, complimentary excitation energies, and also direct investigations of defects using ESR are required before centre assignments are fully conclusive.

10.7. Implications for OSL Dating

The dose dependences of quartz by IL, XEOL and CL described in this thesis highlight that the geological irradiation history of quartz has the potential to significantly influence its emission spectrum. Although the total dose of the different experiments presented here are up to 14 orders of magnitude greater than experienced by quartz in the natural depositional environment, natural alpha, beta and gamma decay result in the exposure of quartz to much greater energies of up to ~ 4 MeV (Appendix G in Aitken, 1985). As radiolysis of quartz is possible at energies > 9 eV and emission modification is observed to occur, even in the absence of the multiple excited states seen in the XEOL experiments, this provides a partial explanation for why some quartz luminesce more efficiently during OSL than others. Rink (1994) observed that the emission spectrum and TSL properties of granitic quartz were dependent upon irradiation history. The IL and XEOL experiments have contrasted the emission spectra of Scottish (granitic) and calibration quartz material, and their OSL QE are reflected in both their emission spectra, and dose dependent behaviour. Whereas CalQzB8 has the most intense 3.3 eV emission in the IL spectra, the WTUL samples have red emissions which are relatively pronounced in contrast to their UV emissions, suggesting that quartz with greater irradiation histories may luminescence more brightly in the red. This is not observed within the XEOL, and is attributed to different routings of excitons between the two techniques. Within the XEOL experiments, whereas CalQzB34 and the natural hydrothermal macrocrystal samples exhibited significant dose dependencies, the Scottish samples are relatively unaffected.

Table 10.2: Key emission energies observed with the different spectroscopic techniques explored throughout this research. Experiment details are given in Chapters 7, 8 and 9.

Emission Energy (eV)	Excitation Method	Defect Assignment
4.4	XEOL	V_o (Pacchioni and Ieranò, 1997) *E'* (Jones and Embree, 1976)
4.1	XEOL	V_o (Song et al., 2001)
3.8	XEOL	Si-O, Peroxy linkages (this study)
3.6	IL, XEOL	$[AlO_4]^\circ$ charge compensated with $M^+_{(free)}$ (this study)
3.3-3.4	IL	$[AlO_4/M^+]^\circ$ or $[AlO_4/h^+]^\circ$ (e.g. Itoh et al., 2002; Perny et al., 1992; see Chapter 8 for a review)
2.7	IL, XEOL, CL	$[AlO_4/H^+]^\circ$ (this study) *E'*-H^+ (Griscom, 1985b) STE (Itoh et al., 1989; Itoh et al., 2002)
2.1, 2.0	CL, RL	*E'* (Götze et al., 1999; Rink et al., 1993) STE (Itoh et al., 1988; Stevens-Kalceff and Phillips, 1995)
1.9	IL, XEOL, CL	NBOHC, $[Si_3^-/H^+]^\circ$ (see Stevens-Kalceff and Phillips, 1995 for a review)
1.75	IL, CL	Fe^{3+} (Kempe et al., 1999) (Pott and McNicol, 1971)

10.8. Conclusions & Further Research

The luminescence emission of quartz is complex, and is dictated by the interrelationships of a suite of different emission centres and donor defects. The XEOL and IL spectra demonstrate the importance of irradiation history in determining the quartz luminescence emission, and also that samples with the greatest QE are most susceptible to irradiation induced signal depletion.

The CL and RL spectra exhibit little correlation between signal intensity and OSL QE, whereas for the IL and XEOL spectra, CalQz has the brightest emission intensity of the sample suite. Further IL, XEOL, RL and CL investigations are required on quartz of a range of QE in order to confirm this association, and also to explore the influence of annealing on specific centre efficiency. These experiments demonstrate that spectroscopic investigations into the luminescence of quartz, using a range of excitation energies provide valuable insights into its luminescence behaviour, and the interrelationships between the different defect types.

Correlation of the A and *m* values calculated for the different emissions of each of the XEOL samples analysed have indicated a means of exploring dose rate effects. A gradient of -10.5 has been identified for XEOL at 7 keV, and should also be investigated for complimentary sample suites analysed with contrasting x-ray energies. Deviation from a linear gradient is hypothesised to occur once *E* reduces below the point of trap saturation, however achieving sufficient signal to noise ratios at lower excitation energies will be challenging, as indicated by the PL analyses. This could be circumvented through LNT analyses, where the luminescence intensity of quartz increases (Chapter 8), or alternatively through vacuum UV experiments.

Quartz can be sensitized through annealing, reflected in the enhanced CalQz OSL, IL and XEOL QE and attributed to the recovery, and clustering (Martini et al., 2009) of $[AlO_4]^{\circ}$ centres. Mechanical processes such as transport and weathering have also been proposed as signal sensitizers (e.g. Pietsch et al., 2008), however it is unknown which specific process causes the observed increase in luminescence QE for quartz which have undergone multiple depositional and erosional cycles. These effects could be explored through examining the OSL and emission spectra response of either a natural or synthetic quartz macrocrystal, exposed to known stresses and strains. Coupling these experiments with ESR (in which the identity of centres can be modelled and hence identified with greater confidence) would enable monitoring of both the different donor and acceptor defects, facilitating the assignment of changes in QE due to mechanical processes, to specific defect population fluctuations.

Luminescence spectroscopy is a powerful technique when used independently, especially where it is possible to vary excitation energies. However coupling emission spectra with ESR and optical absorption spectra would enable more specific attribution of luminescence defects, and their response to irradiation, heat and weathering.

Chapter 11. Synthesis & Conclusions

11.1. Synthesis & Conclusions

This thesis has sought to identify whether the OSL of quartz and feldspar can be used successfully to determine the transport and depositional processes of a suite of glaciofluvial sediments. If successful, OSL could provide a new provenance analysis tool, useful for Earth scientists seeking to understand sediment transport and depositional pathways. The OSL dose distributions and residual ages of a suite of modern Norwegian quartz and feldspar samples from a range of glaciofluvial catchments have been examined, and it is apparent that the controls on sample OSL are complex but that it does have potential as a depositional pathway tracer. Whereas sample dose distributions are influenced predominately by source sediment σ_d characteristics, residual age is controlled by transport and depositional processes over short (< 10 km) transport distances. Processes that sort sediments least effectively have the greatest overdispersion and residual age. Transport and depositional processes which result in significant sunlight exposure also influence dose distribution signatures. This technique therefore offers the potential for Earth scientists to make inferences about source sediment characteristics, as well as sediment transport and depositional process.

The Norwegian samples have poor OSL sensitivity, which limited these investigations due to low numbers of aliquots. Within this research, this has been accommodated through statistical investigations into the number of aliquots necessary for accurate residual age and dose distribution characterisation. Through bootstrapping sub-samples of various sizes, it is apparent that the minimum sample number required to fully characterise a samples distribution, must be judged on an individual sample basis. Those samples which have the most non-normal distributions require the greatest aliquot numbers. However despite this, sample σ_d is stable, ± 20% where n > 10 aliquots; which is sufficient to differentiate between the various source materials of the glacial catchments explored here.

Further research in a less complex depositional environment, where quartz has greater sensitivity, is required to fully characterise the relationships recorded here. Brighter quartz would enable more precise OSL D_e determinations and also improve aliquot numbers, which may influence some of the dose distributions analysed throughout this thesis. Contrasting the OSL properties of samples deposited along completely different depositional pathways (e.g. aeolian and fluvial) using factor analysis, would also enable better exploration of the value of this technique in elucidating the OSL response of samples to different source materials, transport and depositional processes.

The paired quartz and feldspar samples exhibited different residual ages, which are attributed to more gradual bleaching of the feldspar signal during transport, as well as depositional processes that result in short periods of sunlight exposure (i.e. slope failure

and/or glaciofluvial transport during turbulent flow). However the variation in σ_d between paired quartz and feldspar samples is more difficult to account for, as all grains within a sample should undergo similar transport and depositional processes, and so would be anticipated to have similar σ_d irrespective of bleaching rate. Further research investigating the relative rates of quartz and feldspar bleaching, throughout different processes and light exposures, relative to changing σ_d and dose distributions is required to understand these observations. Laboratory based explorations would best address these questions, as they would enable the different variables to be properly constrained.

In addition to providing information about provenance, understanding the controls on quartz OSL QE may help to improve the precision and accuracy of OSL dating. These controls were investigated using a range of complimentary spectroscopic techniques with different excitation energies on a suite of Norwegian, Scottish and calibration quartz, as well as a natural hydrothermal quartz macro-crystal. IL and XEOL deliver excitation energies similar to natural irradiation, albeit at greater dose rates, and indicate that the radiation history of quartz influences both its sensitivity and emission spectrum. IL spectra suggest that quartz subject to significant geological irradiation, which have not been reworked over large transport distances will luminesce more efficiently in the red part of the emission spectrum, outside of the range conventionally monitored in OSL dating. In contrast the XEOL spectra suggest that irradiation reduces the overall sensitivity of quartz. These results are supported by the OSL properties of the Norwegian samples, as quartz derived from Bergsetdalen which has bedrock geology of quartz monzanite and the highest calculated radiation dose rate, had the lowest sample acceptance. Aliquots were rejected due to poor recycling ratios, low signal intensities and high levels of recuperation, which are all diagnostic of low OSL sensitivity.

This research has demonstrated that valuable insights into quartz OSL sample behaviour can be gained from consideration of its emission spectra, however further work is needed to fully elucidate these relationships. Spectroscopic OSL analyses using different modes and energies of stimulation (e.g. TSL, RL, PL), at different temperatures and resolved in the time domain will allow more conclusive assignments of different donor and acceptor centres within quartz OSL samples. Such experiments should be coupled with high energy spectroscopy (e.g. IL/XEOL) and ESR analyses, on the same sample suite and also synthetic quartz with known defect populations. Minimising sample variability will enable better predictions regarding sample behaviour to be made and tested.

Appendixes

Appendix A. OSL

A.1 Sample List

Table A.1: List of samples analysed, facies, deposit type, GPS co-ordinates and sample elevations. Sediment source and depositional process are determined from sample luminescence properties, grain size characteristics and depositional context, discussed in Chapter 6, and are only listed for those samples fully characterised and included in the factor analyses.

Sample	Facies	Deposit Type	Source Sediment	Process	GPS	GPS	Elevation (m)
Bergsetdalen (61˚38′ N, 7˚05′ E)							
BERG10	Sr:Sl	Point bar	Glaciofluvial	Glaciofluvial	399718	6836324	454
BERG16	Sh	Braided bar	Glaciofluvial	Glaciofluvial	399786	68363260	476
BERG19	Sh	Braided bar	Glaciofluvial	Glaciofluvial	400806	6836026	436
BERG1	Dmm	Paraglacial	Glaciofluvial	Glaciofluvial	399218	6836055	715
BERG21	Fl:Sh	Braided bar	Glaciofluvial	Glaciofluvial	399966	6836244	444
BERG24	Sr	Braided bar	Glaciofluvial	Glaciofluvial	399856	6836249	454
BERG25	Sr	Braided bar	Glaciofluvial	Glaciofluvial	399856	6836249	454
BERG2	Dmm	Paraglacial	Paraglacial	Mass Movement	399172	6836021	713
BERG4	Sm	Braided bar	Glaciofluvial	Glaciofluvial	399841	6836578	435
BERG7	Sh	Point bar	Glaciofluvial	Glaciofluvial	403021	6835899	440
Fåbergstølsdalen (61˚42′ N, 7˚17′ E)							
FAB100			Paraglacial	Glaciofluvial	411449	6843080	547
FAB41	Sh	Reworked Subglacial Deposit	Subglacial	Sheetwash	409830	6843015	745
FAB42	Dmm	Paraglacial	Paraglacial	Avalanche	410016	6843479	737
FAB79	Sh	Point bar	Subglacial	Glaciofluvial	409669	6843511	777
FAB80	Fl	Point bar	Subglacial	Glaciofluvial	410048	6843449	674
FAB81	Sh:Fl	Braided bar	Subglacial	Glaciofluvial	410109	6843448	667
FAB83			-	-	410322	6843412	656
FAB84	Sr	Point bar	Paraglacial	Glaciofluvial	410367	6843411	661
FAB85	Sh:Fl	Paraglacial	Paraglacial	Sheetwash	410559	6843406	645
FAB86	Sr	Paraglacial	Paraglacial	Sheetwash	410645	6843411	631
FAB90	Sh	Point bar	Paraglacial	Glaciofluvial	410876	6843376	630
FAB91	Sr	Point bar	Paraglacial	Glaciofluvial	410896	6843377	616
FAB92	Sh	Point bar	-	-	410917	6843368	625
FAB94	Sh:Fl	Point bar	Paraglacial	Glaciofluvial	410967	6843358	618
FAB95	Sr	Point bar	Paraglacial	Glaciofluvial	410973	6843353	618
FAB98	Sh	Point bar	Paraglacial	Glaciofluvial	411014	6843350	615
FAB99	Sh	Point bar	Paraglacial	Glaciofluvial	411223	6843266	586
FABSUB1	Dmm	Subglacial	Subglacial	Glacial	409914	6843419	752
FABSUB2	Dmm	Subglacial	Subglacial	Glacial	409914	6843419	752
Gaupne (61˚26′ N, 7˚14′ E)							
GAUP1	Sh	Delta	-	-	406489	68133685	85
GAUP2	Sh	Delta	-	-	406489	68133685	85
GAUP40	Sr	River Channel	-	-	406433	6813293	97
GAUP41	Sr	River Channel	-	-	406433	6813293	97
Fåbergstølsgrandane (61˚44′ N, 7˚20′ E)							
GRAN54	Sh	Sandar Braided bar	Subglacial	Sandur Glaciofluvial	412365	6846978	558
GRAN55	Sh	Sandar Braided bar	Glaciofluvial	Sandur Glaciofluvial	412414	6846956	540
GRAN56	Sr	Sandar Braided bar	Glaciofluvial	Sandur Glaciofluvial	412520	6846926	545
GRAN57	Sr	Sandar Braided bar	Glaciofluvial	Sandur Glaciofluvial	412709	6846743	540
GRAN58	Sr	Sandar Braided bar	Subglacial	Sandur Glaciofluvial	412809	6846525	535
GRAN59	Sr	Sandar Braided bar	Subglacial	Sandur Glaciofluvial	412836	6846465	530
GRAN62	Sr	Sandar Braided bar	Glaciofluvial	Sandur Glaciofluvial	413270	6845928	533
GRAN69	Sr	Point bar	Subglacial	Glaciofluvial	412998	6845694	529
GRAN71			-	-	413046	6845354	521
Jostedalen (61˚28′ N, 7˚15′ E)							
JOS51	Sh	Point bar	Glaciofluvial	Glaciofluvial	409102	6830734	192
LEI13	Sr	Braided bar	Paraglacial	Glaciofluvial	407896	6818873	70
LEI14	Sh	Braided bar	Paraglacial	Glaciofluvial	407234	6817852	70
LEI18	Sh	Braided bar	Paraglacial	Glaciofluvial	407202	6817146	71
Stordalen (61˚45′ N, 7˚16′ E)							
LOD4	Sh	Point bar	Subglacial	Glaciofluvial	408762	6848313	680
LOD5	Sr	Point bar	Subglacial	Glaciofluvial	409193	6848118	665
LOD6	Sr	Point bar	Subglacial	Glaciofluvial	411703	6847249	659
Nigardsdalen (61˚40′ N, 7˚12′ E)							
NIG103	Dmm	Subglacial	-	-	405061	6839374	310
NIG3	Sh	Sandar Braided bar	Glaciofluvial	Sandur Glaciofluvial	405605	6839365	285
NIG4	Sh	Sandar Braided bar	Glaciofluvial	Sandur Glaciofluvial	405581	6839351	326
NIG6	Sh	Sandar Braided bar	Subglacial	Sandur Glaciofluvial	405540	6839371	285
NIG7	Sh	Sandar Braided bar	Glaciofluvial	Sandur Glaciofluvial	405658	6839321	289
NIG8	Sh	Sandar Braided bar	Glaciofluvial	Sandur Glaciofluvial	405665	6839314	290
NIG9	Sr	Sandar Braided bar	Glaciofluvial	Sandur Glaciofluvial	405650	6839321	290

*GPS co-ordinates are relative to datum WGS 1984, UTM 32 V.

A.2 Background uncertainty

Background values for each Risø machine were measured following the protocol of Li (2007); six blank discs coated with silicone grease (medium mask) were analysed with the Risø calibration protocol (A.5). No variation in background as a function of stimulation time was observed for either Risø (Figure A.1). The relative standard error was calculated using equation 3 of Galbraith (2002).

Eq. A.1: $$RSE = \frac{\sqrt{Y_0 + \frac{1}{k}\bar{Y}}}{Y_0 + \bar{Y}}$$

where Y_0 is the integrated signal, $\bar{Y}$ is the average background and k is the ratio of the number of channels used for estimating Y_0 to the number used for estimating $\bar{Y}$ (Li, 2007).

The mean background and variance for each aliquot are summarised in Table A.2. Background subtractions are automatically performed prior to curve fitting in Analyst, and a systematic uncertainty of 1.5% was incorporated in all single aliquot D_e determinations.

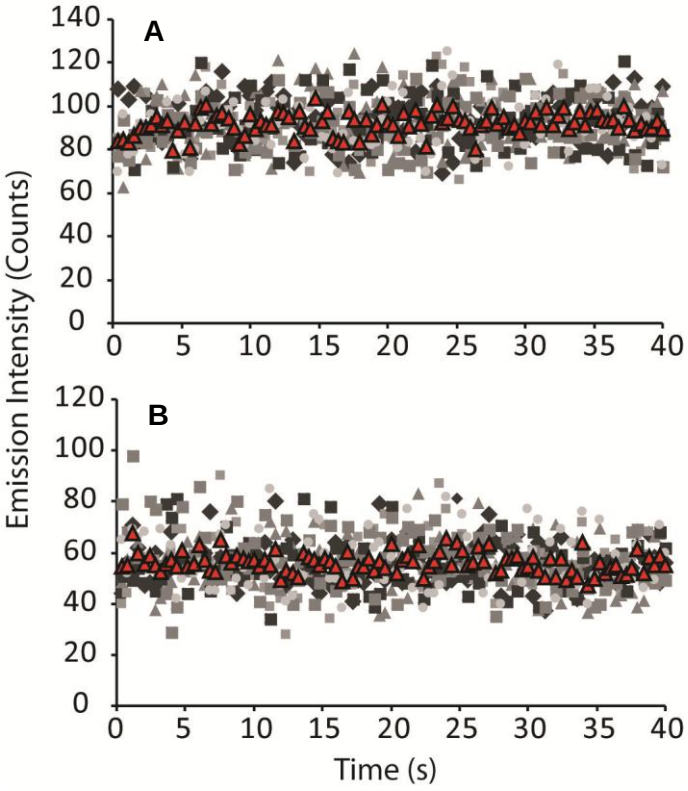

Figure A.1: Background luminescence measurements from six blank (silicone grease coated) stainless steel discs for A) Risø 2 and B) Risø 1, after Li (2007). Red data points are the average emission intensity.

Table A.2: Background mean counts, variance and relative standard error for Risø 1 and Risø 2.

Risø 1 Aliquot	Mean counts/0.4 s	Variance/0.4 s	Mean/Variance	Relative Standard Error
1	56.43	74.89	1.33	0.87
2	55.32	102.62	1.85	1.02
3	55.27	101.34	1.83	1.01
4	55.23	87.46	1.58	0.94
5	57.32	142.96	2.49	1.20
6	56.60	108.58	1.92	1.05
Average	56.03 ± 1.76	102.97 ± 46.15	1.84 ± 0.78	1.01 ± 0.22%
Risø 2 Aliquot	Mean counts/0.4 s	Variance/0.4 s	Mean/Variance	Relative Standard Error
1	93.79	104.37	1.11	1.03
2	92.14	148.32	1.61	1.22
3	92.62	168.24	1.82	1.30
4	92.37	146.77	1.59	1.22
5	90.14	110.90	1.23	1.06
6	91.34	117.06	1.28	1.09
Average	92.07 ± 2.47	132.61 ± 50.81	1.44 ± 0.54	1.15 ± 0.22%

A.3 Environmental Dose Rate Calculation

A.3.1 External Radiation Sources

The contributions of uranium (U), thorium (Th), potassium (K) and rubidium (Rb) are considered when quantifying external ionizing radiation. Uranium and Th produce lightly ionizing gamma rays and beta particles (electrons), as well as heavily ionizing alpha particles. Potassium and Rb do not undergo alpha decay. An infinite matrix assumption is made to overcome the different spatial ranges of gamma rays (0.3 m), alpha (0.03 mm) and beta (3 mm) particles (Aitken, 1985). Etching quartz with HF removes the alpha irradiated portion of the grain (see Section 4.1) however a component of alpha irradiation still affects the feldspar grains, which have not been etched.

Cosmic radiation comprises lightly ionizing radiation. The ‘soft’ component is absorbed within the top 50 cm of sediment, so generally only the lightly ionizing muon radiation is considered (Aitken, 1998). Muon radiation varies spatially with longitude, and also with deposit depth, and the correction factors of Prescott and Hutton (1994) were used in its calculation for these samples.

A.3.2 Internal Radiation Sources

K-feldspars experience an internal contribution to total radiation dose due to the inclusion of K in the crystal structure. It is possible to measure the exact composition of K-feldspar grains using imaging microprobe x-ray analysis (e.g. Godfrey-Smith et al., 2005).

This is not routinely done within the dating community due to equipment availability and time constraints, although recent interest in single grain feldspar analyses prompted a number of labs to report single grain K concentrations at the recent LED meeting (2011) in Toruń. An average K concentration is more conventionally estimated and Godfrey-Smith et al. (2005) proposed 15.4 ± 0.7 % as an appropriate average K_2O content for the > 2.58 g cm^{-3} feldspar separate based on imaging microprobe XRF analyses. This converts to 12.78 ± 0.58 % following conversion to K:

Eq. A.1: $K\ \% = K_2O\ \% / 1.2046$

which is in agreement with Huntley and Baril's (1997) earlier estimate of 12.5 ± 0.5 % K, derived from element concentration mapping with an SEM; and similar to the results of Zhao and Li (2005), who derived a value of 13 – 14 % K from electron microprobe investigations. Godfrey-Smith et al. (2005) and Huntley and Baril (1997) observe anomalous values lower and higher than their reported averages, however these data provide a best estimate in the absence of individual grain K concentration quantification.

The K concentration is often used as the basis for approximating the Rb content of grains, based on a K:Rb of 270:1 identified by Mejdahl (1987). Zhao and Li (2005) contrasted measured and estimated values of the K:Rb relationship and determined that a ratio of 200:1 provided a reliable estimate (Aitken, 1998), however Huntley and Hancock (2001) dispute this approach. They used Neutron Activation Analysis (NAA) to quantify the Rb content of a range of K-feldspars and instead observed that the relationship could be explained as (11 %)(Rb content of the sample + K content of the sample). This relationship is believed to be specific to the igneous source of these feldspar minerals and thus is not applicable to other sample suites. Their average Rb content ranged from 200 – 400 $\mu g.g^{-1}$, and when combined with Mejdahl's (1987) dataset an average value of 400 ± 100 $\mu g.g^{-1}$ was obtained, it is this latter value which has been adopted in these dose rate calculations.

Quartz may also contain radioisotopes as inclusions (the large atom sizes of U, Th, precludes inclusion within the lattice) and Sutton and Zimmerman (1978b) estimated that the internal alpha dose rate from the decay of U and Th may contribute up to 5 % of total dose. The beta dose contribution was regarded as less significant as the majority of the energy for grain sizes < 100 µm is deposited beyond the grain, although this may be significant with the grain size range analysed here (180-212 µm). Sutton and Zimmerman (1978b) also observed that within larger grains clustering of radioisotopes occurs, limiting the effective dose spatially. Quartz internal dosing provides a relatively small contribution to its total dosimetry (Zhao and Li, 2005) in contrast to K-feldspar, and consequently has been ignored.

A.3.3 Environmental Dose Rate Measurement

The environmental dose rate was measured using ICP-MS. Where samples were collected using the opaque bag method, part of the sample bulk was analysed using ICP-MS for U (ppm), Th (ppm), K (%) and Rb (ppm) concentrations; where samples were collected in plastic tubes, the sample ends were used. The Rb concentration was not measured for all samples due to an analytical error, and thus where no direct measurement has been made a value of 100 ppm has been estimated.

Alpha, beta and gamma radiation have conversion factors derived from nuclear tables which quantify the dose rate associated with radioisotope concentrations (Adamiec and Aitken, 1998). Alpha and beta particles, because of their larger size relative to gamma rays, are attenuated by quartz and feldspar grains, this causes dose rate reduction and requires quantification. Water attenuates all radiation types and so soil water content must be calculated. The isolation of quartz from polymineral separates using HF reduces the contribution from alpha irradiation and some beta irradiation, and must be corrected for. The complexity of internal dose rate calculations have already been alluded to, and may exert significant influence on the final D_r.

A.4 Radioisotope measurement, calibration and errors

A.4.1 Inductively coupled plasma mass spectrometry

Unsieved, desiccated samples were prepared for ICP-MS through initial grinding to a fine powder using a Tema mill. Samples were then weighed into platinum-gold crucibles, previously cleaned in HCl; 0.25 ± 0.01 g of sample was mixed with 1.25 ± 0.01 g of flux, which comprised 80 % lithium metaborate and 20 % lithium tetraborate. Six standards were prepared using the same technique (Table A.3). A spatula of ammonium iodide (NH_4I) was added to each of the samples which were then carefully stirred. Ammonium iodide behaves as an oxidant, which acts as a releasing agent, facilitating sample melting.

Samples were placed in a furnace at 1080 ˚C for 20 mins, before being allowed to cool completely. The resultant glass was then dissolved in 5 % nitric acid (N_2O_2) for two hours. Following dissolution, samples were diluted through addition of 5 % nitric acid, up to a volume of 100 ml. 10 ml of the diluted sample was then diluted further with 90 ml of 5 % nitric acid, doped with Ge, Rh and Re prior to analysis with ICP-MS.

Counting errors are assumed to be 5 % for all radioisotopes, although measured standards deviated by < 1 % (Table A.3). A further 3 % ICP-MS calibration error is also incorporated. These two uncertainties are propagated in quadrature, e.g. for K:

Eq. A.2: $$\delta K = K_{count}\sqrt{\left(\frac{\delta K_{count}}{K_{count}}\right)^2 + \left(\frac{\delta cal}{1}\right)^2}$$

where δK is the potassium (K) uncertainty, K_{count} is the potassium concentration (%),δK_{count} is the counting uncertainty (5 %) and δcal is the ICP-MS calibration uncertainty (3 %). All uncertainties are propagated using the same technique.

Table A.3: ICP-MS Standards relative to certified compositions

	Radioisotope			Measurement Deviation from Standard			
	39K	Th	U		39K	Th	U
Standard	%	ppm	ppm				
AC-E	3.72	18.13	4.48	Δ%	0.08	2.00	2.63
Cert	3.72	18.50	4.60	StDev	0.00	0.26	0.09
BE-N	1.17	10.45	2.40	Δ%	1.74	0.48	0.08
Cert	1.15	10.40	2.40	StDev	0.01	0.04	0.00
GS-N	3.84	41.85	7.85	Δ%	0.00	0.36	1.85
Cert	3.84	42.00	8.00	StDev	0.00	0.11	0.10
GSR-1	4.15	54.98	18.99	Δ%	0.00	1.81	1.01
Cert	4.15	54.00	18.80	StDev	0.00	0.69	0.13
GSR-4	0.47	7.25	2.20	Δ%	10.94	3.63	4.76
Cert	0.53	7.00	2.10	StDev	0.04	0.18	0.07
PM-S	0.10	0.06	0.02	Δ%	13.64	14.00	30.00
Cert	0.11	0.05	0.03	StDev	0.01	0.00	0.01
				Average	0.01	0.21	0.07
				SE	0.00	0.09	0.03

A.4.2 Radioisotope conversion factors

Conversion factors are necessary to estimate the dose rate produced by radioelement concentration and/or activity. These have most recently been calculated by Adamiec and Aitken (1998) from nuclear data tables, and their conversion factors are used here (Table A.4).

Table A.4: Conversion factors after Adamiec and Aitken (1998)

Rate (Gy/ka)	Beta	Gamma	Alpha
Th (ppm)	0.0273 ± 0.0008	0.0476 ± 0.0014	0.7320 ± 0.0220
U (ppm)	0.1460 ± 0.0044	0.1130 ± 0.0034	2.7800 ± 0.0834
K (%)	0.7820 ± 0.0235	0.2430 ± 0.0073	
Rb (50 ppm)	0.0190 ± 0.0006		
Rb (1 ppm)	0.000358 ± 0.00001*		

*after Readhead (2002a)

A.4.3 Beta-particle Attenuation

The dose rate from beta particles is moderated through attenuation by the grains, and is influenced by grain size. Mejdahl (1979) calculated the beta-dose attenuation rates for quartz grains of different sizes, which are used here (Table A.5). As the 180 – 212 µm grain size fraction has been used throughout this thesis, an average of the two beta attenuation factors listed, is used in all calculations.

Table A.5: Beta-particle attenuation factors for quartz, after Mejdahl (1979)

Diameter (mm)	^{40}K β	^{232}Th β	^{238}U β	^{87}Rb β
0.180	0.6692	0.8050	0.8630	0.38*
0.200	0.9298	0.7940	0.8540	0.311*
(0.180 + 0.200)/2	0.7995 ± 0.024**	0.8585 ± 0.026**	0.93325 ± 0.028**	0.34 ± 0.010**

*The attenuation value for Rb is taken from Readhead (2002a, b).
**Beta attenuation error is 3%

All quartz extracts were etched with HF during preparation to remove feldspar contamination and also to remove the outer quartz layer, which is subject to alpha irradiation. The influence of alpha irradiation is difficult to quantify because of its dependency on particle energy, unlike beta or gamma radiation (see Adamiec and Aitken, 1998 for a discussion). HF etching also therefore influences grain size and morphology and this was investigated by Bell and Zimmerman (1978) who determined that different types of quartz were affected by HF to different extents, with dissolution occurring at dislocations in the crystal structure (Lang and Miuscov, 1967). In an experiment to contrast the effect of HF dissolution on two quartz types, distinguished by their shiny and cloudy appearances respectively, Bell and Zimmerman (1978) observed that the cloudy quartz lost an average of 10 µm diameter, in contrast to 3 µm for the shiny material. This impacts the amount of alpha and beta dose removed, with Bell and Zimmerman (1978) determining that in most instances ~ 2.5 - 5 % of the alpha dose remains, however in exceptional circumstances > 5 % may remain after etching. However for grains > 100 µm, the residual alpha dose will be negligible, especially after HF etching (Bell, 1979).

Mejdahl (1979) calculated the influence of non-isotropic and isotropic etching on quartz beta attenuation, determining that non-isotropic etching would have no influence, whereas isotropic removal would result in a maximum error of 2 %. Mejdahl (1979) concluded that the overall impact, given the varied response of different quartz grains, would be negligible. However the total received beta dose is reduced by etching by a factor of 0.915 for thorium, 0.940 for uranium and 0.755 for rubidium, whereas the potassium induced beta dose is unaffected (Bell, 1979). These factors have been used in D_r determinations. Brennan (2002) has recently recalculated the dose rate attenuation factor for spherical grains, determining that a factor of 0.92 should be used relative to the conventional 0.90 factor for grains of 100 µm (Aitken, 1985). However, this calculation is

extremely sensitive to anisotropic grain etching and subsequent deviation from sphericity (Bell and Zimmerman, 1978), thus the attenuation factors of Bell (1979) have been used.

A.4.4 Alpha-particle attenuation

Alpha irradiation is generally ignored within quartz analyses, however as the feldspar fraction analysed are not treated with HF, it must be accounted for within their dosimetry. Alpha attenuation values were calculated for materials of 1 – 1000 μm by Bell (1980) (Table A.6), however for a grain of 100 μm diameter, Bell observed a 7 % difference between attenuation for quartz and feldspar grains, reflecting the reduced attenuation caused by the structure of feldspar. Consequently, in the absence of other alpha attenuation values, the quartz alpha attenuation factors have been increased by 7 % for application in feldspar dose rate estimation. It is acknowledged that this is a crude approximation, however in the absence of an alternative it is regarded as better than ignoring alpha attenuation altogether.

In addition to alpha-particle attenuation, an alpha efficiency factor (α-value) must also be used which accounts for the saturation of trapping defects within alpha decay tracks (Aitken, 1985). A factor of 0.15 ± 0.05 has been used (e.g. Balescu and Lamothe, 1994) throughout this research.

Table A.6: Alpha-particle attenuation factors, after Bell (1980)

Diameter (mm)	^{232}Th β	^{238}U β
Quartz 0.200	0.1260 ± 0.0038*	0.1080 ± 0.0038*
Feldspar 0.200	0.1350 ± 0.0040*	0.1160 ± 0.0035*

A.4.5 Attenuation by water

Water has significant attenuating properties which influence the effective dose rate for both quartz and feldspar (Aitken, 1998), consequently it is necessary to estimate the degree of saturation of a sediment throughout its entire depositional history. As the majority of samples analysed throughout this thesis are modern, the water content measured during sample desiccation in the lab is regarded as appropriate, although it is acknowledged that significant environmental changes have occurred throughout deglaciation. The water attenuation factors for gamma, beta and alpha radiation are 1.14, 1.25 and 1.49 respectively (Aitken, 1998), and water attenuation may be calculated:

Eq. A.3: $$D_{moist} = \frac{D_\gamma}{1+HW}$$

where D_{moist} is the wet environmental dose rate, D_γ is the gamma irradiation derived dose rate for example, H is the appropriate attenuation factor as described above, and W is the percentage of water present. Error caused by variation in the water content affects the water attenuation factor:

Eq. A.4: $\delta H = (H + (H * \delta W)) - H$

where δH is the error of the water attenuation factor, and δW the error of the substrate water content, thus the error of D_{moist} is calculated:

Eq. A.5: $$\delta D_{moist} = D_{moist} \sqrt{\left(\frac{\delta D_r}{D_r}\right)^2 + \left(\frac{\delta H}{H}\right)^2}$$

where δD_{moist} is the error of D_{moist}.

A.5 Risø reader calibration

The two Risø readers at the University of St Andrews, primarily used throughout the course of this research were calibrated using CalQz purchased from the Risø National Laboratory, Denmark. Three batches of CalQz were used for this purpose: 8, 34 and 40.

- Batch 8 comprises sedimentary quartz from Jutland, sieved to 180-250 µm and annealed at 500 ˚C. It was irradiated between 1st-16th July, 2004 and has a dose of 4.81 ± 0.06 Gy.
- Batch 34 also comprises sedimentary quartz from Jutland, sieved to 180-250 µm and annealed at 700 ˚C. It was irradiated in February 2009, and has a dose of 4.81 Gy.
- Batch 40 has a dose of 4.81 Gy, no further information was provided for this sample.

Small or medium sized aliquots of approximately 30 to 125 grains were analysed using the protocol listed in Table A.7. Dose rates were calculated:

Eq. A.6: Dose rate (Gy s^{-1}) = CalQz D_P (Gy) / measured D_e (s)

Table A.7: Calibration protocol*

Natural/Regenerative Doses	23, 46, 69 s
TSL	260˚C, 5˚C/s, 10 s
OSL	125˚C, 5˚C/s, Blue LEDs 90% Power, 40 s duration
Test Dose	46 s
TSL	160˚C, 5˚C/s, 0 s
OSL	125˚C, 5˚C/s, Blue LEDs 90% Power, 40 s duration

*note the absence of the IR depletion test

A.5.1 Risø Reader Calibration Error

The calibration error propagation can be propagated:

Eq. A.7: $$\delta D_R = D_R \sqrt{\left(\frac{\delta D_P}{D_P}\right)^2 + \left(\frac{\delta D_e}{D_e}\right)^2}$$

Where δD_R is dose rate error in Gy s^{-1}, D_P *and* δD_P are the palaeodose (Gy) and error of the palaeodose respectively, and D_e and δD_e are the equivalent dose (s) and the

error of the equivalent dose respectively. An additional calibration error of 3 % for source calibration was incorporated in sample age determination after Armitage and Bailey (2005), which accounts for any error in the gamma dosing of the calibration quartz.

The Risø reader quartz calibration is also applied to feldspar, which due to its differing density will actually have a different effective dose rate. However, as the range of feldspar densities encompasses that of quartz, in relation to the other influences affecting dosimetry, this effect is regarded as minor.

A.6 Laboratory Lighting

A.6.1 Sodium lamp Design

Feldspar are susceptible to bleaching under the red light conditions conventionally used in luminescence labs (Jensen and Barbetti, 1979; Smith, 1988; Spooner and Prescott, 1986; Sutton and Zimmerman, 1978a), consequently prior to feldspar sample preparation, a sodium lamp was constructed, which comprises a low pressure 18 W Na lamp, with appropriate control gear and filtering after Spooner et al. (2000).

A.6.2 Sodium Lamp Bleaching Experiment

A bleaching experiment was carried out on six aliquots of the GRAN56 feldspar extract, which had been bleached for 600 minutes on a bright, overcast July day in St Andrews, before being dosed with 6.21 ± 0.28 Gy, and on six aliquots of Batch 40 Calibration quartz (D_e: 4.81 ± 0.06 Gy). Three of each of the aliquots were placed directly in front of the sodium lamp for 60 minutes, whilst the remaining six aliquots (three from each sample) were exposed to the ambient red light in the OSL lab at St Andrews. It should be noted that Spooner et al. (2000) suggest only 3.6 cm^2 of the Na lamp should be exposed, and that this should be angled facing the lab wall, providing a dim light source. In this experiment the window was fully opened (~ 15 cm^2) and the samples exposed fully to the light source, in order that the maximum bleaching influence of the Na lamp could be explored. Following light exposure, all aliquots were analysed to determine lab lighting bleaching effects using the protocols listed in Table A.8 and Table A.9.

Table A.8: Feldspar lab-light bleaching experiment post IR – IRSL (pIR-IRSL) protocol (see Chapter 5 for protocol development details).

Natural/Regenerative	N = 6.2, 2.5, 6.2, 8.6, 0, 2.5 Gy*
Dose	250 ˚C, 60 s, 5 ˚C/s
TSL	50 ˚C, 100 s, 5˚C/s, 90% power
IRSL	250 ˚C, 100 s, 5˚C/s, 90% power

IRSL	6.2 Gy
Test Dose	250 ˚C, 60 s, 5 ˚C/s
TSL	50 ˚C, 100 s, 5˚C/s, 90% power
IRSL	250 ˚C, 100 s, 5˚C/s, 90% power
IRSL	290 ˚C, 100 s, 5˚C/s, 90% power
IRSL	

*All feldspar analyses were carried out on Risø 2, thus a specific dose is cited

Table A.9: Quartz lab-light bleaching experiment protocol

Natural/Regenerative	N = 4.81, 2.1, 6.4 Gy*
Dose	260 ˚C, 10 s, 5 ˚C/s
TSL	125˚C, 100s, 5˚C/s, 90% power
IRSL	6.2 Gy
Test Dose	160 ˚C, 0 s, 5 ˚C/s
TSL	125˚C, 100s, 5˚C/s, 90% power
IRSL	

*These quartz analyses were carried out on Risø 1

A.6.3 Sodium Lamp Bleaching Experiment Results

The feldspar IRSL signal was seriously bleached by Na lamp exposure, and quartz samples were also affected (Table A.10). In contrast, the pIR-IRSL signal of the feldspar was unaffected, indicative of its relatively slow bleaching rate. These results prompted measurement of the lamp emission spectrum, using the spectrometer detailed in Chapter 5. Spectra were collected in a light-tight room at 20 s intervals for 600 s (Figure A.2).

Sodium is solid at room temperature, and a mixture of neon and argon are used to provide an initial discharge of heat (and light), which causes the sodium to melt and vaporise. This initial emission is in the red – IR, and is apparent in the initial spectra (Figure A.2). As more sodium becomes available, and because sodium is ionised preferentially to neon and argon, the emission of the lamp changes over time. The yellow sodium emission dominates after 300 s, and the sodium *d* lines at 589 and 589.5 nm (2.10 eV) (Steck, 2003) are apparent. However, the red – IR emission centred at 1.55 eV is present even after the lamp has been switched on for 3000 s, and it is this emission which is likely to have caused the bleaching in the test experiment, explaining why feldspar are more seriously affected than quartz.

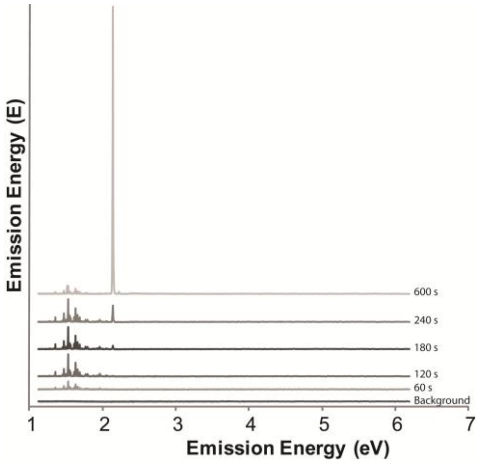

Figure A.2: Emission of the Na lamp as a function of increasing time (s). A background emission spectrum was measured to confirm that observed emissions relate to the Na lamp.

Table A.10: Sodium lamp bleaching experiment results

	CalQz BSL	GRAN56 IRSL	GRAN56 pIR-IRSL
Natural			
D_e (Gy)	4.81 ± 0.06	6.21 ± 0.28	6.21 ± 0.28
Na Lamp			
D_e (Gy)	4.14 ± 0.20	3.72 ± 0.16	6.48 ± 0.23
Δ %	- 14 01	- 40.02	4.35
Red Lights			
D_e (Gy)	4.77 ± 0.22	6.16 ± 0.22	6.29 ± 0.22
Δ %	- 0.79	- 0.79	1.4

The emission spectra of the naked 18 W Na bulb and the bulb filtered through five layers of Lee 101 yellow filter paper and one layer of Lee 216 white diffusion paper (after Spooner et al., 2000) were indistinguishable. This filter stack is advocated by Spooner et al. (2000) to remove the weak, high energy sodium emission lines, however it is insufficient for this Na lamp. Further filtering could be achieved through use of a 'detector trimmer' as described by Lamothe (1995). However, given that the bleaching rates observed are < 1 % under red light conditions, this lighting is adequate for feldspar sample preparation and so further filtering options for the Na lamp were not pursued.

A.7 Quartz Rejection Rates by Sample

Table A.11: Causes of aliquot rejection for subglacial samples

Sample	N	n	Acc. %	RR	Oversat	Sig <3 BG	IRSL	Inad. Regen	Plot	Calc	Recup
FAB_1	86	20	23	22	2	18	13	1	5	-	5
FAB_ 2	61	25	41	15	1	5	8	2	-	1	4
FAB Totals (%)	147	45	30.6	25.2	2.0	15.6	14.3	2.0	3.4	0.7	6.1
NIG103	54	6	11	7	2	10	3	-	3	3	20
NIG Totals (%)	54	6	11.1	13.0	3.7	18.5	5.6	0.0	5.6	5.6	37.0
Deposit Total	201	51		44	5	33	24	3	8	4	29
%	100	25.4		21.9	2.5	16.4	11.9	1.5	4.0	2.0	14.4

Table A.12: Causes of quartz aliquot rejection for Gilbert-style delta samples

Sample	N	n	Acc. %	RR	Oversat	Sig <3 BG	IRSL	Inad. Regen	Plot	Calc	Recup
GAUP2	24	8	33	7	7	-	-	-	-	-	2
GAUP40	12	1	8	-	2	1	-	-	1	1	6
GAUP41	26	13	50	5	-	-	3	-	-	2	3
Deposit Total	62	22		12	9	1	3	0	1	3	11
%	100	35.5		19.4	14.5	1.6	4.8	0.0	1.6	4.8	17.7

Table A.13: Causes of quartz aliquot rejection for fluvial braided channel bar samples

Sample	N	n	Acc. %	RR	Oversat	Sig <3 BG	IRSL	Inad. Regen	Plot	Calc	Recup
FAB81	30	22	73	1	1	1	2	2	-	-	1
FAB Total (%)	30	22		3.3	3.3	3.3	6.7	6.7	0.0	0.0	3.3
BERG4	12	0	0	10	-	-	-	1	-	-	1
BERG16	12	0	0	1	-	3	-	5	3	-	-
BERG19	36	2	6	5	-	9	-	-	2	3	15
BERG21	12	0	0	-	-	-	-	1	-	-	11
BERG24	36	8	22	11	-	9	3	-	-	-	5
BERG25	24	0	0	13	-	8	3	-	-	-	-
BERG Totals (%)	132	10	7.6	30.3	0.0	22.0	4.5	5.3	3.8	2.3	24.2
Total	162	32		41	1	30	8	9	5	3	33
%	100	19.8		25.3	0.6	18.5	4.9	5.6	3.1	1.9	20.4

Table A.14: Causes of quartz aliquot rejection for reworked paraglacial samples

Sample	N	n	Acc. %	RR	Oversat	Sig <3 BG	IRSL	Inad. Regen	Plot	Calc	Recup
FAB_41	36	14	39	7	6	-	-	9	-	-	-
FAB_42	42	27	50	4	1	-	3	4	-	-	3
FAB_85	30	23	77	2	-	-	-	3	-	-	3
FAB_86	112	27	24	23	11	22	1	3	7	2	16
FAB Total (%)	220	91	41.4	16.4	8.2	10.0	1.8	8.6	3.2	0.9	10.0
BERG1	36	0	0	9	-	11	1	-	1	3	11
BERG2	12	0	0	2	-	2	2	-	-	-	6
BERG Total (%)	48	0	0	22.9	0.0	27.1	6.3	0.0	2.1	6.3	35.4
Deposit Total	268	91		47	18	35	7	19	8	5	39
%	100	37.9		16.1	6.4	12.1	3.0	7.0	2.7	1.7	13.4

Table A.15: Causes of quartz aliquot rejection for sandur braided channel samples

Sample	N	n	Acc. %	RR	Oversat	Sig <3 BG	IRSL	Inad. Regen	Plot	Calc	Recup
GRAN_54	24	13	54	2	4	1	1	1	1	1	-
GRAN_55	48	30	63	5	1	6	-	-	-	-	6
GRAN_56	36	5	14	6	1	1	2	-	-	1	20
GRAN_57	36	6	17	2	-	2	-	-	2	-	24
GRAN_58	30	12	40	1	-	6	-	1	1	-	9
GRAN_59	30	24	41	5	1	-	-	-	-	-	-
GRAN_62	29	5	17	16	-	7	-	-	1	-	-
GRAN_71	12	3	25	-	-	-	-	-	-	-	9
Total	245	98		37	7	23	3	2	5	2	68
%	100	40		15.1	2.9	9.4	1.2	0.8	2.0	0.8	27.8

Table A.16: Causes of quartz aliquot rejection for fluvial point bar samples

Sample	N	n	Acc. %	RR	Oversat	Sig <3 BG	IRSL	Inad. Regen	Plot	Calc	Recup
FAB_79	65	28	43	13	14	1	-	9	-	-	-
FAB_80	30	19	63	-	3	-	-	5	-	-	3
FAB_83	2	0	0	-	1	-	-	1	-	-	-
FAB_84	38	19	50	8	4	-	-	-	1	-	6
FAB_90	36	19	53	12	4	-	-	1	-	-	
FAB_91	48	31	65	3	4	2	1	2	1	-	4
FAB_92	52	7	13	11	-	2	4	-	-	-	28
FAB_94	60	43	67	5	5	2	1	3	-	-	1
FAB_95	98	56	57	15	6	1	13	1	1	-	5
FAB_98	72	41	57	11	4	-	1	1	-	-	14
FAB_99	36	18	50	3	1	1	-	3	2	-	8
FAB_100	39	25	64	4	-	-	1	-	1	-	8
FAB Totals (%)	576	306	53.1	14.8	8.0	1.6	3.6	4.5	1.0	0.0	13.4
BERG7	12	0	0	1	-	-	2	-	1	-	8
BERG10	12	3	25	1	-	2	-	3	-	-	3
BERG Totals (%)	24	3	0	8.3	0.0	0.0	16.7	0.0	8.3	0.0	66.7
LOD105	24	1	4	-	6	-	10	1	-	-	6
LOD106	12	2	8	-	-	-	-	-	-	-	10
LOD107	12	0	0	2	-	-	-	-	1	-	9
LOD Totals (%)	48	3	6.3	4.2	12.5	0.0	20.8	2.1	2.1	0.0	52.1
Deposit Total	648	312		89	52	11	33	30	9	0	113
%	100	48.1		13.7	8.0	1.7	5.1	4.6	1.4	0.0	17.4

A.8 Feldspar Rejection Rates

Table A.17: Causes of feldspar aliquot rejection

Summary	N	n	Acc. %	RR	Max. P Error	Max. Td Error	Inad. Regen	SGC sat.
All Samples	1006	994		1	2	3	4	2
%			99					

A.9 Feldspar Samples Fading Rates

	IRSL			pIR-IRSL		
	n	g_{2days} (%/decade)	g_{2days} Error	*n*	g_{2days} (%/decade)	*SE**
GRAN54	12	4.68	2.85	12	4.27	0.30
GRAN55	6	3.30	1.07	12	3.18	0.64
GRAN56	19	3.36	1.20			
GRAN57	6	3.04	1.37	12	1.53	0.61
GRAN58	6	3.63	1.00	12	2.73	0.21
GRAN59	12	4.62	2.85			
GRAN69a	18	3.91	5.91			
GRAN69b	18	4.01	4.44			
FAB81	6	2.63	1.04			
FAB86	6	2.77	0.94			
FAB94	6	2.19	1.07			
FAB100	6	2.26	1.28			
JOS51	17	2.08	5.06			
LEI13	18	2.32	5.19			
LEI14	15	4.09	4.05			
LEI18	18	2.11	3.91			
NIG3	17	5.22	3.53			
NIG4	21	4.66	1.87			
NIG6	12	2.76	1.60			
NIG7	12	2.21	1.14			
NIG8	12	1.78	1.09			
NIG9	6	2.87	1.08			
BERG2	11	6.98	7.61			
GAUP1	6	1.32	2.42			
LOD4	18	3.81	4.47			
LOD5	18	3.57	3.68			
LOD6	18	4.96	3.36			

*The pIR-IRSL *g* values were calculated from a spreadsheet designed by myself, whereas the IRSL *g* values are calculated from curve fitting in the spreadsheet developed by Huot (2006), consequently the uncertainties are calculated differently. Those for the IRSL *g* values are the uncertainty of the curve fitting, whereas the pIR-IRSL *g* values are calculated from the standard error of *g* between the 12 aliquots analysed. It is therefore probable that the uncertainty of the pIR-IRSL *g* values is underestimated, however they are listed here for illustrative purposes.

A.10 Samples Distributions

D_e distributions of samples not given in Chapter 6 are given here, including samples with n < 10. Light grey histograms relate to quartz samples, and dark grey histograms to feldspar samples, all samples are individually labelled.

A.10.1 Reworked paraglacial deposits

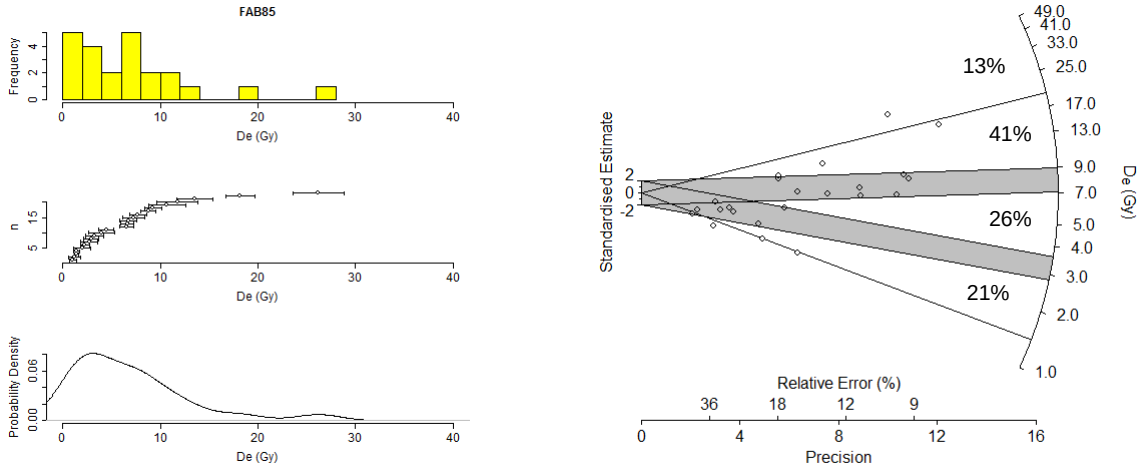

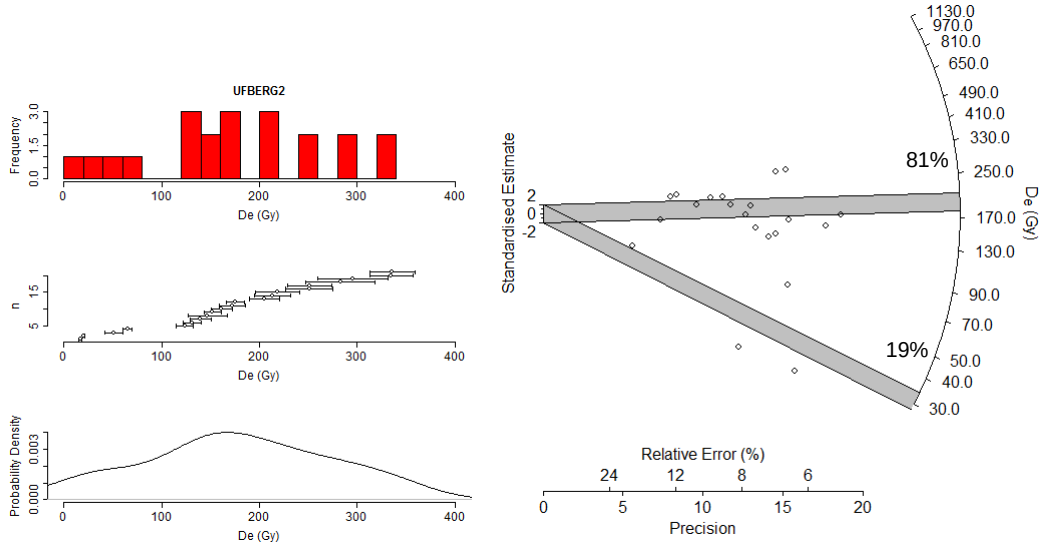

A.10.2 Glaciofluvial Point Bar Deposits

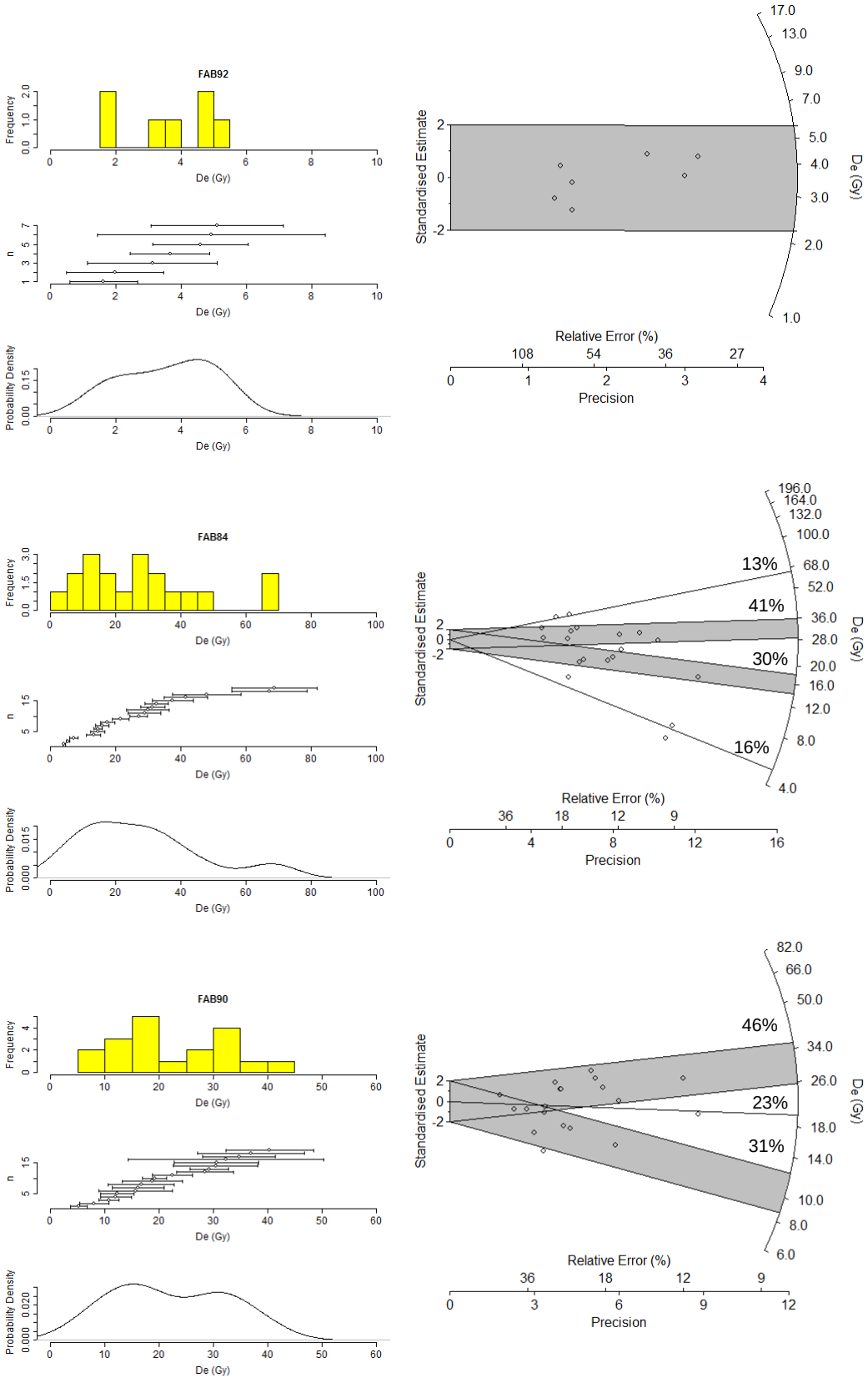

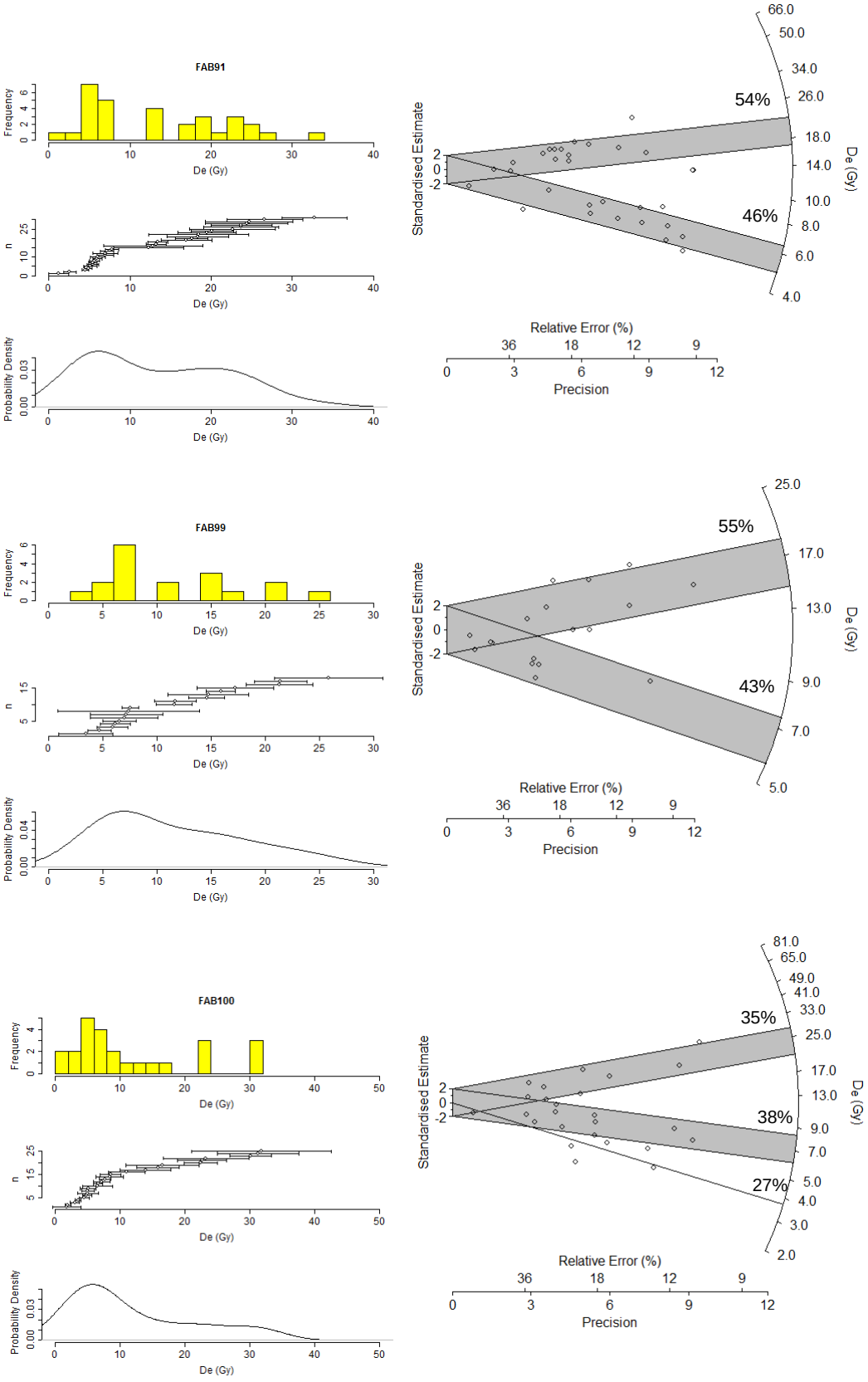
FAB91
Frequency
De (Gy)
n
Probability Density
Standardised Estimate
54%
46%
De (Gy)
Relative Error (%)
Precision
FAB99
55%
43%
FAB100
35%
38%
27%

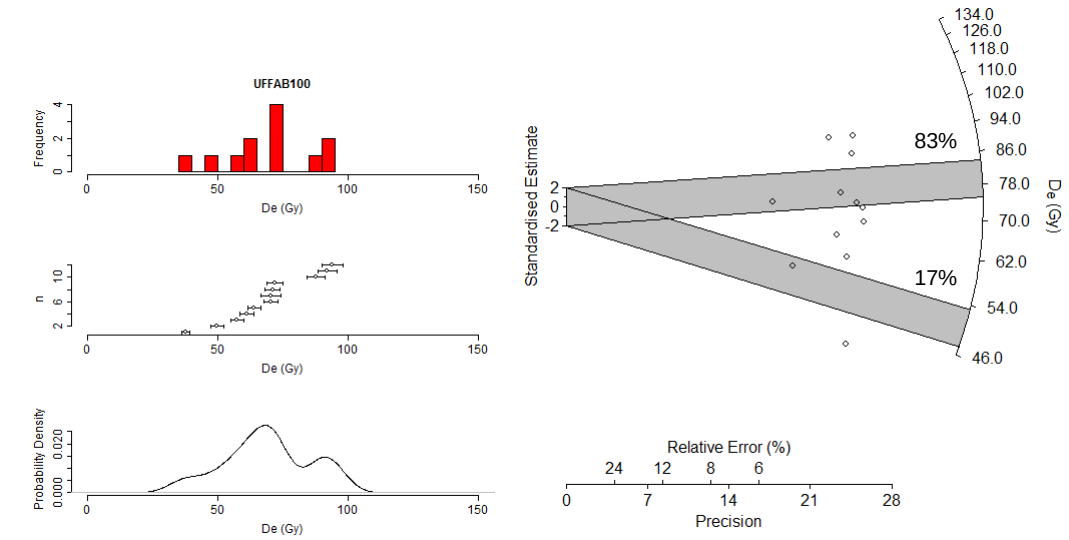
UFFAB100
Frequency
De (Gy)
n
Probability Density
Standardised Estimate
83%
17%
De (Gy)
Relative Error (%)
Precision

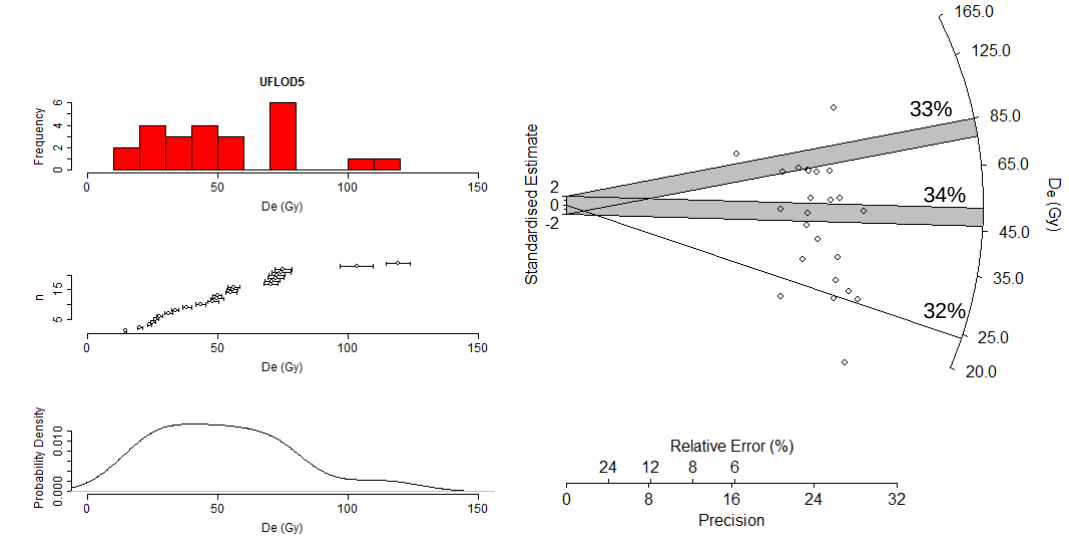
UFLOD5
Frequency
De (Gy)
n
Probability Density
Standardised Estimate
33%
34%
32%
De (Gy)
Relative Error (%)
Precision

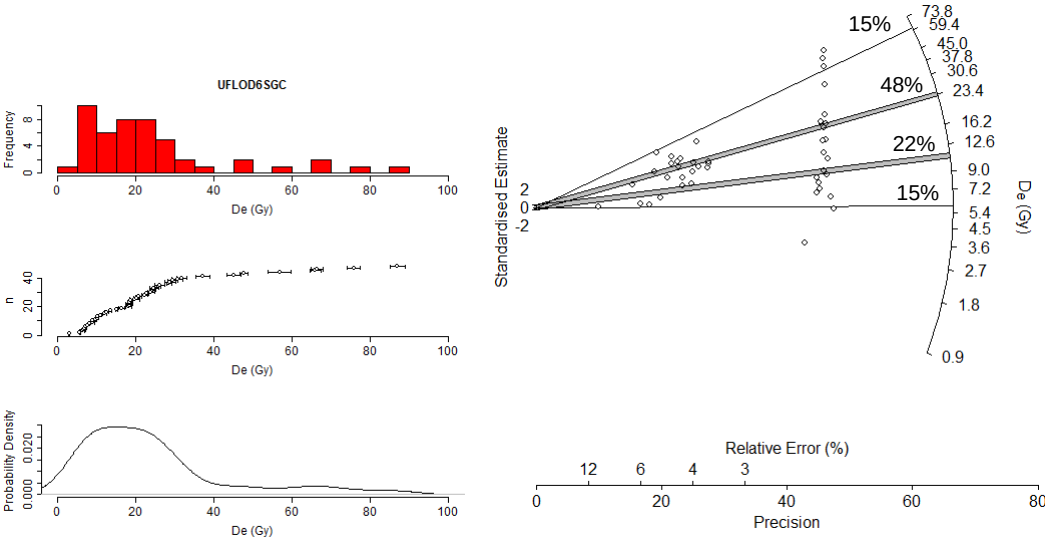
UFLOD6SGC
Frequency
De (Gy)
n
Probability Density
Standardised Estimate
15%
48%
22%
15%
De (Gy)
Relative Error (%)
Precision

A.10.3 Glaciofluvial Braided Channel Bar Deposits

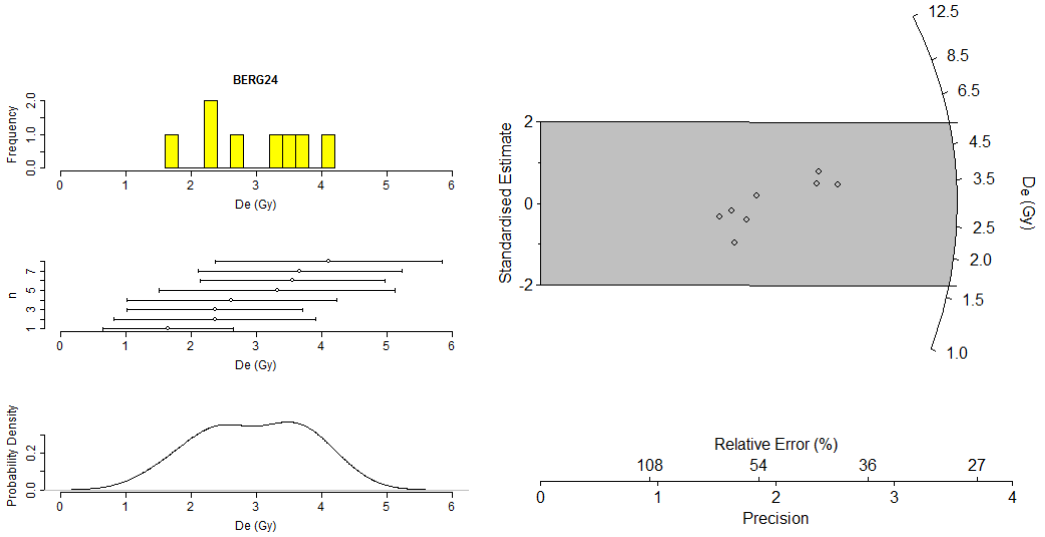

A.10.4 Sandur Braided Bar Deposits

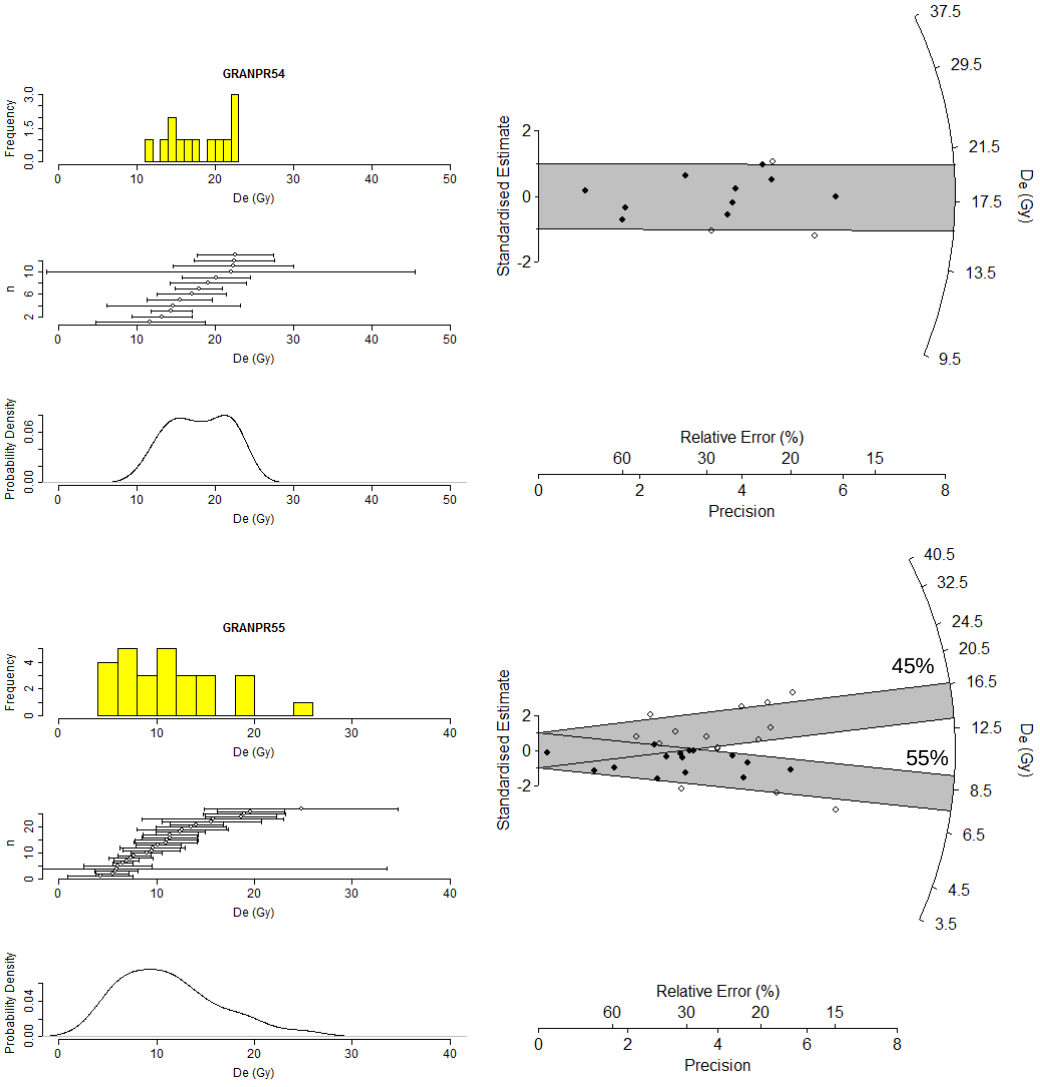

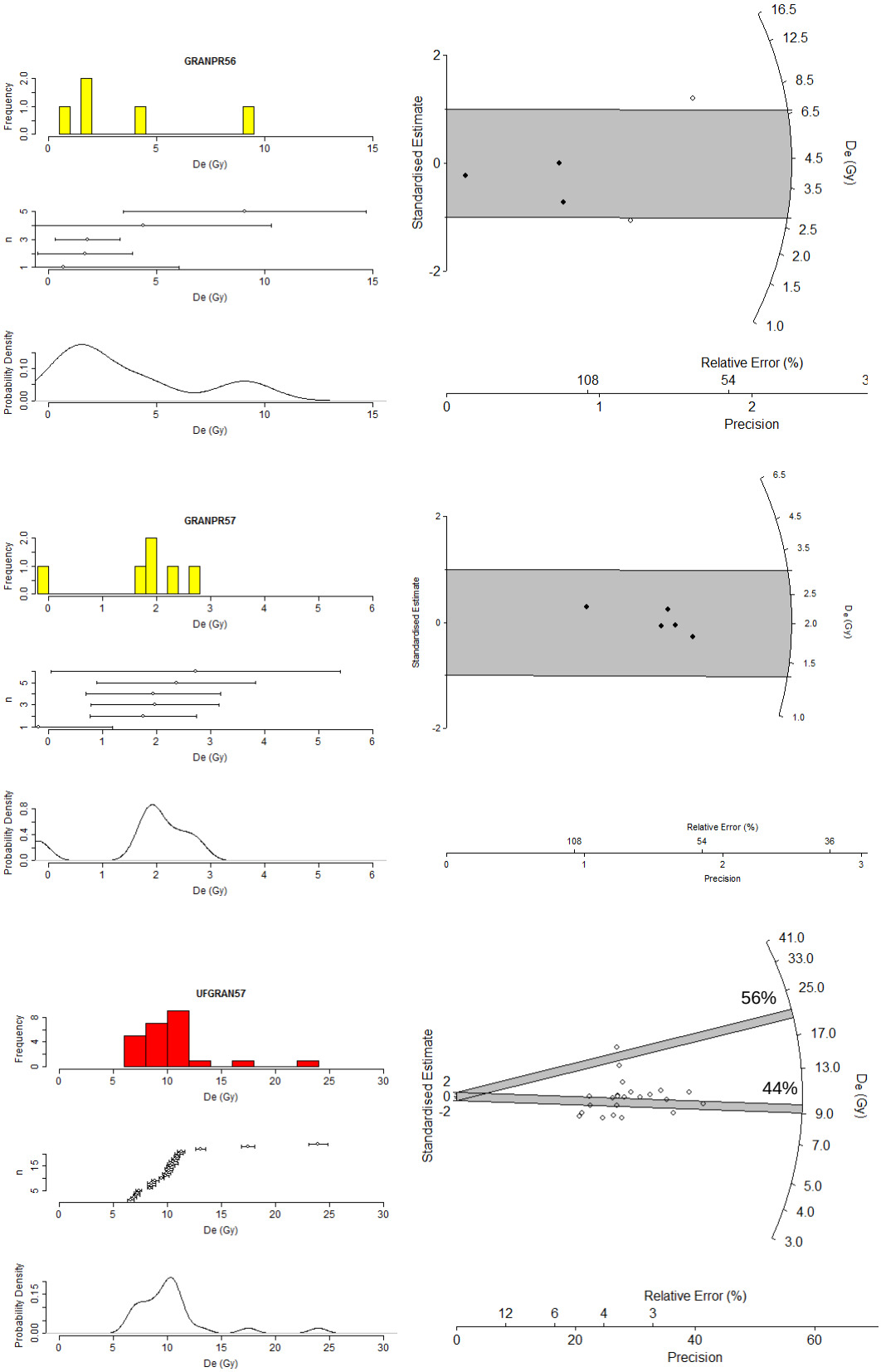
GRANPR56
Frequency
De (Gy)
n
Probability Density
Standardised Estimate
De (Gy)
Relative Error (%)
Precision
GRANPR57
UFGRAN57
56%
44%

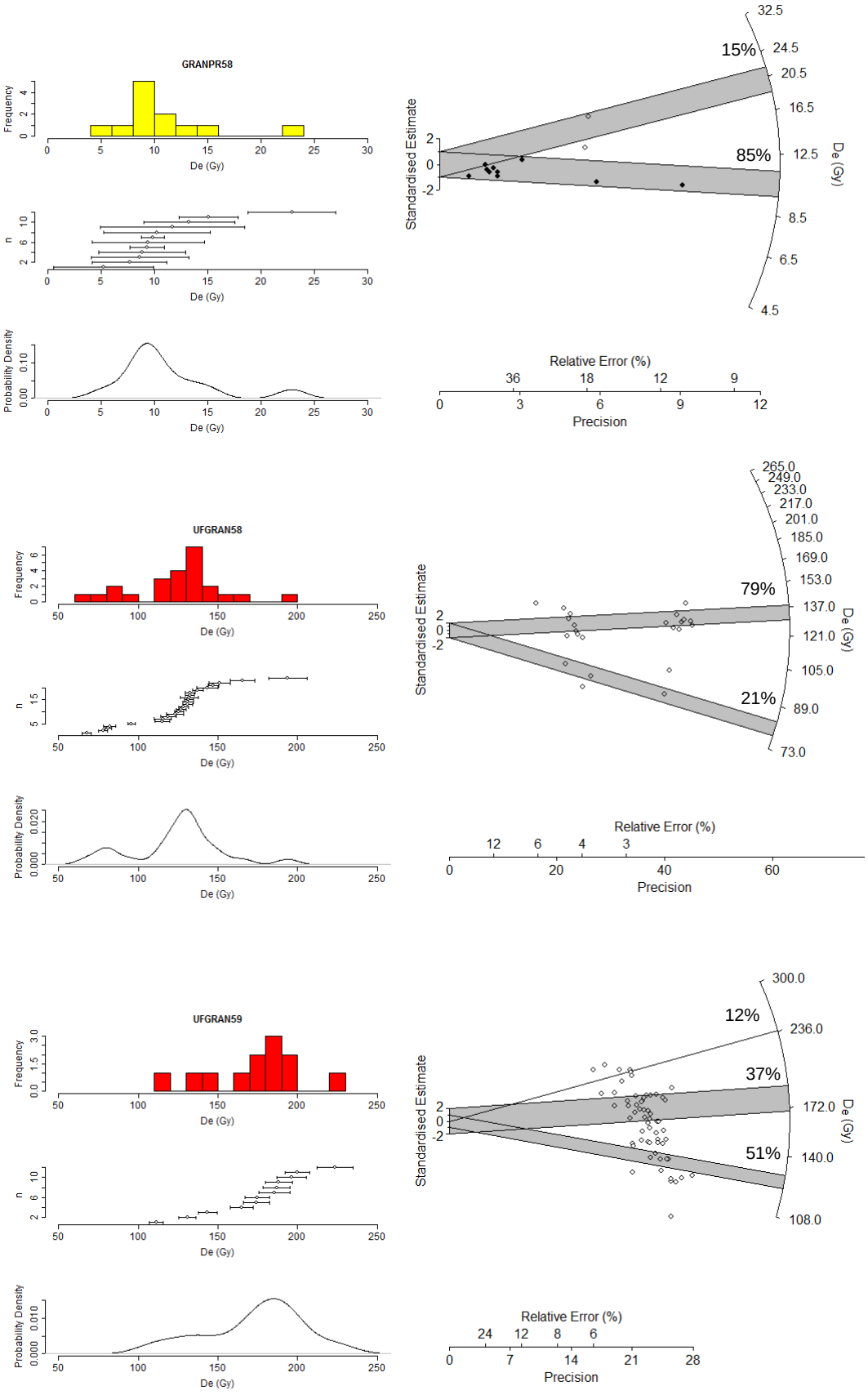
GRANPR58
Frequency
De (Gy)
n
Probability Density
Standardised Estimate
15%
85%
De (Gy)
Relative Error (%)
Precision
UFGRAN58
79%
21%
UFGRAN59
12%
37%
51%

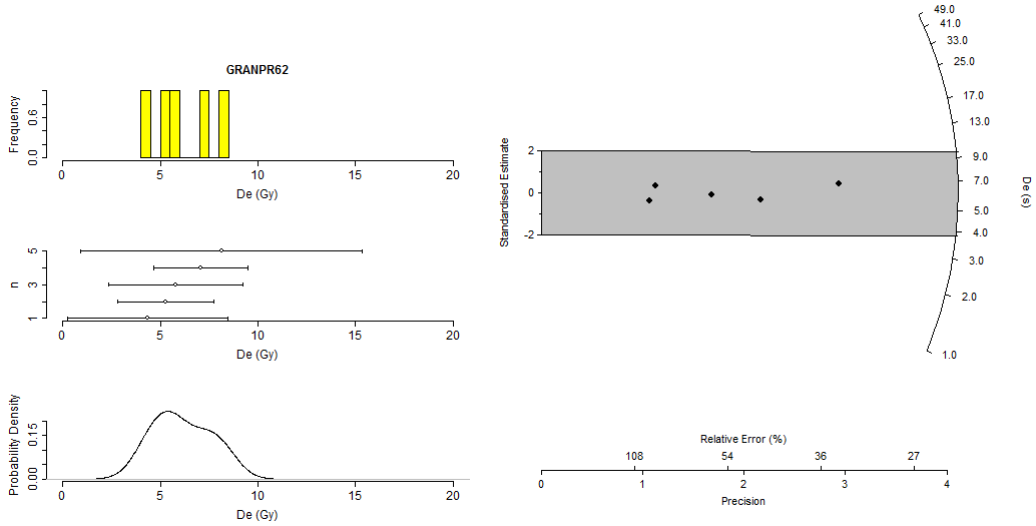
GRANPR62
Frequency
De (Gy)
n
Probability Density
Standardised Estimate
De (s)
Relative Error (%)
Precision

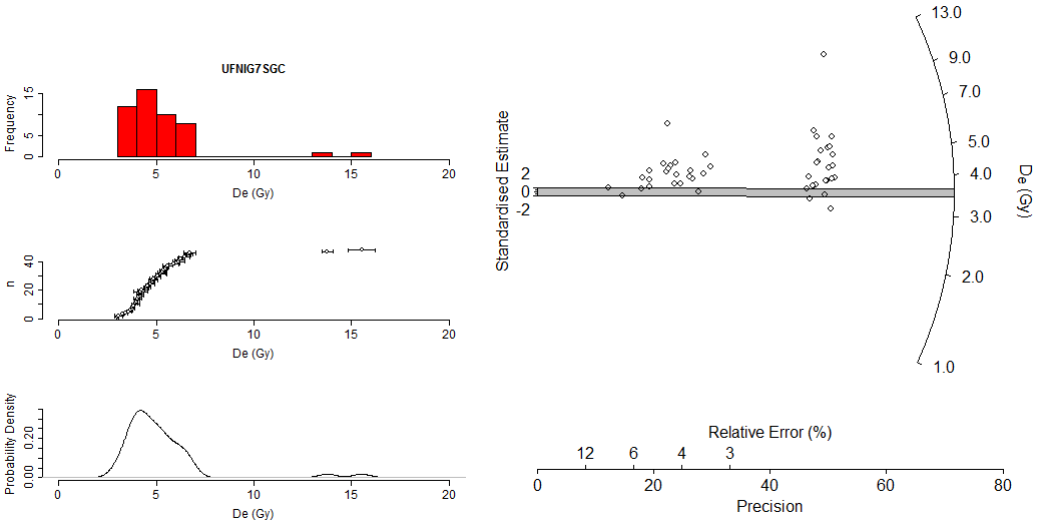
UFNIG7SGC
Frequency
De (Gy)
n
Probability Density
Standardised Estimate
De (Gy)
Relative Error (%)
Precision

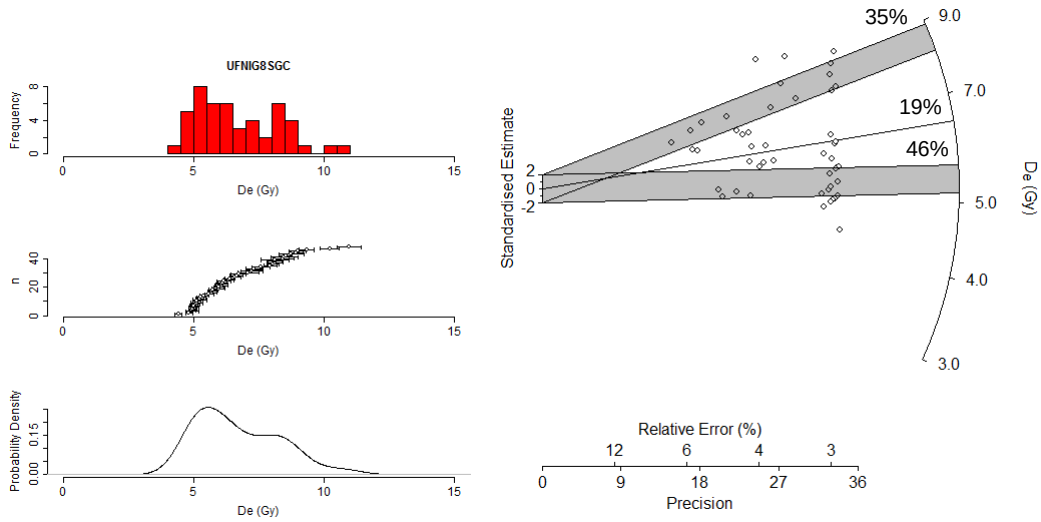
UFNIG8SGC
Frequency
De (Gy)
n
Probability Density
Standardised Estimate
35%
19%
46%
De (Gy)
Relative Error (%)
Precision

A.11 Factor Analysis Loadings

A.11.1 GSA all variables

R-Mode Data: GSA All Variables Unrotated Factor Loadings and Communalities						
Variable	Factor1	Factor2	Factor3	Factor4	Factor5	Communality
%_ V_ COARSE_SAND:	-0.683	-0.696	-0.063	-0.124	0.021	0.972
%_COARSE_SAND:	-0.893	-0.24	0.048	0.332	0.09	0.976
%_MEDIUM_SAND:	-0.248	0.828	-0.089	-0.196	0.279	0.872
%_FINE_SAND:	0.781	0.513	0.057	-0.235	-0.153	0.955
%_V FINE_SAND:	0.956	0.056	0.071	0.033	-0.235	0.979
%_V_COARSE_SILT:	0.962	-0.088	0.004	0.15	-0.136	0.974
%_COARSE_SILT:	0.954	-0.167	-0.044	0.175	0.002	0.97
%_MEDIUM_SILT:	0.931	-0.245	-0.097	0.165	0.128	0.98
%_FINE_SILT:	0.877	-0.335	-0.169	0.123	0.22	0.974
%_V_FINE_SILT:	0.957	-0.194	-0.105	0.088	0.111	0.985
%_CLAY:	0.987	-0.092	-0.058	0.091	-0.047	0.997
Distance_(m)	-0.371	0.212	0.099	0.878	-0.011	0.963
MEAN	0.945	0.305	0.029	0.032	-0.102	0.998
SORTING	0.614	-0.45	0.402	-0.356	0.268	0.939
SKEWNESS	-0.374	-0.312	-0.719	-0.18	-0.328	0.894
KURTOSIS	0.247	0.213	-0.834	0.055	0.28	0.883
Eigenvalues	9.8204	2.2323	1.4606	1.2658	0.5317	15.3107
% Var	0.614	0.14	0.091	0.079	0.033	0.957

Q-Mode Data: GSA All Variables Factor Score Coefficients					
Variable	Factor1	Factor2	Factor3	Factor4	Factor5
%_ V_ COARSE_SAND:	-3.846	1.231	1.461	-2.811	3.357
%_COARSE_SAND:	-3.882	1.441	1.542	-2.46	3.499
%_MEDIUM_SAND:	-2.681	1.456	0.997	-2.062	2.858
%_FINE_SAND:	-2.762	1.39	1.17	-2.226	2.207
%_V FINE_SAND:	-2.463	1.071	1.068	-1.813	1.807
%_V_COARSE_SILT:	-1.123	0.459	0.489	-0.758	0.816
%_COARSE_SILT:	-0.357	0.111	0.151	-0.188	0.404
%_MEDIUM_SILT:	-0.07	-0.043	-0.001	0.012	0.385
%_FINE_SILT:	0.024	-0.123	-0.09	0.05	0.471
%_V_FINE_SILT:	0.054	-0.069	-0.055	0.038	0.248
%_CLAY:	0	0	0	0	0
Distance_(m)	-0.038	0.095	0.068	0.694	-0.022
MEAN	0.096	0.137	0.02	0.026	-0.191
SORTING	0.063	-0.202	0.275	-0.281	0.505
SKEWNESS	-0.038	-0.14	-0.492	-0.142	-0.618
KURTOSIS	0.025	0.095	-0.571	0.043	0.527

A.11.1 GSA reduced variables

R-Mode Data: GSA Reduced Variables Unrotated Factor Loadings and Communalities						
Variable	Factor1	Factor2	Factor3	Factor4	Factor5	Communality
%_ V_ COARSE_SAND:	0.82	0.515	0.169	0.001	-0.108	0.978
%_COARSE_SAND:	0.959	-0.046	-0.204	-0.093	-0.067	0.977
%_MEDIUM_SAND:	0.004	-0.785	0.006	0.589	-0.021	0.965
%_FINE_SAND:	-0.936	-0.198	0.035	0.095	0.056	0.93
%_V_FINE_SAND:CLAY	-0.907	0.195	0.004	-0.331	0.125	0.987
Distance_(m)	0.413	-0.49	-0.507	-0.537	0.041	0.958
MEAN	-0.974	-0.093	-0.025	-0.159	0.104	0.994
SORTING	-0.536	0.72	-0.131	0.188	-0.199	0.898
SKEWNESS	0.485	0.05	0.751	-0.063	0.407	0.971
KURTOSIS	-0.225	-0.4	0.698	-0.328	-0.438	0.998
Variance	4.9841	1.8925	1.3984	0.9349	0.4455	9.6554
% Var	0.498	0.189	0.14	0.093	0.045	0.966

Q-Mode Data: GSA Reduced Variables Factor Score Coefficients					
Variable	Factor1	Factor2	Factor3	Factor4	Factor5
%_ V_ COARSE_SAND:	0.317	0.186	0.119	0.298	-0.479
%_COARSE_SAND:	0.346	-0.112	-0.148	0.199	-0.386
%_MEDIUM_SAND:	0.108	-0.476	0.003	0.839	-0.213
%_FINE_SAND:	-0.073	-0.17	0.023	0.325	-0.052
%_V_FINE_SAND:CLAY	0	0	0	0	0
Distance_(m)	0.083	-0.259	-0.363	-0.574	0.091
MEAN	-0.195	-0.049	-0.018	-0.17	0.233
SORTING	-0.107	0.38	-0.094	0.201	-0.447
SKEWNESS	0.097	0.026	0.537	-0.067	0.914
KURTOSIS	-0.045	-0.212	0.499	-0.351	-0.984

A.11.2 GSA final

R-Mode Data: GSA Final Unrotated Factor Loadings and Communalities						
Variable	Factor1	Factor2	Factor3	Factor4	Factor5	Communality
%_ V_ COARSE_SAN	-0.846	-0.463	-0.17	-0.012	0.115	0.972
%_COARSE_SAND:	-0.956	0.114	0.205	0.012	0.097	0.979
%_MEDIUM_SAND:	0.101	0.736	-0.007	-0.642	0.132	0.981
%_FINE_SAND:	0.957	0.127	-0.036	-0.017	-0.1	0.944
Distance_(m)	-0.423	0.558	0.51	0.447	-0.069	0.954
MEAN	0.955	0.046	0.025	0.212	-0.15	0.983
SORTING	0.498	-0.767	0.129	-0.076	0.205	0.901
SKEWNESS	-0.505	-0.002	-0.75	-0.036	-0.381	0.964
KURTOSIS	0.234	0.403	-0.697	0.372	0.396	0.999
Variance	4.2056	1.8489	1.3984	0.8034	0.4211	8.6772
% Var	0.467	0.205	0.155	0.089	0.047	0.964

Q-Mode Data: GSA Final Factor Score Coefficients					
Variable	Factor1	Factor2	Factor3	Factor4	Factor5
%_ V_ COARSE_SAND:	-0.201	-0.251	-0.121	-0.015	0.274
%_COARSE_SAND:	-0.227	0.062	0.147	0.014	0.231
%_MEDIUM_SAND:	0.024	0.398	-0.005	-0.799	0.312
%_FINE_SAND:	0.228	0.069	-0.025	-0.021	-0.238
Distance_(m)	-0.101	0.302	0.365	0.556	-0.163
MEAN	0.227	0.025	0.018	0.264	-0.356
SORTING	0.118	-0.415	0.092	-0.095	0.487
SKEWNESS	-0.12	-0.001	-0.536	-0.045	-0.904
KURTOSIS	0.056	0.218	-0.499	0.464	0.941

A.11.3 Quartz luminescence all variables

R-Mode Data: LUM All variables Unrotated Factor Loadings and Communalities						
Variable	Factor1	Factor2	Factor3	Factor4	Factor5	Communality
Age (ka)	-0.412	0.872	-0.122	0.105	-0.05	0.959
Max Age (ka)	0.465	0.01	-0.491	0.578	-0.455	0.999
c	0.864	0.383	-0.033	-0.02	0.288	0.978
K	0.806	0.525	-0.031	-0.096	0.218	0.983
% Acc	0.198	-0.018	0.826	0.525	0.034	0.999
Average Tx	0.53	0.085	0.329	-0.432	-0.645	0.998
Od	0.609	-0.724	-0.175	-0.01	0.167	0.954
Variance	2.4734	1.7158	1.0799	0.8169	0.7837	6.8698
% Var	0.353	0.245	0.154	0.117	0.112	0.981

Q-Mode Data: LUM All variables Factor Score Coefficients					
Variable	Factor1	Factor2	Factor3	Factor4	Factor5
Age (ka)	-0.167	0.508	-0.113	0.128	-0.064
Max Age (ka)	0.188	0.006	-0.455	0.707	-0.58
c	0.349	0.223	-0.03	-0.025	0.367
K	0.326	0.306	-0.029	-0.118	0.278
% Acc	0.08	-0.01	0.765	0.643	0.043
Average Tx	0.214	0.049	0.305	-0.529	-0.822
Od	0.246	-0.422	-0.162	-0.012	0.213

A.11.4 Quartz luminescence incl. distance

R-Mode Data: LUM incl. Distance Unrotated Factor Loadings and Communalities						
Variable	Factor1	Factor2	Factor3	Factor4	Factor5	Communality
Age (ka)	-0.572	-0.737	-0.275	-0.063	0.035	0.951
Max Age (ka)	0.46	-0.098	-0.346	-0.7	0.41	0.998
c	0.744	-0.573	0.005	0.008	-0.28	0.961
K	0.69	-0.675	-0.057	0.109	-0.207	0.989
% Acc	0.087	-0.136	0.875	-0.381	-0.096	0.946
Average Tx	0.468	-0.23	0.326	0.394	0.679	0.995
Od	0.735	0.561	0.018	-0.087	-0.151	0.887
Distance (m)	-0.719	-0.309	0.284	-0.164	0.022	0.72
Variance	2.853	1.8174	1.1515	0.8401	0.7844	7.4464
% Var	0.357	0.227	0.144	0.105	0.098	0.931

Q-Mode Data: LUM incl. Distance Factor Score Coefficients					
Variable	Factor1	Factor2	Factor3	Factor4	Factor5
Age (ka)	-0.201	-0.405	-0.239	-0.075	0.044
Max Age (ka)	0.161	-0.054	-0.3	-0.833	0.523
c	0.261	-0.315	0.004	0.009	-0.356
K	0.242	-0.371	-0.049	0.129	-0.264
% Acc	0.03	-0.075	0.76	-0.454	-0.123
Average Tx	0.164	-0.126	0.283	0.469	0.866
Od	0.258	0.309	0.016	-0.104	-0.193
Distance (m)	-0.252	-0.17	0.247	-0.196	0.028

A.11.5 GSA and quartz luminescence

R-Mode Data: GSA and LUM Data Unrotated Factor Loadings and Communalities						
Variable	Factor1	Factor2	Factor3	Factor4	Factor5	Communality
% V COARSE SAND:	-0.949	-0.27	0.031	0.08	0.059	0.984
% COARSE SAND:	-0.883	0.021	0.352	-0.199	-0.158	0.968
% MEDIUM SAND:	0.138	0.795	0.342	-0.123	-0.401	0.944
MEAN	0.952	-0.094	-0.216	0.064	0.1	0.977
SORTING	0.391	-0.751	0.301	0.103	0.219	0.866
SKEWNESS	-0.835	-0.014	-0.411	0.054	0.148	0.891
KURTOSIS	-0.173	0.13	-0.646	0.509	-0.404	0.887
Distance (m)	0.526	0.714	0.157	0.298	0.112	0.911
Age (ka)	0.231	0.064	-0.775	-0.515	-0.046	0.925
c	0.295	-0.737	-0.414	0.031	-0.362	0.933
Average Tx	0.253	-0.499	0.576	-0.369	-0.384	0.929
Od	-0.004	-0.247	0.276	0.81	-0.129	0.81
Variance	3.9668	2.663	2.1699	1.4861	0.7421	11.0279
% Var	0.331	0.222	0.181	0.124	0.062	0.919

Q-Mode Data: GSA and LUM Data Factor Score Coefficients					
Variable	Factor1	Factor2	Factor3	Factor4	Factor5
% V COARSE SAND:	-0.239	-0.101	0.014	0.054	0.08
% COARSE SAND:	-0.223	0.008	0.162	-0.134	-0.213
% MEDIUM SAND:	0.035	0.299	0.158	-0.083	-0.541
MEAN	0.24	-0.035	-0.1	0.043	0.134
SORTING	0.099	-0.282	0.139	0.069	0.295
SKEWNESS	-0.211	-0.005	-0.189	0.036	0.2
KURTOSIS	-0.044	0.049	-0.298	0.343	-0.545
Distance (m)	0.132	0.268	0.073	0.2	0.151
Age (ka)	0.058	0.024	-0.357	-0.346	-0.062
c	0.074	-0.277	-0.191	0.021	-0.487
Average Tx	0.064	-0.188	0.266	-0.249	-0.517
Od	-0.001	-0.093	0.127	0.545	-0.174

A.11.6 Feldspar luminescence all variables

R-Mode Data: LUM All variables excl. De (Gy) Unrotated Factor Loadings and Communalities						
Variable	Factor1	Factor2	Factor3	Factor4	Factor5	Communality
Age (ka)	0.753	0.451	-0.369	-0.006	-0.306	1
Max Age (ka)	0.685	0.612	-0.262	0.011	0.296	1
c	-0.905	0.072	-0.394	0.089	-0.015	0.988
k	-0.847	0.055	-0.513	0.076	0.03	0.99
Average Tx	0.643	-0.525	-0.194	0.522	0.025	1
Od	-0.479	0.645	0.437	0.403	-0.048	1
Variance	3.2151	1.2771	0.8512	0.4483	0.1853	5.977
% Var	0.536	0.213	0.142	0.075	0.031	0.996

Q-Mode Data: LUM All variables excl. De (Gy) Factor Score Coefficients					
Variable	Factor1	Factor2	Factor3	Factor4	Factor5
Age (ka)	0.234	0.353	-0.433	-0.014	-1.65
Max Age (ka)	0.213	0.479	-0.308	0.023	1.599
c	-0.281	0.057	-0.463	0.199	-0.08
k	-0.263	0.043	-0.603	0.171	0.161
Average Tx	0.2	-0.411	-0.227	1.164	0.137
Od	-0.149	0.505	0.513	0.898	-0.257

A.11.7 Feldspar luminescence incl. distance

R-Mode Data: LUM all variables excl. De (Gy), incl. Distance Unrotated Factor Loadings and Communalities						
Variable	Factor1	Factor2	Factor3	Factor4	Factor5	Communality
Age (ka)	-0.711	0.519	-0.344	-0.111	0.028	0.907
Max Age (ka)	-0.641	0.667	-0.227	-0.064	0.015	0.912
c	0.915	0.057	-0.263	-0.204	0.191	0.988
k	0.869	0.059	-0.394	-0.22	0.162	0.989
Average Tx	-0.621	-0.441	-0.394	0.371	0.355	0.999
Od	0.487	0.586	0.472	0.328	0.294	0.998
Distance (m)	0.676	0.199	-0.416	0.485	-0.308	1
Age (ka)	-0.711	0.519	-0.344	-0.111	0.028	0.907
Variance	3.5893	1.2995	0.9457	0.5868	0.3716	6.7929
% Var	0.513	0.186	0.135	0.084	0.053	0.97

Q-Mode Data: LUM all variables excl. De (Gy) incl. Distance Factor Score Coefficients					
Variable	Factor1	Factor2	Factor3	Factor4	Factor5
Age (ka)	-0.198	0.4	-0.363	-0.19	0.076
Max Age (ka)	-0.179	0.514	-0.24	-0.11	0.042
c	0.255	0.044	-0.278	-0.347	0.514
k	0.242	0.045	-0.416	-0.375	0.436
Average Tx	-0.173	-0.339	-0.417	0.631	0.956
Od	0.136	0.451	0.499	0.559	0.792
Distance (m)	0.188	0.153	-0.44	0.827	-0.829
Age (ka)	-0.198	0.4	-0.363	-0.19	0.076

A.11.8 GSA and feldspar luminescence

R-Mode Data: GSA and LUM all variables excl. De (Gy), incl. Distance Unrotated Factor Loadings and Communalities						
Variable	Factor1	Factor2	Factor3	Factor4	Factor5	Communality
MEAN	0.739	-0.109	-0.407	-0.524	0.03	1
SORTING	0.668	0.669	-0.032	0.052	0.308	0.992
Max Age (ka)	0.73	-0.633	-0.201	0.128	0.055	0.993
Distance (m)	-0.65	-0.587	0.387	-0.178	0.101	0.959
Od	-0.57	-0.104	-0.791	0.144	-0.064	0.986
Average Tx	0.932	-0.243	-0.003	0.247	0.024	0.989
c	-0.846	-0.368	-0.183	0.048	0.303	0.98
Age (ka)	0.835	-0.515	0.142	0.043	-0.006	0.985
Variance	4.5549	1.6758	1.0355	0.4111	0.2055	7.8828
% Var	0.569	0.209	0.129	0.051	0.026	0.985

Q-Mode Data: GSA and LUM all variables excl. De (Gy) incl. Distance Factor Score Coefficients					
Variable	Factor1	Factor2	Factor3	Factor4	Factor5
MEAN	0.162	-0.065	-0.393	-1.275	0.148
SORTING	0.147	0.399	-0.031	0.126	1.498
Max Age (ka)	0.16	-0.378	-0.194	0.312	0.269
Distance (m)	-0.143	-0.35	0.374	-0.432	0.494
Od	-0.125	-0.062	-0.763	0.349	-0.31
Average Tx	0.205	-0.145	-0.003	0.602	0.117
c	-0.186	-0.22	-0.176	0.116	1.475
Age (ka)	0.183	-0.307	0.137	0.104	-0.027

A.11.9 Combined quartz and feldspar

R-Mode Data: LUM All variables excl. De (Gy) quartz & feldspar Unrotated Factor Loadings and Communalities						
Variable	Factor1	Factor2	Factor3	Factor4	Factor 5	Communality
Age (ka)	-0.572	-0.737	-0.275	-0.063	0.035	0.951
Max Age (ka)	0.46	-0.098	-0.346	-0.7	0.41	0.998
c	0.744	-0.573	0.005	0.008	-0.28	0.961
K	0.69	-0.675	-0.057	0.109	-0.207	0.989
% Acc	0.087	-0.136	0.875	-0.381	-0.096	0.946
Average Tx	0.468	-0.23	0.326	0.394	0.679	0.995
Od	0.735	0.561	0.018	-0.087	-0.151	0.887
Distance (m)	-0.719	-0.309	0.284	-0.164	0.022	0.72
Variance	2.853	1.8174	1.1515	0.8401	0.7844	7.4464
% Var	0.357	0.227	0.144	0.105	0.098	0.931

Q-Mode Data: LUM All variables excl. De (Gy) quartz & feldspar Factor Score Coefficients					
Variable	Factor1	Factor2	Factor3	Factor4	Factor5
Age (ka)	-0.201	-0.405	-0.239	-0.075	0.044
Max Age (ka)	0.161	-0.054	-0.3	-0.833	0.523
c	0.261	-0.315	0.004	0.009	-0.356
K	0.242	-0.371	-0.049	0.129	-0.264
% Acc	0.03	-0.075	0.76	-0.454	-0.123
Average Tx	0.164	-0.126	0.283	0.469	0.866
Od	0.258	0.309	0.016	-0.104	-0.193
Distance (m)	-0.252	-0.17	0.247	-0.196	0.028

A.11.10 GSA and combined quartz and feldspar

R-Mode Data: Quartz & feldspar luminescence and GSA Unrotated Factor Loadings and Communalities									
Variable	Factor1	Factor2	Factor3	Factor4	Factor5	Factor6	Factor7	Factor8	Communal
% V COARSE SAND:	0.707	-0.486	-0.445	-0.095	0.146	0.107	-0.026	-0.107	0.988
% COARSE SAND:	0.868	-0.411	0.137	-0.037	-0.051	0.092	0.158	-0.004	0.978
% MEDIUM SAND:	0.098	0.358	0.343	0.503	-0.583	0.359	0.001	0.116	0.992
MEAN	-0.864	0.406	0.142	-0.075	0.114	-0.2	-0.021	0.079	0.998
SORTING	-0.59	-0.149	-0.468	-0.528	-0.073	0.212	-0.021	0.16	0.944
SKEWNESS	0.47	-0.011	-0.413	0.575	0.353	-0.154	-0.165	0.317	0.999
KURTOSIS	0.075	0.721	0.006	0.267	0.518	0.231	-0.06	-0.219	0.969
Age (ka)	-0.594	-0.479	0.215	0.382	0.358	-0.041	0.201	-0.074	0.951
Od	0.322	0.701	-0.351	-0.17	0.15	0.029	0.458	0.115	0.994
c	0.354	0.191	0.523	-0.491	0.434	0.227	-0.202	0.119	0.972
Average Tx	-0.564	-0.591	0.197	0.153	0.304	0.328	0.136	0.127	0.964
Distance (m)	0.468	-0.068	0.786	-0.159	0.067	-0.242	0.113	0.098	0.953
Variance	3.7042	2.3519	1.8436	1.4148	1.2109	0.5318	0.38	0.2637	11.71
% Var	0.309	0.196	0.154	0.118	0.101	0.044	0.032	0.022	0.975

Q-Mode Data: Quartz & feldspar luminescence and GSA Factor Score Coefficients								
Variable	Factor1	Factor2	Factor3	Factor4	Factor5	Factor6	Factor7	Factor8
% V COARSE SAND:	0.191	-0.207	-0.241	-0.067	0.121	0.202	-0.069	-0.406
% COARSE SAND:	0.234	-0.175	0.074	-0.026	-0.042	0.174	0.415	-0.014
% MEDIUM SAND:	0.026	0.152	0.186	0.356	-0.482	0.676	0.001	0.442
MEAN	-0.233	0.173	0.077	-0.053	0.094	-0.377	-0.056	0.301
SORTING	-0.159	-0.063	-0.254	-0.373	-0.061	0.398	-0.056	0.605
SKEWNESS	0.127	-0.005	-0.224	0.407	0.291	-0.29	-0.434	1.2
KURTOSIS	0.02	0.307	0.003	0.189	0.427	0.434	-0.157	-0.829
Age (ka)	-0.16	-0.204	0.117	0.27	0.296	-0.076	0.53	-0.282
Od	0.087	0.298	-0.19	-0.12	0.124	0.055	1.206	0.437
c	0.096	0.081	0.284	-0.347	0.358	0.428	-0.532	0.452
Average Tx	-0.152	-0.251	0.107	0.108	0.251	0.617	0.357	0.482
Distance (m)	0.126	-0.029	0.426	-0.112	0.055	-0.455	0.296	0.373

Appendix B. R Code

B.1 EBG code (Section 4.6.2)

```
### change names

NOR35_2<-read.table("C:\\Program Files\\R\\R-2.11.1\\NOR35_2.txt",header=T)
attach(NOR35_2)
names(NOR35_2)

### ensure that t and I are correct headers

nlc<-nls.control(maxiter = 1000, minFactor = 1/10000, warnOnly=TRUE)
model3<-nls(I~((n1*b1*(exp(-b1*t)))+(n2*b2*(exp(-b2*t)))+(n3*b3*(exp(-b3*t)))),
start=list(n1=1000,b1=1.97,n2=1000,b2=0.48,n3=1000,b3=0.11),control=nlc,trace=FALSE)
summary(model3)

### add more variables as appropriate
dev.new(width=4.8,height=4.8)
plot(log(t),I,col="black",
ylab="Signal Intensity (counts)",
xlab="log(Time) (s)",
ylim=c(0,1500),xlim=c(-2,4))

y1<-(coef(model3)["n1"]*(coef(model3)["b1"])*exp(-(coef(model3)["b1"]*t)))
y2<-(coef(model3)["n2"]*(coef(model3)["b2"])*exp(-(coef(model3)["b2"]*t)))
y3<-(coef(model3)["n3"]*(coef(model3)["b3"])*exp(-(coef(model3)["b3"]*t)))
lines(log(t),y1,lty=1,col="blue")
lines(log(t),y2,lty=1,col="grey")
lines(log(t),y3,lty=1,col="red")
lines(log(t),(y3+y2+y1),lty=3,col="red")

### to plot the relative contribution of the different variables (log scale)

dev.new(width=4.8,height=4.8)
plot(log(t),y1/(y1+y2+y3),ylim=c(0,1.0),col="blue",
ylab="Proportional Contribution to Total Signal",
xlab="log(Time) (s)")
points(log(t),y2/(y1+y2+y3),col="grey")
points(log(t),y3/(y1+y2+y3),col="red")

### to plot the relative contribution of the different variables (non-log scale)
### having to amend plot size in this file and then save manually as eps

dev.new(width=4.8,height=4.8)
plot(t,y1/(y1+y2+y3),ylim=c(0,1.0),col="blue",
ylab="Proportional Contribution to Total Signal",
xlab="Time (s)")
points(t,y2/(y1+y2+y3),col="grey")
points(t,y3/(y1+y2+y3),col="red")

### to highlight the overlap of the different components in non-log space

dev.new(width=4.8,height=4.8)
plot(t,y1/(y1+y2+y3),ylim=c(0,1.0), xlim=c(0,10),col="blue",
ylab="Proportional Contribution to Total Signal",
xlab="Time (s)")
points(t,y2/(y1+y2+y3),col="grey")
points(t,y3/(y1+y2+y3),col="red")

### to calculate a second model with different starting parameters

model4<-nls(I~((n1*b1*(exp(-b1*t)))+(n2*b2*(exp(-b2*t)))+(n3*b3*(exp(-b3*t)))),
start=list(n1=100,b1=2.2,n2=100,b2=0.44,n3=1000,b3=0.02),control=nlc,trace=FALSE)
summary(model4)

dev.new(width=4.8,height=4.8)
plot(log(t),I,col="black",
ylab="Signal Intensity (counts)",xlab="log(Time) (s)",ylim=c(0,1500),xlim=c(-2,4))

y1<-(coef(model4)["n1"]*(coef(model4)["b1"])*exp(-(coef(model4)["b1"]*t)))
y2<-(coef(model4)["n2"]*(coef(model4)["b2"])*exp(-(coef(model4)["b2"]*t)))
y3<-(coef(model4)["n3"]*(coef(model4)["b3"])*exp(-(coef(model4)["b3"]*t)))
lines(log(t),y1,lty=1,col="blue")
lines(log(t),y2,lty=1,col="grey")
lines(log(t),y3,lty=1,col="red")
lines(log(t),(y3+y2+y1),lty=3,col="red")

### to plot the relative contribution of the different variables (log scale)
```

```
dev.new(width=4.8,height=4.8)
plot(log(t),y1/(y1+y2+y3),ylim=c(0,1.0),col="blue",
ylab="Proportional Contribution to Total Signal",
xlab="log(Time) (s)")
points(log(t),y2/(y1+y2+y3),col="grey")
points(log(t),y3/(y1+y2+y3),col="red")

### to plot the relative contribution of the different variables (non-log scale)

dev.new(width=4.8,height=4.8)
plot(t,y1/(y1+y2+y3),ylim=c(0,1.0),col="blue",
ylab="Proportional Contribution to Total Signal",
xlab="Time (s)")
points(t,y2/(y1+y2+y3),col="grey")
points(t,y3/(y1+y2+y3),col="red")

### to highlight the overlap of the different components in non-log space

dev.new(width=4.8,height=4.8)
plot(t,y1/(y1+y2+y3),ylim=c(0,1.0), xlim=c(0,10),col="blue",
ylab="Proportional Contribution to Total Signal",
xlab="Time (s)")
points(t,y2/(y1+y2+y3),col="grey")
points(t,y3/(y1+y2+y3),col="red")

### RSE calculations for different integration intervals

RSE1<-(sqrt
        (((sum(I[1]))+
        ((1/0.33)*
        (mean(I[2:4])))+
        (1+(1/0.33))*
        ((27.2*0.33)-
        (13.05*0.33)))/
        ((sum(I[1]))-(mean(I[2:4])))*100)
RSE2<-(sqrt
        (((sum(I[1:2]))+
        ((1/0.33)*
        (mean(I[3:7])))+
        (1+(1/0.33))*
        ((27.2*0.33)-
        (13.05*0.33)))/
        ((sum(I[1:2]))-(mean(I[3:7])))*100)
RSE3<-(sqrt
        (((sum(I[1:3]))+
        ((1/0.33)*
        (mean(I[4:11])))+
        (1+(1/0.33))*
        ((27.2*0.33)-
        (13.05*0.33)))/
        ((sum(I[1:3]))-(mean(I[4:11])))*100)
RSE4<-(sqrt
        (((sum(I[1:4]))+
        ((1/0.33)*
        (mean(I[5:14])))+
        (1+(1/0.33))*
        ((27.2*0.33)-
        (13.05*0.33)))/
        ((sum(I[1:4]))-(mean(I[5:14])))*100)
RSE5<-(sqrt
        (((sum(I[1:5]))+
        ((1/0.33)*
        (mean(I[6:18])))+
        (1+(1/0.33))*
        ((27.2*0.33)-
        (13.05*0.33)))/
        ((sum(I[1:4]))-(mean(I[5:14])))*100)
RSE6<-(sqrt
        (((sum(I[1:6]))+
        ((1/0.33)*
        (mean(I[7:21])))+
        (1+(1/0.33))*
        ((27.2*0.33)-
        (13.05*0.33)))/
        ((sum(I[1:6]))-(mean(I[7:21])))*100)
RSE7<-(sqrt
        (((sum(I[1:7]))+
        ((1/0.33)*
```

```
        (mean(I[8:25])))+
        (1+(1/0.33))*
        ((27.2*0.33)-
        (13.05*0.33)))/
        ((sum(I[1:7]))-(mean(I[8:25])))*100)
RSE8<-(sqrt
        (((sum(I[1:8]))+
        ((1/0.33)*
        (mean(I[9:28])))+
        (1+(1/0.33))*
        ((27.2*0.33)-
        (13.05*0.33)))/
        ((sum(I[1:8]))-(mean(I[9:28])))*100)
RSE9<-(sqrt
        (((sum(I[1:9]))+
        ((1/0.33)*
        (mean(I[10:32])))+
        (1+(1/0.33))*
        ((27.2*0.33)-
        (13.05*0.33)))/
        ((sum(I[1:9]))-(mean(I[10:32])))*100)
RSE10<-(sqrt
        (((sum(I[1:10]))+
        ((1/0.33)*
        (mean(I[11:35])))+
        (1+(1/0.33))*
        ((27.2*0.33)-
        (13.05*0.33)))/
        ((sum(I[1:10]))-(mean(I[11:35])))*100)
```

B.2 Bootstrapping Experiments

B.2.1 Boot50 & Shapiro-Wilk test code (Section 4.12)

```
CalQzB8<-read.table("C:\\Program Files\\R\\R-2.12.0\\ CalQzB8.txt",header=T)
attach(CalQzB8)
names(CalQzB8)
testdat1 <- replicate( 20, CalQzB8 [sample(nrow(CalQzB8), 24, rep=TRUE),], simplify=FALSE)

write.table(testdat1, file="C:/Users/Georgina/Documents/Academic/Statistics/Boot/ CalQzB8_Boot50.txt", append=FALSE,
quote=TRUE, sep = " ", eol = "\n", dec = ".", row.names = TRUE, col.names = TRUE, qmethod = "double")

CalQzB8<- read.table("C:/Users/Georgina/Documents/Academic/Statistics/Boot/CalQzB8_Boot50.txt")

attach(CalQzB8)
names (CalQzB8)

t1 <-shapiro.test(cd)
t2 <-shapiro.test(cd.1)
t3 <-shapiro.test(cd.2)
t4 <-shapiro.test(cd.3)
t5 <-shapiro.test(cd.4)
t6 <-shapiro.test(cd.5)
t7 <-shapiro.test(cd.6)
t8 <-shapiro.test(cd.7)
t9 <-shapiro.test(cd.8)
t10 <-shapiro.test(cd.9)
t11 <-shapiro.test(cd.10)
t12 <-shapiro.test(cd.11)
t13 <-shapiro.test(cd.12)
t14 <-shapiro.test(cd.13)
t15 <-shapiro.test(cd.14)
t16 <-shapiro.test(cd.15)
t17 <-shapiro.test(cd.16)
t18 <-shapiro.test(cd.17)
t19 <-shapiro.test(cd.18)
t20 <-shapiro.test(cd.19)
t21 <-shapiro.test(cd.20)
t22 <-shapiro.test(cd.21)
t23 <-shapiro.test(cd.22)
t24 <-shapiro.test(cd.23)
t25 <-shapiro.test(cd.24)
t26 <-shapiro.test(cd.25)
t27 <-shapiro.test(cd.26)
```

```
t28 <-shapiro.test(cd.27)
t29 <-shapiro.test(cd.28)
t30 <-shapiro.test(cd.29)
t31 <-shapiro.test(cd.30)
t32 <-shapiro.test(cd.31)
t33 <-shapiro.test(cd.32)
t34 <-shapiro.test(cd.33)
t35 <-shapiro.test(cd.34)
t36 <-shapiro.test(cd.35)
t37 <-shapiro.test(cd.36)
t38 <-shapiro.test(cd.37)
t39 <-shapiro.test(cd.38)
t40 <-shapiro.test(cd.39)
t41 <-shapiro.test(cd.40)
t42 <-shapiro.test(cd.41)
t43 <-shapiro.test(cd.42)
t44 <-shapiro.test(cd.43)
t45 <-shapiro.test(cd.44)
t46 <-shapiro.test(cd.45)
t47 <-shapiro.test(cd.46)
t48 <-shapiro.test(cd.47)
t49 <-shapiro.test(cd.48)
t50 <-shapiro.test(cd.49)
list(t1)
list(t2)
list(t3)
list(t4)
list(t5)
list(t6)
list(t7)
list(t8)
list(t9)
list(t10)
list(t11)
list(t12)
list(t13)
list(t14)
list(t15)
list(t16)
list(t17)
list(t18)
list(t19)
list(t20)
list(t21)
list(t22)
list(t23)
list(t24)
list(t25)
list(t26)
list(t27)
list(t28)
list(t29)
list(t30)
list(t31)
list(t32)
list(t33)
list(t34)
list(t35)
list(t36)
list(t37)
list(t38)
list(t39)
list(t40)
list(t41)
list(t42)
list(t43)
list(t44)
list(t45)
list(t46)
list(t47)
list(t48)
list(t49)
list(t50)
```

B.2.2 $Boot_{10,000}$ mean dependency on *n* code (Section 4.12)

```
library(boot)
CalQzB8<-read.table("C:\\Program Files\\R\\R-2.12.0\\CalQzB8.txt",header=T)
attach(CalQzB8)
names(CalQzB8)
testdat1 <- sample(CalQzB8$cd,5, replace=TRUE)

mymean<-function(testdat1,i) mean(testdat1[i])
myboot1<-boot(testdat1,mymean,R=10000)

testdat2 <- sample(CalQzB8$cd,10, replace=TRUE)

mymean<-function(testdat2,i) mean(testdat2[i])
myboot2<-boot(testdat1,mymean,R=10000)

testdat3 <- sample(CalQzB8$cd,15, replace=TRUE)

mymean<-function(testdat3,i) mean(testdat3[i])
myboot3<-boot(testdat1,mymean,R=10000)

testdat4 <- sample(CalQzB8$cd,20, replace=TRUE)

mymean<-function(testdat4,i) mean(testdat4[i])
myboot4<-boot(testdat4,mymean,R=10000)

testdat5 <- sample(CalQzB8$cd,25, replace=TRUE)

mymean<-function(testdat5,i) mean(testdat5[i])
myboot5<-boot(testdat5,mymean,R=10000)

testdat6 <- sample(CalQzB8$cd,30, replace=TRUE)

mymean<-function(testdat6,i) mean(testdat6[i])
myboot6<-boot(testdat6,mymean,R=10000)

testdat7 <- sample(CalQzB8$cd,35, replace=TRUE)

mymean<-function(testdat7,i) mean(testdat7[i])
myboot7<-boot(testdat7,mymean,R=10000)

testdat8 <- sample(CalQzB8$cd,40, replace=TRUE)

mymean<-function(testdat8,i) mean(testdat8[i])
myboot8<-boot(testdat8,mymean,R=10000)

myboot1
myboot2
myboot3
myboot4
myboot5
myboot6
myboot7
myboot8
```

B.2.3 Resample σ_d dependency on *n* code (Section 4.12)

```
CalQzB8<-read.table("C:\\Program Files\\R\\R-2.12.0\\CalQzB8.txt",header=T)
attach(CalQzB8)
names(CalQzB8)

testdat1 <- replicate( 5, CalQzB8[sample(nrow(CalQzB8), 1, rep=TRUE),], simplify=FALSE)
```

```
write.table(testdat1, file="C:/Users/Georgina/Documents/Academic/Statistics/Boot/Od n/CalQzboot5.txt", append=FALSE,
quote=FALSE, sep = " ", eol = "\n", dec = ".", row.names = FALSE, col.names = FALSE, qmethod = "double")

testdat2 <- replicate( 10, CalQzB8[sample(nrow(CalQzB8), 1, rep=TRUE),], simplify=FALSE)

write.table(testdat2, file="C:/Users/Georgina/Documents/Academic/Statistics/Boot/Od n/CalQzboot10.txt", append=FALSE,
quote=FALSE, sep = " ", eol = "\n", dec = ".", row.names = FALSE, col.names = FALSE, qmethod = "double")

testdat3 <- replicate( 15, CalQzB8[sample(nrow(CalQzB8), 1, rep=TRUE),], simplify=FALSE)

write.table(testdat3, file="C:/Users/Georgina/Documents/Academic/Statistics/Boot/Od n/CalQzboot15.txt", append=FALSE,
quote=FALSE, sep = " ", eol = "\n", dec = ".", row.names = FALSE, col.names = FALSE, qmethod = "double")

testdat4 <- replicate( 20, CalQzB8[sample(nrow(CalQzB8), 1, rep=TRUE),], simplify=FALSE)

write.table(testdat4, file="C:/Users/Georgina/Documents/Academic/Statistics/Boot/Od n/CalQzboot20.txt", append=FALSE,
quote=FALSE, sep = " ", eol = "\n", dec = ".", row.names = FALSE, col.names = FALSE, qmethod = "double")

testdat5 <- replicate( 25, CalQzB8[sample(nrow(CalQzB8), 1, rep=TRUE),], simplify=FALSE)

write.table(testdat5, file="C:/Users/Georgina/Documents/Academic/Statistics/Boot/Od n/CalQzboot25.txt", append=FALSE,
quote=FALSE, sep = " ", eol = "\n", dec = ".", row.names = FALSE, col.names = FALSE, qmethod = "double")

testdat6 <- replicate( 30, CalQzB8[sample(nrow(CalQzB8), 1, rep=TRUE),], simplify=FALSE)

write.table(testdat6, file="C:/Users/Georgina/Documents/Academic/Statistics/Boot/Od n/CalQzboot30.txt", append=FALSE,
quote=FALSE, sep = " ", eol = "\n", dec = ".", row.names = FALSE, col.names = FALSE, qmethod = "double")

testdat7 <- replicate( 35, CalQzB8[sample(nrow(CalQzB8), 1, rep=TRUE),], simplify=FALSE)

write.table(testdat7, file="C:/Users/Georgina/Documents/Academic/Statistics/Boot/Od n/CalQzboot35.txt", append=FALSE,
quote=FALSE, sep = " ", eol = "\n", dec = ".", row.names = FALSE, col.names = FALSE, qmethod = "double")

testdat8 <- replicate( 40, CalQzB8[sample(nrow(CalQzB8), 1, rep=TRUE),], simplify=FALSE)

write.table(testdat8, file="C:/Users/Georgina/Documents/Academic/Statistics/Boot/Od n/CalQzboot40.txt", append=FALSE,
quote=FALSE, sep = " ", eol = "\n", dec = ".", row.names = FALSE, col.names = FALSE, qmethod = "double")
```

B.2.4 $Boot_{10,000}$ distribution statistic bias code (Section 4.12.1)

```
Library(boot)

FAB94<-read.table("C:\\Program Files\\R\\R-2.12.0\\FAB94.txt",header=T)
attach(FAB94)
names(FAB94)

mymean<-function(cd,i) mean(cd[i])
myboot<-boot(cd,mymean,R=10000)
myboot

#The output is interpreted as follows. The original is the mean of the whole sample
#mean(cd)
#bias is the difference between arithmetic mean and the mean of the bootstrapped samples which are in the #variable
called myboot$t
#mean(myboot$t)-mean(cd)
#and std. error is the sdev of the simulated samples in myboot$t
#sqrt(var(myboot$t))

hist(myboot$t)

skew<-function(x){
m3<-sum((cd-mean(x))^3)/length(x)
s3<-sqrt(var(x))^3
m3/s3 }

#function taken from Crawley

myskew<-function(cd,i) skew(cd[i])

myboot2<-boot(cd,myskew,R=10000)
myboot2
hist(myboot2$t)

kurt<-function(x) {
m4<-sum((x-mean(x))^4)/length(x)
```

```
s4<-var(x)^2
m4/s4 - 3 }

mykurt<- function(cd,i) kurt(cd[i])

myboot3<-boot(cd,mykurt,R=10000)
myboot3
hist(myboot3$t)

tiff("C:\\Users\\Georgina\\Documents\\Academic\\Statistics\\Boot\\Sample Test\\FAB94.tiff")

par(mfrow=c(3,1))

hist(myboot$t,main=" ", col=8, ylab="Frequency",xlab="De (Gy)", bty="n", cex.axis=1, cex.main=1, cex.lab=1)
hist(myboot2$t,main=" ",col=8, ylab="Frequency",xlab="Skewness", bty="n", cex.axis=1, cex.main=1, cex.lab=1)
hist(myboot3$t,main=" ",col=8, ylab="Frequency",xlab="Kurtosis", bty="n", cex.axis=1, cex.main=1, cex.lab=1)
dev.off()


myboot
myboot2
myboot3
```

B.2.5 Boot synthetic sample development code (Section 4.12.1)

```
CalQzB8<-read.table("C:\\Program Files\\R\\R-2.12.0\\ CalQzB8.txt",header=T)
attach(CalQzB8)
names(CalQzB8)
testdat1 <- sample(CalQzB8$cd,3000, replace=TRUE)

mymean<-function(testdat1,i) mean(testdat1[i])
myboot<-boot(testdat1,mymean,R=5000)
myboot

myskew<-function(testdat1,i) skew(testdat1[i])

myboot2<-boot(testdat1,myskew,R=5000)
myboot2

mykurt<- function(testdat1,i) kurt(testdat1[i])

myboot3<-boot(testdat1,mykurt,R=5000)
myboot3

shapiro.test(myboot$t)
shapiro.test(myboot2$t)
shapiro.test(myboot3$t)
```

Appendix C. Sample Descriptions

C.1 Bergsetdalen

C.1.1 BERG1 & 2

- Process: Slope failure, slumping and gullying
- Classification: Paraglacial
- Description & location: Gullied paraglacial deposits on the south valley side of Bergsetdalen.
- Facies: Dmm
- Texture: silt – boulders, angular – sub-angular, consolidated, unsorted
- Bedding: Massive
- Scale: Valley side drift > 3 m thick
- Quartz and feldspar of BERG2 analysed, only quartz analysed for BERG1

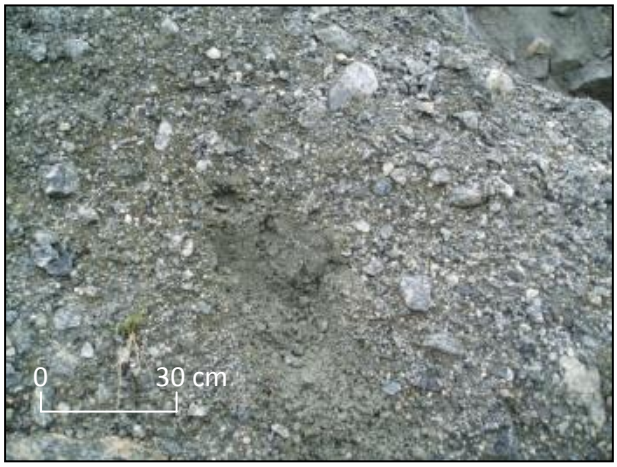

C.1.2 BERG4

- Process: Glaciofluvial
- Classification: Braided bar deposit sampled from the Bergsetdøla.
- Sampled at the point of bar clast transition from cobbles to pebbles. Sample forms a veneer over the cobble deposits.
- Facies: Sm
- Texture: coarse-medium sand, fining upwards
- Bedding: Massive
- Scale: > 10 cm thick
- Quartz analysed (prepared and measured by DBL under guidance of GEK, analysed by GEK)

C.1.3 BERG7

- Process: Glaciofluvial
- Classification: Point bar deposit sampled from the Bergsetdøla.
- Facies: Sh
- Texture: coarse-medium sand matrix (4 cm), overlaying sand matrix supported medium sub-well rounded pebbles (4 cm)
- Bedding: Low angle cross lamination, conformable contacts between medium (1 cm) and coarse (1 cm) units
- Scale: ~ 8 cm thick
- Quartz analysed (prepared and measured by DBL under guidance of GEK, analysed by GEK)

C.1.4 BERG10

- Process: Glaciofluvial
- Classification: Point bar deposit sampled from the Bergsetdøla.
- Facies: Sr:Sl
- Texture: coarse to fine sand, consolidated
- Bedding: Ripple cross laminated (~ 1 cm thick) with some horizontal and draped lamination of fine sand
- Scale: ~ 10 cm thick
- Quartz analysed (prepared and measured by DBL under guidance of GEK, analysed by GEK)

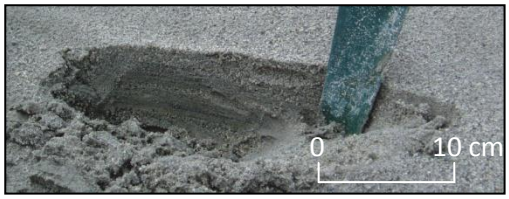

C.1.5 BERG16

- Process: Glaciofluvial
- Classification: Braided bar-tail deposit sampled from the Bergsetdøla.
- Facies: Sh
- Texture: coarse to fine sand, overlaying sub-rounded cobbles, consolidated
- Bedding: Sharp conformable contacts between coarse and medium-fine grained sand
- Scale: ~ 8 cm thick
- No image of the exact sample location is available, but this image shows depositional context.
- Quartz analysed (prepared and measured by DBL under guidance of GEK, analysed by GEK)

C.1.6 BERG19

- Process: Glaciofluvial
- Classification: Braided bar deposit sampled from the Bergsetdøla.
- Facies: Sh
- Texture: medium to fine sand (5 cm), overlaying gravels
- Scale: ~ 5 cm thick
- Quartz analysed (prepared and measured by DBL under guidance of GEK, analysed by GEK)

C.1.7 BERG21

- Process: Glaciofluvial
- Classification: Braided bar deposit sampled from the Bergsetdøla.
- Facies: Fl:Sh
- Texture: silt to coarse sand (5 cm), overlaying sub-angular cobbles and gravels, poorly consolidated
- Bedding: Ripple cross bedding of coarse sand, fining up section to medium sand (1 cm) interbedded with fine laminated silts (< 0.5 cm)
- Scale: ~ 5 cm thick
- Quartz analysed (prepared and measured by DBL under guidance of GEK, analysed by GEK)

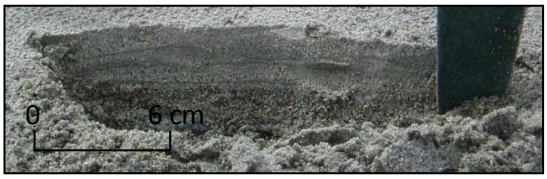

C.1.8 BERG24 & BERG25

- Process: Glaciofluvial
- Classification: Braided bar deposit sampled from the Bergsetdøla.
- Facies: Sr
- Texture: ranges from gravel to silt (10 cm)
- Bedding: Ripple cross bedding, alternating from coarse sands (3 cm), medium sands (1 cm) to finer laminations of silt. Some lenses of gravel are also present.
- Scale: ~ 10 cm thick
- The image showing depositional context does not relate to either of the samples described.
- Quartz analysed (prepared and measured by DBL under guidance of GEK, analysed by GEK)

C.2 Fåbergstølsgrandane

C.2.1 FABSUB1 & FABSUB2

- Process: Glacial
- Classification: Subglacial
- Description & location: Subglacial material sampled from beneath the glacier snout.
- Facies: Dmm
- Texture: silt – boulders, angular – sub-angular, consolidated
- Bedding: Massive
- Scale: > 1 m thick
- Quartz analysed

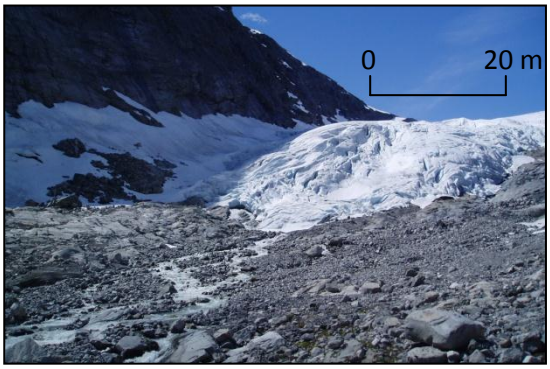

C.2.2 FAB41

- Process: Slope failure, sheet wash
- Classification: Paraglacial
- Description & location: Sampled adjacent to a meltwater stream on the north valley side.
- Facies: Sh
- Texture: medium to coarse sand
- Bedding: Horizontal to low angle bedding
- Scale: > 15 cm thick
- Quartz analysed

C.2.3 FAB42

- Process: Slope failure, snow avalanche
- Classification: Paraglacial
- Description & location: Debris covered snow ridge from the north valley side.
- Facies: Dmm
- Texture: poorly sorted, coarse sand to sub-angular pebbles
- Bedding: Massive
- Scale: < 5 cm thick
- Quartz analysed

C.2.4 FAB79

- Process: Glaciofluvial
- Classification: Channel point bar
- Description & location: Meltwater deposit collected ~ 100 m from Fåbergstølsbreen snout
- Facies: Sh
- Texture: fine to medium sand layers and medium to coarse sand layers
- Bedding: low angle cross lamination, units ~ 1 cm thick
- Scale: ~ 10 cm thick
- Quartz analysed

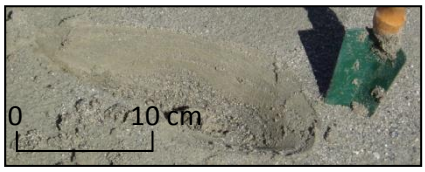

C.2.5 FAB80

- Process: Glaciofluvial
- Classification: Channel point bar
- Description & location: Meltwater deposit collected ~ 100 m from Fåbergstølsbreen snout
- Facies: Fl
- Texture: fine sand to silt, overlaying medium sand
- Bedding: low angle cross lamination, units ~ 1 cm thick
- Scale: ~ 10 cm thick
- Quartz analysed

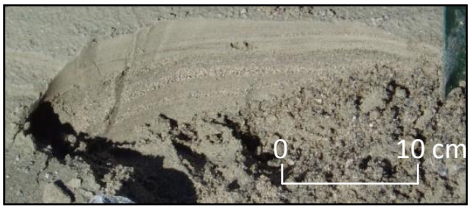

C.2.6 FAB81

- Process: Glaciofluvial
- Classification: Braided channel bar
- Description & location: Meltwater deposit collected at the confluence of a meltwater stream and the main meltwater channel.
- Facies: Sh:Fl
- Texture: fine sand overlaying coarse gravel
- Bedding: low angle - horizontal bedding, units indistinct
- Scale: ~ 5 cm thick. As the deposit was so shallow some of the coarser underlying material was also sampled.
- Quartz and feldspar analysed

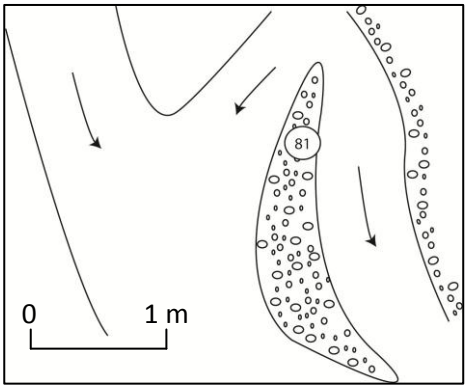

C.2.7 FAB83

- Process: Glaciofluvial
- Classification: Channel point bar
- Description & location: Meltwater deposit collected from the main meltwater channel point bar ~ 200 m from the snout of Fåbergstølsbreen
- Facies: Sh
- Texture: well sorted, fine-coarse sand
- Bedding: variation from fine to coarse sand units
- Scale: ~ 10 cm thick
- Quartz analysed

C.2.8 FAB84

- Process: Glaciofluvial
- Classification: Channel point bar
- Description & location: Meltwater deposit collected from the main meltwater channel point bar ~ 160 m from the snout of Fåbergstølsbreen
- Facies: Sr
- Texture: well sorted
- Bedding: ripple cross bedded, units ~ 1 cm to 6 cm
- Scale: ~ 30 cm thick.
- Quartz analysed

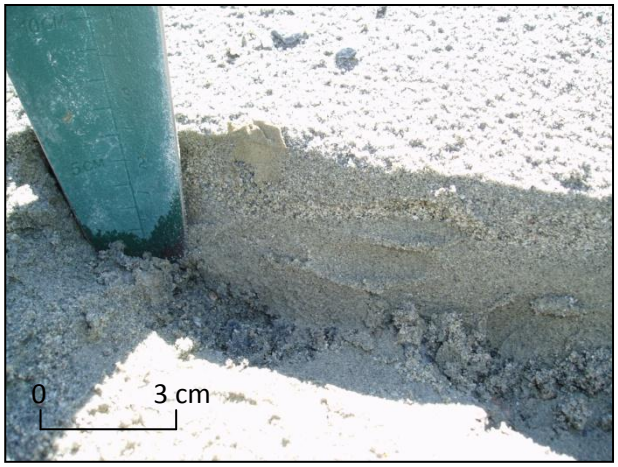

C.2.1 FAB85

- Process: Sheet wash
- Classification: Paraglacial
- Description & location: Deposit collected ~ 5 m above the main channel, indicating provenance from valley side.
- Facies: Sh:Fl
- Texture: well sorted
- Bedding: horizonally bedded, units < 0.5 cm
- Scale: ~ 5 cm thick.
- Quartz analysed

C.2.2 FAB86

- Process: Sheet wash
- Classification: Paraglacial
- Description & location: Meltwater deposit from the confluence of a valley side meltwater stream and the main meltwater channel.
- Facies: Sr
- Texture: fine to medium sand
- Quartz and feldspar analysed

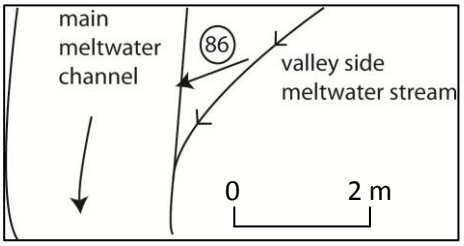

C.2.3 FAB90

- Process: Glaciofluvial
- Classification: Channel point bar
- Description & location: Deposit from the stoss side of a boulder adjacent to the main meltwater stream.
- Facies: Sh
- Texture: fine sand – silt, loosely consolidated, well sorted
- Bedding: horizontally bedded, units ~ 1 cm to 3 cm
- Scale: ~ 30 cm thick.
- Quartz analysed

C.2.4 FAB91

- Process: Glaciofluvial
- Classification: Channel point bar
- Description & location: Meltwater deposit from the main meltwater stream, ~ 450 m from the snout of Fåbergstølsbreen.
- Facies: Sr
- Texture: moderately sorted, fine sand – coarse gravel
- Bedding: ripple cross bedded, units vary in clast size from gravels to sands and are between ~ 1 cm to 3 cm thick
- Scale: ~ 15 cm thick.
- Quartz analysed

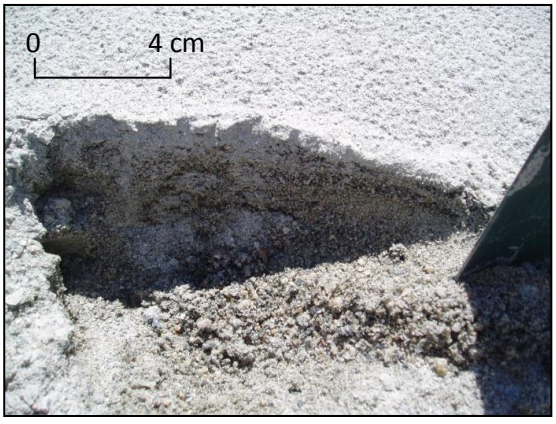

C.2.5 FAB92

- Process: Glaciofluvial
- Classification: Channel point bar
- Description & location: Meltwater deposit adjacent to the main meltwater stream.
- Facies: Sh
- Texture: moderately sorted fine sand to gravel
- Bedding: horizontally bedded, 1 cm thick veneer of fine sand overlaying coarse sand and gravel
- Scale: ~ 15 cm thick. Quartz analysed

C.2.6 FAB94

- Process: Glaciofluvial
- Classification: Channel point bar
- Description & location: Wet meltwater deposit collected from the confluence of a valley side stream and the main meltwater channel, ~ 500 m distal from the snout of Fåbergstølsdalen.
- Facies: Sh:Fl
- Texture: moderately sorted fine sand to silt
- Bedding: structure difficult to identify but some evidence for horizontal bedding, 5 cm thick layer of fine sand to silt overlaying coarse sand and gravel
- Scale: ~ 10 cm thick.
- Quartz analysed

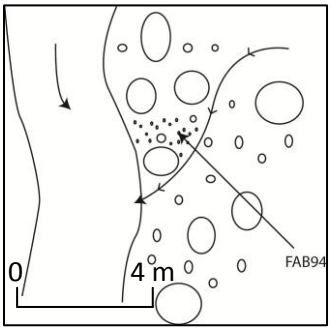

C.2.7 FAB95

- Process: Glaciofluvial
- Classification: Channel point bar
- Description & location: Meltwater deposit collected from the stoss side of a boulder ~ 3 m from the main meltwater channel.
- Facies: Sr
- Texture: well sorted medium to coarse sand
- Bedding: interbedded medium and coarse sand units, 2-3 cm thick
- Scale: ~ 30 cm thick.
- Quartz analysed

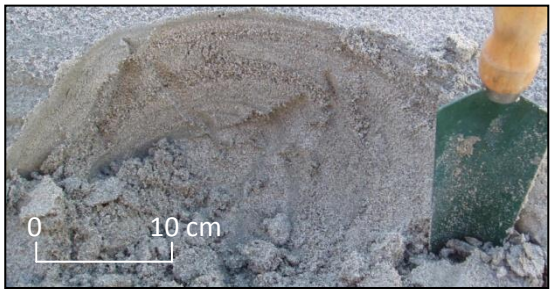

C.2.8 FAB98

- Process: Glaciofluvial
- Classification: Channel point bar
- Description & location: Meltwater deposit collected from the lee side of a boulder.
- Facies: Sh
- Texture: well sorted, medium sand
- Bedding: interbedded medium and coarse sand units, 2-3 cm thick
- Scale: ~ 30 cm thick.
- Quartz analysed

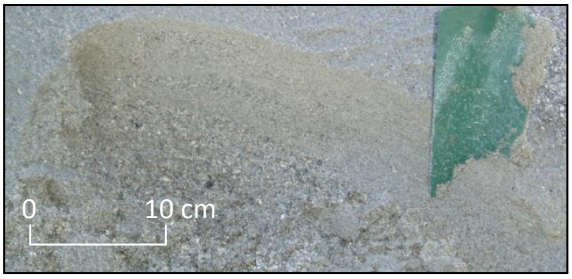

C.2.9 FAB99

- Process: Glaciofluvial
- Classification: Channel point bar
- Description & location: Meltwater deposit taken from adjacent to the main meltwater channel ~650m from the glacial snout.
- Facies: Sh
- Quartz analysed

C.2.10 FAB100

- Process: Glaciofluvial
- Classification: Channel point bar
- Description & location: Meltwater deposit collected from a point bar deposit at the point where the valley widens. The river splits into various meltwater channels at this point, ~800m from the glacier.
- Facies: Sh
- Quartz and feldspar analysed

C.3 Stordalen

C.3.1 LOD4

- Process: Glaciofluvial
- Classification: Side attached, channel point bar
- Description & location: Meltwater deposit collected from adjacent to the only meltwater stream draining Stordalen. No obvious source of paraglacial material influx, although active valley sides.
- Facies: Sh
- Texture: well sorted medium sand
- Scale: ~ 30 cm thick.
- Quartz and feldspar analysed

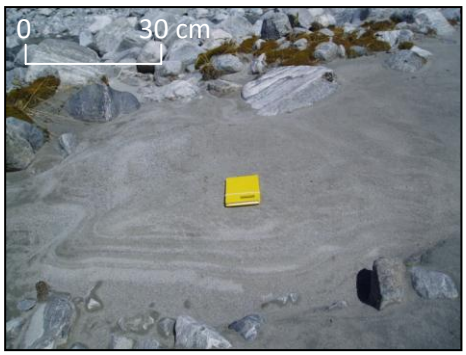

C.3.2 LOD5

- Process: Glaciofluvial
- Classification: Side attached, channel point bar
- Description & location: Meltwater deposit collected downstream from where the meltwater stream dissects a relict moraine.
- Facies: Sr
- Texture: well sorted medium to coarse sand
- Scale: ~ 30 cm thick
- Quartz and feldspar analysed

C.3.3 LOD6

- Process: Glaciofluvial
- Classification: Side attached, channel point bar
- Description & location: Meltwater deposit collected just before the confluence of the Stordalen meltwater stream and Fåbergstølsgrandane.
- Facies: Sr
- Texture: well sorted coarse to medium sand
- Scale: ~ 30 cm thick
- Quartz and feldspar analysed

C.4 Jostedøla

C.4.1 JOS51

- Process: Fluvial (with glacial source region)
- Classification: Side attached, channel point bar
- Description & location: River channel deposit collected from the bank of the Jostedøla.
- Facies: Sh
- Texture: well sorted medium to fine sand
- Bedding: low angle cross-bedding, units grade from medium to fine sand and are ~ 2 cm thick. Some organic lenses are present.
- Scale: ~ 30 cm thick
- Feldspar analysed

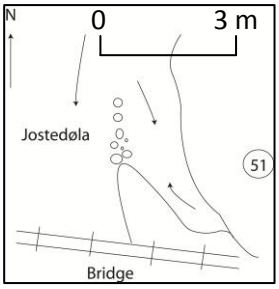

C.4.2 LEI13

- Process: Fluvial (with glacial source region)
- Classification: Braided channel bar
- Description & location: Bar downstream of Leirdal. Pebble/sandy bar tail.
- Facies: Sr
- Feldspar analysed

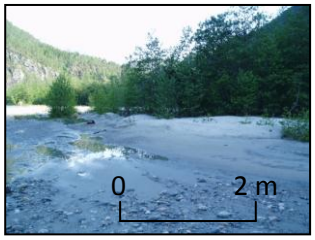

C.4.3 LEI14

- Process: Fluvial (with glacial source region)
- Classification: Braided channel bar
- Description & location: Sample collected from mid portion of an established bar, birch trees present but the bar edge is sandy.
- Facies: Sh
- Texture: well sorted coarse to medium sand, overlaying fine sand to silt
- Bedding: Horizontally bedded units 10 cm thick, gradational contacts
- Scale: 0.5 m thick
- Feldspar analysed

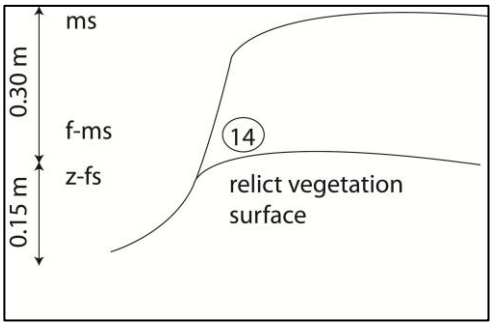

Sample LEI14 is the bottom sample in the photo, samples LEI15 and LEI16 were not analysed due to time restrictions.

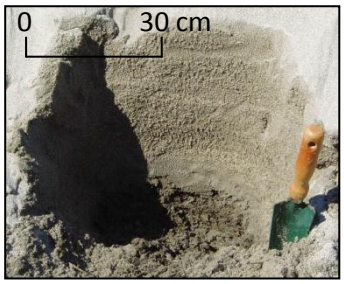

C.4.4 LEI18

- Process: Fluvial (with glacial source region)
- Classification: Braided channel bar
- Description & location: Sample collected from the tail of a recently developed bar (~30 m in length) comprising unconsolidated sand and well-rounded pebbles of ~ 8 cm diameter.
- Facies: Sh
- Texture: well sorted, medium to coarse sand
- Bedding: Horizontally bedded units 10 cm thick, gradational contacts
- Scale: 20 cm thick
- Feldspar analysed

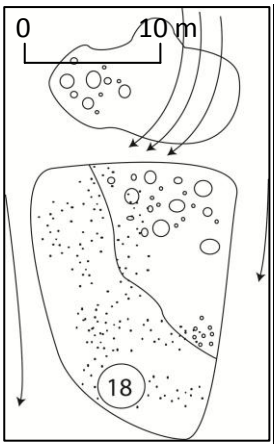

C.5 Nigardsdalen

C.5.1 NIG3

- Process: Glaciofluvial
- Classification: Braided channel bar
- Description & location: Sampled from the tail of a longitudinal bar.
- Facies: Sh
- Texture: well sorted, medium to fine sand
- Feldspar analysed

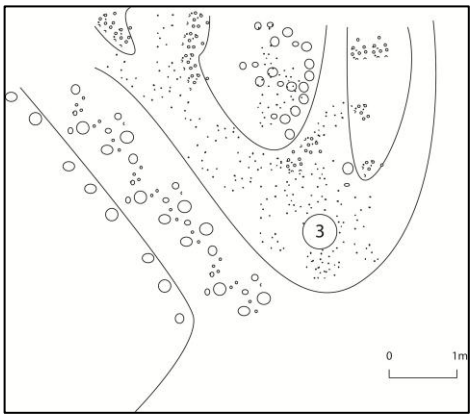

C.5.2 NIG4

- Process: Glaciofluvial
- Classification: Braided channel bar
- Description & location: Sampled from the mid-section of the same composite bar feature than NIG3 is sampled from. Depositional direction is lateral-oblique.
- Facies: Sh
- Texture: well sorted, medium to coarse sand
- Feldspar analysed

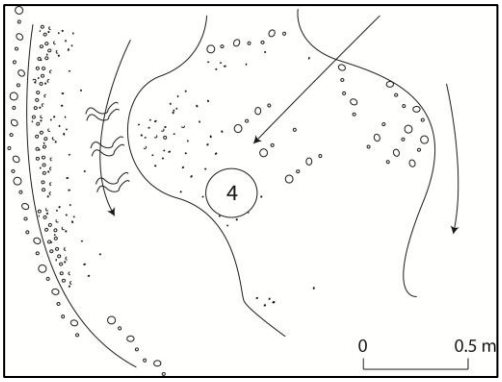

C.5.3 NIG6

- Process: Glaciofluvial
- Classification: Braided channel bar
- Description & location: Sampled from the head of a medial bar feature, which forms part of a suite of bar features related to the bar that NIG3 and NIG4 are sampled from.
- Facies: Sh
- Texture: well sorted, medium to coarse sand, sample is saturated
- Feldspar analysed

C.5.4 NIG7

- Process: Glaciofluvial
- Classification: Braided channel bar
- Description & location: Sampled from the tail region of a large sandy landform within the proglacial delta of Nigardsvatnet.
- Facies: Sh
- Texture: moderately sorted, well sorted upper layer, poorly sorted underlying material. medium to fine sand, overlaying coarse sand. Bar tail is granular to coarse sand
- Bedding: horizontal bedding, 6 cm thick medium to fine sand upper unit
- Scale: 20 cm thick
- Feldspar analysed

C.5.5 NIG8

- Process: Glaciofluvial
- Classification: Braided channel bar
- Description & location: Sampled from mid way along the edge of the large sandy landform sampled for NIG7.
- Facies: Sh
- Texture: well sorted, medium to coarse sand
- Bedding: horizontal bedding, 5 cm thick upper unit
- Scale: 30 cm thick
- Feldspar analysed

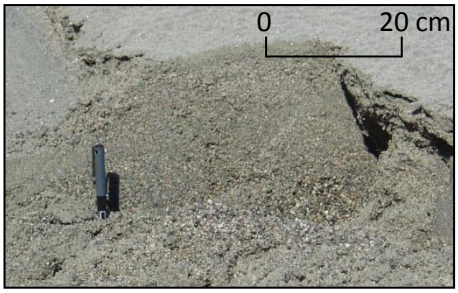

C.5.6

C.5.7 NIG9

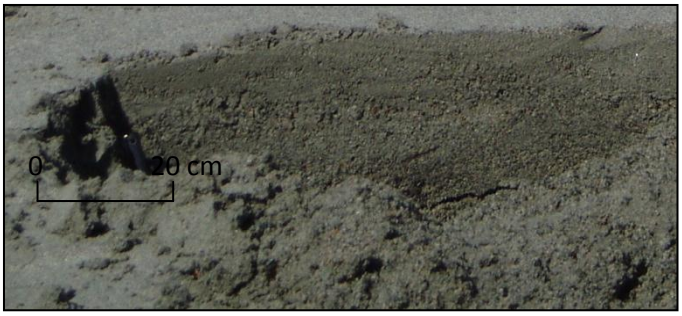

- Process: Glaciofluvial
- Classification: Braided channel bar
- Description & location: Sampled from a side attached bar deposit which is more ice proximal than the large sandy landform sampled for NIG7/8, but part of the same deposit suite.
- Facies: Sr
- Texture: well sorted, medium to fine sand
- Bedding: cross bedded upper unit (~ 5 cm thick), horizontally bedded lower unit
- Scale: 30 cm thick
- Feldspar analysed

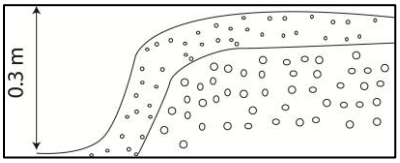

C.5.8 NIG103

- Process: Glacial
- Classification: Subglacial
- Description & location: Subglacial material sampled from beneath the glacier snout.
- Facies: Dmm
- Texture: silt – boulders, angular – sub-angular, consolidated
- Bedding: Massive
- Scale: > 1 m thick
- Quartz analysed

C.6 Fåbergstølsgrandane

C.6.1 GRAN54

- Process: Glaciofluvial
- Classification: Sandur braided channel bar
- Description & location: Sampled from the head of a longitudinal bar deposit.
- Facies: Sh
- Texture: well sorted fine to medium sand, although overlays well rounded, cobble sized clasts and gravel
- Bedding: horizontal bedding, lateral gradations into coarser sand
- Scale: 10 cm thick
- Quartz & feldspar analysed

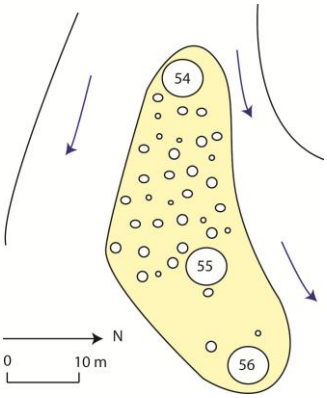

C.6.2 GRAN55

- Process: Glaciofluvial
- Classification: Sandur braided channel bar
- Description & location: Sampled from the mid-point of the same longitudinal bar deposit as GRAN54.
- Facies: Sh
- Texture: well sorted fine to medium sand, although overlays well rounded, cobble sized clasts and gravel
- Bedding: horizontal bedding, lateral gradations into coarser sand
- Scale: 10 cm thick
- Quartz & feldspar analysed

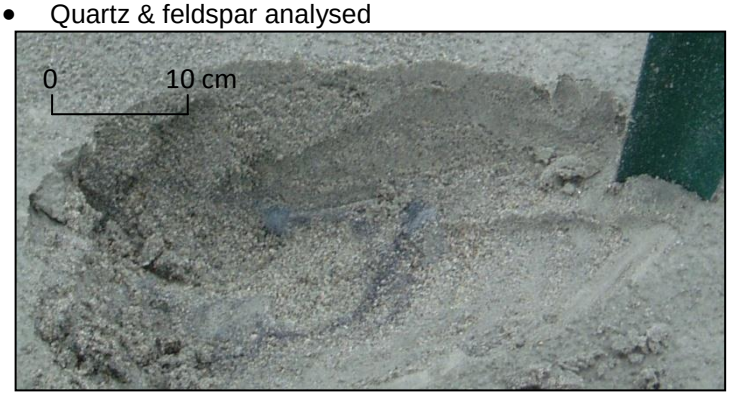

C.6.3 GRAN56

- Process: Glaciofluvial
- Classification: Sandur braided channel bar
- Description & location: Sampled from the tail of the same longitudinal bar deposit as GRAN54/55.
- Facies: Sr
- Texture: well sorted fine sand fine sand, although overlays well medium to coarse sand
- Bedding: cross bedded fine sand (~ 1 cm thick), the deposit fines vertically
- Scale: 10 cm thick
- Quartz & feldspar analysed

C.6.4 GRAN57

- Process: Glaciofluvial
- Classification: Sandur braided channel bar
- Description & location: Sampled from the tail of a longitudinal bar.
- Facies: Sr
- Texture: well sorted fine to medium sand
- Bedding: cross bedded fine sand, the deposit fines vertically
- Scale: 10 cm thick
- Quartz & feldspar analysed

C.6.5 GRAN58

- Process: Glaciofluvial
- Classification: Sandur braided channel bar
- Description & location: Sampled from the head of a longitudinal bar.
- Facies: Sr
- Texture: well sorted fine to medium sand
- Bedding: cross bedded fine sand
- Scale: 10 cm thick
- Quartz & feldspar analysed

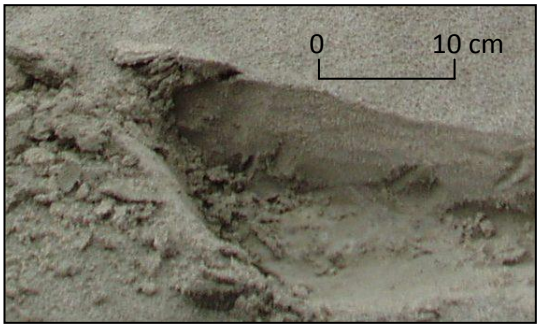

C.6.6 GRAN59

- Process: Glaciofluvial
- Classification: Sandur braided channel bar
- Description & location: Sampled from the head of a longitudinal bar.
- Facies: Sr
- Texture: well sorted fine to medium sand, also contains some clay lenses but these were avoided during sampling
- Bedding: cross bedded fine sand
- Scale: 10 cm thick
- Feldspar analysed

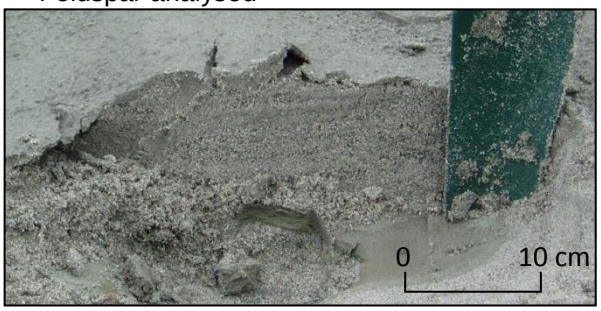

C.6.7 GRAN62

- Process: Glaciofluvial
- Classification: Sandur braided channel bar
- Description & location: Sampled from the mid-section of a longitudinal bar.
- Facies: Sr
- Texture: well sorted, silt, fine to medium sand
- Bedding: fine cross bedding silt to fine sand layers ~ 1 cm thick
- Scale: 20 cm thick
- Quartz analysed

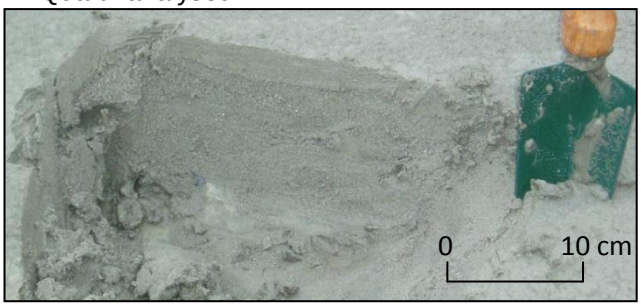

C.6.8 GRAN69

- Process: Glaciofluvial
- Classification: Side attached, channel point bar
- Description & location: Sampled from adjacent to the main meltwater stream.
- Facies: Sr
- Texture: well sorted, medium sand
- Bedding: fining upwards
- Feldspar analysed

C.6.9 GRAN71

- Process: Glaciofluvial
- Classification: Sandur braided channel bar
- Description & location: Sampled from the head of a longitudinal bar.
- Facies: Sr
- Texture: well sorted fine to medium sand, overlies coarser sand
- Bedding: cross bedded fine sand
- Quartz analysed

C.7 Gaupne

C.7.1 GAUP1 & GAUP2

- Process: Fluvial (glacial origin)
- Classification: Delta bottomset
- Description & location: Sampled from a horizontally bedded sand deposit, overlain by gilbard delta foresets.
- GAUP1: Sh, F-MS
- GAUP2: Sh, FS and CS units
- Facies: Sh
- Texture: well sorted, poorly consolidated fine to coarse sand deposits
- Bedding: horizontally bedded, dipping at 20˚.
- Scale: Part of 10 m thick sequence (see sediment logs in Chapter 6)
- GAUP1: Quartz analysed
- GAUP2: Feldspar analysed

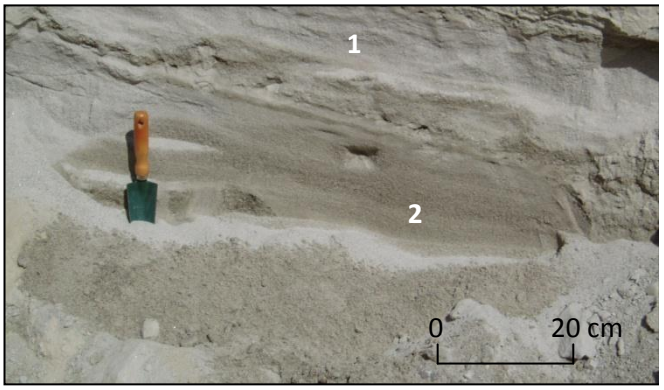

C.7.2 GAUP40 & GAUP41

- Process: Fluvial (glacial origin)
- Classification: In-filled river channel
- Description & location: Cross bedded layer overlaying delta foresets, at the deposit surface stratigraphically.
- Facies: Sr
- Texture: well sorted, medium sand with some sub-rounded pebbles interbedded (not sampled)
- Bedding: Ripple cross bedding, highlighted by coarser gravel – pebble deposits ~ 5 cm thick.
- Scale: 0.5 m thick (see sediment logs in Chapter 6)
- Quartz and feldspar analysed

Appendix D. Water of Tulla OSL

D.1 WTUL Samples

D.1.1 Sample OSL analysis & characterisation

Samples were collected from the Water of Tulla (56˚34' N, 4˚41'E) using the opaque tube method detailed in Chapter 3, and were hammered into the cleaned exposure face (Figure D.1). Three samples were collected, however as WTUL3 did not contain sufficient material within the 180-212 µm grain size fraction, it was not analysed. Samples were prepared as detailed in Section 4.1, and the quartz extract analysed. The initial OSL protocol used is listed in Table D.1. Samples were initially decanted by hand and then using the medium mask described in Chapter 4, aliquot sizes are approximately equal.

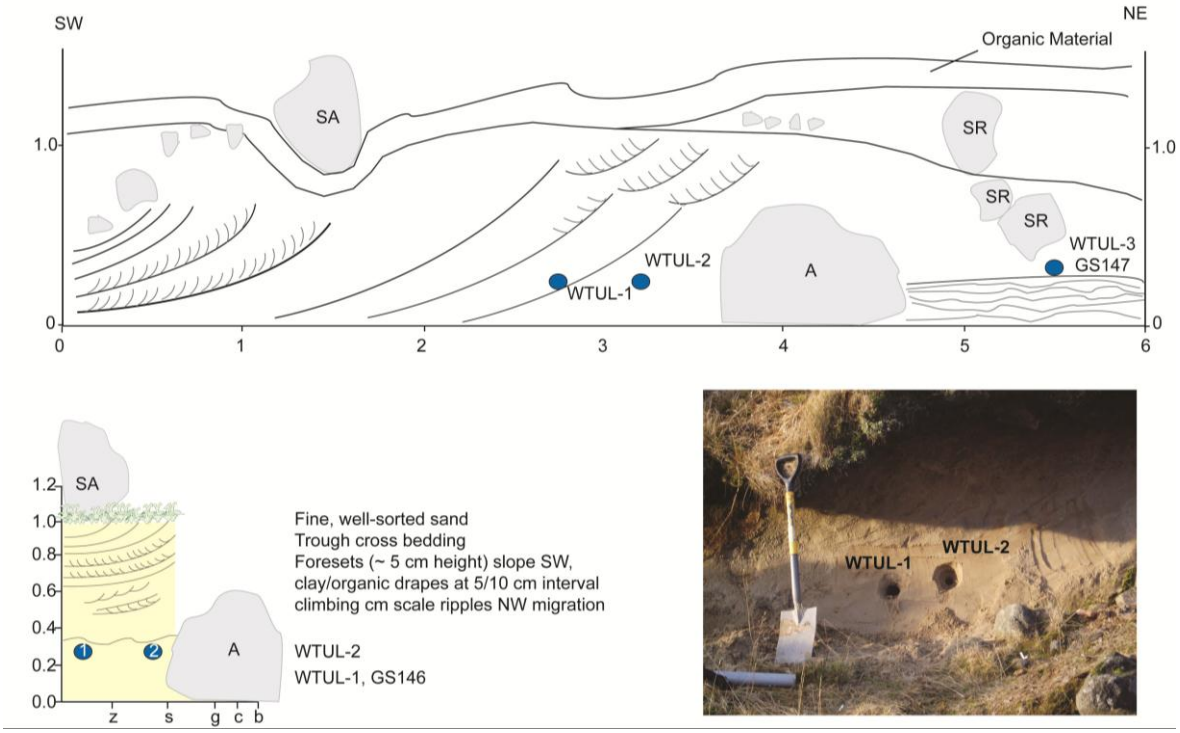

Figure D.1: Sedimentary log, sketch and photo of the WTUL sample site.

Table D.1: Initial SAR protocol

Natural/Regenerative Dose	N, 12.2, 24.4, 36.6, 48.8, 0, 12.2, 12.2 Gy
TSL	260 ˚C, 10 s, 5 ˚C/s
OSL	125 ˚C, 40 s, 5 ˚C/s, 90 % power (Lx)
(IRSL	40 ˚C, 40 s, 5 ˚C/s, 90 % power)*
Test Dose	4.89 Gy**
TSL	220 ˚C, 10 s, 5 ˚C/s
OSL	125 ˚C, 40 s, 5 ˚C/s, 90 % (Tx)
OSL	280 ˚C, 40 s, 5 ˚C/s, 90 %

*IR depletion test is included in the final analysis cycle only
**Dose rates relate to Risø 1, although both Risø machines were used to analyse these samples

The WTUL samples have low luminescence sensitivity (Figure D.2) and exhibit significant thermal dependence which was explored with a series of preheat plateau dose

response experiments, summarised in Figure D.3. Dose recovery is most accurate where a 190 °C PH is used, followed by a cut-heat of 180 °C. The HB was omitted as no systematic improvement in dose recovery or acceptance rate was observed, the selected protocol is summarised in Table D.2. The T_D was increased significantly to ~ 20 Gy in order to improve sample acceptance through improved T_x signal to noise.

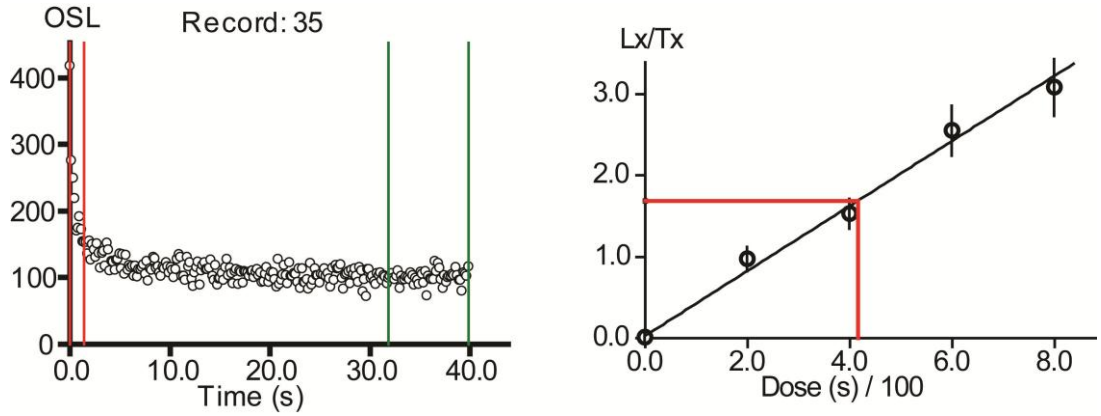

Figure D.2: (A) L_n decay curve and (B) regenerative dose curve for an aliquot of WTUL1

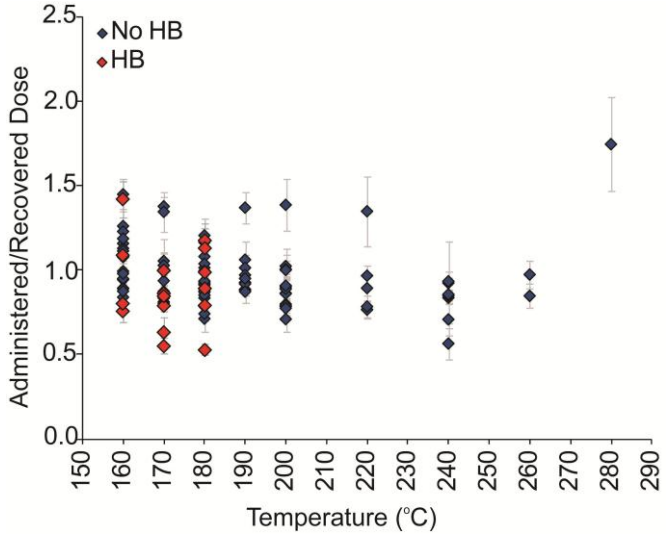

Figure D.3: Summary of preheat plateau dose recovery experiments for the WTUL samples. Those samples treated with a hot bleach (HB) are highlighted in red.

Table D.2: Final SAR protocol

Natural/Regenerative Dose	N, 19.6, 39.1, 58.7, 0, 19.6, 19.6 Gy
TSL	190 ˚C, 10 s, 5 ˚C/s
OSL	125 ˚C, 40 s, 5 ˚C/s, 90 % power (Lx)
IRSL	40 ˚C, 40 s, 5 ˚C/s, 90 % power
Test Dose	19.6 Gy*
TSL	180 ˚C, 10 s, 5 ˚C/s
OSL	125 ˚C, 40 s, 5 ˚C/s, 90 % (Tx)

*IR depletion test is included in the final analysis cycle only
**Dose rates relate to Risø 1, although both Risø machines were used to analyse these samples

Samples were initially treated with a single 40 minute 40% HF treatment, which failed to fully remove feldspar and isolate a pure quartz extract, reflected in the high rejection rate of aliquots based on the IR depletion test, where a 15% depletion limit was enforced. A second 40 min, 40% HF etch effectively removed the feldspar contamination,

improving aliquot acceptance significantly, although some aliquots were still rejected due to failure of the IR depletion ratio.

Samples were analysed using Analyst version 3.22b (Duller, 2005), signals were integrated over the first 1.6 s, with the background subtracted from the final 8 s of stimulation. Acceptance criteria were that the recycling ratio was within 15 % between the first and final regenerative doses, that the IR depletion ratio was < 15 % and that signals were > 3 σ above background. No maximum T_x or P error acceptance criteria were included as this would have resulted in the rejection of too many aliquots associated with low signal to noise ratios, furthermore as these errors are incorporated in the final age estimate the precision is appropriately reduced. Almost 400 aliquots were analysed and 54 were accepted for WTUL1 and 37 for WTUL2, the causes of individual aliquot rejection are listed in Table D.3.

After the bulk of the luminescence measurements had been made, a double SAR protocol was investigated, whereby a post-IR BSL signal is measured, to remove the malign effects of any IR-responsive signal (see Roberts, 2007 for a review). For WTUL1 the percentage difference between L_x/T_x of the post-IR BSL and conventional BSL signal were ~ 1% for WTUL1 and ~ 15% for WTUL2, indicating that this may have provided a suitable alternative analysis protocol, which would have resulted in greater aliquot acceptance.

Table D.3: Summary table by deposit type

Summary	N	n	Acc.%	RR	Oversat	Sig <3 BG	IRSL	Inad. Regen	Plot	Recup
WTUL1	201	53		10	1	2	115	3	11	6
%			*24*	*5*	*1*	*1*	*58*	*2*	*6*	*3*
WTUL2	181	38		8	2	0	119	7	3	4
%			*21*	*4*	*1*	*0*	*66*	*4*	*2*	*2*
Total All Aliquots	382	91		18	3	2	234	10	14	10
%			*24*	*5*	*1*	*1*	*61*	*2*	*4*	*2*

D.2 Age Determinations

Samples were overdispersed (56 ± 3 % for WTUL1 and 32 ± 3 % for WTUL2), using the modified selection criteria of Bailey and Arnold (2006) after Thrasher et al. (2009b) (see Chapter 4 for a discussion), both samples were initially modelled using the MAM-3 model. However, the MAM-3 D_e for WTUL1 was significantly affected by a single aliquot with D_e of 6.36 ± 0.20 Gy (Figure D.4).This aliquot was removed due to its effect on the age model (Figure D.5), and the analysis repeated.

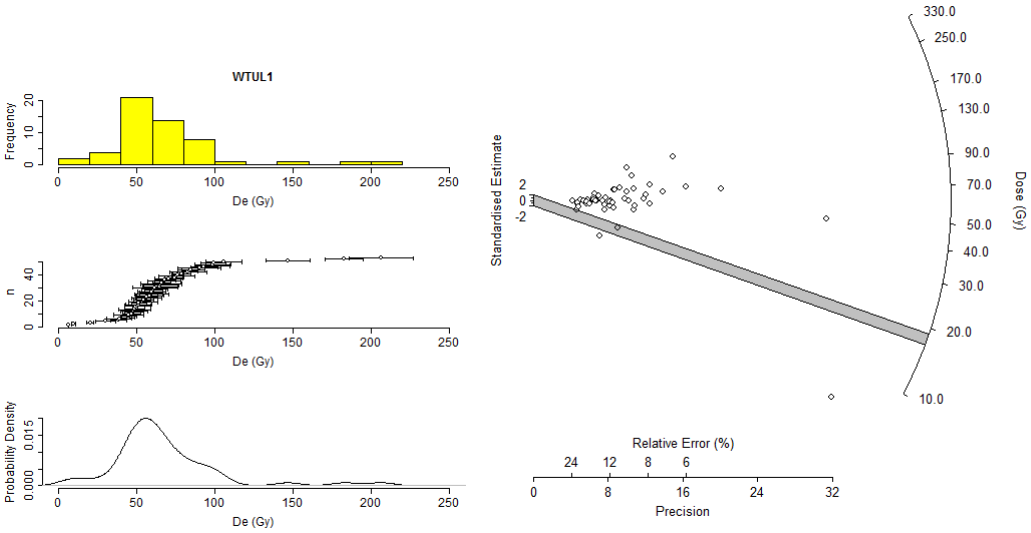

Figure D.4: Histogram, probability density function, scatter graph and radial plots of WTUL1.

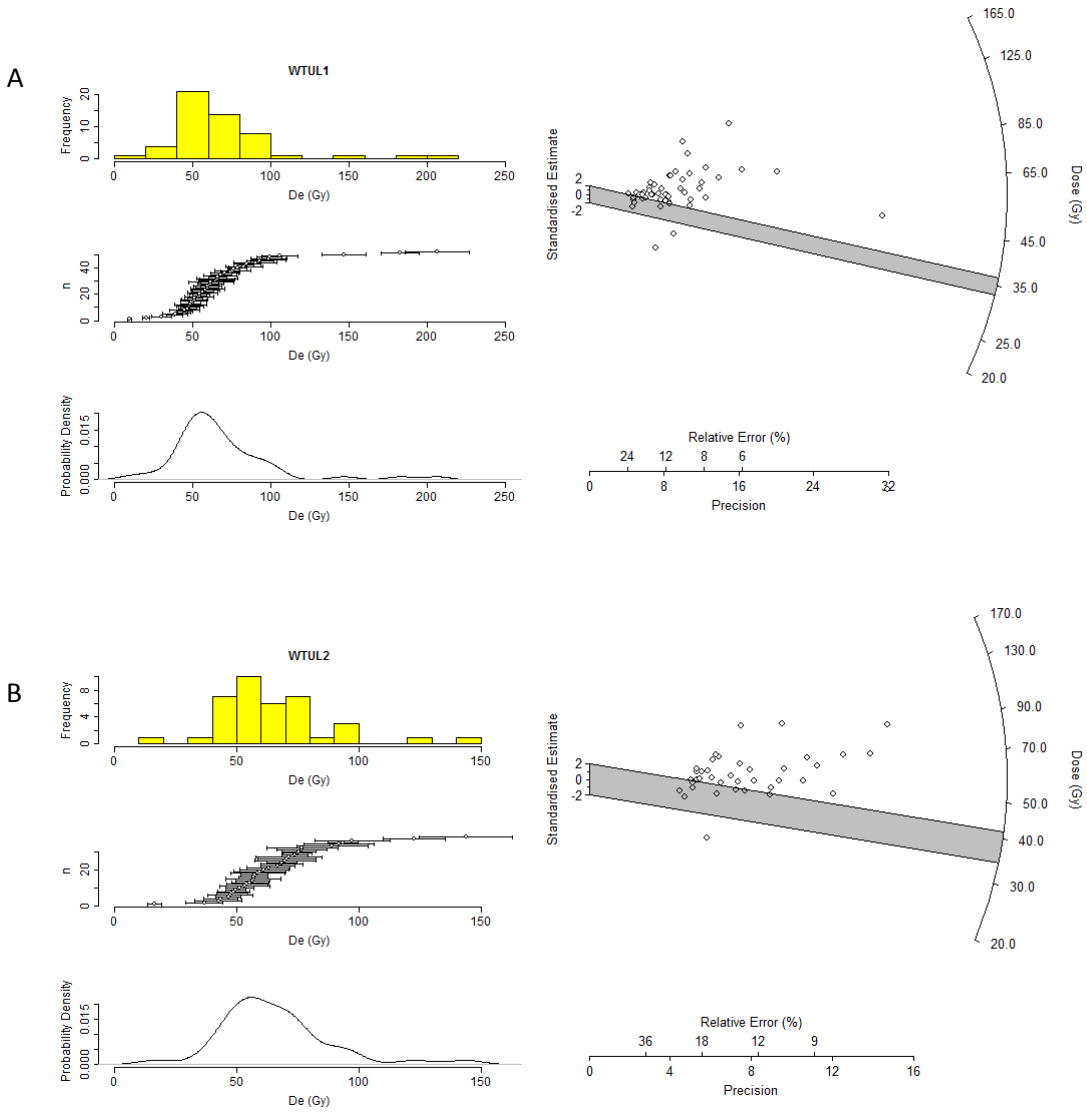

Figure D.5: Histograms, probability density functions, scatter graphs and radial plots of (A) WTUL1 following rejection of an aliquot of dose 6.36 ± 0.20 Gy, and (B) WTUL2.

The D_r was calculated from ICP-MS of material collected from each of the sample sites (Table D.4), using the method given in Appendix A.3. Sample ages are 14.90 ± 1.69 ka for WTUL1 and 17.45 ± 1.84 ka for WTUL2 which are inconsistent with other chronologies of the final deglaciation of Scotland following the Loch Lomond Stadial at ~ 12.9-11.5 ka (see Ballantyne, 2010 for a review). The older age estimates reported here may relate to sediment partial bleaching, which is known to affect glaciofluvial deposits, and which has been discussed in greater depth in Chapter 6.

Table D.4: Environmental dose rates and associated age determinations for WTUL1 and WTUL2.

	D_e (Gy)	K (%)	Th (ppm)	U (ppm)	Rb (ppm)	% Water	Depth (cm)	Wet D_r (Gy ka^{-1})	Age (ka)
WTUL1	35.94±3.33	1.81±0.09	5.44±0.27	1.99±0.10	100±10	13.5±5.0	110	2.41±0.13	14.90±1.67
WTUL2	44.79±3.79	1.86±0.09	5.94±0.30	2.24±0.11	100±10	12.4±5.0	95	2.57±0.14	17.45±1.84

References

Abesser, C., Robinson, R., Soulsby, C., 2006. Iron and manganese cycling in the storm runoff of a Scottish upland catchment. Journal of Hydrology 326, 59-78.

Adamiec, G., Aitken, M.J., 1998. Dose-rate conversion factors: update. Ancient TL 16, 37-46.

Aitken, M.J., 1985. Thermoluminescence Dating. Academic Press, London.

Aitken, M.J., 1998. Introduction to Optical Dating. Oxford University Press, New York.

Aitken, M.J., Smith, B.W., 1988. Optical dating: Recuperation after bleaching. Quaternary Science Reviews 7, 387-393.

Alexanderson, H., 2007. Residual OSL signals from modern Greenlandic river sediments. Geochronometria 26, 1-9.

Alonso, P.J., Halliburton, L.E., Kohnke, E.E., Bossoli, R.B., 1983. X-ray-induced luminescence in crystalline SiO_2. Journal of Applied Physics 54, 5369-5375.

Andersen, T.B., 1998. Extensional tectonics in the Caledonides of southern Norway, an overview. Tectonophysics 285, 333-351.

Armitage, S.J., Bailey, R.M., 2005. The measured dependence of laboratory beta dose rates on sample grain size. Radiation Measurements 39, 123-127.

Armitage, S.J., Duller, G.A.T., Wintle, A.G., 2000. Quartz from southern Africa: sensitivity changes as a result of thermal pretreatment. Radiation Measurements 32, 571-577.

Armitage, S.J., King, G.E., Submitted. Optically stimulated luminescence dating of hearths from the Fazzan Basin, Libya: A tool for determining the timing and pattern of Holocene occupation of the Sahara. Quaternary Geochronology.

Arnold, L.J., 2006. Optical dating and computer modelling of arroyo epicycles in the American Southwest. St Peter's College, University of Oxford.

Arnold, L.J., Bailey, R.M., Tucker, G.E., 2007. Statistical treatment of fluvial dose distributions from southern Colorado arroyo deposits. Quaternary Geochronology 2, 162-167.

Arnold, L.J., Roberts, R.G., 2009. Stochastic modelling of multi-grain equivalent dose (De) distributions: Implications for OSL dating of sediment mixtures. Quaternary Geochronology 4, 204-230.

Auclair, M., Lamothe, M., Huot, S., 2003. Measurement of anomalous fading for feldspar IRSL using SAR. Radiation Measurements 37, 487-492.

Aune, B., 1993. Air temperature normals, normal period 1961-1990., Klima. Det norske meteorologiske institutt, Oslo.

Bailey, R.M., 2000. The slow component of quartz optically stimulated luminescence. Radiation Measurements 32, 233-246.

Bailey, R.M., 2001. Towards a general kinetic model for optically and thermally stimulated luminescence of quartz. Radiation Measurements 33, 17-45.

Bailey, R.M., 2003. Paper I: The use of measurement-time dependent single-aliquot equivalent-dose estimates from quartz in the identification of incomplete signal resetting. Radiation Measurements 37, 673-683.

Bailey, R.M., 2004. Paper I--simulation of dose absorption in quartz over geological timescales and its implications for the precision and accuracy of optical dating. Radiation Measurements 38, 299-310.

Bailey, R.M., Arnold, L.J., 2006. Statistical modelling of single grain quartz D-e distributions and an assessment of procedures for estimating burial dose. Quaternary Science Reviews 25, 2475-2502.

Bailey, R.M., Singarayer, J.S., Ward, S., Stokes, S., 2003. Identification of partial resetting using De as a function of illumination time. Radiation Measurements 37, 511-518.

Bailey, R.M., Smith, B.W., Rhodes, E.J., 1997. Partial bleaching and the decay form characteristics of Quartz OSL. Radiation Measurements 27, 123-136.

Bakke, J., Dahl, S.O., Nesje, A., 2005. Lateglacial and early Holocene palaeoclimatic reconstruction based on glacier fluctuations and equilibrium-line altitudes at northern Folgefonna, Hardanger, western Norway. Journal of Quaternary Science 20, 179-198.

Balescu, S., Lamothe, M., 1992. The blue emission of K-feldspar coarse grains and its potential for overcoming TL age underestimation. Quaternary Science Reviews 11, 45-51.

Balescu, S., Lamothe, M., 1994. Comparison of TL and IRSL age estimates of feldspar coarse grains from waterlain sediments. Quaternary Science Reviews 13, 437-444.

Ballantyne, C.K., 1979. A sequence of Lateglacial ice-dammed lakes in East Argyll. Scottish Journal of Geology 15, 153-160.

Ballantyne, C.K., 1995. Paraglacial debris-cone formation on recently deglaciated terrain, western Norway. The Holocene 5, 25-33.

Ballantyne, C.K., 2010. Extent and deglacial chronology of the last British–Irish Ice Sheet: implications of exposure dating using cosmogenic isotopes. Journal of Quaternary Science 25, 515-534.

Ballantyne, C.K., Benn, D.I., 1994. Paraglacial Slope Adjustment and Resedimentation Following Recent Glacier Retreat, Fåbergstølsdalen, Norway. Arctic and Alpine Research 26, 255-269.

Ballarini, M., Wallinga, J., Duller, G.A.T., Brouwer, J.C., Bos, A.J.J., Van Eijk, C.W.E., 2005. Optimizing detection filters for single-grain optical dating of quartz. Radiation Measurements 40, 5-12.

Banerjee, D., Botter-Jensen, L., Murray, A.S., 2000. Retrospective dosimetry: estimation of the dose to quartz using the single-aliquot regenerative-dose protocol. Applied Radiation and Isotopes 52, 831-844.

Baril, M.R., 2002. Spectral Investigations of Luminescence in Feldspars, Physics. Unpublished PhD Thesis, Simon Fraser University, Vancouver, p. 278.

Baril, M.R., Huntley, D.J., 2003. Optical excitation spectra of trapped electrons in irradiated feldspars. Journal of Physics: Condensed Matter 15, 8011.

Bates, D.M., Watts, D.G., 1988. Nonlinear Regression Analysis and Its Applications. Wiley, New York.

Becker, R.A., Chambers, J.M., Wilks, A.R., 1988. The New S Language. Wadsworth & Brooks/Cole.

Bell, W.T., 1979. Attenuation factors for the absorbed radiation dose in quartz inclusions for thermoluminescence dating. Ancient TL 8, 1-12.

Bell, W.T., 1980. Alpha dose attenuation in quartz grains for thermoluminescence dating. Ancient TL 12, 4 - 8.

Bell, W.T., Zimmerman, D.W., 1978. The effect of HF acid etching on the morphology of quartz inclusions for thermoluminescence dating. Archaeometry 20, 63-65.

Benn, D.I., Evans, D.J.A., 1998. Glaciers and Glaciation. Arnold, London.

Berger, G.W., 1990. Effectiveness of natural zeroing of the thermoluminescence in sediments. Journal of Geophysical Research 95, 12,375-312,397.

Berger, G.W., Luternauer, J.J., 1987. Preliminary fieldwork for thermoluminescence dating studies at the Fraser River delta, British Columbia, Geological Survey of Canada Paper 87-1A, pp. 901-904.

Bettiol, A.A., Nugent, K.W., Jamieson, D.N., 1997. The characterisation of high-grade synthetic quartz, corundum and spinel using ionoluminescence (IL). Nuclear Instruments and Methods in Physics Research Section B: Beam Interactions with Materials and Atoms 130, 734-739.

Bickerton, R.W., Matthews, J.A., 1993. Little ice age variations of outlet glaciers from the jostedalsbreen ice-cap, Southern Norway: A regional lichenometric-dating study of ice-marginal moraine sequences and their climatic significance. Journal of Quaternary Science 8, 45-66.

Blair, M.W., Yukihara, E.G., McKeever, S.W.S., 2005. Experiences with single-aliquot OSL procedures using coarse-grain feldspars. Radiation Measurements 39, 361-374.

Blair, M.W., Yukihara, E.G., McKeever, S.W.S., 2006. Progress towards a polymineral single-aliquot OSL dating procedure. Radiation Protection Dosimetry 119, 450-453.

Blott, S.J., Croft, D.J., Pye, K., Saye, S.E., Wilson, H.E., 2004. Particle size analysis by laser diffraction. Geological Society, London, Special Publications 232, 63-73.

Blott, S.J., Pye, K., 2001. GRADISTAT: a grain size distribution and statistics package for the analysis of unconsolidated sediments. Earth Surface Processes and Landforms 26, 1237-1248.

Boe, A.-G., Murray, A., Dahl, S.O., 2007. Resetting of sediments mobilised by the LGM ice-sheet in southern Norway. Quaternary Geochronology

LED 2005, 11th International Conference on Luminescence and Electron Spin Resonance Dating 2, 222-228.

Boggs, S., Jr., Kwon, Y.-I., Goles, G.G., Rusk, B.G., Krinsley, D., Seyedolali, A., 2002. Is Quartz Cathodoluminescence Color a Reliable Provenance Tool? A Quantitative Examination. JOURNAL OF SEDIMENTARY RESEARCH 72, 408-415.

Botis, S., Nokhrin, S.M., Pan, Y., Xu, Y., Bonli, T., 2005. Naturation radiation-induced damage in Quartz 1. Correlations between cathodoluminescence colours and paramagnetic defects. The Canadian Mineralogist 43, 1565-1580.

Botis, S., Pan, Y., Bonli, T., Xu, Y., Zhang, A., Nokhrin, S., Sopuck, V., 2006. Natural radiation-induced damage in Quartz. II. Distribution and implications for Uranium mineralization in the Athabasca basin, Saskatchewan, Canada. Can Mineral 44, 1387-1402.

Bøtter-Jensen, L., Bulur, E., Duller, G.A.T., Murray, A.S., 2000. Advances in luminescence instrument systems. Radiation Measurements 32, 523-528.

Bøtter-Jensen, L., McKeever , S.W.S., Wintle, A.G., 2003. Optically Stimulated Luminescence Dosimetry. Elsevier Science, Amsterdam.

Boyce, J.I., Eyles, N., 2000. Architectural element analysis applied to glacial deposits: Internal geometry of a late Pleistocen till sheet, Ontario, Canada. Bulletin of the Geological Society of America 112, 98-118.

Brennan, B.J., 2002. Beta doses to spherical grains. Radiation Measurements 37, 299-303.

Bridge, J.S., 2003. Rivers and Floodplains. Blackwell Science, Oxford.

Bridge, J.S., Bennett, S.J., 1992. A model for the entrainment and transport of sediment grains of mixed sizes, shapes and densities. Water Resources Research 28, 337-363.

Bridge, R.S., Demicco, R.V., 2008. Earth Surface Processes, Landforms and Sediment Deposits. Cambridge University Press, Cambridge.

Brookfield, M.E., Martini, I.P., 1999. Facies architecture and sequence stratigraphy in glacially influenced basins: basic problems and water-level/glacier input-point controls (with an example from the Quaternary of Ontario, Canada). Sedimentary Geology 123, 183-197.

Brooks, R.J., Hole, D.E., Townsend, P.D., 2002. Ion beam induced luminescence of materials. Nuclear Instruments and Methods in Physics Research Section B: Beam Interactions with Materials and Atoms 190, 136-140.

Brooks, R.J., Ramachandran, V., Hole, D.E., Townsend, P.D., 2001. Dose rate effects in ion beam luminescence. Radiation Effects and Defects in Solids: Incorporating Plasma Science and Plasma Technology 155, 177 - 181.

Bryhni, I., Sturt, B.A., 1985. Caledonides of southwestern Norway, in: Gee, D.E., Sturt, B.A. (Eds.), The Caledonide Orogen. John Wiley & Sons, Chichester, p. 619.

Bulur, E., 1996. An alternative technique for optically stimulated luminescence (OSL) experiment. Radiation Measurements 26, 701-709.

Bulur, E., Duller, G.A.T., Solongo, S., Bøtter-Jensen, L., Murray, A.S., 2002. LM-OSL from single grains of quartz: a preliminary study. Radiation Measurements 35, 79-85.

Burbidge, C.I., Duller, G.A.T., Roberts, H.M., 2006. D-e determination for young samples using the standardised OSL response of coarse-grain quartz. Radiation Measurements 41, 278-288.

Buylaert, J.P., Murray, A.S., Thomsen, K.J., Jain, M., 2009. Testing the potential of an elevated temperature IRSL signal from K-feldspar. Radiation Measurements 44, 560-565.

Buylaert, J.P., Vandenberghe, D., Murray, A.S., Huot, S., De Corte, F., Van den Haute, P., 2007. Luminescence dating of old (>70 ka) Chinese loess: A comparison of single-aliquot OSL and IRSL techniques. Quaternary Geochronology 2, 9-14.

Chen, R., Hag-Yahya, A., 1997. A new possible interpretation of the anomalous fading in thermoluminescent materials as normal fading in disguise. Radiation Measurements 27, 205-210.

Choi, J.H., Duller, G.A.T., Wintle, A.G., 2006. Analysis of quartz LM-OSL curves. Ancient TL 24, 9-20.

Choi, J.H., Murray, A.S., Jain, M., Cheong, C.S., Chang, H.W., 2003. Luminescence dating of well-sorted marine terrace sediments on the southeastern coast of Korea. Quaternary Science Reviews 22, 407-421.

Church, M., Ryder, J.M., 1972. Paraglacial sedimentation: a consideration of fluvial processes conditioned by glaciation. Geological Society of America Bulletin 83, 3059-3071.

Clark, R.J., Bailiff, I.K., 1998. Fast time-resolved luminescence emission spectroscopy in some feldspars. Radiation Measurements 29, 553-560.

Corazza, A., Crivelli, B., Martini, M., Spinolo, G., Vedda, A., 1996. Photoluminescence and optical absorption in neutron-irradiated crystalline quartz. Physical Review B 53, 9739.

Cunningham, A.C., Wallinga, J., 2010. Selection of integration time intervals for quartz OSL decay curves. Quaternary Geochronology In Press, Corrected Proof.

Curry, A.M., 1999. Paraglacial modification of slope form. Earth Surface Processes and Landforms 24, 1213-1228.

Curry, A.M., Ballantyne, C.K., 1999. Paraglacial Modification of Glacigenic Sediment. Geografiska Annaler: Series A, Physical Geography 81, 409-419.

Dahl, S.O., Nesje, A., Lie, Ø., Fjordheim, K., Matthews, J.A., 2002. Timing, equilibrium-line altitudes and climatic implications of two early-Holocene glacier readvances during the Erdalen Event at Jostedalsbreen, western Norway. The Holocene 12, 17-25.

Davis, J.C., 1986. Statistics and Data Analysis in Geology, 2 ed. John Wiley & Sons, Chichester.

Deer, W.A., Howie, R.A., Zussman, J., 2001. Framework Silicates: Feldspars 2nd Ed. Geological Society of London, London, Bath.

Deer, W.A., Howie, R.A., Zussman, J., 1992. An Introduction to the Rock-Forming Minerals 2nd Ed. Longman, Harlow.

Demars, C., Pagel, M., Deloule, E., Blanc, P., 1996. Cathodoluminescence of quartz from sandstones; interpretation of the UV range by determination of trace element distributions and fluid-inclusion P-T-X properties in authigenic quartz. American Mineralogist 81, 891-901.

Ditlefsen, C., 1992. Bleaching of K-Feldspars in Turbid Water Suspensions - a Comparison of Photoluminescence and Thermoluminescence Signals. Quaternary Science Reviews 11, 33-38.

Drouin, D., Couture, A.R., Joly, D., Tastet, X., Aimez, V., Gauvin, R., 2007. CASINO V2.42—A Fast and Easy-to-use Modeling Tool for Scanning Electron Microscopy and Microanalysis Users. Scanning 29, 92-101.

Duller, G.A.T., 1992. Luminescence chronology of raised marine terraces, south-west North Island, New Zealand. University of Wales, Aberystwyth.

Duller, G.A.T., 1997. Behavioural studies of stimulated luminescence from feldspars. Radiation Measurements 27, 663-694.

Duller, G.A.T., 2000. Dating methods: geochronology and landscape evolution. Progress in Physical Geography 24, 111-116.

Duller, G.A.T., 2003. Distinguishing quartz and feldspar in single grain luminescence measurements. Radiation Measurements 37, 161-165.

Duller, G.A.T., 2004. Luminescence dating of Quaternary sediments: recent advances. Journal of Quaternary Science 19, 183-192.

Duller, G.A.T., 2005. Luminescence Analyst. University of Wales, Aberystwyth.

Duller, G.A.T., 2006. Single grain optical dating of glacigenic deposits. Quaternary Geochronology 1, 296-304.

Duller, G.A.T., 2008. Single-grain optical dating of Quaternary sediments: why aliquot size matters in luminescence dating. Boreas 37, 589-612.

Duller, G.A.T., Augustinus, P.C., 2006. Reassessment of the record of linear dune activity in Tasmania using optical dating. . Quaternary Science Reviews 25, 2608–2618.

Duller, G.A.T., Bøtter-Jensen, L., Murray, A.S., 2000. Optical dating of single sand-sized grains of quartz: sources of variability. Radiation Measurements 32, 453-457.

Duller, G.A.T., Murray, A.S., 2000. Luminescence dating of sediments using individual mineral grains. Geologos 5, 88-106.

Duller, G.A.T., Wintle, A.G., 1991. On infrared stimulated luminescence at elevated temperatures. Nuclear Tracks and Radiation Measurements 18, 379-384.

Durcan, J.A., Duller, G.A.T., 2011. The fast ratio: a rapid measure for testing the dominance of the fast component in the initial OSL signal from quartz. . Radiation Measurements 46, 1195-1334

Durrani, S.A., Khazal, K.A.R., McKeever, S.W.S., Riley, R.J., 1977. Studies of changes in the thermoluminescence sensitivity in quartz induced by proton and gamma irradiations. Radiation Effects and Defects in Solids: Incorporating Plasma Science and Plasma Technology 33, 237 - 244.

Efron, B., Tibshirani, R.J., 1993. An Introduction to the Bootstrap. Chapman & Hall/CRC, New York.

Eyles, N., Eyles, C.H., Miall, A.D., 1983. Lithofacies types and vertical profile models; an alternative approach to the description and environmental interpretation of glacial diamict and diamitite sequences. Sedimentology 30, 393-410.

Fattahi, M., Stokes, S., 2004. Absorbed dose evaluation in feldspar using a single-aliquot regenerative-dose (SAR) infrared-stimulated red luminescence protocol. Radiation Measurements 38, 127-134.

Feathers, J.K., 2003. Single-grain OSL dating of sediments from the Southern High Plains, USA. Quaternary Science Reviews 22, 1035-1042.

Finch, A.A., Garcia-Guinea, J., Hole, D.E., Townsend, P.D., Hanchar, J.M., 2004. Ionoluminescence of zircon: rare earth emissions and radiation damage. Journal of Physics D: Applied Physics 37, 2795.

Finch, A.A., Klein, J., 1999. The causes and petrological significance of cathodoluminescence emissions from alkali feldspars. Contributions to Mineralogy and Petrology 135, 234-243.

Folk, R.L., 1954. The distinction between grain size and mineral composition in sedimentary-rock nomenclature. Journal of Geology 62, 344-359.

Folk, R.L., Ward, W.C., 1957. Brazos River bar: a study in the significance of grain size parameters. Journal of Sedimentary Petrology 27, 3-26.

Førland, E., 1993. Precipitation normals, normal period 1961-1990, Klima. Det norske meteoroligiske institutt - klimaavdelingen, Oslo.

Forman, S.L., Ennis, G., 1991. The effect of light intensity and spectra on the reduction of thermoluminescence of near-shore sediments from Spitsbergen, Svalbard: Implications for dating Quaternary water-lain sequences. Geophysical Research Letters 18.

Forman, S.L., Ennis, G., 1992. Limitations of thermoluminescence to date waterlain sediments from glaciated fiord environments of western spitsbergen, svalbard. Quaternary Science Reviews 11, 61-70.

Fragoulis, D., Stoebe, T.G., 1990. Relationship of Anomalous Fading to Feldspar Inclusions in Quartz. Radiation Protection Dosimetry 34, 65-68.

Fragoulis, D.V., Readhead, M.L., 1991. Feldspar inclusions and the anomalous fading and enhancement of thermoluminescence in quartz grains. International Journal of Radiation Applications and Instrumentation. Part D. Nuclear Tracks and Radiation Measurements 18, 291-296.

Friebele, E.J., Griscom, D.L., Marrone, M.J., 1985. The optical absorption and luminescence bands near 2 eV in irradiated and drawn synthetic silica. Journal of Non-Crystalline Solids 71, 133-144.

Friebele, E.J., Griscom, D.L., Stapelbroek, M., Weeks, R.A., 1979. Fundamental Defect Centers in Glass: The Peroxy Radical in Irradiated, High-Purity, Fused Silica. Physical Review Letters 42, 1346.

Friis, H., 2009. Luminescence Spectroscopy of Natural and Synthetic REE-bearing Minerals, School of Geography & Geosciences. University of St Andrews, p. 145.

Friis, H., Finch, A., Williams, C., 2011. Multiple luminescent spectroscopic methods applied to the two related minerals, leucophanite and meliphanite. Physics and Chemistry of Minerals 38, 45-57.

Fuchs, M., Lang, A., 2001. OSL dating of coarse-grain fluvial quartz using single-aliquot protocols on sediments from NE Peloponnese, Greece. Quaternary Science Reviews 20, 783-787.

Fuchs, M., Owen, L.A., 2008. Luminescence dating of glacial and associated sediments: review, recommendations and future directions. Boreas 37, 636-659.

Fujita, H., Hashimoto, T., 2006. Influence of Radioluminescence on Optically Stimulated Luminescence from Natural Quartz grains. Radioisotopes 55, 117-123.

Galbraith, R., 2002. A note on the variance of a background-corrected OSL count. Ancient TL 20, 49-51.

Galbraith, R.F., Green, P.F., 1990. Estimating the component ages in a finite mixture. Nuclear Tracks and Radiation Measurements 17, 197-206.

Galbraith, R.F., Laslett, G., 1993. Statistical models for mixed fission track ages. Radiation Measurements 21, 459-470.

Galbraith, R.F., Roberts, R.G., Laslett, G.M., Yoshida, H., Olley, J.M., 1999. Optical dating of single and multiple grains of quartz from jinmium rock shelter, northern Australia, part 1, Experimental design and statistical models. Archaeometry 41, 339-364.

Galbraith, R.F., Roberts, R.G., Yoshida, H., 2005. Error variation in OSL palaeodose estimates from single aliquots of quartz: A factorial experiment. Radiation Measurements 39, 289-307.

Garcia-Guinea, J., Correcher, V., Sanchez-Muñoz, L., Finch, A.A., Hole, D.E., Townsend, P.D., 2007a. On the luminescence emission band at 340 nm of stressed tectosilicate lattices. Nuclear Instruments and Methods in Physics Research Section A: Accelerators, Spectrometers, Detectors and Associated Equipment 580, 648-651.

Garcia-Guinea, J., Finch, A., Can, N., Hole, D., Townsend, P., 2007b. Orientation dependence of the ion beam and cathodoluminescence of albite. physica status solidi (c) 4, 910-913.

Gee, C.M., Kastner, M., 1979. Intrinsic-Defect Photoluminescence in Amorphous SiO_{2}. Physical Review Letters 42, 1765.

Gemmell, A.M.D., 1988. Thermo-Luminescence Dating of Glacially Transported Sediments - Some Considerations. Quaternary Science Reviews 7, 277-285.

Gemmell, A.M.D., 1994. Thermoluminescence in Suspended Sediment of Glacier Meltwater Streams. Journal of Glaciology 40, 158-166.

Gemmell, A.M.D., 1997. Fluctuations in the thermoluminescence signal of suspended sediment in an alpine glacial meltwater stream. Quaternary Science Reviews 16, 281-290.

Gemmell, A.M.D., 1999. IRSL from fine-grained glacifluvial sediment. Quaternary Science Reviews 18, 207-215.

Gilman, J.J., 2008. Electronic basis of hardness and phase transformations (covalent crystals). Journal of Physics D: Applied Physics 41, 074020.

Godfrey-Smith, D.I., Huntley, D.J., Chen, W.H., 1988. Optical dating studies of quartz and feldspar sediment extracts. Quaternary Science Reviews 7, 373-380.

Godfrey-Smith, D.I., Scallion, P., Clarke, M.L., 2005. Beta dosimetry of potassium feldspars in sediment extracts using imaging microprobe analysis and beta counting. Geochronometria 24, 7-12.

Götte, T., Pettke, T., Ramseyer, K., Koch-Müller, M., Mullis, J., In Press. Cathodoluminescence properties and trace element signatures of hydrothermal quartz: A fingerprint of growth dynamics. American Mineralogist.

Götze, J., 1996. Kathodolumineszenz von Quartz-Grundlagen und Anwendung in den Geowissenschaften. Der Aufshcluss 47, 145-164.

Götze, J., 2009. Chemistry, textures and physical properties of quartz - geological interpretation and technical application. Mineral Mag 73, 645-671.

Götze, J., Plötze, M., Fuchs, H., Habermann, D., 1999. Defect structure and luminescence behaviour of agate - results of electron paramagnetic resonance (EPR) and cathodoluminescence (CL) studies. Mineralogical Magazine 63, 149-163.

Götze, J., Plötze, M., Graupner, T., Hallbauer, D.K., Bray, C.J., 2004. Trace element incorporation into quartz: A combined study by ICP-MS, electron spin resonance, cathodoluminescence, capillary ion analysis, and gas chromatography. Geochimica et Cosmochimica Acta 68, 3741-3759.

Götze, J., Plötze, M., Habermann, D., 2001. Origin, spectral characteristics and practical applications of the cathodoluminescence (CL) of quartz – a review. Mineralogy and Petrology 71, 225-250.

Gower, J.C., 1966. Some distance properties of latent root and vector methods used in multivariate analysis. Biometrika 53, 325-338.

Griscom, D.L., 1980. *E'* center in glassy SiO_2: ^{17}O, ^{1}H, and "very weak" ^{29}Si superhyperfine structure. Physical Review B 22, 4192-4202.

Griscom, D.L., 1985a. Defect structure of glasses: Some outstanding questions in regard to vitreous silica. Journal of Non-Crystalline Solids 73, 51-77.

Griscom, D.L., 1985b. Diffusion of radiolytic molecular hydrogen as a mechanism for the post-irradiation buildup of interface states in SiO_2 structures. Journal of Applied Physics 58, 2524-2533.

Grun, R., 1989. Present Status of Esr-Dating. Applied Radiation and Isotopes 40, 1045-1055.

Guralnik, B., Matmon, A., Avni, Y., Porat, N., Fink, D., 2011. Constraining the evolution of river terraces with integrated OSL and cosmogenic nuclide data. Quaternary Geochronology 6, 22-32.

Gurkovskii, E.V., Leko, V.K., Stepanova, I.A., 1974. Absorption spectra of quartz glasses. Glass and Ceramics 31, 102-103.

Halliburton, L.E., Koumvakalis, N., Markes, M.E., Martin, J.J., 1981. Radiation effects in crystalline SiO_2: The role of aluminum. Journal of Applied Physics 52, 3565-3574.

Halperin, A., Sucov, E.W., 1993. Temperature dependence of the X-ray induced luminescence of Al-Na-containing quartz crystals. Journal of Physics and Chemistry of Solids 54, 43-50.

Hamilton, T.D.S., Munro, I.H., Walker, G., 1978. Luminescence Instrumentation, in: Lumb, M.D. (Ed.), Luminescence Spectroscopy. Academic Press, London, pp. 149-238.

Hansen, L., Funder, S., Murray, A.S., Mejdahl, V., 1999. Luminescence dating of the last Weichselian Glacier advance in East Greenland. Quaternary Science Reviews 18, 179-190.

Hayes, W., Kane, M.J., Salminen, O., Wood, R.L., Doherty, S.P., 1984. ODMR of recombination centres in crystalline quartz. Journal of Physics C: Solid State Physics 17, 2943.

Henke, B.L., Gullikson, E.M., Davis, J.C., 1993. X-ray interactions: photoabsorption, scattering, transmission, and reflection at E=50-30000 eV, Z=1-92. Atomic Data and Nuclear Data Tables 54, 181-342.

Hibbert, F.D., Austin, W.E.N., Leng, M.J., Gatliff, R.W., 2010. British Ice Sheet dynamics inferred from North Atlantic ice-rafted debris records spanning the last 175 000 years. Journal of Quaternary Science 25, 461-482.

Hochman, M.B.M., Ypma, P.J.M., 1988. Changes in the artificial thermoluminescence glow curves of quartz associated with uranium deposits. International Journal of Radiation Applications and Instrumentation. Part D. Nuclear Tracks and Radiation Measurements 14, 105-111.

Holtedahl, O., 1960. Geology of Norway. I Kommisjon Hos H. Aschehoug & Co., Oslo, p. 540.

Holtedahl, O., Dons, J.A., 1960. Geologisk kart over Norge Berggrunnskart (Geological map of Norway (Bedrock), Norges Geologiske Undersøkelse Nr. 208, Oslo.

Hornyak, W., Franklin, A., Chen, R., 1993. A model for mid-term fading in TL dating. Ancient TL 11, 21-26.

Hoya-Optics, 2011. http://www.hoyaoptics.com/pdf/U340.pdf.

Hungr, O., Evans, S.G., Bovis, M.J., Hutchinson, J.N., 2001. A review of the classification of landslides of the flow type. Environmental and Engineering Geoscience 7, 221-238.

Huntley, D.J., Baril, M.R., 1997. The K content of the K-feldspars being measured in optical dating or in thermoluminescence dating. Ancient TL 15, 11-13.

Huntley, D.J., Godfrey-Smith, D.I., Thewalt, M.L.W., 1985. Optical dating of sediments. Nature 313, 105-107.

Huntley, D.J., Hancock, R.G.V., 2001. The Rb content of the K-feldspar grains being measured in optical dating. Ancient TL 19, 43-46.

Huntley, D.J., Lamothe, M., 2001. Ubiquity of anomalous fading in K-feldspars and the measurement and correction for it in optical dating. Canadian Journal of Earth Sciences 38, 1093-1106.

Huntley, D.J., Lian, O.B., 2006. Some observations on tunnelling of trapped electrons in feldspars and their implications for optical dating. Quaternary Science Reviews 25, 2503-2512.

Huot, S., 2006. A recipe book of fading. Risø, p. 9.

Huot, S., Lamothe, M., 2003. Variability of infrared stimulated luminescence properties from fractured feldspar grains. Radiation Measurements 37, 499-503.

Hütt, G., Jaek, I., Tchonka, J., 1988. Optical dating: K feldspars optical response stimulation spectra. Quaternary Science Reviews 7, 381-385.

Hütt, G., Jungner, H., 1992. Optical and TL dating on glaciofluvial sediments. Quaternary Science Reviews 11, 161-163.

Itoh, C., Tanimura, K., Itoh, N., 1988. Optical studies of self-trapped excitons in SiO 2. Journal of Physics C: Solid State Physics 21, 4693.

Itoh, C., Tanimura, K., Itoh, N., Itoh, M., 1989. Threshold energy for photogeneration of self-trapped excitons in SiO2. Physical Review B 39, 11183.

Itoh, N., Stoneham, D., Stoneham, A.M., 2002. Ionic and electronic processes in quartz:Mechanisms of thermoluminescence and optically stimulated luminescence. Journal of Applied Physics 92, 5036-5044.

Jacobs, Z., Duller, G.A.T., Wintle, A.G., 2006. Interpretation of single grain D-e distributions and calculation of D-e. Radiation Measurements 41, 264-277.

Jacobs, Z., Wintle, A.G., Duller, G.A.T., Roberts, R.G., Wadley, L., 2008. New ages for the post-Howiesons Poort, late and final Middle Stone Age at Sibudu, South Africa. Journal of Archaeological Science 35, 1790-1807.

Jain, M., Ankjærgaard, C., 2011. Towards a non-fading signal in feldspar: Insight into charge transport and tunnelling from time-resolved optically stimulated luminescence. Radiation Measurements 46, 292-309.

Jain, M., Bøtter-Jensen, L., S. Murray, A., Jungner, H., 2002. Retrospective Dosimetry: Dose Evaluation using Unheated and Heated Quartz from a Radioactive Waste Storage Building. Radiation Protection Dosimetry 101, 525-530.

Jain, M., Choi, J.H., Thomas, P.J., 2008. The ultrafast OSL component in quartz: Origins and implications. Radiation Measurements 43, 709-714.

Jain, M., Lindvold, L.R., 2007. Blue light stimulation and Linearly Modulated Optically Stimulated Luminescence. Ancient TL 25, 69-80.

Jain, M., Murray, A.S., Botter-Jensen, L., 2003. Characterisation of blue-light stimulated luminescence components in different quartz samples: implications for dose measurement. Radiation Measurements 37, 441-449.

Jain, M., Murray, A.S., Bøtter-Jensen, L., 2001. Luminescence characteristics of a thermally unstable fast component in quartz. Abstract volume Luminescence and ESR dating meeting, 17-19 September. University of Glasgow.

Jensen, H., Barbetti, M., 1979. More on filters for laboratory illumination. Ancient TL 7, 10.

Jerlov, N.G., 1976. Marine Optics. Elsevier, New York, p. 231.

Jones, C.E., Embree, D., 1976. Correlations of the 4. 77 eV--4. 28 eV luminescence band in silicon dioxide with the oxygen vacancy. Final report 1 Jul 1975--30 Jun 1976, p. Medium: X; Size: Pages: 39.

Jopling, A.V., Walker, R.G., 1968. Morphology and origin of ripple-drift cross laminations, with examples from the Pleistocene of Massachusetts. Journal of Sedimentary Petrology 38, 971-984.

Jürgensen, A., Anderson, A., Sham, T.-K., 2009. An X-ray excited optical luminescence study of a zoned quartz crystal from an emerald-bearing quartz vein, Hiddenite, North Carolina, USA. Physics and Chemistry of Minerals 36, 207-216.

Kars, R.H., Wallinga, J., Cohen, K.M., 2008. A new approach towards anomalous fading correction for feldspar IRSL dating -- tests on samples in field saturation. Radiation Measurements 43, 786-790.

Kempe, U., Goetze, J., Dandar, S., Habermann, D., 1999. Magmatic and metasomatic processes during formation of the Nb-Zr-REE deposits Khaldzan Buregte and Tsakhir (Mongolian Altai); indications from a combined CL-SEM study. Mineral Mag 63, 165-177.

Kibar, R., Garcia-Guinea, J., Çetin, A., Selvi, S., Karal, T., Can, N., 2007. Luminescent, optical and color properties of natural rose quartz. Radiation Measurements 42, 1610-1617.

King, G.E., 2007. Single grain laser luminescence dating of burnt rocks from the Libyan Sahara, Department of Geography. Royal Holloway, London, p. 95.

King, G.E., Finch, A.A., Robinson, R.A.J., Hole, D.E., 2011a. The problem of dating quartz 1: Spectroscopic ionoluminescence of dose dependence. Radiation Measurements 46, 1-9.

King, G.E., Finch, A.A., Robinson, R.A.J., Taylor, R.P., Mosselmans, J.F.W., 2011b. The problem of dating quartz 2: Synchrotron generated X-ray excited optical luminescence (XEOL) from quartz. Radiation Measurements 46, 1082-1089.

Kiyak, N.G., Polymeris, G.S., Kitis, G., 2007. Component resolved OSL dose response and sensitization of various sedimentary quartz samples. Radiation Measurements 42, 144-155.

Kiyak, N.G., Polymeris, G.S., Kitis, G., 2008. LM-OSL thermal activation curves of quartz: Relevance to the thermal activation of the 110 °C TL glow-peak. Radiation Measurements 43, 263-268.

Klasen, N., Fiebig, M., Preusser, F., Radtke, U., 2006. Luminescence properties of glaciofluvial sediments from the Bavarian Alpine Foreland. Radiation Measurements 41, 866-870.

Klasen, N., Fiebig, M., Preusser, F., Reitner, J.M., Radtke, U., 2007. Luminescence dating of proglacial sediments from the Eastern Alps. Quaternary International 164-165, 21-32.

Komuro, K., Horikawa, Y., Toyoda, S., 2002. Development of radiation-damage halos in low-quartz: cathodoluminescence measurement after He ion implantation. Mineralogy and Petrology 76, 261-266.

Kononenko, S.I., Kalantaryan, O.V., Muratov, V.I., Zhurenko, V.P., 2007. Silica luminescence induced by fast light ions. Radiation Measurements 42, 751-754.

Kopp, G., Lean, J.L., 2011. A new, lower value of total solar irradiance: Evidence and climate significance. Geophys. Res. Lett. 38, L01706.

Krbetschek, M.R., Götze, J., Dietrich, A., Trautmann, T., 1997. Spectral information from minerals relevant for luminescence dating. Radiation Measurements 27, 695-748.

Krbetschek, M.R., Rieser, U., 1995. Luminescence spectra of alkalifeldspars and plagioclases. Radiation Measurements 24, 473-477.

Krbetschek, M.R., Trautmann, T., 2000. A spectral radioluminescence study for dating and dosimetry. Radiation Measurements 32, 853-857.

Lamothe, M., 1995. Using 600-650 nm light for IRSL sample preperation. Ancient TL 13, 1-4.

Lamothe, M., Auclair, M., Hamzaoui, C., Huot, S., 2003. Towards a prediction of long-term anomalous fading of feldspar IRSL. Radiation Measurements 37, 493-498.

Lang, A.R., Miuscov, V.F., 1967. Dislocations and Fault Surfaces in Synthetic Quartz. Journal of Applied Physics 38, 2477-2483.

Levy, M., Varley, J.H.O., 1955. Radiation Induced Colour Centres in Fused Quartz. Proc. Phys. Soc. B 68, 223-233.

Levy, P., 1979. Thermoluminescence studies having application to geology and archaeology. PACT 3, 466-480.

Li, B., 2007. A note on estimating the error when subtracting background counts from weak OSL signals. Ancient TL 25, 9-14.

Li, B., Li, S.-H., 2006. Comparison of estimates using the fast component and the medium component of quartz OSL. Radiation Measurements 41, 125-136.

Li, B., Li, S.-H., 2011. Thermal stability of infrared stimulated luminescence of sedimentary K-feldspar. Radiation Measurements 46, 29-36.

Li, B., Li, S.-H., In Press. Luminescence dating of K-feldspar from sediments: A protocol without anomalous fading correction. Quaternary Geochronology In Press, Corrected Proof.

Li, S.-H., Yin, G.-M., 2006. Luminescence properties of biotite relevant to dating and dosimetry. Journal of Luminescence 121, 51-56.

Lian, O.B., Roberts, R.G., 2006. Dating the Quaternary: progress in luminescence dating of sediments. Quaternary Science Reviews 25, 2449-2468.

Lie, Ø., Dahl, S.O., Nesje, A., Matthews, J.A., Sandvold, S., 2004. Holocene fluctuations of a polythermal glacier in high-alpine eastern Jotunheimen, central-southern Norway. Quaternary Science Reviews 23, 1925-1945.

Lowe, J.J., Birks, H.H., Brooks, S.J., Coope, G.R., Harkness, D.D., Mayle, F.E., Sheldrick, C., Turney, C.S.M., Walker, M.J.C., 1999. The chronology of palaeoenvironmental changes during the Last Glacial-Holocene transition: towards an event stratigraphy for the British Isles. Journal of the Geological Society 156, 397-410.

Luff, B.J., Townsend, P.D., 1990. Cathodoluminescence of synthetic quartz. Journal of Physics: Condensed Matter 2, 8089-8097.

Luff, B.J., Townsend, P.D., 1993. High sensitivity thermoluminescence spectrometer. Measurement Science and Technology 4, 65.

Lukas, S., 2007. Early-Holocene glacier fluctuations in Krundalen, south central Norway: palaeoglacier dynamics and palaeoclimate. The Holocene 17, 585-598.

Lukas, S., Spencer, J.Q.G., Robinson, R.A.J., Benn, D.I., 2007. Problems associated with luminescence dating of Late Quaternary glacial sediments in the NW Scottish Highlands. Quaternary Geochronology 2, 243-248.

Marfunin, A.S., 1979. Spectroscopy, Luminescence and Radiation Centres in Minerals. Springer-Verlag, Berlin.

Martini, M., Fasoli, M., Galli, A., 2009. Quartz OSL emission spectra and the role of [AlO4]° recombination centres. Radiation Measurements 44, 458-461.

Martini, M., Galli, A., 2007. Ionic mechanisms in the optically stimulated luminescence of quartz. physica status solidi (c) 4, 1000-1003.

Martini, M., Meinardi, F., Vedda, A., 2000. The role of alkali ions in the 190 K TSL peak in quartz. Radiation Measurements 32, 673-677.

Martini, M., Paleari, A., Spinolo, G., Vedda, A., 1995. Role of [AlO_{4}]^{0} centers in the 380-nm thermoluminescence of quartz. Physical Review B 52, 138.

Martins, A.A., Cunha, P.P., Buylaert, J.-P., Huot, S., Murray, A.S., Dinis, P., Stokes, M., 2010. K-feldspar IRSL dating of a Pleistocene river terrace staircase sequence of the Lower Tejo River (Portugal, western Iberia). Quaternary Geochronology 5, 176-180.

Matthews, J.A., 1980. Some problems and implications of 14C dates from a podzol buried beneath an end moraine at Haugabreen, Southern Norway. Geografiska Annaler, Series A, Physical Geography 62, 185-208.

Matthews, J.A., 2005. 'Little Ice Age' glacier variations in Jotunheimen, southern Norwvay: a study in regionally controlled lichenometric dating of recessional moraines with implications for climate and lichen growth rates. The Holocene 15, 1-19.

Matthews, J.A., Dahl, S.O., Berrisford, M.S., Nesje, A., Dresser, P.Q., Dumayne-Peaty, L., 1997. A preliminary history of Holocene colluvial (debris-flow) activity, Leirdalen, Jotunheimen, Norway. Journal of Quaternary Science 12, 117-129.

Matthews, J.A., Innes, J.L., Caseldine, C.J., 1986. 14C dating and palaeoenvironment of the historic lsquolittle ice agersquo glacier advance of Nigardsbreen Southwest Norway. Earth Surface Processes and Landforms 11, 369-375.

Matthews, J.A., Olaf Dahl, S., Nesje, A., Berrisford, M.S., Andersson, C., 2000. Holocene glacier variations in central Jotunheimen, southern Norway based on distal glaciolacustrine sediment cores. Quaternary Science Reviews 19, 1625-1647.

Matthews, J.A., Owen, G., 2008. Endolithic lichens, rapid biological weathering and schmidt hammer R-values on recently exposed rock surfaces: Storbreen glacier foreland, Jotunheimen, Norway. Geografiska Annaler: Series A, Physical Geography 90, 287-297.

Matthews, J.A., Owen, G., 2010. Schmidt hammer exposure-age dating: developing linear age-calibration curves using Holocene bedrock surfaces from the Jotunheimen and Jostedalsbreen regions of southern Norway. Boreas 39, 105-115.

McEwen, L.J., Matthews, J.A., 1998. Channel Form, Bed Material and Sediment Sources of the Sprongdøla, Southern Norway: Evidence for a Distinct Periglacio-Fluvial System. Geografiska Annaler: Series A, Physical Geography 80, 17-36.

McFee, C.J., Tite, M.S., 1994. Investigations into the Thermoluminescence Properties of Single Quartz Grains Using an Imaging Photon Detector. Radiation Measurements 23, 355-360.

McFee, C.J., Tite, M.S., 1998. The detection of insufficiently bleached grains using an imaging photon detector. Archaeometry 40, 153-168.

McKeever , S.W.S., 1984. Thermoluminescence in Quartz and Silica. Radiation Protection Dosimetry 8, 81-98.

McKeever, S.W.S., 1991. Mechanisms of thermoluminescence production: Some problems and a few answers? International Journal of Radiation Applications and Instrumentation. Part D. Nuclear Tracks and Radiation Measurements 18, 5-12.

Mejdahl, V., 1979. Thermoluminescence Dating: Beta-Dose Attenuation in Quartz Grains.

Mejdahl, V., 1987. Internal radioactivity in quartz and feldspar grains. Ancient TL 5, 10-17.

Mejdahl, V., Bøtter-Jensen, L., 1994. Luminescence dating of archaeological materials using a new technique based on single aliquot measurements. Quaternary Science Reviews 13, 551-554.

Miall, A.D., 1985. Architectural-element analysis: A new method of facies analysis applied to fluvial deposits. Earth-Science Reviews 22, 261-308.

Miljøvernavdelinga, F.i.S.o.F., 1994. Forvaltningsplan for Jostedalsbreen Nasjonalpark.

Mineralogy-Database, Biotite.

Minitab, 2010. Minitab Inc., 16.1.0 ed.

Mosselmans, J.F.W., Quinn, P.D., Dent, A.J., Cavill, S.A., Moreno, S.D., Peach, A., Leicester, P.J., Keylock, S.J., Gregory, S.R., Atkinson, K.D., Rosell, J.R., 2009. I18 - the microfocus spectroscopy beamline at the Diamond Light Source. Journal of Synchrotron Radiation 16, 818-824.

Munekuni, S., Yamanaka, T., Shimogaichi, Y., 1990. Various types of nonbridging oxygen hole center in high-purity silica glass. Journal of Applied Physics 68, 1212-1217.

Murray, A.S., Mejdahl, V., 1999. Comparison of regenerative-dose single-aliquot and multiple-aliquot (SARA) protocols using heated quartz from archaeological sites. Quaternary Science Reviews 18, 223-229.

Murray, A.S., Olley, J.M., Caitcheon, G.G., 1995. Measurement of equivalent doses in quartz from contemporary water-lain sediments using optically stimulated luminescence. Quaternary Science Reviews 14, 365-371.

Murray, A.S., Roberts, R.G., 1997. Determining the burial time of single grains of quartz using optically stimulated luminescence. Earth and Planetary Science Letters 152, 163-180.

Murray, A.S., Roberts, R.G., 1998. Measurement of the equivalent dose in quartz using a regenerative-dose single-aliquot protocol. Radiation Measurements 29, 503-515.

Murray, A.S., Wintle, A.G., 1999. Isothermal decay of optically stimulated luminescence in quartz. Radiation Measurements 30, 119-125.

Murray, A.S., Wintle, A.G., 2000. Luminescence dating of quartz using an improved single-aliquot regenerative-dose protocol. Radiation Measurements 32, 57-73.

Murray, A.S., Wintle, A.G., 2003. The single aliquot regenerative dose protocol: potential for improvements in reliability. Radiation Measurements 37, 377-381.

Nasdala, L., Göetze, J., Hanchar, J.M., Gaft, M., Krbetschek, M.R., 2004. Luminescence techniques in Earth Sciences, in: Beran, A., Libowitzky, E. (Eds.), Spectroscopic Methods in Mineralogy. Eötvös University Press, Budapest, pp. 43-91.

Nathan, R.P., Thomas, P.J., Jain, M., Murray, A.S., Rhodes, E.J., 2003. Environmental dose rate heterogeneity of beta radiation and its implications for luminescence dating: Monte Carlo modelling and experimental validation. Radiation Measurements 37, 305-313.

Nesje, A., 1989. Glacier-front variations of outlet glaciers from Jostedalsbreen and climate in the Jostedalsbre region of western Norway in the period 1901-80. Norsk Geografisk Tidsskrift - Norwegian Journal of Geography 43, 3 - 17.

Nesje, A., Kvamme, M., 1991. Holocene glacier and climate variations in western Norway: Evidence for early Holocene glacier demise and multiple Neoglacial events. Geology 19, 610-612.

Nesje, A., Kvamme, M., Rye, N., Løvlie, R., 1991. Holocene glacial and climate history of the Jostedalsbreen region, Western Norway; evidence from lake sediments and terrestrial deposits. Quaternary Science Reviews 10, 87-114.

Nesje, A., Matthews, J.A., Dahl, S.O., Berrisford, M.S., Andersson, C., 2001. Holocene glacier fluctuations of Flatebreen and winter-precipitation changes in the Jostedalsbreen region, western Norvay, based on glaciolacustrine sediment records. The Holocene 11, 267-280.

Nesje, A., Olaf Dahl, S., Andersson, C., Matthews, J.A., 2000. The lacustrine sedimentary sequence in Sygneskardvatnet, western Norway: a continuous, high-resolution record of the Jostedalsbreen ice cap during the Holocene. Quaternary Science Reviews 19, 1047-1065.

Nesje, A., Olaf Dahl, S., Lie, Ø., 2004. Holocene millennial-scale summer temperature variability inferred from sediment parameters in a non-glacial mountain lake: Danntjørn, Jotunheimen, central southern Norway. Quaternary Science Reviews 23, 2183-2205.

Nishikawa, H., Tohmon, R., Ohki, Y., Nagasawa, K., Hama, Y., 1989. Defects and optical absorption bands induced by surplus oxygen in high-purity synthetic silica. Journal of Applied Physics 65, 4672-4678.

Nishikawa, H., Watanabe, E., Ito, D., Ohki, Y., 1994. Decay kinetics of the 4.4-eV photoluminescence associated with the two states of oxygen-deficient-type defect in amorphous SiO2. Physical Review Letters 72, 2101.

Nunnally, J.C., 1978. Psychometric theory, 2 ed. McGraw-Hill., New York.

Nuttall, R.H.D., Weil, J.A., 1980. Two hydrogenic trapped-hole species in [alpha]-quartz. Solid State Communications 33, 99-102.

O'Reilly, E.P., Robertson, J., 1983. Theory of defects in vitreous silicon dioxide. Physical Review B 27, 3780.

Oerlemans, J., 2007. Estimating response times of Vadret da Morteratsch, Vadret da Palu, Briksdalsbreen and Nigardsbreen from their length records. Journal of Glaciology 53, 357-362.

Ollerhead, J., 2001. Light transmittance through dry, sieved sand: some test results. Ancient TL 19, 13-17.

Olley, J., Caitcheon, G., Murray, A., 1998. The distribution of apparent dose as determined by Optically Stimulated Luminescence in small aliquots of fluvial quartz: Implications for dating young sediments. Quaternary Science Reviews 17, 1033-1040.

Olley, J.M., Roberts, R.G., Murray, A.S., 1997. Disequilibria in the uranium decay series in sedimentary deposits at Allen's Cave, Nullarbor Plain, Australia: Implications for dose rate determinations. Radiation Measurements 27, 433-443.

Østrem, G., Liestøl, O., Wold, B., 1976. Glaciological investigations at Nigardsbreen, Norway. Norsk Geografisk Tidsskrift - Norwegian Journal of Geography 30, 187 - 209.

Owen, G., Matthews, J.A., Albert, P.G., 2007. Rates of Holocene chemical weathering, `Little Ice Age' glacial erosion and implications for Schmidt-hammer dating at a glacier—foreland boundary, Fåbergstølsbreen, southern Norway. The Holocene 17, 829-834.

Owen, L.A., Kamp, U., Spencer, J.Q., Haserodt, K., 2002. Timing and style of Late Quaternary glaciation in the eastern Hindu Kush, Chitral, northern Pakistan: a review and revision of the glacial chronology based on new optically stimulated luminescence dating. Quaternary International 97-98, 41-55.

Owen, L.A., Robinson, R., Benn, D.I., Finkel, R.C., Davis, N.K., Yi, C., Putkonen, J., Li, D., Murray, A.S., 2009. Quaternary glaciation of Mount Everest. Quaternary Science Reviews 28, 1412-1433.

Owen, M.R., 1988. Radiation-damage halos in quartz. Geology 16, 529-532.

Pacchioni, G., Ieranò, G., 1997. Computed Optical Absorption and Photoluminescence Spectra of Neutral Oxygen Vacancies in alpha -Quartz. Physical Review Letters 79, 753.

Pagel, M., Barbin, V., Blanc, P., Ohnenstetter, D., 2000. Cathodoluminescence in Geosciences. Springer-Verlag, Berlin.

Pawley, S.M., Bailey, R.M., Rose, J., Moorlock, B.S.P., Hamblin, R.J.O., Booth, S.J., Lee, J.R., 2008. Age limits on Middle Pleistocene glacial sediments from OSL dating, north Norfolk, UK. Quaternary Science Reviews 27, 1363-1377.

Perny, B., Eberhardt, P., Ramseyer, K., Mullis, J., Panrath, R., 1992. Microdistribution of Al, Li, and Na in α quartz: Possible causes and correlation with short-lived cathodoluminescence. American Mineralogist 77, 535-544.

Phillips, M.R., Telg, H., Kucheyev, S.O., Gelhausen, O., Toth, M., 2003. Cathodoluminescence Efficiency Dependence on Excitation Density in n-Type Gallium Nitride. Microscopy and Microanalysis 9, 144-151.

Pietsch, T.J., Olley, J.M., Nanson, G.C., 2008. Fluvial transport as a natural luminescence sensitiser of quartz. Quaternary Geochronology 3, 365-376.

Polymeris, G.S., Afouxenidis, D., Tsirliganis, N.C., Kitis, G., 2009. The TL and room temperature OSL properties of the glow peak at 110 °C in natural milky quartz: A case study. Radiation Measurements 44, 23-31.

Poolton, N.R.J., Bøtter-Jensen, L., Ypma, P.J.M., Johnsen, O., 1994. Influence of crystal structure on the optically stimulated luminescence properties of feldspars. Radiation Measurements 23, 551-554.

Poolton, N.R.J., Mauz, B., Lang, A., Jain, M., Malins, A.E.R., 2006. Optical excitation processes in the near band-edge region of KAlSi3O8 and NaAlSi3O8 feldspar. Radiation Measurements 41, 542-548.

Poolton, N.R.J., Smith, G.M., Riedi, P.C., Bulur, E., Bøtter-Jensen, L., Murray, A.S., Adrian, M., 2000. Luminescence sensitivity changes in natural quartz induced by high temperature annealing: a high frequency EPR and OSL study. Journal of Physics D: Applied Physics 33, 1007-1017.

Porat, N., Botha, G., 2008. The luminescence chronology of dune development on the Maputaland coastal plain, southeast Africa. Quaternary Science Reviews 27, 1024-1046.

Pott, G.T., McNicol, B.D., 1971. Spectroscopic study of the coordination and valence of Fe and Mn ions in and on the surface of aluminas and silicas. Discussions of the Faraday Society 52, 121-131.

Prescott, J.R., Hutton, J.T., 1994. Cosmic ray contributions to dose rates for luminescence and ESR dating: Large depths and long-term time variations. Radiation Measurements 23, 497-500.

Preusser, F., 1999. Luminescence dating of fluvial sediments and overbank deposits from Gossau, Switzerland: fine grain dating. Quaternary Science Reviews 18, 217-222.

Preusser, F., Chithambo, M.L., Götte, T., Martini, M., Ramseyer, K., Sendezera, E.J., Susino, G.J., Wintle, A.G., 2009. Quartz as a natural luminescence dosimeter. Earth-Science Reviews 97, 184-214.

Preusser, F., Müller, B.U., Schlüchter, C., 2001. Luminescence Dating of Sediments from the Luthern Valley, Central Switzerland, and Implications for the Chronology of the Last Glacial Cycle. Quaternary Research 55, 215-222.

Preusser, F., Ramseyer, K., Schlüchter, C., 2006. Characterisation of low OSL intensity quartz from the New Zealand Alps. Radiation Measurements 41, 871-877.

Randall, J.T., Wilkins, M.H.F., 1945. Phosphorescence and Electron Traps. I. The Study of Trap Distributions. Proceedings of the Royal Society of London. Series A. Mathematical and Physical Sciences 184, 365-389.

Readhead, M.L., 2002a. Absorbed dose fraction for ^{87}Rb β particles. Ancient TL 20, 25-28.

Readhead, M.L., 2002b. Addendum to "Absorbed dose fraction for ^{87}Rb β particles". Ancient TL 20, 47.

Reed, M., Olley, J., 2003. Radial Plot, 1.3 ed. CSIRO Land and Water.

Reineck, H.-E., Singh, I.B., 1973. Depositional Sedimentary Environments. Springer-Verlag, Berlin.

Rhodes, E.J., 1988. Methodological considerations in the optical dating of quartz. Quaternary Science Reviews 7, 359-400.

Rhodes, E.J., 2000. Observations of thermal transfer OSL signals in glacigenic quartz. Radiation Measurements 32, 595-602.

Rhodes, E.J., 2007. Quartz single grain OSL sensitivity distributions: Implications for multiple grain single aliquot dating. Geochronometria 26, 19-29.

Rhodes, E.J., Bailey, R.M., 1997. The effect of thermal transfer on the zeroing of the luminescence of quartz from recent glaciofluvial sediments. Quaternary Science Reviews 16, 291-298.

Rhodes, E.J., Pownall, L., 1994. Zeroing of the OSL signal in quartz from young glaciofluvial sediments. Radiation Measurements 23, 581-585.

Rice, S.P., Church, M., 2010. Grain-size sorting within river bars in relation to downstream fining along a wandering channel. Sedimentology 57, 232-251.

Richards, B.W.M., 2000. Luminescence dating of Quaternary sediments in the Himalaya and High Asia: a practical guide to its use and limitations for constraining the timing of glaciation. Quaternary International 65-66, 49-61.

Richards, B.W.M., Benn, D.I., Owen, L.A., Rhodes, E.J., Spencer, J.Q., 2000. Timing of late Quaternary glaciations south of Mount Everest in the Khumbu Himal, Nepal. Geological Society of America Bulletin 112, 1621-1632.

Rieser, U., Hütt, G., Krbetschek, M.R., Stolz, W., 1997. Feldspar IRSL emission spectra at high and low temperatures. Radiation Measurements 27, 273-278.

Rink, W.J., 1994. Billion-year age dependence of luminescence in granitic quartz. Radiation Measurements 23, 419-422.

Rink, W.J., Odom, A.L., 1991. Natural alpha recoil particle radiation and ionizing radiation sensitivities in quartz detected with EPR: Implications for geochronometry. International Journal of Radiation Applications and Instrumentation. Part D. Nuclear Tracks and Radiation Measurements 18, 163-173.

Rink, W.J., Rendell, H., Marseglia, E.A., Luff, B.J., Townsend, P.D., 1993. Thermoluminescence spectra of igneous quartz and hydrothermal vein quartz. Physics and Chemistry of Minerals 20, 353-361.

Ripley, B.D., 1987. Stochastic Simulation. Wiley.

Risø, 2002. The TL/OSL Risø Luminescence Reader.

Risø, 2006. The Risø TL/OSL Luminescence Reader: Model TL/OSL-DA-20.

Roberts, H.M., 2007. Assessing the effectiveness of the double-SAR protocol in isolating a luminescence signal dominated by quartz. Radiation Measurements 42, 1627-1636.

Roberts, H.M., Duller, G.A.T., 2004. Standardised growth curves for optical dating of sediment using multiple-grain aliquots. Radiation Measurements 38, 241-252.

Roberts, R.G., Galbraith, R.F., Yoshida, H., Laslett, G.M., Olley, J.M., 2000. Distinguishing dose populations in sediment mixtures: a test of single-grain optical dating procedures using mixtures of laboratory-dosed quartz. Radiation Measurements 32, 459-465.

Robinson, R.A.J., Brezina, C.A., Parrish, R.R., Horstwood, M.S.A., Oo, N.W., Bird, M.I., Thein, M., Walters, A.S., Oliver, G.J.H., Zhaw, K., Submitted. Co-evolution of Cenozoic river systems in Myanmar and southern Tibet and the eastern Himalayan syntaxis. Nature Geosciences.

Robinson, R.A.J., Slingerland, R.L., 1998. Origin of fluvial grain-size trends in a foreland basin: the Pocono Formation of the Central Appalachian Basin. Journal of Sedimentary Research 68, 473-486.

Robinson, R.A.J., Spencer, J.Q.G., Strecker, M.R., Richter, A., Alonso, R.N., 2005. Luminescence dating of alluvial fans in intramontane basins of NW Argentina. Alluvial Fans: Geomorphology, Sedimentology, Dynamics 251, 153-168.

Rodnight, H., 2008. How many equivalent dose values are needed to obtain a reproducible distribution? Ancient TL 26, 3-9.

Rodnight, H., Duller, G.A.T., Wintle, A.G., Tooth, S., 2006. Assessing the reproducibility and accuracy of optical dating of fluvial deposits. Quaternary Geochronology 1, 109-120.

Rogalev, A., Goulon, J., 2002. X-ray Excited Optical Luminescence Spectroscopies, in: Sham, T.-K. (Ed.), Chemical Applications of Synchrotron Radiation, Part II: X-ray Applications. World Books, Singapore, p. p.707.

Royston, P., 1982a. Algorithm AS 181: The *W* test for Normality. Applied Statistics 31, 176-180.

Royston, P., 1982b. An Extension of Shapiro and Wilk's *W* test for normality to large samples. Applied Statistics 31, 115-124.

Royston, P., 1995. Remark AS R94: A remark on Algorithm AS 181: The *W* test for normality. Applied Statistics 44, 547-551.

Rusk, B.G., Reed, M.H., Dilles, J.H., Kent, A.J.R., 2006. Intensity of quartz cathodoluminescence and trace-element content in quartz from the porphyry copper deposit at Butte, Montana. American Mineralogist 91, 1300-1312.

Sanderson, D.C.W., Bishop, P., Stark, M., Alexander, S., Penny, D., 2007. Luminescence dating of canal sediments from Angkor Borei, Mekong Delta, Southern Cambodia. Quaternary Geochronology 2, 322-329.

Sanderson, D.C.W., Bishop, P., Stark, M.T., Spencer, J.Q., 2003. Luminescence dating of anthropogenically reset canal sediments from Angkor Borei, Mekong Delta, Cambodia. Quaternary Science Reviews 22, 1111-1121.

Sanderson, D.C.W., Clark, R.J., 1994. Pulsed photostimulated luminescence of alkali feldspars. Radiation Measurements 23, 633-639.

Sanzelle, S., Miallier, D., Pilleyre, T., Faïn, J., Montret, M., 1996. A new slide technique for regressing TL/ESR dose response curves-intercomparisons with other regression techniques. Radiation Measurements 26, 631-638.

Schilles, T., Poolton, N.R.J., Bulur, E., Botter-Jensen, L., Murray, A., Smith, G.M., Riedi, P.C., Wagner, G.A., 2001. A multi-spectroscopic study of luminescence sensitivity changes in natural quartz induced by high-temperature annealing. Journal of Physics D: Applied Physics 34, 722.

Shakesby, R.A., Matthews, J.A., Winkler, S., 2004. Glacier variations in Breheimen, southern Norway: relative-age dating of Holocene moraine complexes at six high-altitude glaciers. The Holocene 14, 899-910.

Sham, T.-K., Rosenberg, R.A., 2007. Time-Resolved Synchrotron Radiation Excited Optical Luminescence: Light-Emission Properties of Silicon-Based Nanostructures. ChemPhysChem 8, 2557-2567.

Shapiro, S.S., Wilk, M.B., 1965. An analysis of variance test for normality (complete samples). Biometrika 52, 591-611.

Sigel, G.H., 1973. Ultraviolet Specta of Silicate Glasses: A Review of Some Experimental Evidence. Journal of Non-Crystalline Solids 13, 372-398.

Singarayer, J.S., Bailey, R.M., 2003. Further investigations of the quartz optically stimulated luminescence components using linear modulation. Radiation Measurements 37, 451-458.

Singarayer, J.S., Bailey, R.M., 2004. Component-resolved bleaching spectra of quartz optically stimulated luminescence: preliminary results and implications for dating. Radiation Measurements 38, 111-118.

Sletten, K., Blikra, L.H., 2007. Holocene colluvial (debris-flow and water-flow) processes in eastern Norway: stratigraphy, chronology and palaeoenvironmental implications. Journal of Quaternary Science 22, 619-635.

Smith, B.W., 1988. More cautions on laboratory illumination. Ancient TL 6, 9.

Smith, B.W., Aitken, M.J., Rhodes, E.J., Robinson, P.D., Gerald, D.M., 1986. Optical dating: methodological aspects. Radiation Protection Dosimetry 34, 75-78.

Song, J., Corrales, L.R., eacute, Kresse, G., oacute, nsson, H., 2001. Migration of O vacancies in alpha -quartz: The effect of excitons and electron holes. Physical Review B 64, 134102.

Spencer, J.Q., Owen, L.A., 2004. Optically stimulated luminescence dating of Late Quaternary glaciogenic sediments in the upper Hunza valley: validating the timing of glaciation and assessing dating methods. Quaternary Science Reviews 23, 175-191.

Spooner, N.A., 1994a. The anomalous fading of infrared-stimulated luminescence from feldspars. Radiation Measurements 23, 625-632.

Spooner, N.A., 1994b. On the optical dating signal from quartz. Radiation Measurements 23, 593-600.

Spooner, N.A., Prescott, J.R., 1986. A caution on laboratory illumination. Ancient TL 4, 46-48.

Spooner, N.A., Questiaux, D.G., Aitken, M.J., 2000. The use of sodium lamps for low-intensity laboratory safelighting for optical dating. Ancient TL 18, 45-49.

Srivastava, P., Juyal, N., Singhvi, A.K., Wasson, R.J., Bateman, M.D., 2001. Luminescence chronology of river adjustment and incision of Quaternary sediments in the alluvial plain of the Sabarmati River, north Gujarat, India. Geomorphology 36, 217-229.

Steck, D.A., 2003. Sodium D Line Data. Los Alamos National Laboratory, Los Alamos, p. 29.

Steffen, D., Preusser, F., Schlunegger, F., 2009. OSL quartz age underestimation due to unstable signal components. Quaternary Geochronology 4, 353-362.

Stephens, M.A., 1974. EDF Statistics for Goodness of Fit and Some Comparisons. Journal of the American Statistical Association 69, 730-737.

Stevens-Kalceff, M.A., 2009. Cathodoluminescence microcharacterization of point defects in alpha-quartz. Mineral Mag 73, 585-605.

Stevens-Kalceff, M.A., Phillips, M.R., 1995. Cathodoluminescence microcharacterization of the defect structure of quartz. Physical Review B 52, 3122.

Stokes, S., Bray, H.E., Blum, M.D., 2001. Optical resetting in large drainage basins: tests of zeroing assumptions using single-aliquot procedures. Quaternary Science Reviews 20, 879-885.

Stokes, S., Colls, A.E.L., Fattahi, M., Rich, J., 2000. Investigations of the performance of quartz single aliquot DE determination procedures. Radiation Measurements 32, 585-594.

Stone, A.E.C., Thomas, D.S.G., 2008. Linear dune accumulation chronologies from the southwest Kalahari, Namibia: challenges of reconstructing late Quaternary palaeoenvironments from aeolian landforms. Quaternary Science Reviews 27, 1667-1681.

Strom, K.M., 1948. The Geomorphology of Norway. The Geographical Journal 112, 19-23.

Sutton, S.R., Zimmerman, D.W., 1978a. A blue-UV absorbing filter for laboratory illumination. Ancient TL 5, 5.

Sutton, S.R., Zimmerman, D.W., 1978b. Thermoluminescence dating: radioactivity in quartz. Archaeometry 20, 66-88.

Swift, D.A., Sanderson, D.C.W., Nienow, P.W., Bingham, R.G., Cochrane, I.C., 2010. Anomalous luminescence of subglacial sediment at Haut Glacier d'Arolla, Switzerland – a consequence of resetting at the glacier bed? Boreas, no-no.

Tabachnick, B.G., Fidell, L.S., 1966. Using multivariate statistics, 3 ed. Harper Collins, New York.

Tanimura, K., Halliburton, L.E., 1986. Polarization of the x-ray-induced blue luminescence in quartz. Physical Review B 34, 2933.

Team, R.D.C., 2010. R: A language and environment for statistical computing. R Foundation for Statistical Computing, Vienna, Austria.

Telfer, M.W., Bateman, M.D., Carr, A.S., Chase, B.M., 2008. Testing the applicability of a standardized growth curve (SGC) for quartz OSL dating: Kalahari dunes, South African coastal dunes and Florida dune cordons. Quaternary Geochronology 3, 137-142.

Temple, J.T., 1978. The use of factor analysis in Geology. Journal of the International Association for Mathematical Geology 10, 379-387.

Templer, R.H., 1985. The removal of anomalous fading in Zircon. Nuclear Tracks and Radiation Measurements 10, 531-537.

Templer, R.H., 1986. The localised transition model of anomalous fading. Radiation Protection Dosimetry 17, 493-497.

Thiel, C., 2011. On the applicability of post-IR IRSL dating to different environments, Geowissenschaften. Freien Universitat Berlin, Berlin, p. 186.

Thomas, P.J., Murray, A.S., Kjaer, K.H., Funder, S., Larsen, E., 2006. Optically Stimulated Luminescence (OSL) dating of glacial sediments from Arctic Russia - depositional bleaching and methodological aspects. Boreas 35, 587-599.

Thomsen, K.J., Jain, M., Botter-Jensen, L., Murray, A.S., Jungner, H., 2003. Variation with depth of dose distributions in single grains of quartz extracted from an irradiated concrete block. Radiation Measurements 37, 315-321.

Thomsen, K.J., Murray, A.S., Botter-Jensen, L., 2005. Sources of variability in OSL dose measurements using single grains of quartz. Radiation Measurements 39, 47-61.

Thomsen, K.J., Murray, A.S., Jain, M., Bøtter-Jensen, L., 2008. Laboratory fading rates of various luminescence signals from feldspar-rich sediment extracts. Radiation Measurements 43, 1474-1486.

Thrasher, I.M., Mauz, B., Chiverrell, R.C., Lang, A., 2009a. Luminescence dating of glaciofluvial deposits: A review. Earth-Science Reviews 97, 145-158.

Thrasher, I.M., Mauz, B., Chiverrell, R.C., Lang, A., Thomas, G.S.P., 2009b. Testing an approach to OSL dating of Late Devensian glaciofluvial sediments of the British Isles. Journal of Quaternary Science 24, 785-801.

Townsend, P.D., Karali, T., Rowlands, A.P., Smith, V.A., Vazquez, G., 1999. Recent examples of cathodoluminescence as a probe of surface structure and composition. Mineral Mag 63, 211-226.

Townsend, P.D., Rendell, H., Luff, B.J., 1993. High sensitivity TL spectra of quartz and feldspar. Ancient TL 11, 36-39.

Townsend, P.D., Rowlands, A.P., 2000. Information Encoded in Cathodoluminescence Emission Spectra, in: Pagel, M., Barbin, V., Blanc, P., Ohnenstetter, D. (Eds.), Cathodoluminescence in Geosciences. Springer-Verlag, Heidelberg, pp. 41-57.

Trukhin, A.N., Paludis, A.E., 1979. Investigation of the intrinsic luminescence of SiO_2. Soviet Physics Solid State 21, 644-646.

Truscott, A.J., Duller, G.A.T., Bøtter-Jensen, L., Murray, A.S., Wintle, A.G., 2000. Reproducibility of optically stimulated luminescence measurements from single grains of Al2O3:C and annealed quartz. Radiation Measurements 32, 447-451.

Tsukamoto, S., Denby, P.M., Murray, A.S., Botter-Jensen, L., 2006. Time-resolved luminescence from feldspars: New insight into fading. Radiation Measurements 41, 790-795.

Udden, J.A., 1914. Mechanical composition of clastic sediments. Bulletin of the Geological Society of America 25, 655-744.

Universität-Würzburg, 2008. Institut für Geographie Universität Würzburg. http://www.geographie.uni-wuerzburg.de/arbeisbereiche/physische_geographie/weitere_forschungsarbeiten/norglamo/fabergstolsbreen/,.

Vandenberghe, D., Jain, M., Murray, A., 2008. A note on spurious luminescence from silicone oil. Ancient TL 26, 29-32.

Vandenberghe, D., Kasse, C., Hossain, S.M., Corte, F.D., Haute, P.V.D., Fuchs, M., Murray, A.S., 2004. Exploring the method of optical dating and comparison of optical and ^{14}C ages of Late Weichselian coversands in the southern Netherlands. Journal of Quaternary Science 19, 73-86.

Visocekas, R., 1979. Miscellaneous aspects of artificial TL of calcite: emission spectra, athermal detrapping and anomalous fading. PACT 3, 258-265.

Visocekas, R., 1985. Tunnelling radiative recombination in labradorite: Its association with anomalous fading of thermoluminescence. Nuclear Tracks and Radiation Measurements (1982) 10, 521-529.

Visocekas, R., 2002. Tunneling in afterglow, its coexistance and interweaving with thermally stimulated luminescence. Radiation Protection Dosimetry 100, 45-54.

Visocekas, R., Ceva, T., Marti, C., 1976. Tunneling processes in afterglow of calcite. Physica Status Solidi A: Applied Research 35, 315-327.

Visocekas, R., Tale, V., Zink, A., Tale, I., 1998. Trap spectroscopy and tunnelling luminescence in feldspars. Radiation Measurements 29, 427-434.

Visocekas, R., Zink, A., 1999. Use of the far red TL emission band of alkali feldspars for dosimetry and dating. Quaternary Science Reviews 18, 271-278.

Vorren, T.O., 1973. Glacial geology of the area between Jostedalsbreen and Jotunheimen, South Norway. Norges Geologiske Undersøkelse 291, 1-46.

Walden, J., Smith, J.P., 1995. Factor Analysis: A practical application, in: Maddy, D., Brew, J.S. (Eds.), Statistical Modelling of Quaternary Science Data. Quaternary Research Association, Cambridge, pp. 39-56.

Walden, J., Smith, J.P., Dackombe, R.V., 1992. The Use of Simultaneous R- and Q-Mode Factor Analysis as a Tool for Assisting Interpretation of Mineral Magnetic Data. Mathematical Geology 24, 227-247.

Wallinga, J., 2002. Optically stimulated luminescence dating of fluvial deposits: a review. Boreas 31, 303-322.

Wallinga, J., Bos, A.J.J., Dorenbos, P., Murray, A.S., Schokker, J., 2007. A test case for anomalous fading correction in IRSL dating. Quaternary Geochronology 2, 216-221.

Wallinga, J., Bos, A.J.J., Duller, G.A.T., 2008. On the separation of quartz OSL signal components using different stimulation modes. Radiation Measurements 43, 742-747.

Wallinga, J., Murray, A., Duller, G., 2000a. Underestimation of equivalent dose in single-aliquot optical dating of feldspars caused by preheating. Radiation Measurements 32, 691-695.

Wallinga, J., Murray, A., Wintle, A., 2000b. The single-aliquot regenerative-dose (SAR) protocol applied to coarse-grain feldspar. Radiation Measurements 32, 529-533.

Wallinga, J., Murray, A.S., Duller, G.A.T., Törnqvist, T.E., 2001. Testing optically stimulated luminescence dating of sand-sized quartz and feldspar from fluvial deposits. Earth and Planetary Science Letters 193, 617-630.

Wang, Y., 2007. Luminescence detection of the structural changes in ZnO, KTa-xNbxO_3 and Gd_2O_3: Eu. Beijing Normal University, Beijing.

Ward, S., Stokes, S., Bailey, R., Singarayer, J., Goudie, A., Bray, H., 2003. Optical dating of quartz from young samples and the effects of pre-heat temperature. Radiation Measurements 37, 401-407.

Warnes, G.R., Bolker, B., Bonebakker, L., Gentleman, R., Liaw, W.H.A., Lumley, T., Maechler, M., Magnusson, A., Moeller, S., Schwartz, M., Venables, B., 2010. gplots: Various R programming tools for plotting data., R package version 2.8.0 ed.

WaveMetrics, 2011. Igor Pro 6.2.

Weil, J.A., 1984. A review of electron spin spectroscopy and its application to the study of paramagnetic defects in crystalline quartz. Physics and Chemistry of Minerals 10, 149-165.

Wentworth, C.K., 1922. A scale of grade and class terms for clastic sediments Journal of Geology 30, 377-392.

Westaway, K.E., 2009. The red, white and blue of quartz luminescence: A comparison of De values derived for sediments from Australia and Indonesia using thermoluminescence and optically stimulated luminescence emissions. Radiation Measurements 44, 462-466.

Winkler, S., Matthews, J.A., Shakesby, R.A., Dresser, P.Q., 2003. Glacier variations in Breheimen, southern Norway: dating Little Ice Age moraine sequences at seven low-altitude glaciers. Journal of Quaternary Science 18, 395-413.

Wintle, A.G., 1973. Anomalous fading of thermoluminescence in mineral samples. Nature 245, 143-144.

Wintle, A.G., 1977. Detailed Study of a Thermoluminescent Mineral Exhibiting Anomalous Fading. Journal of Luminescence 15, 385-393.

Wintle, A.G., Murray, A.S., 1997. The relationship between quartz thermoluminescence, photo-transferred thermoluminescence, and optically stimulated luminescence. Radiation Measurements 27, 611-624.

Wintle, A.G., Murray, A.S., 1999. Luminescence sensitivity changes in quartz. Radiation Measurements 30, 107-118.

Wintle, A.G., Murray, A.S., 2006. A review of quartz optically stimulated luminescence characteristics and their relevance in single-aliquot regeneration dating protocols. Radiation Measurements 41, 369-391.

Xie, J., Aitken, M.J., 1991. The hypothesis of mid-term fading and its trial on Chinese loess. Ancient TL 9, 21-25.

Yang, X.H., McKeever, S.W.S., 1990. Point Defects and the Pre-Dose Effect in Quartz. Radiat Prot Dosimetry 33, 27-30.

Zhao, H., Li, S.-H., 2005. Internal dose rate to K-feldspar grains from radioactive elements other than potassium. Radiation Measurements 40, 84-93.

Zhou, D., Chang, T., Davis, J.C., 1983. Dual Extraction of R-Mode and Q-Mode Factor Solutions. Journal of the International Association for Mathematical Geology 15, 581-606.

Ziegler, J.F., Ziegler, M.D., Biersack, J.P., 2008. SRIM-20083.04: The stopping and range of ions in matter. SRIM.com.

Zimmerman, J., 1971. The radiation-induced increase of the 100 C thermoluminescence sensitivity of fired quartz. Journal of Physics C: Solid State Physics 4, 3625-3276.

Zink, A., Visocekas, R., Bos, A.J.J., 1995. Comparison of `blue' and `infrared' emission bands in thermoluminescence of alkali feldspars. Radiation Measurements 24, 513-518.